UNDERSTANDING THE SURFACE CHEMISTRY OF CERIA NANOPARTICLES USING A MULTI-METHOD APPROACH

By

Inder Preet Kaur

A thesis submitted to the University of Birmingham

for the degree of

DOCTOR OF PHILOSOPHY

School of Geography, Earth and Environmental Sciences

College of Life and Environmental Sciences

University of Birmingham, UK

November 2015

Abstract

Nanotechnology and the use of nanoparticles (NPs) has remarkably increased in the past few years and is attracting a lot of public interest. As a result, NPs are increasingly being released into the environment. Ceria NPs, due to their widespread applications, have also attracted a lot of concern about their toxic effects on both human health and environment. Cerium occurs in two oxidation states, Ce (III) and Ce (IV), and has the unique ability to readily switch between these two states. There is a lot of speculation on the redox behaviour of cerium oxide being related to its toxicity but there are large gaps in knowledge of whether Ce (III) or Ce (IV) is responsible for such toxic behaviours, their toxicological mechanism and safety assessment.

The aim of this study is to accurately quantify the ratio of Ce (III) and Ce (IV) in synthesised ceria samples using a multi-method approach thus providing an insight in understanding their surface chemistry and hence biological behaviour. It is known that nanoceria is capable of oxygen storage, which is size and shape dependent. In order to understand the chemistry of these nanoparticles, ceria NPs of different shapes and sizes were synthesised using various cerium salts and reducing agents as precursors. We produced NPs coated with different capping agents, with different strengths of interaction between core and capping agent/no capping agent and with both steric and charge stabilization. In total, four different sizes of nanocubes, seven different sizes of spheres and two different sizes of rods were synthesized using different methodologies. The size, shape and morphology of the as synthesized samples have been determined using DLS and TEM. DLS has also been used to monitor the stability of the particles after 3/6 months post synthesis. The results indicate that reaction time, temperature and concentration of the precursors play an important role towards the shape and size of the particles formed.

The oxidation state of the samples was determined using STEM-EELS and XPS. The $M_{4,5}$-edge spectra were used to evaluate the oxidation state of cerium using STEM-EELS whereas binding energies of individual peaks of the Ce (3d) spectrum from XPS were employed to quantify the oxidation states in different samples. The results suggest that the oxidation state of ceria NPs is not uniform throughout the particle and the amount of Ce (III) increases as the particle size decreases, with particles ≤ 2nm to be completely Ce (III).

Human exposure to nanoceria may promote their entry in human body by inhalation and ingestion, allowing them to reach bloodstream and other body fluids. Later in the study, we investigated the uptake and internalisation of different shapes and sizes of ceria NPs in lung-derived A549 cell lines (Adenocarcinomic human alveolar basal epithelial cells, A549). The characterization of NPs in pristine conditions as well as in biological media is essential to understand their biological behaviour. In this study, NPs were dispersed and characterised in cell culture media to mimic the realistic conditions during uptake assays in order to better understand the behaviour of NPs when treated with the biological media. DLS was used to measure the hydrodynamic diameter and polydispersity index (PdI) of the NPs in sterile water as well in the culture media whereas reflectance confocal microscopy (RCM) was used to detect the aggregation behaviour and visualise the uptake and internalsation of ceria nanoparticles by the human lung epithelial cells (also known as HeLa A549 cells).

The results from *in vitro* ceria uptake experiments conclude that particles with sizes (<10nm) are completely internalised and uptaken by the A549 cells. The data further concluded that the internalisation seems to be more size dependent and to some extent shape and capping dependent. The uptake images depicted that the internalised particles were localised in the cytoplasm and did not seem to enter the nucleus of A549 cells.

This thesis is dedicated

To my Parents; your unconditional love, endless support, prayers and sacrifices have paved the way in fulfilling this dream, mum and dad....this is for you!

To my husband; your love is the greatest gift of my life, this wouldn't have been possible without your support

To my siblings; thank you for being there for me

Acknowledgements

I would like to express my deepest gratitude to my supervisor Professor Jamie R. Lead for his guidance and support throughout this study, and especially for his confidence in me. Thank you so much for your encouragement, expert suggestions and all those developing opportunities you have given me over these years. I would also like to thank my co-supervisor Professor Eugenia Valsami-Jones (Eva) for her generous support throughout. Thank you for your continued interest and guidance. I would also like to thank NERC for providing the funding which made this research possible.

This thesis would not have been possible without the help of so many people in many ways. I am grateful to Dr Ruth Merrifield and Dr. Mohammed Baalousha for providing training on various instruments and characterisation techniques. I am also thankful to Ghulam Raza for all his help during TEM sessions. My sincere thanks goes to Dr Douglas Blom at the Electron Microscopy Centre USC, for providing technical support at STEM-EELS and Dr Shuguo Ma from College of Engineering and Computing, USC, for his kind assistance with XPS measurements. Special thanks go to Dr Julie Mazzolini for all her help and expert guidance with the biological work. Thank you so much Julie for all those brain storming discussions and coffee breaks.

I would also like to thank everyone in the _Nanogroup‘ for sharing their knowledge during group meetings. Thanks Marie for all those cookies and cakes, Ashwini and Yusuf for your cooperation during lab sessions. Special thanks go to Indrani for the wonderful lunch break talks, health tips and encouragement during my intense writing phase.

I am deeply indebted to my parents for giving me such a wonderful upbringing and for all those sacrifices you made to educate me well, my grandparents, wherever you are, I know you are watching from the heavenly skies and are happy for me, my husband for his constant support and trust in me, this wouldn‘t have been possible if it wasn‘t for your love, my beautiful sister and caring brothers for being there for me during stressful times and my in-laws for all their support.

Table of Contents

List of Figures

List of Tables

List of Abbreviations

ADF	Annular dark field
AR	Analytical reagent
BSA	Bovine serum albumin
CCD	Charge-coupled device
CNT	Carbon nanotube
DI	Deionised
DLS	Dynamic light scattering
DLVO	Derjaguin-Landau-Verwey-Overbeek theory
DMEM	Dulbecco‘s modified eagles medium
EDX	Energy dispersive x-rays
EELS	Electron energy loss spectroscopy
ELS	Electrophoretic light scattering
EM	Electron microscopy
ENMs	Engineered nanomaterials
ENPs	Engineered nanoparticles / manufactured nanoparticles
EPM	Electrophoretic mobility
ESCA	Electron spectroscopy for chemical analysis
ESEM	Environmental Scanning Electron Microscope
FCC	Face centered cubic
FBS	Foetal bovine serum
HAADF	High-angle annular dark field
HMTA	Hexamethylenetetramine
HRTEM	High resolution transmission electron microscope
HS	Humic Substances

IEP	Iso-electric point
ICP-MS	Inductively coupled plasma – mass spectrometer (elemental analyser)
MW	Molecular weight
MNPs	Manufactured nanoparticles
MSD	Material safety datasheet
NMs	Nanomaterials
NO	Nitrogen oxide
NOM	Natural organic matter
NPs	Nanoparticles
OS	Oxidative stress
PCS	Photon correlation spectroscopy
PDI	Polydispersity index
PEG	Polyethylene glycol
PVP	Poly vinyl pyrrolidone
QELS	Quasi-elastic light scattering
RCM	Reflectance confocal microscopy
ROS	Reactive oxygen species
SCM	Serum containing media
SEM	Scanning electron micrscopy
SFM	Serum free media
SOD	Superoxide dismutase
SOP	Standard operating procedure
SSA	Specific surface area - weight per area (g cm-3)
STEM	Scanning transmission electron microscopy
SWCNT	Single walled carbon nanotubes

TEM	Transmission electron microscope
UF	Ultrafiltration
UHV	Ultra high vacuum
UV	Ultra violet
WWTP	Waste water treatment plant
XAS	X-ray absorption spectroscopy
XPS	X-ray photoelectron spectroscopy
XRD	X-ray diffraction crystallograp

1 Introduction

1.1 Introduction to nanotechnology and nanoparticles

Nanotechnology involves the design, production, and use of structures at the nanoscale (1–100 nm) (Rotello, 2003, Roco, 2003). A nanometer (nm) is equal to one billionth of a meter (10^{-9} m). Without special measures, the human eye can not see anything much smaller than one tenth of a millimetre wide. Figure 1.1 provides a relative scale of physical size of nanostructures as compared to the common things we can see with human eye, from large- to small- to nano.

Figure 1.1 Relative scale of physical size, nanoscale engineering deals with sizes many orders of magnitude smaller than conventional features (http://www.slideshare.net/PerkinElmer/poster-nanomaterials, 2012)

Nanoparticles (NPs) are usually defined as the particles with size range between 1 and 100 nm (Hosokawa, 2007, Klabunde and Richards, 2009). Although there is no official definition yet, on 18 October 2011, the European Commission defined nanomaterial (NM) as natural, incidental or manufactured material containing particles, in an unbound state or as an aggregate or as an agglomerate and where, for 50% or more of the particles in the number size distribution, one or more external dimensions is in the size range 1 nm – 100 nm (European Commission, 2011). The source of NPs can vary and is classified into naturally occurring and incidental (man-made) nanoparticles. The former are generated during the evolution of earth or other natural processes such as volcanic eruptions (in the form of ashes, soil particles) physical and chemical weathering of rocks, precipitation reactions, and biological processes whereas the latter are either formed as by-product of processes like combustion or are produced intentionally due to their characteristic properties (Nowack and Bucheli, 2007). Theses NPs which are designed and produced deliberately are called engineered nanoparticles (ENPs).

In past decades, extensive research has been carried out in the design and preparation of nanostructures with different shapes and sizes because of their corresponding novel properties and potential applications (Service, 1996, Sun et al., 2003a, Sun et al., 2003b, Alivisatos, 1996). This is due to the reason that NPs possess a much higher specific surface area (SSA) than their larger counterparts of the same material, and the proportion of atoms on the surface versus the interior of the particle is also much larger for NPs. As the size of NPs approaches the range, 20–30 nm, their mechanical, electronic, magnetic, optical, chemical reactivity, catalytic properties and potential toxicity may differ significantly from those of their bulk counterparts (Baalousha and Lead, 2009, Klaine et al., 2008, Auffan et al., 2009c). This is due to an exponential increase in the number of atoms localized at the surface as the

size decreases. These smaller nanoparticles have a size-dependent crystallinity that gives them properties drastically different from the bulk material. Other size-dependent property changes include surface plasmon resonance in some metal particles and superparamagnetism in magnetic materials. These unique properties make NMs physico-chemically different and superior to their bulk counterparts of the same material. For example, copper which is opaque at macroscale can become transparent at nanoscale (Shanmin, 2003), aluminium which is stable at macroscale turns combustible at nanosclale (Shafirovich et al., 2006) and insoluble materials such as gold can become soluble at nanoscale (Pengo et al., 2003). Similarly, silicon, an insulator at macroscale, becomes a conductor of electric cureent at nanoscale (Hu et al., 2003).

Manufactured nanoparticles are already in hundreds of products including sunscreens, cosmetics, foods, food packaging, clothing, agrochemicals, industrial catalysts etc. (Figure 1.2) (El-Sayed et al., 2005, Veiseh et al., 2005, Salata, 2004, Chan and Nie, 1998, Karhanek et al., 2005, Aitken et al., 2006, Chaudhry et al., 2009, Chaudhry, 2005). Chaudhry et al. (Chaudhry, 2005) provided a report on the global distribution of nanotechnology companies (Figure 1.3). It can be seen that the nanotechnology industry is dominated by US companies (49%), followed by Europe (21%) and rest of the world (21%). A report by Wijnhoven et al. provides a comprehensive analysis of the current and projected scales of the use of engineered NMs in consumer products (Wijnhoven et al., 2009). Other reports have also been published, having identified that engineered NMs are produced in high production volumes (Aitken et al., 2008). These include silver, carbon black, amorphous silica, titanium dioxide, zinc oxide, nanoclays, carbon materials (fullerenes and carbon nanotubes), cerium oxide, iron, organic materials and other commercially produced ENMs. As the number and quantity of engineered products in the market are increasing, the potential for their unintended

environmental consequences is also increasing. There is now a worldwide debate about the benefits of the manufactured NMs and their potential harmful effects on environment and human health (Royal, 2004, Breggin and Carothers, 2006, US-EPA, 2005, Owen and Depledge, 2005, Maynard, 2006, Tratnyek and Johnson, 2006, Pitkethly, 2009, Savolainen et al., 2010, Handy and Shaw, 2007, Owen R and RD, 2007).

As mentioned above, shrinking the size of a material to the nanoscale can produce vastly or subtly different properties. However, just as this is true for desirable properties, such as colour, strength and conductivity, it may also be true of undesirable properties such as toxicity. A substance that is normally considered to be inert and non-toxic at a larger scale may become toxic when produced at the nanoscale. The potential toxicity of NPs has been recognized (Barnard, 2006, Brayner et al., 2006, Ju-Nam and Lead, 2008, Nel et al., 2006, Suresh et al., 2010, Thill et al., 2006) and reviews and perspectives are available (Nel et al., 2006, Auffan et al., 2009a, Handy et al., 2008a, Handy et al., 2008b, Klaine et al., 2008, Nowack and Bucheli, 2007). However, very little is known about their environmental fate, transport and accumulation as well their effects on both human health and environment.

Figure 1.2 Applications of Nanoparticles : Manufactured nanoparticles are already in hundreds of products including sunscreens, cosmetics, foods, food packaging, clothing, agrochemicals, industrial catalysts etc (El-Sayed et al., 2005, Veiseh et al., 2005, Salata, 2004, Chan and Nie, 1998, Karhanek et al., 2005, Aitken et al., 2006, Chaudhry et al., 2009, Chaudhry, 2005).

(Source: http://networksandservers.blogspot.co.uk/2011/01/nanotechnology.html)

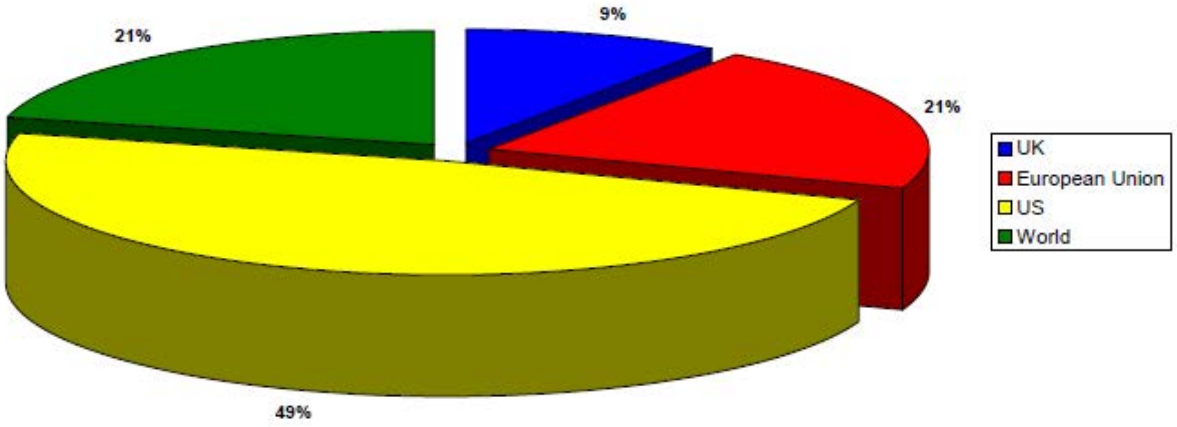

Figure 1.3 The global distribution of nanotechnology companies (Source: (Chaudhry, 2005)

1.2 Cerium oxide (ceria) nanoparticles

Ceria nanoparticles, due to their widespread applications such as their use in the preparation of high temperature ceramics, in catalytic convertors, in fuel cells, solar cells, UV blocks and for polishing materials (Campbell and Peden, 2005, Deluga et al., 2004, Park et al., 2000, Corma et al., 2004) (detailed explanation of applications in section 1.2.2), have also attracted a lot of concern about their toxic effects on both human health and environment. Fluorite-structured ceria; the cations have a coordination number of 8 and the anions have a coordination number of 4, have proved to be a material of exceptional technological importance due to its unique properties, including high mechanical strength, oxygen ion conductivity and oxygen storage capacity (Inaba and Tagawa, 1996, Trovarelli, 1996, Feng et al., 2006). A perfect cerium oxide, CeO_2, (ceria) lattice has cubic fluorite structure (Fig. 1.4a) and in presence of oxygen vacancies it can exist as Ce_2O_3 (sesquioxide) with a hexagonal lattice.

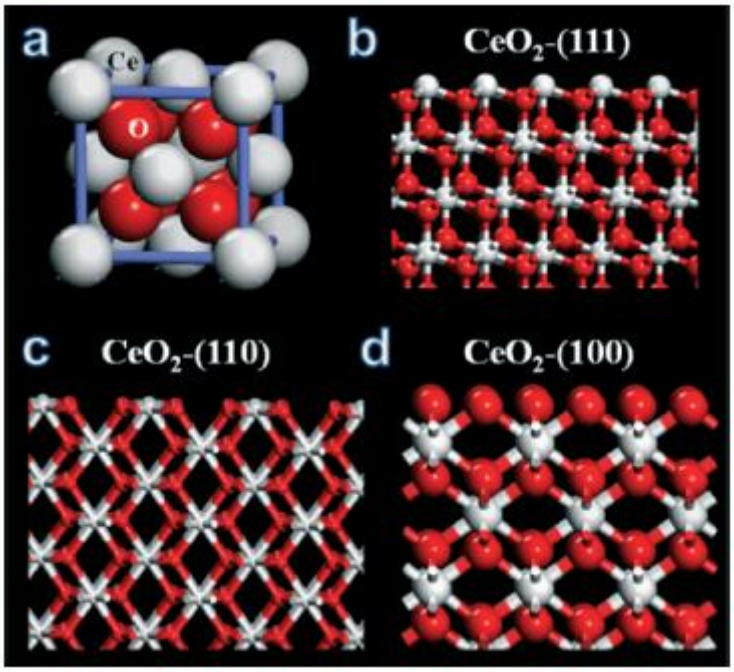

Figure 1.4 (a) Fluorite structure of cerium oxide (CeO2), (b) (111) plane of CeO2, (c) (110) plane CeO2 and (d) (100) plane of CeO2, adapted from (Kumar et al., 2014)

1.2.1 Redox behaviour

Cerium occurs in three oxidation states, Ce (II), Ce (III) and Ce (IV). While Ce (II), because of its instability, is very rarely found and is observed only in CeH_2, CeI_2 and CeS (Patnaik, 2003), both Ce (III) as well as Ce (IV) are commonly found and have the unique ability to readily switch between these two states (Suzuki et al., 2001, Conesa, 1995, Herman, 1999), as shown in figure 1.5. This easy oxidation and reduction (surface catalytic activity) in CeO_{2-x} is known to have several key origins linked to switching between Ce (III) and Ce (IV) oxidation states and the possibility to absorb and release oxygen by inducing oxygen vacancies close to the surface (Turner et al., 2011). However, the detailed mechanism for oxygen buffering in these materials is relatively poorly understood.

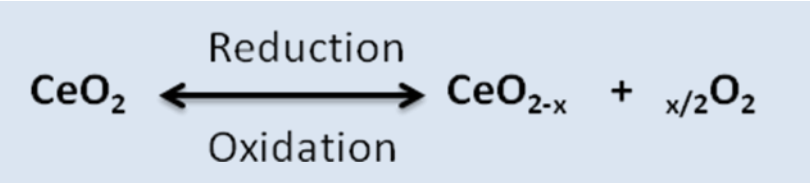

Figure 1.5 The oxidation and reduction reactions of cerium oxide (CeO_{2-x}) nanoparticles (Amin et al., 2011)

1.2.2 Applications

Ceria NPs are currently being used for preparing high temperature ceramics, in catalytic convertors, in fuel cells, solar cells, UV blocks and for polishing materials (Campbell and Peden, 2005, Deluga et al., 2004, Park et al., 2000, Corma et al., 2004). They are produced at industrial scales for their use as a diesel fuel additive for fuel efficiency and as a polishing agent (Park et al., 2003, Park, 2008). The former application is claimed to reduce fuel consumption and particulate emissions. Typically added to diesel at a concentration of 5-10 ppm (5 mg L^{-1}), nano-cerium oxide is claimed to increase fuel efficiency by ~10% and is also known to reduce particulate emission by converting harmful gases such as carbon monoxide (CO) and nitrogen oxide NO (emitted from the vehicle exhaust) and other hydrocarbons to less harmful carbon dioxide (CO_2) and nitrogen and water. Under high-oxygen conditions, the cerium oxide absorbs oxygen, which helps to increase the efficiency by which nitrogen oxide is reduced to nitrogen. Under low-oxygen conditions, the cerium oxide releases stored oxygen and increases the efficiency by which carbon monoxide is oxidized and becomes carbon dioxide (McCartney, 2003). The hydrocarbons are subsequently converted to water vapour and carbon dioxide (Bleiwas, 2013). The catalyst is already in use on a large scale in stage coaches in a number of countries including the UK, Philippines and New Zealand (Aitken et al., 2008). Almost all these uses of nano ceria depend upon the ease with which the ceria particles are reduced and oxidized (Figure 1.5).

1.2.3 Physico-chemical properties of NPs

There is a long list of physico-chemical properties which are considered to be potentially important in assessing the biological behaviour and effects of NPs, including ceria (figure 1.6). Some of these have been grouped and discussed here.

a) Size: The foremost and perhaps the most fundamental measure of nanoparticles is its size. Both mean particle size and particle size distribution are crucial in understanding the behaviour of the NPs in (eco) - toxicological studies. It is known that as the size of NPs approaches the range, 20–30 nm, their mechanical, electronic, magnetic, optical, chemical reactivity, catalytic properties and potential toxicity may differ significantly from those of their bulk counterparts (Baalousha and Lead, 2009, Klaine et al., 2008, Auffan et al., 2009c). This is due to an exponential increase in the number of atoms localized at the surface as the size decreases. These smaller nanoparticles have a size-dependent crystallinity that gives them properties drastically different from the bulk material. Particle size can also enhance processes such as dissolution. For example, It has been found that the bactericidal effect of silver nanoparticles between 1 and 100 nm in diameter was highest in the 1–10-nm range, where there are more highly reactive (111) surfaces (Morones et al., 2005). The interaction of particles with cells is also known to be strongly influenced by particle size (Gratton et al., 2008) but little is known about the independent role played by size in view of other NP properties (Jiang et al., 2009).

b) Aggregation/Agglomeration: The use and meaning of the words 'aggregation' and 'agglomeration' is discipline specific. Here we define 'aggregation' as strongly bonded or

fused collection of particles while 'agglomeration' is a collection of loosely bound particles (or aggregates) held by weaker van der Waals forces. In the environment, Brownian motion (Einstein, 1905) and NP characteristics (e.g., surface properties, particle size) are believed to affect NP agglomeration and aggregation (Farré et al., 2009). The particles are constantly colliding with each other because of Brownian motion, and agglomeration will occur when the energy of either motion or attraction exceeds the energy of repulsion (Lin et al., 2008). The forces involved in the collisions include Born repulsion, diffuse double layer potential, and van der Waals attraction. These forces are described by the extended DLVO theory developed by Derjaguin and Landau in 1941 and Verwey and Overbeck in 1948, hence the name DLVO (Derjaguin and Landau, 1993, Verwey EJW, 1948). It is also known that aggregate size in the solution depends on properties such as initial particle size and concentration (Phenrat et al., 2006). Also the aggregate size may vary among different particle types, zinc oxide NPs dispersed in aqueous solutions aggregate in a wide range of sizes (Pipan-Tkalec et al., 2010, Wang et al., 2009, Lin and Xing, 2008) whereas TiO_2 NPs showed a uniform distribution and agglomeration (Jemec et al., 2008).

c) Morphology: This includes shape of the nanoparticles, including sphericity and aspect ratio. Particle shape is known to play an important role in the fate and behaviour of manufactured NPs into their environment. This could be either because diffusion rates of the material change with the aspect ratio of the material (e.g., higher drag on a tubular structure compared to a perfect sphere) or because of steric hindrance in the collisions as the shape may make it difficult for particles to approach each other (Handy et al., 2008a). Several reports have addressed the role of shape and size on cellular internalization (Geng et al., 2007, Champion and Mitragotri, 2006, Jiang et al., 2009).

d) Chemical composition – The chemistry of the medium is known to influence the electrostatic surface charge of the particles, thereby affecting agglomeration/aggregation rates and particle stability. Most of the manufactured NMs nowadays are coated with surfactants to increase the stability of the suspension. The presence of a surface coating on manufactured NPs may significantly modify their surface chemistry, compared with the uncoated equivalents (Badawy et al., 2010). Similar kind of changes may happen when pristine particles are treated with complex media such as humic acids. For example, adsorption of humic acids on the surface of small aggregates of silver NPs is known to resulted in the disaggregation of the NPs (Fabrega et al., 2009).

e) Surface chemistry:

i. Redox state: The redox process (oxidation and reduction processes) can occur at the surface of nanoparticles leading to change in the crystalline nature. For example cerium oxide NPs. Cerium occurs in both trivalent (III) as well as tetravalent (IV) state and has the unique ability to switch readily between these two states (Suzuki et al., 2001, Herman, 1999, Conesa, 1995). This low energy change gives nanoceria some of its key properties (Turner et al., 2011) but it is known that oxidation state is spatially variable within an individual particle (Merrifield et al., 2013) and is dependent on size (Wu et al., 2004), so understanding of the redox mechanism on the particle surface is really crucial.

ii. Zeta-potential: 'zeta potential‘ is the potential difference between the dispersion medium and the layer of fluid attached to the dispersed particle and is often used as an analogue for colloidal stability, although this is only relevant where NPs are charge stabilized. More details are in Chapter 2

iii. Surface charge: is the charge which arises from adsorption or desorption of protons or other charged material on the nanoparticle surface. This is not synonymous with zeta potential. Details are in chapter 2

f) Solubility/Dissolution: Dissolution is a dynamic process in which the contents of the dissolving substance migrate from the surface to the bulk solution through a diffusion layer (Borm et al., 2006a). The thermodynamic parameter that controls this process is described as solubility (Misra et al., 2012). Metal-based NPs such as zinc oxide are known to dissolve quickly and release ions that are themselves known to be toxic. Thus, the extent of dissolution and the relative toxicities of both the nanoparticulate and dissolved forms need to be considered to better understand the potential NP effects on organisms over time (Tourinho et al., 2012).

Some of the above parameters may also be linked. For example the oxygen storage capacity of ceria is known to be size and shape dependent (Mai et al., 2005, Wu et al., 2004). Also, nanoceria are generally considered to be highly insoluble and so ion effects are likely to be of lower importance (Hoecke et al., 2009) than to other common nanoparticles such as Ag or Zn oxide. However, recent work has shown potential effects of even low level dissolution (Röhder et al., 2014, Schwabe et al., 2015). There is a general assumption that solubility will increase as the particle size decreases and redox state is linked to size (Wu et al., 2004), so solubility and oxidation state may be correlated. So, given the dynamics that are well known to occur, it is really important to perform accurate measurements on the size, shape, morphology, aggregation/ agglomeration, surface charge and dissolution (and related parameters) behaviour of these NPs both in their pristine form as well as their evolvement

through interaction with environment. All the above parameters can be measured by scattering, microscopy, spectroscopy and separation techniques. Some of these techniques have been briefly discussed in Chapter 2.

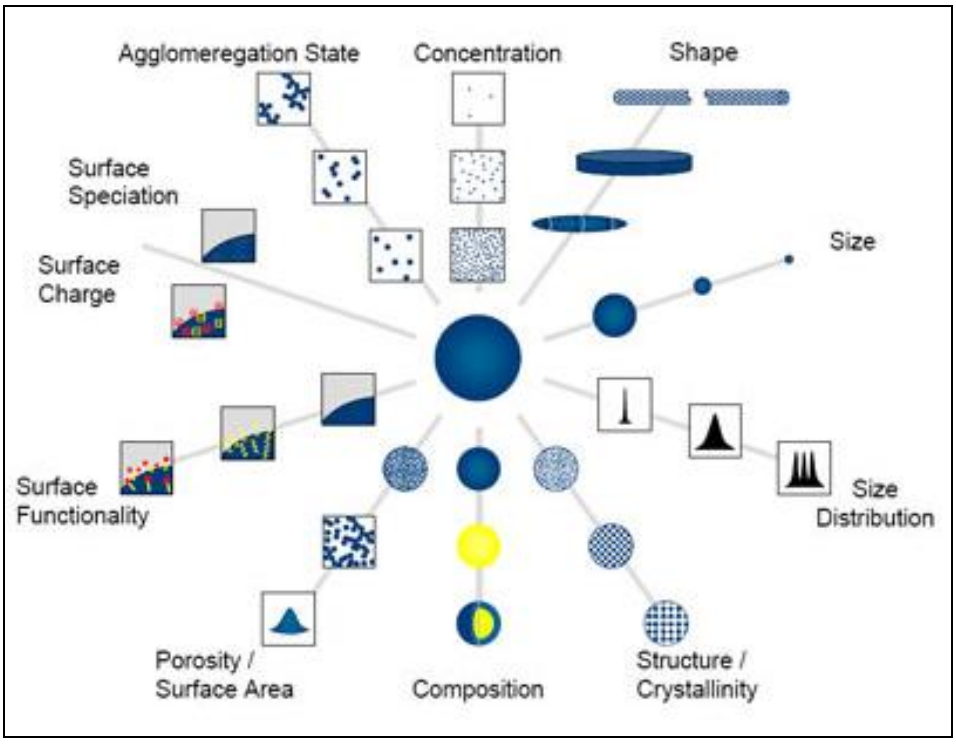

Figure 1.6 Illustration of physico-chemical descriptors for assessing behaviour, fate and environmental/biological effects of NPs, adapted from (Hassellöv and Kaegi, 2009)

1.2.4 Types of synthesis

As such the industrial manufacturing process for nano ceria is not known but over the past few years, many methods have been proposed to produce the ceria NPs, such as sol–gel process (Niederberger, 2007, Laberty-Robert et al., 2005), hydrothermal or solvothermal synthesis, homogenous precipitation (Hakuta et al., 1998, Hirano and Kato, 1999, Uekawa et al., 2004, Wu et al., 2002, Verdon et al., 1995), forced hydrolysis (Dong, 1997),

microemulsion (Masui et al., 1997), etc. Most of these methods are employed for small scale quantities. Typically, these synthetic strategies involve a cerium precursor (usually a Ce (III) source) and an oxidant to convert the cerous ion Ce (III) to less soluble ceric ion Ce (IV) along with the presence of a stabiliser. However, in some cases, the latter plays a dual role of a stabiliser as well as an oxidiser. The general reaction mechanism is based on the concept of preparation of nanoparticle dispersion by condensation from previous supersaturated solution (LaMer and Dinegar, 1950). So, a method of making cerium oxide nanoparticles includes: an aqueous reaction mixture having a source of cerous ion (Ce III)) and a source of hydroxide ion (OH^-), a nanoparticle stabilizer and an oxidant. This leads to the formation of a suspension of cerium hydroxide nanoparticles and further raising the initial temperature achieves oxidation of cerous ion to ceric ion and thereby forming cerium dioxide nanoparticles. The reaction mechanism and the equations (eq 1-4) involved have been summarised below.

$$Ce^{3+} + OH^- \longrightarrow Ce(OH)_3 \qquad \text{eq. (1)}$$

$$Ce^{3+} \longrightarrow Ce^{4+} + e^- \qquad \text{eq. (2)}$$

$$Ce^{4+} + {}_xOH^- + {}_yH_2O \longrightarrow [Ce(OH)_x(H_2O)_y]^{(4-x)+} \qquad \text{eq. (3)}$$

$$[Ce(OH)_x(H_2O)_y]^{(4-x)+} + H_2O \longrightarrow CeO_2.nH_2O + H_3O^+ \qquad \text{eq. (4)}$$

Some of the commonly used stabilizers include alcohols such as primary, secondary and tertiary alcohols (Zhang et al., 2003, Chen and Chang, 2004), polymers such as poly vinyl pyrrolidone (PVP) (Zhou et al., 2007, Merrifield et al., 2013) polyethylene glycol (PEG)

(Zhang, 2007, Karakoti et al., 2011), carboxylic acids (Heckman et al., 2013, Lu et al., 2013) and some organic amines such as ethylenediamine and hexamethylenetetramine also known as HMTA (Kar, 2009, Polezhaeva et al., 2008, Chen and Chen, 1993). Calcination is a commonly employed high temperature technique for the industrial scale production of ceria. The process usually involves high temperature treatment below the melting point of the material in an oxygen rich atmosphere (Grulke et al., 2014). Table 1.1 illustrate a list of selected industrial manufacturers of ceria and their production process.

Table 0.1 Selected industrial manufacturers of ceria and their production processes, adapted from (Grulke et al., 2014)

Manufacturer	production process	Reference
Hitachi	Precipitation (carbonate chemistry prominent); then calcined and milled	(Park et al., 2010)
Rhodia	Precipitation (hydroxide chemistry prominent); then calcined and milled	(Sakurada et al., 2012)
Antaria	Precipitation while being mechanically milled in a NaCl media	(McCormick and Tzuzuki, 2003)
Umicore	Precipitation while being evaporated (thermal spray)	(De Messemaeker et al., 2011)
Evonik	Pyrogenic gas formation from metal alokoxides or metal carboxylates	(Katusic et al., 2009)

1.2.5 Estimated production volumes, environmental release and exposure

While little is known about their environmental fate, transport, and accumulation, cerium oxide is produced at industrial scales for their use as diesel fuel additive and polishing material. Park, et al. projects as much as 1255 tons of CeO_2 will be used as a combustion enhancement additive in diesel fuel in the EU (Park, 2008). The European Commission estimates the global production of nanoceria to be around 10,000 tons (Commission, 2012). Similarly, a comprehensive market study provides an estimate of 7500 to 10 000 tons for the year 2011 (Future Markets, 2012). The emergence of multiple, important applications for ceria NPs and increased industrial production has undoubtedly lead to environmental release of nanoparticles. So far, not many attempts have been made to quantify the release of engineered ceria NPs through use. One of the few studies by Park et al., indicates that 6–100% of CeO_2 will be released during the use phase of diesel fuel additives (Park, 2008). Another article by Ulrich et al. demonstrated that particle filters from diesel cars removed 99.9% of cerium present in fuel additives (Ulrich and Wichser, 2003). However, they did not specify whether the ceria used in additive was at nanoscale. Recently, Collin et al. made some assumptions on the likelihood of environmental release of nanoceria considering the enormous amount of its applications (Collin et al., 2014). They demonstrated that if the batteries carrying nanoceria are not disposed of properly, the most likely environmental compartment would be soil, with negligible release to air, water or wastewater treatment plants (WWTP). Similar assumptions were made for metallurgical products, catalysts in FCC, polishing powders used in industry (which may be released to air or in wastewater), and other applications. Another article by one of the co-authors of the review estimated that nanoceria concentrations in treated WWTP effluent discharged to waterbodies are expected to be in the range of 0.003–1.17 μgL^{-1} (Lazareva and Keller, 2014). In biosolids, nanoceria

concentrations are expected to be around 0.53–9.10 mg kg^{-1} (Lazareva and Keller, 2014). Their initial estimates suggest that the majority of nano-ceria will ultimately end up in landfills, with lesser amounts emitted to air, soil and water. However, this may or may not be the case as the estimated concentrations are expected to change with the increase in global production of nanoceria for different applications, and they are likely be accumulate in soils and sediments further leading to aquifers.

1.2.6 Environmental and human exposure

It is inevitable that NMs are released into the environment during usage, which may adversely affect both the organisms and humans. The human exposure to NMs, as with many other substances in the environment, could include exposure via the air, water or food supply as shown in figure 1.7 (Farré et al., 2009). The source of entry could be through industrial production and transportation or any accidental spills during transfers (Navarro et al., 2008). Particles in solid wastes, wastewater effluents (Mueller and Nowack, 2008), direct discharges, or accidental spillages can be transported to aquatic systems by wind or rainwater runoff. Nanoparticles reaching land have the potential to contaminate soil, migrate into surface and groundwaters, and interact with biota. Amongst other things, it is generally known that the potential of nanomaterials to be released into the environment and the associated risk of direct exposure of nanomaterials to consumers is highly dependent on the location of the nanomaterial within a product (Figure 1.8) (Hansen et al., 2008). Nanomaterials suspended in liquids (e.g. sunscreens) or located on the product surface (e.g. coatings, clothing) pose a higher risk, than products in which nanomaterials are embedded in a solid substance (e.g. tennis rackets) (Hansen, 2008b) (Figure 1.9). If we look at the product category with respect to the location of the NPs present, then most of the cosmetics and sunscreens products contain nanoparticles suspended in liquids whereas most sporting goods

use nanoparticles suspended in solids. If we assume that products that contain nanoparticles "suspended in liquids" and "airborne nanoparticles" are to be expected to reach the environment conveniently, this indicates that ceria nanoparticles used in fuel additives might also be the similar candidates. As far as the humans and other living organisms are concerned, the primary route of entry could be – inhalation, ingestion, and dermal penetration (Oberdörster et al., 2005a, Oberdörster et al., 2005b, Oberdorster, 2012).

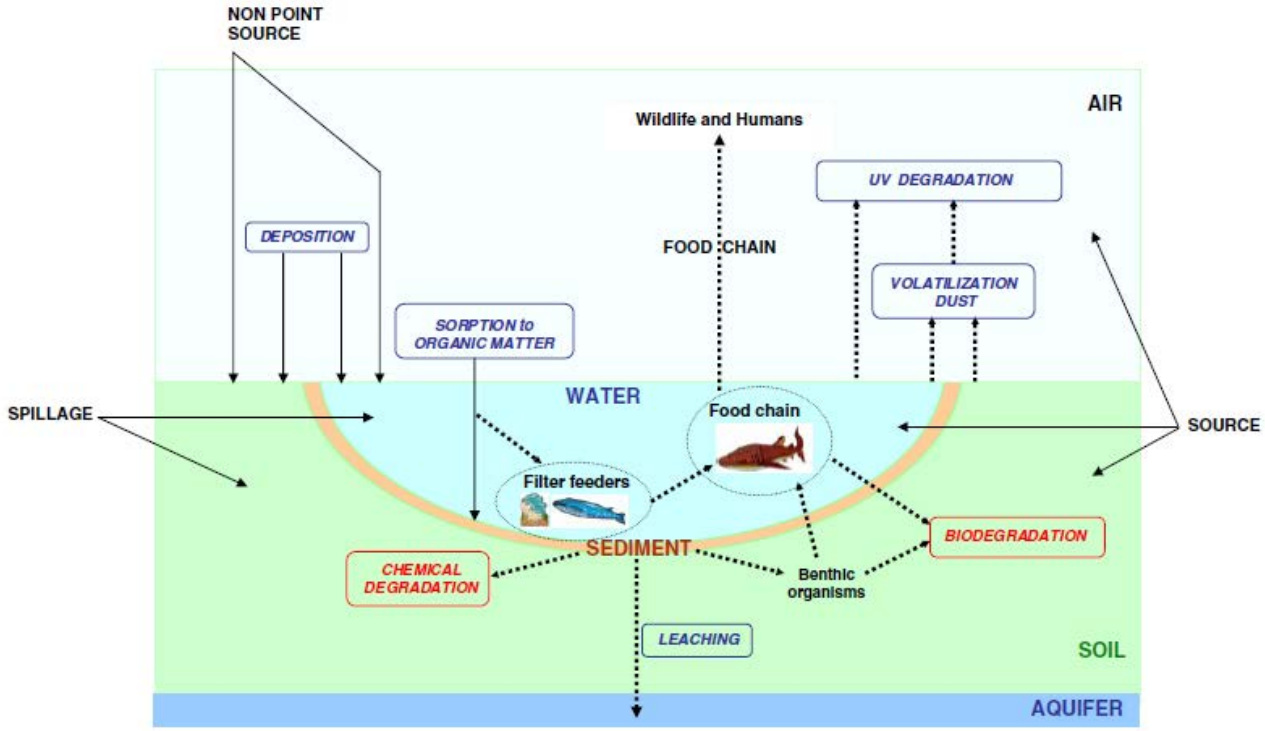

Figure 1.7 Different pathways of entry of ENMs into the environment, adapted from (Farré et al., 2009)

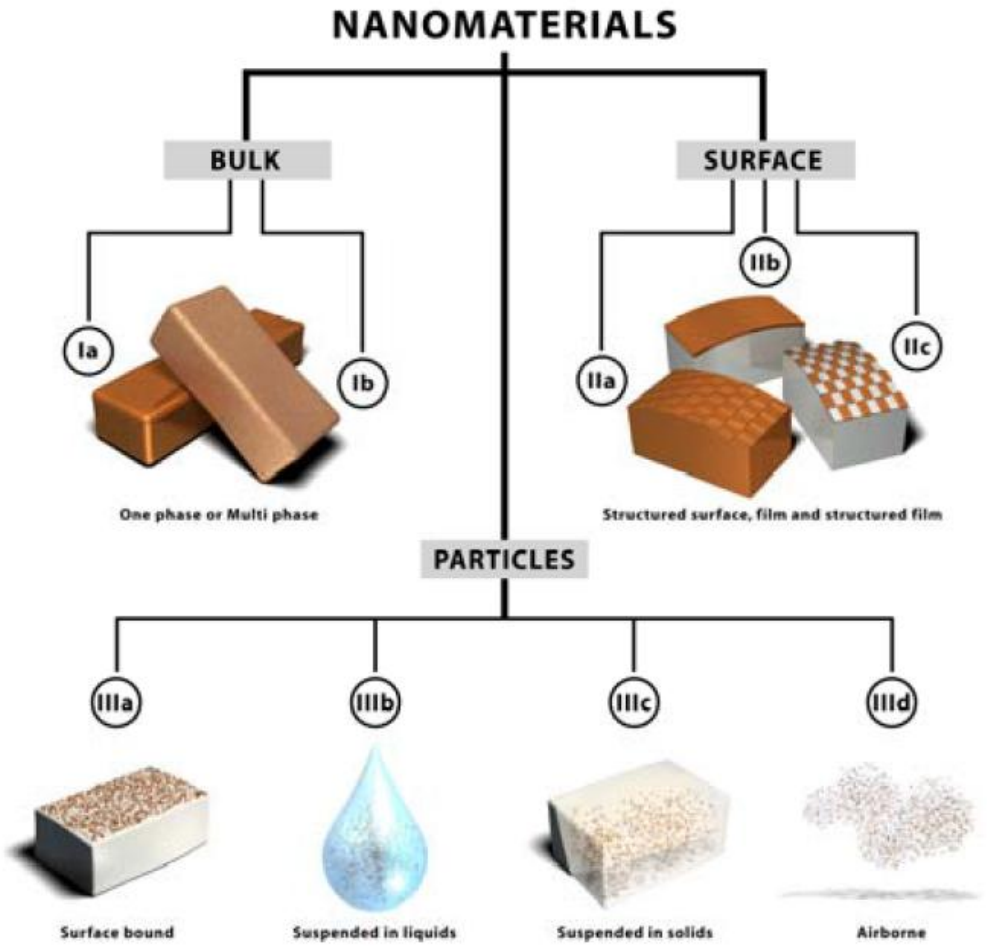

Figure 1.8 The categorisation framework for nanomaterials as suggested by (Hansen et al., 2008)

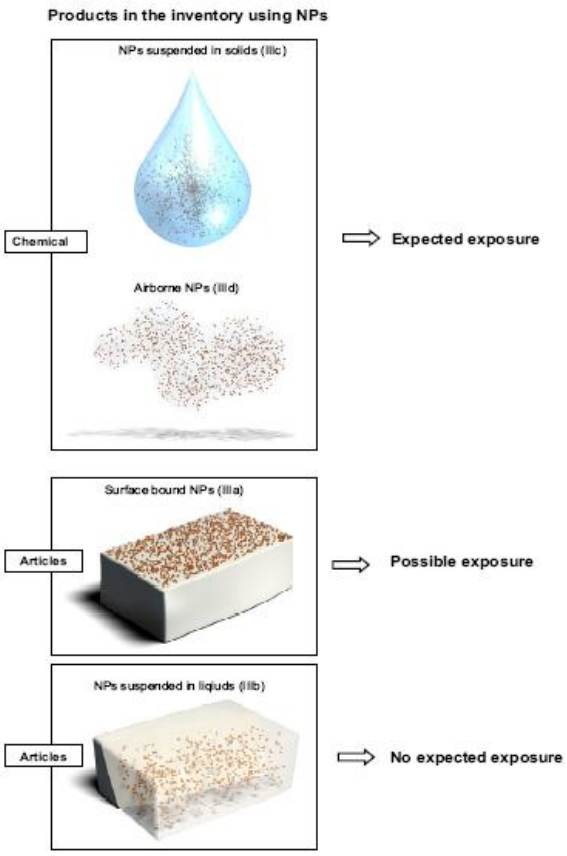

Figure 1.9 Distribution of the products with no, possible and expected exposure within each of the various product categories depending on the location of the nanomaterial in the product as suggested by (Hansen, 2008b)

1.2.7 Health impacts of inhaling airborne particles

The health impacts of inhaling airborne particles have long been recognized and a lot of literature is associated with the lung toxicity caused due to the exposure to ultrafine particles (Maynard and Kuempel, 2005). When particles are inhaled, depending on their size, they may deposit in different regions of the respiratory tract, including the nasal, tracheobronchial, or alveolar (gas-exchange) region. Particles deposited in the respiratory system that are cleared via the mucociliary escalator may be swallowed, leading to exposure to the gastrointestinal

tract (Parent, 1992). Thus, the ingestion route of exposure also occurs when particles are inhaled but there are very few studies available (Oberdörster et al., 2005b). Dermal penetration is another potential route of entry. The extensive use of nanoparticles in sunscreens and cosmetics have raised a big concern over their possible penetration through skin leading to health implications (Royal, 2004). Titanium dioxide and zinc oxide NPs are being used as ultraviolet (UV) blocking agents in sunscreens (Popov et al., 2005, Willander et al., 2005). Ryman-Rasmussen et al. have demonstrated that quantum dots with different sizes (diameter below 10 nm), shapes, and coatings penetrate through the outer layers of pig skin samples in a flow cell, and enter the epidermal and dermal layers (Ryman-Rasmussen et al., 2006, Smijs and Pavel, 2011). There are wider concerns over the photogeneration of hydroxyl radicals by nanosized titanium dioxide and zinc oxide leading to oxidative damage in the skin. However, their surface modification with coatings has shown to suppress free radical generation (Lademann et al., 2000, Wakefield et al., 2004).

1.2.8 Human and eco - toxicity of ceria

Toxicity of ceria NPs has been recognised but various studies have lead to seemingly different assessments. There is a lot of contradiction in literature about the oxidant/antioxidant activity of nanoceria. Park et al. described ceria nanoparticles inducing oxidative stress in human lung epithelial cells (Park, 2008). In other previous reports, nano-ceria was regarded as an exogenous source of reactive oxygen species (ROS) for cells or organisms (Park et al., 2008, Lin et al., 2006). It has been reported that Ce (III) was capable of redox-cycling with peroxide to generate damaging oxygen radicals (Heckert et al., 2008b). They further presumed that Ce (III) accompanied by the oxygen vacancy on the particle

surface was the most likely active sites for ROS generation in the nanotoxicological studies. Figure 1.10 illustrates the redox mediated oxidative stress caused in human fibroblasts. Reactive oxygen species (ROS) are generally produced at low levels in all cells through the electron-transport chain during aerobic respiration and by various constitutively active oxidases. ROS, particularly $O_2^{\bullet-}$ and H_2O_2, are neutralised in cells by some enzymes such as superoxide dismutase (SOD) and catalase which act as antioxidants (Pirmohamed et al., 2010, Dowding et al., 2013). However, excessive ROS production can lead to oxidative stress and cause structural and functional damage to proteins and genes which can further lead to inflammatory diseases (Martin and Leibovich, 2005).

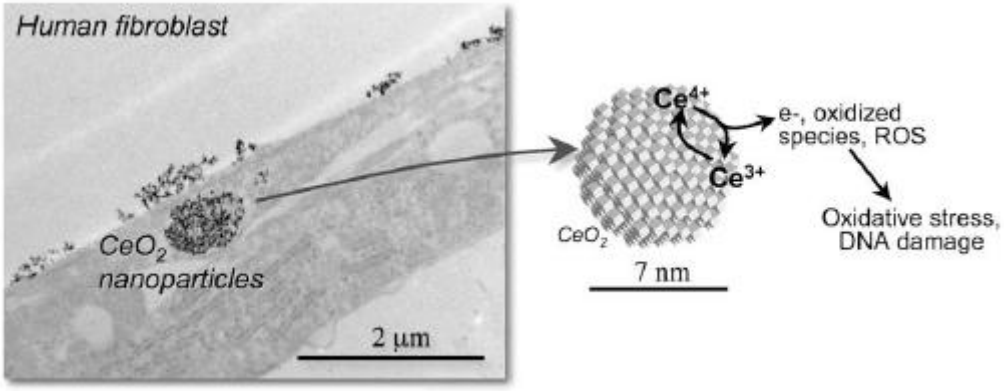

Figure 1.10 Redox evolution of the surface of ceria nanoparticles in contact with human dermal fibroblasts *in vitro*, this redox instability induces an oxidative stress and genotoxic effects, adapted from Auffan et al. (2007).

In contrast, Schubert et al. reported that ceria nanoparticles act as antioxidants and protect cells from oxidative damage (Schubert et al., 2006). Another critical review reveals that ceria NPs have the potential to prevent degenerative diseases that are triggered by oxidative stress (Karakoti et al., 2010a). Few more studies by the same group show that nanoceria remains

deposited in tissues and may decrease ROS, thereby suggesting that cerium oxide nanoparticles may be a useful antioxidant treatment for oxidative stress (Hirst et al., 2013). A study by Xue et al. describes ceria NPs as excellent antioxidants. This activity was proved to be size-dependent and was believed to have a close correlation with Ce (III) at the surface of the particles (Xue et al., 2011). Toxicity has also been reported in daphnia (Gaiser et al., 2011) and algae. Recent findings also suggest that pH and other factors may determine whether ceria nanoparticles destroy or help cells (Perez et al., 2008, Asati et al., 2009). Another study on bacteria by Thill et al. demonstrated that ceria NPs tend to adsorb onto the outer membrane of bacteria (Escherichia coli), and this adsorption and the subsequent reduction of Ce(IV) to Ce(III) was associated with bacterial cytotoxicity (Thill et al., 2006). As is evident, the results are quite conflicting. There is a lot of speculation on the redox behaviour of ceria related to its different biological behaviour however; there is no particular pattern to suggest that ceria NPs have oxidant or anti-oxidant behaviour.

1.2.9 Synthesis dependent behaviour

Recent literature has shown that the synthesis route and different environmental conditions can dramatically influence the properties of nanoceria. Samiee at al used microwave assisted method to prepare ceria NPs and found that different cerium precursors affect the size and optical properties of the ceria NPs formed. They further concluded that Ce (IV) precursors leads to smaller size in relatively shorter reaction time as compared to Ce (III) precursors (Samiee and Goharshadi, 2012). Sakthivel et al. used hydrothermal method to synthesise ceria NPs and concluded that reaction parameters of a hydrothermal method influence the crystallite size, lattice constant, lattice strain, bandgap and oxygen vacancies of ceria

nanostructures. They demonstrated that ceria nanoparticles, nanocubes, and nanorods can be obtained with precisely controlled aspect ratios by varying the synthesis conditions and compositions. They further revealed the concept behind this that in a typical hydrothermal synthesis, the formation of nano- structured materials starts with nucleation from precursor solutions followed by growth of the resulting nuclei. So, by varying synthesis compositions and conditions, both the shape and growth direction of nuclei can be manipulated to obtain nano- structured materials with desirable morphologies (Sakthivel et al., 2013). Recent literature also highlighted that sample preparation methods, synthesis temperature and sample processing may also apparently alter particle behaviour in case of cerium oxide nanoparticles (Karakoti et al., 2012). Karakoti et al. examined different types of the cerium oxide (ceria) particles reported in the literature (table 1.2) in relation to their biological responses observed and categorised them into three different types based on the synthesis temperature and conditions.

a. High temperature: This included nanomaterials heated or calcined at >300°C (e.g., sintering, calcination, high-temperature or flame pyrolysis, and thermal decomposition)
b. Heated in solvent: These included ceria NPs produced when heated in solvents <100°C (e.g., thermal hydrolysis, solvothermal, and hydrothermal)—with or without surfactants/coatings
c. Room temperature: This included NPs synthesized at room temperature (e.g., acid or base hydrolysis or microemulsion)—with or without surfactants/coatings.

They further grouped the biological effects observed from the exposure in three basic responses. All studies indicating inflammatory response from ceria nanoparticles were

grouped as pro-oxidative while all studies reporting beneficial effects were grouped as anti-oxidative. In addition studies that have had mixed response or showed no effect from addition of ceria nanoparticles were grouped as no effect or ambiguous and found that most of the pro-oxidative results reported on ceria nanoparticles involved the NPs synthesized at direct high-temperatures whereas studies using ceria NPs synthesized by low heat in solvents or at room temperature more often reported little or ambiguous response or anti-oxidative response. However, there were few exceptions.

Table 0.2 Classification of biological responses of ceria NPs based on their synthesis temperature, adapted from (Karakoti et al., 2012)

* Biological effects observed as pro-oxidative are indicated in red, anti-oxidative in blue and where no effect or ambiguous or neutral have been indicated in green. The references are in chronological order as observed in table and are summarised here.

36 (Cho et al., 2010), 28 (Eom and Choi, 2009), 37 (Park EJ, 2010), 34 (Yokel et al., 2009), 30 (Lin et al., 2006), 31 (Cassee et al., 2012, Ma et al., 2011), 32 (Park et al., 2008), 69 (D'Angelo, 2009), 70 (Niu et al., 2007), 71 (Xia et al., 2008a), 72 (Park et al., 2007), 73 (Park, 2008), 74 (Gojova et al., 2009), 44 (Thill et al., 2006), 41 (Pierscionek, 2010), 43 (Safi et al., 2010), 27 (Auffan et al., 2009b) , 39 (Hardas et al., 2010), 35 (Zhang et al., 2011a), 75 (Perez et al., 2008), 76 (Schubert et al., 2006), 77 (Niu et al., 2011), 22 (Alili et al., 2011), 23 (Chen et al., 2006), 24 (Colon et al., 2009), 25 (Das et al., 2007), 26 (Tarnuzzer et al., 2005), 48 (Karakoti et al., 2009), 52 (Heckert et al., 2008a), 53 (Hirst et al., 2009), 55 (Karakoti et al., 2010b), 56 (Korsvik et al., 2007).

Synthesis	Study	Response	Ref
High temperature	Inflammation in lungs by metal oxide nanoparticles	Pro-oxidative	[36]
	Oxidative stress of ceria nanoparticles in bronchial epithelial cells	Pro-oxidative	[28]
	Inflammatory response in mice treated with ceria nanoparticles by intratracheal instillation	Pro-oxidative	[37]
	Biodistribution and oxidative stress of commercial ceria nanomaterials	Pro-oxidative	[34]
	Toxicity of cerium oxide nanoparticles in human lung cancer cells	Pro-oxidative	[30]
	Ceria-nanoparticle-induced pulmonary inflammation in rats	Pro-oxidative	[31]
	Oxidative stress induced by ceria nanoparticles in BEAS-2B cells	Pro-oxidative	[32]
	Cerium oxide nanoparticles trigger neuronal survival	Anti-oxidative	[69]
	Cardioprotective effects of ceria nanoparticles	Anti-oxidative	[70]
	Comparison of toxicity of zinc oxide and ceria nanoparticles based on dissolution of metal ions	Anti-oxidative	[71]
	Screening nanoparticulate ceria as a diesel fuel additive	Neutral or Both	[72]
	Hazard and risk assessment of ceria nanoparticles	Neutral or Both	[73]
	Effect of ceria nanoparticles in vascular endothelial cells	Neutral or Both	[74]
Heated in Solvent	Cytotoxicity of ceria nanoparticles for *E coli*	Neutral or Both	[44]
	Nanoceria exhibits no detrimental effects on eye lens proteins	Neutral or Both	[41]
	Interaction between ceria nanoparticles and 3T3 fibroblasts	Neutral or Both	[43]
	DNA damage in human dermal fibroblasts by ceria nanoparticles	Pro-oxidative	[27]
	Brain distribution and toxicological evaluation of ceria nanoparticles	Neutral or Both	[39]
	Adverse effects of ceria nanoparticles at environmentally relevant concentrations	Pro-oxidative	[35]
Room Temperature	Altered vascular reactivity and ischemia-reperfusion injury following ceria nanoparticle instillation	Pro-oxidative	[45]
	pH-dependent antioxidant activity of ceria nanoparticles	Anti-oxidative	[75]
	Yttria and ceria nanoparticles are neuroprotective	Anti-oxidative	[76]
	Ceria nanoparticles inhibit oxidative stress in H9c2 cardiomyocytes exposed to cigarette smoke	Anti-oxidative	[77]
	Combined cytotoxic and anti-invasive properties of redox-active nanoparticles in tumor stroma–interactions	Anti-oxidative	[22]
	Rare earth nanoparticles prevent retinal degeneration induced by intracellular peroxides	Anti-oxidative	[23]
	Protection from radiation-induced pneumonitis using cerium oxide nanoparticles	Anti-oxidative	[24]
	Auto-catalytic ceria nanoparticles offer neuroprotection to adult rat spinal cord neurons	Anti-oxidative	[25]
	Vacancy-engineered ceria nanostructures for protection from radiation-induced cellular damage	Anti-oxidative	[26]
	PEGylated Nanoceria as Radical Scavenger with Tunable Redox Chemistry	Anti-oxidative	[48]
	The role of cerium redox state in the SOD mimetic activity of nanoceria	Anti-oxidative	[52]
	Anti-inflammatory properties of cerium oxide nanoparticles	Anti-oxidative	[53]
	Rare earth oxides as nanoadditives in 3-D nanocomposite scaffolds for bone regeneration	Anti-oxidative	[55]
	Superoxide dismutase mimetic properties exhibited by vacancy-engineered ceria nanoparticles	Anti-oxidative	[56]

1.2.10 Summary

It is clear that different synthesis temperatures may lead to different biological responses but this may not be the case always. Additional parameters such as the amount of precursors, reaction timings, presence/absence of capping agents, sample storage and handling, impurities and Ce (III)/Ce (IV) ratio in a particular sample may be responsible towards contradictions in biological responses. A recent study by Dowding et al. has also elaborated the fact that cellular interaction and toxicity depend on physicochemical properties and surface modification of redox-active nanomaterials (Dowding et al., 2013). The literature available also reveals that the bulk particles are dominated by Ce (IV) and the ceria NPs contain a large amount of Ce (III) however the percentage of Ce (III) and Ce (IV) may also depend on the type of synthesis method and the size and morphology of the NPs (Baalousha et al., 2010, Wu et al., 2004, Zhang et al., 2004). There is concern that nanoceria, due to its small particle size and enhanced reactivity by design, may present unique hazards to ecological receptor species. Of critical importance are the redox properties of ceria which enables it to transition between Ce (III) and Ce (IV). There is a lot of speculation on the redox behaviour of ceria being related to its different biological behaviour.

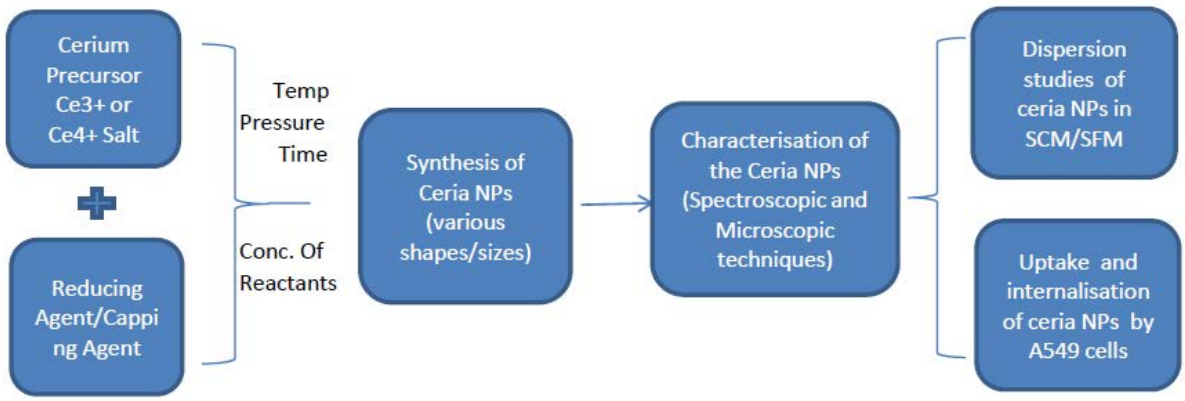

Figure 1.11 Research design

1.3 Research aims and objectives

1. To synthesise shape and size selected ceria nanoparticles, both with and without capping agents.
2. To characterise the physico-chemical properties of manufactured ceria nanoparticles for their size, shape, aggregation, surface charge, composition and oxidation state.
3. To quantify the Ce (III) and Ce (IV) ratios in as-synthesised samples using STEM-EELS and XPS and the technique comparison.
4. To perform dispersion and aggregation studies of ceria nanoparticles in cell culture media which is serum containg media (SCM) and serum free media (SFM)
5. To perform uptake and internalisation studies of selected ceria NPs in human lung epithelial cells (Adenocarcinomic human alveolar basal epithelial cells, A549)

Aim 1 and 2 have been discussed in Chapter 3, aim 3 in Chapter 4 whereas aim 4 and 5 have been discussed in chapter 5 (Research design, figure 1.11).

2 Laboratory techniques and nanoparticle characterisation

2.1 Chapter overview

As discussed in Chapter 1, characterisation of NPs is an important step to understand the chemistry of these nanoparticles in both their synthesized form as well as their evolvement through applications (Karakoti et al., 2012). Size, shape, particle size distribution, surface area and surface charge are one of the most important parameters in understanding the nature of these nanoparticles (Hassellöv and Kaegi, 2009). This chapter summarises the use of various microscopic and spectroscopic techniques used to characterise the ceria NPs. Characterization of the synthesised NPs has been carried out using a combination of existing techniques. The size, shape and morphology of the samples synthesised has been determined using DLS and TEM while STEM+EELS along with XPS have been used to quantify ceria oxidation states. The purpose of this chapter is to highlight the detailed background information about the techniques used with their principle, advantages and disadvantages and how they have been employed to analyse the synthesised ceria NPs as well as understanding their interaction with biological systems. The chapter is also devoted to some other laboratory techniques used either during the synthesis or post synthesis during sample preparation and refinement. All these have been summed up at the bottom of the chapter.

2.2 Laboratory techniques

2.2.1 Chemicals

All the chemicals used in this study were Analytical reagent (AR) grade and used without further purification. They were purchased from Sigma Aldrich and Fisher scientific and all

water used in the experiments was Ultrapure of resistivity 18 MΩ.cm resistivity. All the chemicals were stored according to their material safety datasheets (MSD) and chemicals like Cerium nitrate hexahydrate were kept in dessicator due to their hygroscopic properties.

2.2.2 Glassware preparation

All the glassware and plastic required for the experiments was washed before and after use with 10% nitric acid (HNO_3) for a minimum of 24 hrs and then rinsed thoroughly with ultrapure water ensuring no traces of acid remained. The glassware was then air dried and kept in sterile boxes until next use.

2.2.3 Filtration

Filtration was used in order to remove any large particles or aggregates which may have formed during synthesis. This step is also important in order to eliminate any contamination or impurities in the form of dust which may have entered the sample. A Millipore sterfill filtration system from Sigma-Aldrich, a receiver flask and funnel with filters of cellulose nitrate membrane, pore size 0.1 μm and a diameter of 47 mm, were used.

The set up is a closed unit designed to protect the sample and filtrate from contamination and could be connected to a low pressure vacuum system in order to speed up the filtration process. For every filtration carried out, the filter was first washed and flushed by filtering some ultra pure water before filtering the sample in order to remove any impurities intact with the filter. The setup is shown in the figure 2.1

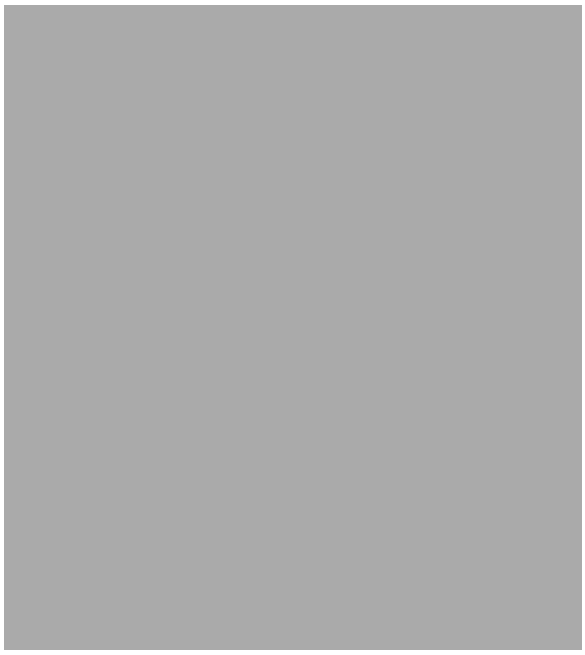

Figure 2.1 A Millipore sterfill filtration system (adapted from Sigma-Aldrich)

2.2.4 Centrifugation and ultracentrifugation

Centrifugation technique (an Eppendorf 5804 R) was used post synthesis with a maximum speed of 5000 rpm at 4 ^{0}C for 10 minutes to separate the nanoparticle pellets collected at the bottom from the rest of the reaction mixture (Figure 2.2). The technique was also used to wash the nanoparticles repeatedly in order to get rid of any excessive capping agent and in some cases to achieve size based separation of the nanoparticles by centrifuging the washed sample for longer periods (40-60 minutes).

Ultracentrifugation was used as an alternative approach for the preparation of TEM grids apart from the drop method. TEM samples for this work were prepared by ultracentrifugation using a Beckman ultracentrifuge (L7-65 ultracentrifuge) with a swing-out rotor SW40Ti (Figure 2.13). Nanoparticles were immobilised on a 300 mesh holey carbon films by immersing the grid in diluted solutions of nanoparticles and ultracentrifuging at 30,000 rpm

for 1 hour at 5 ^{0}C . The technique is considered to be ideal for preparing uniform TEM grids (Mavrocordatos et al., 2007).

Figure 2.2 The Eppendorf 5804 R centrifuge and Beckman ultracentrifuge (L7-65 ultracentrifuge) used in the project

2.2.5 Ultrasonication

Ultrasonication is a technique used to disperse nanoparticles in different matrices. It is commonly used for dispersing and de-agglomerating the nanoparticles in water. Ultrasonic cavitation generates high shear forces that break particle agglomerates into single dispersed particles and improve uniformity and stability of the sample.

Ultrasonication (Branson 1510) has been carried out on synthesised ceria nanoparticles for 1 minute before treating them with the serum containing media and serum free media in order to understand the aggregation behavior of these particles in these media (Figure 2.3). Ultrasonication assisted synthesis has also been carried out to synthesise pegylated ceria nanoparticles using different molecular weights of polyethelene glycol (PEG) as a capping agent (details in chapter3).

Figure 2.3 Branson 1510 sonicator used in the project

2.3 Nanoparticle characterisation techniques

2.3.1 Transmission Electron microscopy (TEM)

Transmission electron microscopy is a well known and one of the most powerful techniques to visualise nanoparticles. It is used to produce images from a sample by illuminating the sample with electrons (electron beam) within a high vacuum, and detecting the electrons that are transmitted through the sample. It allows visualisation and analysis of specimens in the realms of microspace (1μm = 10^{-6}m) to nanospace (1nm = 10^{-9}m).

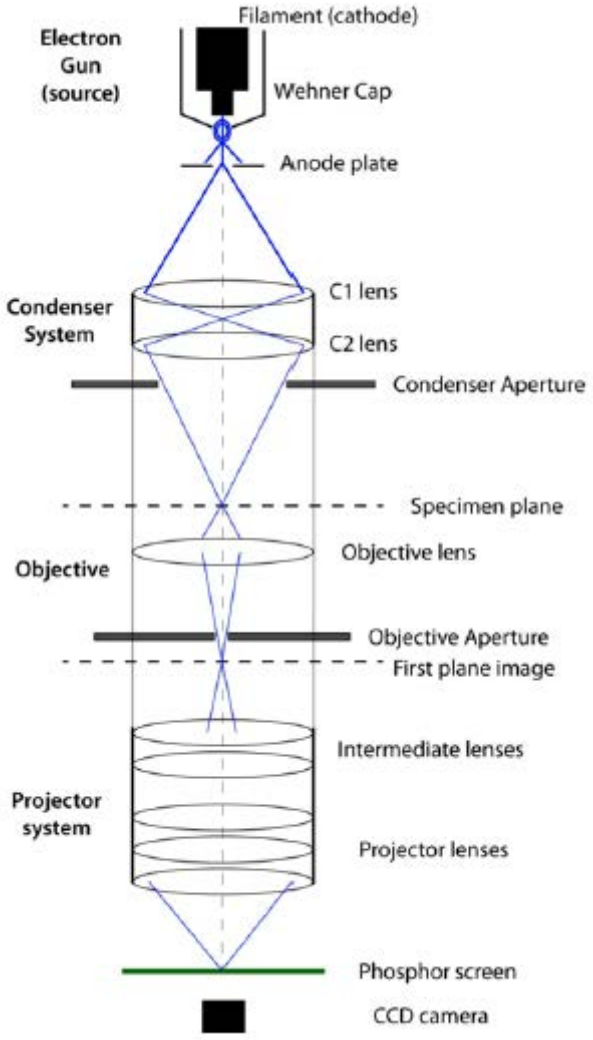

Figure 2.4 Schematic diagram showing the main TEM components (Bortolini, 2014)

The first TEM was built by Max Knoll and Ernst Ruska in 1931 (Knoll, 1932) and the first commercial TEM was developed in 1939 after significant improvements to the quality of magnification. Since then, it has been used in a number of different fields such as life sciences, nanotechnology, medical, biological and material research, forensic analysis and metallurgy as well as industry and education. A schematic representation of the electron path in TEM is shown in Figure 2.4

Starting from the top, a TEM consists of an electron source also known as field emission gun (FEG), which may be a tungsten filament, or a lanthanum hexaboride (LaB_6) source (Egerton,

2005). This high voltage source (typically ~40–120 kV) emits electrons into the vacuum and a system of electromagnetic lenses focuses the electron beam on the sample (Kuntsche et al., 2011). The condenser system (usually made up of two lenses) converges the electron beam to a focus at the plane of the specimen and the objective lens acts as an important component in enhancing the contrast and improving the image quality. One or several lenses are situated in an intermediate position between objective and projector lenses and this projects the image either on the fluorescent screen or the charge-coupled device (CCD) camera (Bortolini, 2014). The image is formed as a result of the interaction of the electrons with the specimen. The technique has sub-nanometer scale resolution and provides 2D image of the sample. The contrast formation in the TEM depends on the mode of operation. The most common mode of operation is the bright field imaging mode in which the contrast is formed directly by absorption of electrons in the sample. Thicker regions of the sample, or regions with a higher atomic number will appear dark, whilst regions with no sample in the beam path will appear bright – hence the term "bright field". So it produces high-resolution black and white images. The lighter areas of the image represent the places where a greater number of electrons were able to pass through the sample and the darker areas reflect the dense areas of the object. These differences provide information on the structure, texture, shape and size of the sample.

This technique not only provides direct visual images but can be applied to determine other properties such aggregation, dispersion, sorption, size, structure and shape of the NPs (Mavrocordatos. D, 2004) but there are a number of drawbacks. Many materials require extensive sample preparation to produce a sample thin enough to be electron transparent. The technique require sample drying, have to be operated under vacuum conditions, electron beam leads to sample destruction and only small amount of samples can be analyzed at a given time.

Figure 2.5 Jeol 1200EX TEM used in this project (courtesy of Centre of Electron Microscopy, University of Birmingham)

Transmission electron microscopy samples for this work were prepared by ultracentrifugation using a Beckman ultracentrifuge (L7-65 ultracentrifuge) with a swing-out rotor SW40Ti. Nanoparticles were immobilised on a 300 mesh holey carbon films by immersing the grid in diluted solutions of nanoparticles and ultracentrifuging at 30,000 rpm for 1 hour (Mavrocordatos et al., 2007). The grids were then washed with ultra pure water and allowed to air dry while kept covered to prevent contamination. The bright field images have been taken at Jeol 1200EX TEM (Figure 2.5). The TEM has an operating voltage ranging from 40 to 120 keV and is fitted with a LaB_6 filament however; most of these images have been taken at 80 kV. Images were collected digitally using a Gatan Dual Vision 300W digital camera. Shape and size quantification has been carried out using image J® software. In all cases, at least 100 NPs were analyzed from TEM images to construct a representative shape and particle size distribution. The size distribution and form factor ((4π*area)/(perimeter2)) of the NP suspensions were measured using image J®. The edges of the particles were defined by

using a watershed algorithm in image J where the background is removed by excluding pixels of a threshold value, leaving just the particles contributing to the image. The diameters, areas, circularity and roundness values are then automatically calculated and used for quantification. The particles at the edges of the image and overlapping particles were excluded (an example is shown in Appendix C). In some cases, where the agglomeration seemed to complicate the accuracy of data obatined, manual measurements were carried out by calibrating the scale bar and taking measurements by visual inspection.

2.3.2 Scanning transmission electron microscopy (STEM)

Scanning transmission electron microscopy (STEM) combines the principles of transmission electron microscopy (TEM) and scanning electron microscopy (SEM). A fine, highly focused beam of electrons is scanned over a thin specimen. Unlike TEM, STEM works on the principle of focusing the electron beam into a narrow spot which is scanned over the sample in a raster. The transmitted electrons at high scattering angle can be collected to form high-resolution, chemically sensitive, atomic number (Z-) contrast images. Both STEM and TEM were initially developed at about the same time (von Ardenne, 1938, Knoll, 1932) but the evolution of STEM was much slower and was not developed until the work of Crewe et al. in 1970 demonstrated its potential and developed the field emission gun (Crewe et al., 1969). Usually a STEM is a conventional transmission electron microscope equipped with additional scanning coils and detectors to it but nowadays dedicated STEM are manufactured and used. Figure 2.6 represents a schematic diagram of the main components of a high-resolution dedicated STEM.

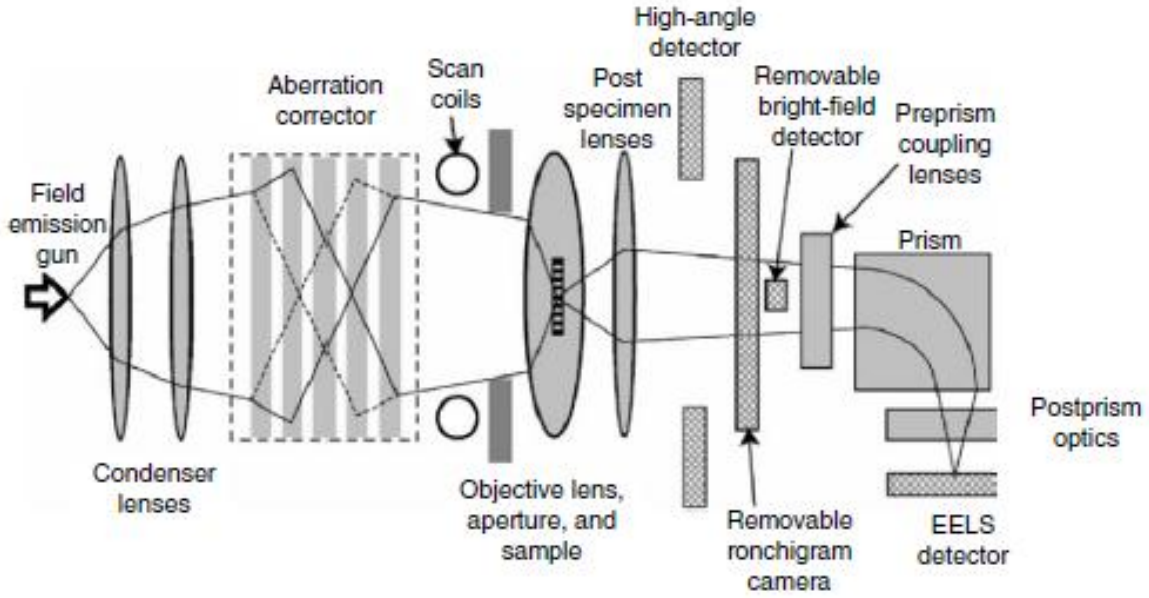

Figure 2.6 Illustration of the main components of a high-resolution dedicated STEM, adapted from (Pennycook et al., 2007)

Electrons are accelerated from a source (usually a heated tungsten filament, a LaB_6 pointed filament, a Schottky or thermal-assisted field emission source) and focused into a point on the specimen by a set of condenser lenses and an objective lens. The probe is serially scanned in a two dimensional raster across the specimen by the set of scan coils, just above the objective lens. The image formed can be collected by multiple detectors providing different but complementary information. The usual detectors include a bright field detector that intercepts the transmitted beam and an annular dark field (ADF) detector that surrounds the transmitted beam to collect scattered electrons. The number of electrons scattered at each point on the sample is fed into a computer that builds up an incoherent Z (atomic number) contrast image pixel by pixel. This is often referred to as a Z-contrast or high-angle ADF (HAADF) image**.** STEM when coupled with energy dispersive x-ray (EDX) and electron energy loss

spectroscopy (EELS) can provide elemental mapping and chemical composition with precision. It is discussed in the next section

2.3.3 Electron Energy Loss Spectroscopy (EELS)

In **electron energy loss spectroscopy** (**EELS**), a material is exposed to a beam of electrons with a known, narrow range of kinetic energies. Some of the electrons will undergo inelastic scattering, which means that they lose energy and have their paths slightly and randomly deflected (Figure 2.7).

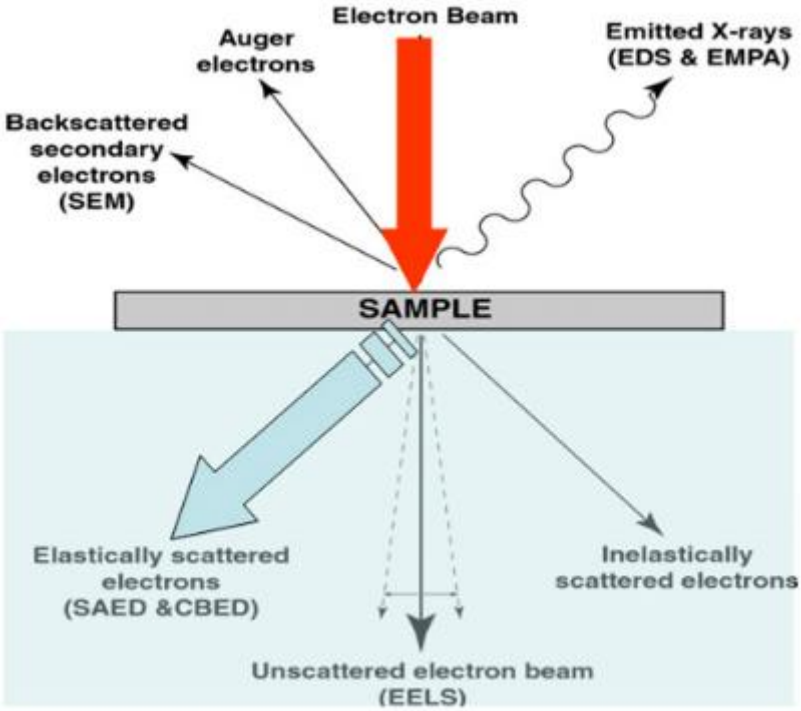

Figure 2.7 Illustration of the Electron Energy Loss Spectroscopy (EELS) principle

The amount of energy loss can be measured via an electron spectrometer and interpreted in terms of what caused the energy loss. So, EELS is based on the principle of loss of energy of the incident electron through the sample and is capable of measuring atomic composition, chemical bonding, valence and conduction band electronic properties, surface properties, and

element-specific pair distance distribution functions (Egerton, 1996) and also works well for low atomic numbers. Electron energy loss spectroscopy (EELS) coupled with TEM/ STEM (Scanning transmission electron microscopy) can provide chemical composition of the particles and especially in case of ceria, can provide oxidation state data with precision (Wu et al., 2004). Quantification of the spectrum enables determination of (local) concentrations of elements. The fine structure in the EELS spectra provides information on the chemical binding of the atoms involved. The combination of EELS and STEM allows 1-D and 2-D mapping of the lateral distribution of elements (Koninklijke, 2012).

EELS is considered to be a unique surface profiling technique as the scan can be selectively acquired at different points of a single particle and oxidation state can be assessed in a localised way. The technique has some disadvantages too. Long beam exposure durations lead to sample destruction. The results obtained also significantly depend upon the method used for the signals extraction and data processing.

Electron energy loss spectra (EELS) for this work has been generated using JEOL 2100F with CEOS GmbH hexapole STEM probe corrector coupled with an X-EDS from Oxford Instruments and EELS from Gatan, Inc. (Figure 2.8) This instrument is an advanced field emission electron microscope with an accelerating voltage of 80 to 200kV and can be operated in either TEM or STEM (scanning transmission electron microscope) mode. In general, TEM mode was used to obtain high resolution images and STEM mode was used to obtain EELS spectra for individual particles. A short EELS acquisition time of 2 s was used as we know that electron beam irradiation for longer periods may damage the particles and also result in the change of oxidation from Ce (IV) to Ce (III), due to loss of oxygen (Baalousha et al., 2012b). The STEM probe size was ~1 Å. The spatial resolution of the

EELS is comparable to that of the STEM probe size and the energy resolution of ~1 eV. The spectra were collected with a convergence angle of 2α = 8.2mrad, a collection angle of 2β = 8.9 and a 1.0 mm EELS aperture. The EELS data have been collected across the diameter of the particle in order to investigate the change in oxidation state as we go from the center of the particle towards the edge.

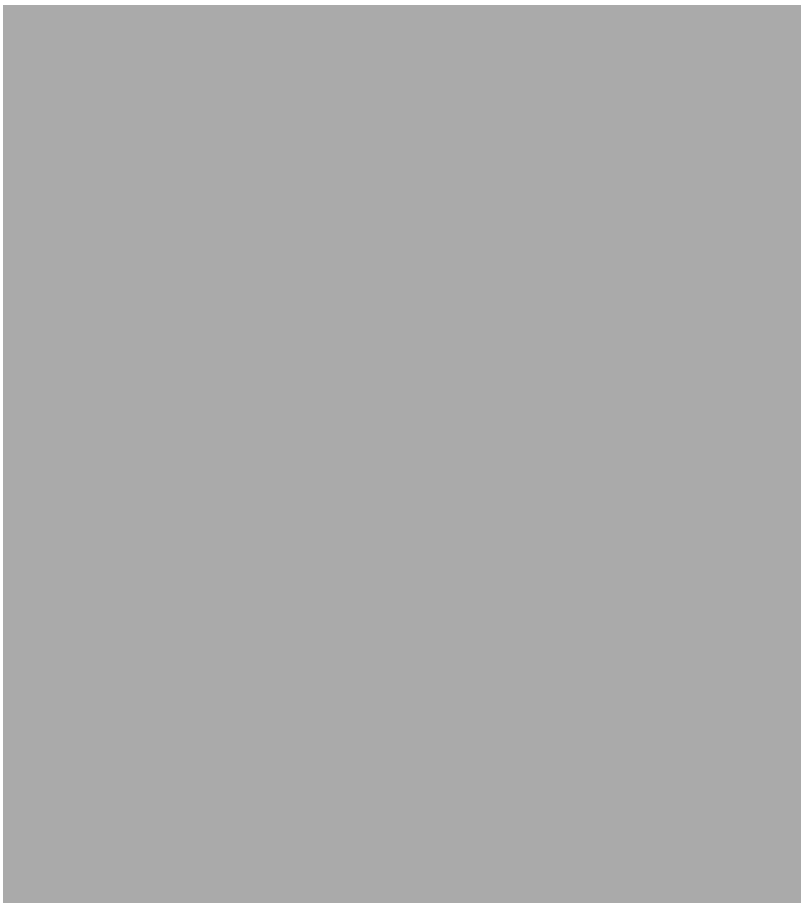

Figure 2.8 JEOL 2100F TEM (courtesy of http://www.jeolusa.com/)

Cerium oxidation states have been measured using Cerium M_5/M_4 white line ratios obtained from the EELS spectra, the two peaks at ~883 eV and ~901 eV indicated the cerium M5/M4 edge (double white line). $CeNO_3$ was used as a Ce (III) standard and bulk CeO_2 was used as a Ce(IV) standard. Ce (III) and Ce (IV) standards have been effectively used giving M_5/M_4 white line ratios of 1.23±0.05 and 0.82±0.03 respectively. These values agree with those previously calculated by others (Wu et al., 2004) (Merrifield et al., 2013) (Fortner et al.,

1997). These are high quality standards and have been previously used in our group and data published. A number of methods have already been developed to measure the M_5/M_4 ratios (Yang et al., 2006) (Manoubi et al., 1990) but in this work, the second derivative method have been used since it is insensitive to thickness variations (Fortner et al., 1997). Because of the noise in the spectra, the raw data of the spectra have been smoothed using the low-band pass smooth function and the M5/M4 ratios have been determined by extracting the integrated signal of the smoothed second derivative (Figure 2.9)

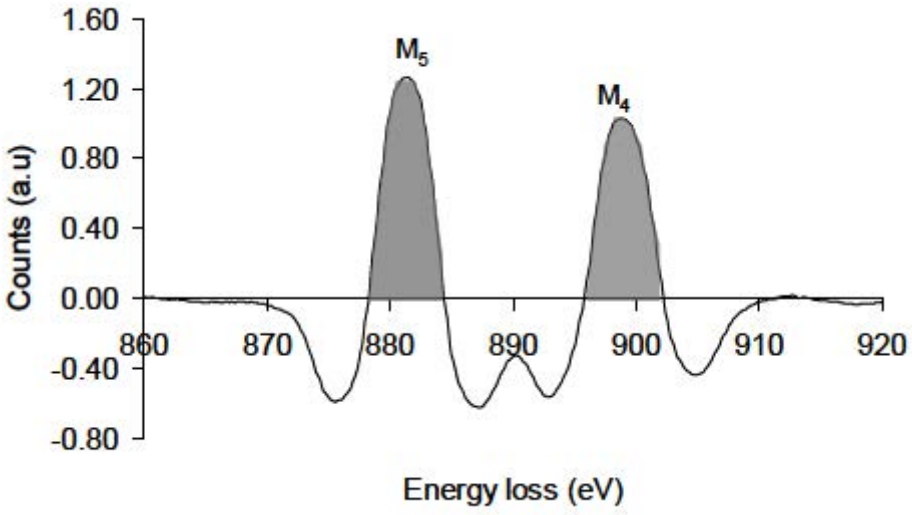

Figure 2.9 Typical electron energy loss spectroscopy spectra of Ce (III) standard, illustrating spectrum analysis procedure by second derivative (Baalousha et al., 2010)

It is also known that the relative intensity of the white lines (M_4 and M_5) of the cerium in the EELS can be used to determine the oxidation state of the ceria nanoparticles i.e a bigger M_5 peak corresponds to the presence of a significant Ce (III) oxidation state whereas it is the vice versa in case of a bigger M_4 peak (Figure 2.9). The EELS measurements and experiments are detailed in Chapter 4.

2.3.4 X-ray Photoelectron Spectroscopy (XPS)

X-ray photoemission spectroscopy (XPS) is another surface sensitive technique used to determine atomic compositions and learn information about the types of bonding within the specimen. It is a quantitative technique in which the number of electrons recorded for a given transition is proportional to the number of atoms at the surface and is interpreted in the form of spectra where each peak is a result of certain recorded binding energy. The technique, also known as ESCA (Electron Spectroscopy for Chemical Analysis), was first developed in the mid-1960s by Kai Siegbahn and his research group at the University of Uppsala, Sweden. The phenomenon is based on the photoelectric effect outlined by Einstein in 1905 where the energy of a photon of all types of electromagnetic radiation is given by the relationship E= hv, where h is planks constant and v is the frequency (in hertz) of the radiation however XPS, uses monochromatic sources of radiation, either Mg K_α radiation : hv = 1253.6 eV or Al K_α radiation : hv = 1486.6 eV, leading to ionization and the emission of a core shell electron from the top atomic layers of the surface of the material and the number of emitted photoelectrons as a function of their kinetic energies is measured using an energy analyser and a spectrum is recorded. Since these binding energies are a characteristic of a specific element and their peak intensities are related to the concentration of the element in the sampled region, quantitative information about the surface composition can be calculated with precision. The only drawback is that a variety of background algorithms are used to measure the peak area and therefore represent a source for uncertainty when computing the peak area.

X-ray photoelectron spectroscopy (XPS) measurements of the dry nanoparticle samples (powder) were performed using the high performance Kratos Axis Ultra DLD instrument equipped with a monochromated Al K_α x-ray source and hemispherical analyzer capable of

an energy resolution of 0.5 eV (Figure 2.10). The NP samples were placed on a standard sample stud using double-sided adhesive tape, and the takeoff angle was fixed at 90^0. Low resolution survey spectra were obtained over a binding energy range of 0.0 to 1200 eV. High-resolution spectra were obtained over a binding energy range of 870 to 925 eV using 0.1 eV increments. The binding energy (BE) scale was calibrated with respect to the C 1s at 285 eV.

The Ce 3d features were collected from reference material (CeO_2 and $CeNO_3$) and the peaks were investigated in order to determine the positions of various components and was deconvoluted using the peak fitting process in casaXPS softeware version 2.3.16 PR 1.6 (licensed to us). The relative amounts of Ce (III) and Ce (IV) have been calculated from XPS data by spectral curve fitting the Ce 3d binding energy region. Curve fittings have been done using shirley calculations in the casaXPS software using the procedure used by others in previous XPS studies of cerium oxide and of nanoceria (Deshpande et al., 2005).

Figure 2.10 X-ray photoelectron spectroscopy (XPS) instrument used in the study (Image courtesy, Shuguo Ma, college of engineering and computing , USC)

2.3.5 Dynamic Light Scattering (DLS)

Dynamic Light Scattering (DLS), also known Quasi-Elastic Light Scattering (QELS) or Photon-Correlation Spectroscopy (PCS), is a widely used, non-invasive technique to measure the size , size distribution and aggregation behaviour of particles in solution (Ledin, 1994). DLS is used across the spectrum of polymer and particle science, while synthetic chemist use it to understand the size of pristine particles as well as complex media, on the other hand biologist use it for proteins and other molecules. It is based on the principle of Brownian motion and measures light scattering and provides an intensity weighted average hydrodynamic diameter of a collection of particles (figure 2.11).

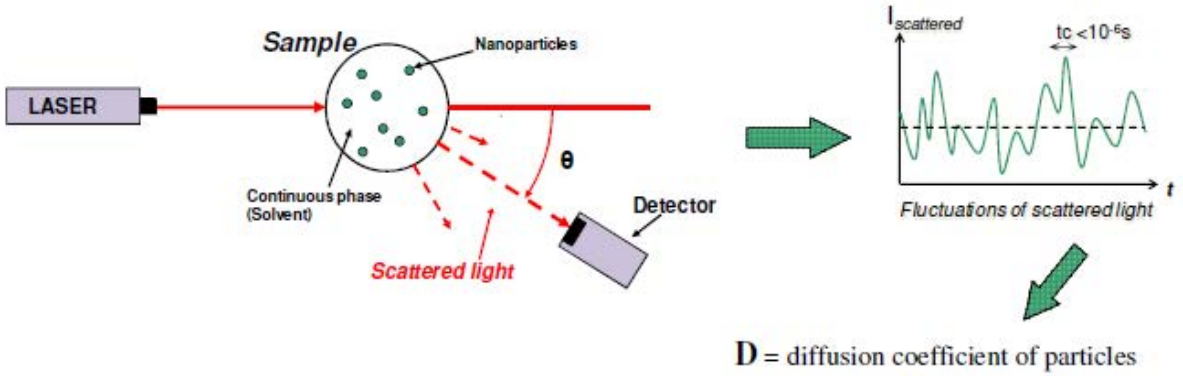

Figure 2.11 Illustration of the dynamic light scattering principle (Maxit, 2010)

It works on measuring the intensity of light scattered by the particles in the sample as a function of time. For example, when light is scattered by a particle, it would be constant if the particle was stationary. However, since all the particles in solution diffuse with Brownian motion in relation to the detector, there will be random changes (constructive and destructive) in the intensity of light scattered. So, by measuring the time scale of light intensity fluctuations, DLS can provide information regarding the average size, size distribution, and

polydispersity of particles in the solution. This Brownian motion of particles in the suspension is modelled by the Stokes-Einstein equation (2.1) below (Einstein, 1905)

$$D_h = \frac{k_B T}{3\pi\eta D_t} \tag{2.1}$$

Where D_h is the hydrodynamic diameter, D_t is the translational diffusion coefficient, k_B is Boltzmann's constant, T is thermodynamic temperature and η is dynamic viscosity of the solvent. The calculations are done within the instrument software. However, the equation does serve as an important reminder that the sample temperature and viscosity are important factors and that the particle size determined by DLS is the hydrodynamic size (Figure 2.12). The hydrodynamic diameter is reported as the intensity-weighted Z-average, with the polydispersity index width (PdI) representing the standard deviation about the Z average assuming a monomodal distribution (Darlington et al., 2009). The Z-Average size or Z-average mean used in dynamic light scattering is a parameter also known as the cumulants mean. It is insensitive to noise and is the primary and most stable parameter produced by the technique. The Z-Average defines the mean value as the _harmonic intensity averaged particle diameter'.

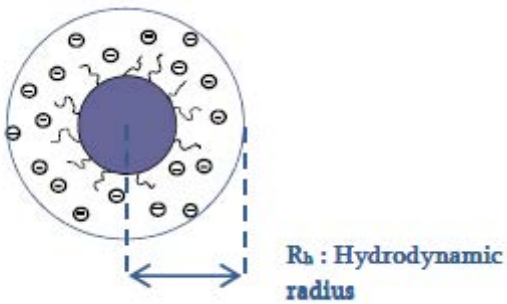

Figure 2.12 Hydrodynamic radius of a particles coated with ionic polymer (Maxit, 2010)

Advantages and disadvantages of the technique: An important characteristic of DLS is its ability to measure particles as they exist in solution. It provides size measurements from 1nm up to ten microns (Zetasizer nanao from Malvern). The instrument set up is simple and requires no sample preparation. The measurements are fully automated and can be carried out at samples with higher concentrations as well as turbid samples. The instrument offers repeatable particle size analysis in few minutes.

Although DLS provides fast, *in situ* analysis, it has certain limitations. Firstly, it is only applicable to fairly simple and homogeneous systems, so the data obtained from samples containing particles with heterogeneous size distributions is difficult to interpret (details below in section 2.3.5.1). The detection limits are at high particle concentrations ($1mgL^{-1}$) much higher than environmentally relevant concentrations (μgL^{-1} levels or less) (Gottschalk F, 2009). Secondly, DLS calculates particle size based on the assumption of spherical geometry and non-permeability less applicable to high aspect ratio systems. Also, the presence of dust particles or other undesirable particles could lead to interferences hence giving wrong results.

Figure 2.13 Zetasizer nano from Malvern instruments

2.3.5.1 The case of strong aggregation

In case of strong aggregation and high polydispersity, the Z-average values obtained from the instrument may vary significantly from the intensity distributed sizes. For a perfectly monodisperse sample, the two results should be the same, that is the z-average should be the same as the mean of the (one and only) peak in the distribution. In real applications, even for monodisperse samples, this is likely not the case and there will be small to large differences (Nobbmann, 2014).

Explanations for the three potential scenarios are:

(a) Z-average smaller than peak size: The cumulant fit only is to the initial part of the correlation function, so in a way, overemphasizes the initial decay from the smaller part of the distribution.

(b) Z-average the same as peak size: Ideal, probably monodisperse sample. In very odd situations it could be a very polydisperse sample where one of the peaks happens to match the overall average size.

(c) Z-average larger than peak size: The distribution shows a small and a large component, the average of the two is somewhere in between. Under peculiar circumstances, there may actually not be a smaller or a larger peak when the smaller peak is smaller than the lowest display cutoff and when the largest peak is larger than the large cutoff. This is a typical scenario of very large aggregates or particles sedimenting at different rates (Washington, 1992). High polydispersity index is another indicator of such systems. In this case, the intensity distribution result is recommended to quote instead of z-average. So for studies with a focus towards detecting strong aggregation, the recommended choice in most cases is the intensity

distribution values. However, this is a sensitive detector for the presence of large material in the sample.

Measurements in this work were obtained using Zetasizer nano from Malvern instruments and the hydrodynamic diameter (Z-average) was calculated (Figure 2.13). In case of discrepancy between the z- average and intensity distribution values obtained, intensity distribution result is quoted with a comment on the sample status. Standard operating procedure (SOP) files were created for cerium oxide nanoparticles using the refractive index value from the Malvern manual and also feeding in the absorption, viscosity and type of dispersant. Low volume disposable cuvettes were used throughout and the sample was injected using syringe or pipettes to avoid any air bubbles. At least three measurements were collected and averaged to report the size. The samples were equilibrated for 2 minutes and all the measurements were taken at 20^0C unless specified.

2.3.6 Electrophoretic mobility (EPM) and zeta potential (ZP)

Zeta potential is a measure of the magnitude of the electrostatic or charge repulsion/attraction between particles, and is one of the fundamental parameters known to affect stability. In particular, the concentration and type of ions and buffer species in solution, as well as the pH, strongly affect the zeta potential.

Electrophoretic light scattering (ELS) is a technique used to measure the electrophoretic mobility of particles in dispersion, or molecules in solution. This mobility is often converted to zeta potential to enable comparison of materials under different experimental conditions.

By directly measuring the electrophoretic mobility of a particle, the zeta potential may then be determined using the Henry Equation

$$U_E = \frac{2\varepsilon z f(Ka)}{3\eta} \quad (1)$$

Where U_E is the electrophoretic mobility, ε is the dielectric constant, z is the zeta potential, f(Ka) is Henry‘s function, and η is the viscosity.

In solution, the presence of a net charge on a particle affects the distribution of ions surrounding it, resulting in an increase in the concentration of counter-ions. The region over which this influence extends is called the electrical double layer (Zasoski, 2008) (Figure 2.14). It consists of an inner region of strongly bound ions known as the Stern layer and an outer layer of loosely associated ions called the diffuse layer. Due to an applied charge, the ions move with the particles in the solution but there is a 'boundary' beyond which the ions do not move with the particle. This is known as the surface of hydrodynamic shear, or the slipping plane, and exists somewhere within the diffuse layer. The potential that exists at this slipping plane or boundary is defined as the zeta potential. The zeta potential is positive for low pH values and negative for high pH values. The pH at which the zeta is zero is called the isoelectric point (IEP). When two particles come so close that their double layers overlap, they repel each other (Borm et al., 2006b). The strength of this electrostatic force depends on the zeta potential. If the zeta potential is too small (typically less than about 25 mV in magnitude), the repulsive force won‘t be strong enough to overcome the Van der Waals attraction between the particles and they will begin to agglomerate, the suspension is said to be unstable when this happens.

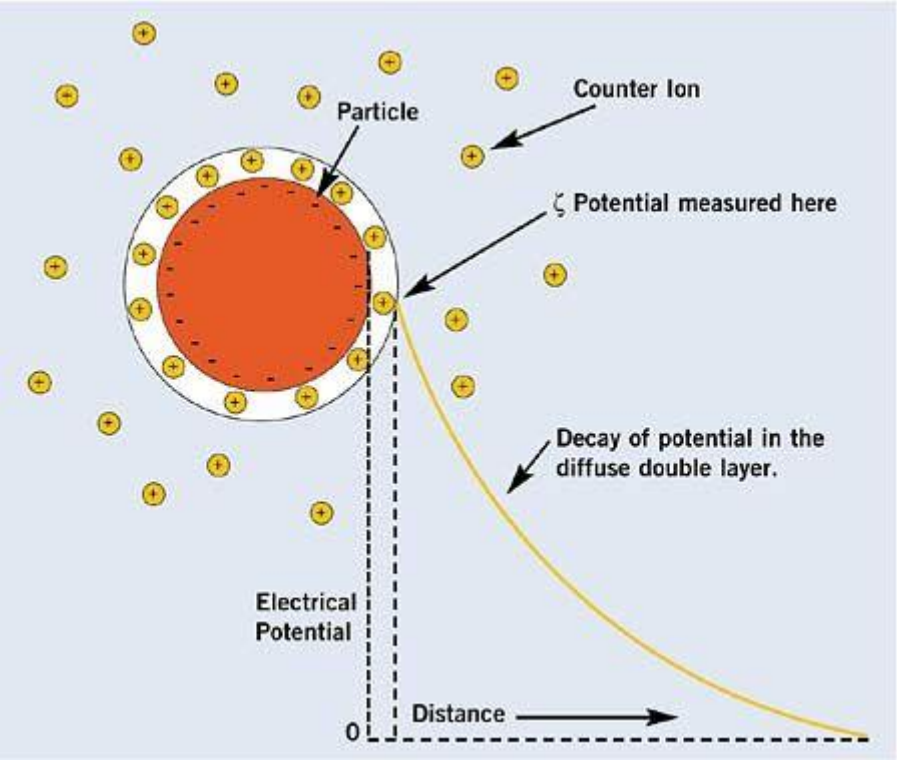

Figure 2.14 Schematic of the electrical double layer at the surface of solution-phase nanoparticles

2.3.7 Reflectance Confocal Microscopy (RCM)

The concept of confocal imaging was first developed and later patented by Marvin Minsky in 1957 (Minsky, 1988). In a conventional widefield microscope, a specimen is placed on microscope stage and the entire field of the specimen is illuminated by light and visualized. However, in confocal microscopy, the point of illumination is brought to focus in the specimen by the objective lens and laterally scanned using a scanning device within the computer (Figure 2.15). The sequences of points of light from the specimen are detected by a photomultiplier tube (PMT) through a pinhole, and the output from the PMT is displayed by the computer in the form of an image (Nikon) (Nwaneshiudu Adaobi, 2012). This technique allows the specimen to be imaged one –point" at a time. One of the main advantages is that unstained specimens can be viewed using light reflected back from the specimen. It provides

very-high-quality images with fine detail and more contrast than conventional microscopy. It can be utilized to gather additional structural information from a specimen by reconstructing the virtual 3D image of the specimen when multiple sections are combined. The specimen preparation is fairly simple and requires minimum effort however; the technique is costlier than conventional microscopes.

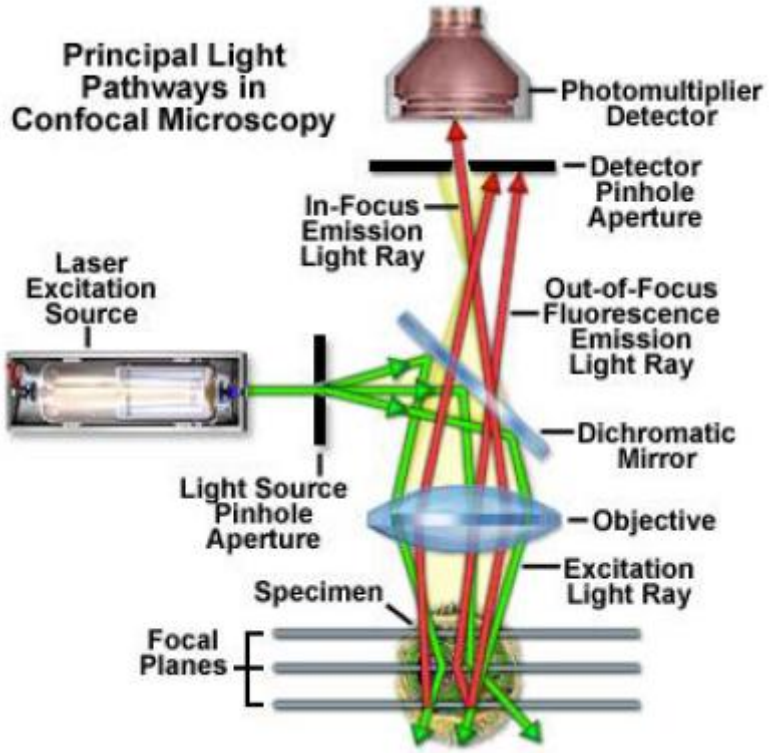

Figure 2.0.15 Simplified view of confocal microscope (Nikon)

Reflectance Confocal Microscopy (RCM) was used in this work to detect the aggregation behaviour and visualise the uptake and internalisation of ceria nanoparticles by the human lung epithelial cells (also known as HeLa A549 cells). Reflectance confocal image acquisitions were obtained using the laser 488 and the reflectance option from confocal

microscope (Zeiss LSM 710 Confocor 3) equipped with an oil immersion objective (PLAPO 63x/1.40 oil DIC M27). Z-series of images were taken at 0.2 μm increment.

2.4 Summary

The characterization of ceria nanoparticles has been performed using a combination of techniques listed above and is a part of a multimethod strategy to understand and quantify the size, shape and oxidation state of the synthesised ceria NPs. The techniques used and the parameters obtained have been summed below (Table 2.1)

Table 2.1 List of characterisation techniques being used as a part of multi-method approach

Analytical Techniques	Particle Size	Particle Size Distribution	Surface Charge	Oxidation state	Shape	Agglomeration	Structure	Composition
DLS	■	■				■		
TEM	■	■			■	■	■	■
Zeta Potential by Zetasizer-nano			■					
XPS				■				
STEM+EELS				■	■		■	■

3 Synthesis and characterisation of ceria nanoparticles

3.1 Chapter summary

As discussed above in Chapter 1, there are scattered observations in literature about the behaviour such as oxidant/antioxidant activity of nanoceria (Chapter 1, sections 1.2.8 and 1.2.9). Differences in behaviour could be attributed to many factors, such as the origin of the precursors used to synthesise these nanoparticles, presence/absence of a capping agent, reaction conditions for example, whether the synthesis was carried out under low/ high /room temperature conditions, what were the physical and chemical properties of the nanoparticles formed (synthesis dependent) and the amount of Ce (III) and Ce (IV) present in the sample. It is also known that nanoceria is capable of oxygen storage, which is size and shape dependent (Mai et al., 2005). So there is an emerging need to understand the chemistry of these nanoparticles in both their synthesized form as well as their evolvement through applications.

In this project, we have tried to address some of these issues. A systematic study has been carried out to look into the effects of some of the potential thermodynamic variables such as precursors and their concentrations, preparation methods, synthesis temperature and sample processing. Ceria nanoparticles of various shapes and sizes have been synthesised using different forms of cerium salts and reducing agents as precursors. Amongst other differences between syntheses, the synthetic procedures have been performed both in the presence and absence of a capping agent. The reactions have been monitored at different concentrations of the precursors and temperature of the reaction mixtures and a batch of samples have been obtained. These nanoparticles are quite stable when dispersed in D.I water. The samples have been characterised for their size, shape, aggregation, surface charge, composition and

oxidation state using a combination of existing techniques such as DLS, TEM, STEM-EELS, XPS along with XAS. This chapter covers the characterisation using DLS and TEM.

3.2 Types of synthesis

Over the past few years, many methods have been proposed to produce the ceria NPs, such as sol–gel process (Niederberger, 2007, Laberty-Robert et al., 2005), hydrothermal or solvothermal synthesis (Hakuta et al., 1998, Hirano and Kato, 1999, Uekawa et al., 2004, Wu et al., 2002, Verdon et al., 1995), forced hydrolysis (Dong, 1997), microemulsion (Masui et al., 1997), homogenous precipitation (Polezhaeva et al., 2008) etc. Most of these methods are employed for small scale quantities. The industrial scale production has been discussed in chapter 1.

3.2.1 Hydrothermal and solvothermal synthesis

A typical hydrothermal synthesis utilizes single or heterogeneous phase reactions in aqueous media at elevated temperature and pressure to crystallize the metal oxide directly from solution (Riman et al., 2002). However, if the water is replaced by a non-aqueous solvent such as alcohols, it is termed as solvothermal synthesis. Typical sol-gel processing consists of hydrolysis and condensation of precursors. It is a multi-step process occurring sequentially and in parallel.

3.2.2 Microemulsion synthesis

Microemulsion synthesis typically involves a colloidal ‗nano-dispersion' of water in oil (or oil in water) stabilized by a surfactant film which can be used to carry out synthesis of nanoparticles (Bumajdad et al., 2009). So microemulsions are nearly transparent quasi-homogeneous, thermodynamically stable mixtures of two immiscible liquids, one is polar such as water and the other is non-polar, such as an organic oil, stabilized by surfactants (or mixture of surfactants).

3.2.3 Hydrolysis

Forced hydrolysis is another popular technique used in industrial applications because of its cheap raw materials, ease of handling and large-scale production. Hydrolysis means cleavage of chemical bonds by the addition of water. A typical forced hydrolysis synthesis involves a carbonyl group carrying ester or amide, alcohol as solvent, a strong base such as ammonia, and desired amount of water. It is called thermal hydrolysis when involves the reaction of cerium(IV) ammonium nitrate $(NH4)_2Ce(NO_3)_4$ with ammonia or other stronger base such as sodium hydroxide at elevated temperatures (Lu et al., 2013, Hirano et al., 2000).

3.2.4 Precipitation method

Precipitation method is one of the simplest processes for the synthesis and scale up of nanoceria (Sahu et al., 2013). They are further categorised into aqueous precipitation (typically involves an aqueous solution of a surfactant such as PEG and cerium nitrate $(Ce(NO_3)_3.6H_2O)$ along with hydrogen peroxide stirred at high temperatures), homogenous precipitation (synthesis involves mixing of equi-volume solutions of cerium nitrate with HMTA or ammonia) (Polezhaeva et al., 2008), co-precipitation (typically involves aging of

solutions containing cerium nitrate after treatment with elevated temperatures (100 ^{0}C) for 5 hrs). The precipitation method is attractive because it can produce fine, spherical particles with improved chemical purity, better chemical homogeneity and controlled particle size.

3.2.5 Sonochemical method

Sonochemical method is another method widely used in the synthesis of nanoparticles. Sonochemistry is the process of generating cavitations, which involves the creation, growth and collapse of bubbles (often called hot spots) formed in the liquid due to the irradiation of high intensity ultra sound (Yin et al., 2002). In laboratory, this process is used in the sonicator. There is no direct interaction of ultrasound field with the chemical species and the chemical reaction is driven by the cavitation effects caused by the agitation of the liquid. The enormous local temperature, pressure and extraordinary heating/cooling rates generated by cavitational collapse provide an unusual mechanism for generating high energy chemistry.

3.3 Synthesis strategy and research design

In this study, we have used hydrolysis, precipitation and sonochemical methods for the production of ceria NPs. Typically, these synthetic strategies involve a cerium precursor and an oxidant to convert the cerous ion Ce (III) to less soluble ceric ion Ce (IV) along with the presence of a stabiliser. However, in some cases, the latter plays a dual role of a stabiliser as well as an oxidiser. The general reaction mechanism is based on the concept of preparation of nanoparticle dispersion by condensation from previous supersaturated solution (LaMer and Dinegar, 1950) and is mediated by the formation of $Ce(OH)_3$ as intermediate. Detailed mechanism has been discussed in Chapter 1, section 1.2.4.

A systematic study has been carried out to look into the effects of some of the potential thermodynamic variables such as types of precursors and their concentrations, capping agents, preparation methods, synthesis temperature and sample processing as they are known to influence both reaction and crystallization kinetics. Thermodynamic variables are known to affect the overall nucleation and growth rates, which control crystal size and morphology, so the reaction conditions have been carefully monitored and documented. We have also looked into the non-thermodynamic variables such as addition speed of the oxidant in the reaction mixture, stirring speed and sonication time as they are also known to influence the particle size by orders of magnitude (Suchanek et al., 2005, Farré et al., 2009).

Characterization of the synthesised NPs has been carried out using different microscopic and spectroscopic techniques. This chapter covers the characterisation using DLS and TEM. STEM+EELS along with XPS have been used to quantify ceria oxidation states and have been discussed in detail in Chapter 4. All the synthesis and characterisation has been carried out by myself.

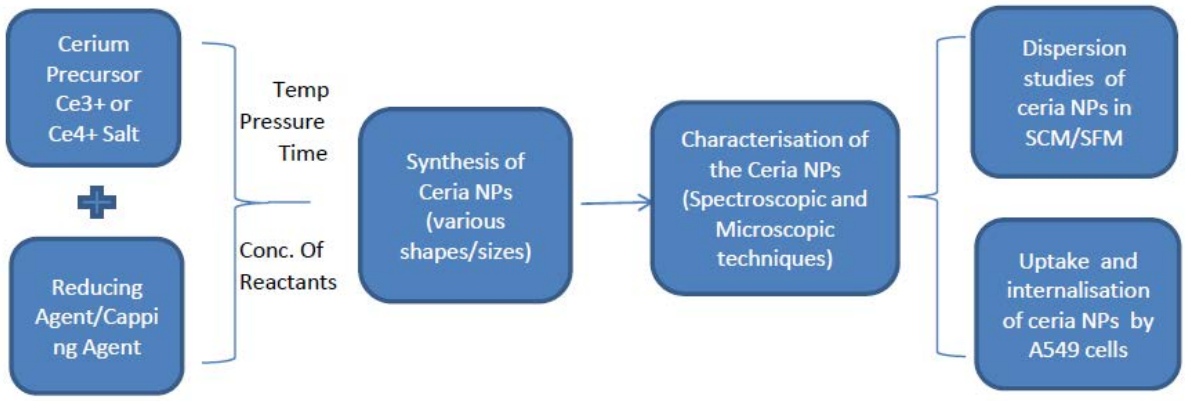

Figure 3.1 Research design

3.3.1 Aims and objectives

1. Synthesis of shape and size selected ceria nanoparticles, both with and without capping agents.

2. Physico-chemical characterization of the manufactured ceria nanoparticles for their size, shape, aggregation, surface charge, composition and oxidation state.

3. Quantification of the Ce (III) and Ce (IV) ratios in as-synthesised samples using STEM-EELS and XPS and the technique comparison.

4. Dispersion and aggregation studies of ceria nanoparticles in cell culture media which is serum containg media (SCM) and serum free media (SFM)

5. Uptake and internalisation studies of ceria NPs in human lung epithelial cells (Adenocarcinomic human alveolar basal epithelial cells, A549)

Aim 1 and 2 has been discussed here whereas aim 3, 4 and 5 has been discussed in chapter 4 and 5 respectively (Research design, figure 3.1).

3.3.2 Materials and methodology

All the chemicals used in this study were Analytical Reagent (AR) grade and used without further purification and all water used in the experiments was ultrapure with the resistivity of of 18 (MΩ.cm). The various precursors and stabilisers used are:

Cerium nitrate hexahydrate: $Ce(NO_3)_3 \cdot 6H_2O$

Ammonium Ce(IV) nitrate

Sodium hydroxide

Ammonium hydroxide

Hexamethylene tetramine (HMTA)

Polyethylene glycol (PEG): Molecular weights used are 600 and 1500

Ethylenediamine

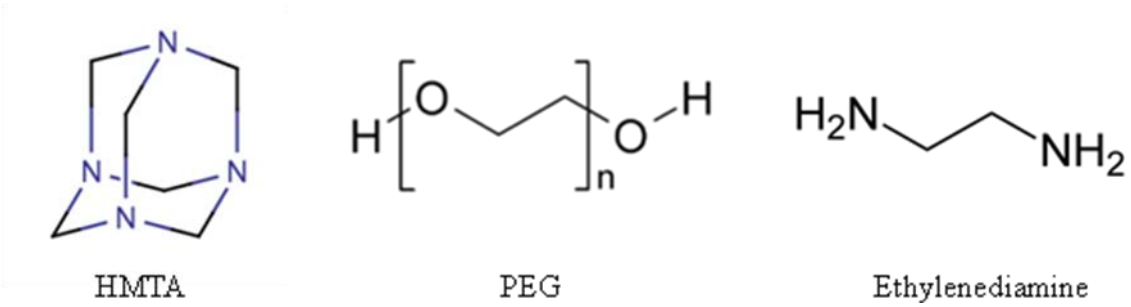

We understand that small changes in synthetic conditions could lead to dramatic changes in particle properties, so we have synthesised similar type of shapes and sizes using different methodologies and looked at their properties in order to identify the synthesis dependent changes.

3.4 Experimental section

3.4.1 Synthesis 1: Homogenous precipitation

Ceria nanoparticles were prepared using a modified method as described in (Polezhaeva et al., 2008), by precipitating CeO_2 from aqueous solutions of cerium(III) nitrate hexahydrate and hexamethylene tetramine (HMTA). The starting chemicals used were $Ce(NO_3)_3 \cdot 6H_2O$ and HMTA. The initial cerium nitrate concentration was, 0.065, 0.08, and 0.1 M; and the initial HMTA concentration was 0.0750, 0.15, and 0.3 M. The solutions were mixed in molar ratios of 1: 10, 1 : 20, and 1 : 40 and were then left standing at room temperature for 24 h, followed by thermostating at a temperature range of 50-80°C for 7hrs. The solutions were

magnetically stirred during thermostating. The contents were cooled down at room temperature and the solutions were kept for ageing overnight. The particles were recovered by centrifugation followed by washing in ethyl alcohol and finally with water. The particles were re-dispersed in ultrapure water.

3.4.1.1 Results and discussion

The 1: 10 and 1: 20 molar ratio solutions became turbid after 15-20 minutes of heating at 70 °C (along with continuous stirring). However, the 1 : 40 molar ratio solution was initially yellow in colour and gradually turned turbid after one hour of heating. The nanoparticles obtained are cubic in structure. The experiments were carried out by changing the concentration of the precursors as well as the reaction temperatures. It was observed that changing the temperature of the reaction from 50-80°C did not have any major effect on the shape and size of the nanocubes formed. However, changing the concentration of the precursors yielded nanocubes of three different sizes. It was observed that increasing the ratio of HMTA yielded nanocubes of smaller sizes however cerium(III) nitrate hexahydrate concentration had very little or almost no effect on the NPs formed. For example when the aqueous solutions of cerium(III) nitrate hexahydrate and hexamethylene tetramine (HMTA) were mixed in the ratio of 1 : 10 and heated at a temperature of 70 °C for 7hrs, nanocubes of size of 30.8±7.3 nm (TEM) were formed. For this work, the sample has been labelled as C1 whereas under similar condition, when the precursors were mixed in the ratio of 1 : 20 and 1 : 40, the particle size decreased to 20.6±7.3 and 15.8±4.6 nm (TEM) respectively (labelled as C2 and C3 respectively). However, all the three samples retained the same nanocubic shape. The pH of the final dispersions is +6.9 (C1), +7.1 (C2) and +7.2 (C3). The exact mechanism of this reaction is not known. However, it is believed that HMTA slowly hydrolyzes in

aqueous solutions to form ammonium hydroxide and formaldehyde and ceria NPs are formed through intermediate compounds such as insoluble Ce(III) carbonates and hydroxycarbonates, which are stable at low temperatures but rapidly oxidize to form cerium oxide at higher temperatures (Polezhaeva et al., 2008). The low and high resolution TEM micrographs (Figure 3.3 and 3.4) clearly illustrate the sizing in ceria particles formed as a function of the change in the concentration of the precursors. The crystallinity of the NPs was determined using high resolution transmission electron microscopic (HRTEM) studies. Figure 3.2 illustrates the size distribution by intensity data obtained by DLS. The results are summarised in table 3.1. Shape and size quantification has been carried out using image J® software. In all cases, at least 100 NPs were analyzed from TEM images to construct a representative shape and particle size distribution (Figure 3.5). All the three samples are very stable when dispersed in ultrapure water and stay stable up to three months when kept at 5 °C in the refrigerator. The DLS data 3/6 months post synthesis has been illustrated in Figure 3.2 and table 3.1. The experimental sizes as calculated by DLS indicate that in all the three samples except C2, the polydispersity index (PDI) significantly increases after 6 months of production confirming that the samples were aggregating.

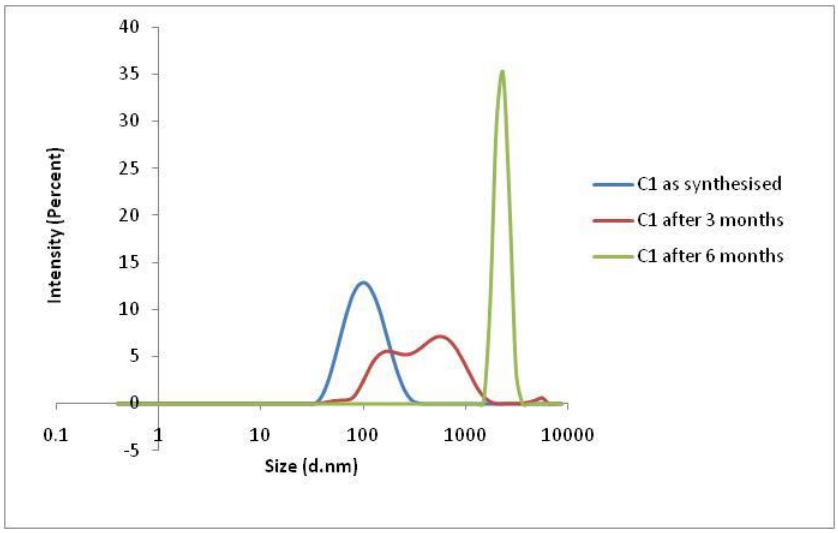

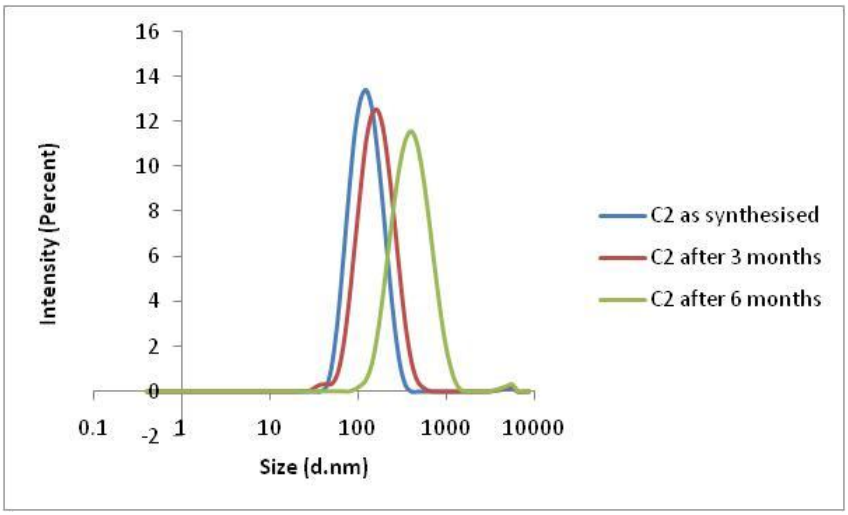

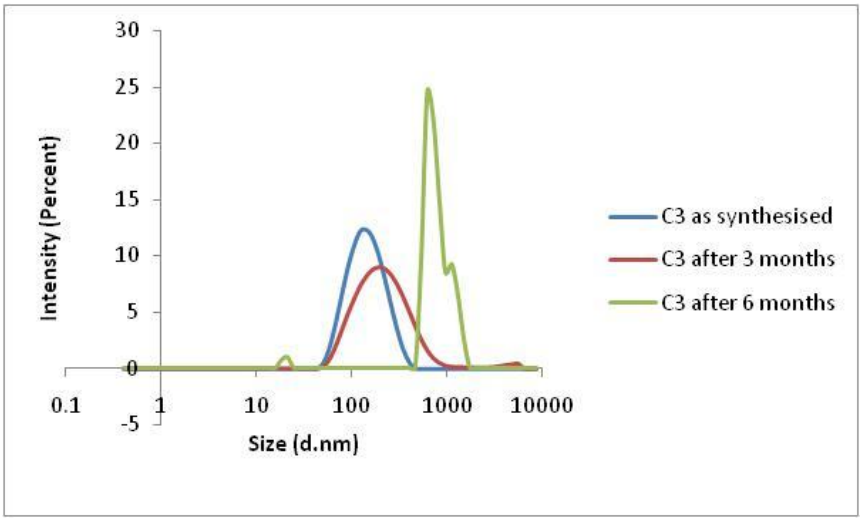

Figure 3.2 Size distributions by intensity obtained with DLS for nanocubes (C1-3), each coloured line represents an average of minimum three measurements

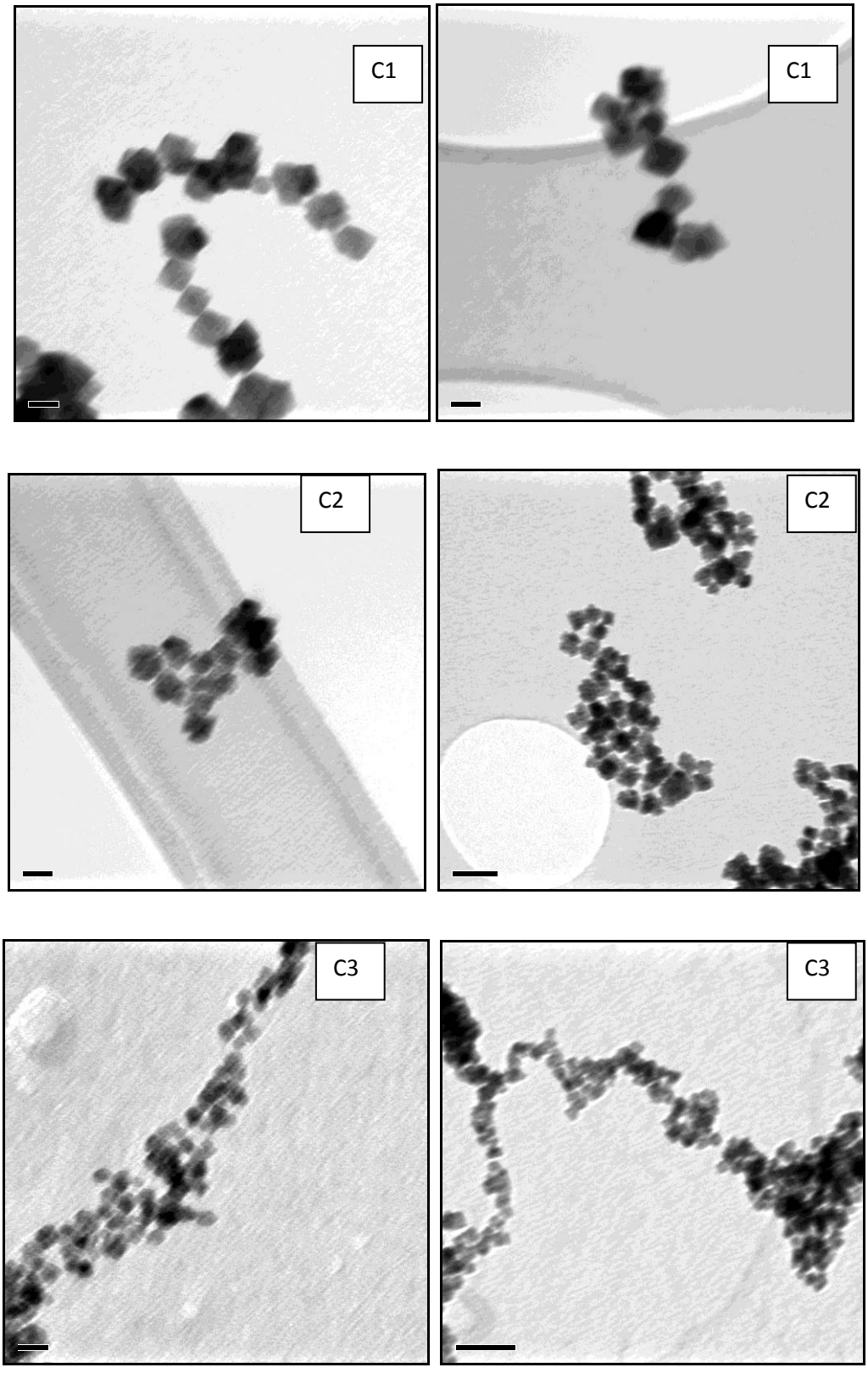

Figure 3.3 Bright field TEM images of the synthesised nanocubes (C1-3)

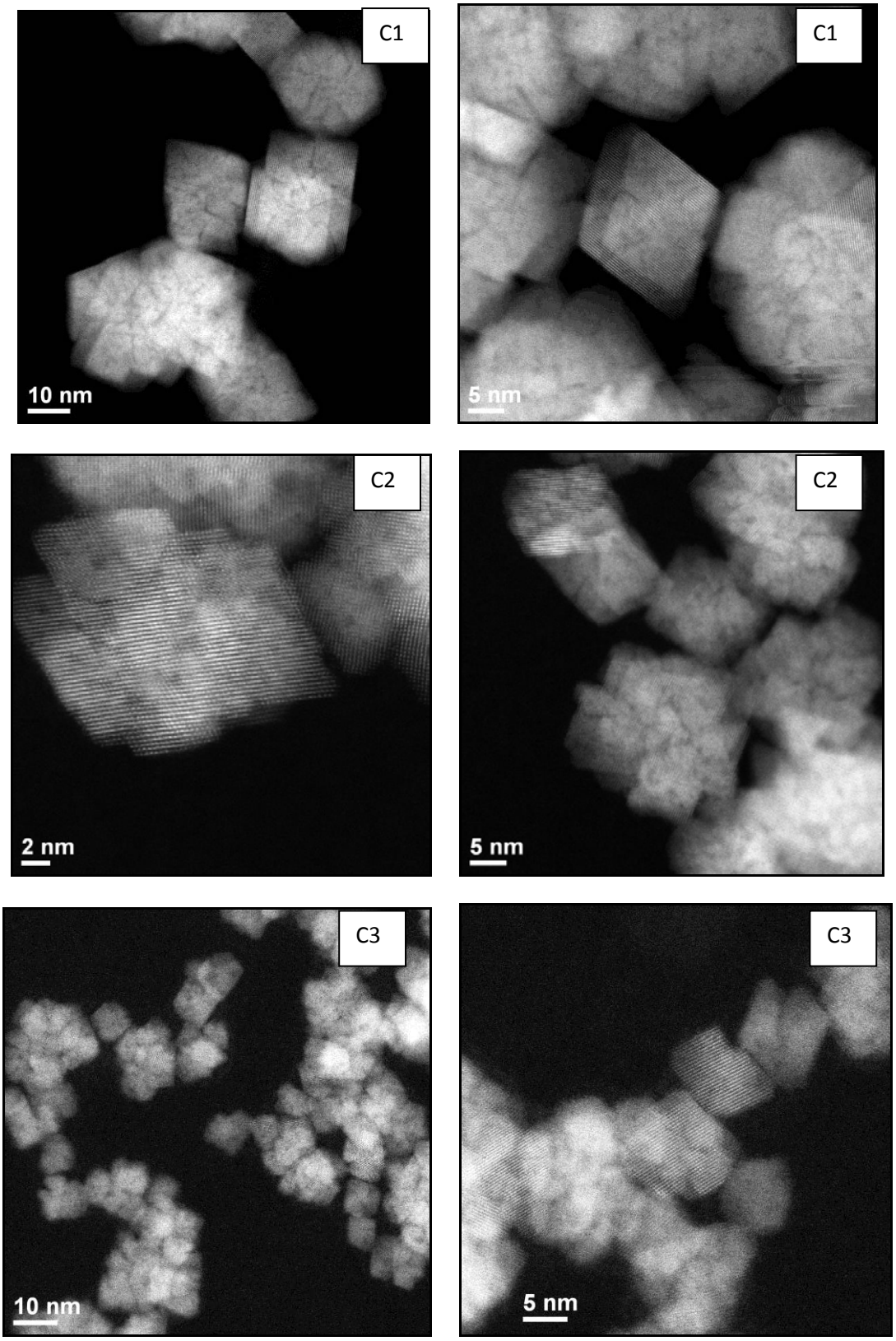

Figure 3.4 Dark field high resolution TEM images of the synthesised nanocubes (C1-3)

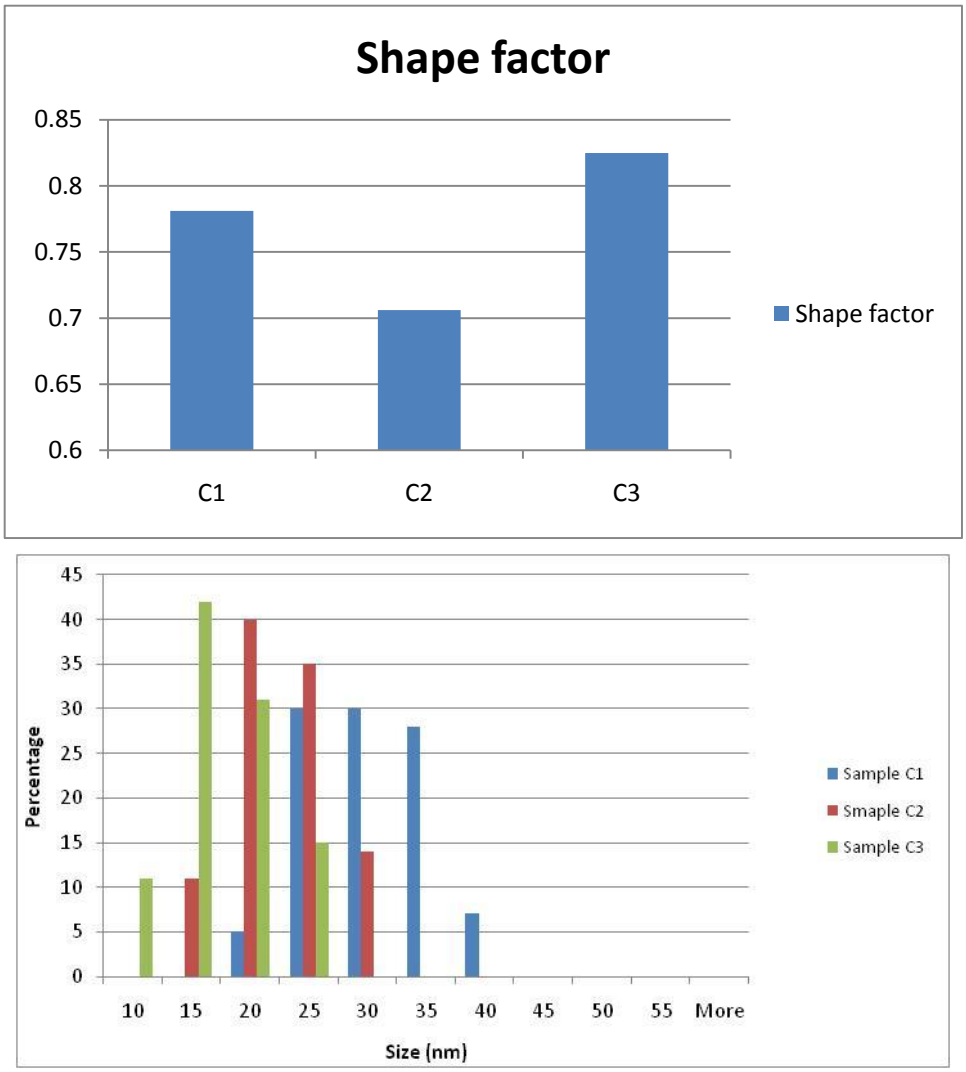

Figure 3.5 Histograms showing shape and size distributions for nanocubes (C1-3)

Table 3.1 Results from synthesis 1

Sample code	Morphology	Shape Factor	Size (nm)		Stability by DLS (nm)		Zeta-Potential (mV)
			DLS	TEM	3 months	6 months	
C1	Nanocube	0.78±0.17	93.7±0.8 PdI- 0.152	30.8±7.3	289±5 PdI- 0.373	2305±285 PdI- 0.316	+ 5.7±0.1 at pH+6.9
C2	Nanocube	0.70±0.23	113.4±0.5 PdI- 0.150	20.6±7.3	152±5 PdI- 0.226	317±28 PdI- 0.203	+ 26.9±1.7 at pH+7.1
C3	Nanocube	0.82±0.13	132.8±3.2 PdI- 0.115	15.8±4.6	166±6 PdI- 0.241	1736±372 PdI- 0.671	-2.2±0.3 at pH+7.2

3.4.2 Synthesis 2: Sonochemical synthesis

The synthetic scheme has been adapted from (Zhang, 2007). In a typical synthesis, 1.25g of cerium nitrate hexahydrate was first dissolved in 15ml of ultra pure water. To this solution, polyethylene glycol (PEG) molecular weight 1500 (250 mg in 10ml of water) was dispersed by ultrasonication at room temperature, and then NaOH solution (250mg in 50ml water) was added gradually (5 ml min^{-1}) into the above mixed solutions with vigorous stirring during the ultrasonication until the pH value was 10. Finally, the mixture solution was further sonicated for 4 hours and the solution was kept for ageing overnight. Ceria nanoparticles were

recovered by centrifugation after repeated washings with alcohol to get rid of any excess PEG 1500 (molecular weight). The particles were re-dispersed in ultrapure water.

3.4.2.1 Results and discussion

The nanoparticles obtained by the above method are spherical in shape. The solutions started turning turbid with the gradual addition (5 ml min^{-1}) of NaOH solution and intermittently had an appearance of purplish tinge in them. We believe that ultrasonication accelerates the release of OH^- groups, resulting in immediate reaction to form a stable cerium oxide suspension. The experiment has also been carried out by raising the temperature of the reaction mixture however, it resulted in larger aggregates. This could be attributed to the degradation of PEG at higher temperatures or to the fact that steric hindrance of PEG is relatively weaker at higher temperatures and so it is weakly adsorbed onto the particle surface. So, it was made sure that the temperature of the ultrasonic bath stayed constant (at room temperature) throughout the experiment. This was done by changing the water of the ultrasonic bath every 30 minutes. It was also observed that addition of the sodium hydroxide solution at a higher rate (10 ml min^{-1}) also leads to aggregation whereas slow (5ml min^{-1}) addition of the NaOH solution with vigorous stirring during ultrasonication leads to well dispersed stable particles. The experiment was also performed by changing the molecular weight (MW) of the capping agent used. So PEG 1500 (MW) as well as PEG 600 (MW) have been used and both yielded monodisperse spherical nanospheres. They have been named as S1 and S2 respectively. The experimental pH of the samples S1 and S2 is + 7.9 and + 7.3 respectively. The size and morphology of the as-synthesised samples have been obtained using high resolution TEM images, Figure 3.6 and 3.8 respectively, and the hydrodynamic diameter has also been obtained using DLS (figure 3.7 and 3.9). Shape and size quantification

has been carried out using image J® software. The size, shape, morphology and zeta potential data as well as the stability data after 3 and 6 months of synthesis is tabulated in table 3.2. According to the experimental data, both the samples are very stable when dispersed in ultrapure water and stay stable up to six months when kept at 5 °C in the refrigerator. The DLS data 3/6 months post synthesis has been illustrated in Figure 3.7 and 3.9 and table 3.2.

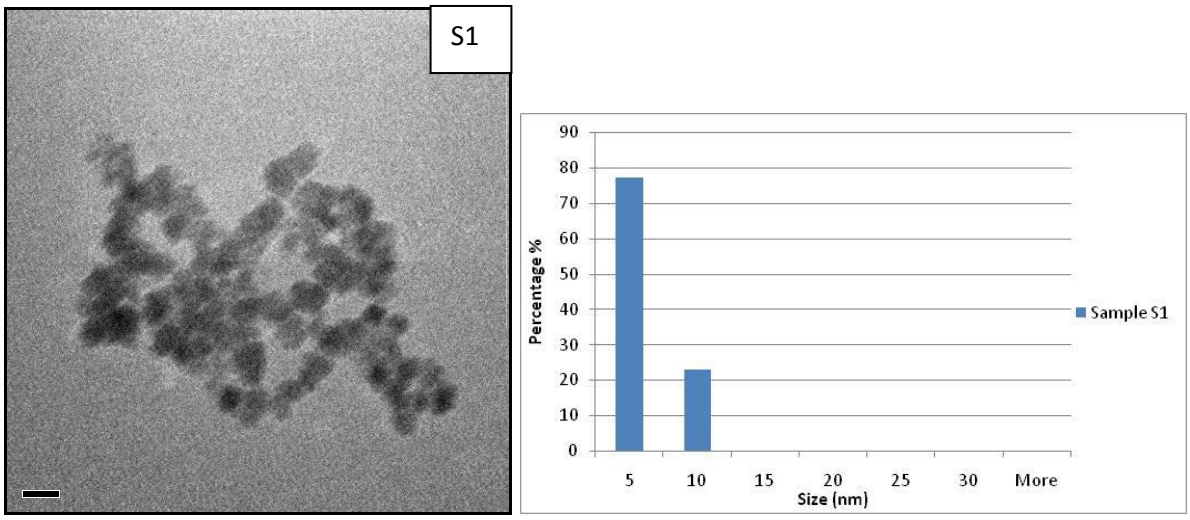

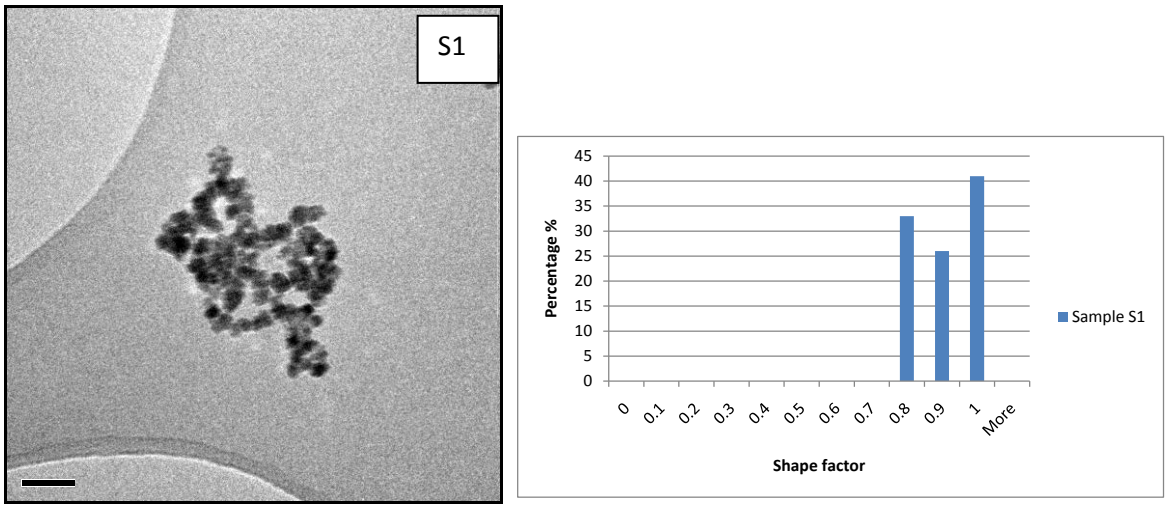

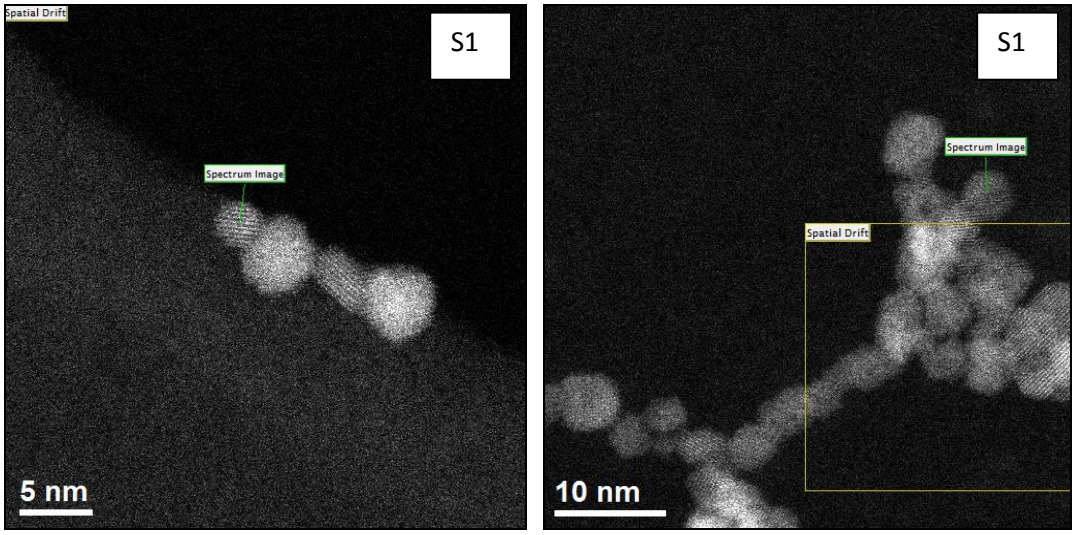

Figure 3.6 Bright field and dark field high resolution TEM images along with histograms showing shape and size distributions for nanospheres (S1)

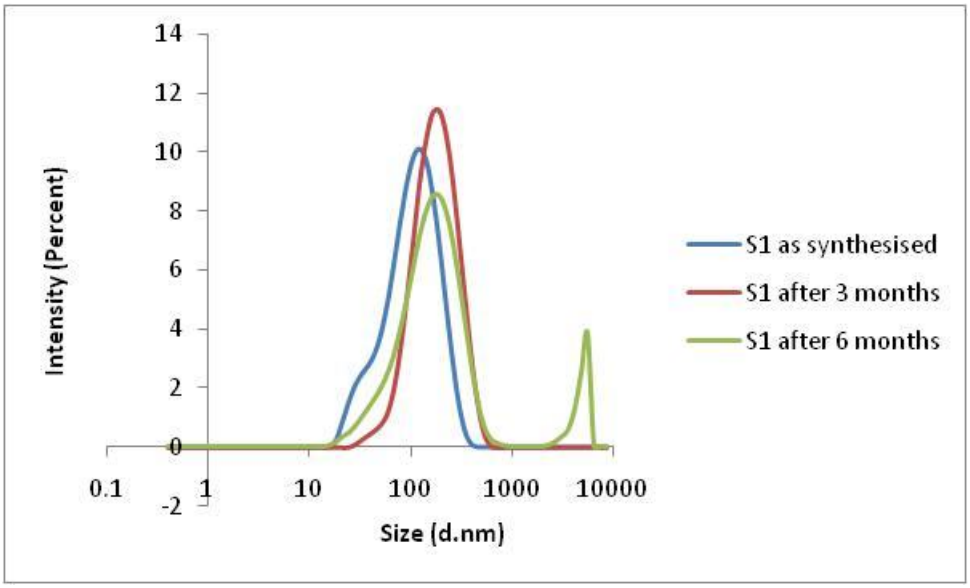

Figure 3.7 Size distribution by intensity obtained with DLS for nanospheres (S1), each coloured line represents an average of minimum three measurements

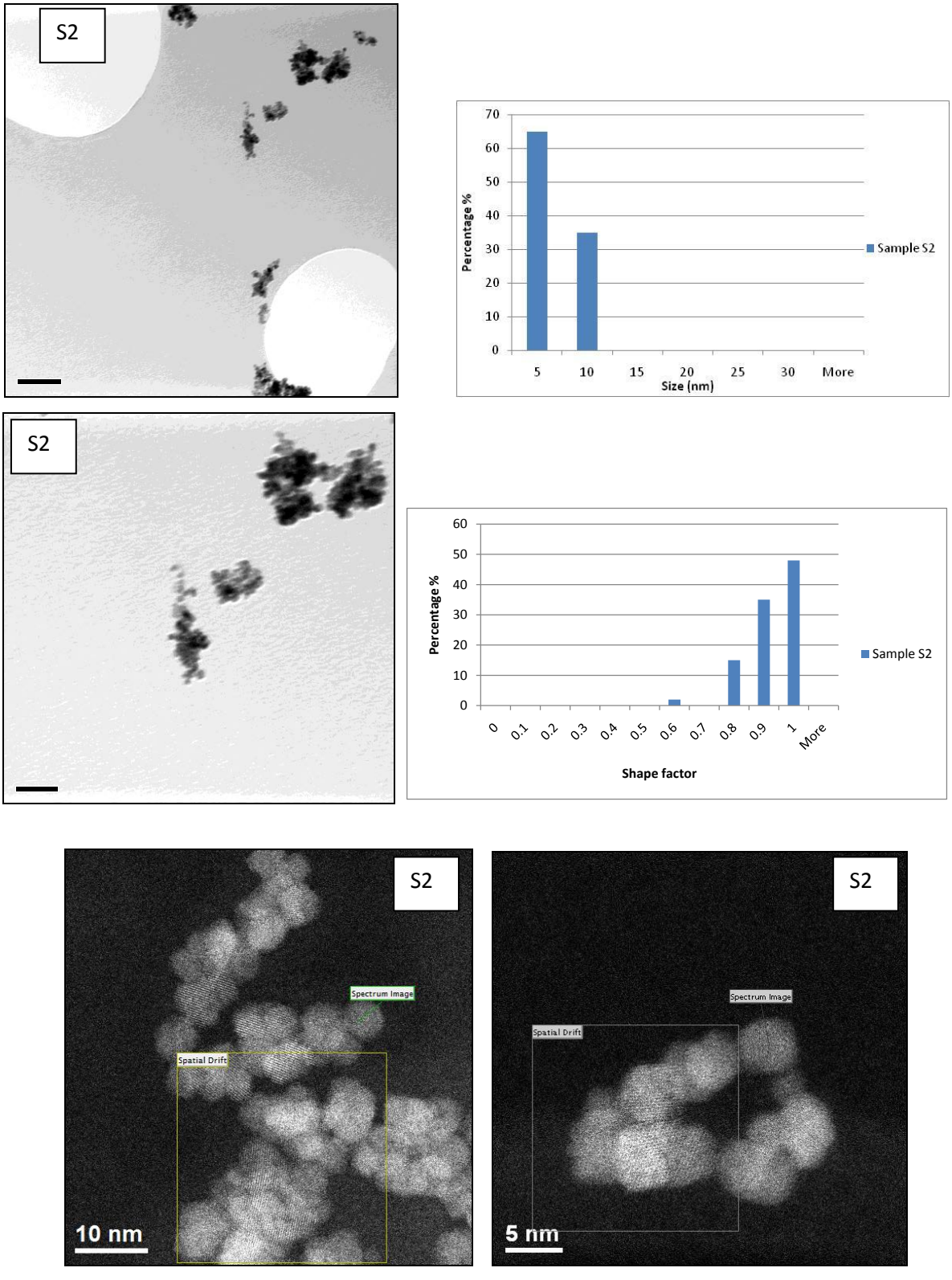

Figure 3.8 Bright field and dark field high resolution TEM images along with histograms showing shape and size distributions for nanospheres (S2)

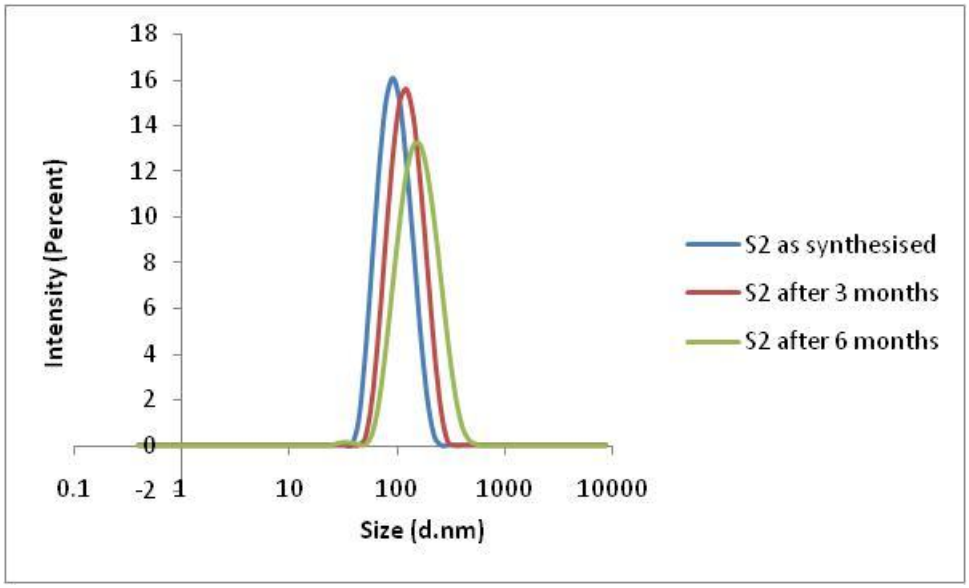

Figure 3.9 Size distributions by intensity obtained with DLS for nanospheres (S2), each coloured line represents an average of minimum three measurements

Table 3.2 Results from synthesis 2

Sample code	Morphology	Shape Factor	Size (nm)		Stability by DLS (nm)		Zeta Potential (mV)
			DLS	TEM	3 months	6 months	
S1	Nanosphere	0.89±0.09	85.5±0.4 PdI:0.247	4.5±2.5	150±2 PdI:0.222	157±5 PdI:0.537	0.024±0.012 at pH +7.9
S2	Nanosphere	0.86±0.09	89.0±0.3 PdI:0.092	6.0±3.0	116±2 PdI:0.108	138±4 PdI:0.132	0.094±0.023 at pH +7.3

3.4.3 Synthesis 3: Homogenous precipitation (scheme a), Co-precipitation (scheme b and c)

Ceria nanoparticles were prepared using a modified method as described in (Kar, 2009).

Scheme a - In a typical synthesis, 0.234 g of Ce $(NO_3)_3.6H_2O$ was first taken in a round bottom flask. To this, 32 mL of ethylenediamine was added by continuous stirring and the reaction mixture was stirred on a magnetic plate for 24 hours at room temperature. The thick dark yellow contents were poured down in a centrifuge tube and the ceria NPs were recovered by centrifugation followed by washing in ethyl alcohol and finally with water. The particles were re-dispersed in DI water to obtain a faint yellow solution.

Scheme b - The same experiment was repeated at 100 °C. In a typical synthesis, 0.234 g of Ce $(NO_3)_3.6H_2O$ was first taken in a round bottom flask. To this solution, 32 mL of ethylenediamine was added by continuous stirring and the reaction mixture was refluxed using a condenser at 100^0C for 7hrs (Figure 3.10). The dark yellow contents were cooled down at room temperature and the particles were recovered by centrifugation followed by washing in ethyl alcohol and finally with water. The particles were re-dispersed in DI water to obtain a faint yellow solution.

Scheme c - Another experiment was carried out by changing the concentration of the precursors used. In a typical synthesis, 0.234 g of Ce $(NO_3)_3.6H_2O$ was first taken in a round bottom flask and dissolved in 16ml of DI water. To this solution, 16 mL of ethylenediamine was added by continuous stirring and the reaction mixture was refluxed using a condenser at 100^0C for 7hrs (Figure 3.10). The light brown contents were cooled down at room temperature and the particles were recovered by centrifugation followed by washing in ethyl

alcohol and finally with water. The particles were re-dispersed in DI water to obtain a dark yellow solution. All these particles form a stable suspension when dispersed in ultra pure water.

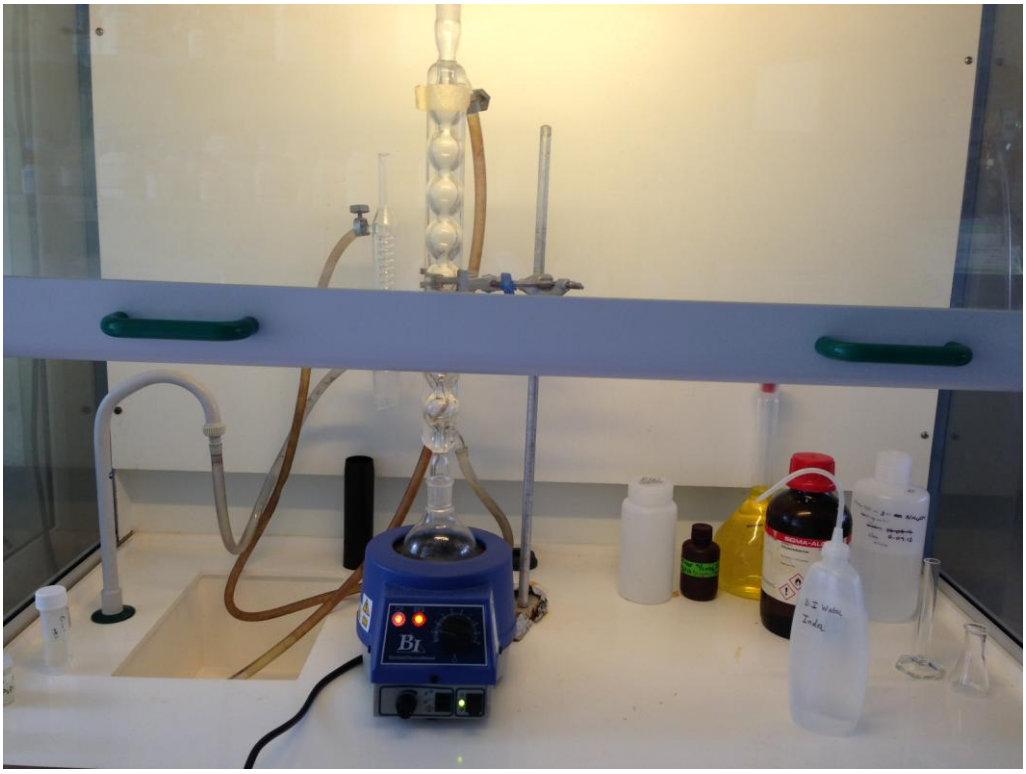

Figure 3.10 Experimental set up for synthesis 3 scheme b and c

3.4.3.1 Results and discussion

The nanoparticles obtained by scheme ‗a' and ‗b' are spherical in shape whereas scheme c yielded nanorods. The samples have been named as S3, S4 and R1 respectively. As is clear from the schemes used, the reactions have been carried out by varying the concentration of the precursors as well as the reaction conditions. All the three solutions were clear at the starting point and eventually turned to thick dark yellow (scheme a), dark yellow (scheme b) and light brown (scheme c) by the end of the synthesis. It was observed that changing the

temperature of the reaction from room temperature to 100°C did not have any major effect on the shape of the particle as both appear to be spherical in shape (by TEM).

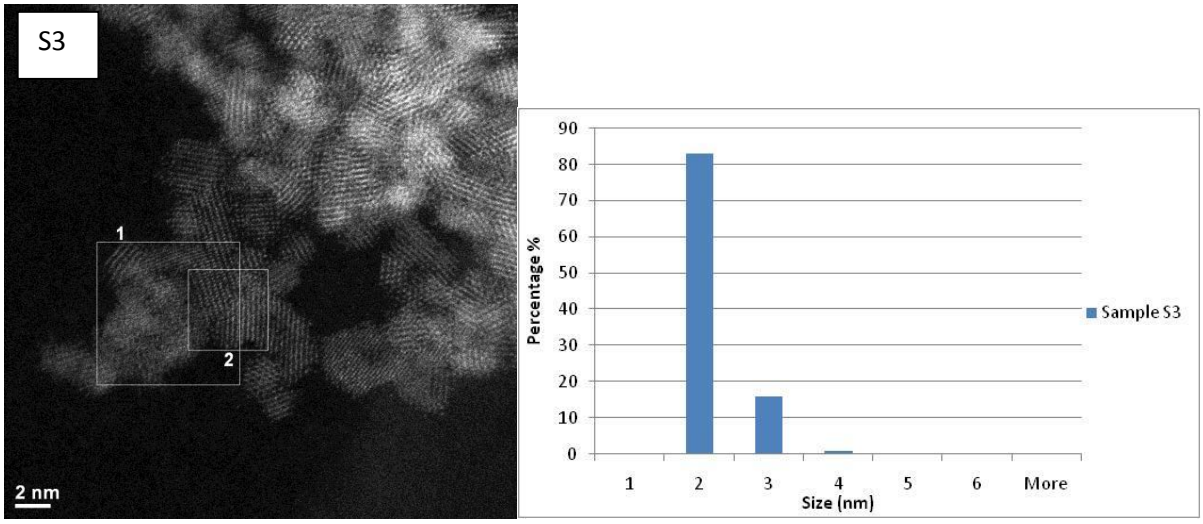

Figure 3.11 Dark field high resolution TEM images along with histogram showing size distribution for nanospheres (S3)

The crystallanity of the spheres formed has been determined using high resolution TEM images; however, the crystallanity of S4 is obscured by some agglomeration (figure 3.11 and 3.12). The size and shape quantification has been illustrated in figure 3.11 and 3.12 however the shape quantification for S3 could not be carried out. The DLS data of the as synthesised NPs and post synthesis after 3 and 6 months has been illustrated in Figure 3.14. It was further observed that the addition of water and higher temperature in the scheme c yielded nanorods (R1) of the size of 83±56 nm in length and 16±6 nm by width (TEM). The crystallinity of the NPs has been determined using high resolution transmission electron microscopic (HRTEM) studies. The low and high resolution TEM micrographs (Figure 3.13) clearly illustrate the sizing of ceria nanorods formed as a function of the change in the concentration of the precursors at 100°C. The histograms clearly depict the size and shape quantification. The experimental sizes as obtained by DLS are illustrated in Figure 3.14 and the results obtained from all the three schemes have been summarised in table 3.3.

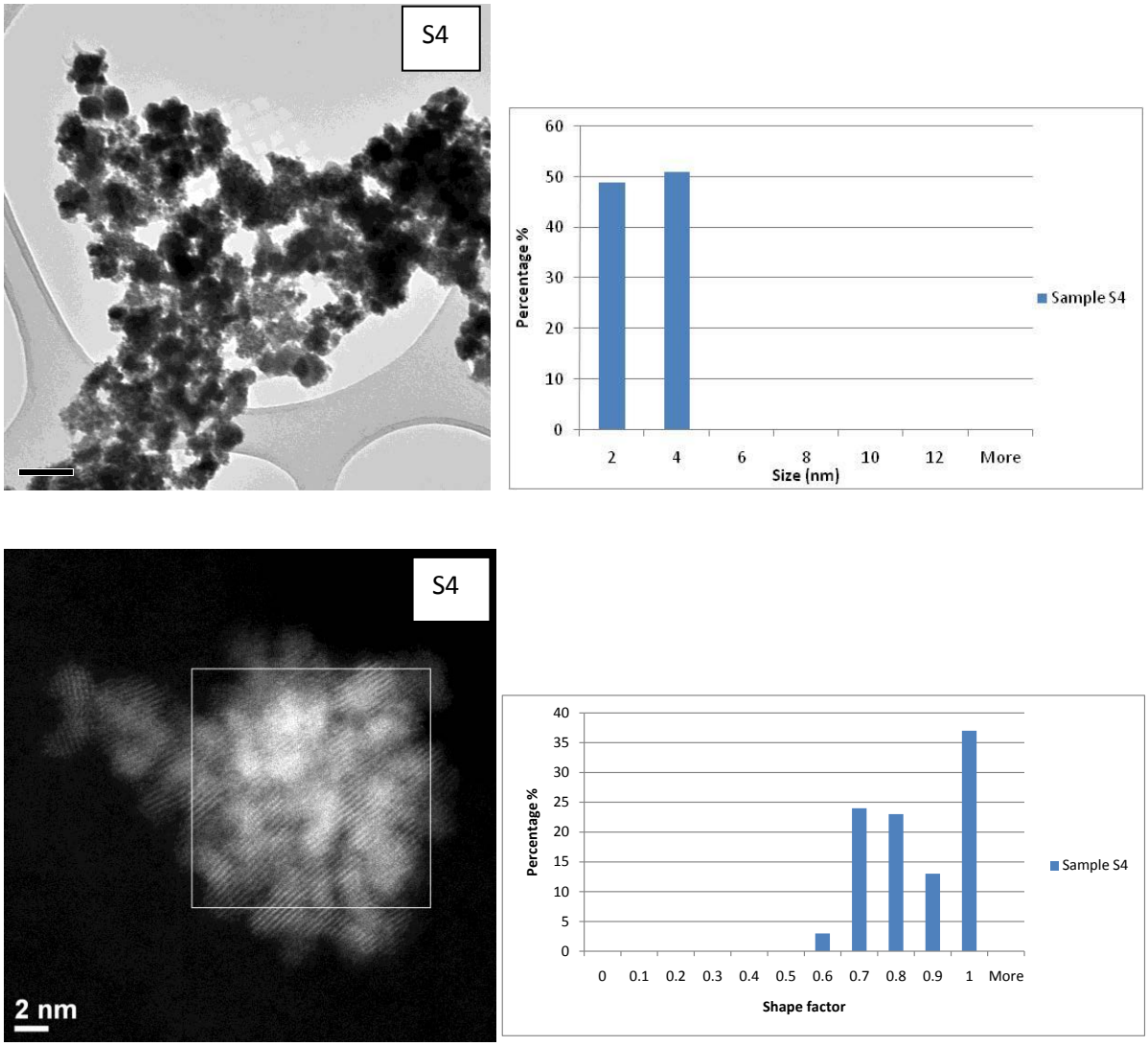

Figure 3.12 Bright field and dark field high resolution TEM images along with histograms showing shape and size distributions for nanospheres (S4)

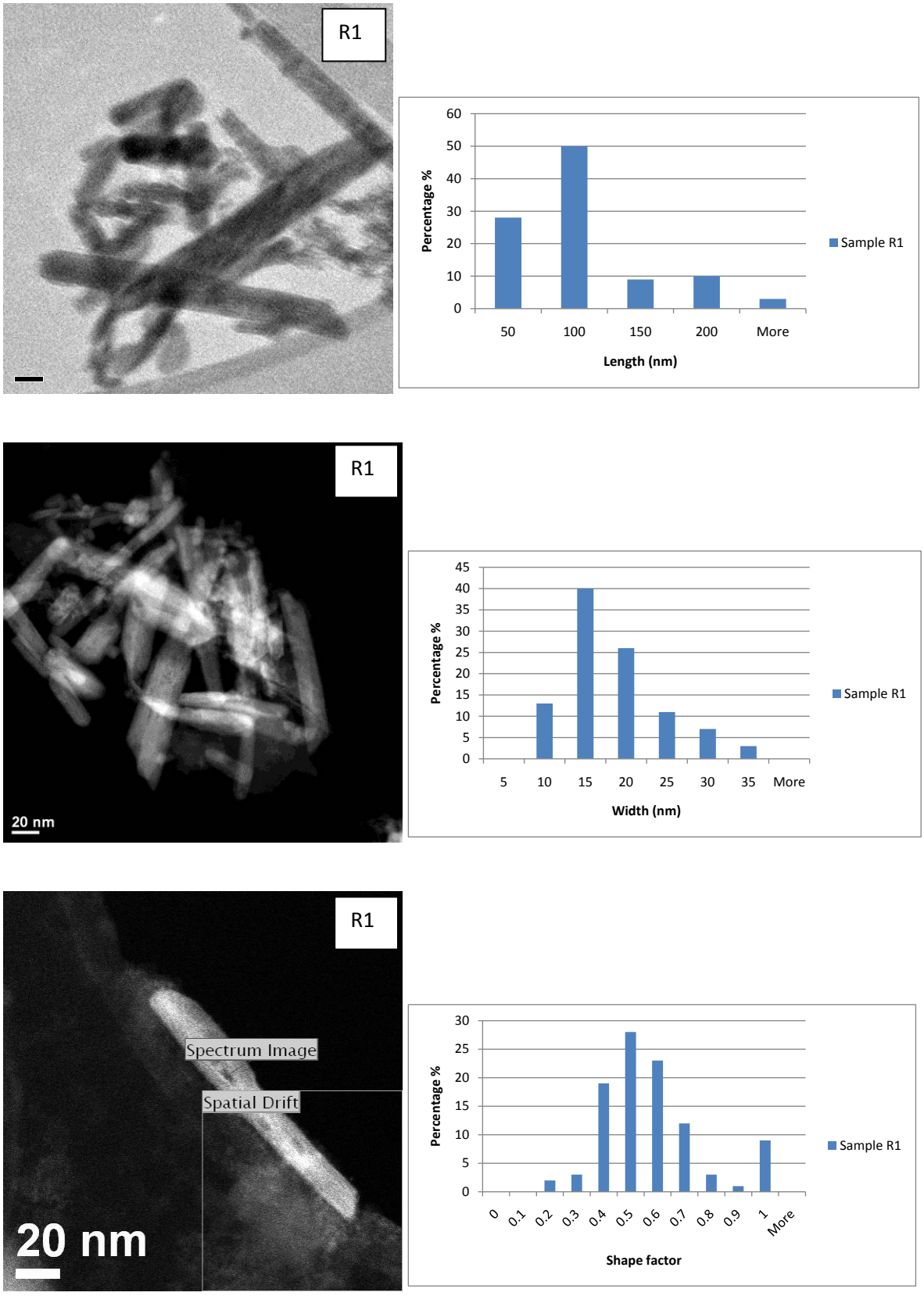

Figure 3.13 Bright field and dark field high resolution TEM images along with histograms showing shape and size distributions for nanorods (R1)

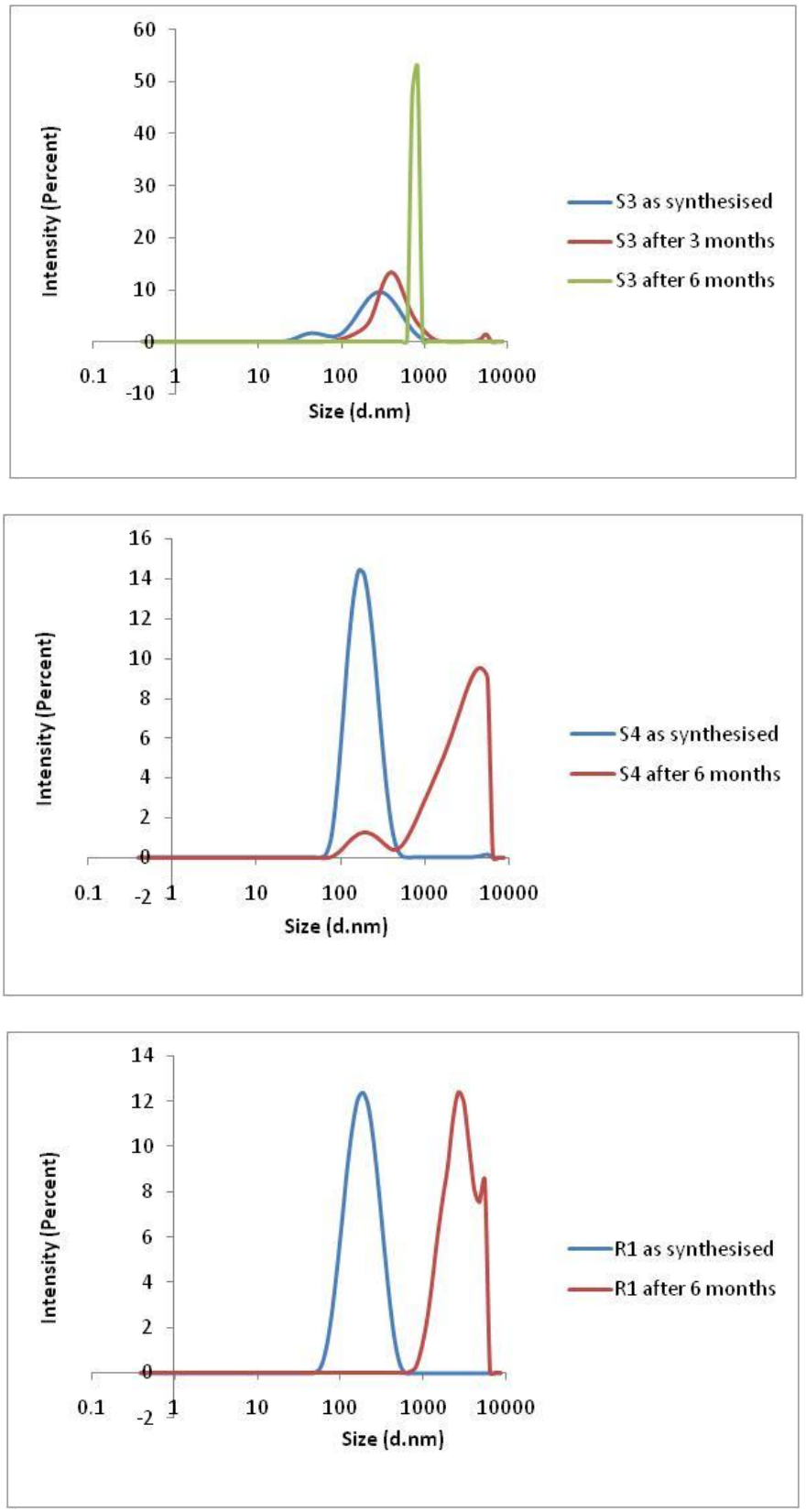

Figure 3.14 Size distributions by intensity obtained with DLS for nanospheres (S3 and S4) and nanorods (R1), each coloured line represents an average of minimum three measurements

Table 3.3 Results from synthesis 3

Sample code	Morphology	Shape Factor	Size (nm)		Stability by DLS (nm)	
			DLS	TEM	After three months	After six months
S3	Nanosphere	_	175±2 PdI:0.470	3±1	427±19 PdI:0.386	825±126 PdI:0.512
S4	Nanosphere	0.82±0.14	171±2 PdI:0.110	3±1	_	1508±180 PdI:0.607
R1	Nanorod	0.52±0.19	168±2 PdI:0.167	83±56 (Length) 16±6 (width)	_	2893±76 PdI:0.252

3.4.4 Synthesis 4: Hydrolysis (Scheme a) and thermal hydrolysis (scheme b)

This method of synthesis is a modified form of synthetic scheme 2. Here Ce (IV) ions were used a starting material instead of Ce (III). Here we have used ammonium Ce (IV) nitrate as a starting material as compared to the cerium nitrate hexahydrate used previously and no capping agent has been used.

Hydrolysis is known to be greatly accelerated by increasing the solution temperature (Hirano et al., 2000), therefore, in order to explore that, we performed thermal hydrolysis at temperatures of 100°C

Scheme a- In a typical synthesis (hydrolysis), 2.78 g of ammonium Ce (IV) nitrate and 2.0 g of sodium hydroxide were dissolved separately in ultrapure water and then mixed together in a conical flask using a magnetic stirrer until the pH value turned 10. The yellow contents

were allowed to stir overnight at room temperature. Ceria NPs were recovered by centrifugation at 5000 rpm for 20 minutes and washed with water three times before dispersing them in ultrapure water.

Scheme b- The same experiment was repeated at 100 °C (thermal hydrolysis). In a typical synthesis, 2.78 g of ammonium Ce (IV) nitrate and 2.0 g of sodium hydroxide were dissolved separately in ultrapure water and then mixed together in a round bottom flask using a magnetic stirrer until the pH value turned 10. The reaction mixture was then fitted with a reflux condenser and refluxed at 100 ^{0}C for 7hrs. The dark yellow contents were cooled down at room temperature and the particles were recovered by centrifugation followed by washing with water. The particles were re-dispersed in ultra pure water to obtain a faint yellow solution.

3.4.4.1 Results and discussion

The nanoparticles obtained from scheme ‗a' are spherical in shape whereas scheme b yielded cubes. The samples have been named as S5 and C4 respectively. As is clear from the above schemes used, the reactions have been carried out by varying the temperature of the reaction mixture from room temperature to 100°C. It was observed that both the solutions turned turbid with the gradual addition of NaOH solution however, the final colour of the crude solution before centrifugation in scheme ‗a' and scheme ‗b' was faint yellow and dark yellow respectively. The experimental pH of the final dispersions is + 7.3 and + 7.9 respectively. It was observed that changing the temperature of the reaction mixture from room temperature to 100 °C had a significant impact on the shape of the NPs formed. The sample S5 is spherical

in shape while C4 has cubic structure (TEM). The crystallinity of both the samples is evident from the high resolution TEM micrographs (figure 3.15). The size obtained from TEM micrographs are 3.3±1.3 nm for S5 and 2.4±0.6 nm for C4 respectively. Shape and size quantification has been carried out using image J® software and is illustrated in figure 3.15. The size, shape and morphology data as well as the stability data after 3 months of synthesis is tabulated in table 3.4. According to the experimental data, both the samples are very stable when dispersed in ultrapure water and stay stable up to three months when kept at 5 °C in the refrigerator. The DLS data of the as synthesised samples as well as after 3 months post synthesis has been illustrated in Figure 3.16 and table 3.4.

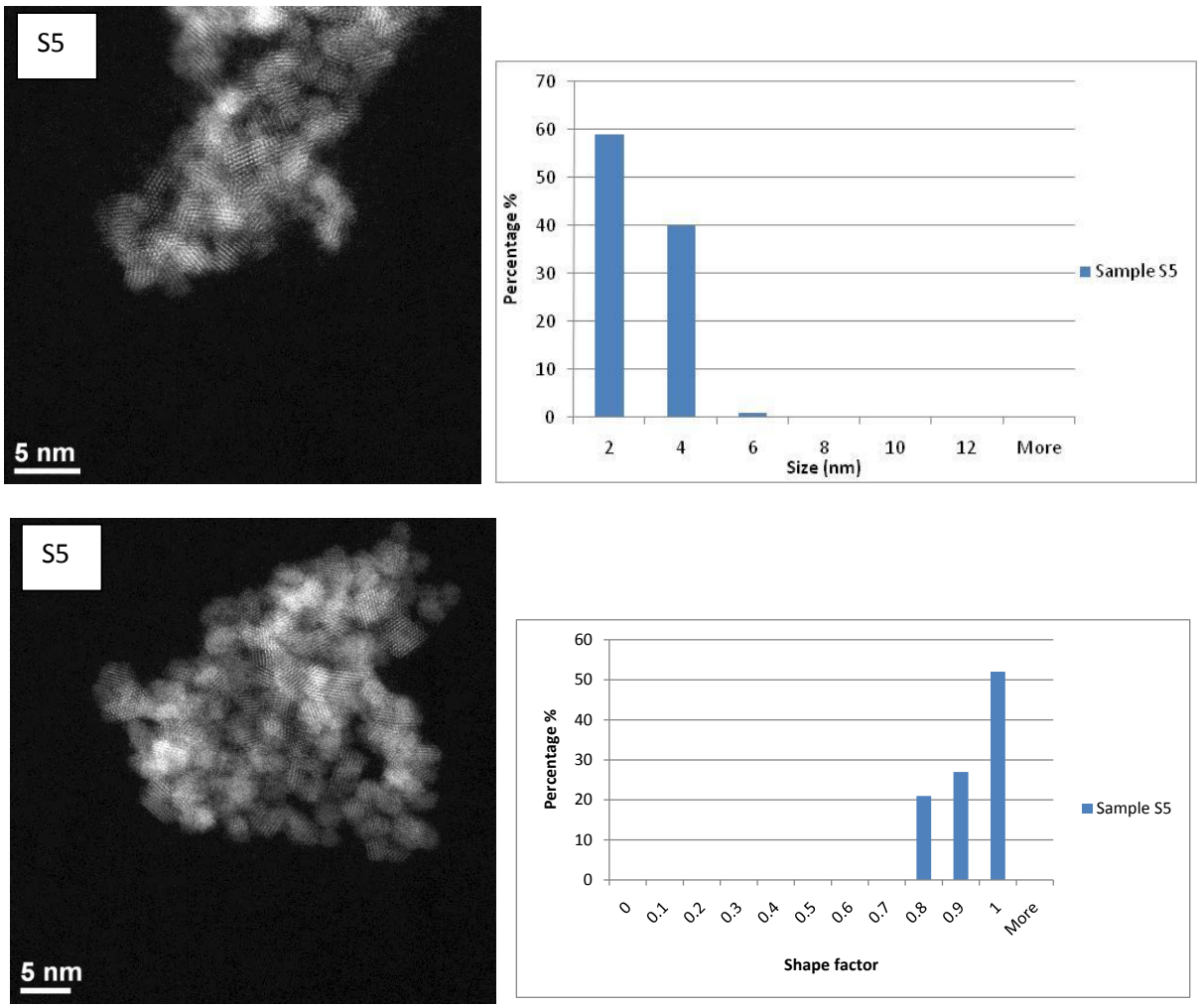

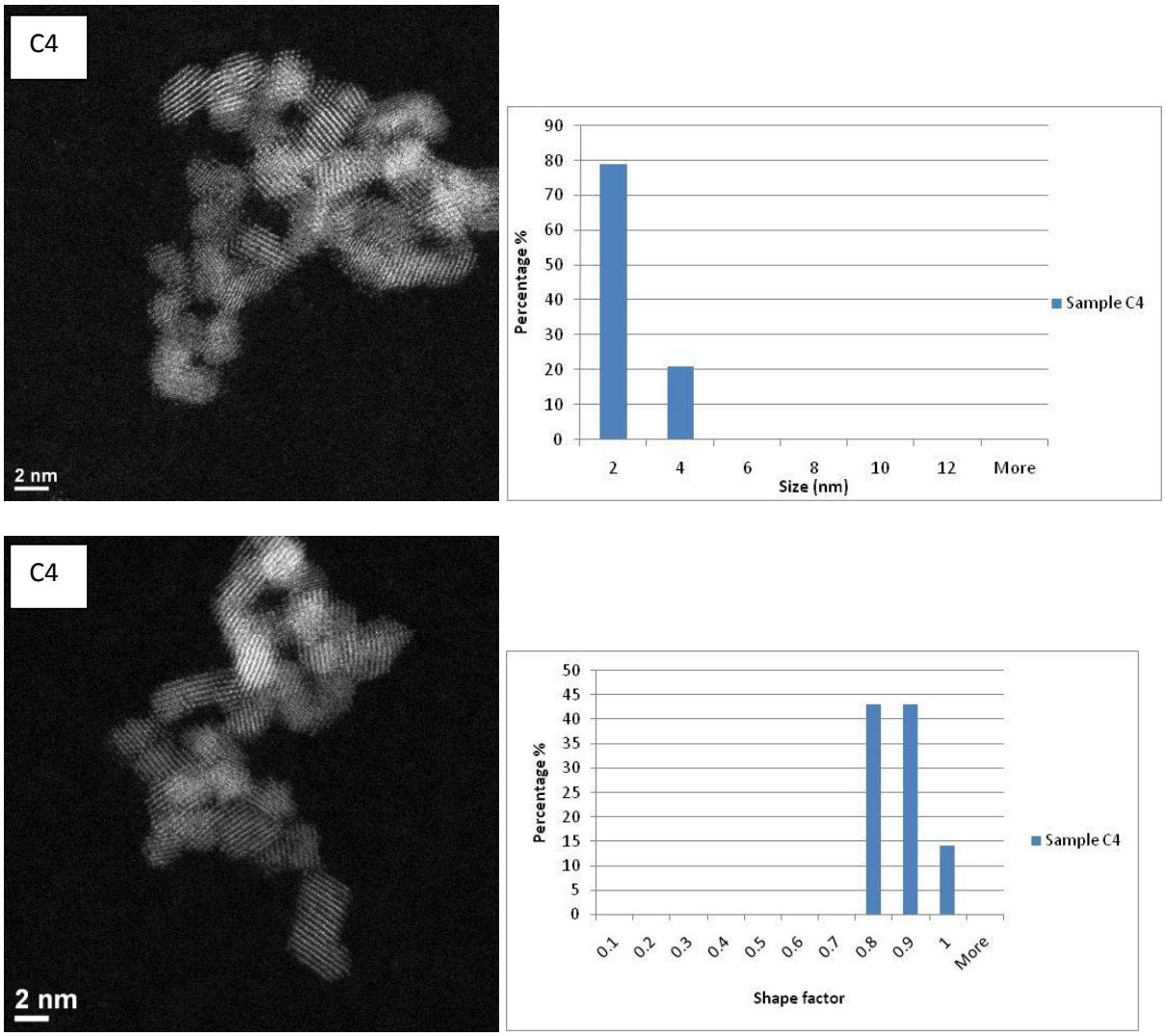

Figure 3.15 Dark field high resolution TEM images along with histograms showing shape and size distributions for nanospheres (S5) and nanocubes (C4)

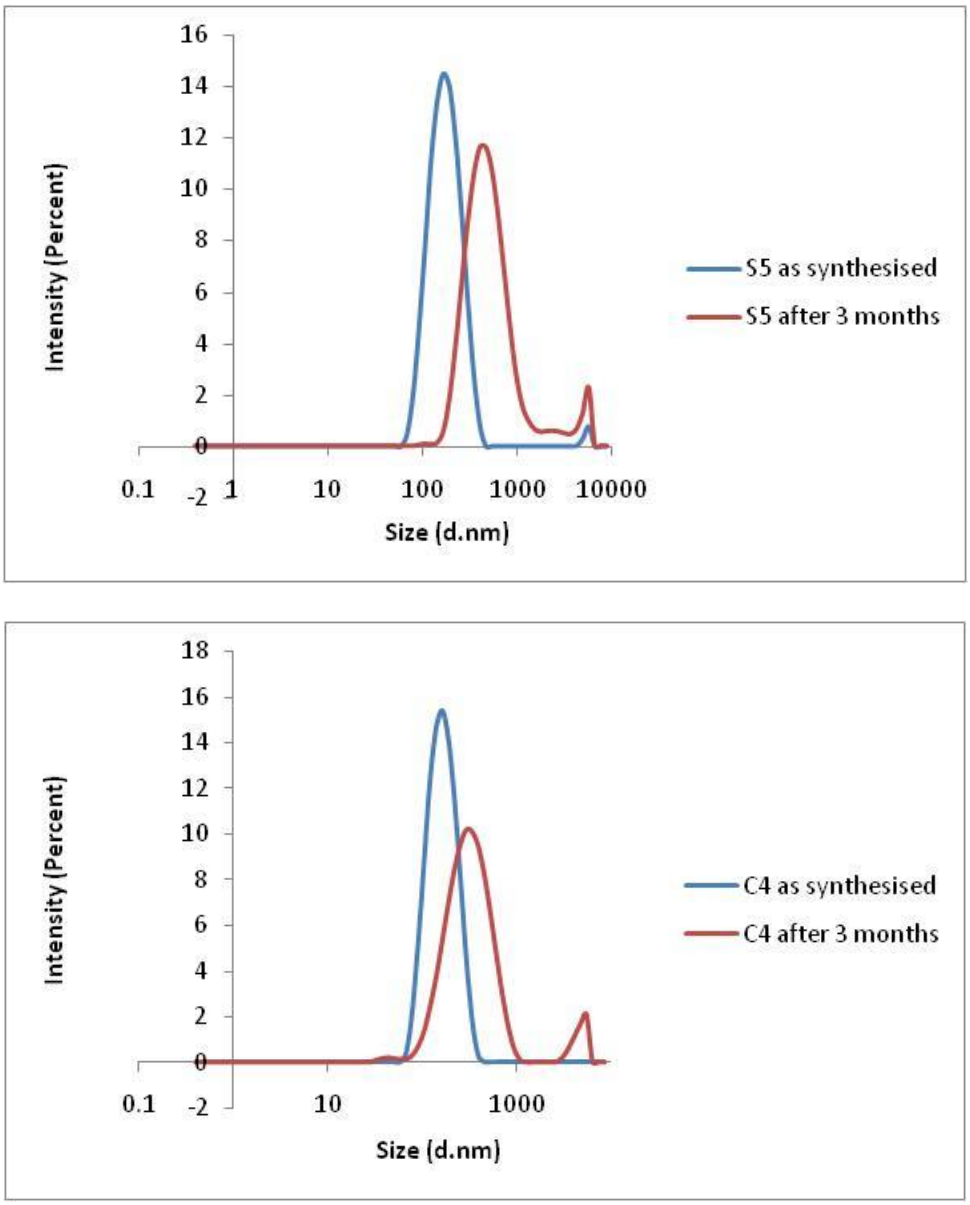

Figure 3.16 Size distributions by intensity obtained with DLS for nanospheres (S5) and nanocubes (C4), each coloured line represents an average of minimum three measurements

Table 3.4 Results from synthesis 4

Sample code	Morphology	Shape Factor	Size (nm)		Stability by DLS (nm)
			DLS	TEM	3 months
S5	Nanosphere	0.88±0.08	148±6 PdI: 0.203	3.3±1.3	495±7 PdI:0.304
C4	Nanocube	0.81±0.06	153±5 PdI:0.098	2.4±0.6	296±26 PdI:0.339

3.4.5 Synthesis 5: Co-precipitation

In a typical synthesis, 1 g of Ce $(NO_3)_3.6H_2O$ was first taken a conical flask and dissolved in 10 ml of absolute ethanol. The solution was subjected to continuous magnetic stirring for another fifteen minutes and then ammonia solution was added drop wise to the reaction mixture with continuous stirring at room temperature until the pH of the solution turned + 6. The dark brown contents were kept for ageing at room temperature overnight and were recovered the following day by centrifugation at 5000 rpm for 20 minutes and washed with water three times before dispersing them in ultrapure water.

3.4.5.1 Results and discussion

The original Ce $(NO_3)_3.6H_2O$ dissolved in absolute ethanol was clear in colour and it was observed that it gradually turned to yellow with the addition of ammonia solution and finally turning to dark brown by the end. The pH turned to + 6 with only 5 drops of ammonia solution. The nature of the reaction was highly exothermic and so the addition was carried out at a very low pace keeping the temperature down to room temperature. The NPs obtained are

spherical in shape and the sample has been named as S6. The colour of the final ceria dispersion in ultra pure water is yellow. The absolute ethanol used as a solvent is highly inflammable in nature so due to concern of the risk involved, the experiment has not been carried out at higher temperatures. The pH of the final dispersion was 7. The low and high resolution TEM micrographs (Figure 3.18) clearly illustrate the sizing in ceria particles formed. The size as observed from TEM is 8.2±2.5 nm and 12±6 nm by DLS. Shape and size quantification has been carried out using image J® software and is illustrated in Figure 3.18. The crystallinity of the NPs has been determined using high resolution transmission electron microscopic (HRTEM) studies. Figure 3.17 illustrates the size distribution by intensity data obtained by DLS. The results are summarised in table 3.5. The sample is quite stable when dispersed in ultrapure water and stay stable up to three months when kept at 5 °C in the refrigerator. The DLS data after 3 months of synthesis has been illustrated in Figure 3.17

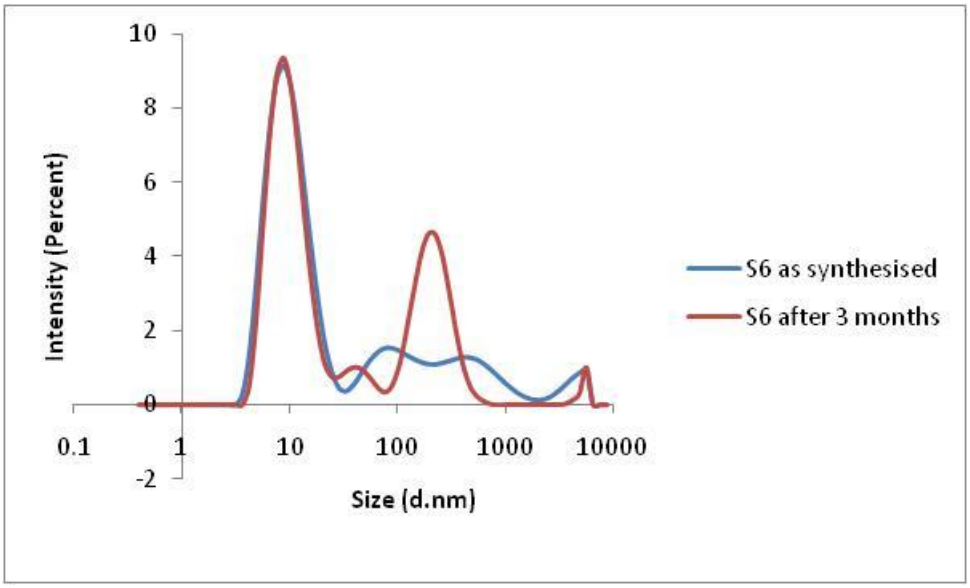

Figure 3.17 Size distributions by intensity obtained with DLS for nanospheres (S6), each coloured line represents an average of minimum three measurements

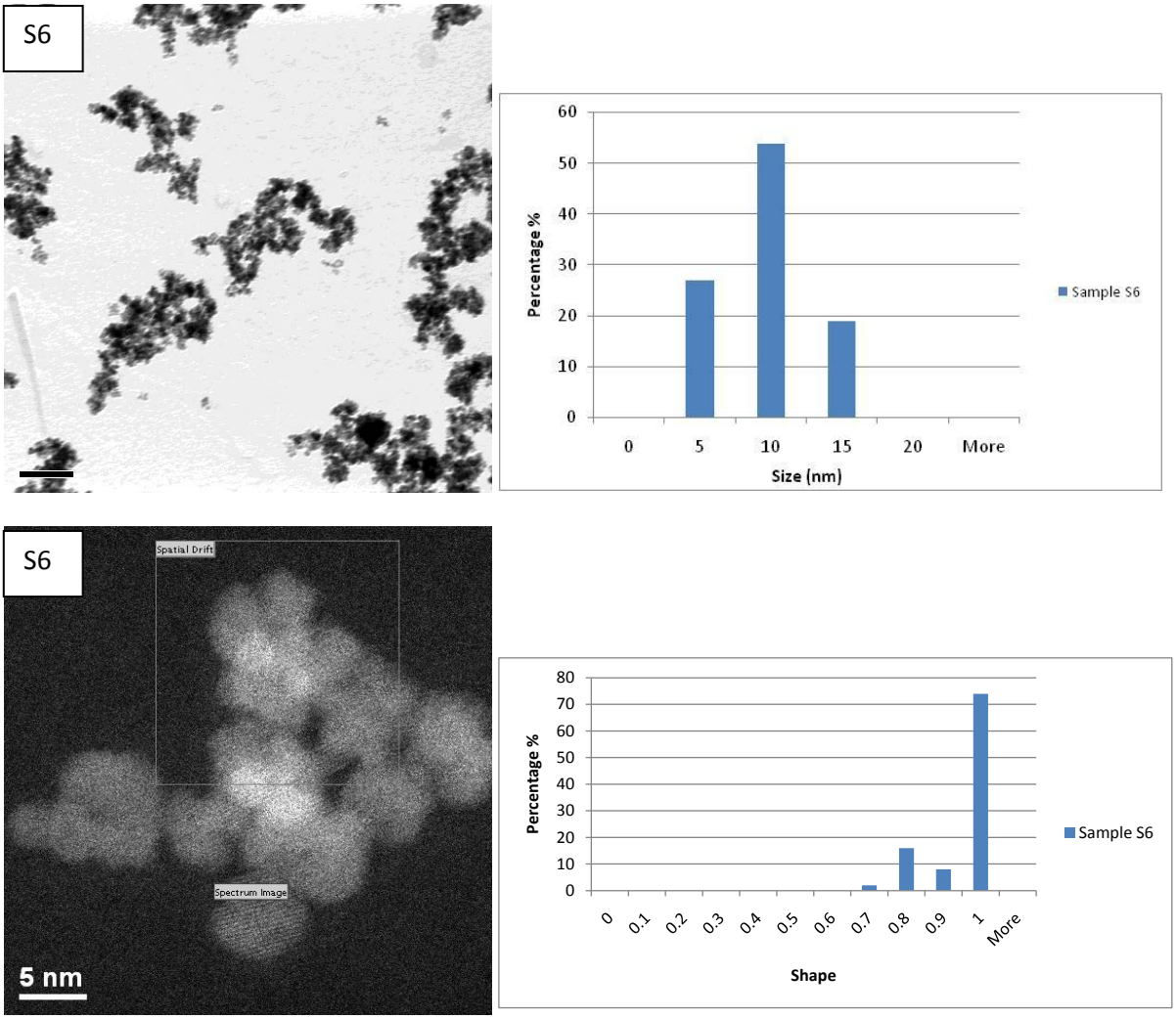

Figure 3.18 Bright field and dark field high resolution TEM images along with histograms showing shape and size distributions for nanospheres (S6)

Table 3.5 Results from synthesis 5

Sample code	Morphology	Shape Factor	Size (nm)		Stability by DLS (nm)
			DLS	TEM	3 months
S6	Nanosphere	0.92±0.09	12±6 PdI:0.441	8.2±2.5	63±24 PdI:0.206

3.4.6 Synthesis 6: Precipitation method

This method of synthesis is a modified form of synthesis 2 (sonochemical method) and has been used without the addition of any capping agent. Also in this method, magnetic stirring has been used instead of sonication.

Scheme a- In a typical synthesis, 0.434 g Ce $(NO_3)_3.6H_2O$ was first dissolved in 10ml of ultra pure water and then sodium hydroxide solution (2g dissolved in 22 ml of water) was added drop wise to it followed by 48 hrs magnetic stirring. The resulting white precipitate was collected by centrifugation at 5000 rpm for 10 minutes and washed several times in water. The particles were re-dispersed in ultra pure water to obtain a creamish yellow solution.

Scheme b- The same experiment was repeated at 50 °C. In a typical synthesis, 0.434 g Ce $(NO_3)_3.6H_2O$ was first dissolved in 10ml of ultra pure water and then sodium hydoxide solution (2g dissolved in 22 ml of water) was added drop wise to it with continuous stirring. After the addition was complete, the reaction mixture was heated at a temperature of 50 °C for 48 hours. The resulting cream precipitates were collected by centrifugation at 5000rpm for 10 minutes and washed several times in water. The particles were re-dispersed in ultra pure water to obtain a creamish yellow solution.

3.4.6.1 Results and discussion

It was observed that nanospheres were formed from scheme a whereas scheme b yielded a mixture of rods and spheres in the ratio of 3 : 1. The samples have been named as S7 and R2. It was observed that in both the schemes, the solutions started turning turbid with the gradual

addition of NaOH and intermittently had an appearance of purplish tinge in them. The final colour of the sample S7 is creamish yellow whereas R2 is yellow in colour. The size and morphology of the synthesized NPs has been confirmed through TEM. An interesting thing observed in TEM micrographs was the self assembly of the nanospheres to form rod like structures. It was observed that the nanospheres formed had arranged themselves in the form of rods though they all exist as spheres only. Further scheme b yielded nanorods with the presence of few spherical structures. In order to understand how the shape formation takes place, the experiments were carried out by changing the concentration of sodium hydroxide used as well as the reaction temperatures. It was observed that changing the concentration of NaOH (we used 1g (S7a), 2g (S7b), 3g (S7c) and 4g (S7d) NaOH) as well as the temperature did not have any major effect on the the shape and size of the NPs formed (DLS data in figure 3.19). The reaction was also carried out for 24 hours instead of 48 hours, but the particles formed are large aggregates with high PdI of 1.000 (size by DLS = 678± 143 nm). The DLS of contents obtained after 24 hours is illustrated in figure 3.19. The reaction was repeated many times but sole rods could not be obtained by scheme b. We found that the exclusive nanorods or nanospheres were hard to obtain by this method. The mechanism of particle shape formation in the above method is very complex and is not very clear whether small particles are clubbing together to form rods or the nanorods are splitting into smaller beads. However, all the batches obtained seemed to be crystalline as is evident from high resolution transmission electron microscope (HRTEM) images (Figure 3.20 and 3.21). The low and high resolution TEM micrographs (Figure 3.20) as well as the DLS data (Figure 3.19) clearly illustrate that there has been very less or almost no change in the size of ceria particles formed as a function of the change in the concentration of sodium hydroxide. All the samples are very stable when dispersed in ultrapure water and stay stable up to six months when kept at 5 °C in the refrigerator. The DLS data after six months of synthesis has been

illustrated in Figure 3.19. The experimental sizes as calculated by DLS indicate that in all the samples except S7a, the polydispersity index (PDI) stays low even after 6 months of production confirming that the samples were not aggregating quickly. All the results are summarised in table 3.6.

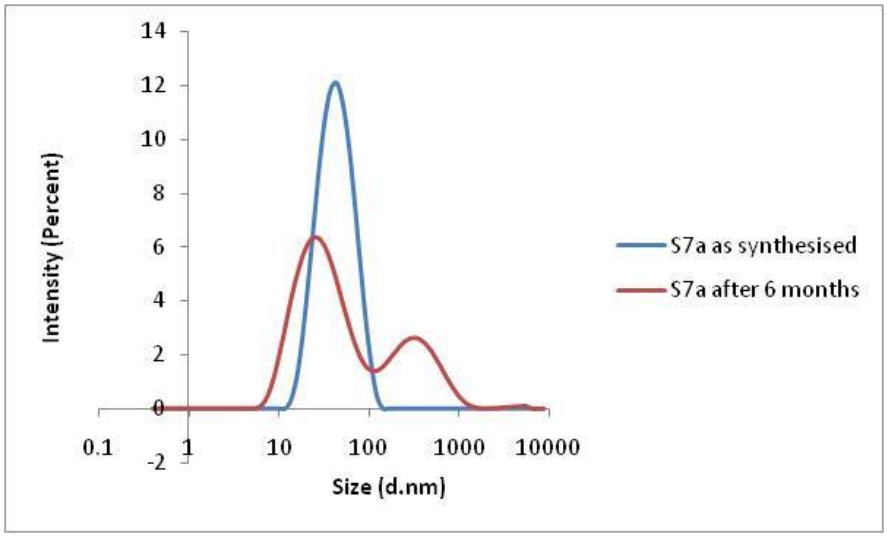

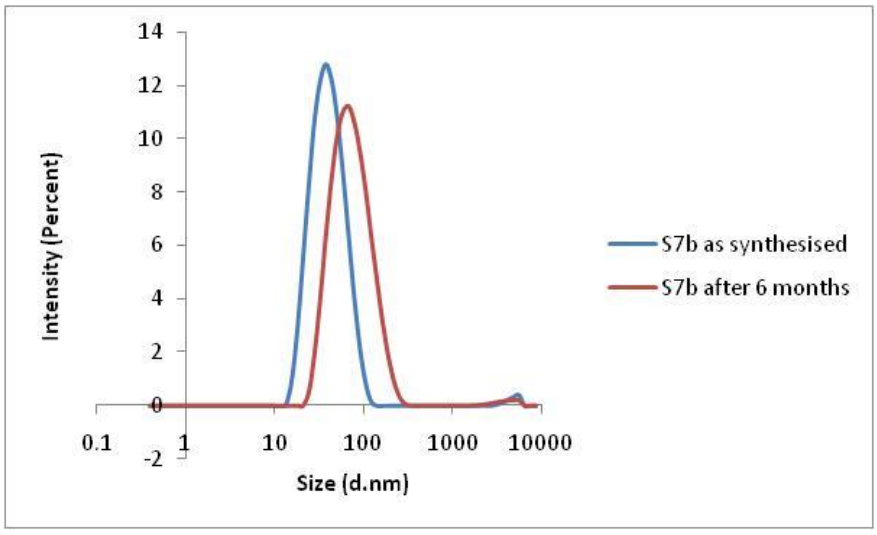

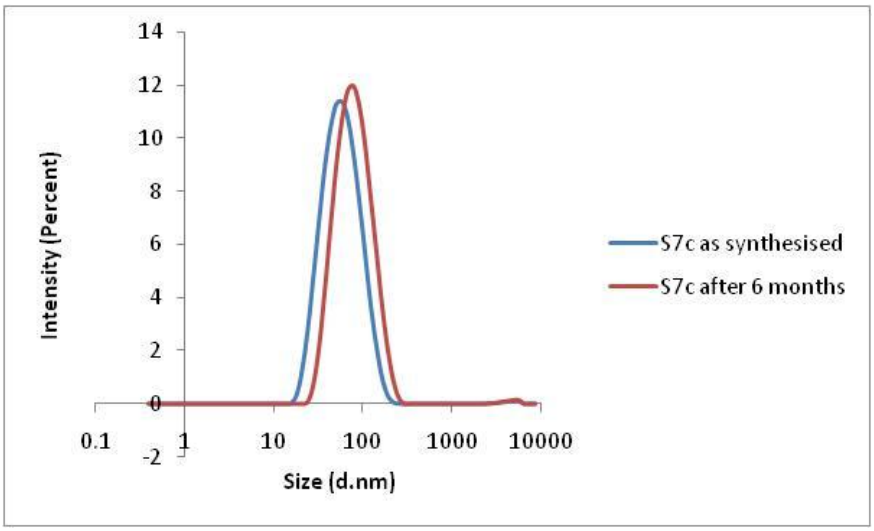
14
12
10
8
6
4
2
0
-2
Intensity (Percent)
0.1
1
10
100
1000
10000
Size (d.nm)
S7c as synthesised
S7c after 6 months

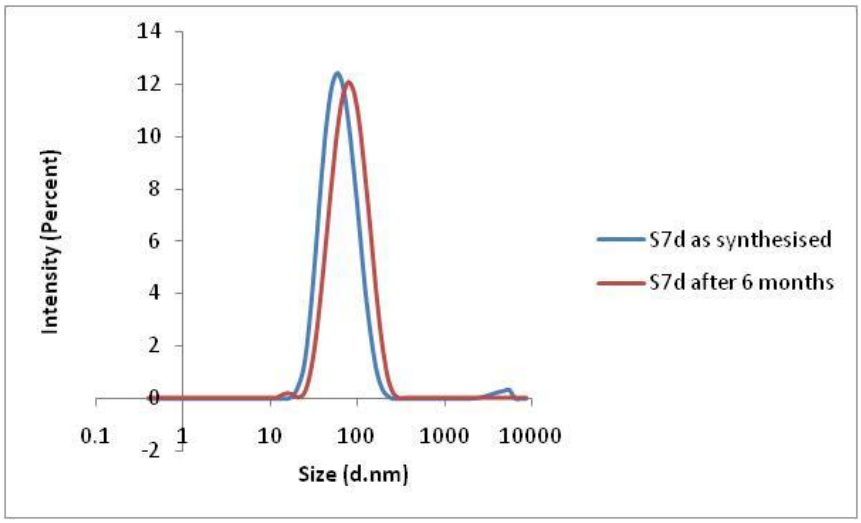
14
12
10
8
6
4
2
0
-2
Intensity (Percent)
0.1
1
10
100
1000
10000
Size (d.nm)
S7d as synthesised
S7d after 6 months

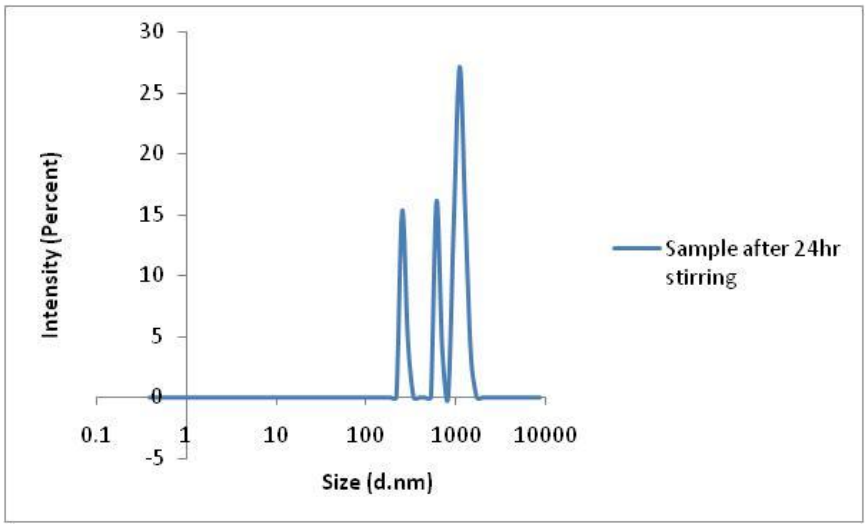
30
25
20
15
10
5
0
-5
Intensity (Percent)
0.1
1
10
100
1000
10000
Size (d.nm)
Sample after 24hr stirring

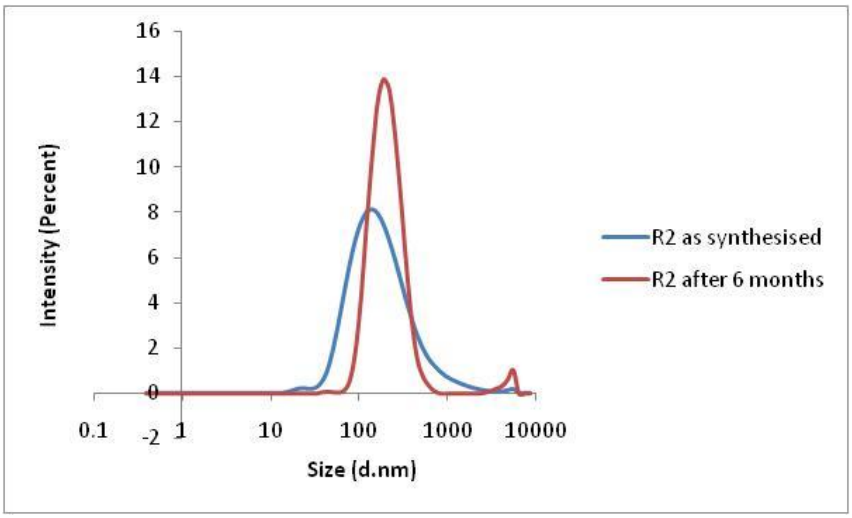

Figure 3.19 Size distributions by intensity obtained with DLS for nanospheres (S7a-d), each coloured line represents an average of minimum three measurements

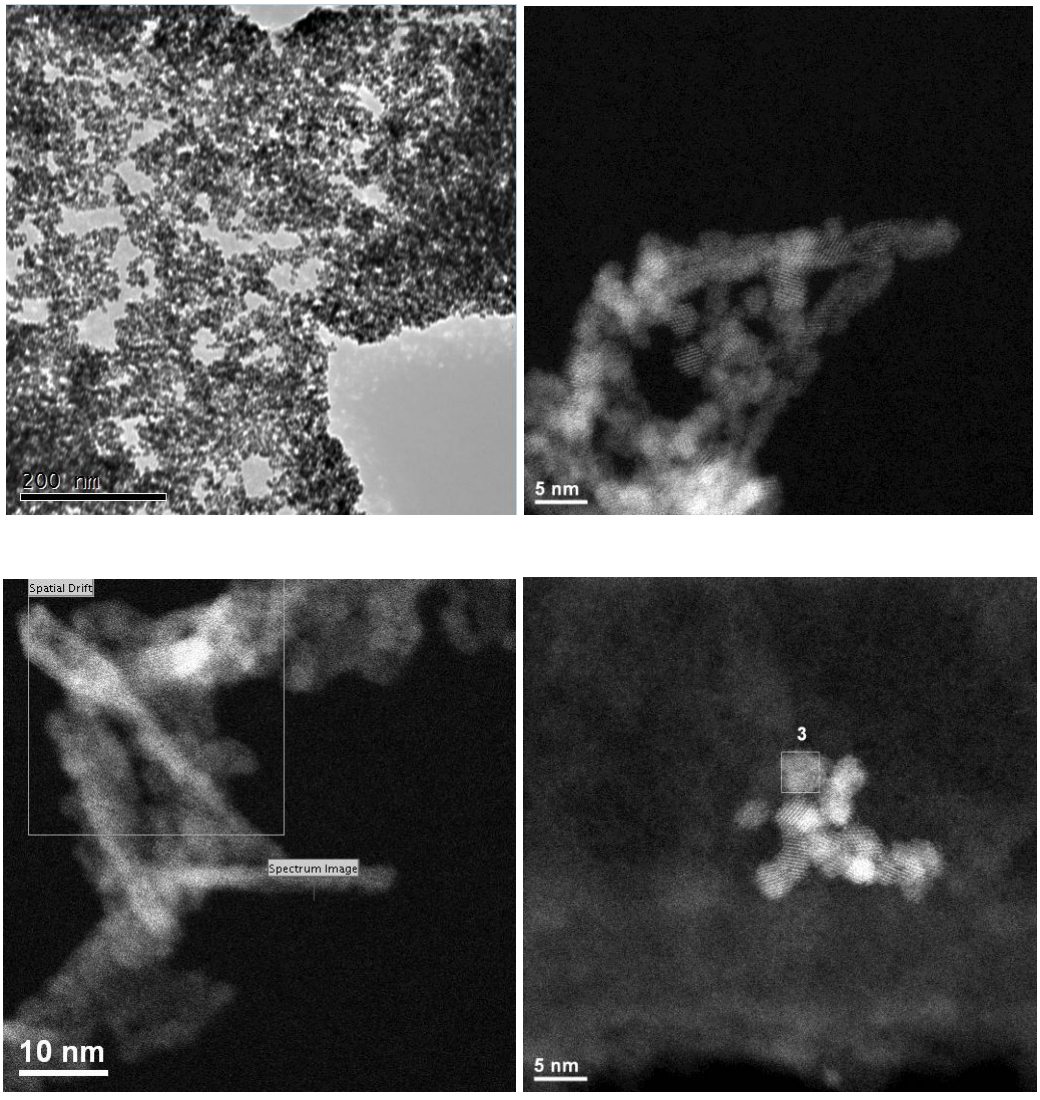

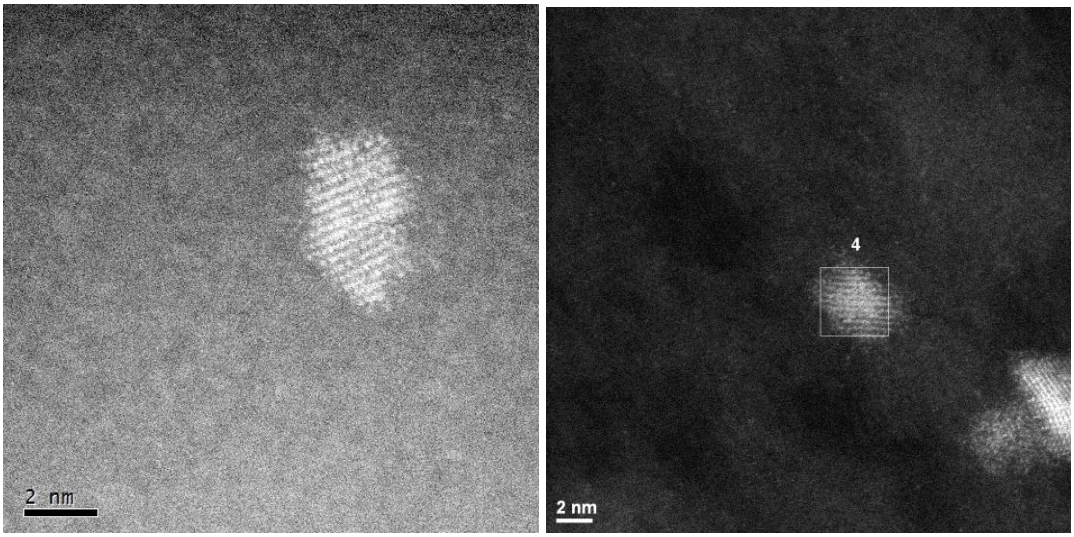

Figure 3.20 Bright field and dark field high resolution TEM images for nanospheres (S7)

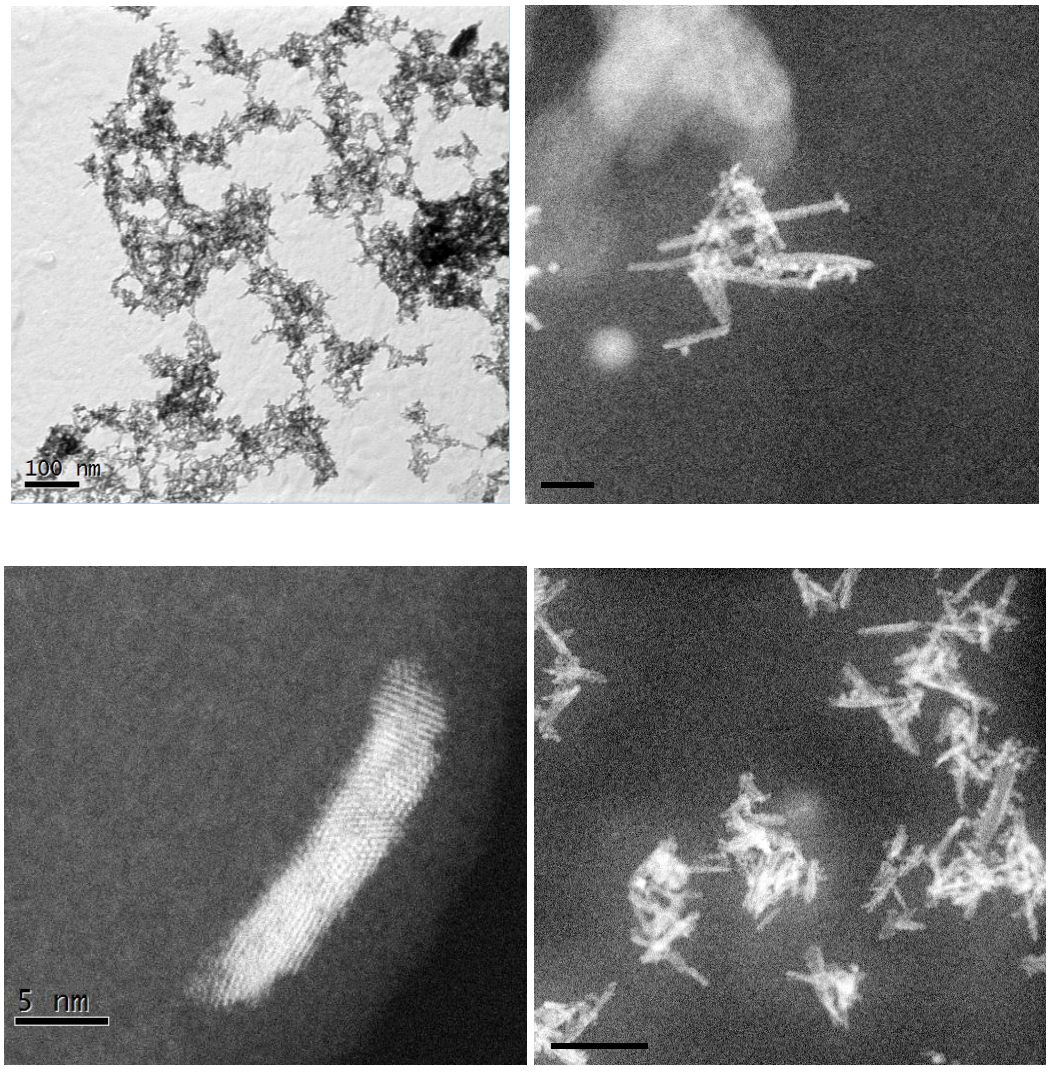

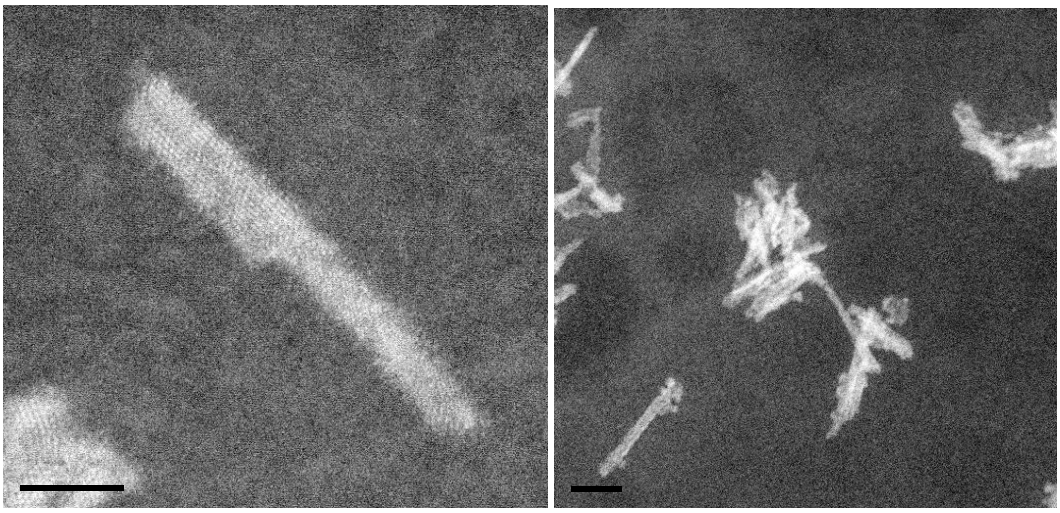

Figure 3.21 Bright field and dark field high resolution TEM images for nanorods (R2)

Table 3.6 Results from synthesis 6

Sample code	Morphology	Size (nm)		Stability by DLS (nm)
		DLS	TEM	3 months
S7	Nanosphere	52±1 PdI:0.176	6±2	70±15 PdI:0.156
R2	Nanorod	147±19 PdI:0.389	30±15(Length) 8±4(width)	200±3 PdI:0.249

3.5 Conclusions

Ceria nanoparticles have been synthesized using sonochemical, thermal hydrolysis and precipitation methods. We have produced NPs coated with different capping agents, with different strengths of interaction between core and capping agent/no capping agent and with both steric and charge stabilization. The various shapes obtained are nanospheres (S1-7),

nanocubes (C1-4) and nanorods (R1-2). The reactions have been monitored at different concentrations of the precursors and temperature of the reaction mixtures and a batch of samples have been obtained. Almost all the synthesised NPs are quite stable when dispersed in ultra pure water and stay stable up to a minimum of three months.

In the experimental data, it has been commonly found that spheres are generally formed at room temperatures whereas higher temperatures and longer reaction times favoured an increase in particle size as well as formation of other shapes such as cubes and rods. However, this may not be the case always. In particular, all the precipitation methodologies performed at room temperatures lead to the formation of nanospheres irrespective of the type of precipitant used. Another important point is that in all the above methodologies used to synthesise ceria NPs, the change in concentration of the ceria precursor had very little or almost no effect on the size and shape of the NPs formed. However, change in concentration of the oxidant lead to different sizes with increase in the temperature. Temperature also had a great impact on the aspect ratio of the ceria nanorods formed. Both the ceria samples (R1 and R2) synthesised using precipitation methodologies at higher temperature yielded nanorods but rods (R1) obtained at 100 ^{0}C temperature in synthesis 3 (scheme b) are larger in size and width as compared to the nanorods (R2) obtained at 50 ^{0}C.

Non-thermodynamic variables also seemed to play an important role. For example synthesis 2 was carried out under ultrasonication conditions however, synthesis 6 was carried out using common laboratory magnetic stirrer and we observed that synthesis 2 yielded spherical ceria NPs quickly (4 hours) as compared to synthesis 6 (48 hours) when carried at room temperature with similar concentration of the precursors. This could be attributed to the fact that ultrasonication accelerates the release of OH^{-} groups, resulting in immediate reaction to form a stable cerium oxide suspension. Hence, reaction with sonochemical method was faster

than from conventional stirring. Also the addition of PEG during ultrasonification leads to more stable nanospheres (S1 and S2) as compared to (S7). This is due to the fact that PEG strongly adsorbs on the particle surface because of the strong agitation in the sonication and the strong asymmetrical collision between the PEG adsorbed particles prevents the aggregation between the suspension due to steric hinderance effect.

Another important process is the appearance of purple-violet colour during the synthesis which ultimately changes to light yellow or dark yellow by the end of the synthesis. This purple tinge could be a characteristic of the not so well defined poor redox change within the reaction and during the synthesis because of the formation of intermediate species such as hydroxides of cerium and finally gives a characteristic yellow colour to the ceria suspension indicating the formation of cerium oxide. It is also known that Ce (III) oxidation state is less stable in air or alkaline conditions as compared to the Ce (IV), so this intermediate could be Ce (III) hydroxide finally converting to stable Ce (IV) (Zhang et al., 2007). However, the exact mechanism is not very understood. It has also been found that the final suspensions which were creamish yellow or light yellow in colour resulted in particles with smaller sizes (after characterisation with DLS and TEM) as compared to the dark yellow suspensions.

It is quite evident now that reaction time, temperature and concentration of the precursors, especially the concentration of oxidants, play an important role towards the shape and size of the particles formed. Keeping this in view, all these parameters have been carefully recorded during the experiments. The size, shape and morphology of all the as synthesized samples has been determined using DLS and TEM. Zeta potential has also been measured for some samples. DLS has been used to monitor the stability of the particles after 3/6 months post synthesis and revealed that many samples stay stable up to a minimum of three months when kept at colder temperatures of 5 ^{0}C. In the next chapter, the oxidation state studies have been

carried out on the synthesised samples using XPS and STEM-EELS and the surface chemistry of these particles has been analysed. The oxidation states of the samples have been quantified as well as the technique comparison has been made.

To summarise, the various experimental procedures performed along with their reaction conditions and products obtained have been tabulated in table 3.7. In total, four different sizes of nanocubes (C1-4), seven different sizes of spheres (S1-7) and two different sizes of rods (R1-2) have been synthesized using different methodologies. The data is summarised below.

Table 3.7 Reaction Conditions of the experimental procedures and the products obtained

Synthesis type	Precursors	Reaction temperature (℃)	Stirring hours	Product morphology	Colour of the final product	Sample code
Homogenous precipitation	$Ce(NO_3)_3 \cdot 6H_2O$ + HMTA Ratio 1: 10	70	7	Nanocube	Pale yellow	C1
Homogenous precipitation	$Ce(NO_3)_3 \cdot 6H_2O$ + HMTA Ratio 1: 20	70	7	Nanocube	Yellow	C2
Homogenous precipitation	$Ce(NO_3)_3 \cdot 6H_2O$ + HMTA Ratio 1: 40	70	7	Nanocube	Yellow	C3
Sonochemical	$Ce(NO_3)_3 \cdot 6H_2O$ + PEG 1500 + NaOH	Room Temperature (25)	4	Nanosphere	Creamish yellow	S1

Sonochemical	$Ce(NO_3)_3 \cdot 6H_2O$ + PEG 600 + NaOH	Room Temperature (25)	4	Nanosphere	Creamish yellow	S2
Homogenous precipitation	$Ce(NO_3)_3 \cdot 6H_2O$ + Ethylenediamine	Room Temperature (25)	24	Nanosphere	Faint yellow	S3
Co-precipitation	$Ce(NO_3)_3 \cdot 6H_2O$ + Ethylenediamine	100	7	Nanosphere	Faint yellow	S4
Co-precipitation	$Ce(NO_3)_3 \cdot 6H_2O$ + Ethylenediamine + Water	100	7	Nanorod	Dark yellow	R1
Hydrolysis	Ammonium Ce(IV) nitrate + NaOH	Room Temperature (25)	24	Nanosphere	Pale Yellow	S5
Thermal hydrolysis	Ammonium Ce(IV) nitrate + NaOH	100	7	Nanocube	Dark yellow	C4
Co-precipitation	$Ce(NO_3)_3 \cdot 6H_2O$ + Ammonia	Room Temperature (25)	1	Nanosphere	Yellow	S6
precipitation	$Ce(NO_3)_3 \cdot 6H_2O$ + NaOH	Room Temperature (25)	48	Nanosphere	Creamish yellow	S7
precipitation	$Ce(NO_3)_3 \cdot 6H_2O$ + NaOH	50	48	Mixture of nanosphere and nanorods	Yellow	R2

4 Oxidation state determination using STEM-EELS and XPS

4.1 Chapter overview

This chapter is focussed on understanding the surface chemistry of synthesised ceria NPs as a function of their size and shape. As discussed in chapter 1, there is some contradiction in literature about the oxidant/antioxidant activity of nanoceria and the speculation is on the redox behaviour of cerium oxide being responsible for these assessments but there are large gaps in knowledge of the redox mechanism of these nanoparticles and whether Ce (III) or Ce (IV) is responsible for such behaviours. There is a need to quantify and understand the presence of Ce (III) and Ce (IV) ratios in synthesised samples and then use them in further toxicological and eco-toxicological studies in order to verify whether it is Ce (III) or Ce (IV) which is leading to toxicity. In this chapter, we have discussed the oxidation state quantification of all the synthesised samples (explained in chapter 3) using two well established techniques, EELS and XPS. Given the uncertainties and contradictions in literature, use of two methods would allow us to be more accurate. Both the techniques are surface profile techniques but are based on different principles. The detailed background has been explained in chapter 2 (section 2.2.3 and 2.2.4 respectively).

There are few studies in literature on synthesised ceria NPs that have employed X-ray photoelectron spectroscopy (XPS) and electron energy loss spectroscopy (EELS) for oxidation state quantification of pristine samples (Deshpande et al., 2005, Paparazzo, 2011, Zhang et al., 2011b, Wu et al., 2004, Merrifield et al., 2013, Han et al., 2005, Haigh et al.,

2011, Gao et al., 2010, Baalousha et al., 2010) but in most of the cases, either of these techniques has been used to identify the oxidation states except (Baalousha et al., 2010) where both the methods have been employed to evaluate commercial samples of ceria. In this study we use a combination of STEM+EELS along with XPS to quantify ceria oxidation states of the as synthesised samples.

4.2 Oxidation state quantification using EELS

4.2.1 Methodology

4.2.1.1 Ceria NPs used for the experiment

All the ceria nanoparticles used for EELS experiments have been synthesised by myself and their synthetic schemes have been discussed in chapter 3.

4.2.1.2 Characterisation

All the samples used in this chapter have been characterised for their size and shape using DLS and TEM (details in chapter 3)

4.2.1.3 Sample preparation for EELS

A good quality sample preparation is one of the most important step in EELS experiments. Good quality means that the sample should be free from any contamination with no surface artefacts and should have a large thin area with a good collection of nanoparticles to analyse. Considering the sample requirements, the samples for EELS experiments were prepared by ultracentrifugation (Mavrocordatos et al., 2007) (details of the technique and sample preparation are explained in chapter 2, section 2.2.6). Another familiar contamination during EELS experiments includes the carbon contamination. There are many sources responsible for it such as dust from the air or vacuum pump as well as sample handing during preparation

and while loading the sample into the sample holder before EELS experiment. In order to avoid this, the sample grids were kept covered while drying and were stored in clean grid boxes throughout. The sample was put into the microscope quickly after taking it out of the grid box and the vacuum pump was cooled down by the liquid nitrogen.

4.2.1.4 EELS measurements

EELS measurements were performed by Dr Douglas Blom from the Electron Microscopy Centre at University of South Carolina, USA with my assistance. My assistance involved loading the sample grid on the sample holder and inserting it in the vacuum chamber and later removing the sample grid off the sample holder, alignment of the electron beam by setting the condensers and the gun, focussing the image and finding a large thin area with a good collection of nanoparticles to analyse and then switching to the STEM mode for diffraction imaging. All the EELS measurements were carried out under his directions. His wider experience and in depth knowledge in STEM-EELS not only helped me in generating some very good images and spectra but also taught me how to generate a quality data. All the raw data collected have been analysed by myself using the Gatan Microscopy Suite at the University of Birmingham. I took a four day training course at the Gatan suite at the University of Birmingham and learnt how to analyse and interpret the signals from the raw EELS data generated and further quantification steps under the guidance of Dr. Ian Jones.

The spectra have been generated using JEOL 2100F with CEOS GmbH hexapole STEM probe corrector coupled with an X-EDS from Oxford Instruments and EELS from Gatan, Inc. Further information on theory and details of the instrument used have been discussed earlier in chapter 2, section 2.2.3). The samples were given a beam shower of five minutes in order to reduce the chances of carbon contamination during the experiments. In this procedure, the

sample and the grid was pre irradiated with a dose of defocussed beam and scanned at a magnification of 50,000X, with the purpose to avoid contamination during subsequent STEM imaging at high magnifications (Egerton et al., 2004).

Cerium oxidation states have been measured using Cerium M_5/M_4 white line ratios obtained from the EELS spectra, the two peaks at ~883 eV and ~901 eV indicated the cerium M5/M4 edge (double white line). $CeNO_3$ was used as a Ce (III) standard and bulk CeO_2 was used as a Ce(IV) standard, These were high quality standards and have been previously used by our group and data published (Merrifield et al., 2013). Ce (III) and Ce (IV) standards have been effectively used giving M_5/M_4 white line ratios of 1.23±0.05 and 0.82±0.03 respectively. These values agree with those previously calculated by others (Fortner et al., 1997, Wu et al., 2004, Merrifield et al., 2013). A number of methods have already been developed to measure the M_5/M_4 ratios (Manoubi et al., 1990, Yang et al., 2006) but in this work, the second derivative method have been used since it is insensitive to thickness variations (Fortner et al., 1997). Because of the noise in the spectra, the raw data of the spectra have been smoothed and the M_5/M_4 ratios have been determined by extracting the integrated signal of the smoothed second derivative. The percentage of Ce (III) and Ce (IV) were calculated using the method used by Wu et al (Wu et al., 2004).

For almost all the samples, line scans have been collected across the diameter of the particle from the centre towards the edge of the particle except for very small particles where a line scan seemed to have been damaging the particle surface. So area scans have been carried out on different sections of the same sample instead of line scans. They are illustrated in the below sections.

4.2.1.5 Quantification steps

Figure 4.1 (a) shows a cerium oxide spectrum over a few hundred electron volts with two distinct edges, the oxygen K edge at around 532 eV and the cerium $M_{4,5}$-edge from 880 eV upwards. We will be concentrating on the second edge which is characterised by the pair of M_5 and M_4 signals. For quantification, the first step is to assign the characteristic peaks (white lines) as signals and the rest as the background (figure 4.1 b) and then the signal is extracted from the spectrum. Because of the noise in the spectra, the extracted signal was band-pass filtered (using the smooth low band-pass filter function) and the second derivative (figure 4.1 c) was calculated using the digital micrograph software. The M_5/M_4 ratio have been determined by extracting the integrated signal of the smoothed second derivative (figure 4.1 d) and comparing these with the M_5/M_4 ratios obtained from the cerium standards. The steps are clearly explained in figure 4.1 (a-c).

4.2.1.6 Beam damage

Electron beam induced damage is an important aspect which needs to be to be considered and recognised (if any), during EELS experiments. This damage can be studied either using electron diffraction patterns or high-resolution images, or by changes in spectral features. In case of cerium oxide, the beam damage can induce change in oxidation state from Ce (IV) to Ce (III), hence leading to an overestimation of the Ce (III) within the sample. According to literature, the beam damaged spectrum of cerium oxide can possibly show the following changes (a) decreases in energies of the M_5 andM_4 maxima; (b) changes in shape of the near-edge structure; (c) inversion of the M_5/M_4 branching ratio; and (d) increase in the M_5/M_4 area ratio (Sauer et al., 1993, Garvie and Craven, 1994, Garvie and Buseck, 1999, Riedl et al., 2006, Tan et al., 2012).

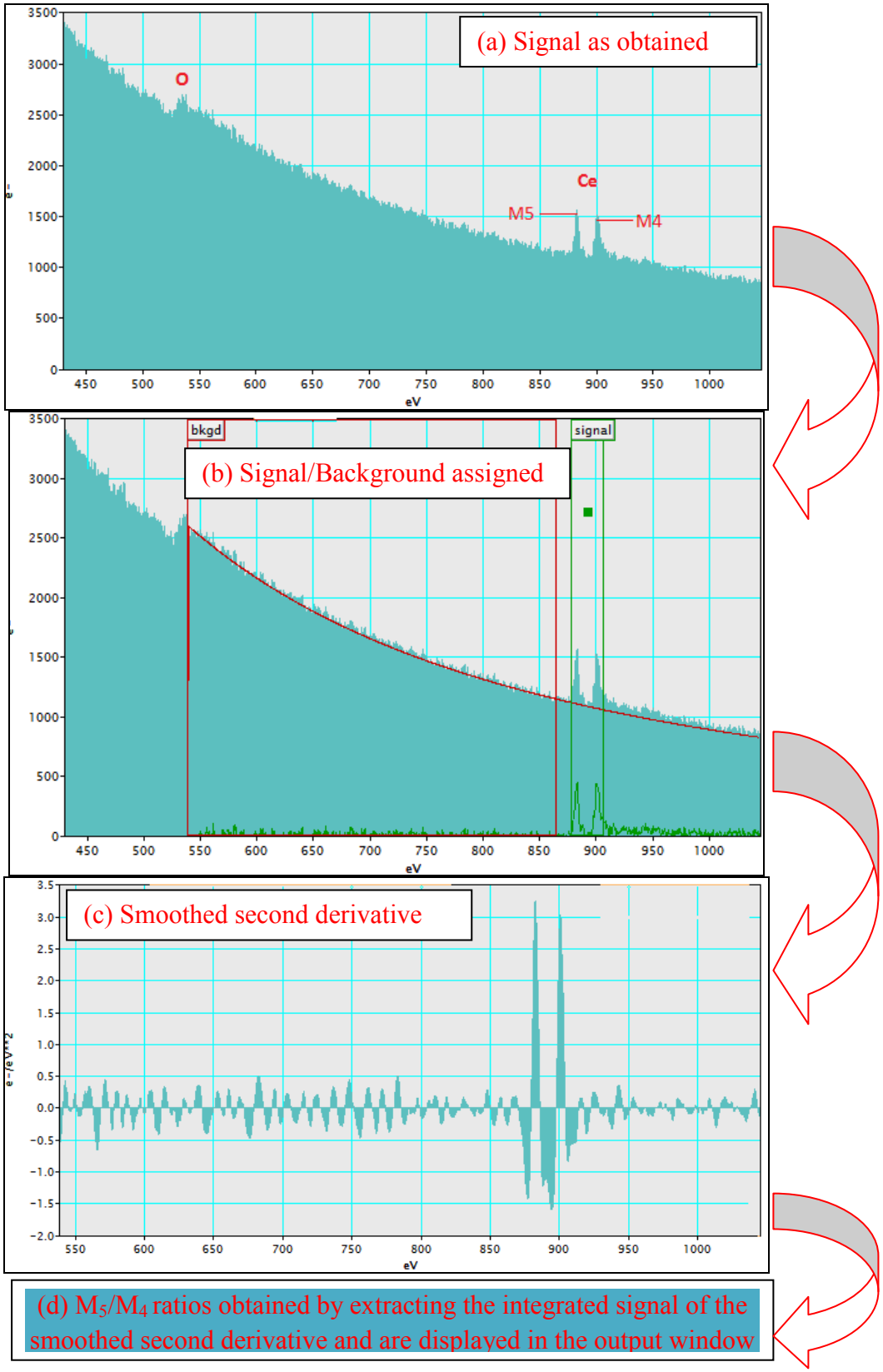

Figure 4.1 (a-c) Illustration of the various steps involved during EELS quantification

The extent of electron-beam damage depends on factors such as the probe current density, accelerating voltage, chemistry and structure of the solid, and dimensions of the irradiated volume, however, there are strategies to identify and minimise the beam damage (Egerton et al., 2004). Beam damaged degradation of the crystalline structure can also be identified from the high resolution images taken before and after the spectral imaging (SI) and conclusions can be made on whether there is a beam damage or not. An example of a beam damaged degradation of the crystalline perfection is explained below. Garvie et al followed the reduction of Ce (IV) in cerium oxide by observing changes in the shape of the Ce $M_{4,5}$ edge by EELS. They reported that the energy-loss near-edge structure of the beam-damaged cerium oxide exhibits Ce $M_{4,5}$ edge shapes that are consistent with reduction to a Ce (III) oxide. They also observed a decrease in the energy of M_5 and M_4 maxima as well as an increase in M_5/M_4 ratio. Ce $M_{4,5}$ edges of Ce (IV) and Ce (III) bearing materials were investigated for example monazite—$CePO_4$, loparite—$(Ce, Na, Ca)_2(Ti, Nb)_2O_6$, and cerianite—$CeO_2$ as shown in figure 4.2 (a). They highlighted the effect of increasing electron dose leading to the beam damaged reduction of Ce (IV) to Ce (III), shown in figure 4.2 (b). Beam irradiation may also lead to the displacement of atoms thereby distorting the crystal perfection, also known as displacement damage (Egerton et al., 2004). This effect can be diagnosed by examining the diffraction pattern before and after the spectral imaging through the high resolution images. Figure 4.3 represents an illustration of a visual inspection of a typical example of beam damage to the crystal structure, however this can be minimised by lowering the acquisition time during spectral imaging. It is also known that beam damage to a larger extent is thickness dependent. So thinner specimen are more prone to structural and spectral changes caused due to electron damage (Garvie and Craven, 1994). All these things were carefully considered and much attention was paid while running the EELS measurements. The chosen acquisition time of 2 seconds was monitored for any beam

damage to the reference CeO_2 and consecutive reduction of Ce (IV) to Ce (III) and no beam damage was observed.

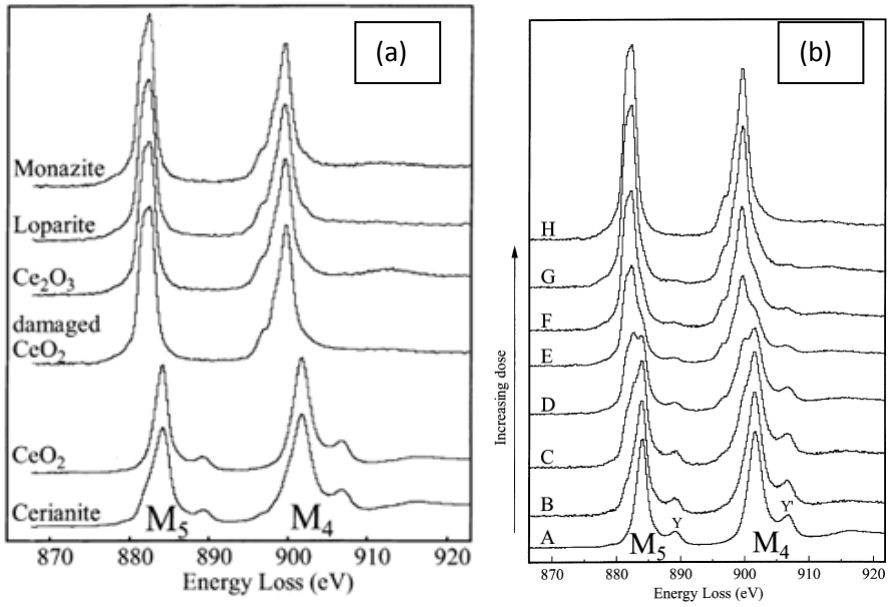

Figure 4.2 (a) Ce $M_{4,5}$ edges of Ce (IV) and Ce (III) bearing materials were investigated for example monazite—$CePO_4$, loparite—$(Ce, Na, Ca)_2(Ti, Nb)_2O_6$, and cerianite—$CeO_2$ and observed for their shape, energy positions and M_5/M_4 area ratio (b) Damage sequence from fresh (A) to damaged (H) CeO_{2-x} from a sample of thickness 0.17 x inelastic mean free path. After H the edge showed no further changes with electron dose. The estimated doses in e/$A^{\circ 2}$ are (a) 3 x 105; (b) 6 x 105; (c) 2 x 106; (d) 3 x 106; (e) 7 x 106; (f) 1 x 107; (g) 2 x 107; and (h) 5 x 107, adapted from (Garvie and Buseck, 1999)

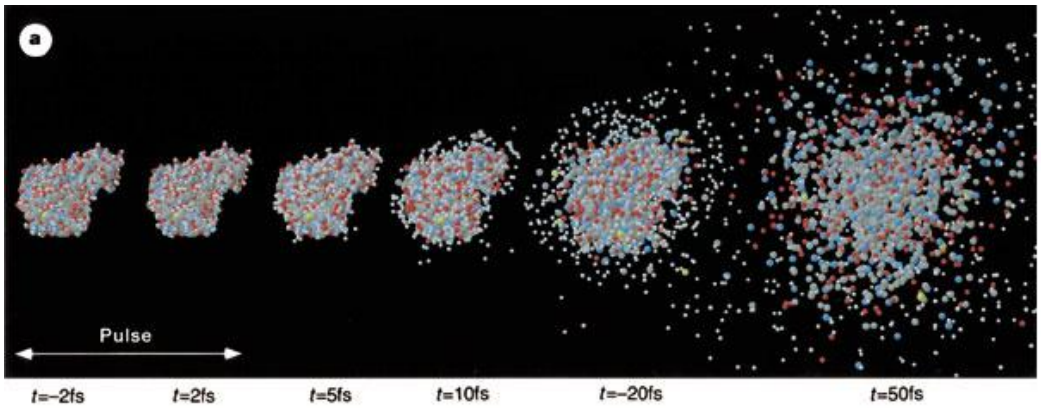

Figure 4.3 An illustration of the beam induced damage to the crystal structure with longer acquisition times, adapted from (Neutze et al., 2000)

4.3 Oxidation state quantification experiments for sample C1, C2 and C3 using EELS

The ceria nanocubes C1, C2 and C3 were synthesised by myself and their synthetic scheme has been discussed in chapter 3 (section 3.2.1, synthesis 1). The particles have been characterised for their size and shape by DLS and TEM (chapter 3, section 3.2.1, Synthesis 1).

4.3.1 EELS measurements on nanocubes C1, C2 and C3

The EELS scan for the nanocubes C1 (30.8±7.3 nm), C2 (20.6±7.3 nm) and C3 (15.8±4.6 nm) have been collected at three points called A, B, C which have been assigned as shown in the figure 4.4 (a) where A indicates the center of the particle, B is the point between the center and edge of the particle and C is the outmost edge of the particle and the M_5/M_4 ratio extracted from this line scan across the particle indicates the variation of cerium oxidation state across the particle as we go from centre towards the edge of the particle.

4.3.1.1 Results and discussion of EELS measurements on nanocubes C1

The M_5/M_4 ratios extracted from the center of the nanocube with diameter (20 nm) from sample C1 is close to that of Ce (IV), while that from the edge is close to Ce (III) (Table 4.1, particle1). Figure 4.4 (a) clearly illustrates the different intensities of M5 and M4 white lines for particle 1 as the line scan was carried out from center towards the edge of the nanocube (C1).

Table 4.1 M_5/M_4 ratio at points A, B and C for sample C1

	Sample C1				**$CeNO_3$ as standard**	**Bulk CeO_2 as standard**
Depth	Particle 1	Particle 2	Particle 3	Particle 4	Ce (III)	Ce (IV)
A (at 8nm)	0.949	0.876	1	0.973	1.23	0.82
B (at 4nm)	0.898	1.01	0.885	0.942		
C (< 1nm)	1.1	1.01	1.24	1.19		

A number of measurements have been carried out on different nanoparticles of the same sample as well as around the perimeter of the particles (Figure 4.2 (b-d)). The results obtained have been illustrated in table 4.1. It has been observed that the nanocubes in sample C1 had Ce (III) present in the top 1nm layer of the particle. However, the core of the NPs contained only Ce (IV). Figure 4.4 (a-d) illustrate different NPs from sample C1 with an approximate size of about 18-20 nm. In all the cases, Ce (III) has been found only in the top 1nm layer (M) whereas the core (A= 9-10 nm deep) as well as the point between the center and the edge (B= 4-5 nm deep) had only Ce (IV) present. This indicates that the oxidation state of the ceria NPs is not uniform throughout the particle and the valence reduction process is predominant at the surface as compared to the interior of the particle.

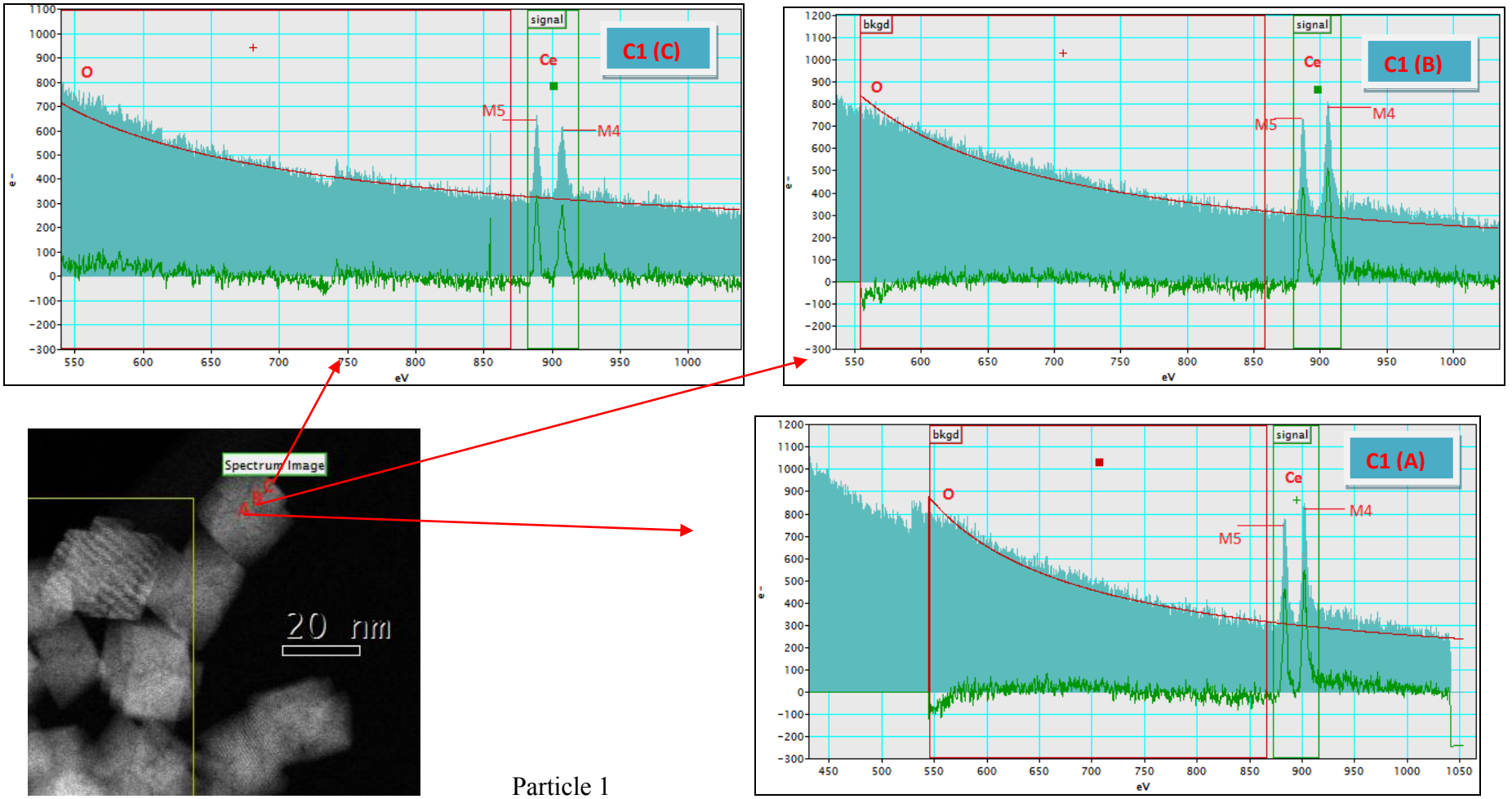

Figure 4.4 (a) EELS spectra illustrating different intensities of M_5 and M_4 white lines for particle 1 as the line scan was carried out from center towards the edge of the nanocube (C1)

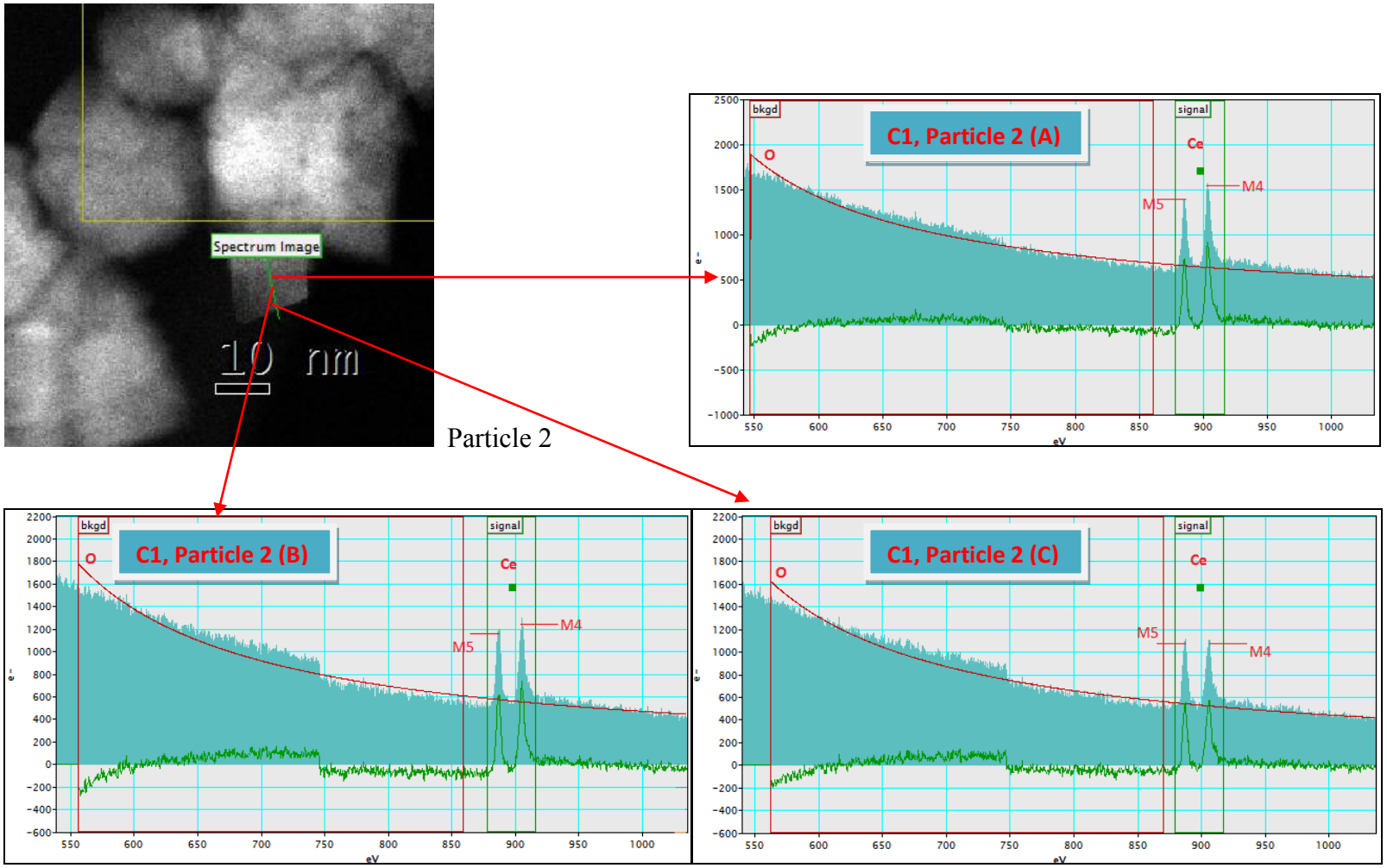

Figure 4.4 (b) EELS spectra illustrating different intensities of M_5 and M_4 white lines for particle 2 as the line scan was carried out from center towards the edge of the nanocube (C1)

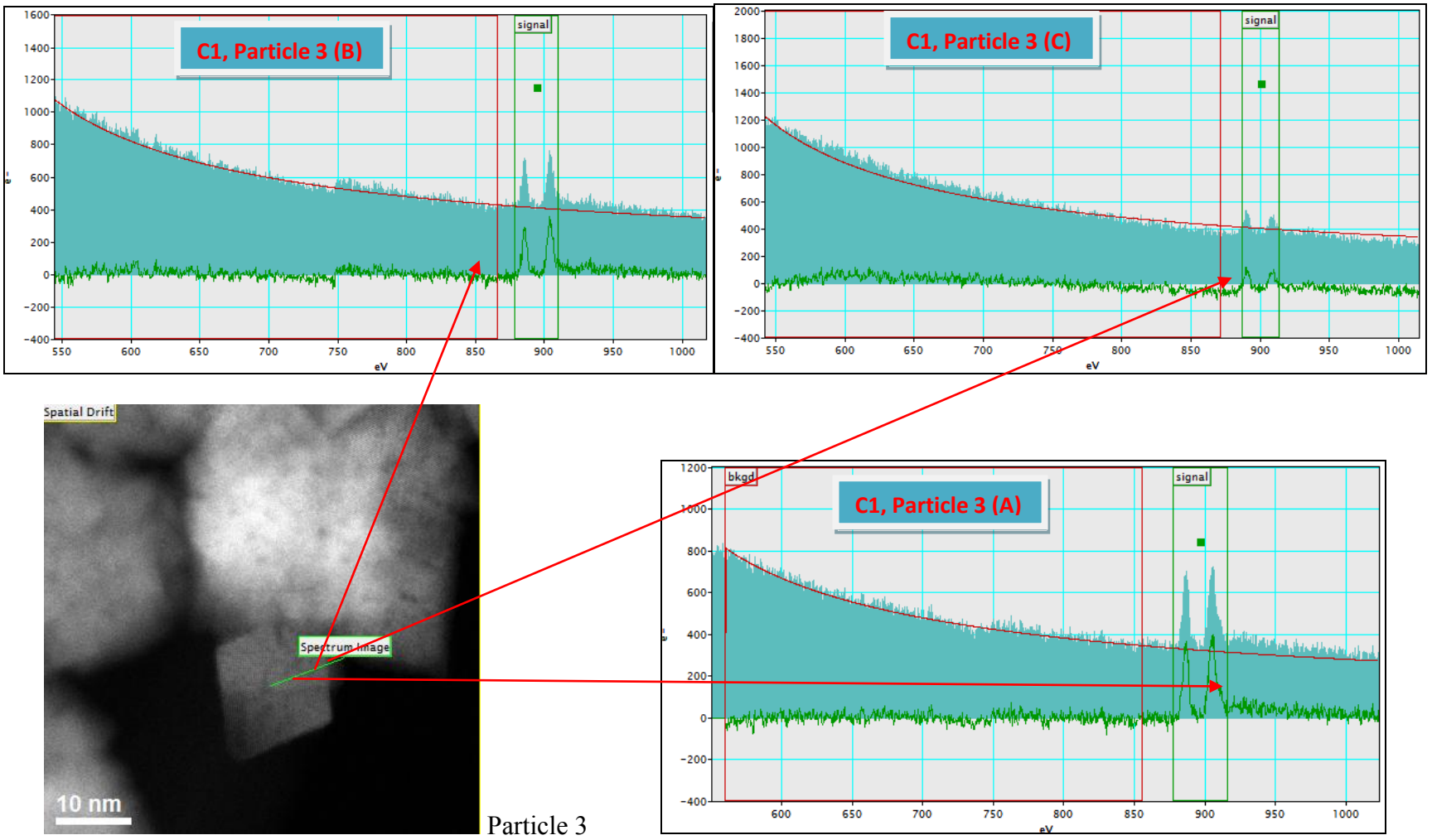

Figure 4.4 (c) EELS spectra illustrating different intensities of M_5 and M_4 white lines for particle 3 as the line scan was carried out from center towards the edge of the nanocube (C1)

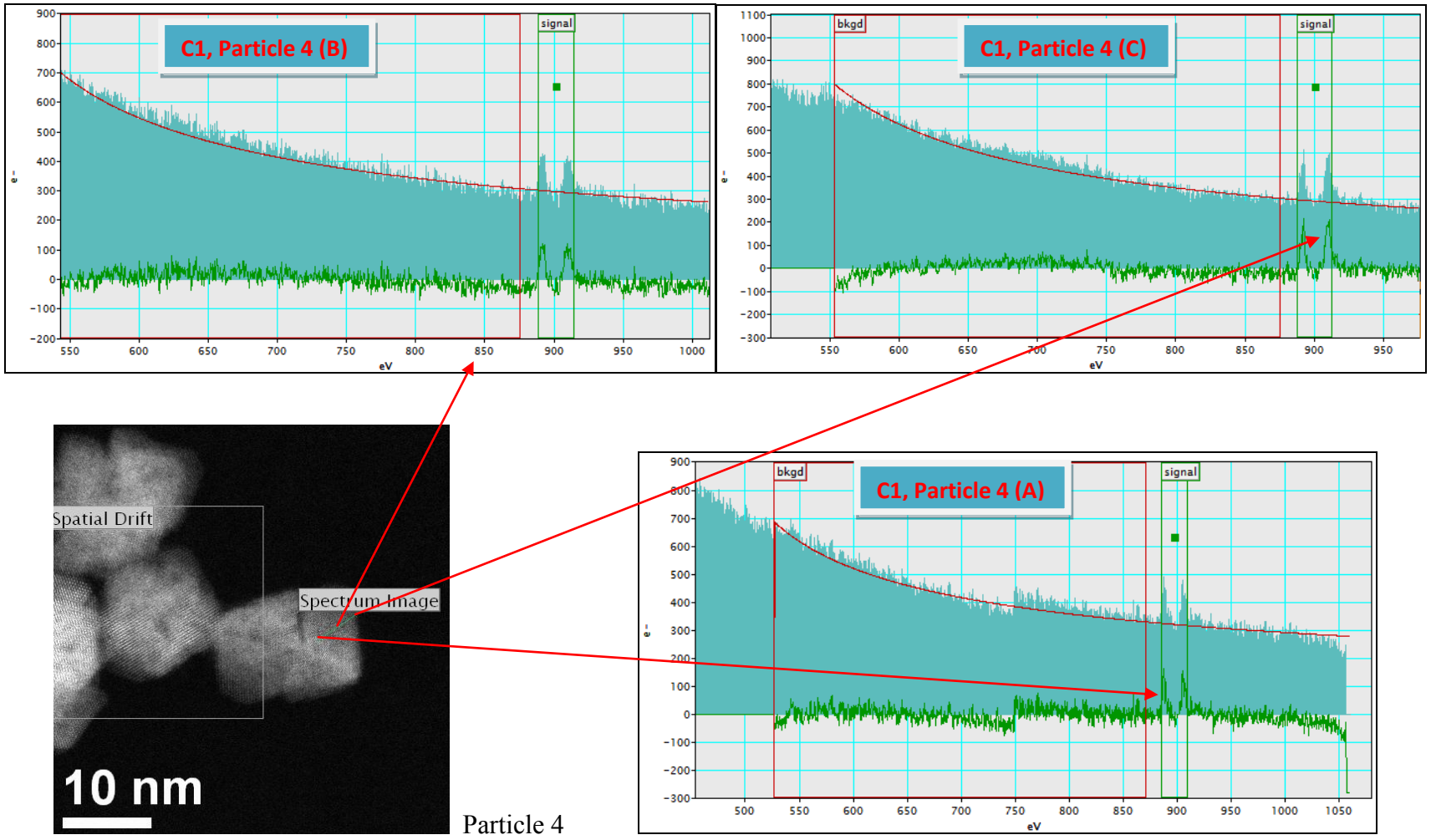

Figure 4.4 (d) EELS spectra illustrating different intensities of M_5 and M_4 white lines for particle 4 as the line scan was carried out from center towards the edge of the nanocube (C1)

It is also known that the relative intensity of the white lines (M_4 and M_5) of the cerium in the EELS can be used to determine the valence of the ceria nanoparticles, a high intensity M_5 peak (peak height) corresponds to the presence of a significant Ce (III) oxidation state whereas it is the vice versa in case of a low intensity M_4 peak. This has been observed for all the measurements (Figure 4.4 (a-d)). It was found that the M_5 signal was more intense at the edges only whereas the M_4 signal was bigger when the probe was at points A and B (at center of the particle and between the center and edge of the particle). The results obtained are in good agreement with the second derivative methodology used here but since the intensity method is dependent on the thickness of the sample, the results have not been compared and discussed here. The M_5/M_4 ratios obtained during various line scans (figure 4.4 (a-d)) are summarised in tables 4.1. After the quantitative analysis of the M_5/M_4 ratios obtained from the investigated particles at different depths of the particle, the data shows that there is 32 % Ce (III) present in the core and 77 % Ce (III) present on the edges of the sample C1.

4.3.1.2 Results and discussion of EELS measurements on nanocubes C2

Nanocubes in sample C2 are comparatively smaller in size (20.6±7.3 nm by TEM) as compared to C1 (30.8±7.3nm by TEM). Figure 4.5 (a-d) illustrate the survey scans carried out on NPs from sample C2. It was observed that for sample C2 (Figure 4.5 (a)) the particles with diameter of approx 14nm had Ce (III) present in the top 1 nm layer (C) as well as at a depth of 4nm from the edge of the particle (B) whereas the core (A) of the particle approximately at the depth of 7nm still had only Ce (IV) present (table 4.2), for example particle 1 (table 4.2). However, the particles with larger sizes again had Ce (III) present in the top 1nm layer of the particle only while the core of the NPs contained only Ce (IV) for example particle 3 and 4 with a core size of 16-18nm had Ce (III) present in the top 1 nm

layer (at the surface of the particle, point C). However the core of the particles (point A) and between the center and edge of the particles (point B) had Ce (IV).

Table 4.2 M_5/M_4 ratios at points A, B and C for sample C2

	Sample C2				**$CeNO_3$ as standard**	**Bulk CeO_2 as standard**
Depth	Particle 1	Particle 2	Particle 3	Particle 4	Ce (III)	Ce (IV)
A (at 7nm)	0.944	1.04	1.01	0.99	1.23	0.82
B (at 4nm)	1.17	1.08	1.02	0.982		
C (<1nm)	1.14	1.28	1.18	1.19		

This indicates that the valence reduction process is predominant at the surface as compared to the interior of the particle. As discussed earlier, the relative intensity of the white lines (M_4 and M_5) of the cerium in the EELS can also be used to determine the oxidation state of the ceria nanoparticles, a bigger M_5 signal corresponds to the presence of a significant Ce (III) oxidation state whereas it is the vice versa in case of a bigger M_4. This has been observed for the measurements on particle 1 with diameter of 14nm (figure 4.5 a). The M_5 peak is bigger at points B and C whereas it is smaller at point A. Similarly for particle 3 and 4, M_5 peak is bigger only at the edge of these particles (C) whereas it is smaller and less intense at points A and B (figure 4.5 c and d). The results obtained are in good agreement with the second derivative methodology (table 4.2). The results show that there is 43 % Ce (III) present in the core and 93 % Ce (III) present on the edges of the sample C2.

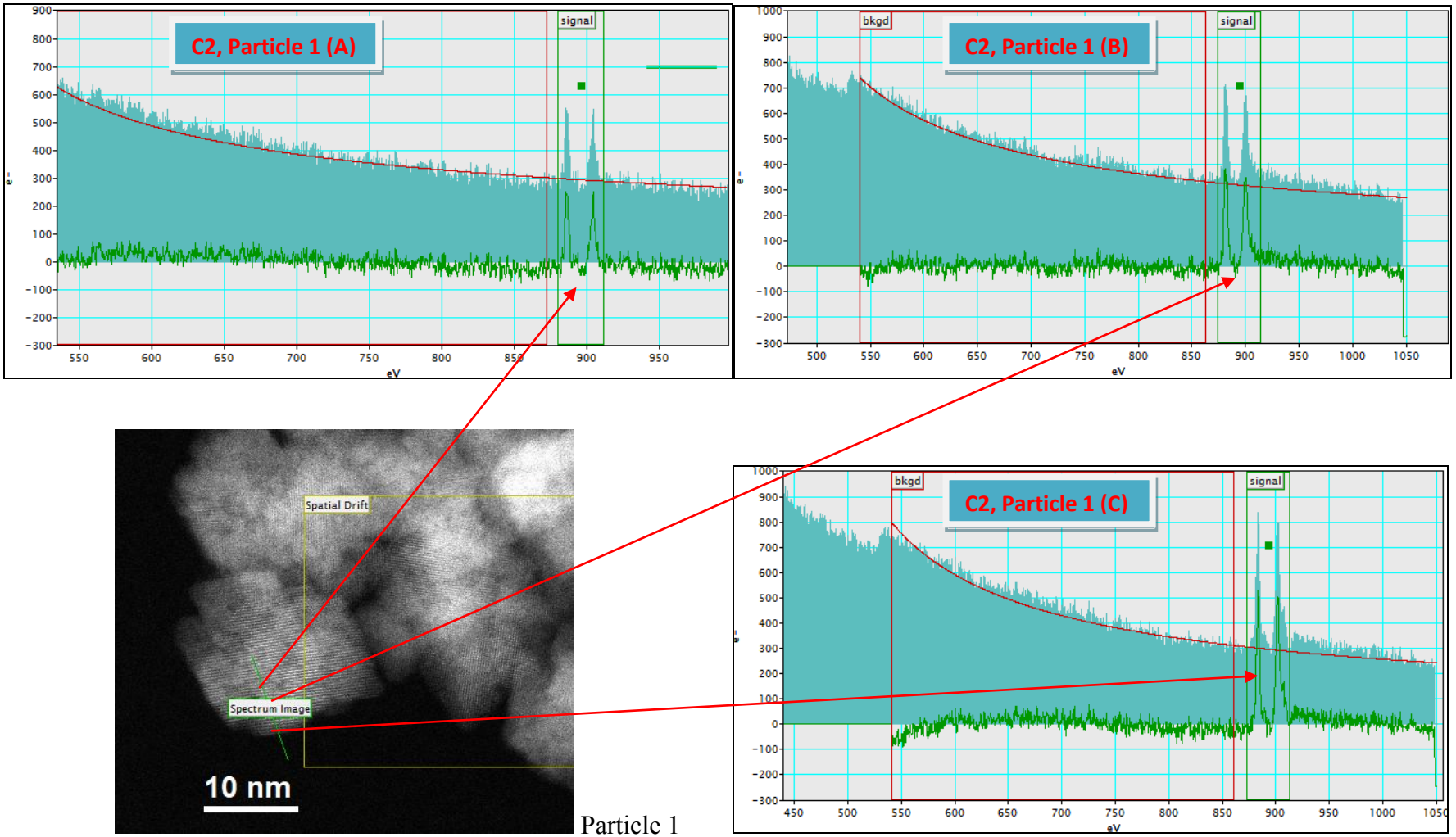

Figure 4.5 (a) EELS spectra illustrating different intensities of M_5 and M_4 white lines for particle 1 as the line scan was carried out from center towards the edge of the nanocube (C2)

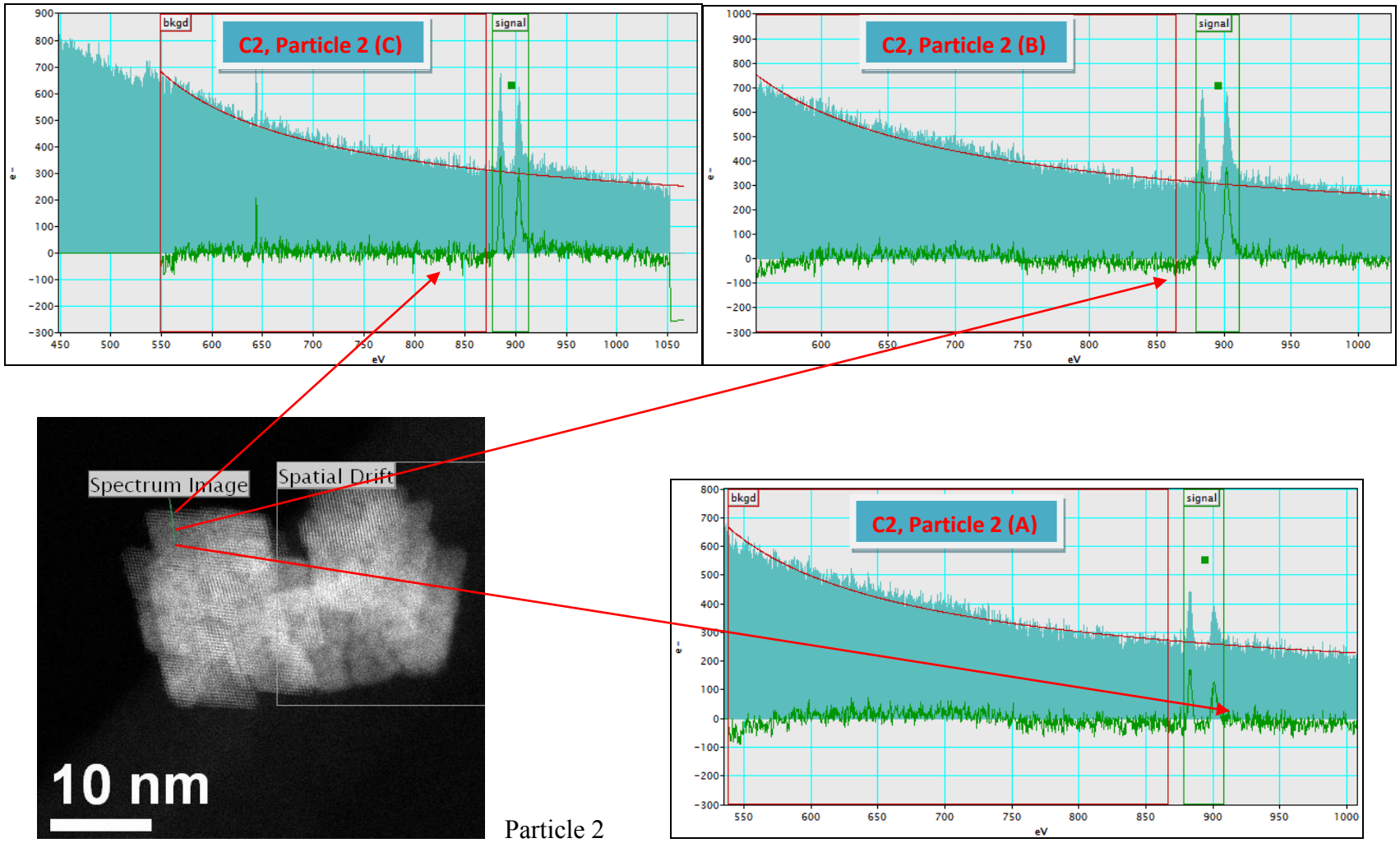

Figure 4.5 (b) EELS spectra illustrating different intensities of M_5 and M_4 white lines for particle 2 as the line scan was carried out from center towards the edge of the nanocube (C2)

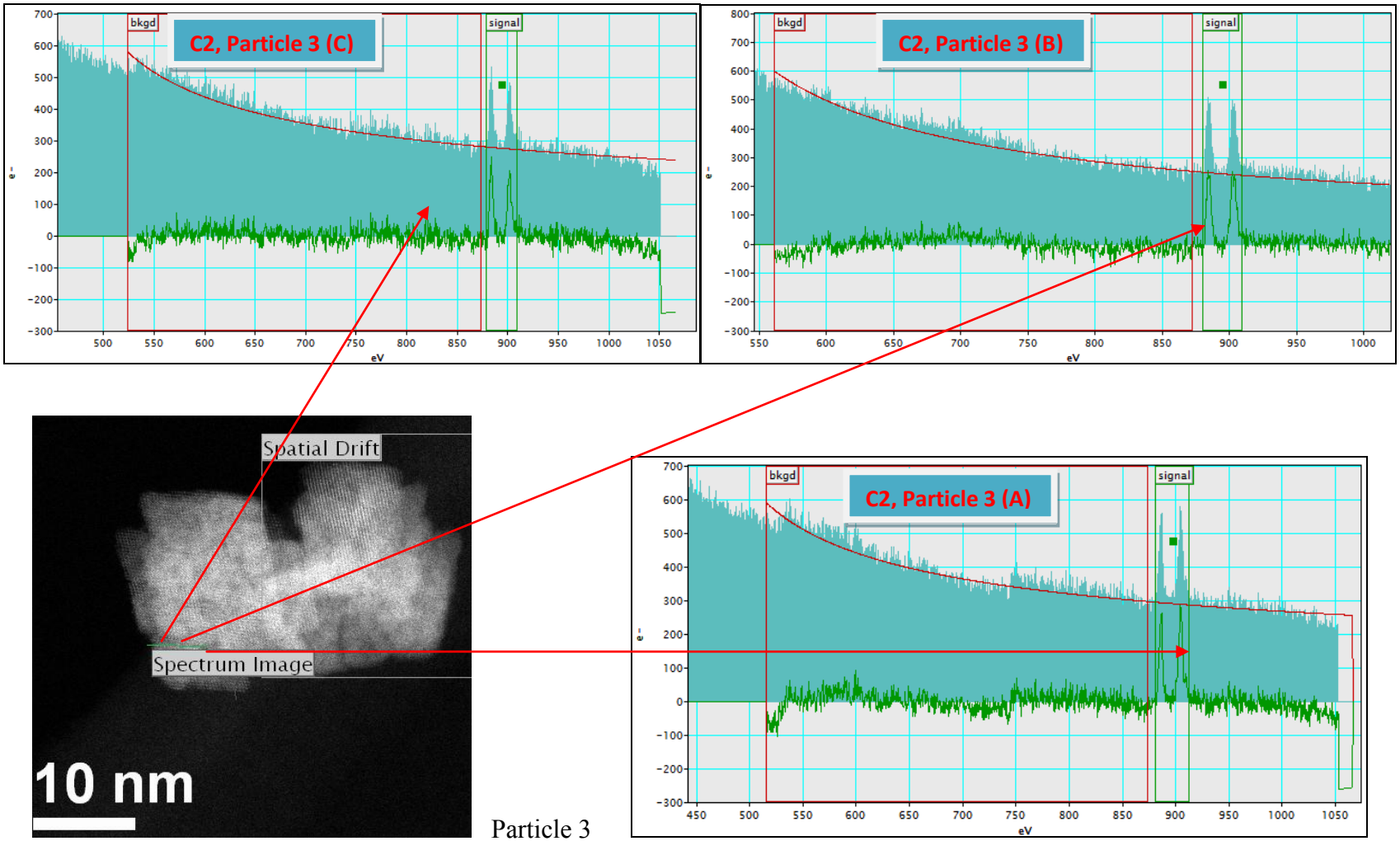

Figure 4.5 (c) EELS spectra illustrating different intensities of M_5 and M_4 white lines for particle 3 as the line scan was carried out from center towards the edge of the nanocube (C2)

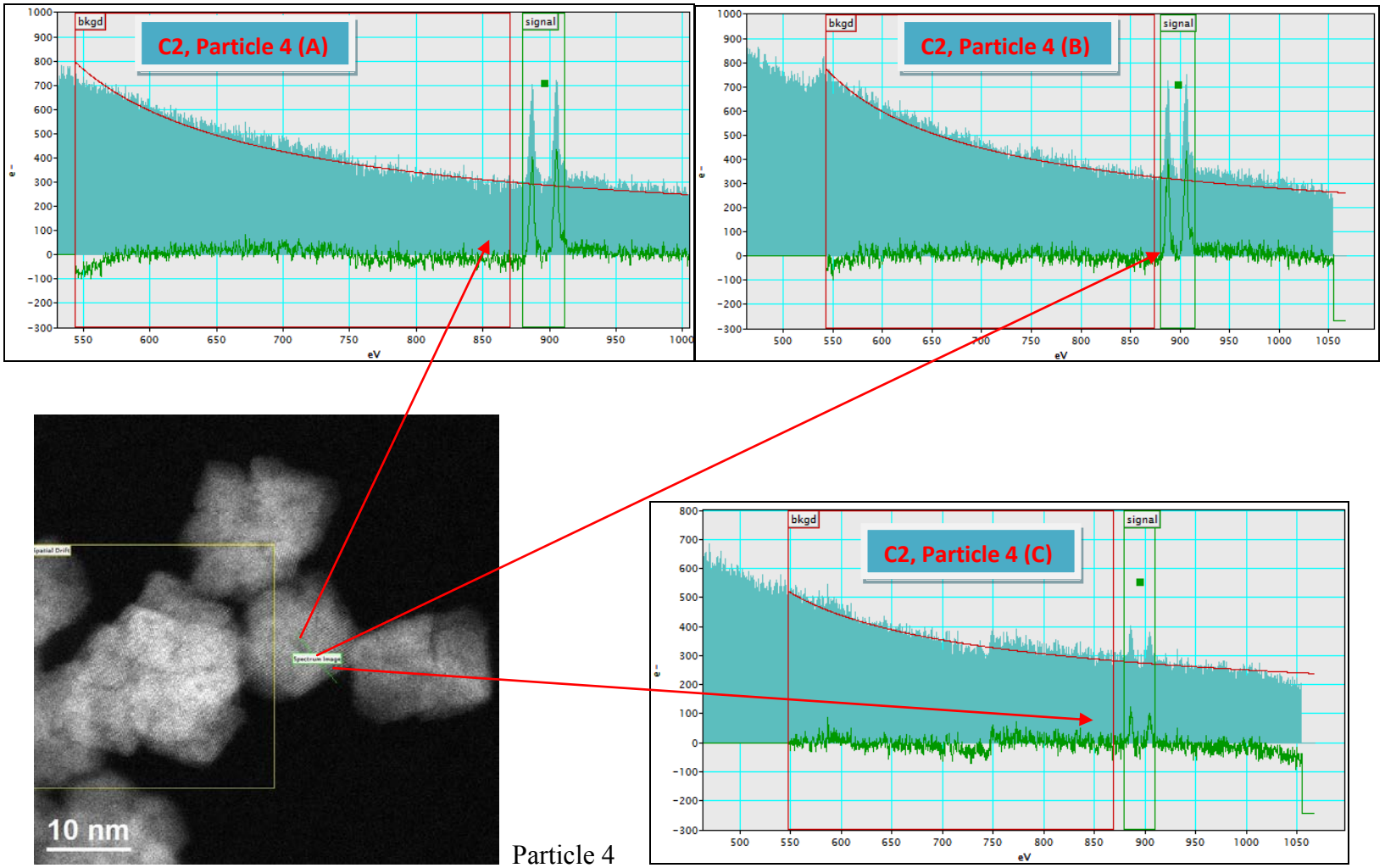

Figure 4.5 (d) EELS spectra illustrating different intensities of M_5 and M_4 white lines for particle 4 as the line scan was carried out from center towards the edge of the nanocube (C2)

4.3.1.3 Results and discussion of EELS measurements on nanocubes C3

The nanocubes in C3 (15.8±4.6 nm) are smaller than nanocubes in C1 (30.8±7.3 nm) and C2 (20.6±7.3 nm) as obtained by TEM. Figure 4.6 (a-d) illustrate the survey scans carried out on NPs from sample C3. Similar kind of results was observed as discussed earlier for sample C2. The amount of Ce (III) increased as the particle size decreased. The M_5/M_4 ratios obtained during various line scans (figure 4.6 (a-d)) are summarised in tables 4.3.

Table 4.3 M_5/M_4 ratio at points A, B and C for sample C3

	Sample C3				**$CeNO_3$ as standard**	**Bulk CeO_2 as standard**
Depth	Particle 1	Particle 2	Particle 3	Particle 4	Ce (III)	Ce (IV)
A (at 5nm)	0.997	0.973	1.03	1.02	1.23	0.82
B (at 3nm)	1.05	1.20	1.24	1.29		
C (< 1nm)	1.29	1.45	1.29	1.31		

All the NPs in C3 with approximate diameter of 10 nm or less (particle 2, 3 and 4) had Ce (III) present till 3nm deep inside the particle however, the core (approx. 5nm deep) had only Ce (IV) as oxidation state. This could be attributed to the increased presence of oxygen vacancies in smaller ceria nanoparticles than those in larger nanoparticles. Similar results were obtained from the M_5/M_4 ratios extracted out of different NPs from sample C3. The results indicate that the oxidation state of the ceria NPs is not uniform throughout the particle. Looking at the intensity of the M_5 and M_4 peaks in the EELS spectrum, all the NPs in C3 with diameter of 10nm or less showed bigger M_5 peak till 3nm deep from the surface of the

particle (at point B) however, it became shorter when the EELS was carried out at the center of the particle at point A (figure 4.6 a-d). The results match with the second derivative methodology used (table 4.3) and are evident from the figures 4.6 (a-d). After the quantitative analysis of the M_5/M_4 ratios obtained from the investigated particles at different depths of the particle, the data shows that there is 45 % Ce (III) present in the core and 100 % Ce (III) present on the edges of the sample C3.

4.3.2 Summary and conclusions of the EELS experiments carried out on nanocubes C1, C2 and C3

In summary, we have carried out systematic EELS experiments on three different samples of nanocubes, C1, C2 and C3, with different sizes. The $M_{4,5}$-edge spectra have been used to evaluate the oxidation state of cerium using STEM-EELS. Line scans have been carried out looking at local oxidation state variation across the particle as we go from the centre towards the edge of the particle. The data has been collected at three points A, B and C where A indicates the center of the particle, B is the point between the center and edge of the particle and C is the outmost edge of the particle. The results clearly suggest that the oxidation state of ceria NPs is not uniform throughout the particle and the amount of Ce (III) increases as the particle size decreases. The results obtained for the three nanocube samples C1, C2 and C3 have been tabulated in table 4.4 and figure 4.7 clearly demonstrates the M5/M4 ratios obtained across the diameter of the particles investigated. M_5/M_4 ratios were plotted against the particle depth illustrating the oxidation state pattern observed for C1, C2 and C3 as we go from center of the particle towards the edge. STEM images have been collected both before and after the EELS scan was carried out and no damage to the nanoparticle under investigation has been observed. So the data shown is due to the amount of energy loss collected during the experiment and not an over or under estimation of the sample.

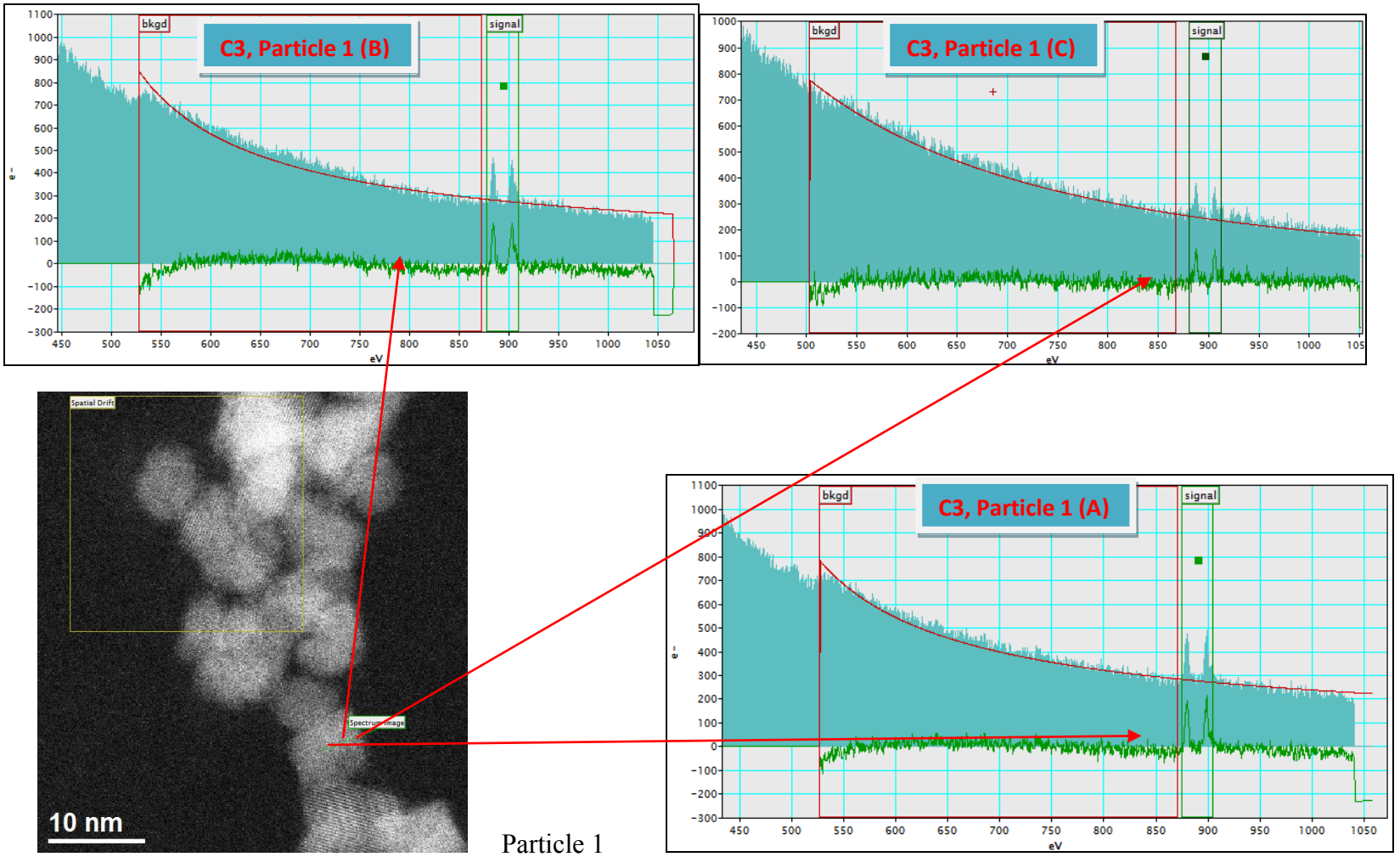

Figure 4.6 (a) EELS spectra illustrating different intensities of M_5 and M_4 white lines for particle 1 as the line scan was carried out from center towards the edge of the nanocube (C3)

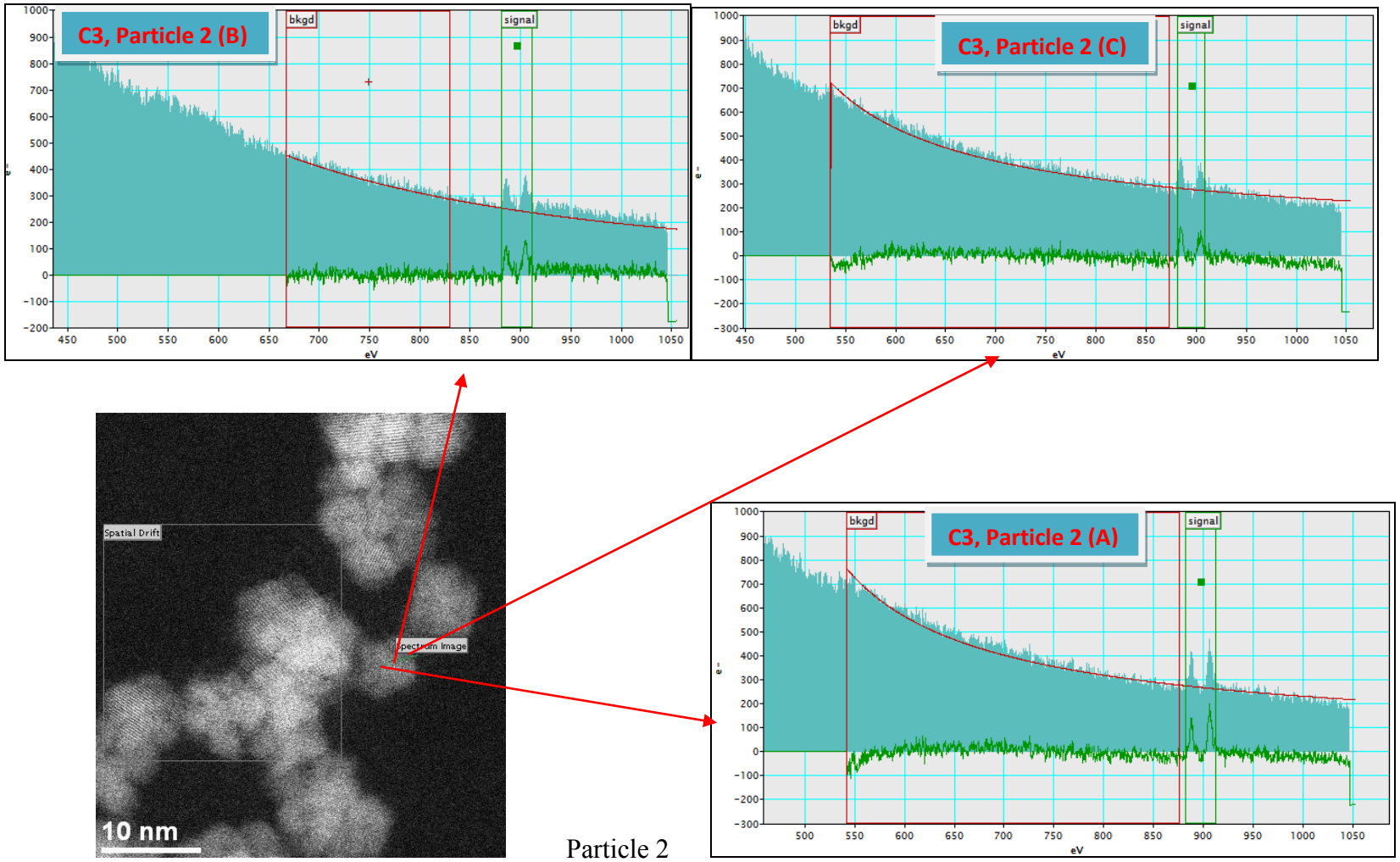

Figure 4.6 (b) EELS spectra illustrating different intensities of M_5 and M_4 white lines for particle 2 as the line scan was carried out from center towards the edge of the nanocube (C3)

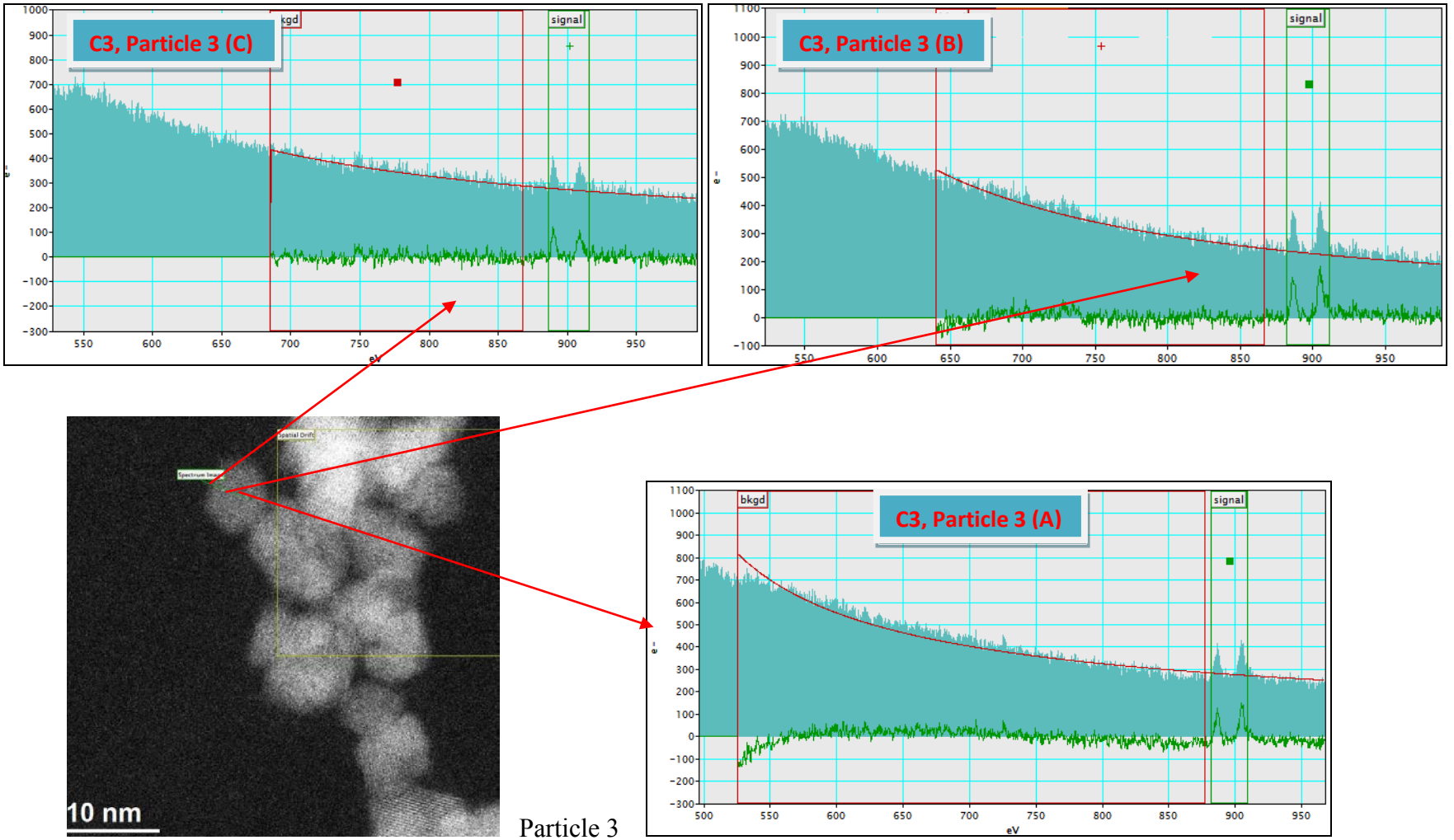

Figure 4.6 (c) EELS spectra illustrating different intensities of M_5 and M_4 white lines for particle 3 as the line scan was carried out from center towards the edge of the nanocube (C3)

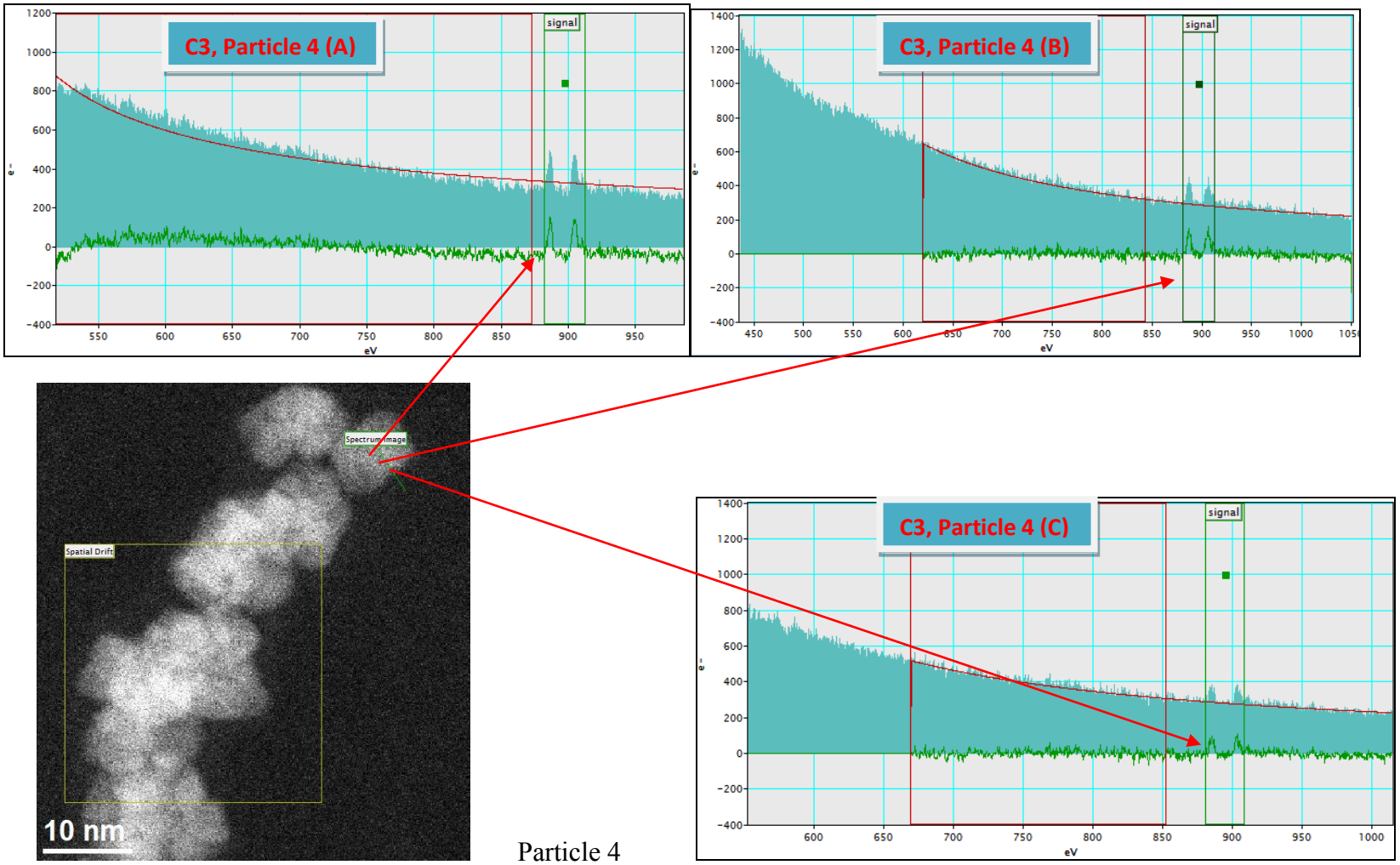

Figure 4.6 (d) EELS spectra illustrating different intensities of M_5 and M_4 white lines for particle 4 as the line scan was carried out from center towards the edge of the nanocube (C3)

Table 4.4 Oxidation state quantification data for the nanocubes C1, C2 and C3 as obtained from EELS

Sample code	Morphology	Size (nm)		EELS (%)	
		DLS	TEM	Ce (III) Center	Ce (III) Edge
C1	Nanocube	93.7±0.8	30.8±7.3	32	77
C2	Nanocube	113.4±0.5	20.6±7.3	43	87
C3	Nanocube	132.8±3.2	15.8±4.6	45	100

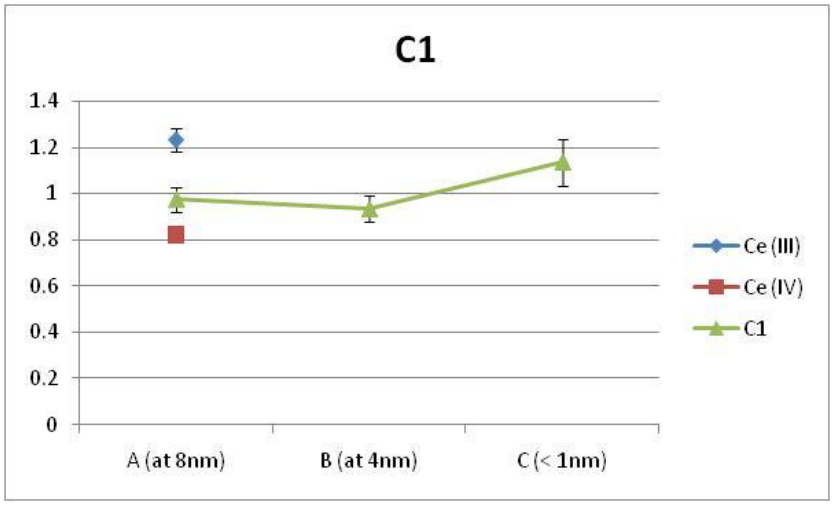

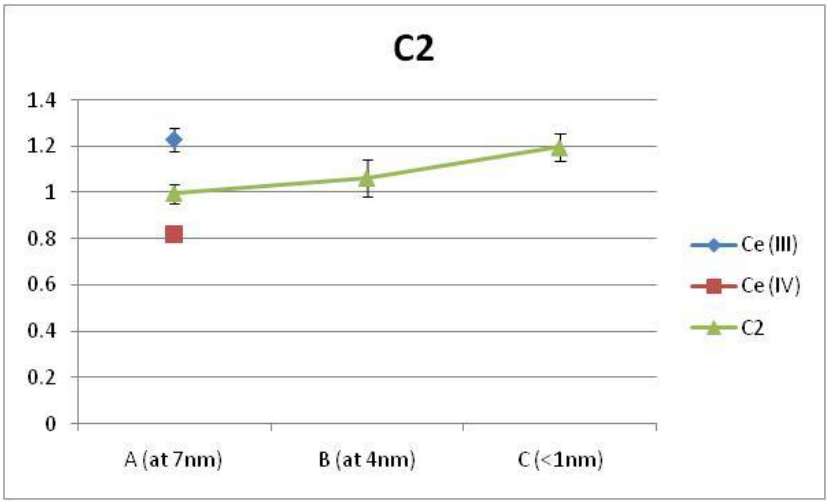

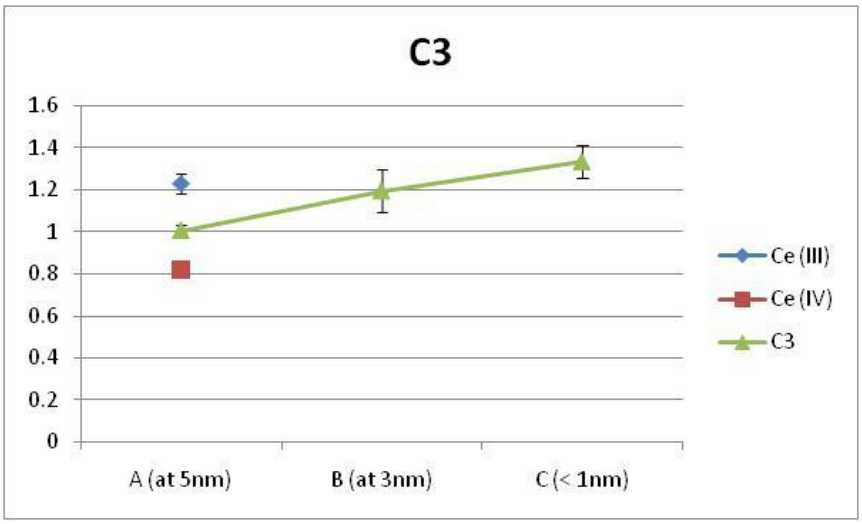

Figure 4.7 The M_5/M_4 ratios obtained across the diameter of the particles investigated are plotted against the particle depth illustrating the oxidation state pattern observed for C1, C2 and C3.

4.4 Oxidation state quantification of nanospheres sample S1 and S2 using EELS

The ceria nanospheres S1 and S2 have been synthesised by myself and their synthetic scheme has been discussed in chapter 3. The particles have been characterised for their size and shape by DLS and TEM. Details in chapter 3.

4.4.1 EELS measurements on nanospheres S1 and S2

The EELS scan for the nanospheres S1 (4.5±2.5 nm) and S2 (6.0±3.0 nm) with primary particle size of as small as 2nm have also been collected at three points called A, B, C (as discussed previously in section 4.3.1) where A indicates the center of the particle, B is the point between the center and edge of the particle and C is the outermost edge of the particle and the M_5/M_4 ratio extracted from this line scan across the particle indicates the local variation of cerium oxidation state across the particle as we go from centre towards the edge of the particle.

4.4.1.1 Results and discussion of EELS measurements on nanospheres S1

The M_5/M_4 ratios extracted from the center of the nanosphere (at point A) with diameter (3 nm) from sample S1 (particle 1) is 1.1 which is closer to that of Ce (III), while that from the edge (at point C) is 1.31, also close to Ce (III) (Table 4.8, particle1). Figure 4.6 (a) clearly illustrates the different intensities of M_5 and M_4 white lines for particle 1 as the line scan was carried out from center towards the edge of the nanosphere (S1).

Table 4.5 M_5/M_4 ratio at points A, B and C for sample S1

Depth	Sample S1							
	Particle 1	Particle 2	Particle 3	Particle 4	Particle 5	Particle 6	Particle 7	Particle 8
A	1.10	1.08	1.17	1.098	1.27	1.29	1.19	1.19
B	1.11	1.48	1.2	1.099	1.04	1.21	1.18	1.29
C	1.30	1.57	1.2	1.1	1.14	1.16	w/s	w/s
* w/s= weak signal								

A number of measurements have been carried out on different nanospheres of the same sample (Figure 4.8 (b-h)). The results obtained have been illustrated in table 4.5. We found that all the nanospheres in sample S1 between the size of 2-3 nm had Ce (III) present at points A, B and C and no Ce (IV) was detected. Figure 4.8 (a-h) clearly illustrate different NPs from sample S1 with an approximate size of about 2-7 nm. In all the cases, it was found that with spherical particles ≤ 3 nm, only Ce (III) was detected at the surface as well as at the core of the particle. However, with larger sized particles, it was observed that the extracted M_5/M_4 ratios were closer to Ce (III) at the surface (point C) as well as between the center and edge of the particle (point B) while the core (point A) had only Ce (IV) present. For example,

the M_5/M_4 ratios extracted from points A and B of a particle size 5nm (particle 4 in table 4.5) were closer to Ce (III) whereas those extracted from point C clearly suggest the presence of Ce (III). This indicates that for larger particle (>3nm), the valence reduction process is predominant at the surface as compared to the interior of the particle. The investigated particles 1, 3, 6, 7 and 8 are in the range of 2-3nm in diameter and all showed the complete presence of Ce (III) in them at points A, B and C. The results illustrate comparatively higher amount of Ce (III) present in smaller nanoparticles with particles ≤ 3nm to be completely Ce (III). During the analysis, some regions showed very low intensity spectrum. This is generally due to very thin areas under investigation and is commonly observed on the edges. Since, the intensity of the signal obtained is very weak, it is difficult to extract the signal out of the spectrum and hence no information could be obtained. These observations have been marked as w/s in the table 4.5 and have not been used for the quantification process.

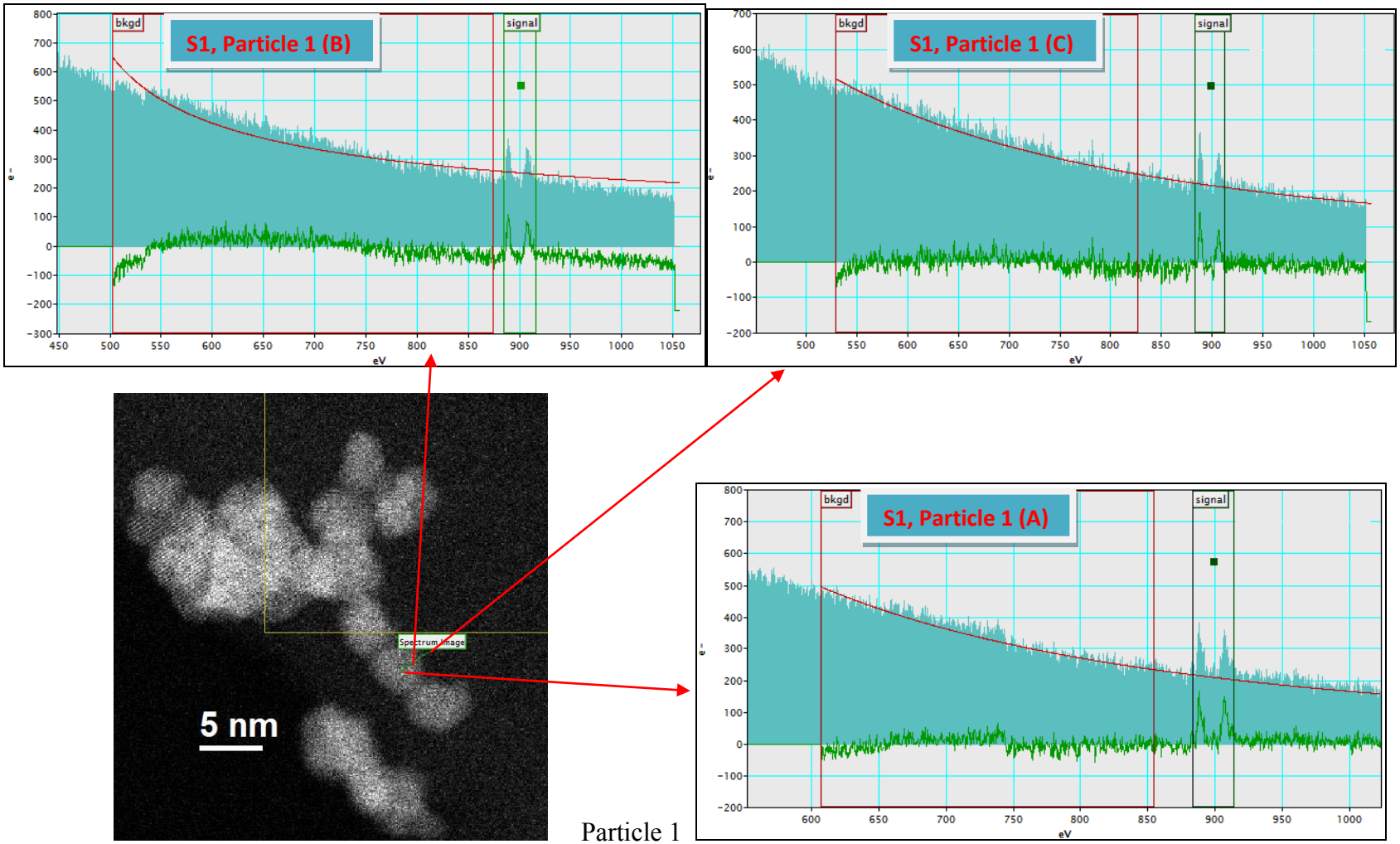

Figure 4.8 (a) EELS spectra illustrating different intensities of M_5 and M_4 white lines for particle 1 as the line scan was carried out from center towards the edge of the nanosphere (S1)

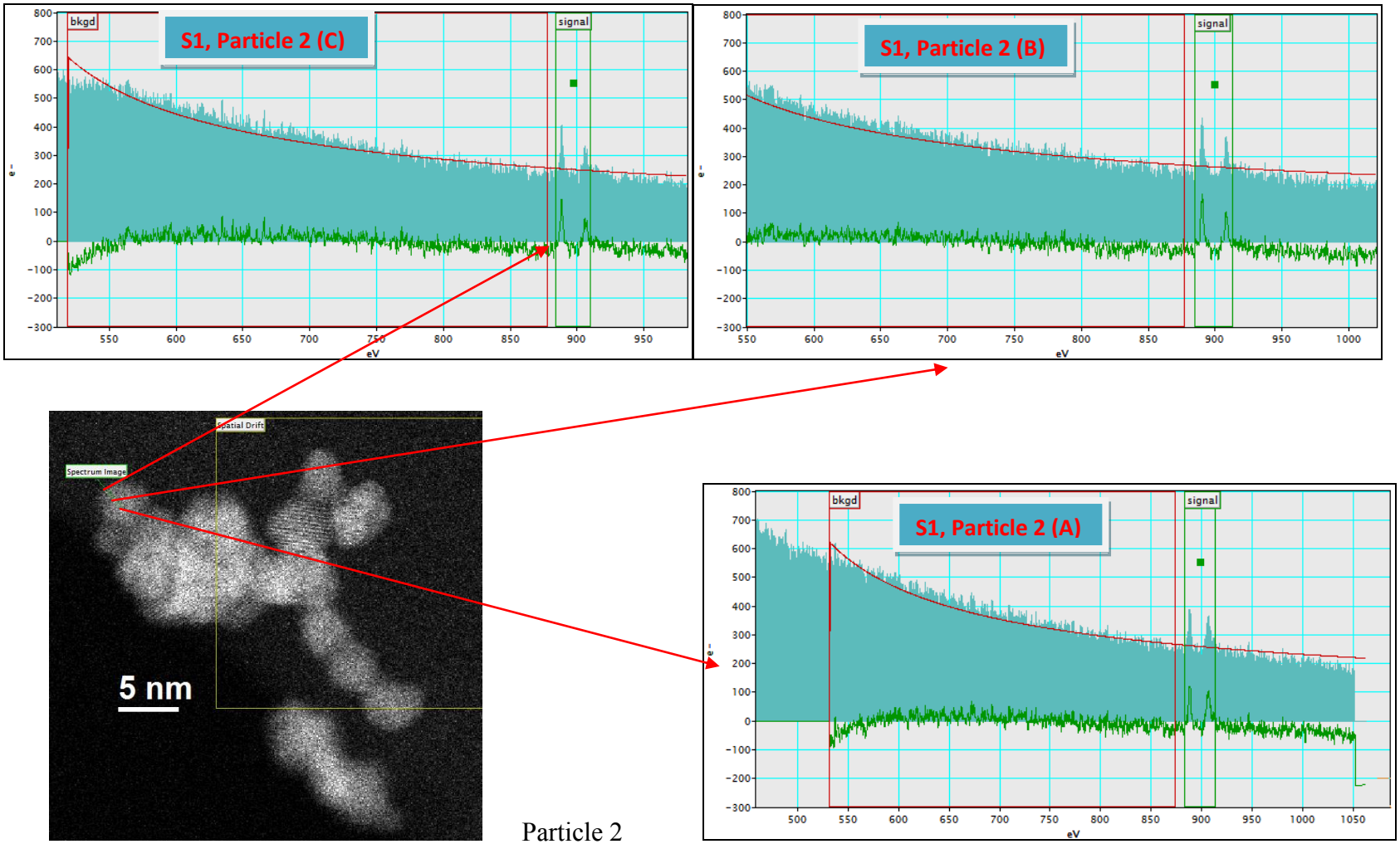

Figure 4.8 (b) EELS spectra illustrating different intensities of M_5 and M_4 white lines for particle 2 as the line scan was carried out from center towards the edge of the nanosphere (S1)

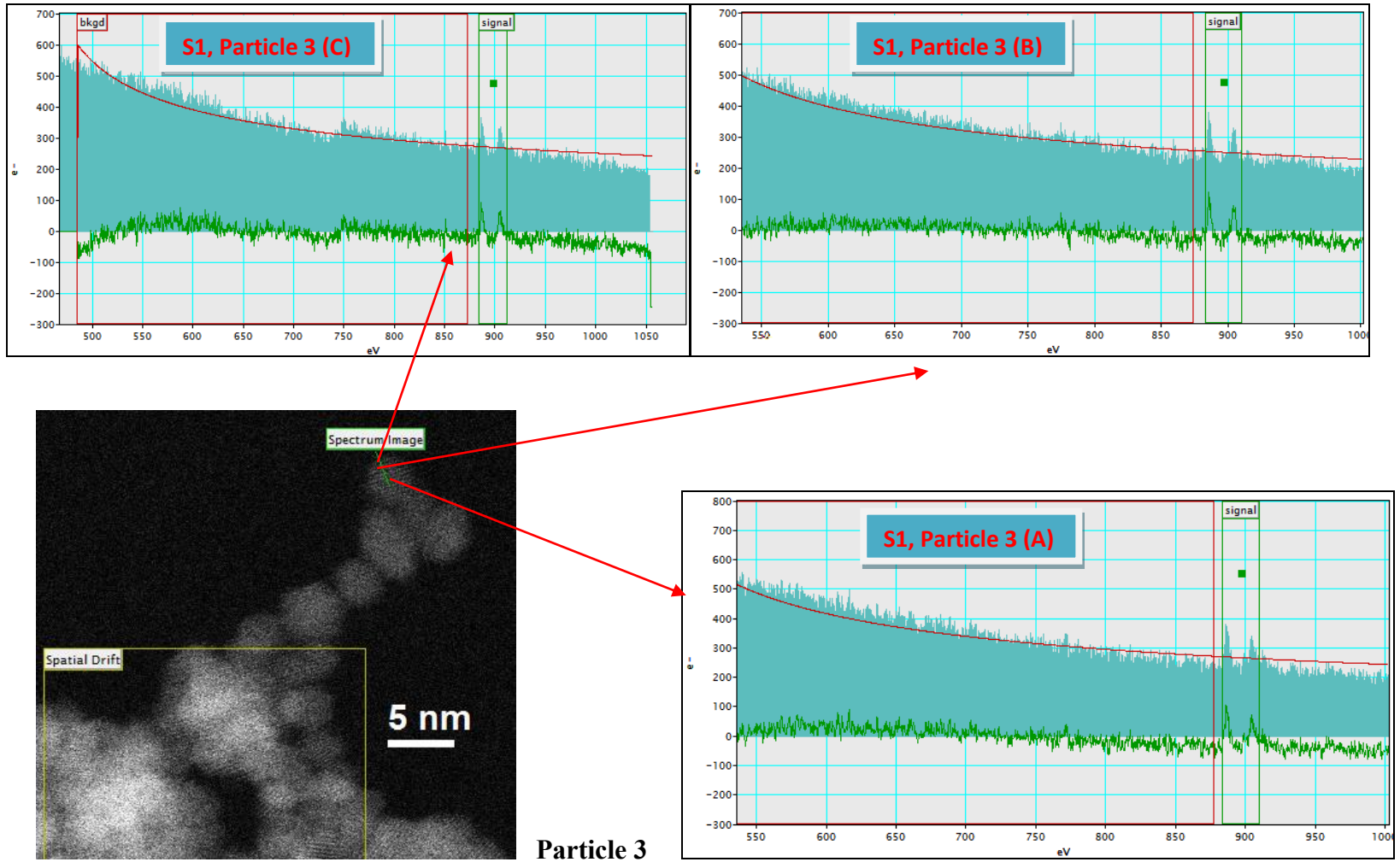

Figure 4.8 (c) EELS spectra illustrating different intensities of M_5 and M_4 white lines for particle 3 as the line scan was carried out from center towards the edge of the nanosphere (S1)

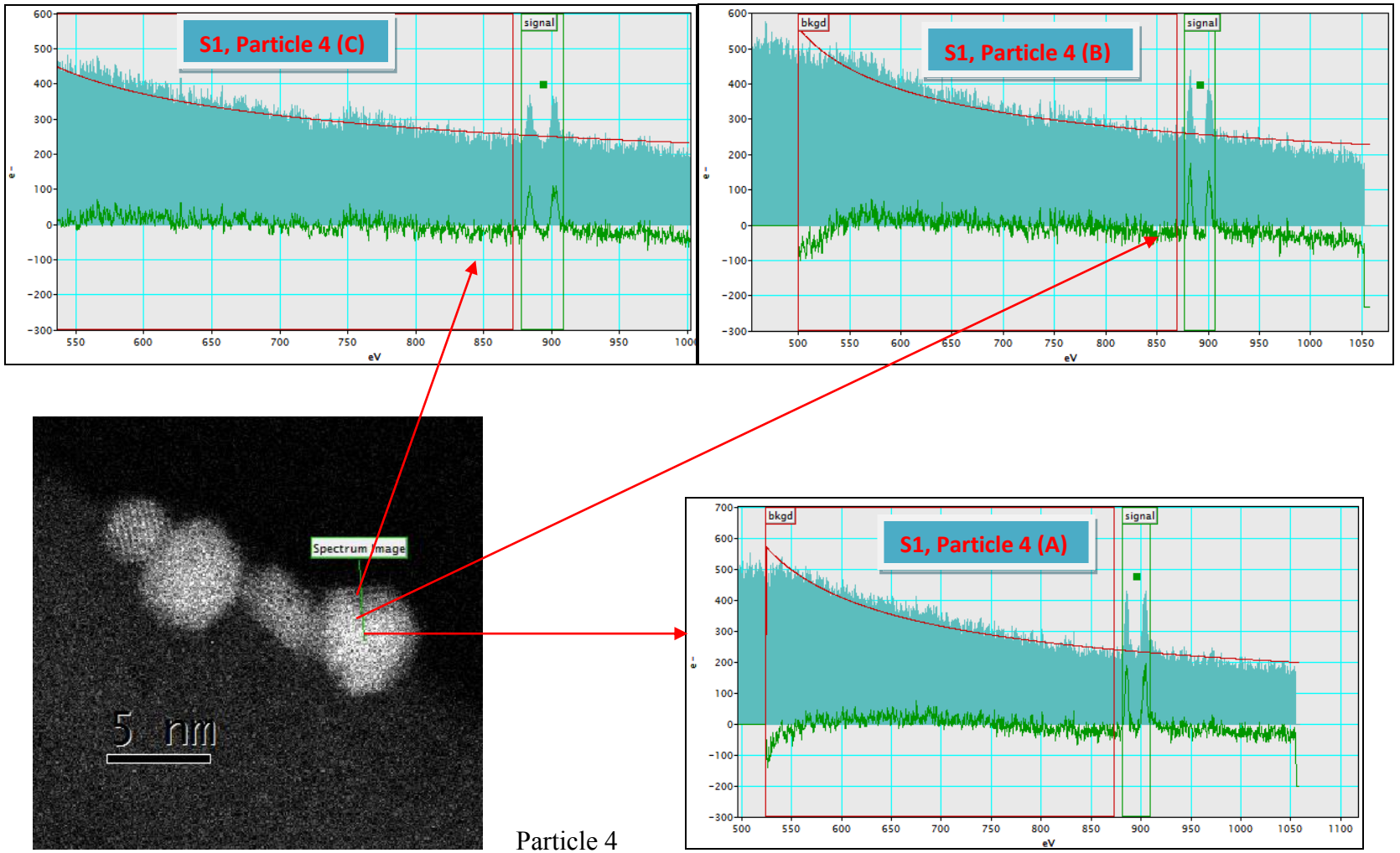

Figure 4.8 (d) EELS spectra illustrating different intensities of M_5 and M_4 white lines for particle 4 as the line scan was carried out from center towards the edge of the nanosphere (S1)

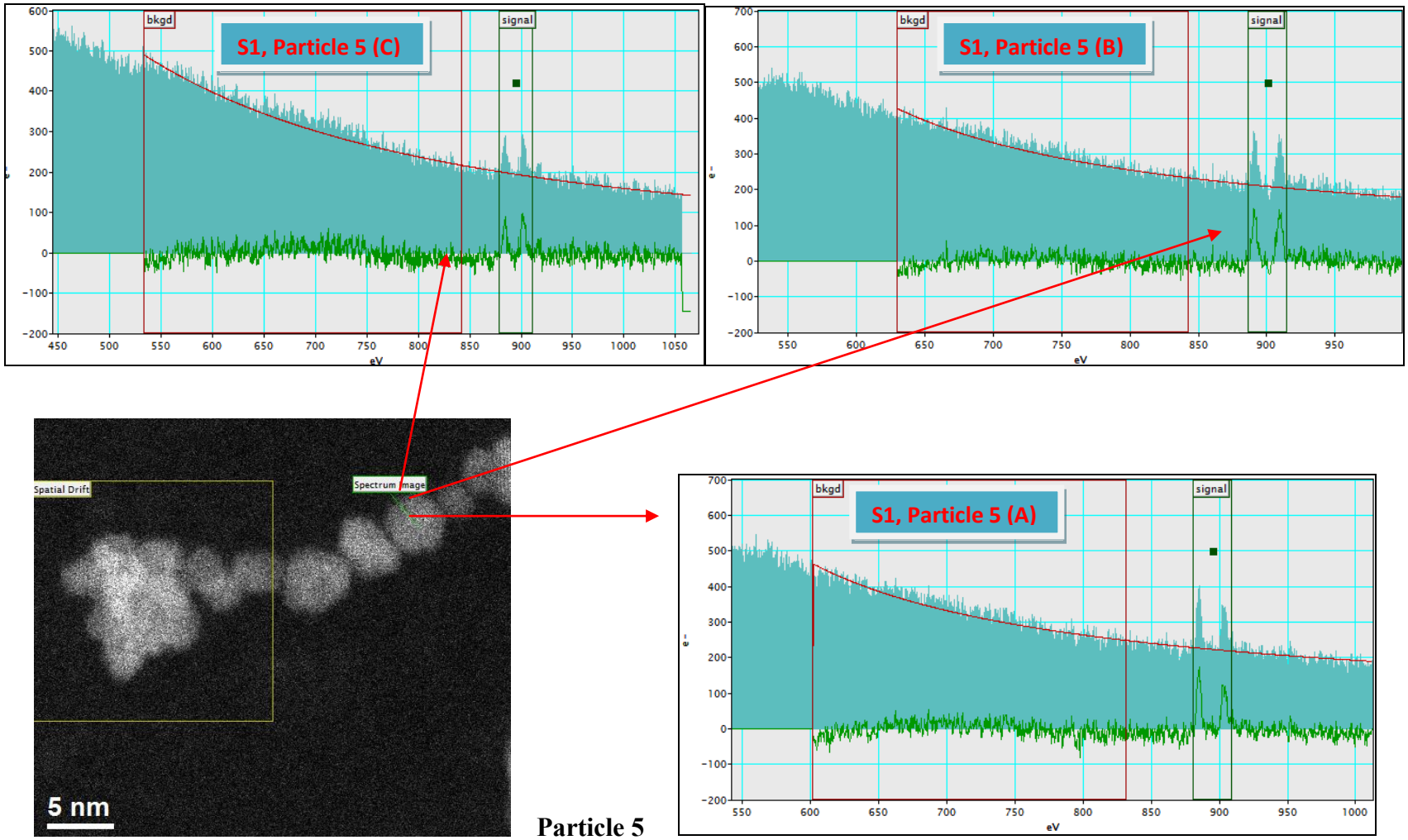

Figure 4.8 (e) EELS spectra illustrating different intensities of M_5 and M_4 white lines for particle 5 as the line scan was carried out from center towards the edge of the nanosphere (S1)

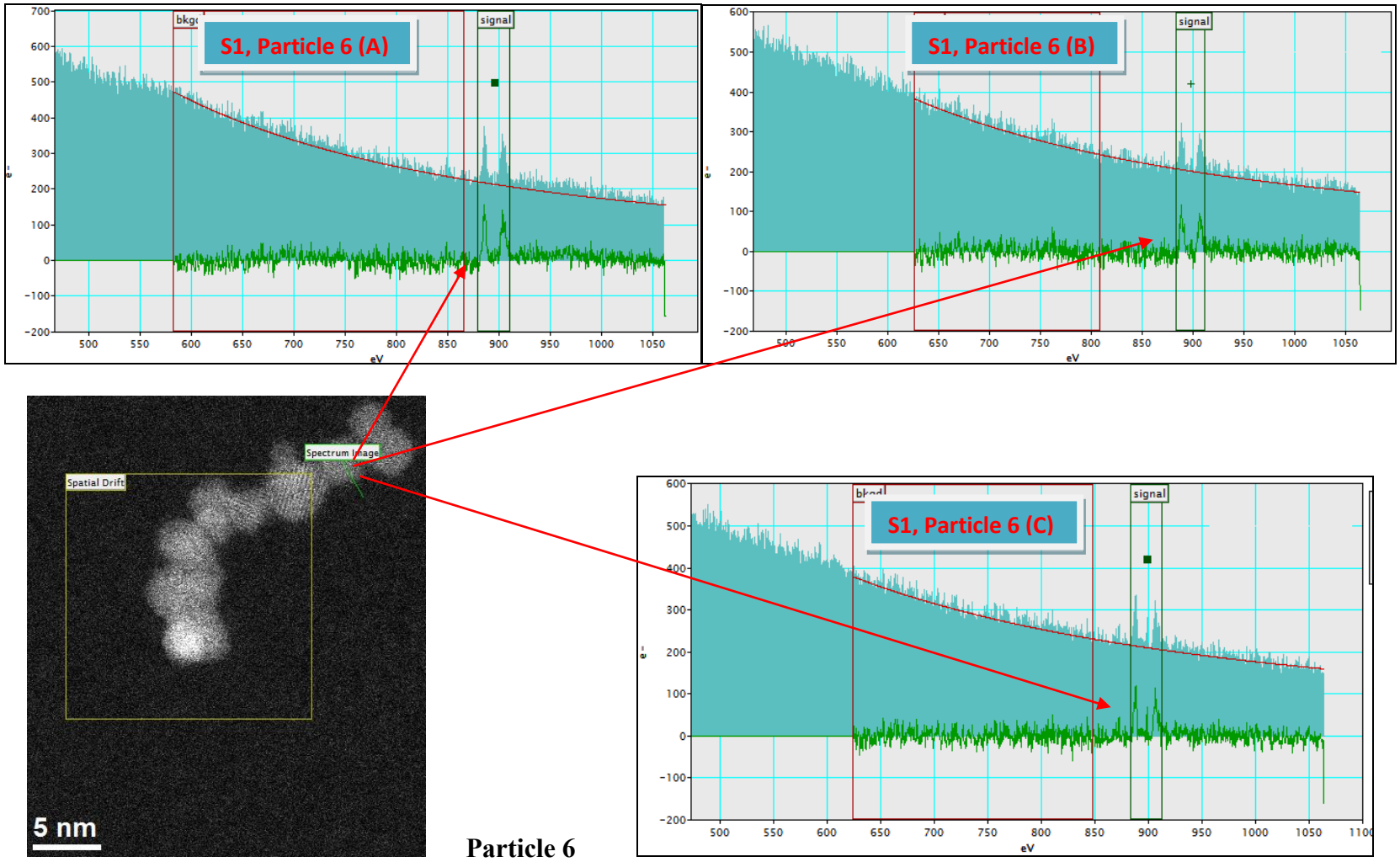

Figure 4.8 (f) EELS spectra illustrating different intensities of M_5 and M_4 white lines for particle 6 as the line scan was carried out from center towards the edge of the nanosphere (S1)

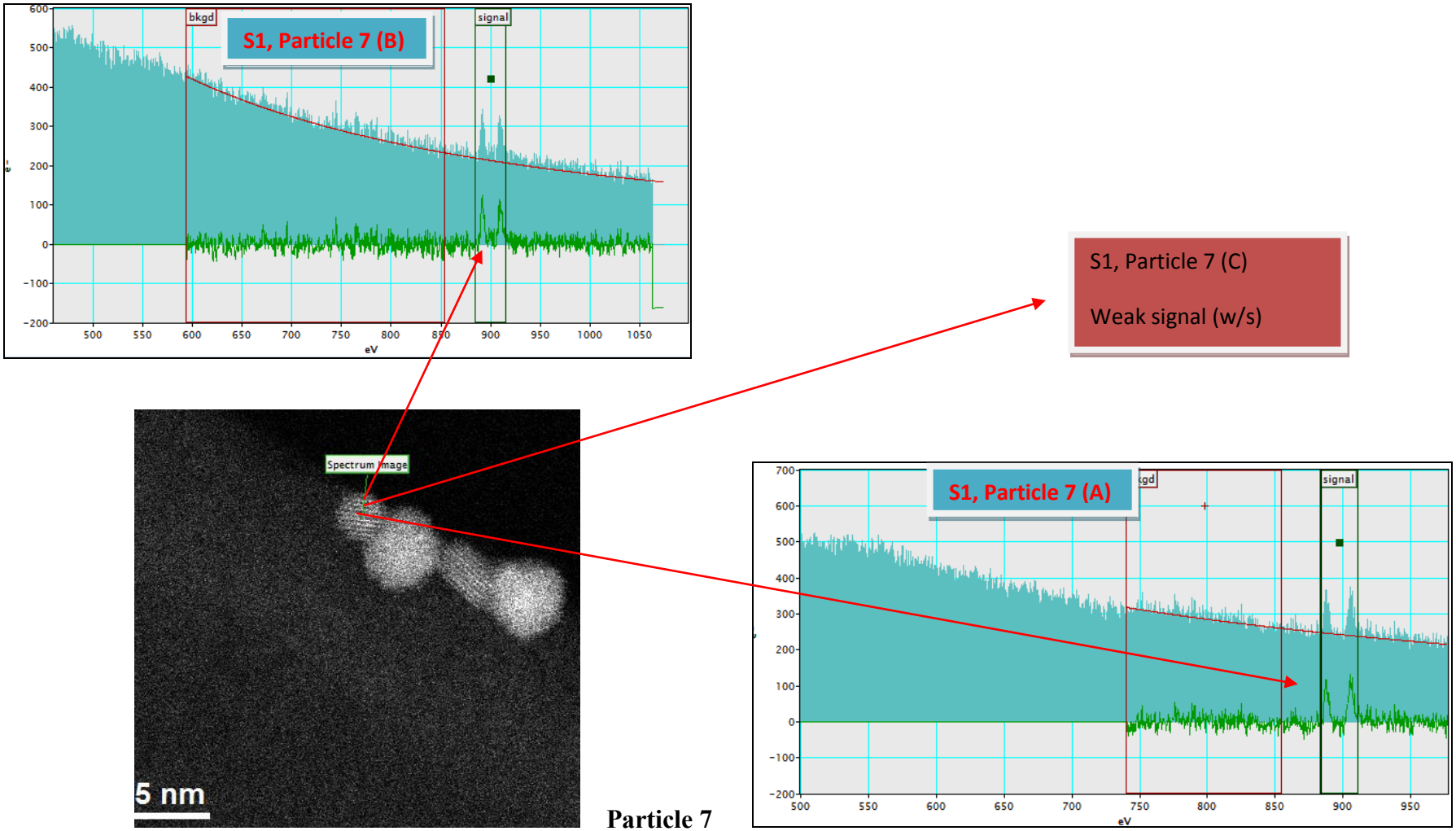

Figure 4.8 (g) EELS spectra illustrating different intensities of M_5 and M_4 white lines for particle 7 as the line scan was carried out from center towards the edge of the nanosphere (S1)

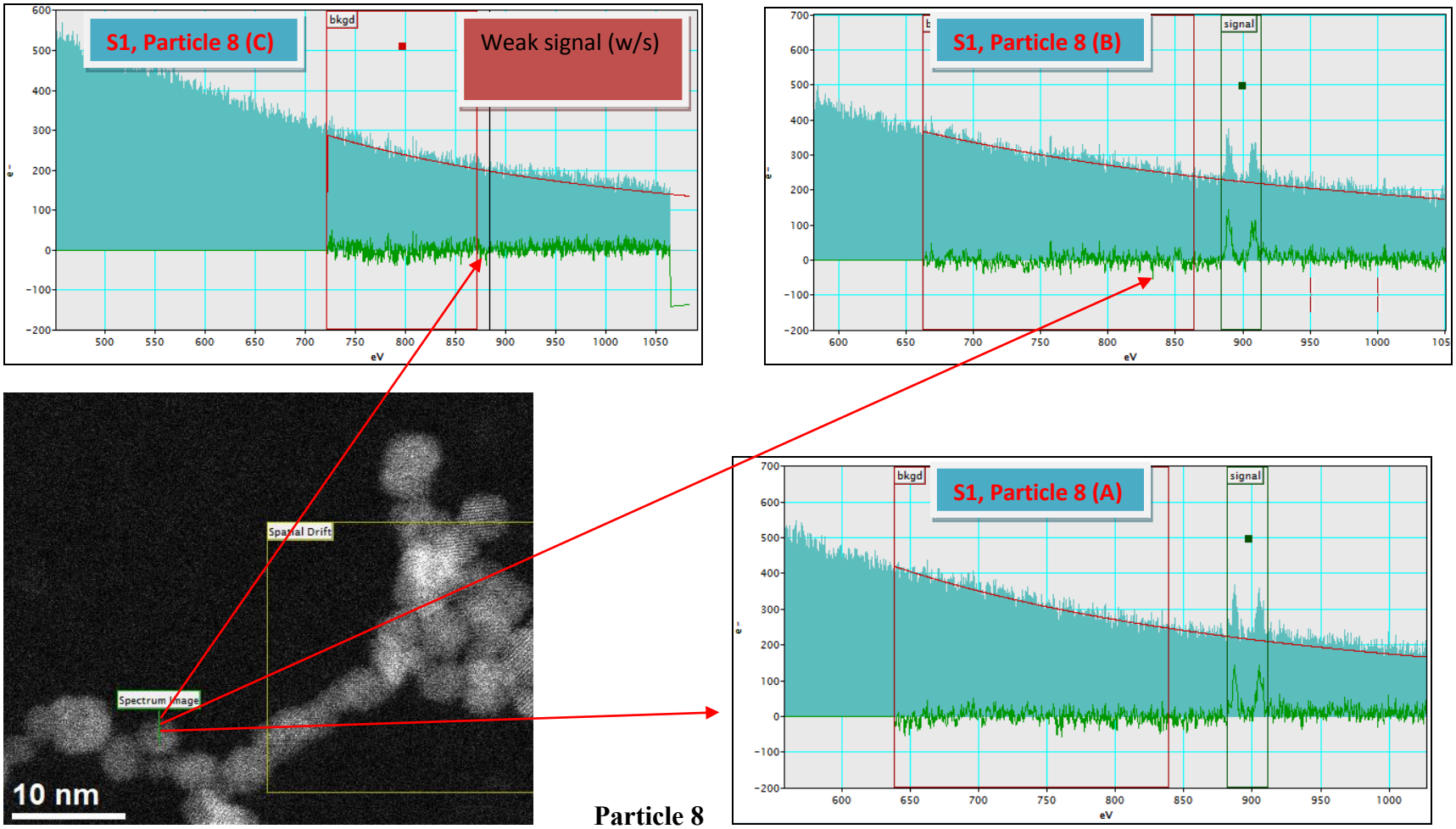

Figure 4.8 (h) EELS spectra illustrating different intensities of M_5 and M_4 white lines for particle 8 as the line scan was carried out from center towards the edge of the nanosphere (S1)

Investigation of the peak intensities in the EELS spectrum also gave similar results (figure 4.8 a-h). In almost all the NPs with diameter of 3nm or less, the M_5 signal was bigger at all the points (A, B and C) of the nanoparticle. However, it became smaller when the EELS was carried out at the center of the larger particles (for example particle 4). The M_5/M_4 ratios obtained during various line scans (figure 4.8 (a-h)) are summarised in tables 4.5. After the quantitative analysis of the M_5/M_4 ratios obtained from all the investigated particles at different depths of the particle, the data shows that there is 86 % Ce (III) present in the core and 100 % Ce (III) present at the edges of the sample S1.

4.4.1.2 Results and discussion of EELS measurements on nanospheres S2

The nanospheres in sample S2 (6.0±3.0 nm) are of similar size to that of S1 (4.5±2.5 nm), as obtained by TEM. Figure 4.9 (a-g) illustrate the survey scans carried out on NPs from sample S2. Similar kind of results has been observed as discussed earlier for sample S1. The amount of Ce (III) increased as the particle size decreased. The M_5/M_4 ratios obtained during various line scans (figure 4.9 (a-g)) are summarised in tables 4.6.

Table 4.6 M_5/M_4 ratio at points A, B and C for sample S2

Depth	Sample S2						
	Particle 1	Particle 2	Particle 3	Particle 4	Particle 5	Particle 6	Particle 7
A	1.04	0.972	0.759	1.02	1.21	1.099	0.946
B	1.24	0.871	0.846	1.10	0.957	1.13	0.985
C	1.11	1.21	1.01	1.23	1.124	1.15	1.38

Figure 4.9 (a-g) illustrate different NPs from sample S2 with an approximate size of about 3-7 nm. In all the cases, it was found that with spherical particles ≤ 3 nm, only Ce (III) was detected at the edge (point C) between the edge and the center (point B) as well as at the core of the particle (point A). However, with larger sized particles, it was observed that the extracted M_5/M_4 ratios were closer to Ce (III) at the edge (C) and sometimes between the edge and center of the particle at point B (depending on particle size) while the core (A) had only Ce (IV) present. For example, the M_5/M_4 ratios extracted from points A and B of a particle size 6nm (particle 3 in table 4.6) were closer to Ce (IV) whereas those extracted from the edge (point C) clearly suggest the presence of Ce (III). Similar results were obtained for particle 2 (d= 5nm) and particle 7 (d=6nm) however, particle 4 (d=3nm) showed the presence of Ce (III) all over the surface as wells as the core of the particle i.e points A, B and C. This again indicates that for larger particles (>3nm), the valence reduction process is predominant at the surface as compared to the interior of the particle. The investigated particle 4 is in the range of 2-3nm in diameter and showed complete presence of Ce (III) whereas the other investigated particles are in the range of 4-7nm and contain a mixture of Ce (III) and Ce (IV) with all the particles predominantly carrying Ce (III) at the surface. After the quantitative analysis of the M_5/M_4 ratios obtained from all the investigated particles at different depths of the particle, the data shows that there is 45 % Ce (III) present inthe core and 86 % Ce (III) present at the edges of the sample S2.

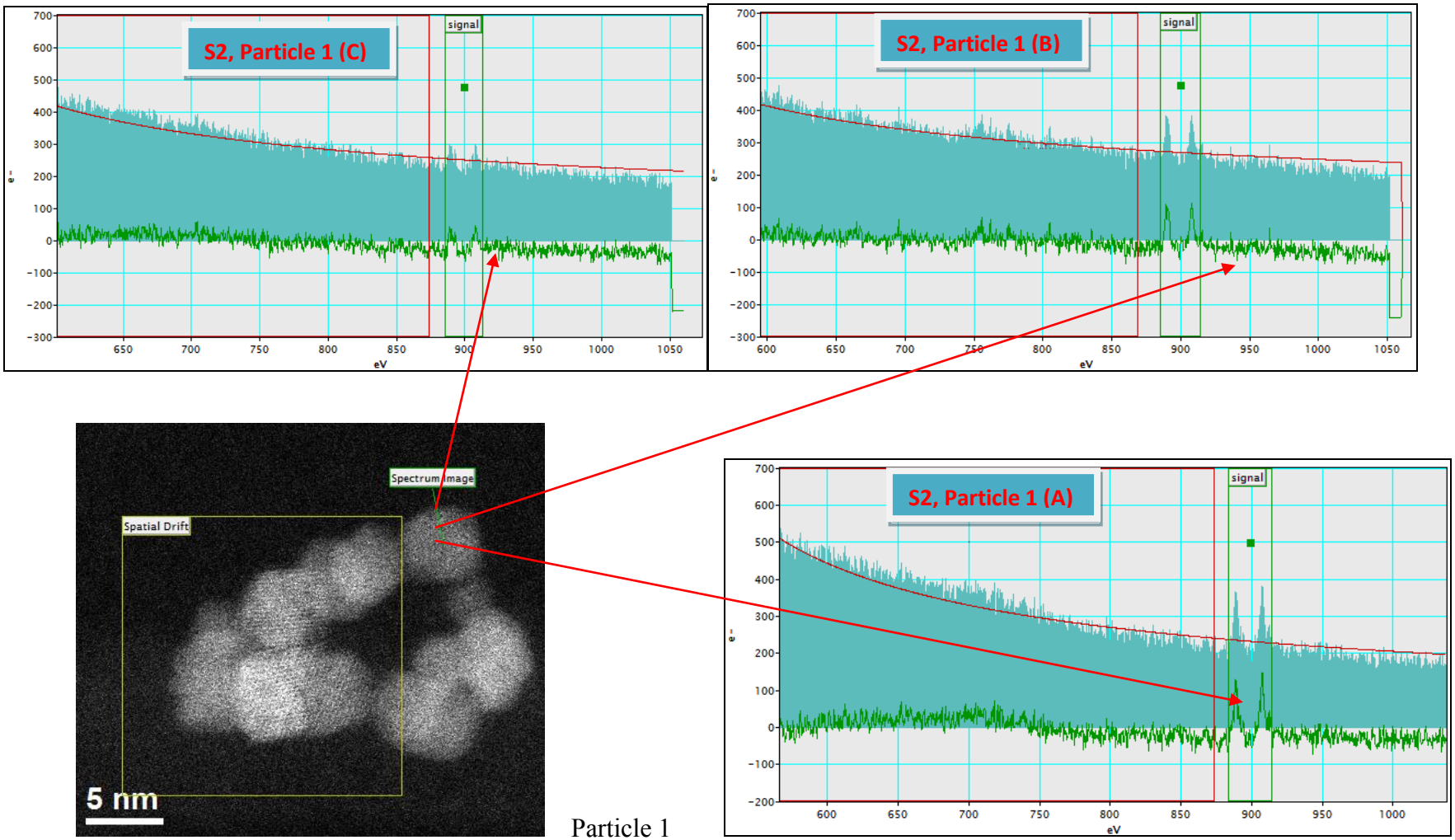

Figure 4.9 (a) EELS spectra illustrating different intensities of M_5 and M_4 white lines for particle 1 as the line scan was carried out from center towards the edge of the nanosphere (S2)

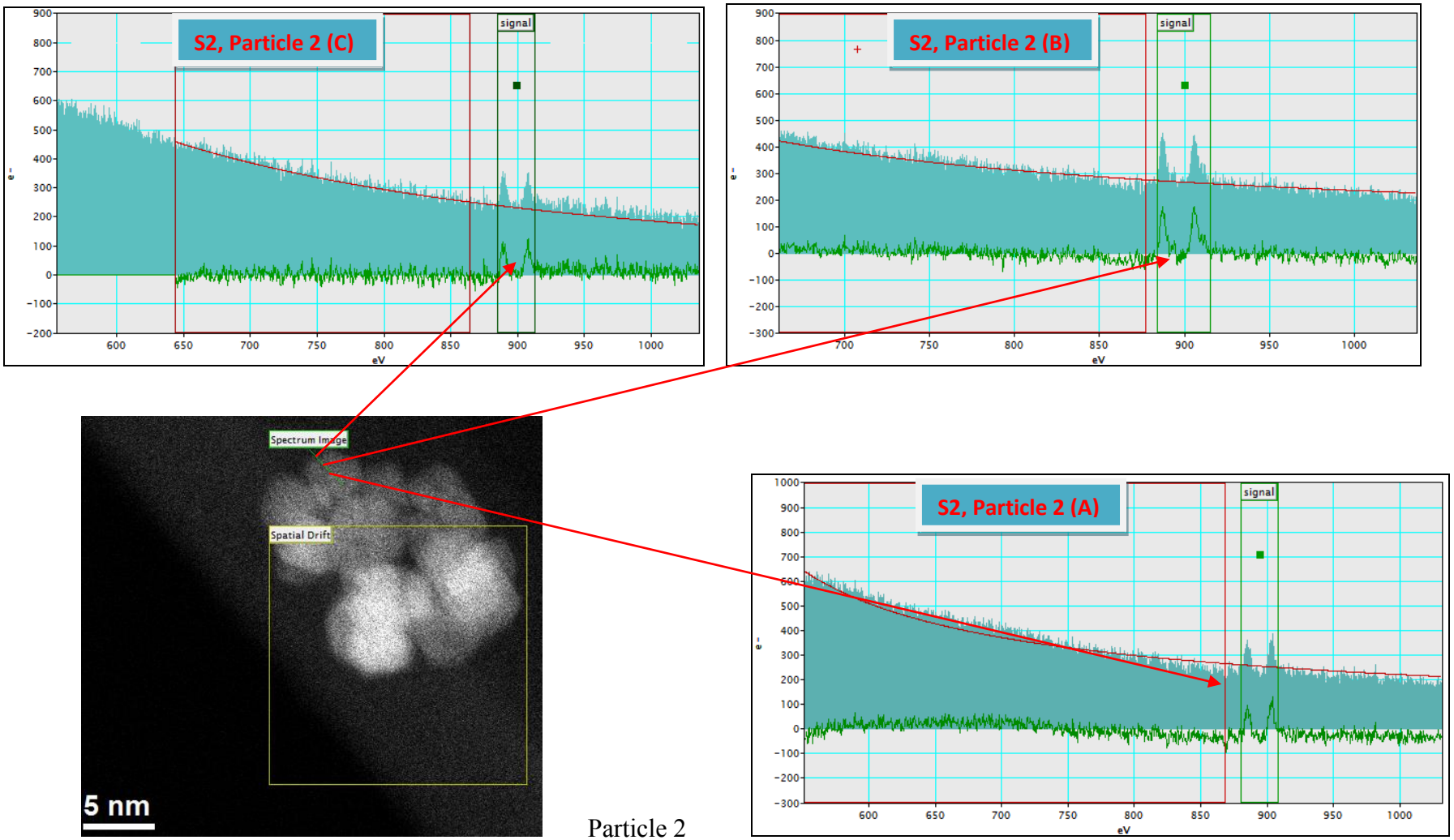

Figure 4.9 (b) EELS spectra illustrating different intensities of M_5 and M_4 white lines for particle 2 as the line scan was carried out from center towards the edge of the nanosphere (S2)

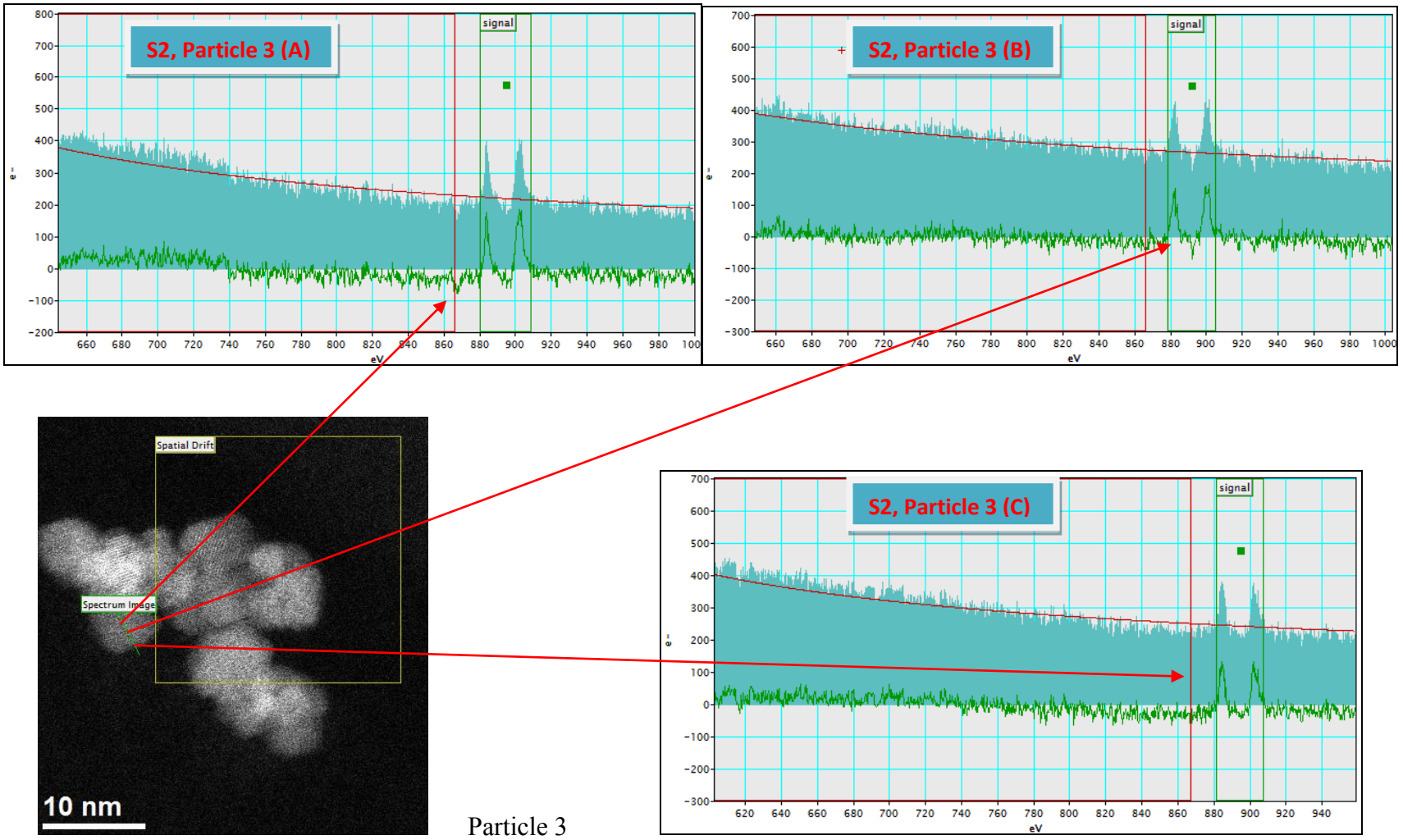

Figure 4.9 (c) EELS spectra illustrating different intensities of M_5 and M_4 white lines for particle 3 as the line scan was carried out from center towards the edge of the nanosphere (S2)

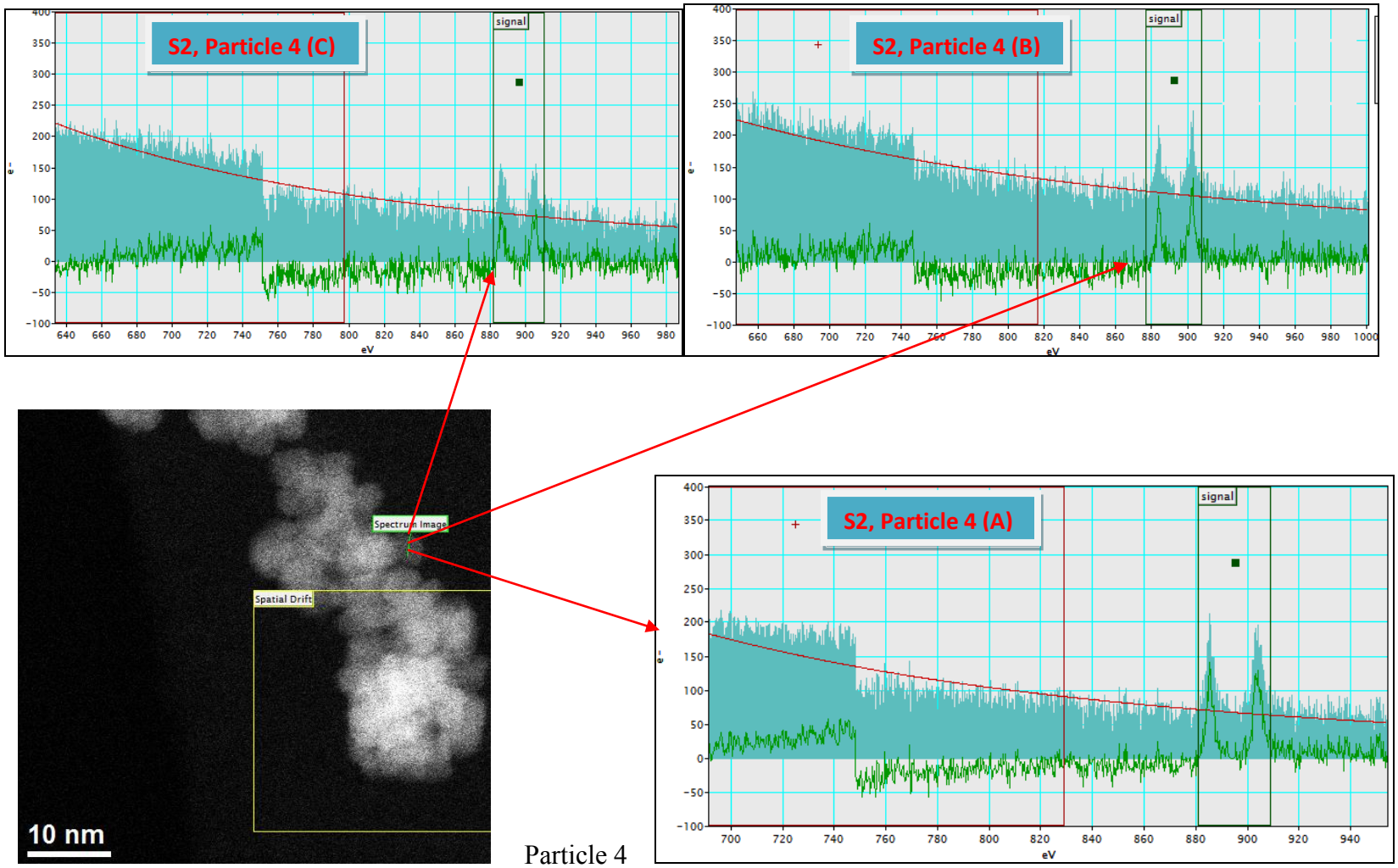

Figure 4.9 (d) EELS spectra illustrating different intensities of M_5 and M_4 white lines for particle 4 as the line scan was carried out from center towards the edge of the nanosphere (S2)

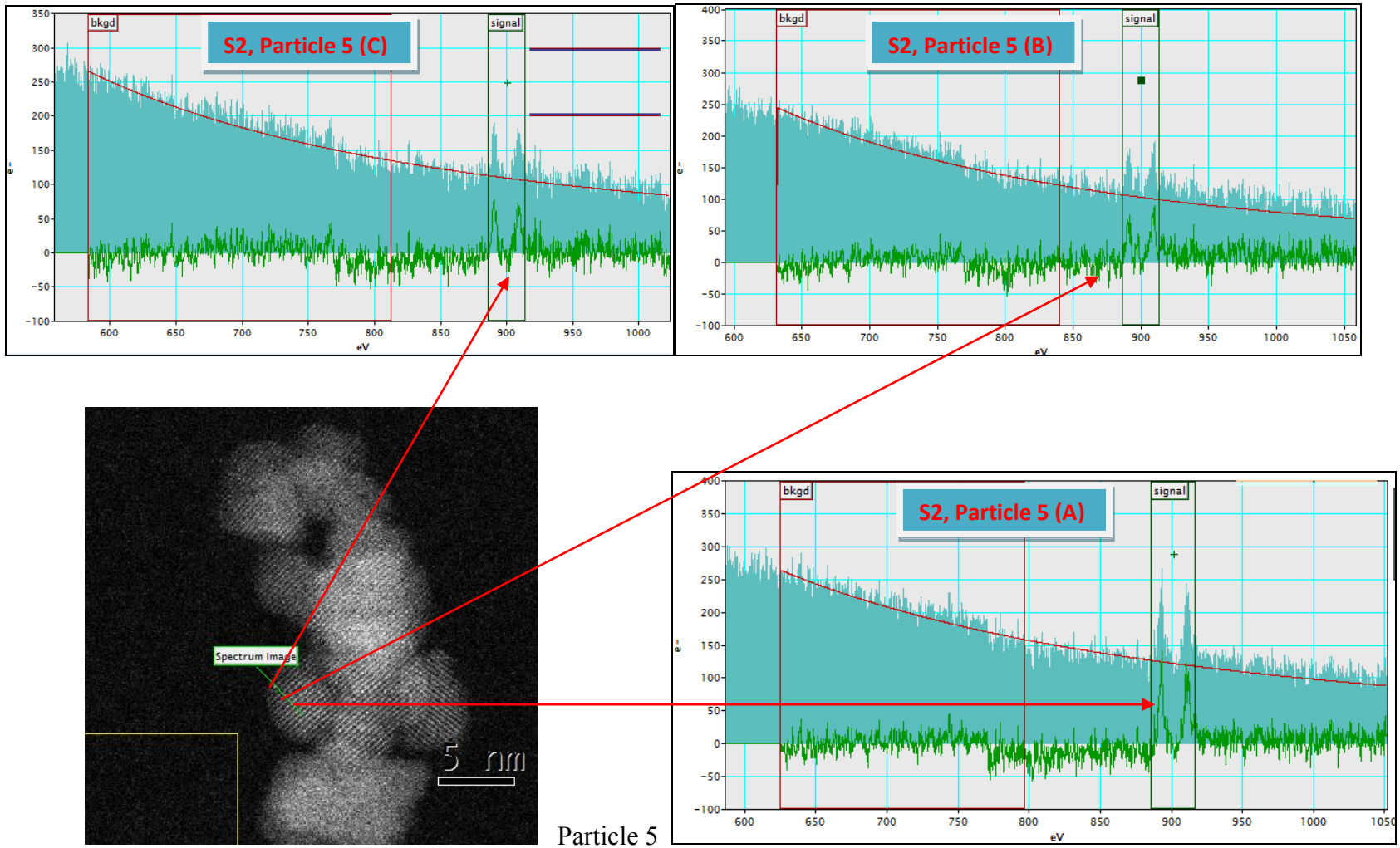

Figure 4.9 (e) EELS spectra illustrating different intensities of M_5 and M_4 white lines for particle 5 as the line scan was carried out from center towards the edge of the nanosphere (S2)

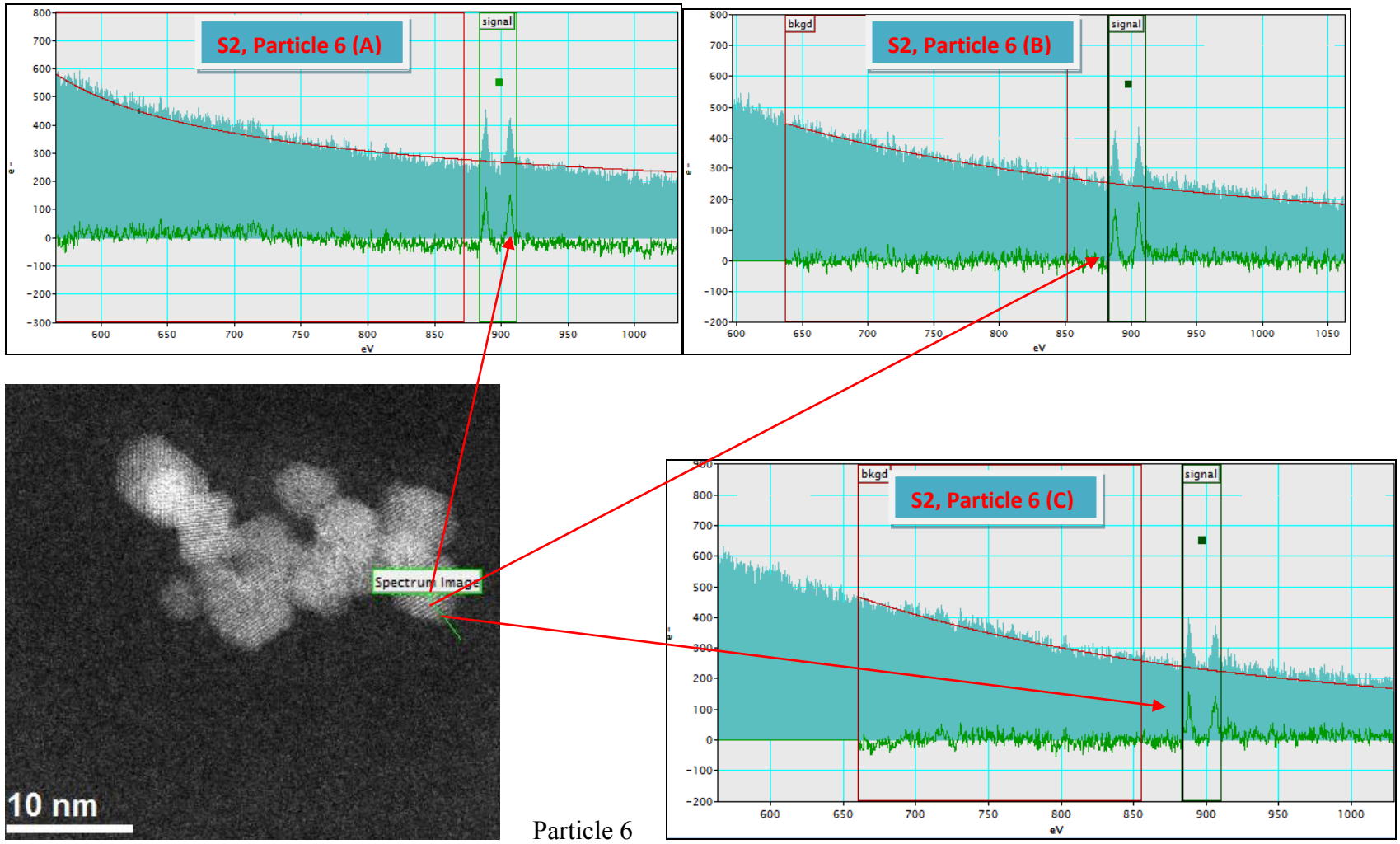

Figure 4.9 (f) EELS spectra illustrating different intensities of M_5 and M_4 white lines for particle 6 as the line scan was carried out from center towards the edge of the nanosphere (S2)

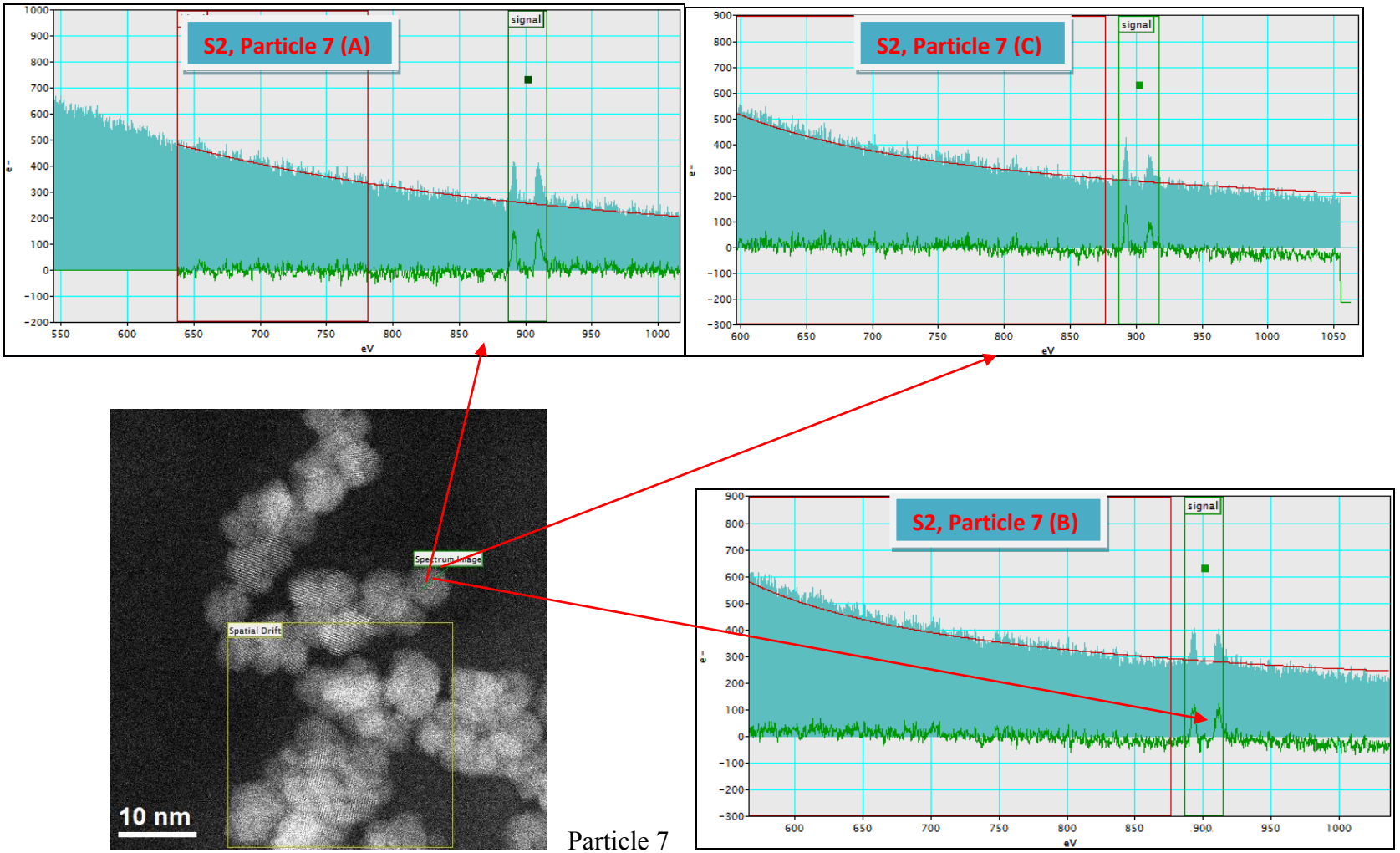

Figure 4.9 (g) EELS spectra illustrating different intensities of M_5 and M_4 white lines for particle 7 as the line scan was carried out from center towards the edge of the nanosphere (S2)

4.4.2 Summary and conclusions of the EELS experiments carried out on nanospheres S1 and S2

In summary, we have carried out systematic EELS experiments on two different samples of nanospheres, S1 and S2 with very similar sizes. The $M_{4,5}$-edge spectra have been used to evaluate the oxidation state of cerium using STEM-EELS. Line scans have been carried out looking at local oxidation state variation across the particle as we go from the centre towards the edge of the particle. STEM images have been collected before and after the EELS experiments and no particle damage has been observed. The results suggest that oxidation state is related to size. The amount of Ce (III) increases as the particle size decreases with particles ≤ 3nm to be completely Ce (III). The oxidation state for larger ceria NPs is not uniform throughout. For larger particles, the valence reduction process is predominant at the surface as compared to the interior of the particle. The results obtained for the spherical samples S1 and S2 have been tabulated in table 4.7.

Table 4.7 Oxidation state quantification data for the nanospheres S1 and S2 as obtained from EELS

Sample code	Morphology	Size (nm)		EELS (%)	
		DLS	TEM	Ce (III) Center	Ce (III) Edge
S1	Nanosphere	85.5±0.4	4.5±2.5	0.86	1.00
S2	Nanosphere	89.0±0.3	6.0±3.0	0.45	0.86

4.5 Oxidation state quantification of nanosphere samples S3 and S4 using EELS

The ceria nanospheres S3 and S4 have been synthesised by myself and their synthetic scheme has been discussed in chapter 3, synthesis 3, scheme a and b respectively. (section 3.2.1). The particles have been characterised for their size and shape by DLS and TEM (details in chapter 3).

4.5.1 EELS measurements on nanospheres S3 and S4

The EELS measurements for the nanospheres S3 (3±1 nm) have also been collected using the same methodology as discussed before. The only difference is that the line scan has been collected at two points A and C where A indicates the center of the particle and C is the outermost edge of the particle (figure 4.10 a). The M_5/M_4 ratio extracted from this line scan across the particle indicate the local variation of cerium oxidation state across the particle as we go from centre towards the edge of the particle (figure 4.10 a-d). Some survey scans were showing very weak or almost no signal (figure 4.10 e), spectrum shown in Appendix B. So a few area scans were carried out on six different regions of the sample. The EELS spectrum generated and the areas under investigation have been illustrated in figures 4.11 (a-c). Area scans have also been generated for nanospheres S4 (3±1 nm), The EELS spectrum generated and the areas under investigation have been illustrated in figure 4.14 (a-c).

4.5.1.1 Results and discussion of EELS measurements on nanospheres S3

The M_5/M_4 ratios collected from the survey scans indicate that there is complete Ce (III) present at the center of the particle (point A) as well as at the edge of the particle (point C) for particle sizes ≤2 nm (table 4.8). Whereas, for larger particles, the core is closer to Ce (IV)

while the edge still carries Ce (III). For example, the M_5/M_4 ratios extracted from a particle with d= 2nm (particle 6), both the core and the edges showed the presence of Ce (III) whereas for larger particles, such as particle 1 with d= 4.5 nm, the core showed the presence of Ce (IV) while the surface of the particle detected Ce (III). Similar results have been obtained for the other particles under investigation (Figure 4.10 (a-d)). The results obtained have been illustrated in table 4.8.

Table 4.8 M_5/M_4 ratio at points A and B for sample S3

Depth	**Sample S3**						
	Particle 1	Particle 2	Particle 3	Particle 4	Particle 5	Particle 6	Particle 7
A	0.956	w/s	1.23	1.06	w/s	1.30	w/s
C	1.25	w/s	1.21	1.29	w/s	1.25	w/s
* w/s=weak signal							

The STEM images in figures 4.10 (a-e) clearly depict the particle size and NPs under investigation. Some survey scans were showing very weak or almost no signal. For example, for particle 2, 5 and 7, the signal came out be very weak, so no conclusions could be drawn based on these scans. The particles are shown in figure 4.10 (e). Considering, that some of the NPs from sample S3 yielded very weak signals, area scans were performed on six different regions of the sample. The EELS spectrum generated and the areas under investigation have been illustrated in figures 4.11 (a-c). The M_5/M_4 ratios extracted by second derivative method are tabulated in table 4.9.

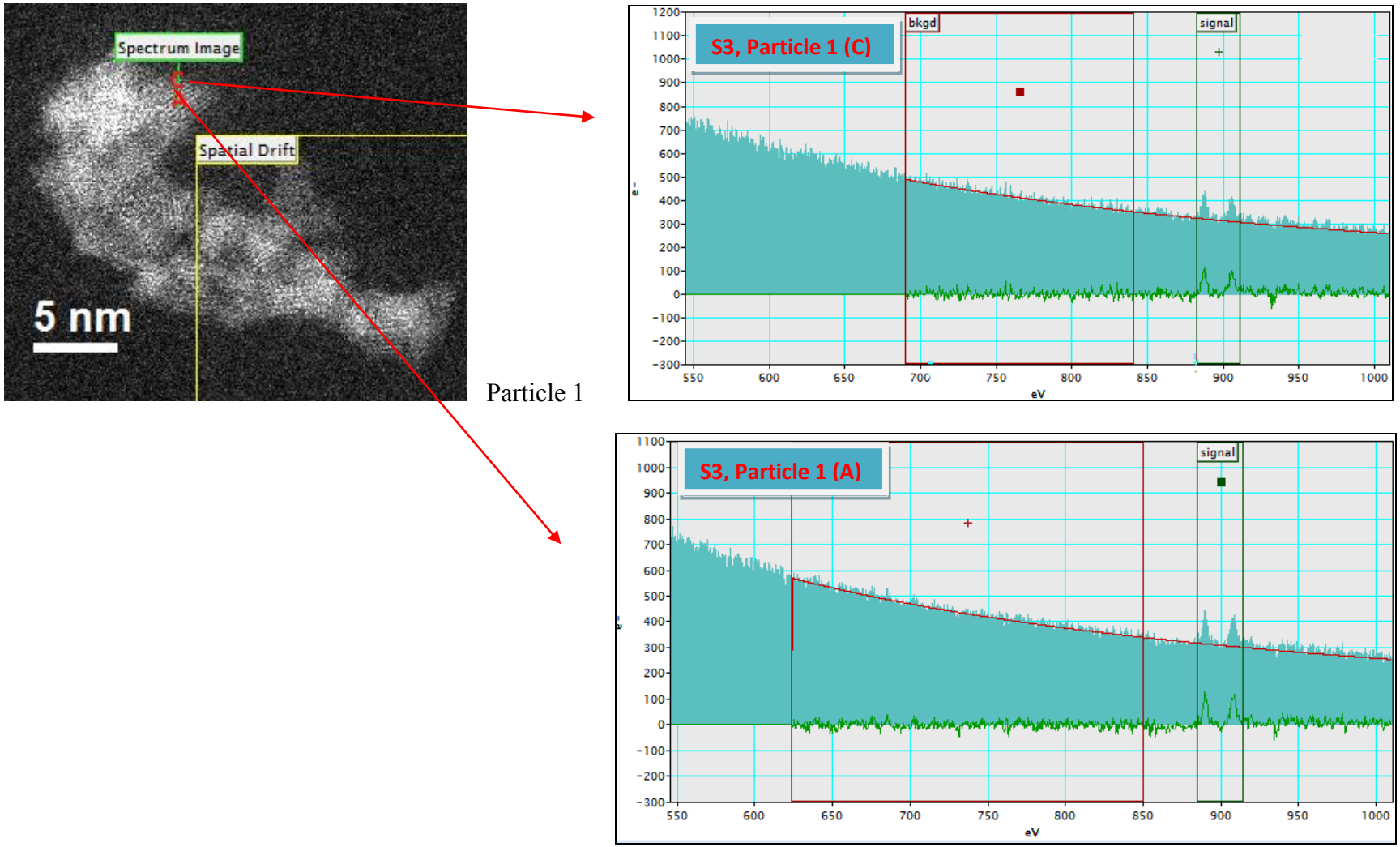

Figure 4.10 (a) EELS spectra illustrating different intensities of M_5 and M_4 white lines for particle 1 as the line scan was carried out from center towards the edge of the nanosphere (S3)

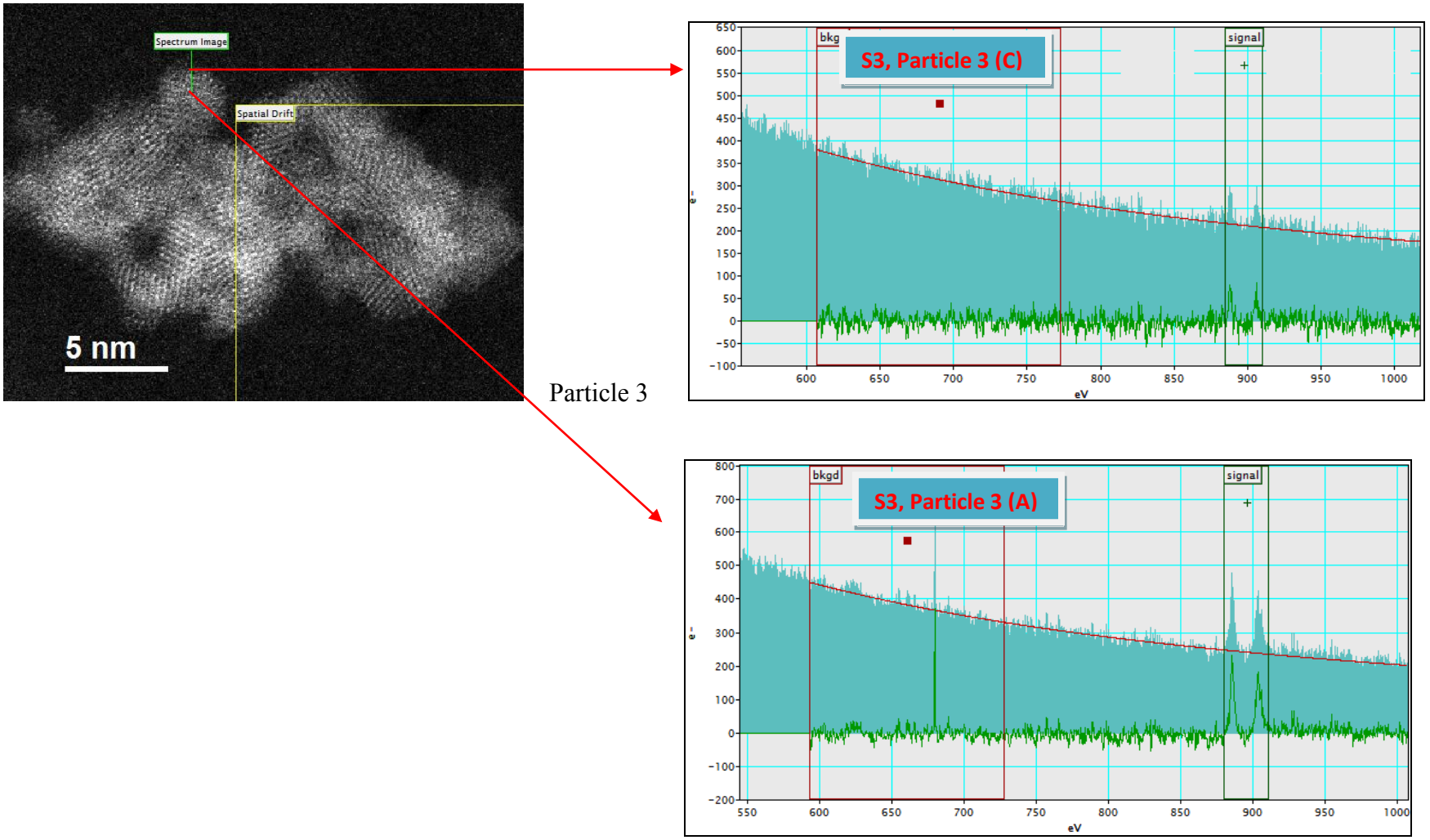

Figure 4.10 (b) EELS spectra illustrating different intensities of M_5 and M_4 white lines for particle 3 as the line scan was carried out from center towards the edge of the nanosphere (S3)

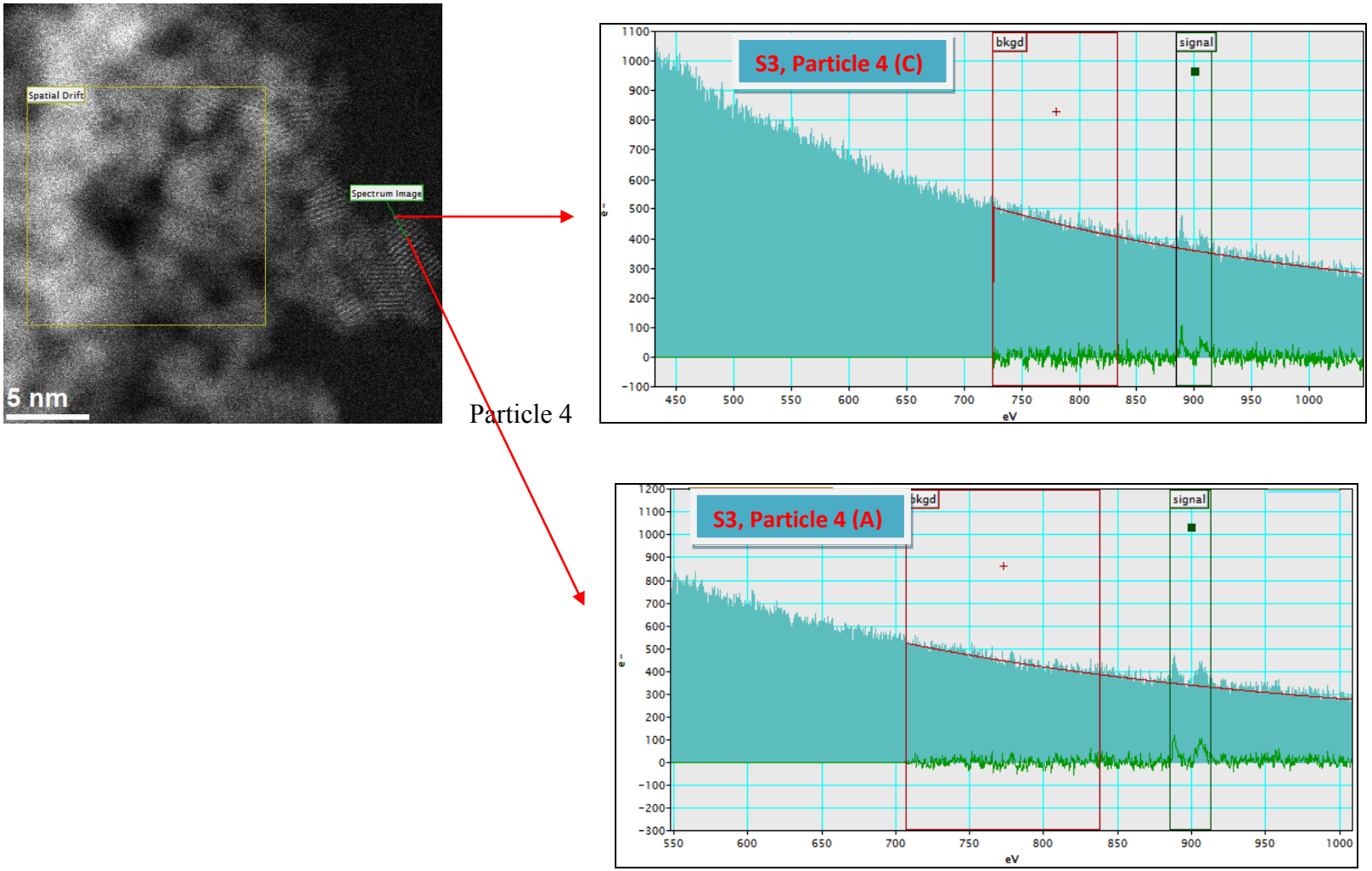

Figure 4.10 (c) EELS spectra illustrating different intensities of M_5 and M_4 white lines for particle 4 as the line scan was carried out from center towards the edge of the nanosphere (S3)

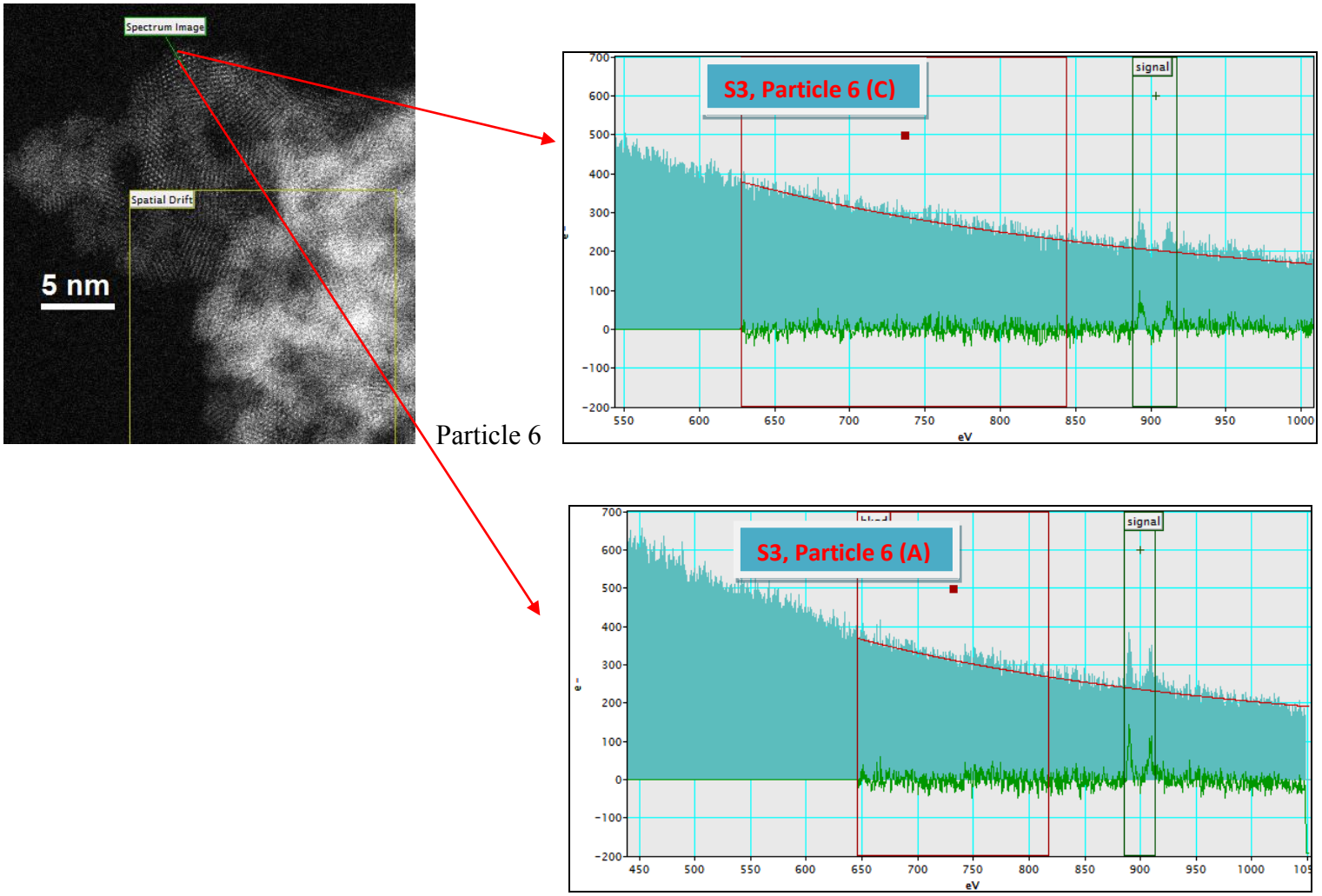

Figure 4.10 (d) EELS spectra illustrating different intensities of M_5 and M_4 white lines for particle 6 as the line scan was carried out from center towards the edge of the nanosphere (S3)

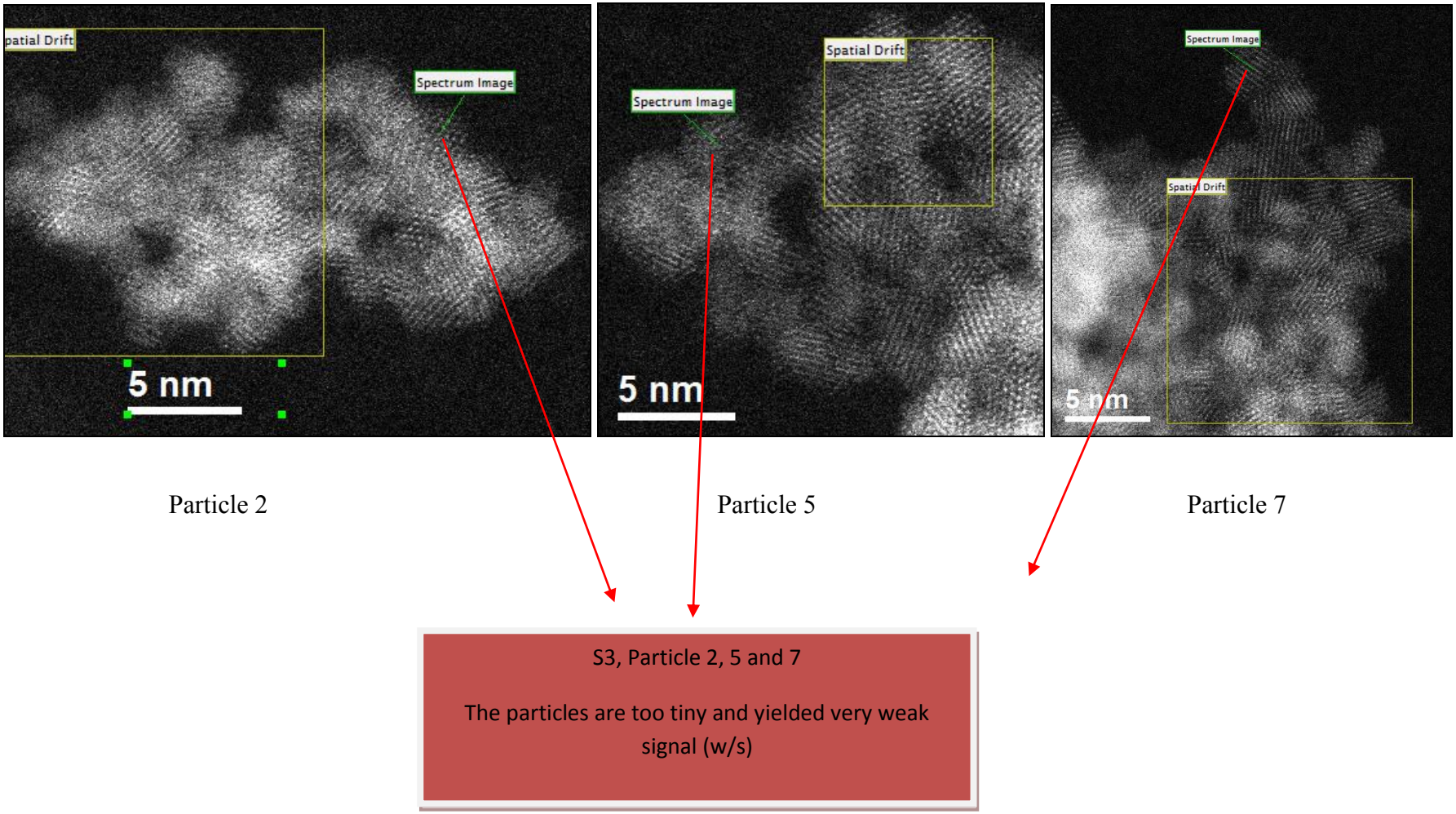

Figure 4.10 (e) The line scan carried out on particle 2, 5 and 7 of the sample S3 yielded very weak signal

The EELS spectrum generated and the areas under investigation have been illustrated in figures 4.11 (a-c). The M_5/M_4 ratios extracted by second derivative method are tabulated in table 4.9.

Table 4.9 M_5/M_4 ratios obtained from area scans carried out on sample S3

Sample S3 - area scans		**$CeNO_3$ as standard**	**Bulk CeO_2 as standard**
	M5/M4	Ce (III)	Ce (IV)
Area 1	1.28	1.23	0.82
Area 2	1.34		
Area 3	1.40		
Area 4	1.33		
Area 5	1.30		
Area 6	1.28		

The results obtained suggest that the sample mainly contains Ce (III). The M_5/M_4 ratios extracted are closer to that obtained from Ce (III) standard and no Ce (IV) was detected. After the quantitative analysis of the M_5/M_4 ratios obtained from the investigated particles at different depths of the particle, the line scan data shows that there is 77 % Ce (III) present in the core and 100 % Ce (III) present at the edges of the sample S3 whereas the area scan quantification shows that there is 100% Ce (III) present in the sample. The results have been summarised in table 4.11. Figure 4.12 represents the average of M_5/M_4 ratios obtained for different areas from sample S3.

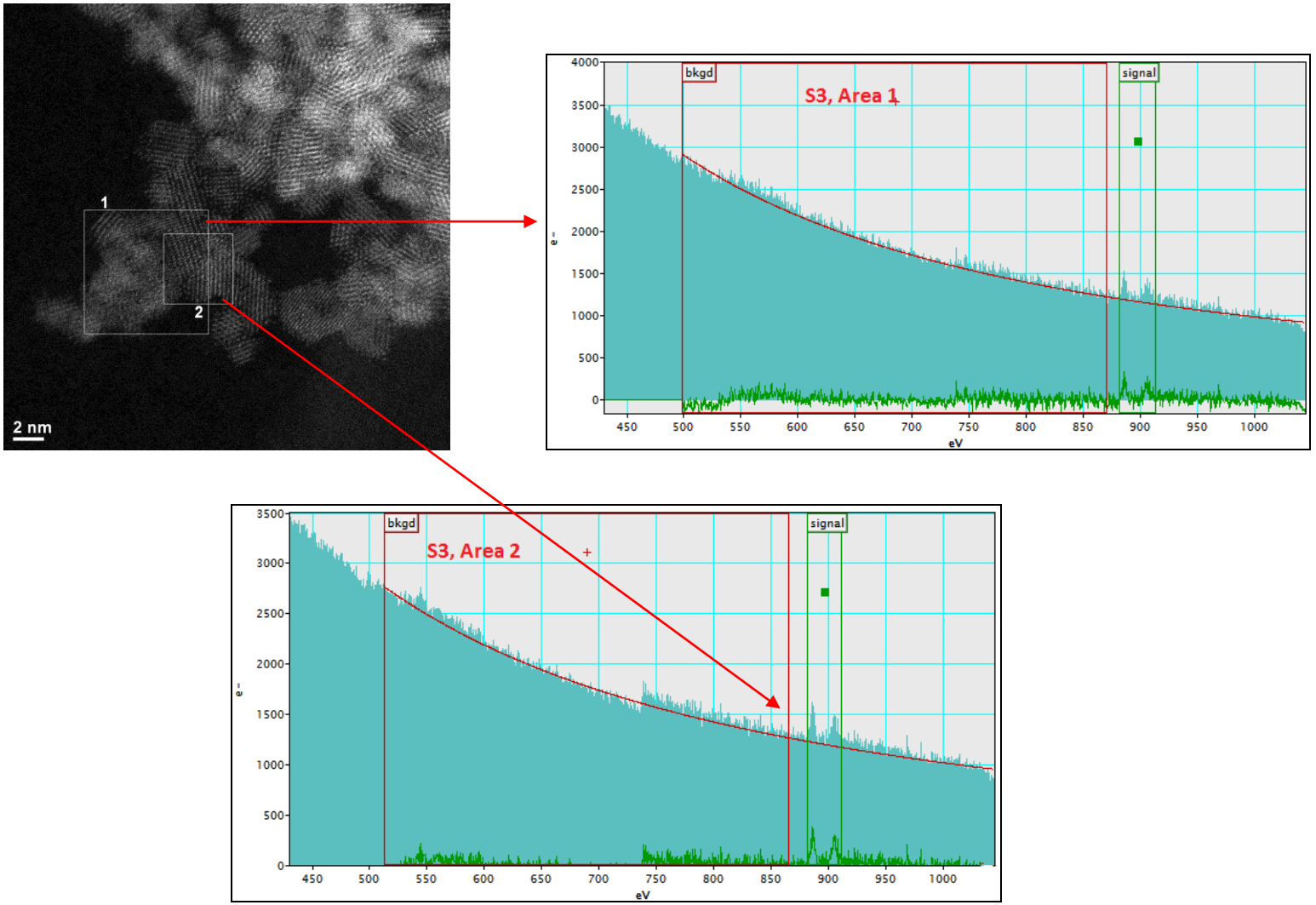

Figure 4.11 (a) STEM image from sample S3 and EELS spectrum generated out of the area 1 and 2 of the sample

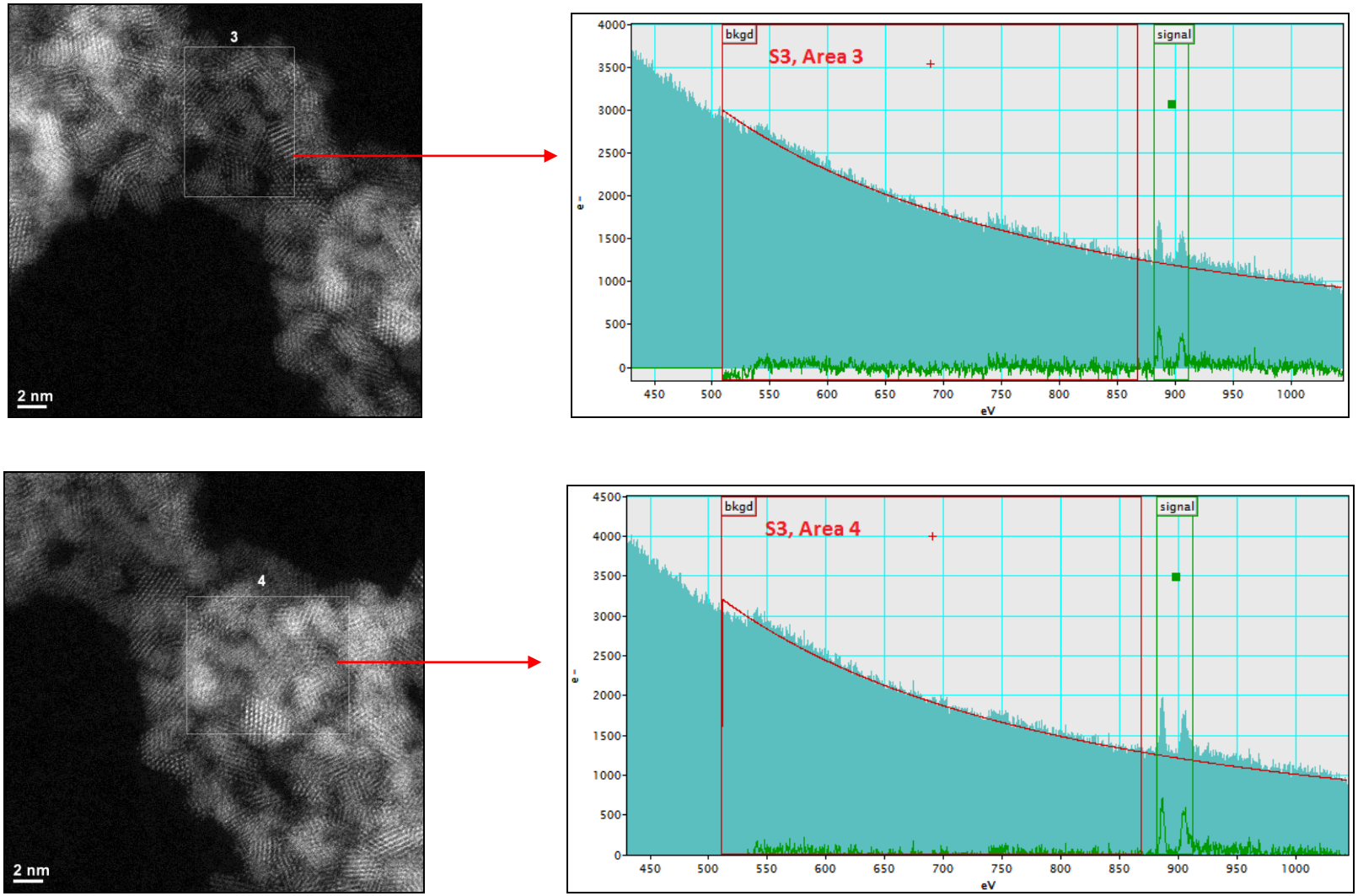

Figure 4.11 (b) STEM images from sample S3 and EELS spectrum generated out of the area 3 and 4 of the sample

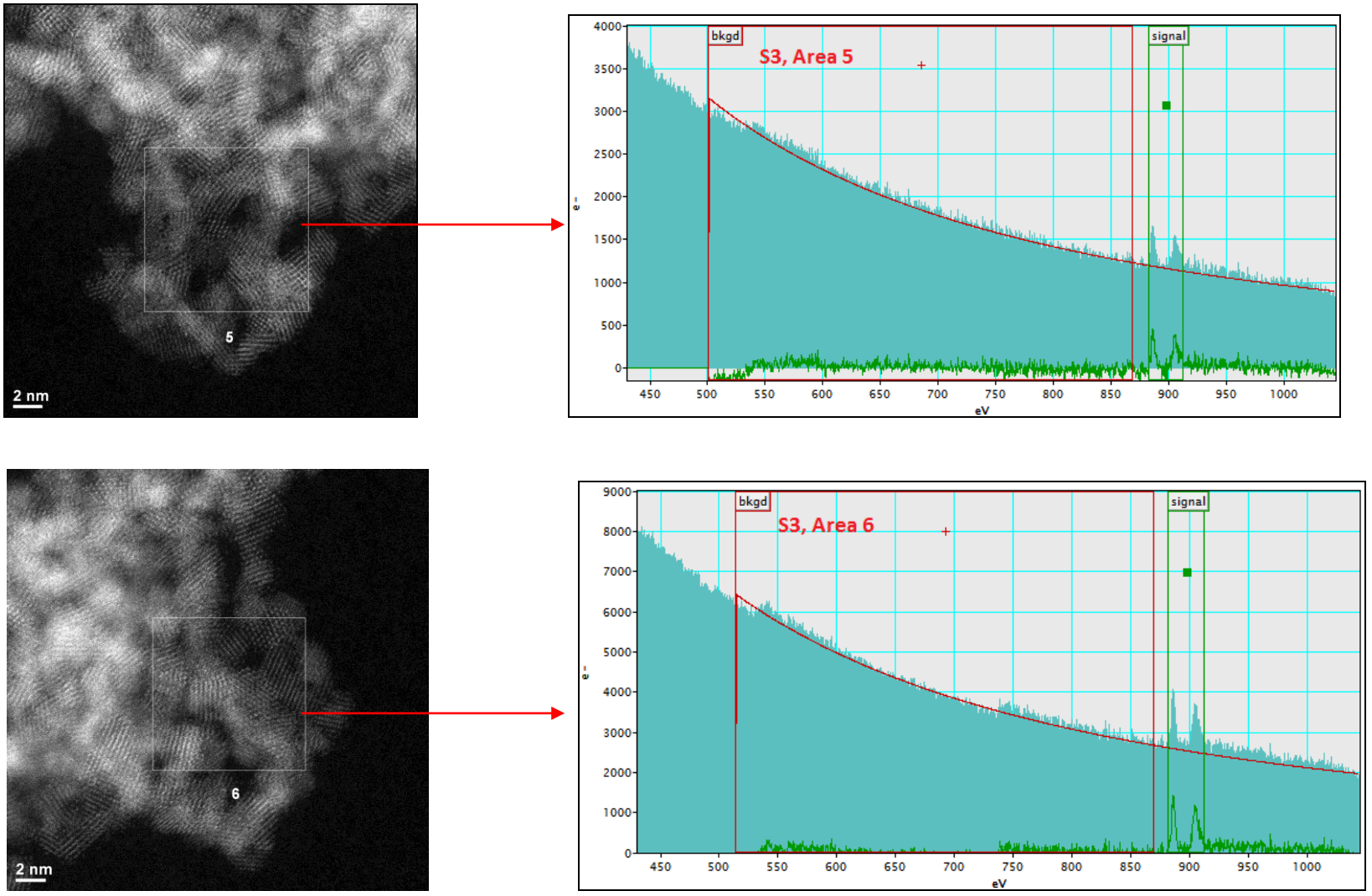

Figure 4.11 (c) STEM images from sample S3 and EELS spectrum generated out of the area 5 and 6 of the sample

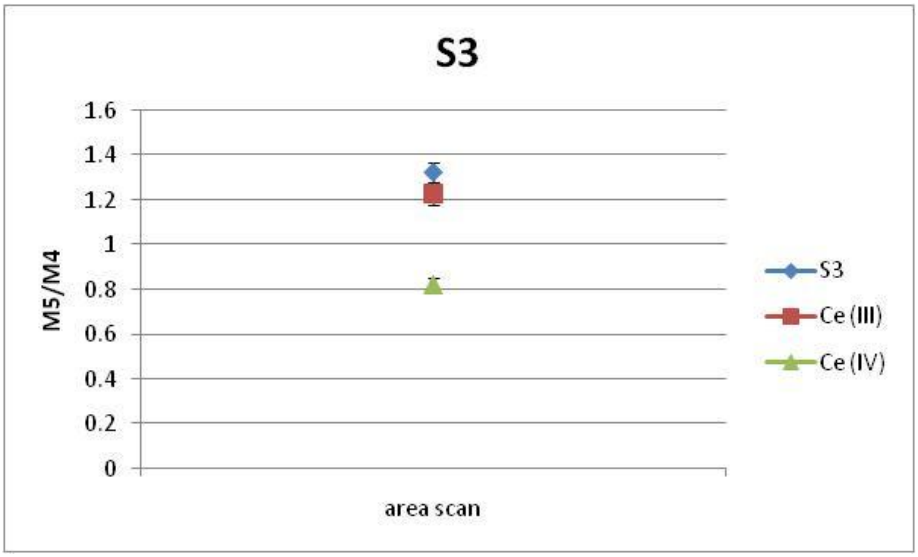

Figure 4.12 Average of M_5/M_4 ratios obtained from area scans carried out on sample S3

4.5.1.2 Results and discussion of EELS measurements on nanospheres S4

Area scans have been carried out on five different regions of the sample. The EELS spectrum generated and the areas under investigation have been illustrated in figures 4.14 (a-c). The M_5/M_4 ratios extracted by second derivative method are tabulated in table 4.10.

Table 4.10 M_5/M_4 ratios obtained from area scans carried out on sample S4

Sample S4 - area scans		**$CeNO_3$ as standard**	**Bulk CeO_2 as standard**
	M5/M4	Ce (III)	Ce (IV)
Area 1	1.042	1.23	0.82
Area 2	1.025		
Area 3	1.453		
Area 4	1.151		
Area 5	1.181		

The results obtained suggest that the sample contains a mixture of Ce (III) and Ce (IV). Some of the M_5/M_4 ratios extracted are closer to that obtained from Ce (III) standard while some confirm the presence of Ce (IV). After the quantitative analysis of the M_5/M_4 ratios obtained from the investigated areas, the data shows that there is 86 % Ce (III) and 14 % Ce (IV) present in the sample S4. Figure 4.13 represents the average M_5/M_4 ratios obtained for different areas from sample S4. The results have been summarised in table 4.11.

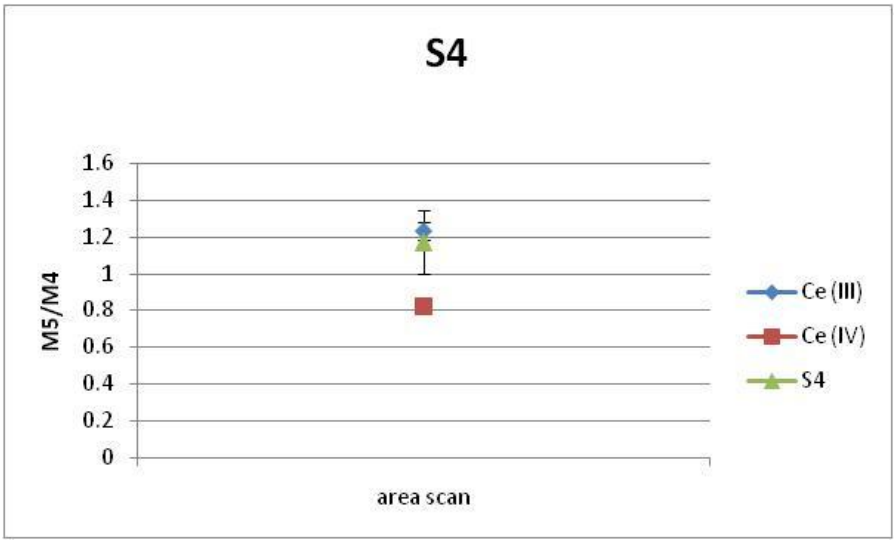

Figure 4.13 Average M_5/M_4 ratios obtained from area scans carried out on sample S4

4.5.2 Summary and conclusion of the EELS experiments carried out on nanospheres S3 and S4

In summary, we have carried out systematic EELS experiments on two different samples of nanospheres, S3 and S4. The $M_{4,5}$-edge spectra have been used to evaluate the oxidation state of cerium using STEM-EELS. Line scans have been carried out for S3 looking at local oxidation state variation across the particles as we go from the centre towards the edge of the particles. The M_5/M_4 ratios collected from the survey scans indicate that the there is complete Ce (III) present at the center of the particle (point A) as well as at the edge of the particle

(point C) for particle sizes ≤2 nm (table 4.8). Whereas, for larger particles, the core is closer to Ce (IV) while the edge still carries Ce (III). The data indicates that for particles >2nm, the valence reduction process is mainly predominant only at the surface and not in the core of the NPs. Some NPs gave very weak signal in the EELS spectrum. STEM images were collected before and after the EELS experiments and some damage to the particles was observed. Considering, that some of the NPs from sample S3 yielded very weak signals and also some beam damage was detected during line scans, area scans were carried out. However, area scans generate an overall picture about the sample and the signals come out of the sample as a whole. So the data generated is an overall review of the sample oxidation state and not of any individual particle. Area scans have also been carried out for S4. The results obtained for the spherical samples S3 and S4 have been summarised in table 4.11.

Table 4.11 Oxidation state quantification data for the nanospheres S3 and S4 as obtained from EELS

Sample code	Morphology	Size (nm)		EELS (%)	
		DLS	TEM	Ce (III)	Ce (IV)
S3	Nanosphere	175±2	3±1	91	7
S4	Nanosphere	171±2	3±1	86	14

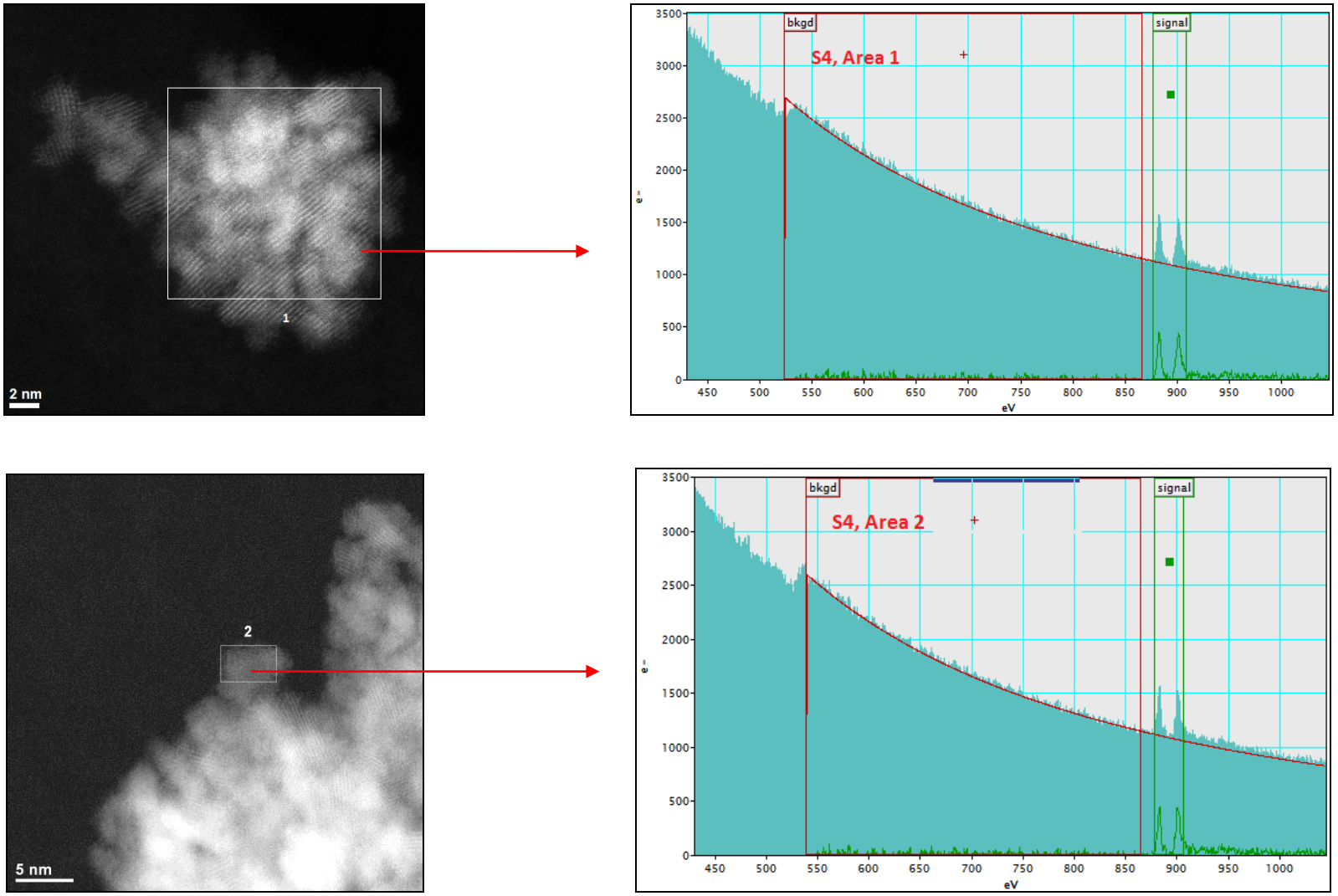

Figure 4.14 (a) STEM images from sample S4 and EELS spectrum generated from area 1 and 2 of the sample

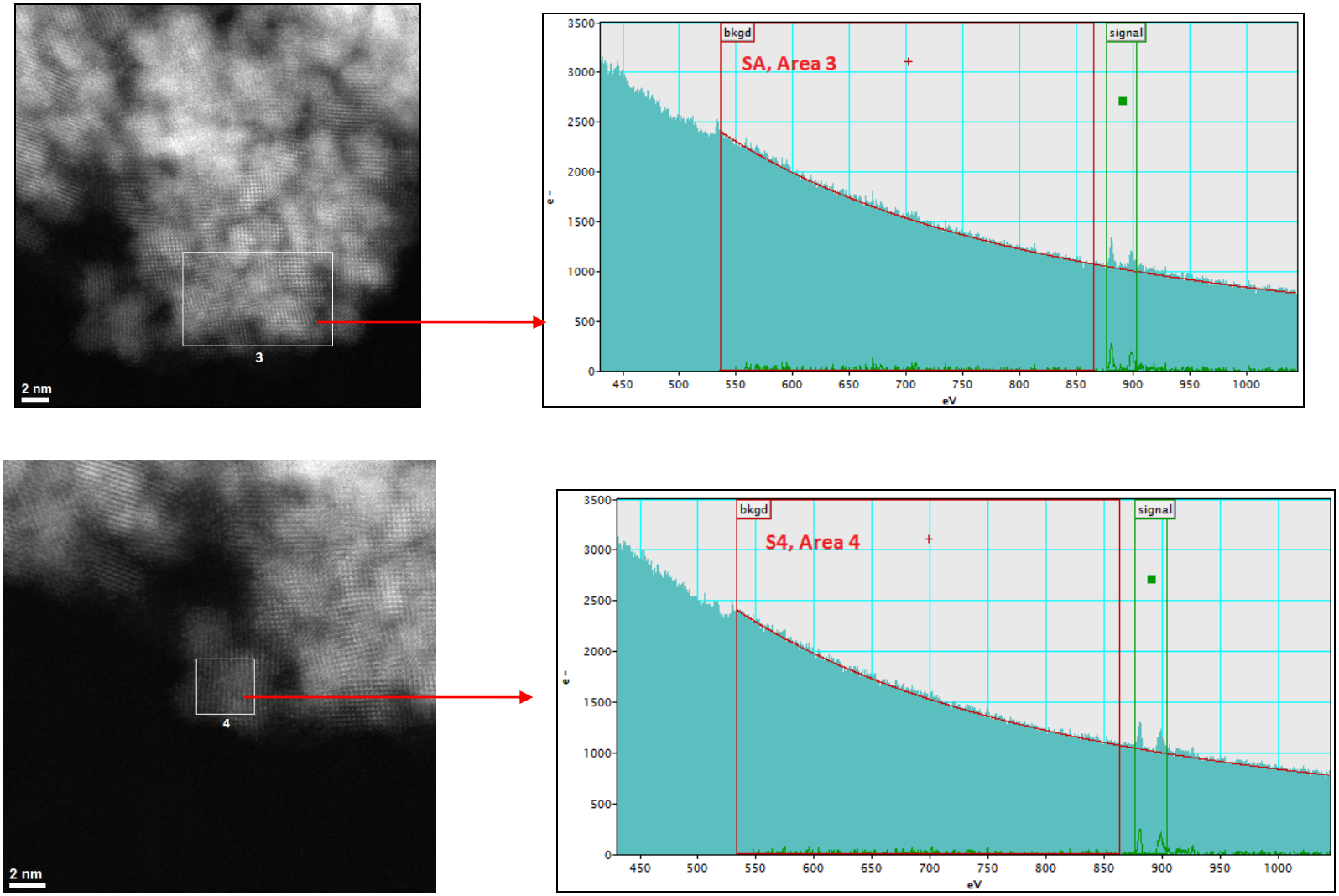

Figure 4.14 (b) STEM images from sample S4 and EELS spectrum generated from area 3 and 4 of the sample

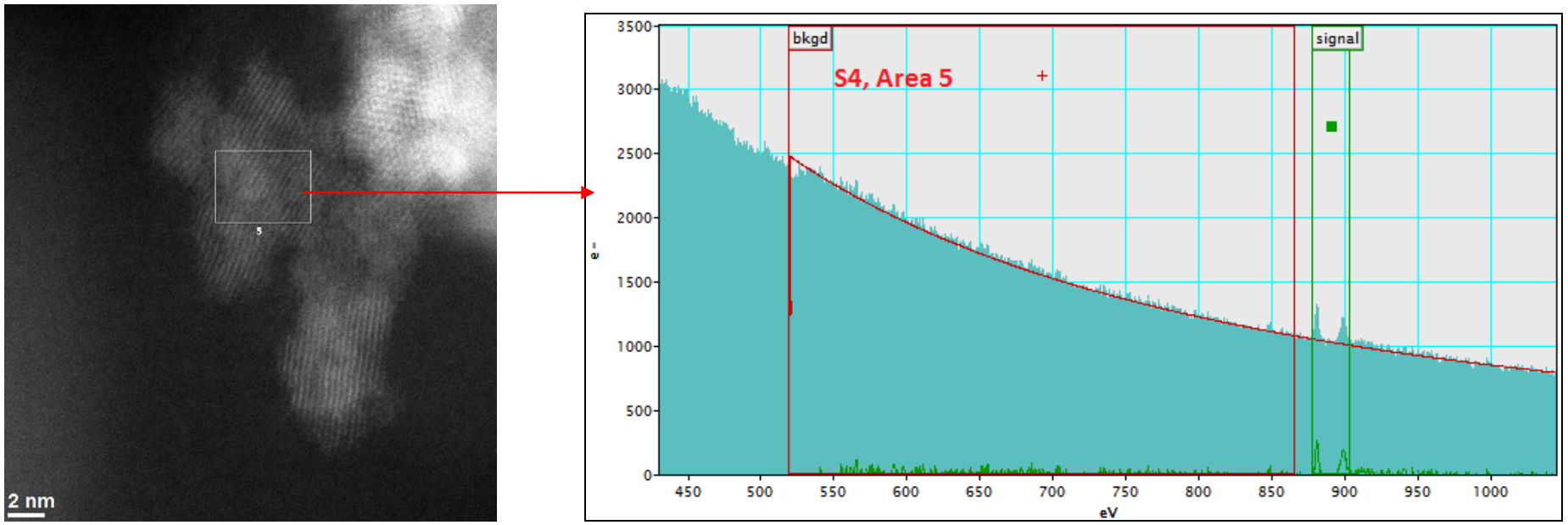

Figure 4.14 (c) STEM image from sample S4 and EELS spectrum generated from area 5 of the sample

4.6 Oxidation state quantification of nanorods sample R1 using EELS

The ceria nanorods R1 were synthesised by myself and their synthetic scheme has been discussed in chapter 3, synthesis 3, scheme c (section 3.2.1). The particles have been characterised for their size and shape by DLS and TEM. The details are in chapter 3.

4.6.1 EELS measurements on nanorods R1

The EELS measurements for the nanorods R1 (83±56 nm long and 16±6 nm wide) have been collected using the same methodology as discussed for previous samples. The survey scan has been carried out at three points called A, B, C where A indicates the center of the rod, B is the point between the center and edge of the rod and C is the outermost edge of the nanorod. The M_5/M_4 ratio extracted from this line scan across the nanorod indicates the variation of cerium oxidation state as we go from the centre towards the edge of the rod.

4.6.2 Results and discussion of EELS measurements on nanorods R1

The M_5/M_4 ratios extracted from the center point A as well as between the center and the edge (point B) of a 70 nm long and 18 nm wide nanorod (particle 1 in figure 4.15 (a) is close to that of Ce (IV), while that from the edge point M is close to Ce (III) (Table 4.12, particle1). Figure 4.15 (a) clearly illustrates the different intensities of M_5 and M_4 white lines for particle 1 as the line scan was carried out from center towards the edge of the nanorod (R1).

Table 4.12 M_5/M_4 ratios at points A, B and C for sample R1

Depth	Sample R1						
	Particle 1	Particle 2	Particle 3	Particle 4	Particle 5	Particle 6	Particle 7
A	0.906	0.956	0.9	0.813	0.841	0.916	0.937
B	0.964	0.89	0.948	0.858	0.906	0.92	0.894
C	1.04	1.144	1.215	1.181	1.164	1.147	1.218

A number of measurements have been carried out on different nanorods of the same sample as well as around the perimeter of the rods (Figure 4.15 (b-g)). The M_5/M_4 ratios extracted after different line scans have been illustrated in table 4.12. Figure 4.15 (a-g) illustrate different nanorods from sample R1 with quite a range of length and widths. All the investigated nanorods had Ce (III) present in the top 3nm layer of the particle (point C), however, the center of the NPs (Point A) and the point between the center and the edge (point B) contained Ce (IV). Only transverse scans have been carried out. The data obtained is in agreement with the EELS data obtained for larger nanocubes C1 (section 4.3.1.1, discussed previously in this chapter). We also found that in all the line scans, the M_5 signal was bigger at the edges (point C) of the nanorods whereas the M_4 signal was bigger when the probe was at points A and B (Figure 4.15 (a-g)). After the quantitative analysis of the M_5/M_4 ratios obtained from all the investigated particles at different depths of the rods, the data shows that R1 contains 19 % of Ce (III) present in the core and and 83 % of Ce (III) present at the edges.

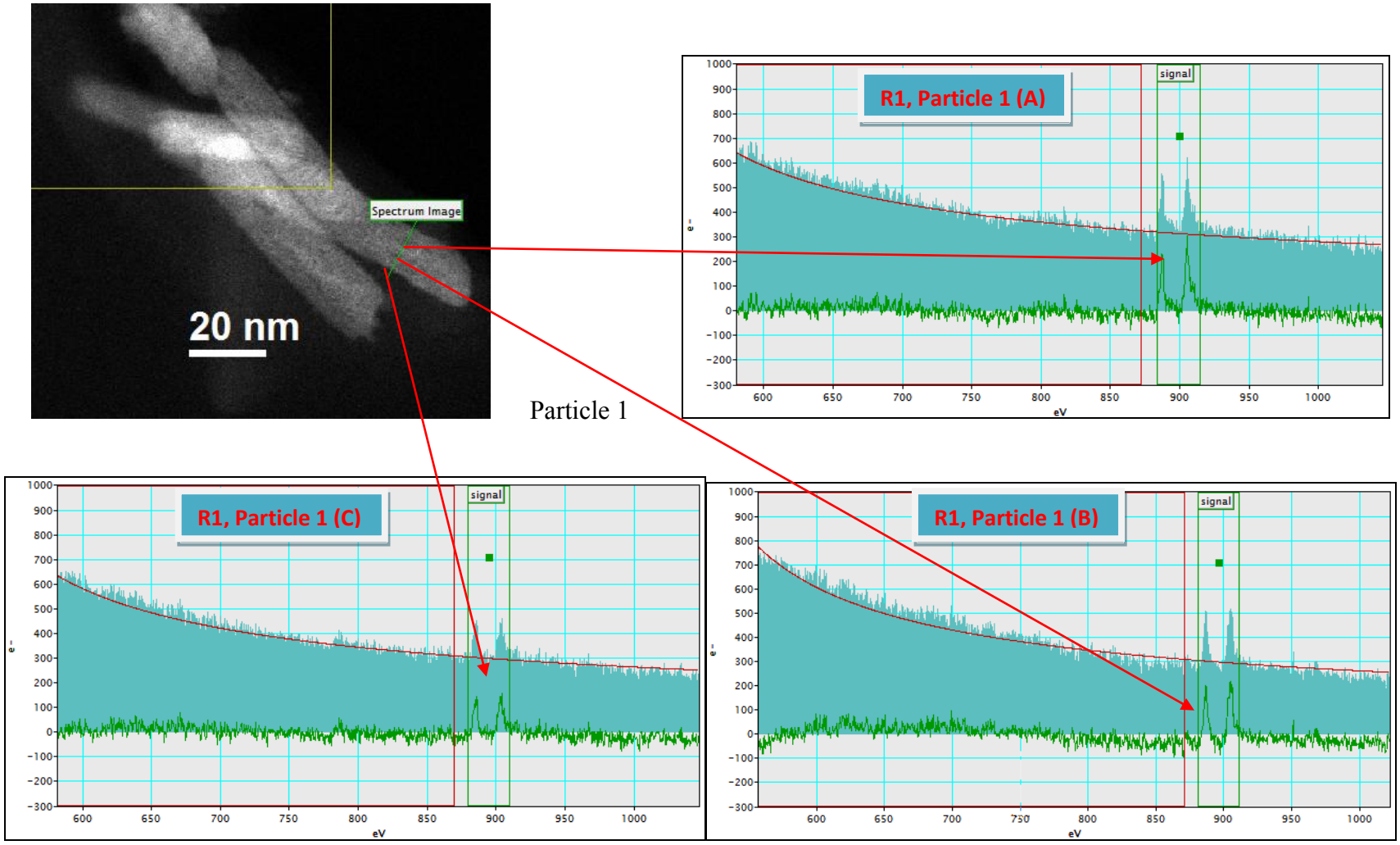

Figure 4.15 (a) EELS spectra illustrating different intensities of M_5 and M_4 white lines for particle 1 as the line scan was carried out from center towards the edge of the nanorod (R1)

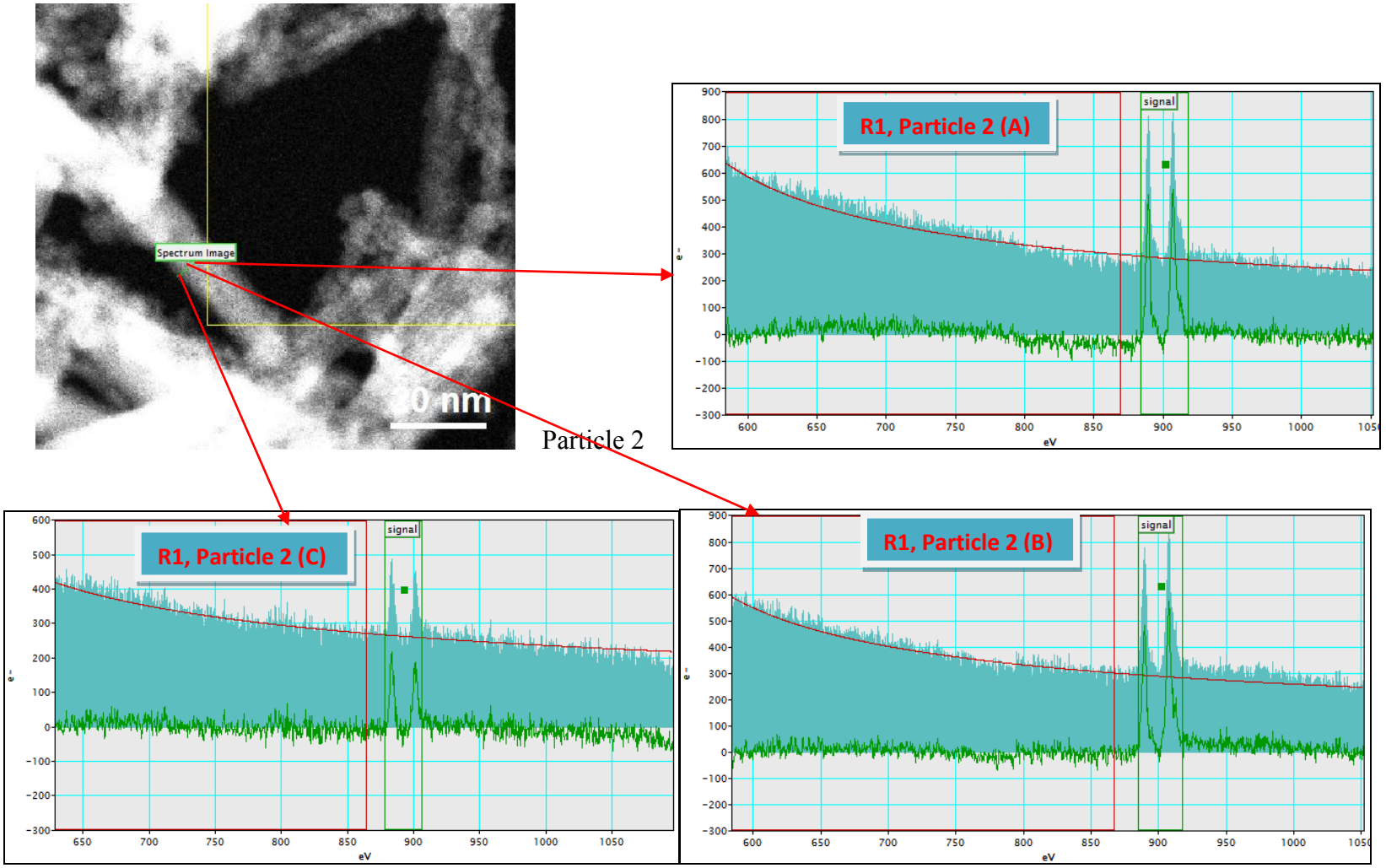

Figure 4.15 (b) EELS spectra illustrating different intensities of M_5 and M_4 white lines for particle 2 as the line scan was carried out from center towards the edge of the nanorod (R1)

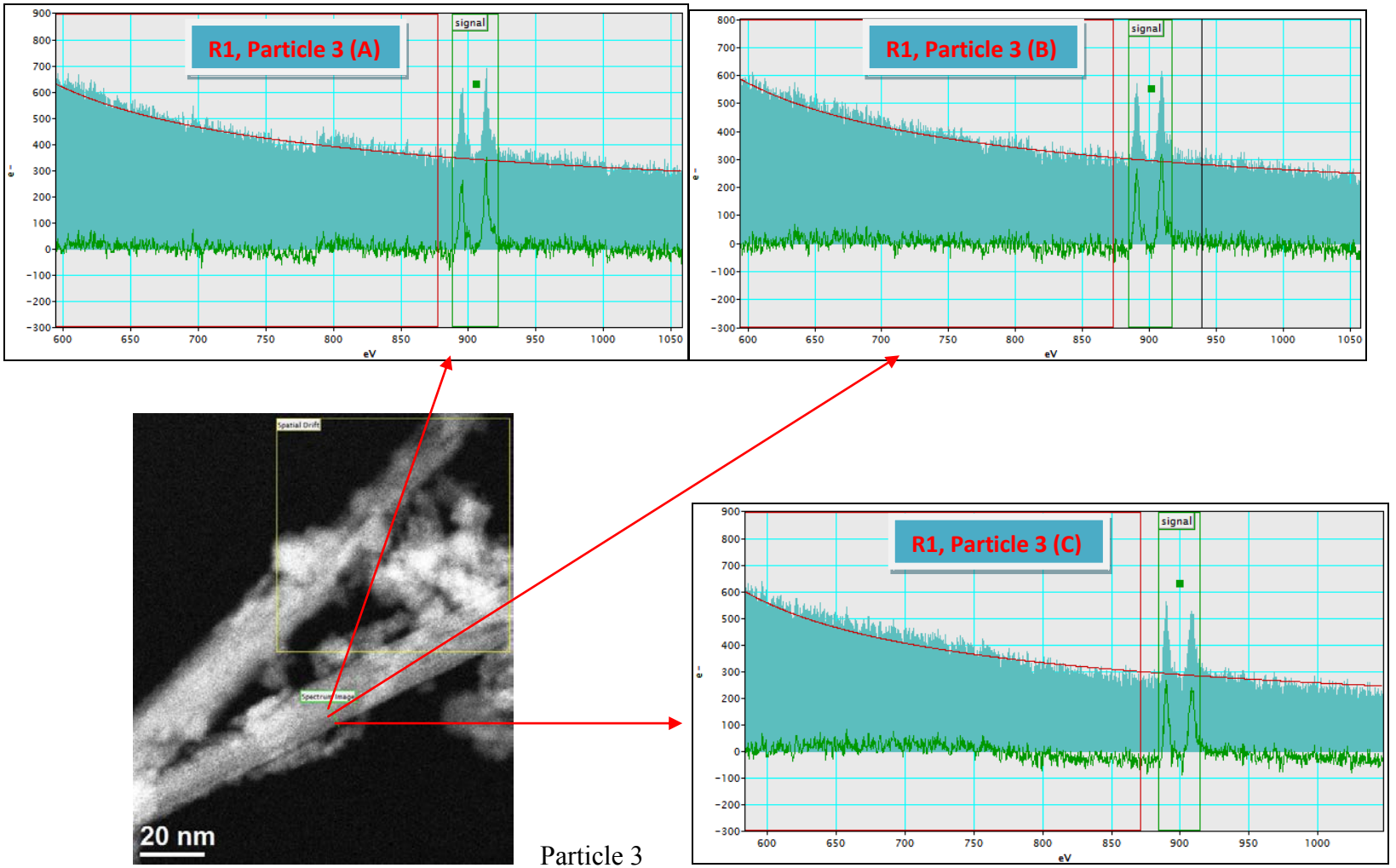

Figure 4.15 (c) EELS spectra illustrating different intensities of M_5 and M_4 white lines for particle 3 as the line scan was carried out from center towards the edge of the nanorod (R1)

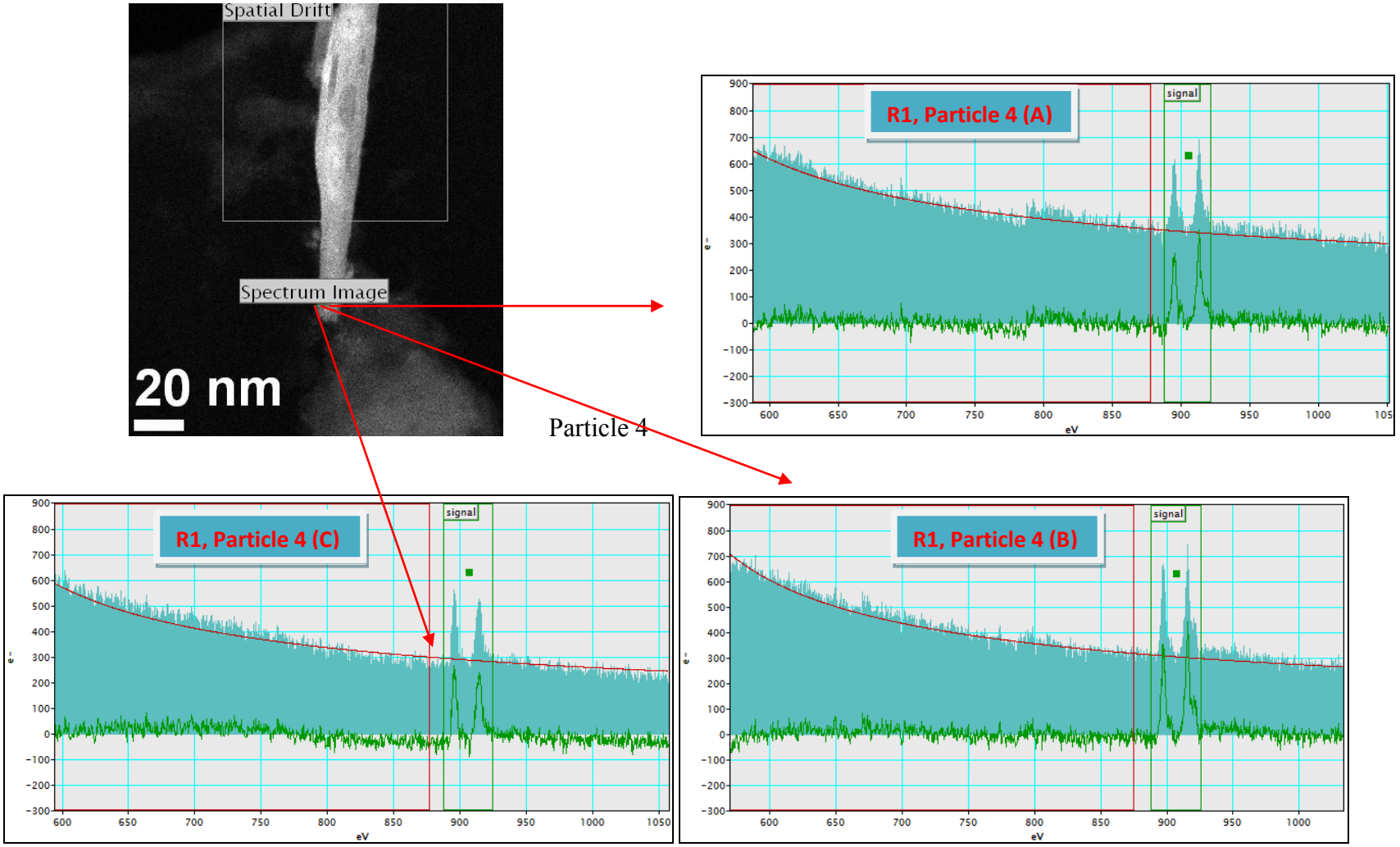

Figure 4.15 (d) EELS spectra illustrating different intensities of M_5 and M_4 white lines for particle 4 as the line scan was carried out from center towards the edge of the nanorod (R1)

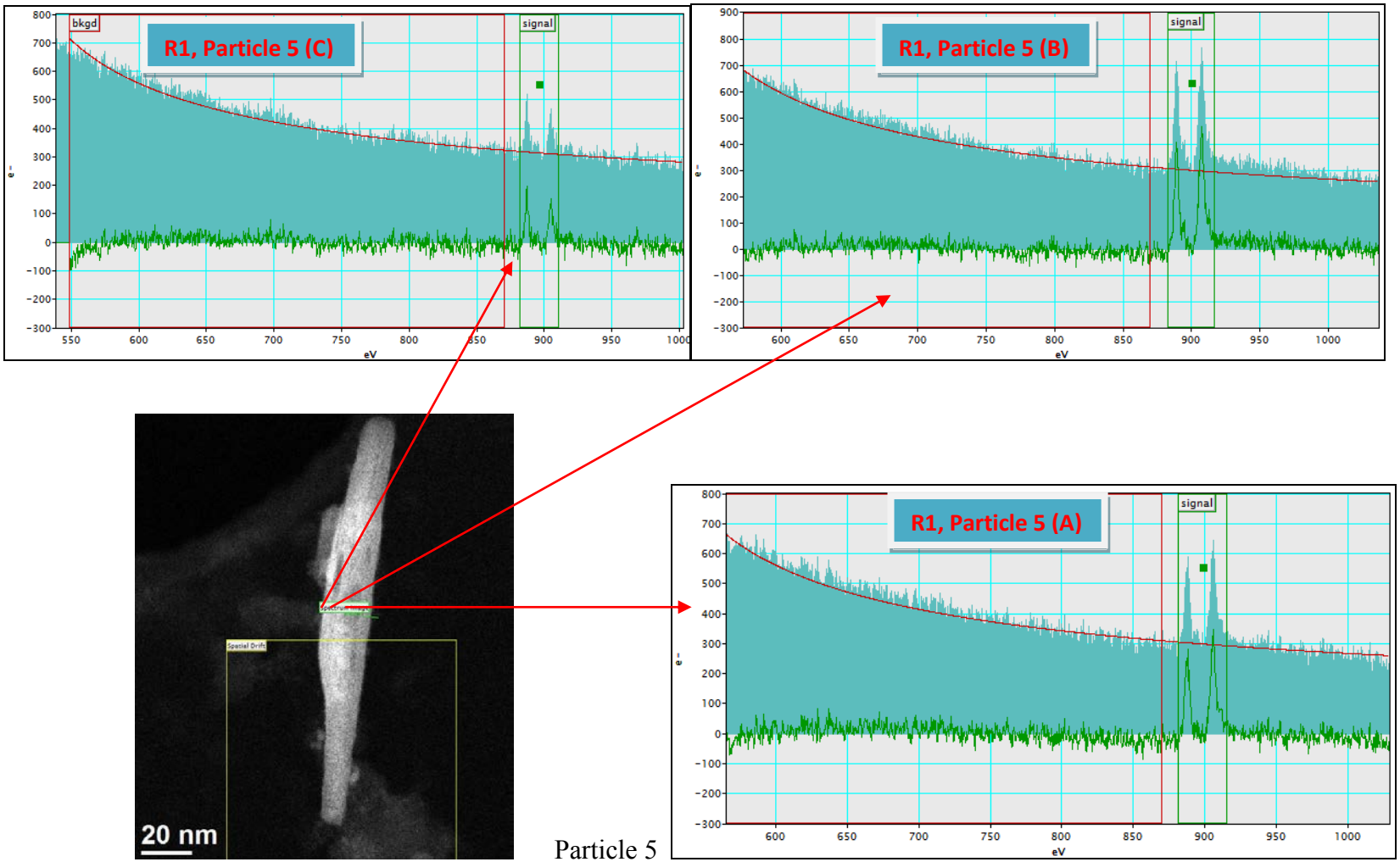

Figure 4.15 (e) EELS spectra illustrating different intensities of M_5 and M_4 white lines for particle 5 as the line scan was carried out from center towards the edge of the nanorod (R1)

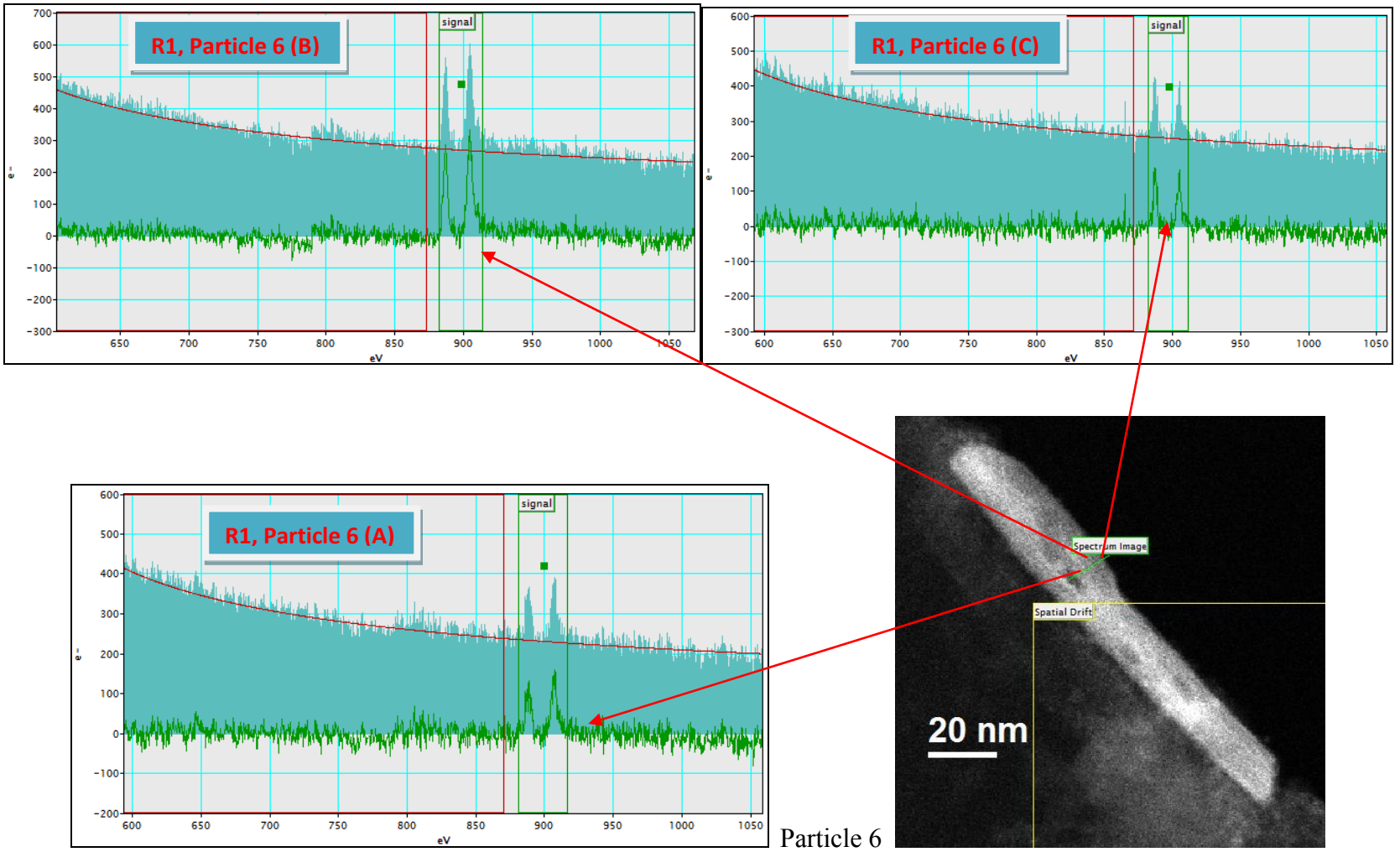

Figure 4.15 (f) EELS spectra illustrating different intensities of M_5 and M_4 white lines for particle 6 as the line scan was carried out from center towards the edge of the nanorod (R1)

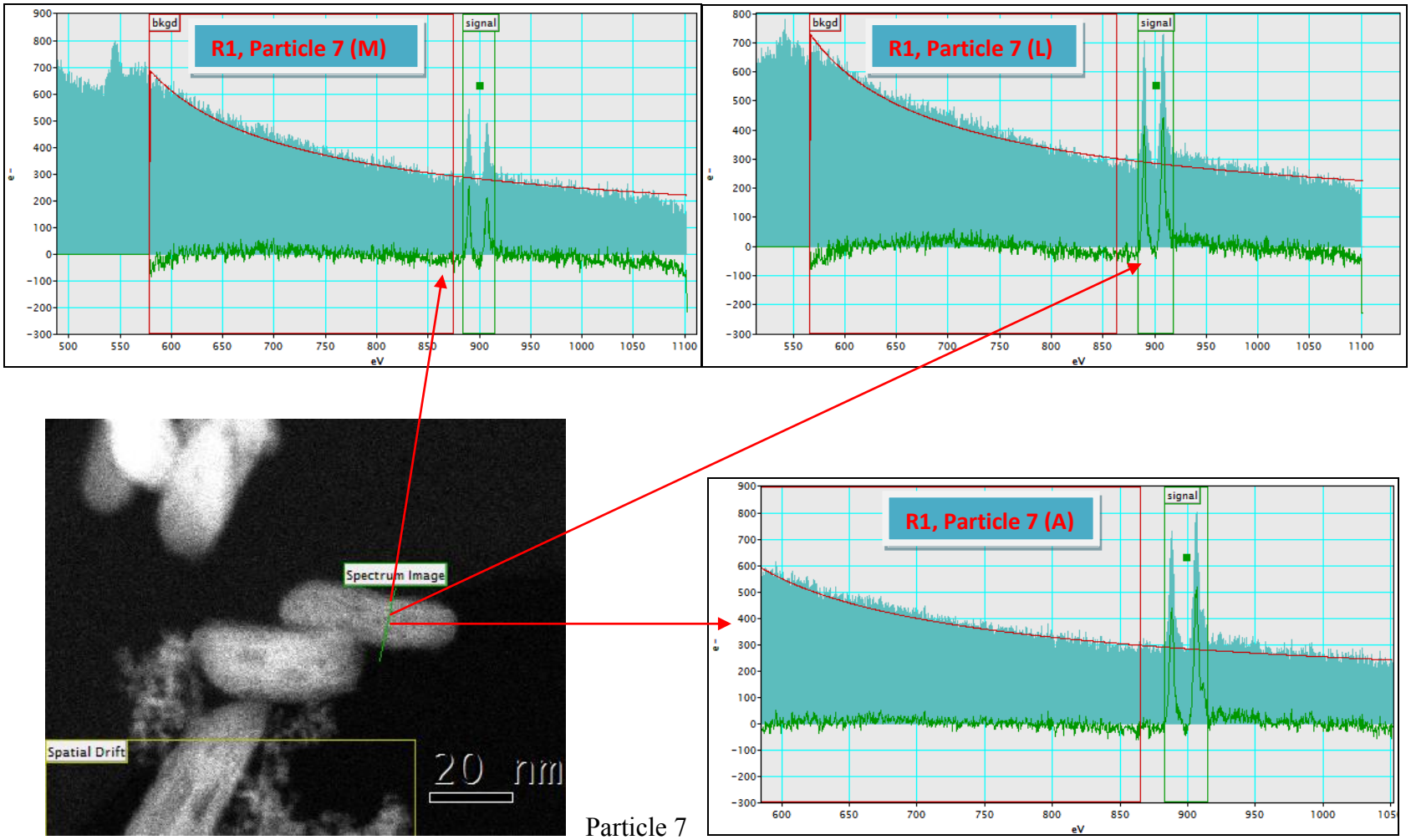

Figure 4.15 (g) EELS spectra illustrating different intensities of M_5 and M_4 white lines for particle 7 as the line scan was carried out from center towards the edge of the nanorod (R1)

4.6.3 Summary and conclusion of the EELS experiments carried out on nanorods R1

In summary, we have carried out systematic EELS experiments on nanorods R1. The $M_{4,5}$-edge spectra have been used to evaluate the oxidation state of cerium using STEM-EELS. Line scans have been carried out for R1 looking at local oxidation state variation across the particle as we go from the centre towards the edge of the particle. The M_5/M_4 ratios collected from the survey scans indicate that Ce (III) present in the top 3nm layer of the particle (point C), however, the center of the NPs (Point A) and the point between the center and the edge (point B) contained Ce (IV). Only transverse scans have been carried out and similar pattern has been observed. The data indicates that the valence reduction process is mainly predominant only at the surface and not in the core of the nanorods. STEM images were collected before and after the EELS experiments and no particle damage has been observed. Figure 4.16 clearly demonstrates the pattern of cerium oxidation states, as calculated from the average of M_5/M_4, from the center of the rod (A) towards the edge at points B and C. The quantification data is summarised in table 4.13.

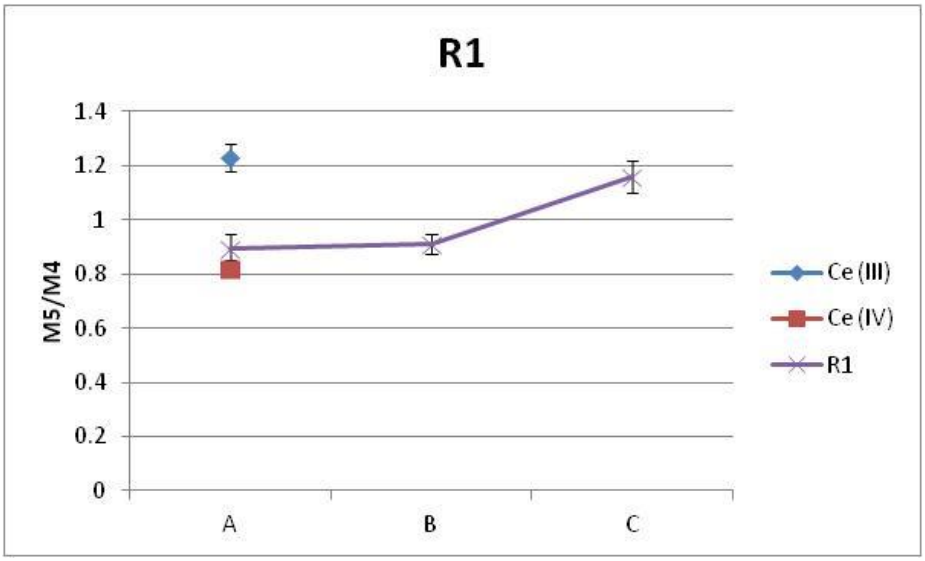

Figure 4.16 The M_5/M_4 ratios obtained across the diameter of the investigated nanorods are plotted against the particle depth illustrating the oxidation state pattern for sample R1.

Table 4.13 Oxidation state quantification data for the nanorods R1 as obtained from EELS

Sample code	Morphology	Size (nm)		EELS (%)	
		DLS	TEM	Ce (III) Center	Ce (IV) Edge
R1	Nanorods	168±2	83±56(Length) 16±6(width)	19	83

4.7 Oxidation state quantification of nanospheres S5 using EELS

The ceria nanospheres S5 were synthesised by myself and their synthetic scheme has been discussed in chapter 3, synthesis 4, scheme a (section 3.2.1). The particles have been characterised for their size and shape by DLS and TEM. The details are in chapter 3.

4.7.1 EELS measurements on nanospheres S5

The nanospheres S5 are 3.3±1.3 nm in size as calculated by TEM. The line scans carried out for EELS measurements seemed to be damaging the particle surface, so area scans have been carried out. Area scans have been carried out on five different regions of the sample. The EELS spectrum generated and the areas under investigation have been illustrated in figures 4.17 (a-c). The M_5/M_4 ratios extracted by second derivative method are tabulated in table 4.14.

Table 4.14 M_5/M_4 ratios obtained from area scans carried out on sample S5

Sample S5 - area scans		**$CeNO_3$ as standard**	**Bulk CeO_2 as standard**
	M_5/M_4	Ce (III)	Ce (IV)
Area 1	1.16	1.23	0.82
Area 2	1.07		
Area 3	1.22		
Area 4	1.01		
Area 5	1.08		

4.7.2 Results and discussion of EELS measurements on nanospheres S5

The results obtained suggest that the sample contains a mixture of Ce (III) and Ce (IV). Some of the M_5/M_4 ratios extracted are closer to that obtained from Ce (III) standard, for example area 2 and 4 while some confirm the presence of Ce (IV), for example area 1 and 3. After the quantitative analysis of the M_5/M_4 ratios obtained from all the investigated areas, the data shows that there is 70 % Ce (III) and 30 % Ce (IV) present in the sample S5.

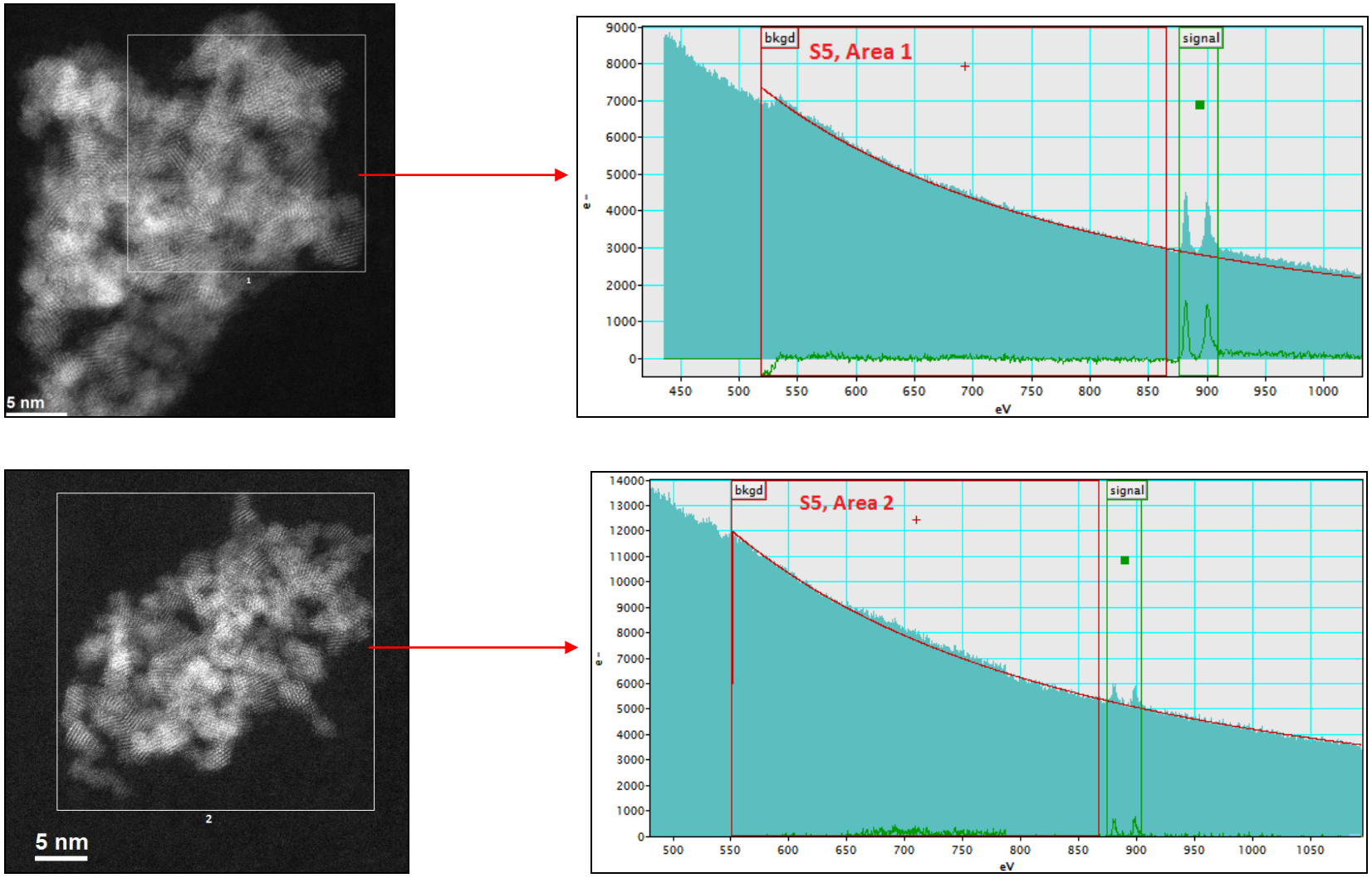

Figure 4.17 (a) STEM images from sample S5 and EELS spectrum generated from area 1 and 2 of the sample

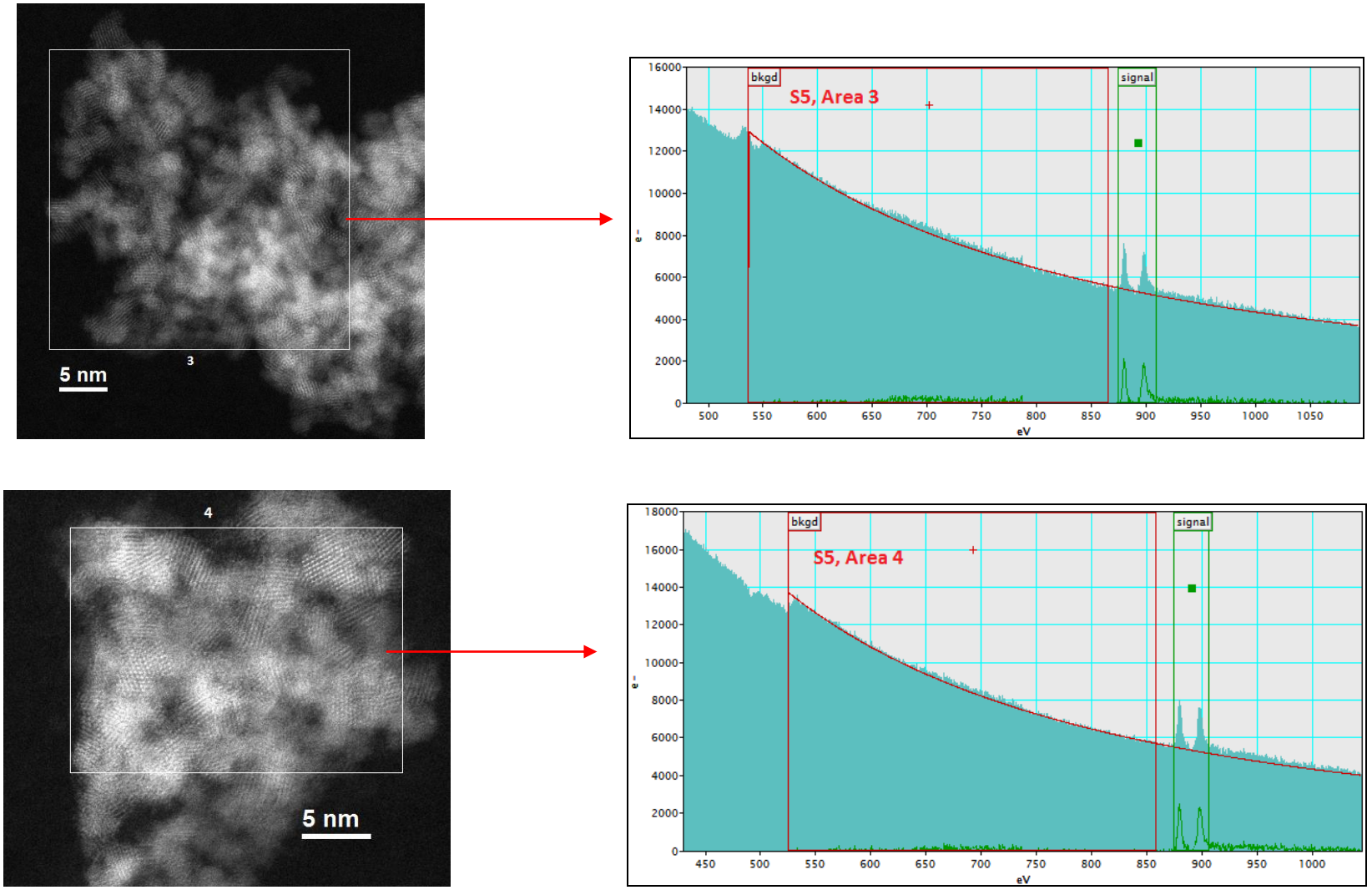

Figure 4.17 (b) STEM images from sample S5 and EELS spectrum generated from area 3 and 4 of the sample

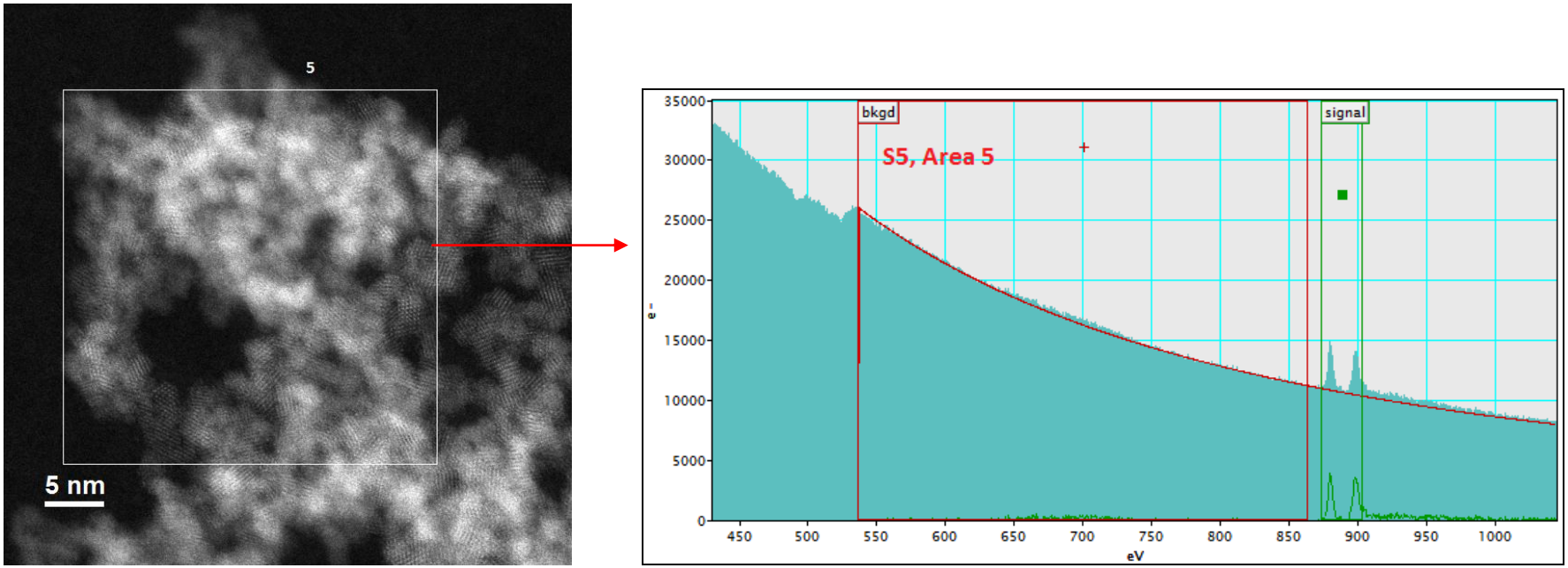

Figure 4.17 (c) STEM image from sample S5 and EELS spectrum generated from area 5 of the sample

4.7.3 Summary and conclusion of the EELS experiments carried out on nanospheres S5

EELS experiments have been performed on nanospheres from sample S5. The line scans carried out during EELS measurements seemed to be damaging the particle surface. STEM images taken before and after the experiment showed damage to the particles (Appendix D). The sample deformation could be clearly seen indicating that the electron beam destroyed some of the particle surface. Considering the damage, area scans were safely carried out on five different regions of the sample S5, Appendix E shows STEM images after the scans. This is a safer way of analysing the samples. However, area scans generate an overall picture about the sample and the signals come out of the sample as a whole. So the data generated is an overall review of the sample oxidation state and not of any individual particle. This method is particularly very helpful for samples where no line scans can be carried out. The EELS spectrum generated and the areas under investigation have been illustrated in figures 4.17 (a-c). The M_5/M_4 ratios extracted by second derivative method are tabulated in table 4.15. Figure 4.18 represents the average M_5/M_4 ratios obtained for different areas from sample S5. The quantitative results have been summarised in table 4.15.

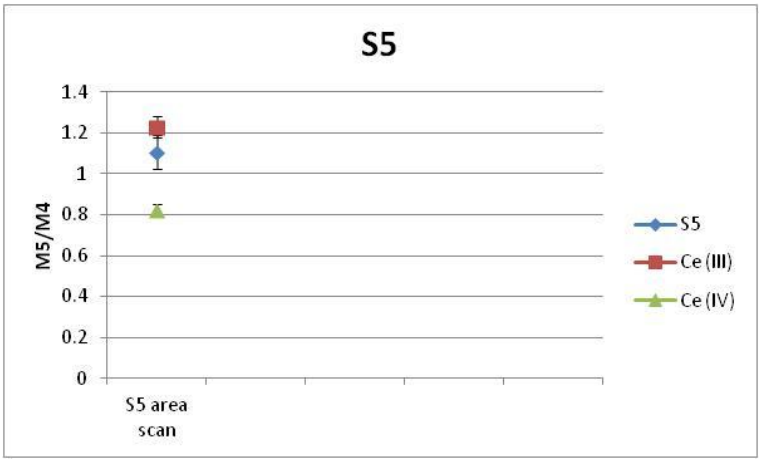

Figure 4.18 M_5/M_4 ratios obtained from area scans carried out on sample S5

Table 4.15 Oxidation state quantification data for the nanospheres S5 as obtained from EELS

Sample code	Morphology	Size (nm)		EELS (%)	
		DLS	TEM	Ce (III)	Ce (IV)
S5	Nanosphere	147.7±6.2	3.3±1.3	70	30

4.8 Oxidation state quantification of nanocubes C4 using EELS

The ceria nanocubes C4 were synthesised by me and their synthetic scheme has been discussed in chapter 3, synthesis 4, and scheme b. The particles have been characterised for their size and shape by DLS and TEM. The details are in chapter 3.

4.8.1 EELS measurements on nanocubes C4

The EELS maesurements on the nanocubes C4 (2.4±0.6 nm by TEM) have been performed using the same methodology as discussed for previous line scans. The survey scan has been carried out at three points called A, B, C where A indicates the center of the cube, B is the point between the center and edge of the cube and C is the outermost edge. The M_5/M_4 ratio extracted from this line scan across the nanocube indicates the variation of cerium oxidation state as we go from the centre towards the edge of the cube.

4.8.2 Results and discussion of EELS measurements on nanocubes C4

The M_5/M_4 ratios extracted from the center point A of particle 1 (d=3.5nm) is close to that of Ce (IV) figure 4.19 (a), while that from the center B and edge of the particle C is close to Ce (III) (Table 4.16, particle1). Figure 4.19 (a) clearly illustrates different intensities of M_5 and

M_4 white lines observed for particle 1 as the line scan was carried out from center towards the edge of the nanoparticle.

Table 4.16 M_5/M_4 ratios at points A, B and C for sample C4

Depth	Sample C4					
	particle 1	particle 2	particle 3	particle 4	particle 5	particle 6
A	0.966	1.33	w/s	w/s	1.3	1.3
B	1.38	1.11	w/s	w/s	1.12	1.12
C	1.33	1.26	w/s	w/s	1.33	1.33
* w/s = weak signal						

A number of measurements have been carried out on different NPs of the same sample. It was found that for NPs ≤ 2 nm, there was Ce (III) detected at each point i.e at points A, B as well as C. For example, the M_5/M_4 ratios detected for particle 2 (d=2nm) (Figure 4.19 b) are 1.33, 1.11 and 1.26 for points A, B and C respectively which match with the M_5/M_4 ratios of the Ce (III) standard. The M_5/M_4 ratios extracted after different line scans have been illustrated in table 4.16 and the different particles investigated are illustrated in Figure 4.19 (a-d). Two other NPs investigated (particle 3 and 4) gave very weak signals, so their signals could not be extracted and used for quantification purposes, spectrum shown in Appendix B.

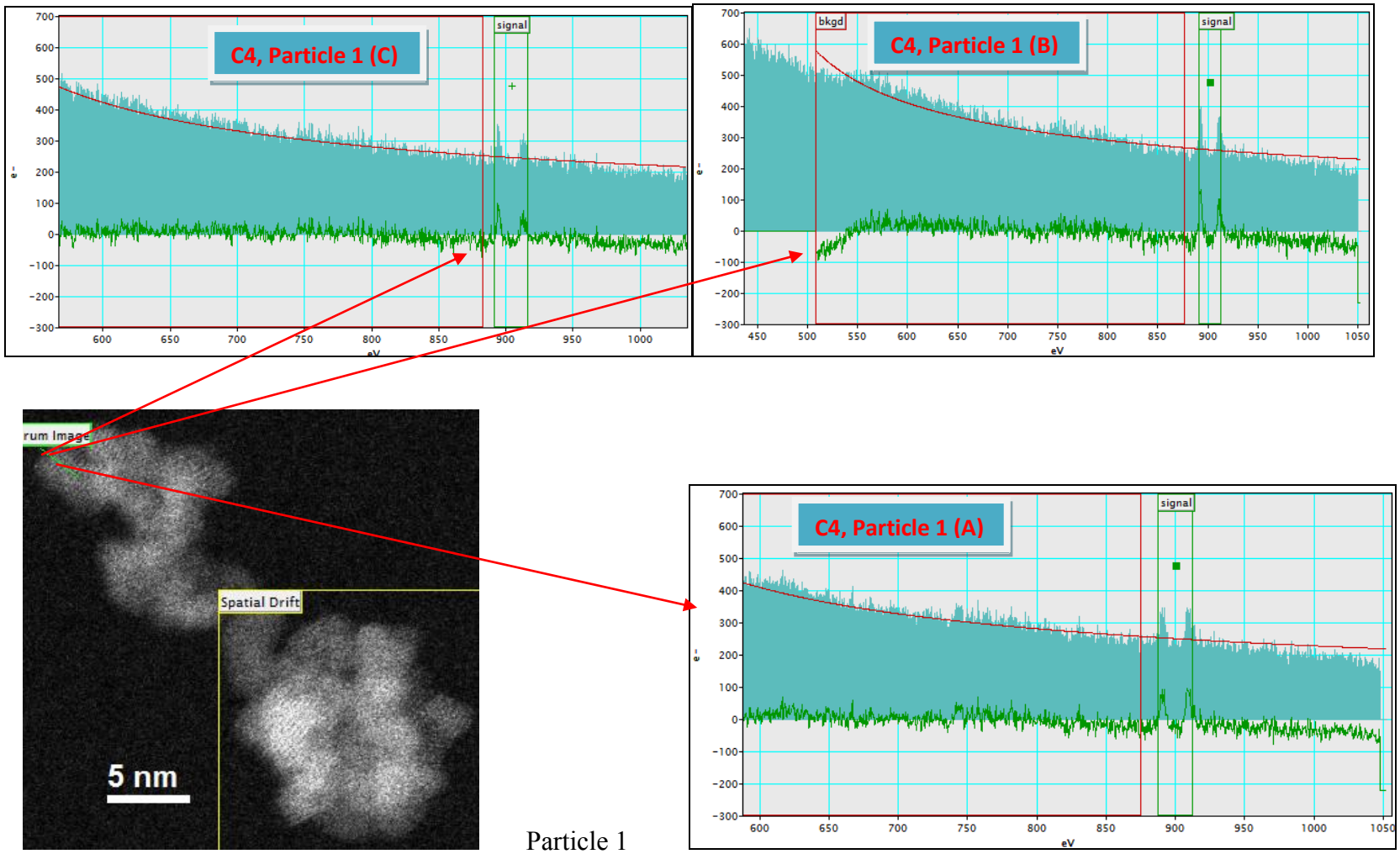

Figure 4.19 (a) EELS spectra illustrating different intensities of M_5 and M_4 white lines for particle 1 as the line scan was carried out from center towards the edge of the nanocube (C4)

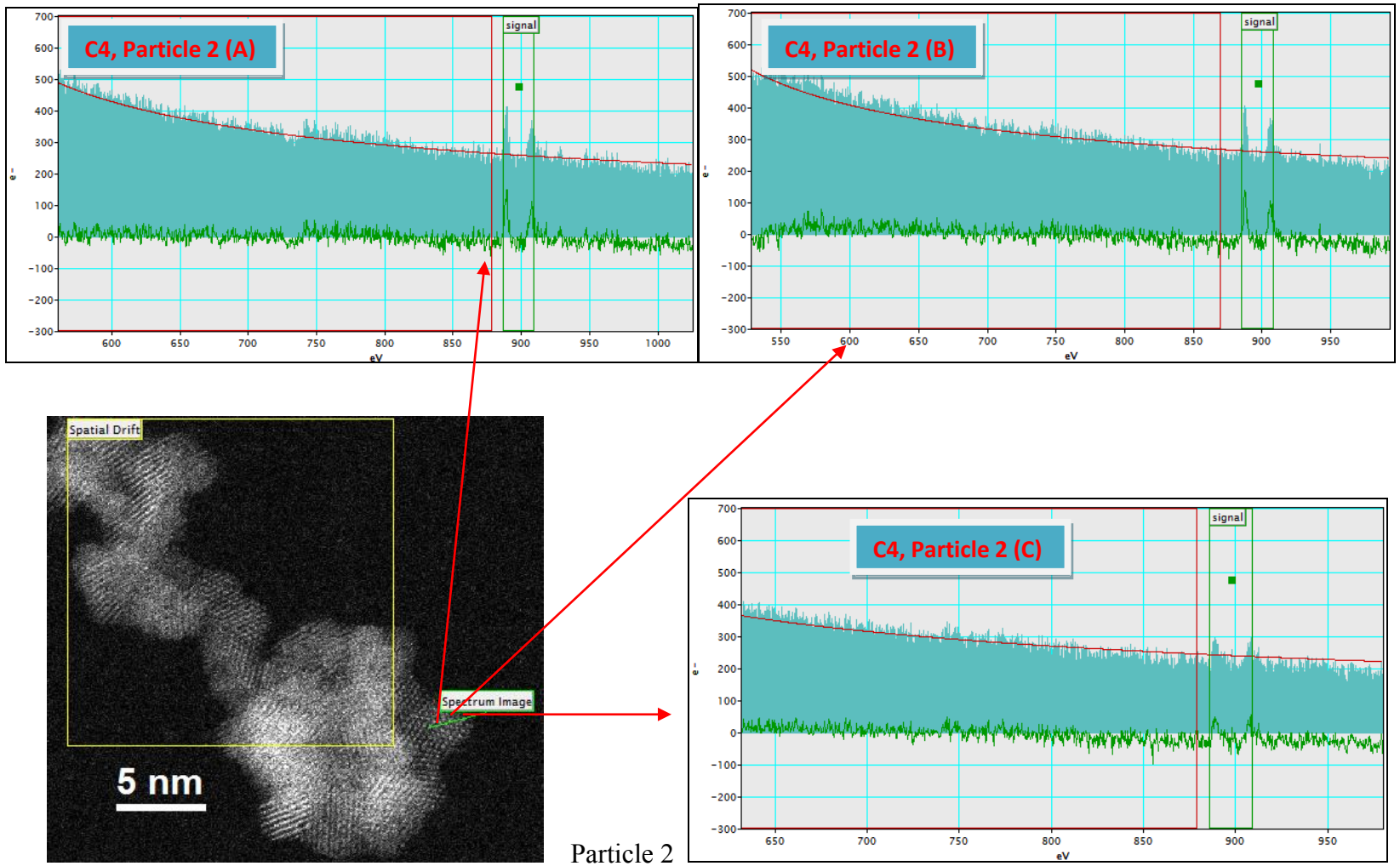

Figure 4.19 (b) EELS spectra illustrating different intensities of M_5 and M_4 white lines for particle 2 as the line scan was carried out from center towards the edge of the nanocube (C4)

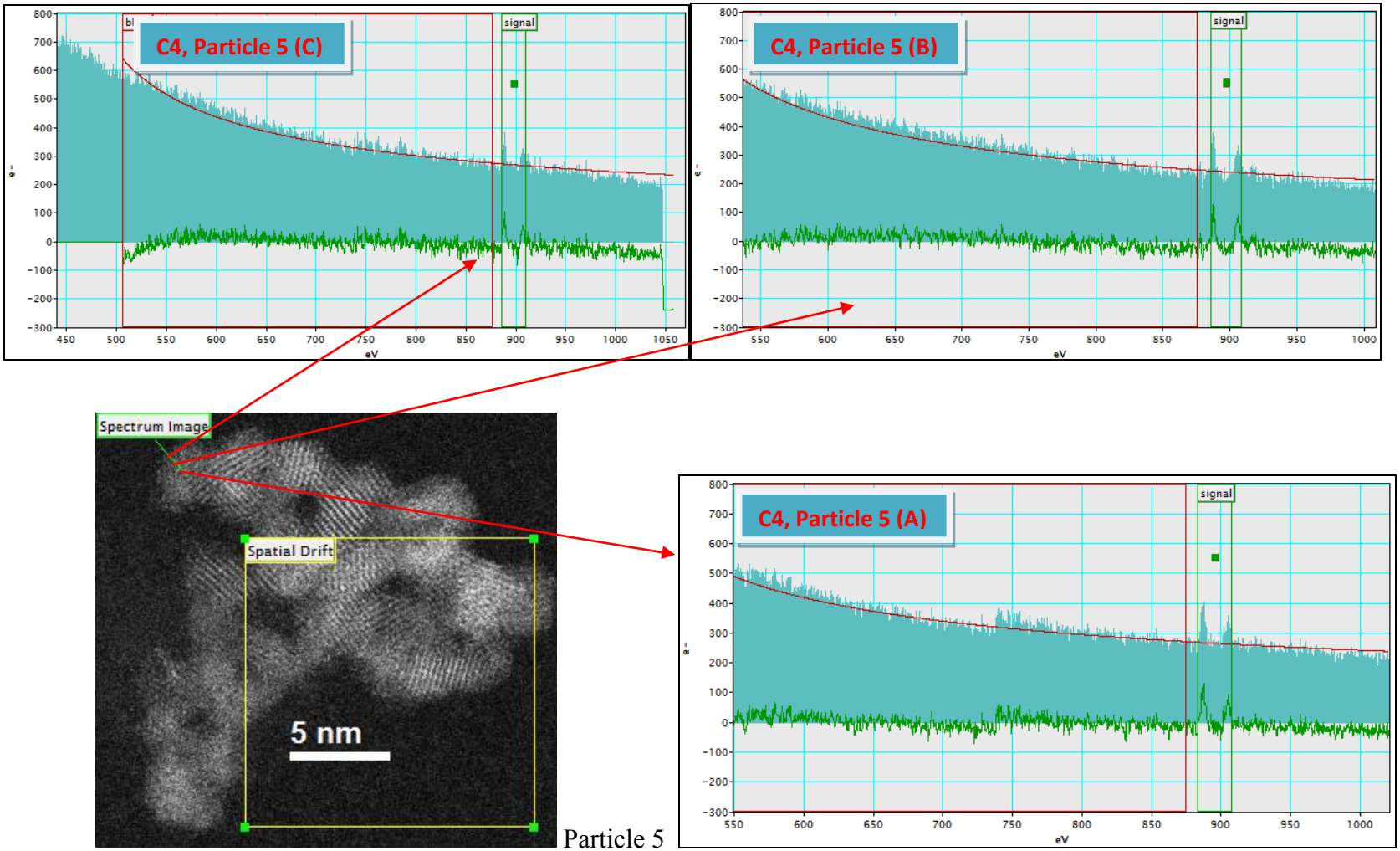

Figure 4.19 (c) EELS spectra illustrating different intensities of M_5 and M_4 white lines for particle 5 as the line scan was carried out from center towards the edge of the nanocube (C4)

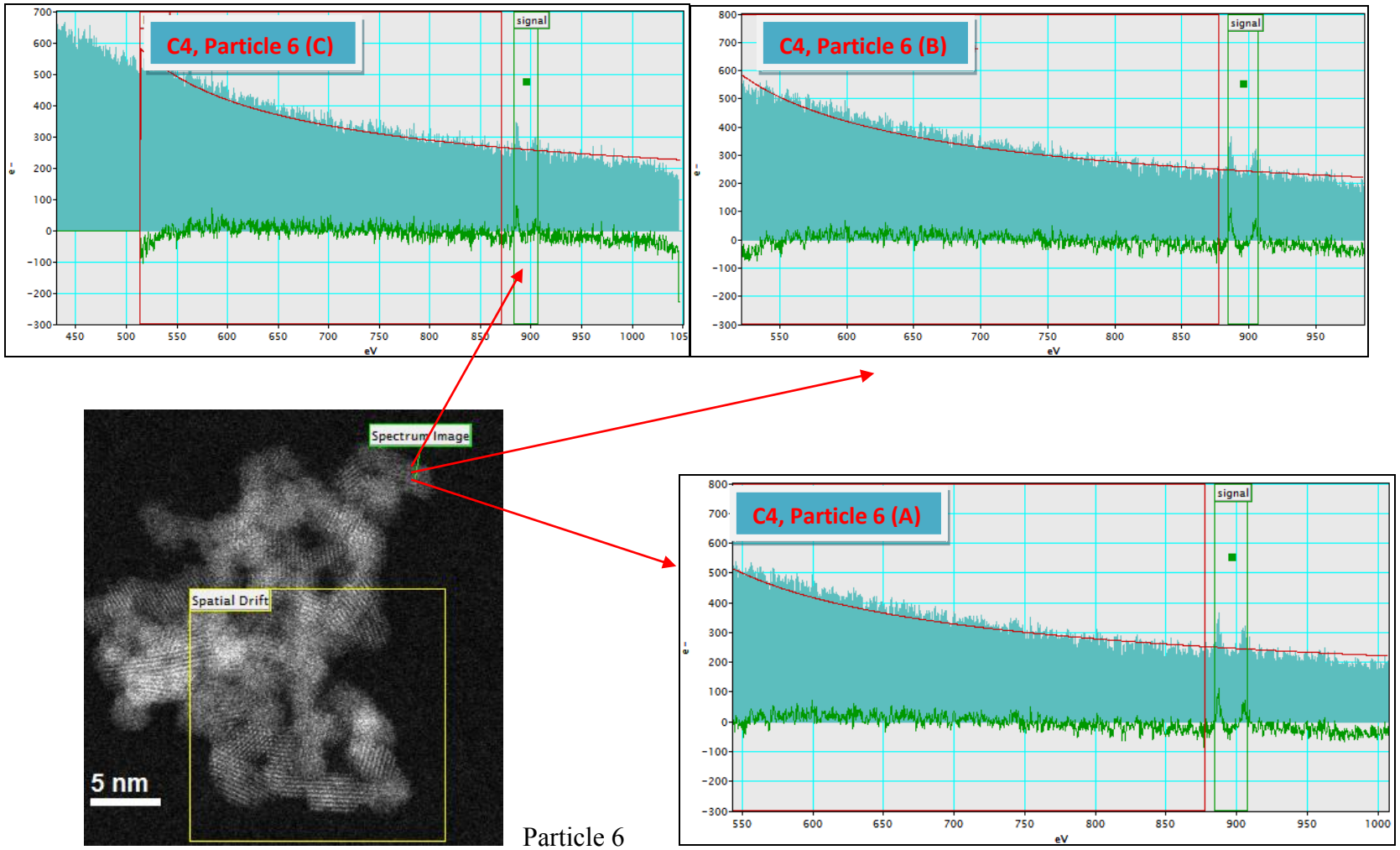

Figure 4.19 (d) EELS spectra illustrating different intensities of M_5 and M_4 white lines for particle 6 as the line scan was carried out from center towards the edge of the nanocube (C4)

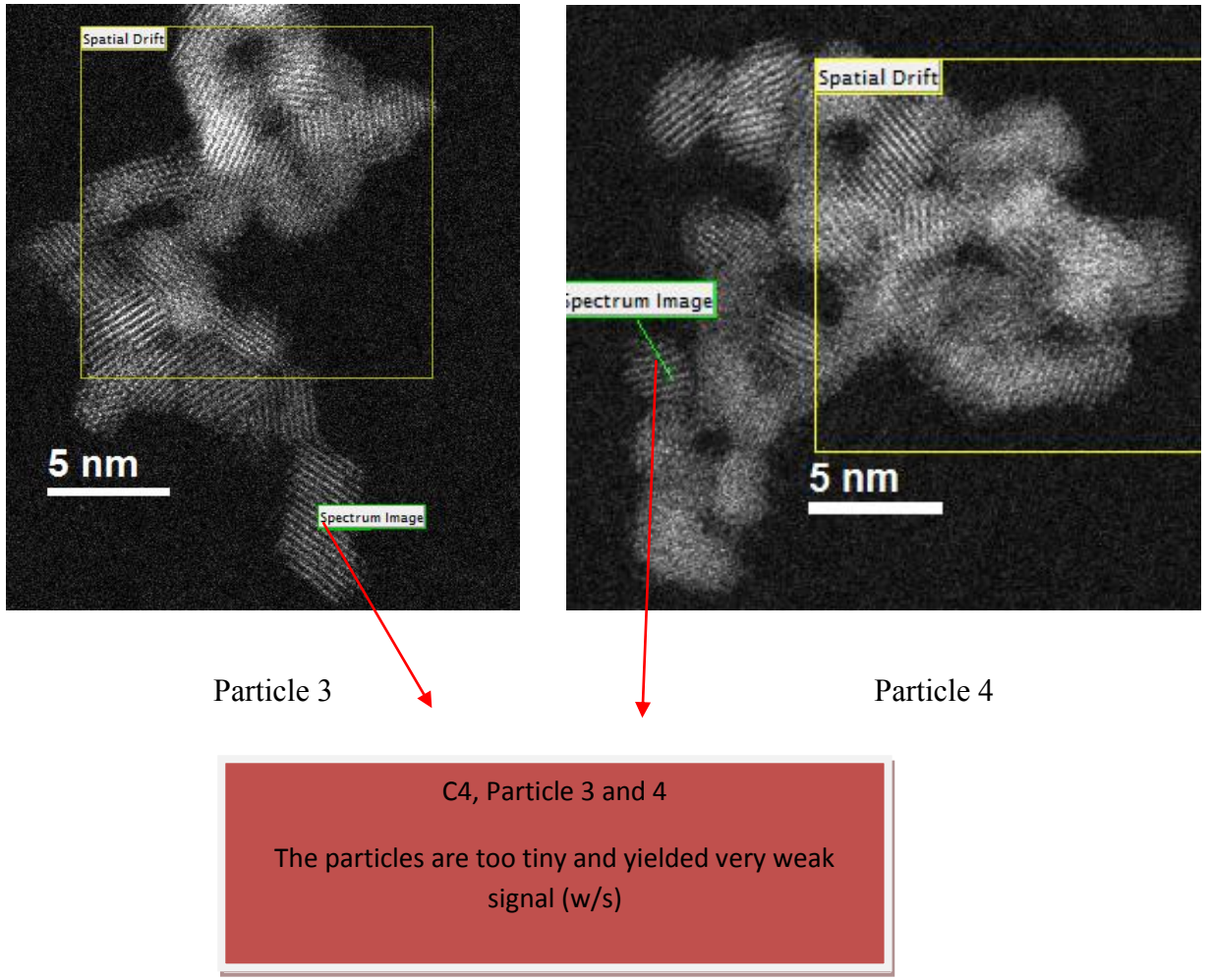

Figure 4.19 (e) The line scan carried out on particle 3 and 4 of the sample C4 yielded very weak signal

The results indicate that the sample contains mainly Ce (III) with very little amount of Ce (IV). The M_5/M_4 ratios extracted from the line scans for all the particles are closer to that obtained from Ce (III) standard while few confirm the presence of Ce (IV). After the quantitative analysis of the M5/M4 ratios obtained from all the investigated particles at different depths of the particle, the data shows that there is 98 % Ce (III) in the core and 100 % Ce (III) present at the edges of sample C4..

4.8.3 Summary and conclusion of the EELS experiments carried out on nanocubes C4

In summary, we have carried out systematic EELS experiments on nanocubes C4. The $M_{4,5}$-edge spectra have been used to evaluate the oxidation state of cerium using STEM-EELS. Line scans have been carried out looking at local oxidation state variation across the particle as we go from the centre towards the edge of the particle. The results suggest that the amount of Ce (III) increases as the particle size decreases with particles $\leq$ 2nm to be completely Ce (III). This could be ascribed to the more number of oxygen vacancies in particles with smaller sizes. The results obtained are in good agreement with the previous samples (S1, S2) with 2nm sized particles. Some of the NPs investigated (particle 3 and 4) gave very weak signals, so their signals couldn't be extracted during spectrum processing and hence were not used for quantification purposes (Appendix B). Figure 4.20 clearly demonstrates the M_5/M_4 ratios obtained across the diameter of the particles investigated and are plotted against the particle depth illustrating the oxidation state pattern observed for cubes C4 as we go from center towards the edge of the particle. The oxidation state quantification data has been summarised in table 4.17

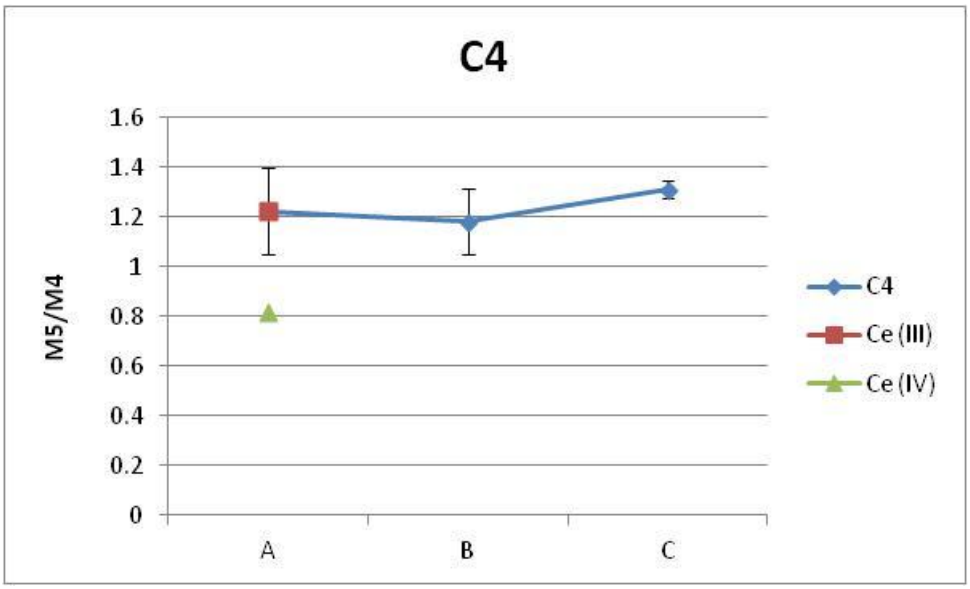

Figure 4.20 The M_5/M_4 ratios obtained across the diameter of the particles investigated are plotted against the particle depth illustrating the oxidation state pattern observed for C4.

Table 4.17 Oxidation state quantification data for the sample C4 as obtained from EELS

Sample code	Morphology	Size (nm)		EELS (%)	
		DLS	TEM	Ce (III) Center	Ce (III) Edge
C4	Nanocubes	152.8±4.6	2.4±0.6	98	100

4.9 Oxidation state quantification of nanospheres S6 using EELS

The ceria nanospheres S6 were synthesised by me and their synthetic scheme has been discussed in chapter 3, section 3.2.1, and synthesis 5. The particles have been characterised for their size and shape by DLS and TEM. The details are in chapter 3.

4.9.1 EELS measurements on nanospheres S6

The EELS measurements on the nanospheres S6 (8.2±2.5 nm by TEM) have been collected using the same methodology as discussed for previous line scans. The survey scan has been carried out at three points called A, B and C where A indicates the center of the particle, B is the point between the center and edge of the sphere and C is the outermost edge and the M_5/M_4 ratio extracted from this line scan across the nanosphere indicates the variation of cerium oxidation state as we go from the centre towards the edge of the particle.

4.9.2 Results and discussion of EELS measurements on nanospheres S6

The M_5/M_4 ratios extracted from the center point A of particle 2 (d=7 nm) as well as between the center and edge of the particle (point B) are close to that of Ce (IV) figure 4.21 (b), while that extracted from the edge of the particle (at point C) is close to Ce (III) (Table 4.18, particle 2). Figure 4.21 (b) clearly illustrates different intensities of M_5 and M_4 white lines observed for particle 2 as the line scan was carried out from center towards the edge of the nanoparticle. A number of measurements have been carried out on different NPs of the same sample. We found that for NPs ≤ 2 nm, there was Ce (III) present at points A, B as well as C. For example, the M5/M4 ratios detected for particle 3 (d=2nm) (Figure 4.21 c) are 1.31, 1.3 and 1.26 for points A, B and C respectively which match with the M_5/M_4 ratios of the Ce (III) standard. Similar results were obtained for other investigated particles of 2nm sizes. The EELS measurements have been performed on a range of particle sizes and the M_5/M_4 ratios extracted after different line scans have been illustrated in table 4.18. The various particles investigated are illustrated in Figure 4.21 (a-g). Two other NPs investigated (particle 1 and 7) gave very weak signals at the edges so their signals couldn't be extracted and used for quantification purposes. They have been marked with w/s (weak signal) in table 4.18, shown

in Appendix B. After the quantitative analysis of the M_5/M_4 ratios obtained from all the investigated particles at different depths of the particle, the data shows that there is 55 % Ce (III) present in the core and 100 % Ce (III) present at the edges of sample S6.

Table 4.18 M_5/M_4 ratios at points A, B and C for sample S6

Depth	**Sample S6**						
	particle 1	particle 2	particle 3	particle 4	particle 5	particle 6	particle 7
A	1.098	0.89	1.31	0.87	1.03	1.21	0.95
B	1.35	0.88	1.3	0.85	1.42	0.8	1.25
C	w/s	1.27	1.26	1.29	1.4	1.46	w/s
***w/s = weak signal**							

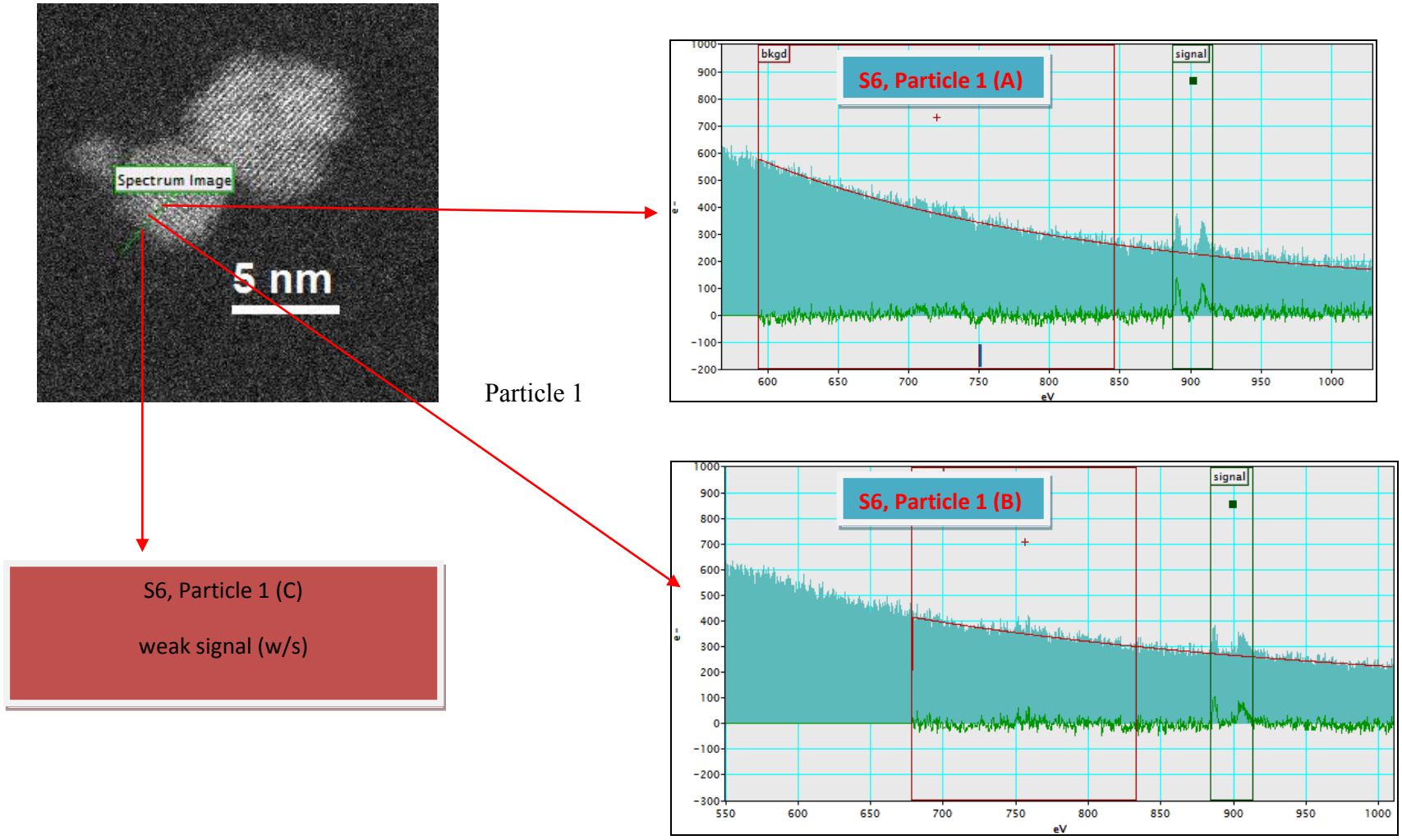

Figure 4.21 (a) EELS spectra illustrating different intensities of M_5 and M_4 white lines for particle 1 as the line scan was carried out from center towards the edge of the nanosphere (S6)

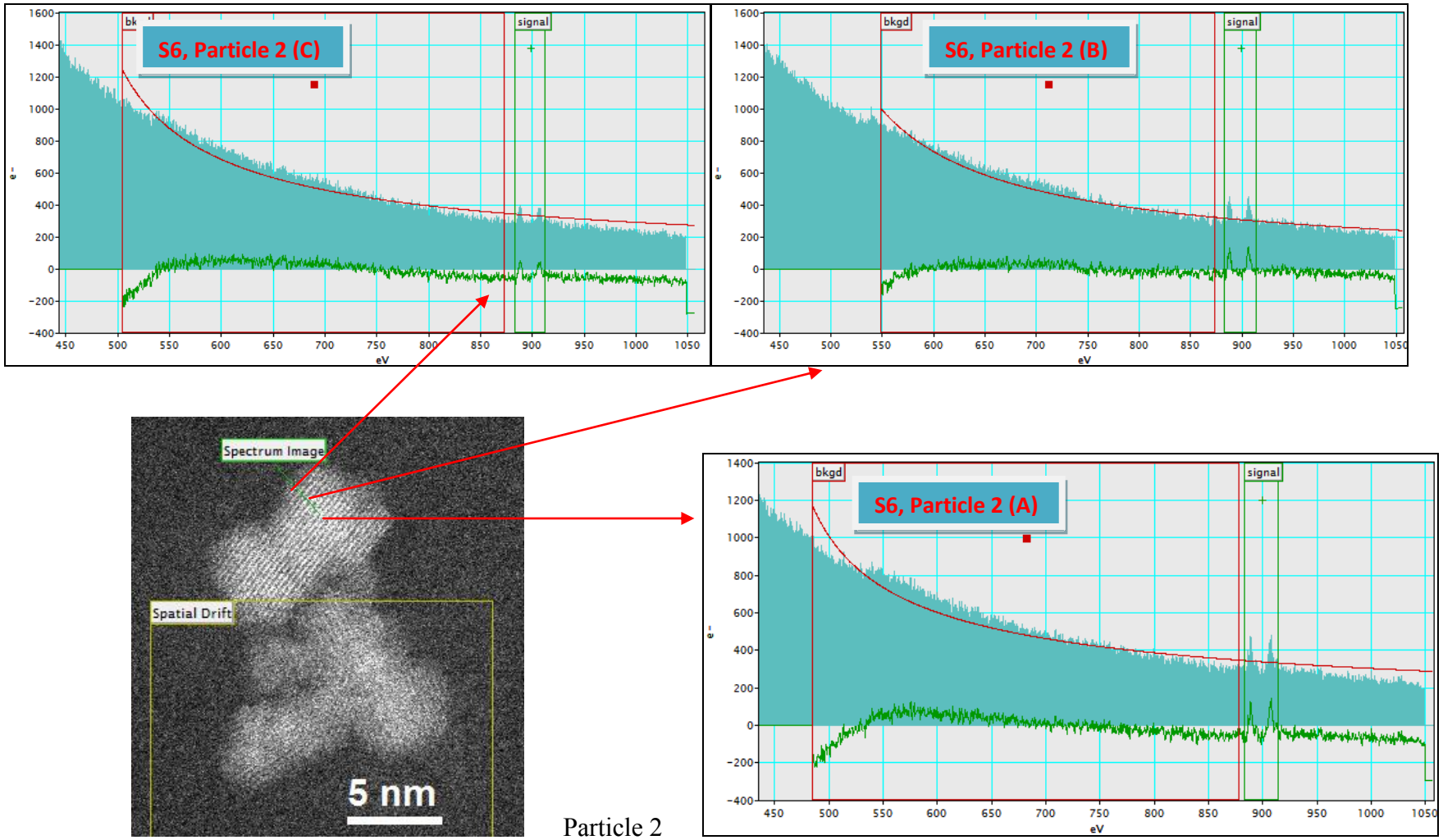

Figure 4.21 (b) EELS spectra illustrating different intensities of M_5 and M_4 white lines for particle 2 as the line scan was carried out from center towards the edge of the nanosphere (S6)

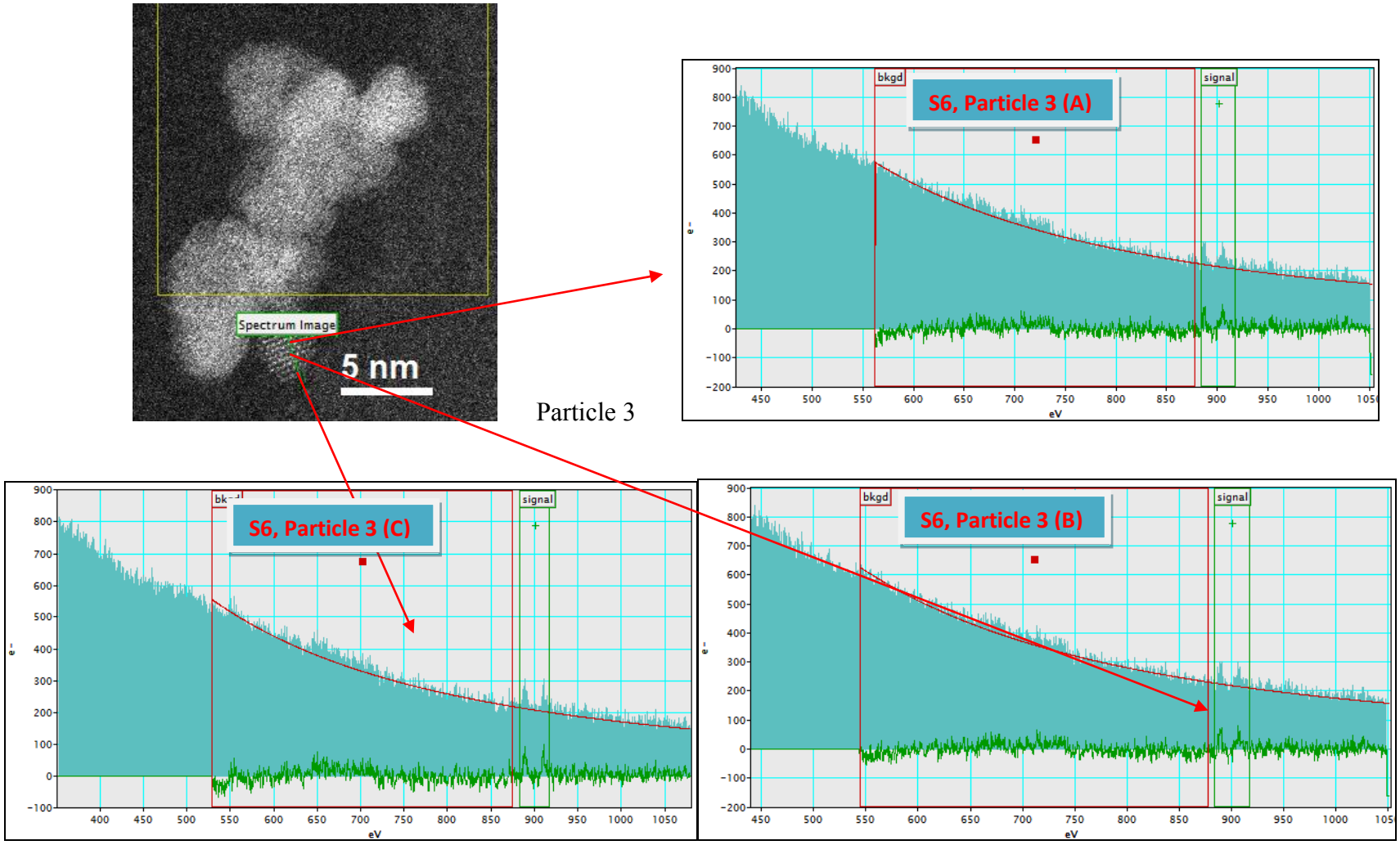

Figure 4.21 (c) EELS spectra illustrating different intensities of M_5 and M_4 white lines for particle 3 as the line scan was carried out from center towards the edge of the nanosphere (S6)

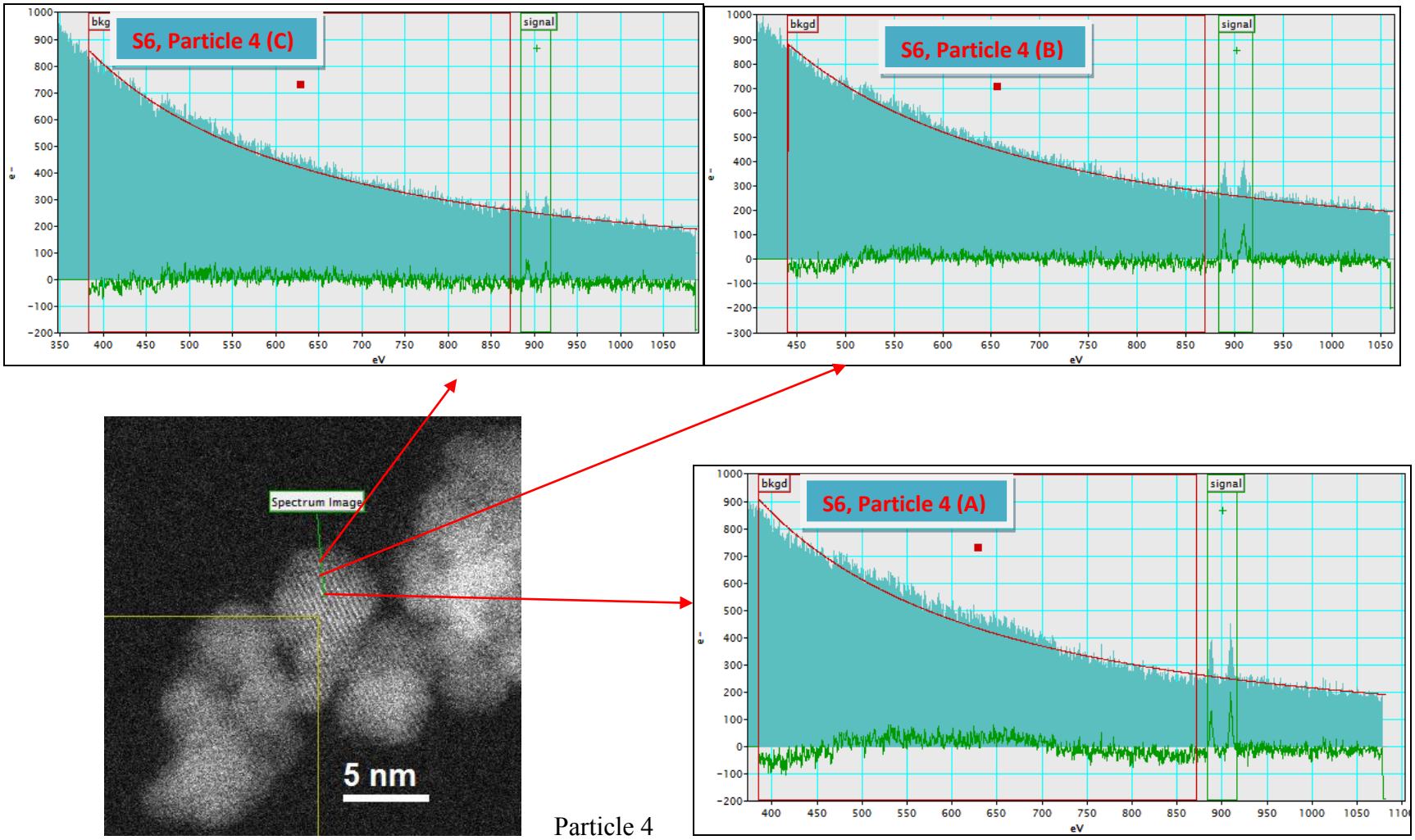

Figure 4.21 (d) EELS spectra illustrating different intensities of M_5 and M_4 white lines for particle 4 as the line scan was carried out from center towards the edge of the nanosphere (S6)

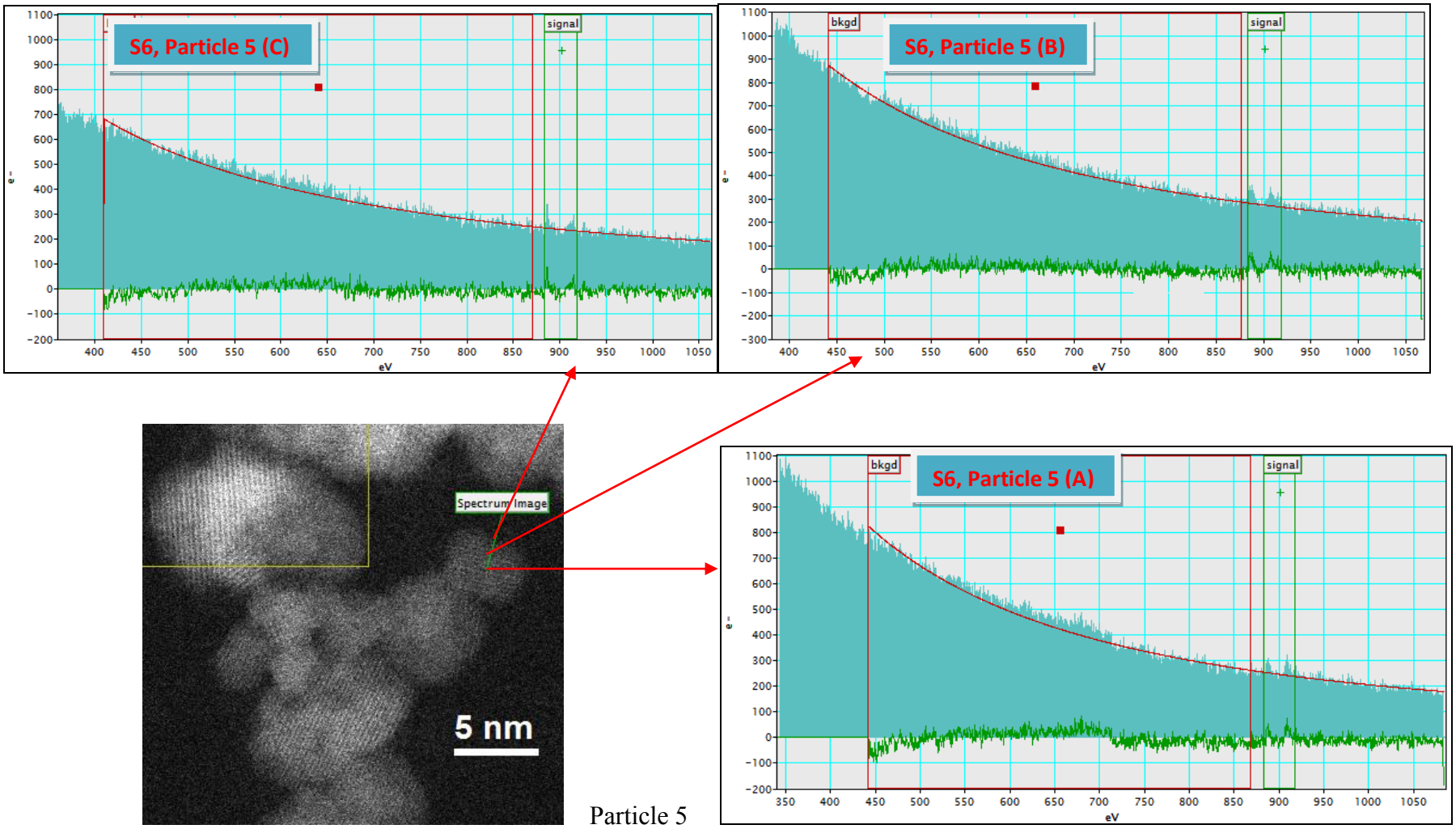

Figure 4.21 (e) EELS spectra illustrating different intensities of M_5 and M_4 white lines for particle 5 as the line scan was carried out from center towards the edge of the nanosphere (S6)

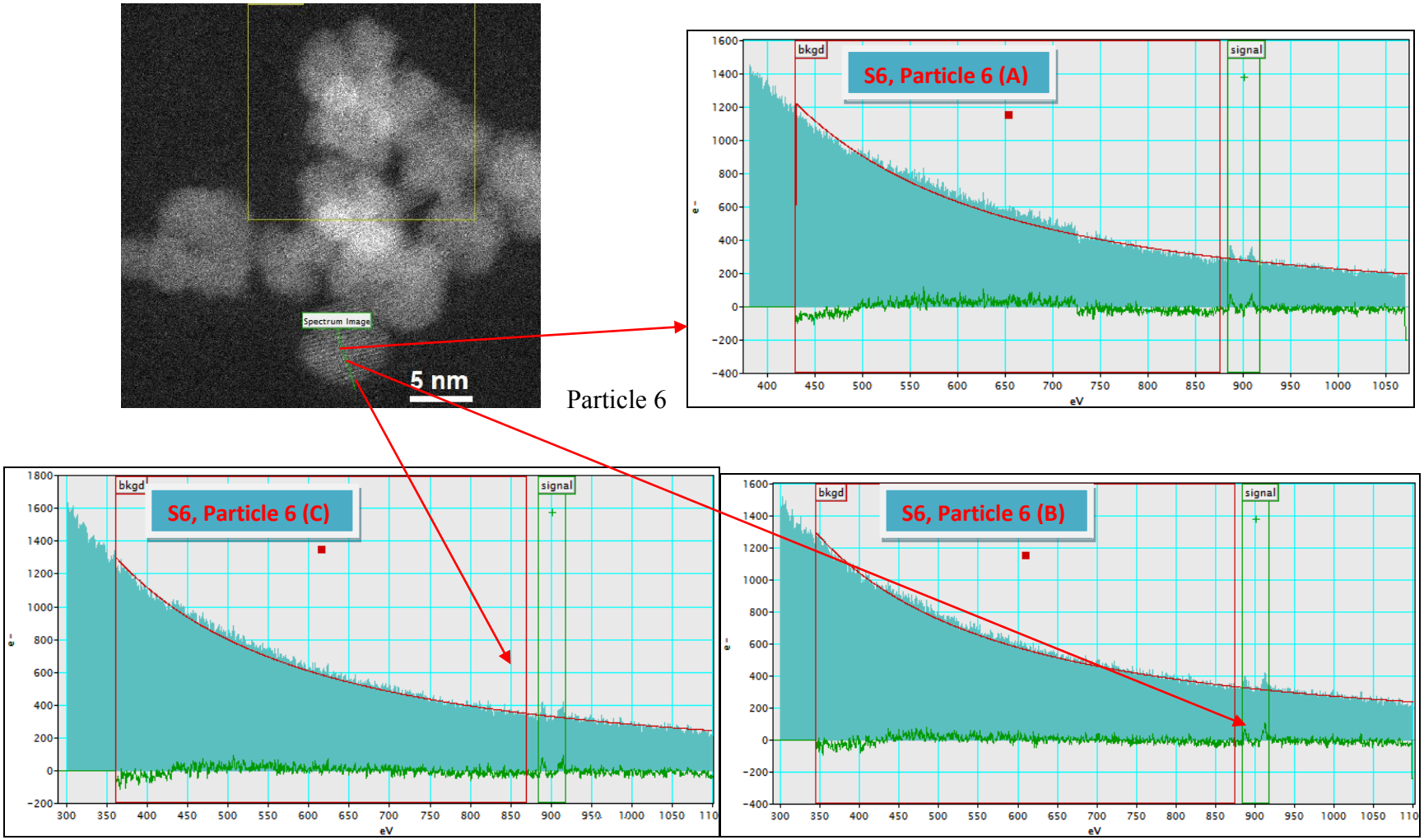

Figure 4.21 (f) EELS spectra illustrating different intensities of M_5 and M_4 white lines for particle 6 as the line scan was carried out from center towards the edge of the nanosphere (S6)

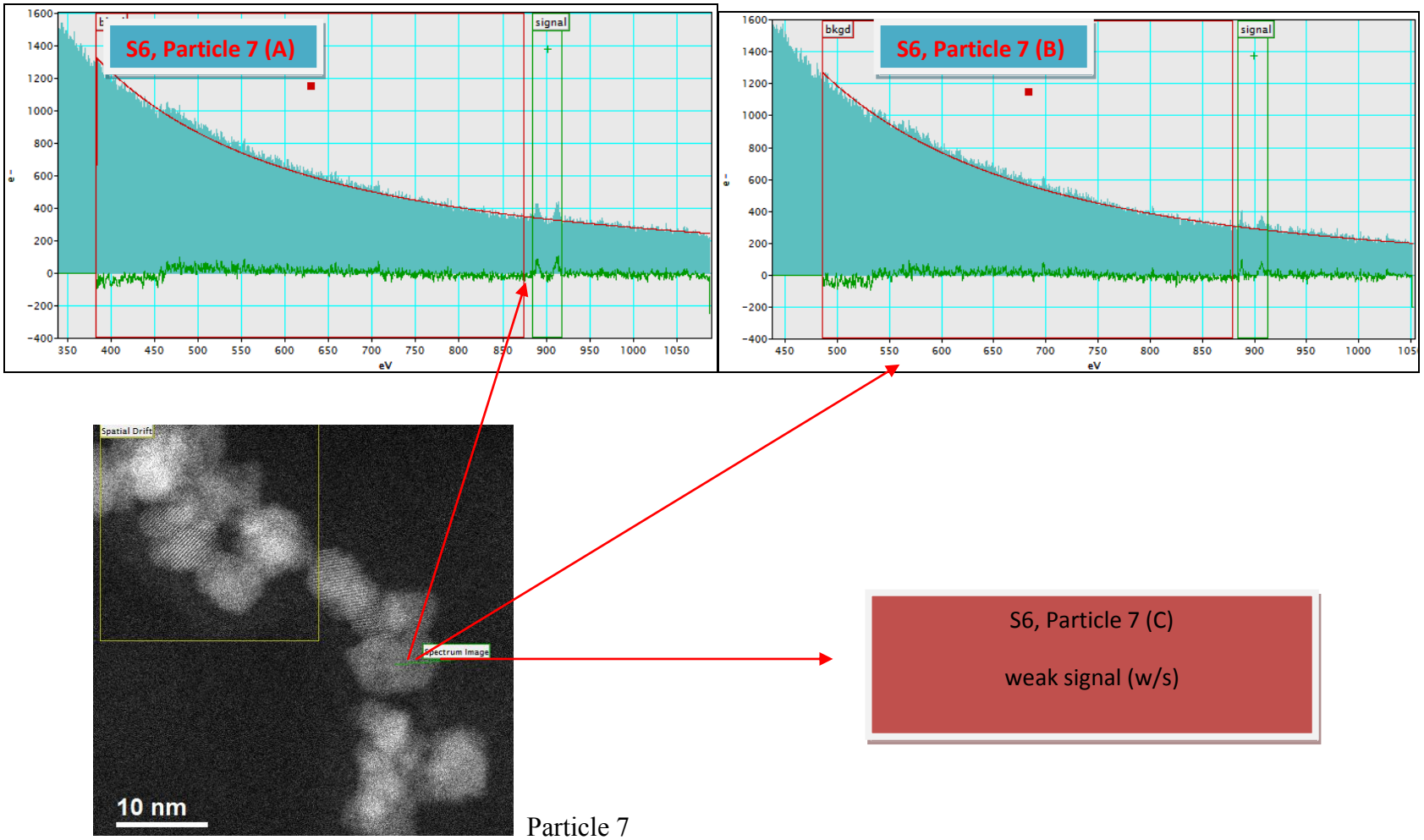

Figure 4.21 (g) EELS spectra illustrating different intensities of M_5 and M_4 white lines for particle 7 as the line scan was carried out from center towards the edge of the nanosphere (S6)

4.9.3 Summary and conclusions of the EELS experiments carried out on nanospheres S6

In summary, we have carried out systematic EELS experiments on nanospheres S6. The $M_{4,5}$-edge spectra have been used to evaluate the oxidation state of cerium using STEM-EELS. Line scans have been carried out looking at local oxidation state variation across the particle as we go from the centre towards the edge of the particle. The results suggest that the amount of Ce (III) increases as the particle size decreases with particles ≤ 2nm to be completely Ce (III). The EELS measurements have been performed on a range of particle sizes (figure 4.21 a-g) and the M_5/M_4 ratios extracted after different line scans have been illustrated in table 4.18. The analysis suggests that for larger particles, the oxidation state is not uniform throughout the particle and valence reduction mainly occurs at the surface. Some of the NPs investigated (particle 1 and 7) gave very weak signals at the edges, so their signals couldn't be extracted during spectrum processing and hence were not used for quantification purposes.

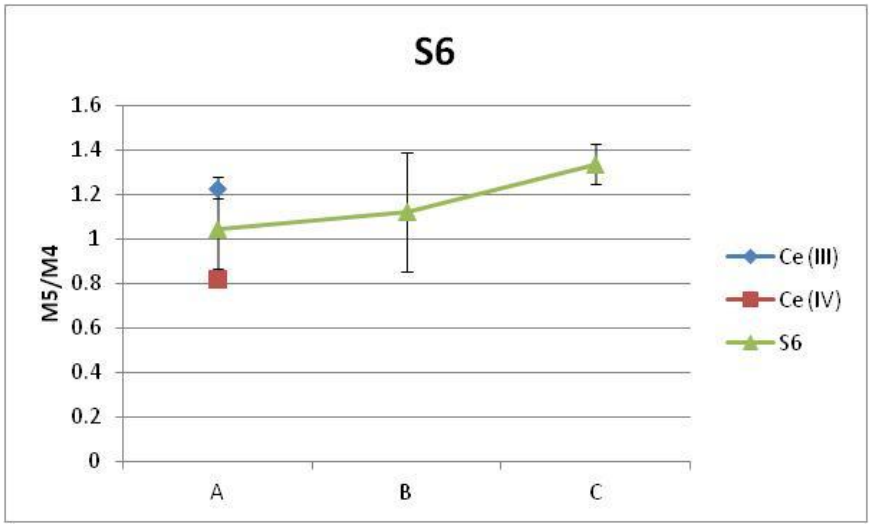

Figure 4.22 The average M_5/M_4 ratios obtained across the diameter of the particles investigated are plotted against the particle depth illustrating the oxidation state pattern observed for S6.

Figure 4.22 clearly demonstrates the M_5/M_4 ratios obtained across the diameter of the particles investigated and are plotted against the particle depth illustrating the oxidation state pattern observed for cubes C4 as we go from center towards the edge of the particle. The oxidation state quantification data has been summarised in table 4.19

Table 4.19 Oxidation state quantification data for the sample S6 as obtained from EELS

Sample code	Morphology	Size (nm)		EELS (%)	
		DLS	TEM	Ce (III) Center	Ce (III) Edge
S6	Nanospheres	12.1±6.1	8.2±2.5	55	100

4.10 Oxidation state quantification of nanospheres S7 using EELS

The ceria nanospheres S7 were synthesised by myself and their synthetic scheme has been discussed in chapter 3, synthesis 6, scheme a. The particles have been characterised for their size and shape by DLS and TEM. The details are in chapter 3.

4.10.1 EELS measurements on nanospheres S7

The nanospheres S7 are 3-8 nm in size as calculated by TEM. The line scans carried out for EELS measurements seemed to be damaging the particle surface, so area scans have been carried out. Area scans have been carried out on six different regions of the sample. The EELS spectrum generated and the areas under investigation have been illustrated in figures 4.24 (a-c). The M_5/M_4 ratios extracted by second derivative method are tabulated in table 4.20.

Table 4.20 M_5/M_4 ratios obtained from area scans carried out on sample S7

Sample S7 - area scans		$CeNO_3$ as standard	Bulk CeO_2 as standard
	M_5/M_4	Ce (III)	Ce (IV)
Area 1	1.04	1.23	0.82
Area 2	0.76		
Area 3	0.9		
Area 4	1.42		
Area 5	1.38		
Area 6	1.28		

4.10.2 Results and discussion of EELS measurements on nanospheres S7

The results obtained suggest that the sample contains a mixture of Ce (III) and Ce (IV). Some of the M_5/M_4 ratios extracted are closer to that obtained from Ce (III) standard while some confirm the presence of Ce (IV). The M_5/M_4 ratios extracted by second derivative method are tabulated in table 4.20. For example the M_5/M_4 ratios extracted from area 4, 5 and 6 are closer to that of the Ce (III) standard while those obtained from area 1, 2 and 3 are closer to that of Ce (IV) standard. After the quantitative analysis of the M_5/M_4 ratios obtained from all the investigated areas of the sample, the data shows that there is 70 % Ce (III) and 30 % Ce (IV) present in the sample S7.

4.10.3 Summary and conclusion of the EELS experiments carried out on nanospheres S7

EELS experiments have been performed on nanospheres from sample S7. The line scans carried out during EELS measurements seemed to be damaging the particle surface. STEM images taken before and after the experiment showed damage to the particles. So area scans were carried out on six different regions of the sample. The EELS spectrum generated and the areas under investigation have been illustrated in figures 4.24 (a-c). The M_5/M_4 ratios extracted by second derivative method are tabulated in table 4.20. The results obtained suggest that the sample contains a mixture of Ce (III) and Ce (IV). Figure 4.23 represents the average M_5/M_4 ratios obtained for different areas from sample S7. The quantitative results have been summarised in table 4.21.

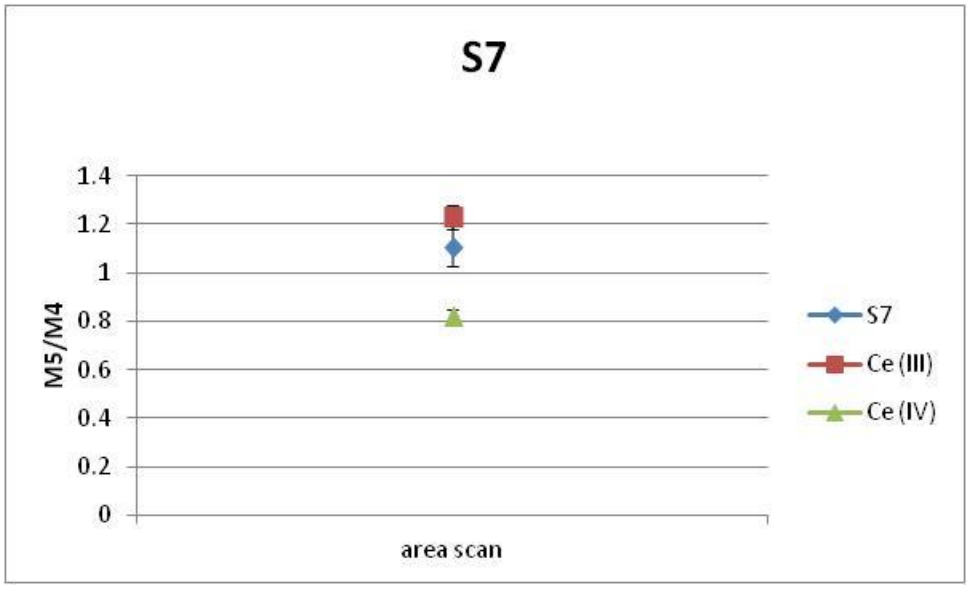

Figure 4.23 The average M_5/M_4 ratios obtained for different area scans from sample S7.

Table 4.21 Oxidation state quantification data for the sample S7 as obtained from EELS

Sample code	Morphology	Size (nm)		EELS (%)	
		DLS	TEM	Ce (III)	Ce (IV)
S7	Nanospheres	35.1±2.1	5.9±2.2	70	30

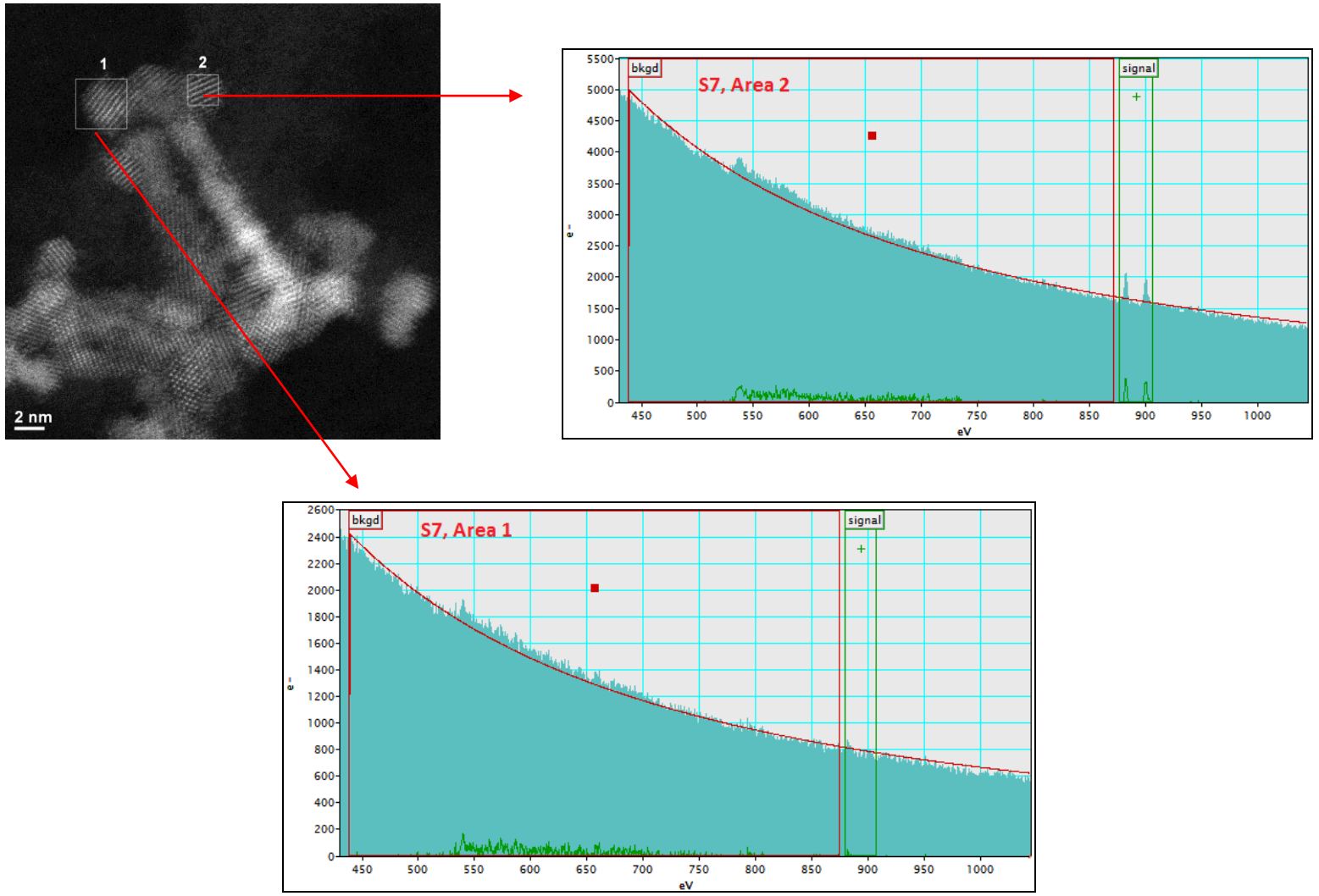

Figure 4.24 (a) STEM image from sample S7 and EELS spectrum generated from area 1 and 2 of the sample

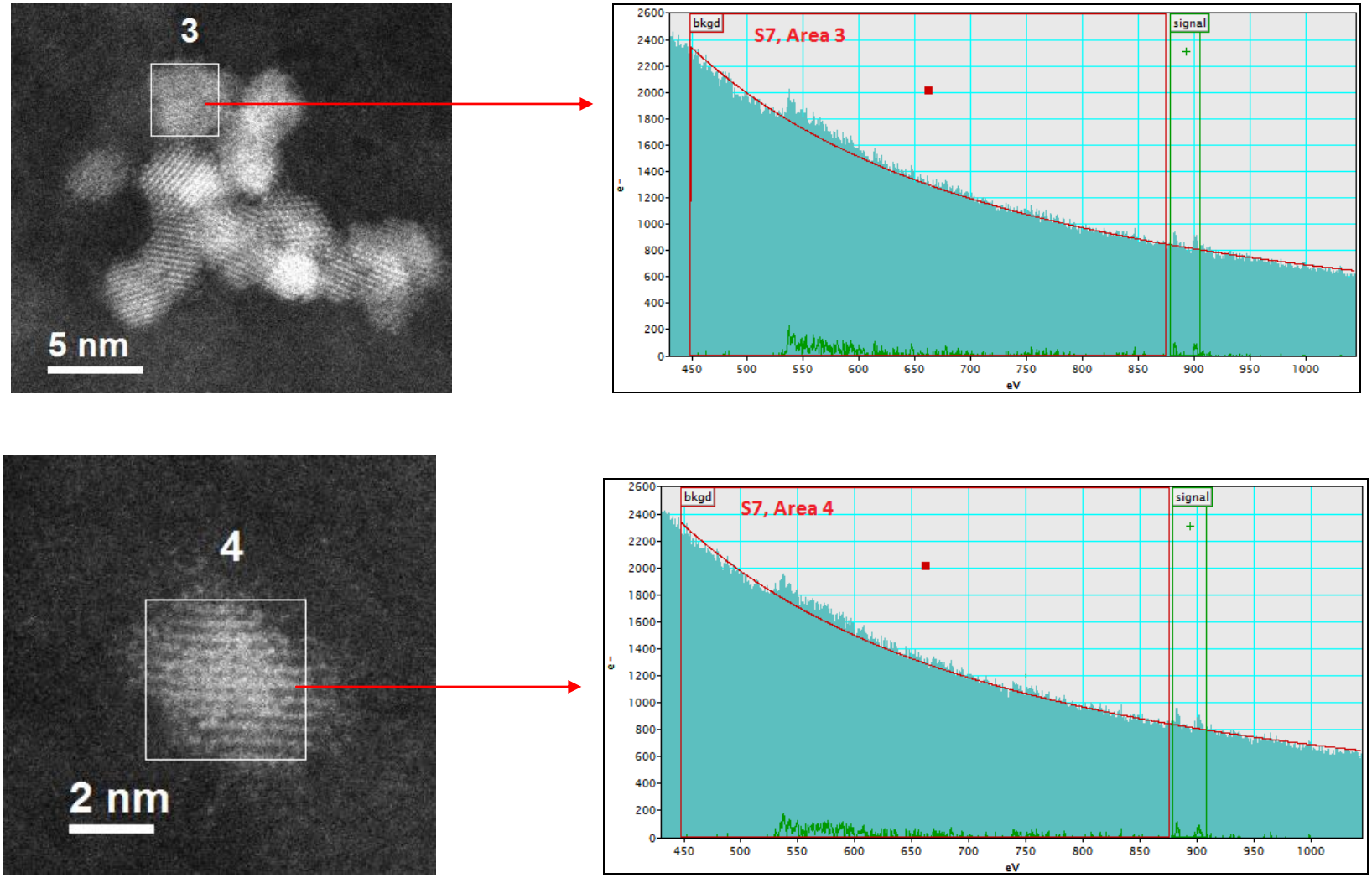

Figure 4.24 (b) STEM image from sample S7 and EELS spectrum generated from area 3 and 4 of the sample

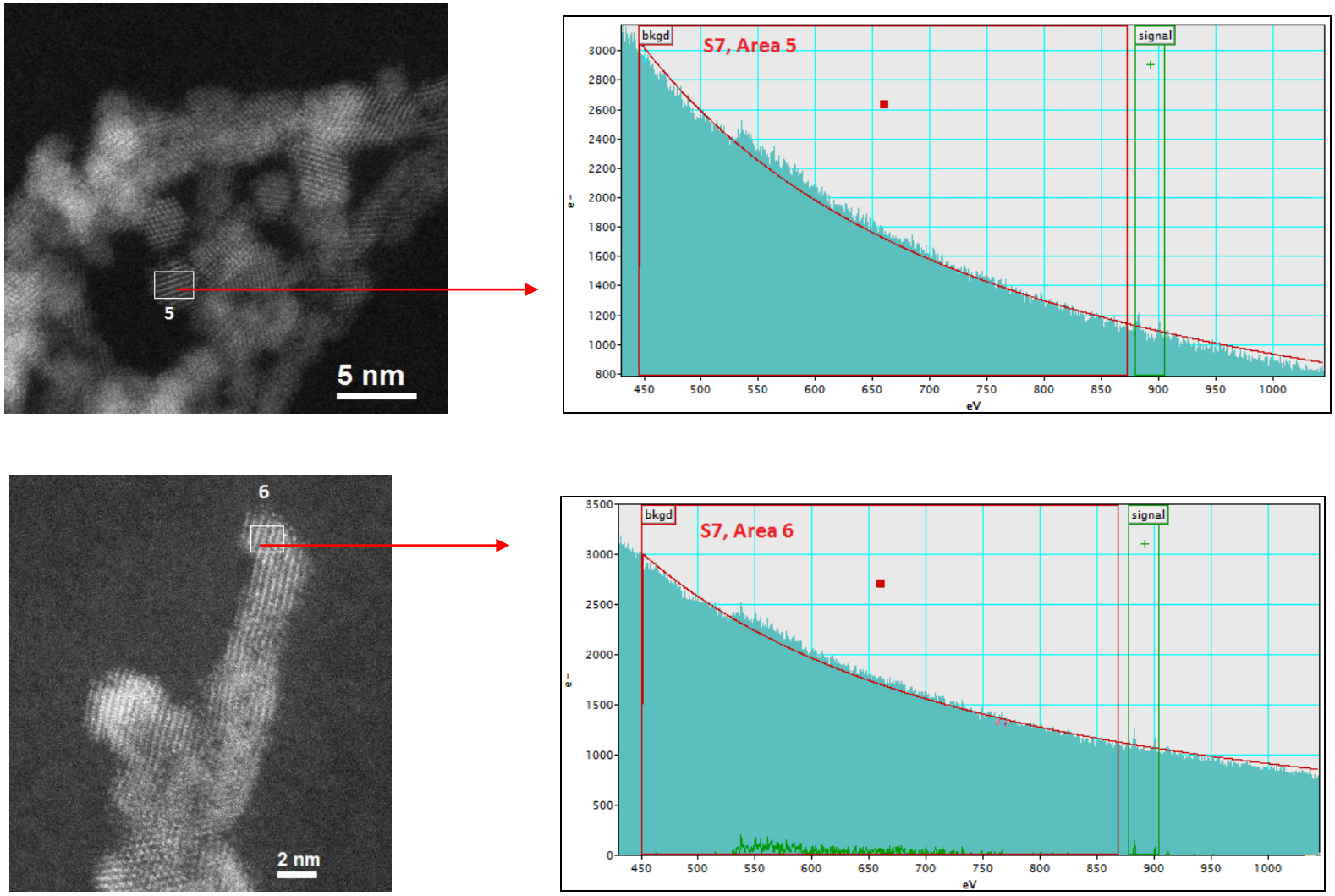

Figure 4.24 (c) STEM image from sample S7 and EELS spectrum generated from area 5 and 6 of the sample

4.11 Oxidation state quantification using XPS

4.11.1 Methodology

X-ray photoelectron spectroscopy (XPS) measurements of the dry nanoparticle samples (powder) were performed using the high performance Kratos Axis Ultra DLD instrument equipped with a monochromated Al K_α x-ray source and hemispherical analyzer capable of an energy resolution of 0.5 eV. The NP samples were placed on a standard sample stud using double-sided adhesive tape, and the takeoff angle was fixed at 90^0. Low resolution survey spectra were obtained over a binding energy range of 0.0 to 1200 eV. High-resolution spectra were obtained over a binding energy range of 870 to 925 eV using 0.1-eV increments. The binding energy (BE) scale was calibrated with respect to the C 1s at 285 eV.

4.11.2 XPS measurements

XPS measurements were performed by Dr Shuguo Ma from the College of Engineering and Computing at University of South Carolina, USA with my assistance. My assistance involved loading the sample on the sample holder and coding the sample names in the computer connected to the machine. The NP powders were uniformly placed on the sample holder with careful patting with a clean spatula in order to avoid any sputtering during the experiments. All the raw data collected have been processed and analysed by myself using the casaXPS softeware version 2.3.16 PR 1.6 (licensed to us), at the University of Birmingham. For this, I attended a two day training workshop on the XPS data processing and analysis organised by the casaXPS software company in Newcastle, UK and learnt how to do sample processing in casaXPS and analyse and quantify the data.

4.11.3 Typical survey spectra and high resolution spectra of cerium oxide

The XPS spectrum from cerium is complex and split into $Ce3d_{3/2}$ and $Ce3d_{5/2}$ with multiple shake up and shake down satellites (Mullins et al., 1998, Romeo et al., 1993). Figure 4.25 illustrates a typical survey scan. The survey scan is a low resolution spectra which gives a general idea of the elements present in the sample but necessarily does not give a very clear information about the chemical bonding or chemistry of the sample as they are taken at a short time of scan. High resolution spectra are obtained over a binding energy range of 870 to 925 eV using 0.1-eV increments to obtain detailed information. Figure 4.26 illustrates a typical high resolution Ce 3d spectrum of cerium oxide.

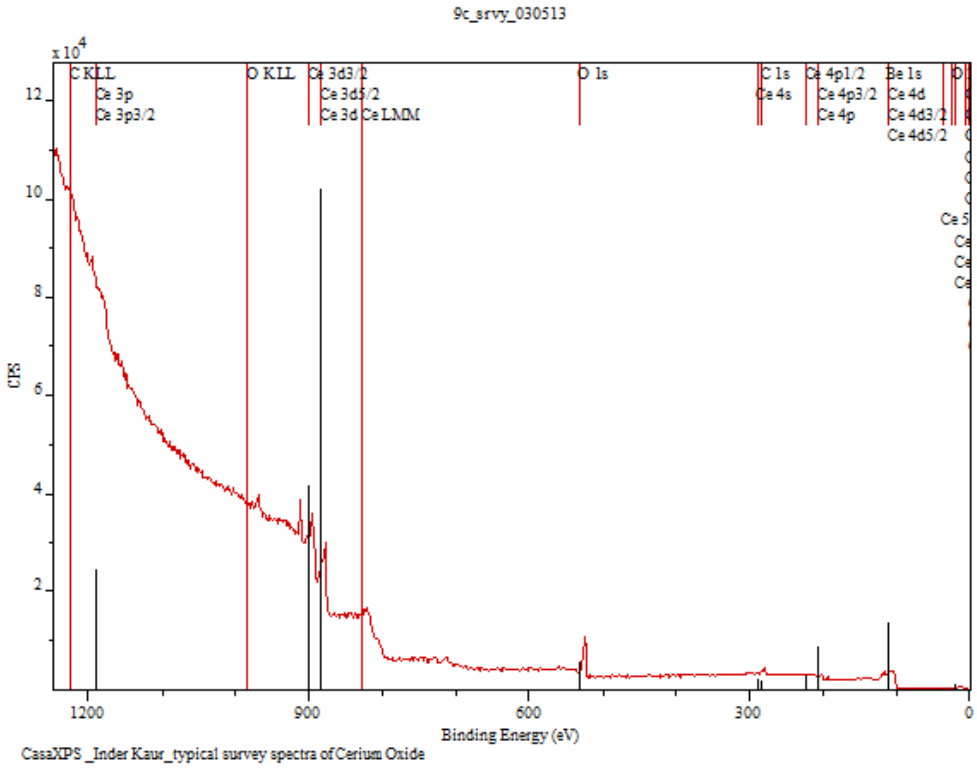

Figure 4.25 Illustration of typical survey spectra of Cerium Oxide

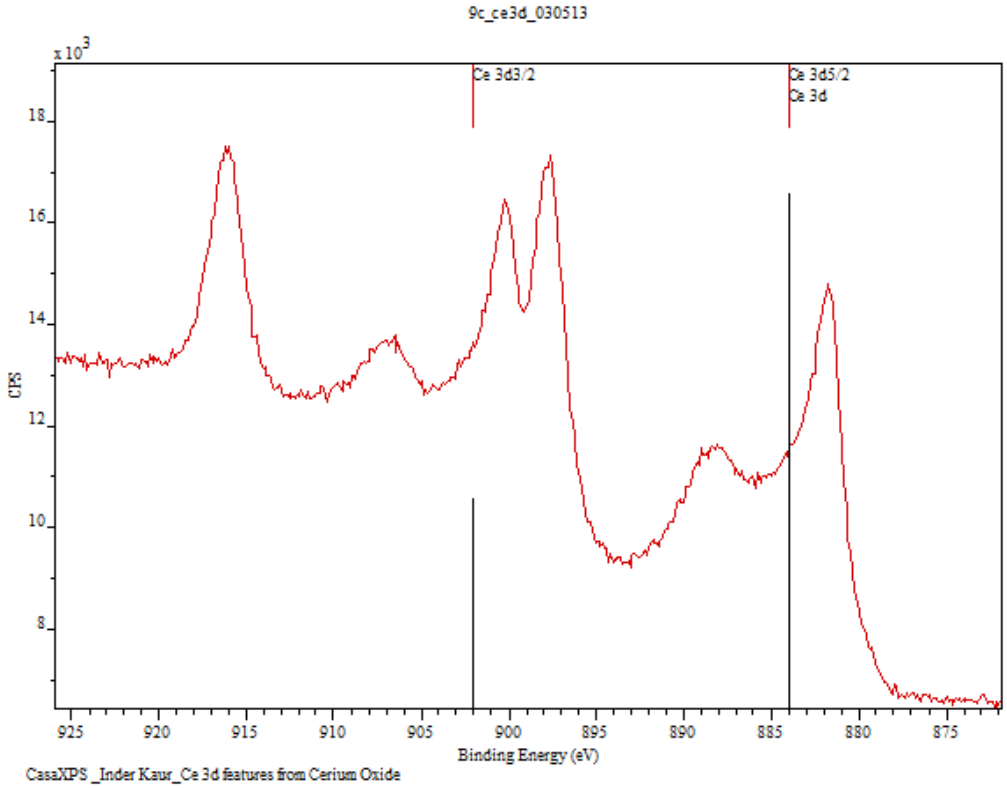

Figure 4.26 Illustration of a typical Ce 3d spectrum of Cerium Oxide

4.11.4 Identification of peaks and curve fitting in casaXPS

The peaks between 880-890 eV belong to $Ce3d_{5/2}$ while peaks between 895-910 eV belong to $Ce3d_{3/2}$ level. The Ce 3d features were collected from reference material (CeO_2 and $CeNO_3$) and the peaks were investigated in order to determine the positions of various components and were deconvoluted using the peak fitting process in casaXPS softeware. The relative amounts of Ce (III) and Ce (IV) have been calculated from XPS data by spectral curve fitting the Ce 3d binding energy regions. Curve fittings have been done using shirley calculations (a set of calculations within the software) in the casaXPS software using the procedure used by others in previous XPS studies of cerium oxide and of nanoceria (Deshpande et al., 2005, Paparazzo, 2011, Bêche et al., 2008). Figure 4.27 shows a typical deconvoluted XPS Ce (3d) spectrum. Similar peak fittings were done for all the samples. In particular, the peaks at 880

eV (v_0), 884 eV (v‘), 900 eV (u_0) and 903 eV (u‘) and are assigned to the Ce (III) oxidation state whereas the peaks at 882 eV (v), 888 eV (v”), 898 eV (v”‘), 901 eV (u), 907 eV (u”) and 917 eV (u”‘) are assigned to cerium in the Ce (IV) oxidation state (Figure 4.24).

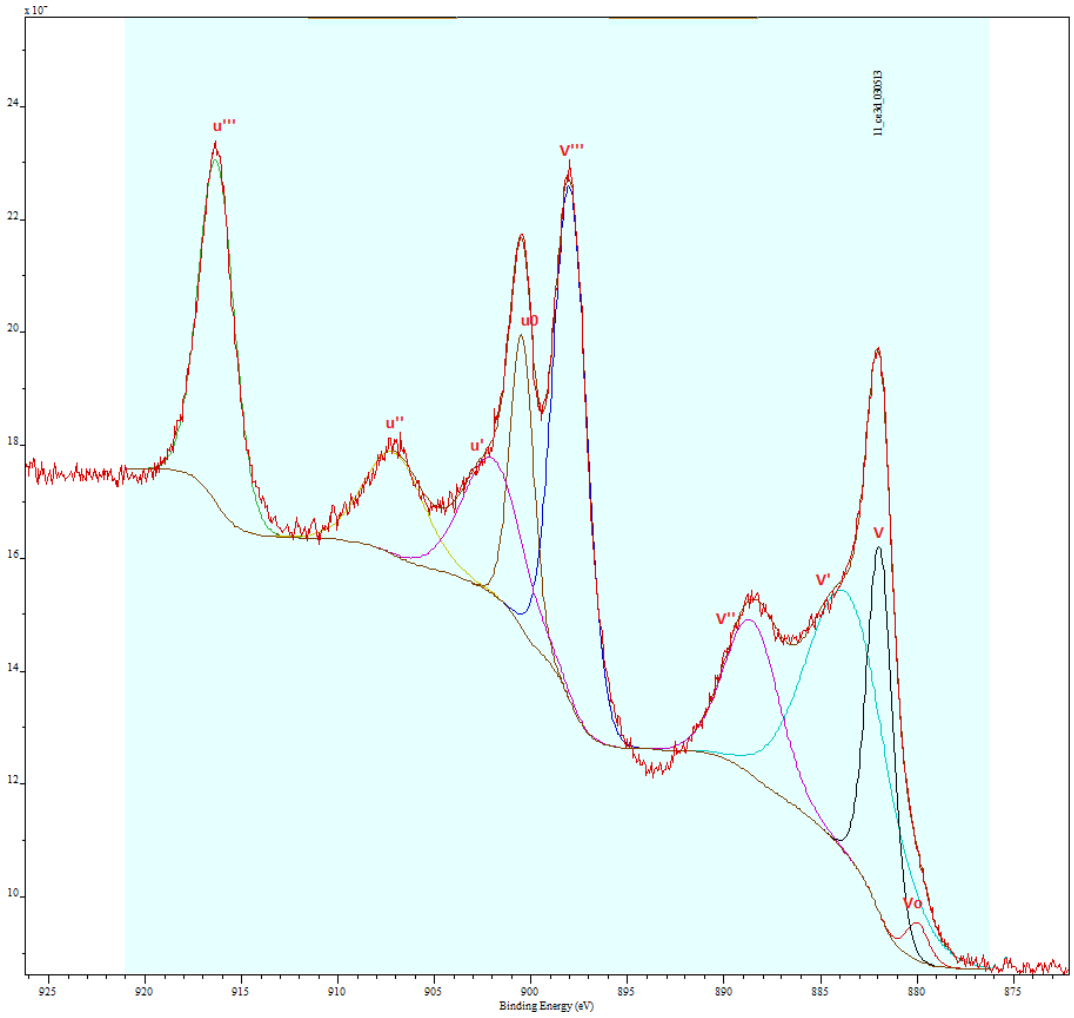

Figure 4.27 Illustration of a typical deconvoluted Ce 3d spectrum of Cerium Oxide

4.11.5 Formula for oxidation state quantifcation

The Ce (III) percentage in the sample, Ce (III) %, is calculated using the relative areas under the peaks according to the equation 4.1

$$\%\ Ce\ (III) = Ce\ (III) / Ce\ (III) + Ce\ (IV) \times 100 \qquad (4.1)$$

where Ce (III) on the right hand side of the equation represents the total area under the v_0, v‘, u_0 and u‘ bands and Ce (IV) represents the total area under the u‘‘‘, u‘‘, u, v‘‘‘, v‘‘ and v bands. The errors are estimated to be of the order of 5 % by this method (Laachir et al., 1991, Borchert et al., 2005). This concept of labelling the ten peaks obtained from the photoemission spectra was first introduced by (Burroughs et al., 1976) and since then has been extensively used in the analysis of cerium oxide and cerium containing compounds such as semiconductors, catalysts and other novel materials.

XPS spectra are usually quantified in terms of peak intensities and positions. The peak intensities correspond to the measure of the amount of material present at the surface whereas the peak positions indicate the elemental and chemical composition. For example, peak broadening or position shifts may indicate a change in the number of bonds contributing towards the peak or the composition of the material. So the peak positions and the relative areas under the peaks have been carefully recorded.

4.11.6 Spectrum processing and quantification steps in casaXPS

Spectrum processing was performed using the options on the spectrum processing dialog window in the toolbar. Quantification regions are created using the Element Library dialog window which helps in specifying the peaks and element markers. The quantification step was performed using the quantification parameter dialog window where the regions and components are created and fitted within the software and extracted quantification information is generated in the form of a report which carries the peak positions, areas under the peak and percentage concentration of the components. These values were used and put in equation 4.1 to evaluate the cerium oxidation state in synthesised samples.

4.11.7 Results

Figure 4.28 (a-j) represent the Ce $3d_{3/2,5/2}$ fitted XPS spectrum collected for various synthesised samples. The peak positions obtained for all the samples are listed in table 4.22 and their relative areas under the peaks are summarised in table 4.23. The results obtained show a mixture of Ce (III) and Ce (IV) in all the samples. More amount of Ce (III) has been detected for smaller spherical samples (S1-7) as compared to the larger nanocubes (C1-3) and rods (R1). The oxidation state data obtained is in table 4.24.

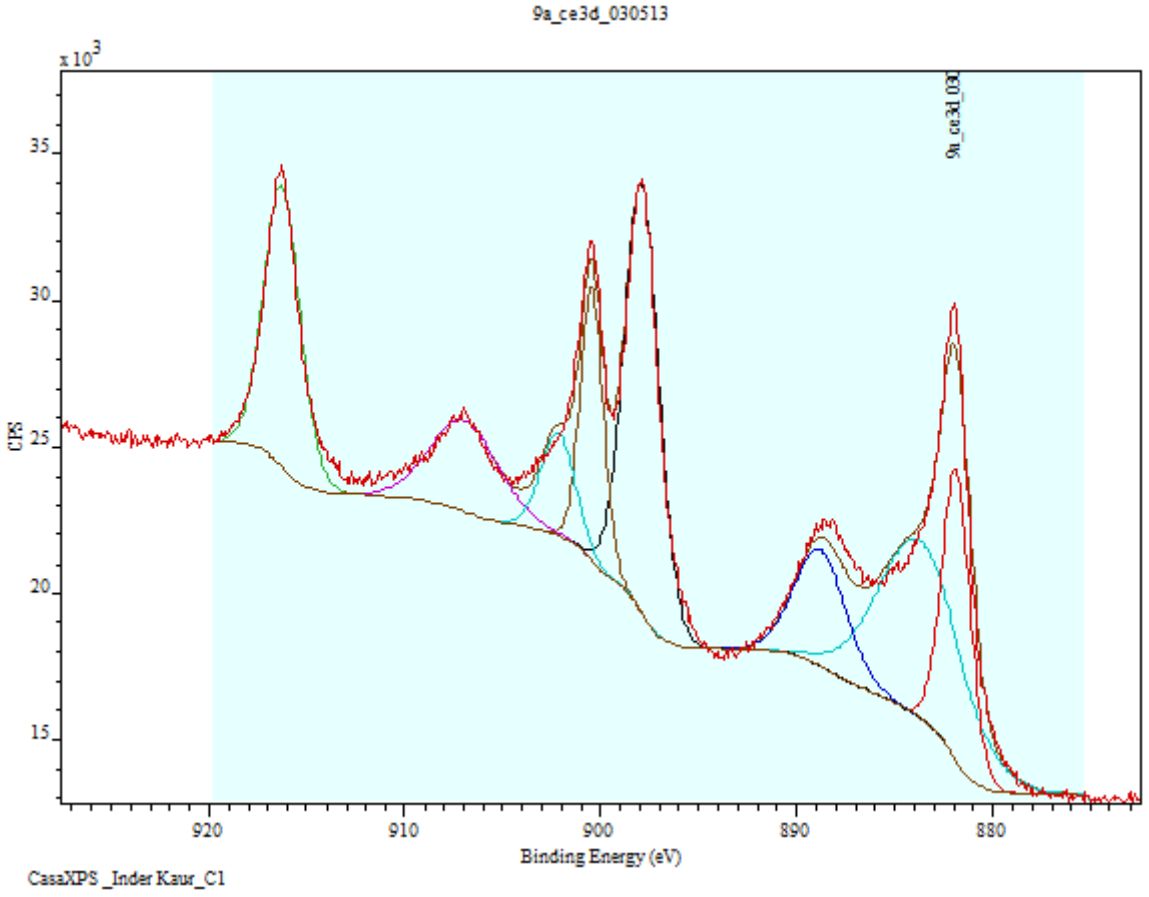

Figure 4.28 (a) Ce $3d_{3/2,5/2}$ fitted XPS spectrum collected for nanocubes C1

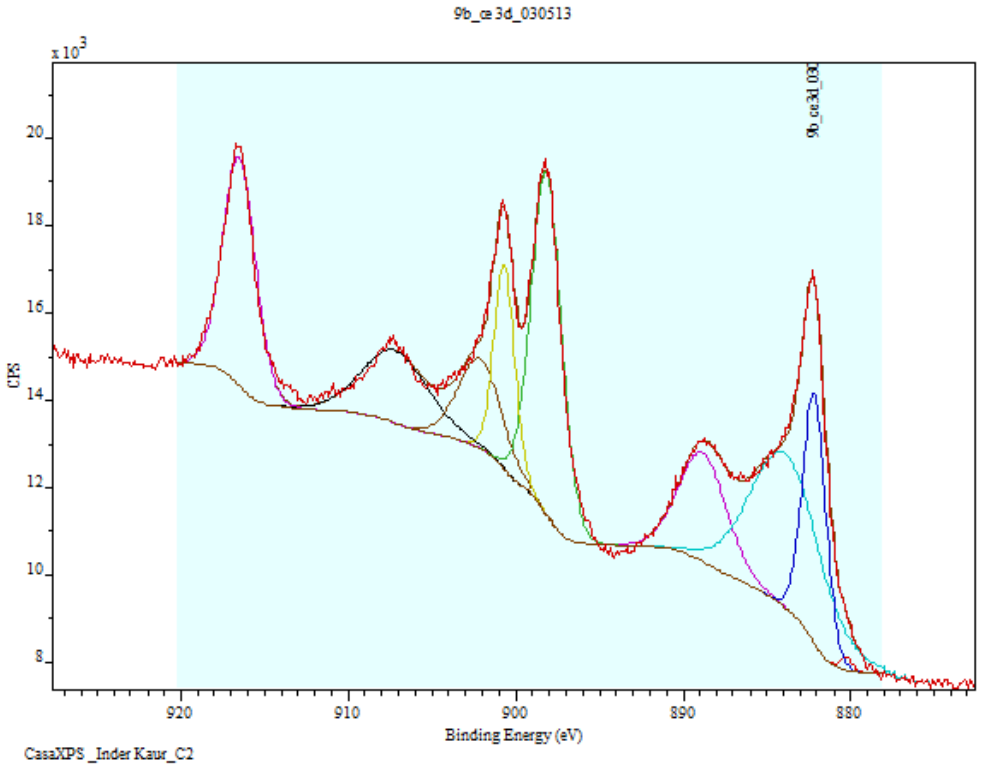

Figure 4.28 (b) Ce $3d_{3/2,5/2}$ fitted XPS spectrum collected for nanocubes C2

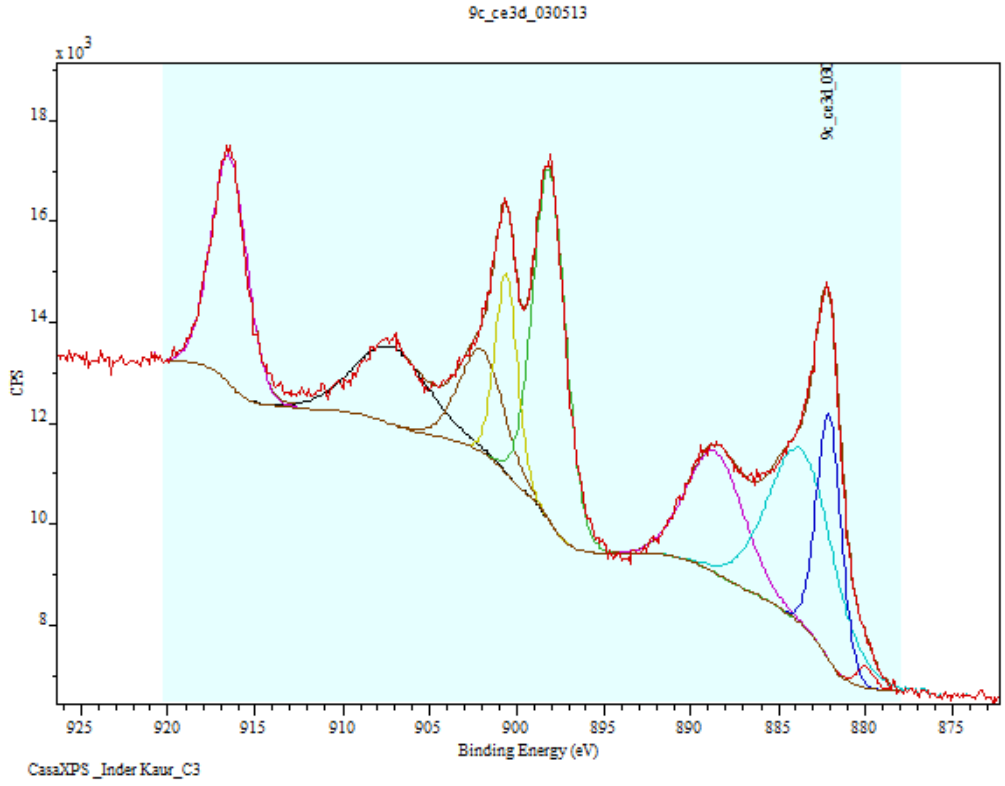

Figure 4.28 (c) Ce $3d_{3/2,5/2}$ fitted XPS spectrum collected for nanocubes C3

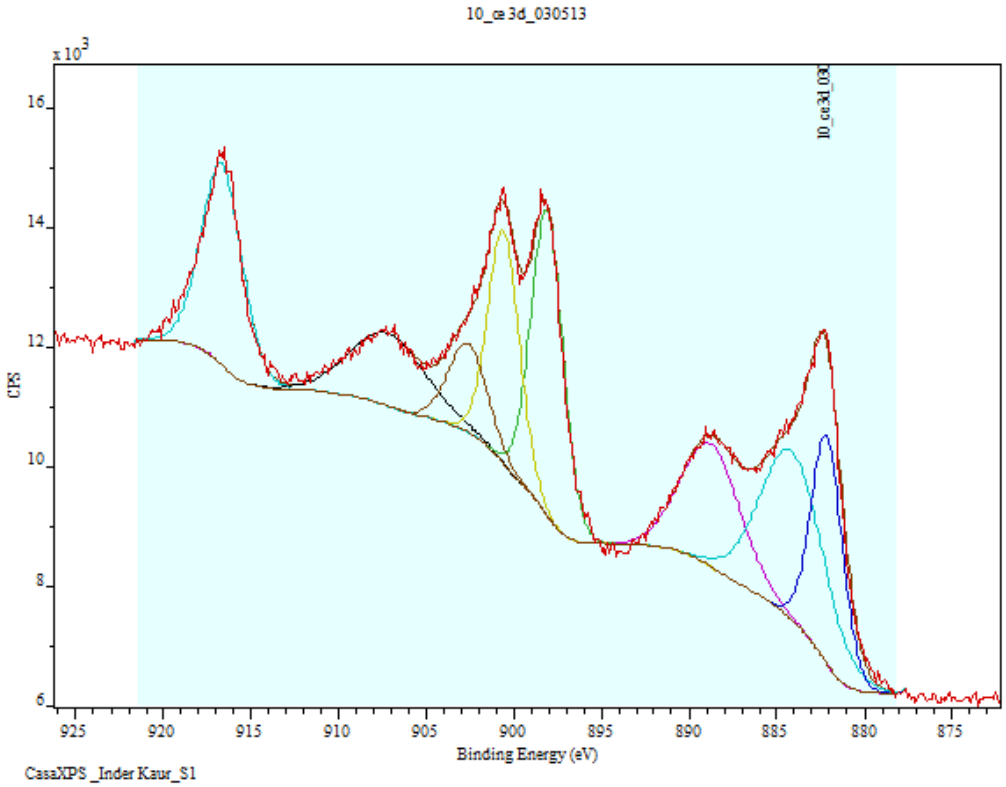

Figure 4.28 (d) Ce $3d_{3/2,5/2}$ fitted XPS spectrum collected for nanospheres S1

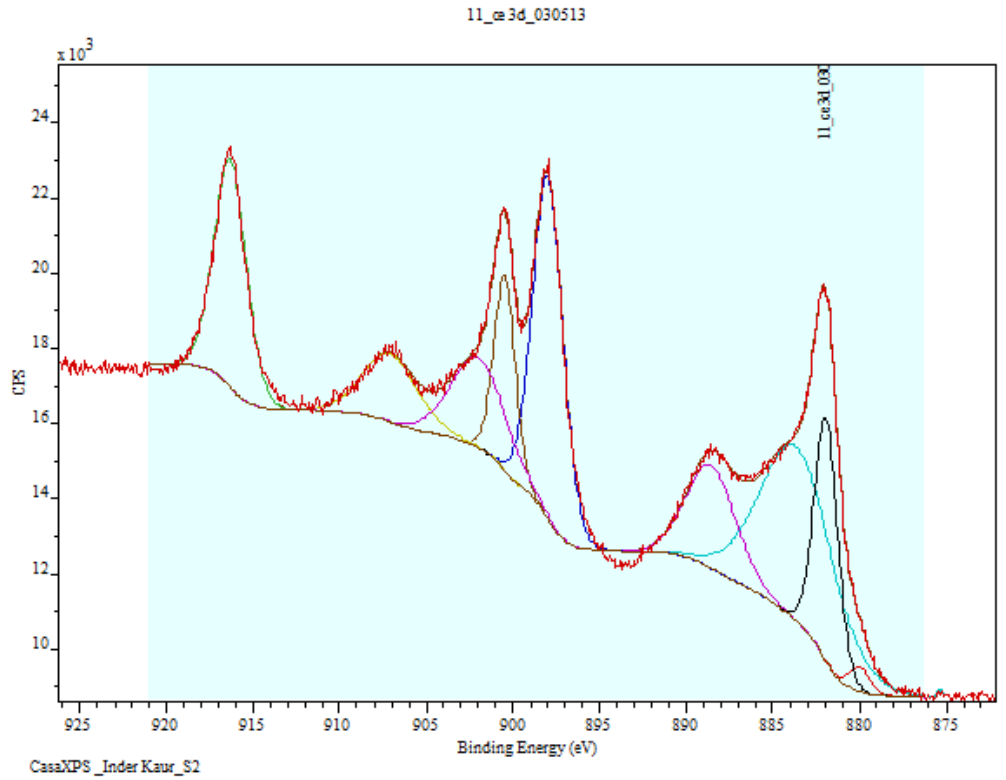

Figure 4.28 (e) Ce $3d_{3/2,5/2}$ fitted XPS spectrum collected for nanospheres S2

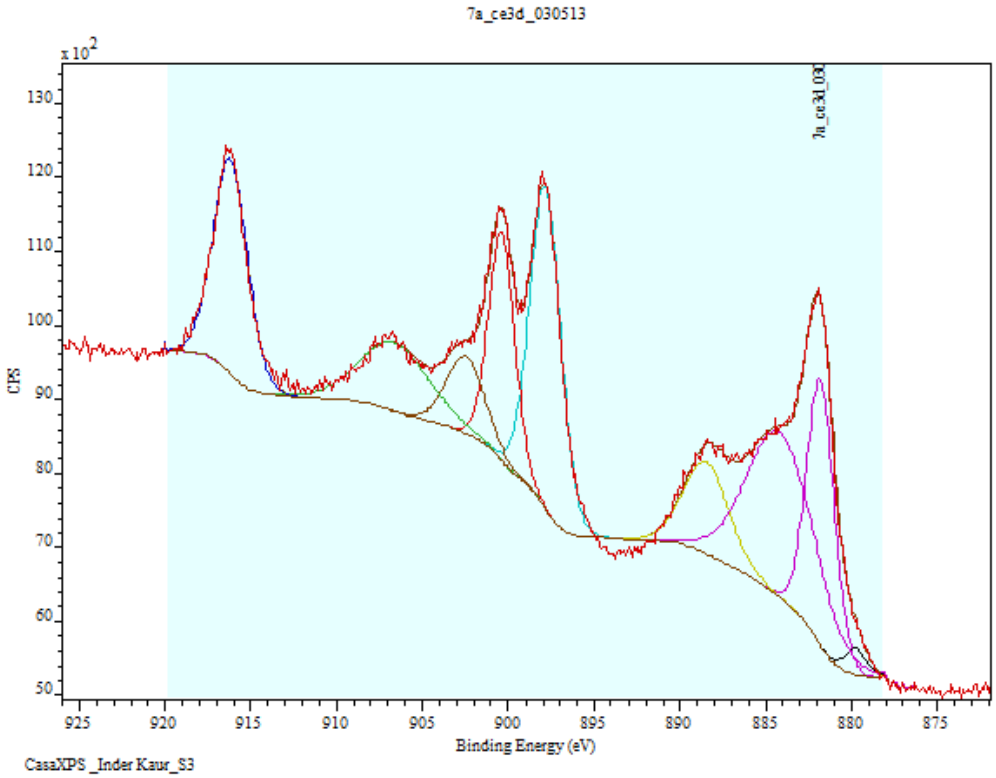

Figure 4.28 (f) Ce $3d_{3/2,5/2}$ fitted XPS spectrum collected for nanospheres S3

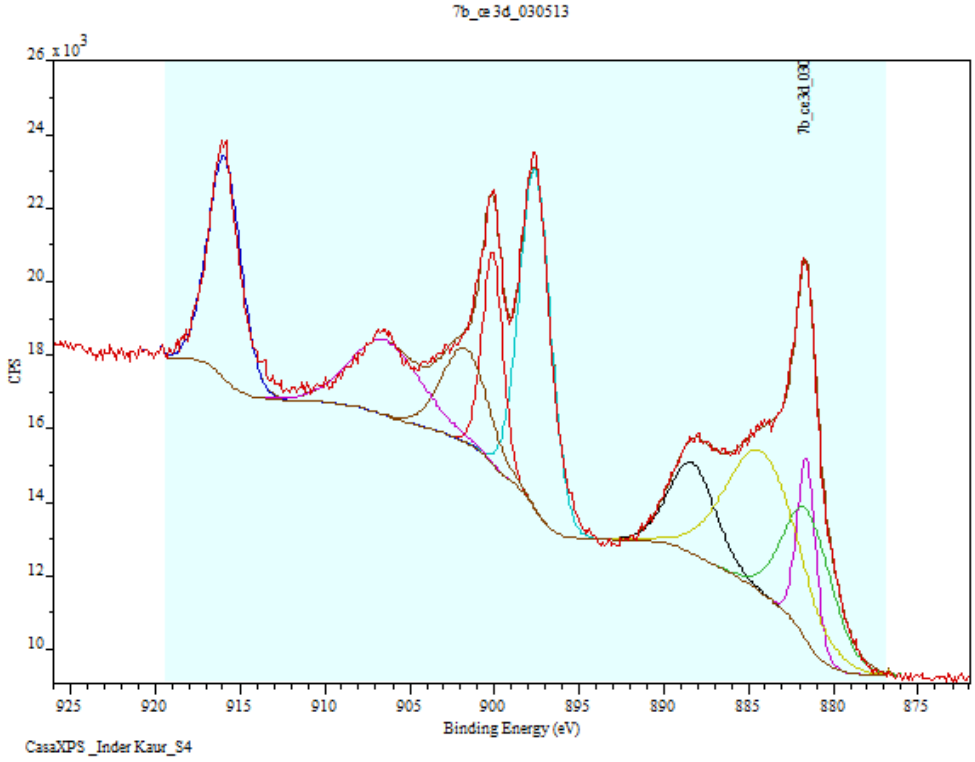

Figure 4.28 (g) Ce $3d_{3/2,5/2}$ fitted XPS spectrum collected for nanospheres S4

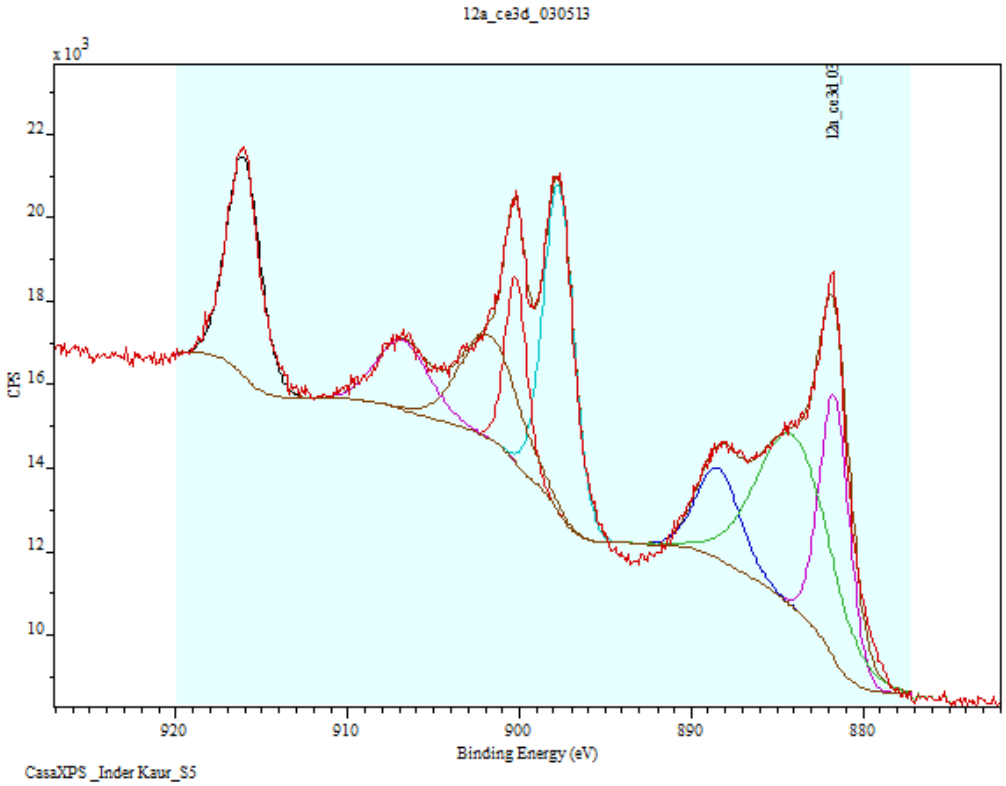

Figure 4.28 (h) Ce $3d_{3/2,5/2}$ fitted XPS spectrum collected for nanospheres S5

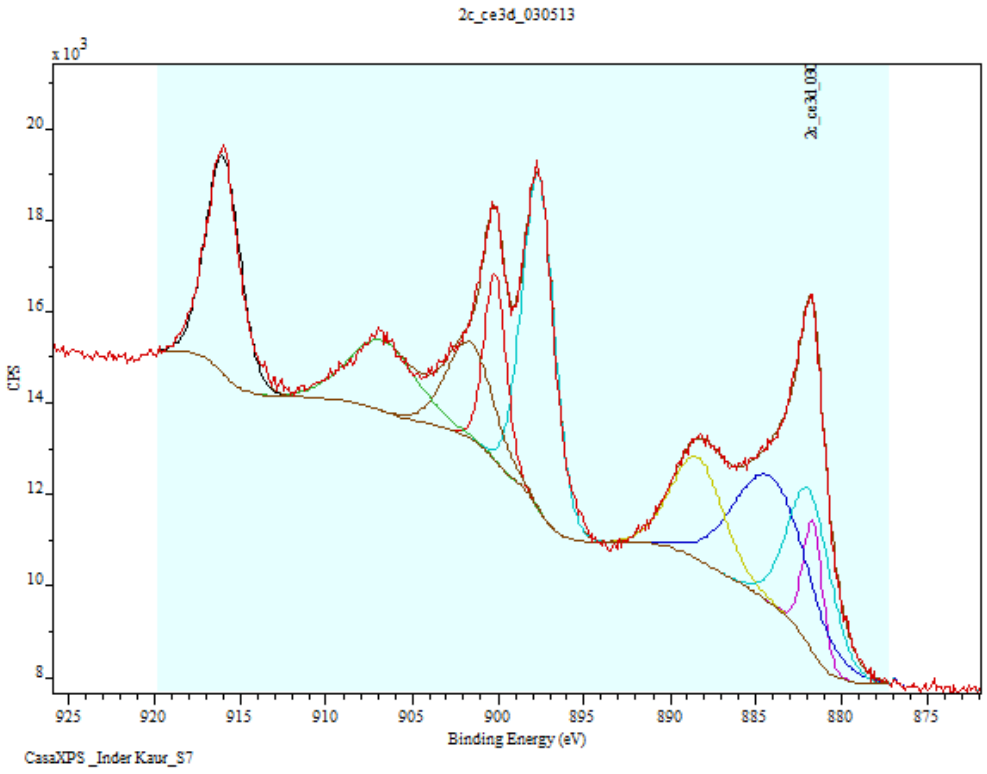

Figure 4.28 (i) Ce $3d_{3/2,5/2}$ fitted XPS spectrum collected for nanospheres S7

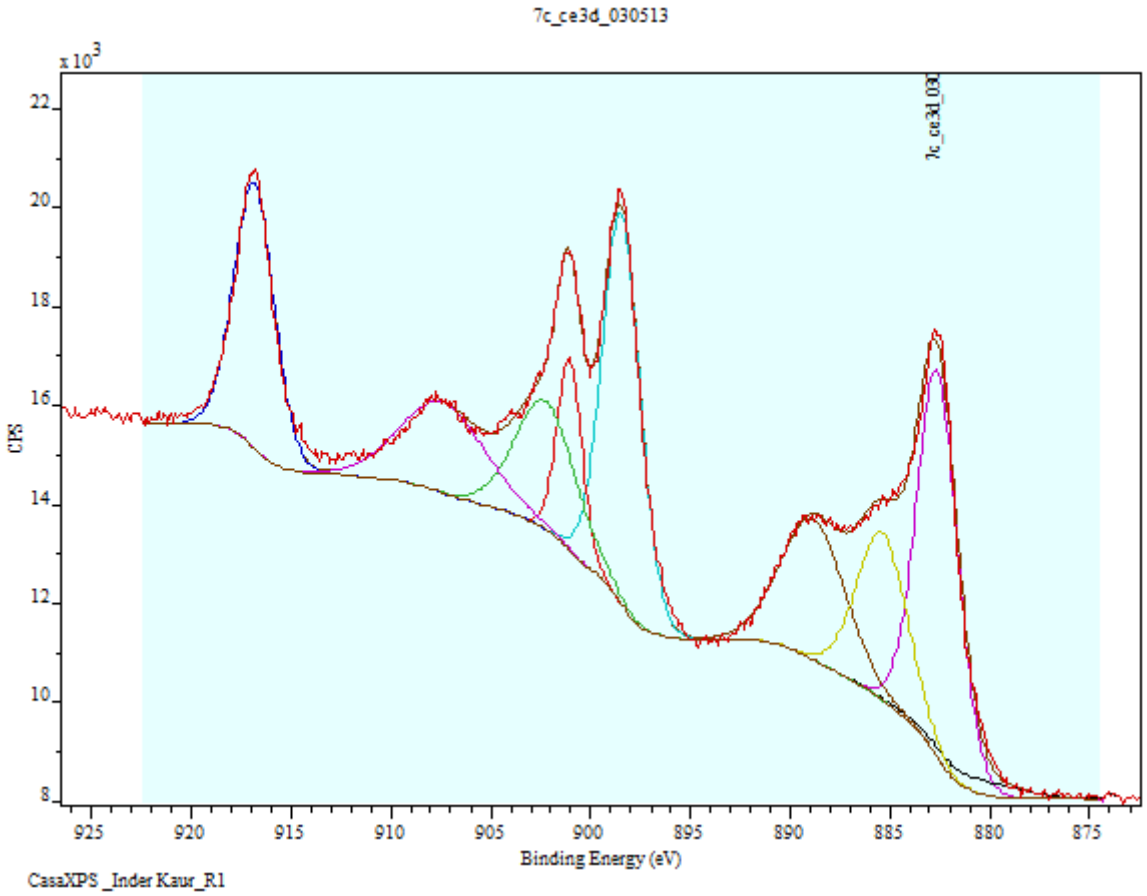

Figure 4.28 (j) Ce $3d_{3/2,5/2}$ fitted XPS spectrum collected for nanorods R1

Table 4.22 XPS binding energies of individual peaks of the Ce (3d) spectrum for different ceria samples

Shape	Ce ($3d_{5/2}$)					Ce ($3d_{3/2}$)				
	v_0	v	v'	v''	v'''	u_0	u	u'	u''	u'''
Nanocube C1	880.10	881.87	883.7	888.79	897.91	900.45	901.00	902.18	906.95	916.26
Nanocube C2	880.25	882.16	884.3	888.81	898.16	900.00	901.00	902.12	907.19	916.51
Nanocube C3	880.0	882.08	884.0	888.6	898.13	900.6	901.1	902.29	907.20	916.49
Nanosphere S1	879.98	881.93	884.10	888.55	897.98	900.46	901.14	902.17	907.1	916.3
Nanosphere S2	880.16	882.11	884.12	888.77	898.13	900.65	901.2	902.35	907.17	916..47
Nanorod R	880.6	882.63	885.39	888.85	898.47	900.0	901.00	903.0	907.41	916.84
Nanosphere S3	879.75	881.81	884.15	888.46	897.84	900.38	901.12	902.47	906.63	916.18
Nanosphere S4	880.98	881.59	884.19	888.31	897.59	900.10	901.72	902.31	906.41	916.00
Nanosphere S5	880.10	881.66	884.04	888.41	897.22	900.20	901.20	902.13	906.78	916.07
Nanocube C4	880.80	882.61	884.92	889.19	898.61	901.14	901.91	902.45	907.61	916.97
Nanosphere S7	880.21	882.10	884.12	888.39	897.65	900.17	901.00	902.10	906.75	916.01

Table 4.23 Integrated areas of individual peaks of the Ce (3d) spectrum for different ceria samples

Shape	Area of Peak								
	Av_0	Av	Av'	Av''	Av'''	Au_0	Au'	Au''	Au'''
Nanocube C1	0.00	5199.28	9356.63	3779.13	9309	3931.81	2205.36	3884.35	6297.46
Nanocube C2	75.92	2859.3	5467.03	2566.5	5077.65	2088.9	1901.52	2353.69	3648.76
Nanocube C3	158.94	2498.6	4766.67	2879.69	4707.41	1815.38	1853.32	2339.11	3309.2
Nanosphere S1	282.28	3165.93	7165.87	2831.45	5729.99	2290.91	2682.46	2036.26	4017.58
Nanosphere S2	269.7	3140.14	5998.18	2284.95	5267.66	2095.95	2178.92	2066.17	3592.08
Nanorod R1	455.87	5852.36	3128.07	3322.52	5401.99	1730.03	2847.42	2803.87	3857.39
Nanosphere S3	162.15	2085.60	3187.57	1174.18	2821.04	1676.40	832.31	1345.82	2074.95
Nanosphere S4	3748.79	1956.11	5945.21	2426.95	6101.72	2534.09	2470.90	3046.03	4183.79
Nanosphere S5	0.00	3972.34	6381.39	1987.16	4997.51	2048.66	3019.31	1836.05	3662.19
Nanocube C4	3337.97	2304.10	5144.13	3409.93	6429.38	2385.74	2618.21	3087.74	4347.12
Nanosphere S7	3119.27	1183.06	4285.09	2441.72	4932.36	1900.49	2063.07	2190.71	3393.53

Table 4.24 Illustrating the Shape, size (by TEM) and quantitative measurements of oxidation states for the synthesised samples using XPS

Sample name	Morphology	Size (nm)	XPS %	
		TEM	Ce III	Ce IV
C1	Nanocube	30.8±7.3	35	65
C2	Nanocube	20.6±7.3	37	63
C3	Nanocube	15.8±4.6	38	62
S1	Nanosphere	4.5±2.5	42	58
S2	Nanosphere	6.0±3.0	40	60
S3	Nanosphere	3.0±1.0	40	60
S4	Nanosphere	3.0±1.0	46	54
S5	Nanosphere	3.3±1.3	42	58
S7	Nanosphere	5.9±2.2	45	55
R1	Nanorod	83.0±56.0(Length) 15.9±6(width)	27	73

4.12 Conclusions

In the present study, we synthesised ceria nanoparticles of various shapes and sizes using a set of methodologies (details in chapter 3). A combination of existing techniques has been used to characterise the samples. The size, shape and morphology of the samples synthesised has been determined using DLS and TEM (explained in chapter 3) while STEM+EELS along with XPS have been used to quantify ceria oxidation states.

We have carried out systematic EELS and XPS measurements on different samples of nanocubes (C1-3), nanospheres (S1-7) and nanorods (R1) with different sizes. The $M_{4,5}$-edge spectra have been used to evaluate the oxidation state of cerium using STEM-EELS whereas binding energies of individual peaks of the Ce (3d) spectrum from XPS have been employed to quantify the oxidation states in different samples.

During EELS experiments, line scans were used to understand the local oxidation state variation across the particle by selectively acquiring the spectra at different points on the particle surface. Area scans were carried out where line scans seemed to be damaging the particles. Both EELS and XPS techniques, despite being surface profiling techniques, are based on different principles with limitations to both. While EELS has an advantage that the scan can be performed on individual particles, it gets easier to look at oxidation state variations locally at any point of the particle whereas XPS provides quantitative compositional information from the top atomic layers of a sample.

One of the objectives of this study was to ascertain if Ce (III) and Ce (IV) oxidation states of different sized and shaped cerium oxide can be consistently determined by these techniques and also to subset the important information that can be obtained about the oxidation state of nanoceria using these techniques and to examine the issues and challenges faced when performing such analysis. We found through EELS analysis that the oxidation state of ceria NPs is not uniform throughout the particle and the amount of Ce (III) increases as the particle size decreases. The results showed higher amount of Ce (III) present in smaller nanoparticles with particles $\leq$ 2nm to be completely Ce (III). Similar results were obtained from XPS experiments. More amount of Ce (III) has been detected for smaller spherical samples (S1-7) as compared to the larger nanocubes (C1-3) and rods (R1). However, the results obtained from both the techniques are not directly comparable. For example, here we compare the

oxidation state data obtained for the three different sized nanocube samples C1 (30.8±7.3 nm), C2 (20.6±7.3 nm), C3 (15.8±4.6 nm) using both the techniques. Both EELS and XPS showed that the amount of Ce (III) increased with decrease in particle size and the order of Ce (III) concentration in the samples is of the order of C3>C2>C1 (table 4.25). However, EELS provided localised information about the oxidation state at different points of the nanoparticle like center or at the edges, whereas, XPS provides a quantitative composition of the whole sample. Both the techniques are complimentary to each other and provide important information about the sample. We also observed that the Ce (III) and Ce (IV) ratios obtained were very similar for different shaped ceria samples with similar core sizes. For example, C3 nanocubes of d=15.8±4.6 nm showed similar amount of Ce (III) present in the sample when compared to nanospheres S2 (6.0±3.0 nm) and S7 (5.9±2.2 nm) of the similar core sizes by TEM. Similarly, 20 nm nanocubes from sample C1 showed similar Ce (III) concentrations when compared to the 21 nm (by width) core sized nanorods R1. The results indicate that oxidation state is mainly size dependent and is independent of the shape of the particles, though we intend to explore this more in our future work.

An advantage of EELS over XPS is the spatial resolution to analyse individual nanoparticles. It is a great tool permitting analysis on a 'per particle' basis. Individual or a collection of nanoparticles can be visualised and data can be collected based on the needs of the study. However, beam damage could inaccuracies and can lead to an overestimation of Ce (III) within the sample. In case of XPS, the particles cannot be seen during experiment. The measurements are carried on the collection of the nanoparticles and hence chemical speciation cannot be identified on a particle basis. Even for nanoparticles, the sampling depth can be considerably smaller than the particle diameter (Zhang et al., 2011a).

There are some other general issues associated with nanoparticles which are useful to consider when analyzing. Though both EELS and XPS are operated under vacuum, XPS requires sample dehydration prior to the study. This may alter some of the important physico-chemical properties of the NPS. It is also believed that the above method (XPS) used for the quantification of oxidation states has an estimated error expectancy of the order of 5 % (Laachir et al., 1991, Borchert et al., 2005). So the amount of Ce (III) and Ce (IV) concentrations observed after the XPS analysis could be an underestimate or overestimate of the original concentrations. Similarly, poor signal to noise ratio in case of EELS can also challenge the accuracy of signal extraction from the background. According to literature, when the noise level in the experimental data is low, signal extraction from the spectra is straightforward and sufficient accuracy can be achieved. However, when the noise level increases, the signal extraction error also increases and is estimated to range from 10-15 % (Riedl et al., 2006, Yakovlev et al., 2012). It is clear that both EELS as well as XPS are complimentary techniques and useful information about the oxidation states of cerium can be obtained from both the techniques. Here we report the Ce (III) data obtained for the analysed samples and tabulated in table 4.25.

Table 4.25 Illustrating the size (by TEM) and quantitative measurements of oxidation states for the synthesised samples using EELS and XPS

Sample name	Morphology	Size (nm)	EELS %			XPS %
		TEM	Ce III Center	Ce III Edge	Ce (III) Area scans	Ce (III)
C1	Nanocube	30.8±7.3	32	77	-	35
C2	Nanocube	20.6±7.3	43	93	-	37
C3	Nanocube	15.8±4.6	45	100	-	38
S1	Nanosphere	4.5±2.5	86	100	-	42
S2	Nanosphere	6.0±3.0	45	86	-	40
S3	Nanosphere	3.0±1.0	77	100	-	40
S4	Nanosphere	3.0±1.0	-	-	86	46
S5	Nanosphere	3.3±1.3	-	-	70	42
S6	Nanosphere	8.2±2.5	55	100	-	-
S7	Nanosphere	5.9±2.2	-	-	70	45
C4	Nanocube	29.0±18.6	98	100	-	-
R1	Nanorod	83±56(Length) 15.9±6.0(width)	19	83	-	27

5 Dispersion and aggregation behaviour of ceria nanoparticles in cell culture media and their uptake and internalisation by human lung epithelial cells (A549 cells)

5.1 Chapter overview

The widespread use of cerium oxide nanoparticles in commercial products has potentially increased the probability of exposure to human and the environment. In particular, the use of cerium oxide as fuel additive, in catalytic convertors and polishing agents (Trovarelli, 1996, Deluga et al., 2004, Park et al., 2000, Campbell and Peden, 2005), their production at an industrial scale and hence their potential direct discharge into the environment has led to an increased amount of research in their biological effects (Ju-Nam and Lead, 2008). As discussed in chapter 1, toxicity of ceria NPs has been recognised and various efforts have led to seemingly different assessments (Lin et al., 2006, Xue et al., 2011), Hirst et al. (2013), (Gaiser et al., 2011, Schubert et al., 2006, Karakoti et al., 2010a, Park et al., 2008, Heckert et al., 2008b, Pirmohamed et al., 2010, Dowding et al., 2013).

As discussed in Chapter 1, the oxidant/antioxidant behaviour of ceria could be ascribed to many factors such as the origin of the materials used for their synthesis (Karakoti et al., 2012), the presence of stabilizing or capping agents (Baer, 2011), the chemical and physical properties of the ceria nanoparticles, the Ce (III)/Ce (IV) ratio in a particular sample, the

behaviour of the synthesised particles in the cell culture media as well as the procedures employed to evaluate toxicity.

In chapter 3 and 4, we reported that ceria nanoparticles of various shapes and sizes have been synthesized using biocompatible raw materials and simple wet lab synthetic routes. We have produced NPs coated with different capping agents, with different strengths of interaction between core and capping agent/no capping agent and with both steric and charge stabilization. The various shapes obtained are nanospheres, nanocubes and nanorods. The size, shape and morphology of the as synthesized samples were determined using DLS and TEM and the oxidation states have been quantified using STEM-EELS and XPS.

As discussed in Chapter1, inhalation and ingestion of nanoceria is likely to promote their entry into the human body, allowing them to reach the bloodstream and other body fluids. In this chapter, we report and discuss the dispersion behaviour of some of the synthesised nanoceria (with known physico-chemical properties) in cell culture media and their uptake and internalisation in lung-derived A549 cell lines (Adenocarcinomic human alveolar basal epithelial cells, A549 cells). More details are in section 5.3.3.

An important requirement is to first understand the behaviour of these NPs in the cell culture media. So here in this chapter, we have used six of our well characterised ceria nanoparticle samples with known size, shape, and oxidation state. The aggregation behaviour of these NPs has been assessed in serum containing media (cell growth medium with foetal bovine serum) and serum free media (cell growth medium without foetal bovine serum) and then later on in the second part of the chapter, their cellular interaction and uptake by human lung epithelial cells has been studied. DLS was used to measure the hydrodynamic diameter, polydispersity index (PDI) and zeta potential of the NPs in the water as well in the culture media whereas

reflectance confocal microscopy (RCM) was used in this work to detect the aggregation behaviour and visualise the uptake and internalsation of ceria nanoparticles by the human lung epithelial cells (also known as HeLa A549 cells). This chapter fulfils the aim 4 and 5 of the project as outlined in chapter 3.

5.2 Physico-chemical properties of NPs and their fate after organismal exposure

Characterization of pristine NPs is an essential step before uptake and toxicity assessment as properties of NPs vary significantly with shape and size (Hussain et al., 2009, Powers et al., 2006, Baalousha et al., 2012a, Powers et al., 2007). The most relevant physicochemical characteristics of NPs are size, shape, surface chemistry, crystallinity, solubility, aggregation tendency and homogeneity of dispersions (Hussain et al., 2009). These properties may also influence their interaction with the biological systems (Kumar et al., 2014) as various biological media contain different buffer ions, biomolecules including proteins, amino acids etc (Chaudhury et al.) and due to the high surface energy, NPs tend to agglomerate or react with ions or absorb proteins present in the media. So it is important to investigate and understand the nanoparticle chemistry in relevant biological media (Patil et al., 2007).

5.2.1 Size dependent interactions

In the recent past, a number of biological studies have demonstrated the size-dependent cellular interaction of various nanoparticles. Although, there are very few on ceria NPs (Arnold et al., 2013), a lot of them have been carried out on gold (Pan et al., 2007), silver (Carlson et al., 2008) and titanium dioxide nanoparticles (Gurr et al., 2005). Arnold et al. investigated that cerium oxide NPs are more toxic than equimolar bulk cerium oxide and

tested it in Caenorhabditis elegans (a nematode) with particle size of 53.34 ± 3.12 nm (by DLS). Another study by Patil et. al demonstrated the size selective uptake by human alveolar basal epithelial cells (A549 cells). They revealed that the A549 cells efficiently took up smaller nanoceria (3-5nm) prepared using a microemulsion method as compared to bigger nanopceria prepared using hydrothermal method (8-10 nm). However, no details of synthesis dependent uptake was provided. There is also literature investigating the effect of agglomeration on uptake. Schrand et al. demonstrated that size dependent uptake does not necessarily apply to agglomerated particles i.e some particles behave as larger particles when in agglomerated state and so the uptake will depend on the size of the agglomerate and not the original particle size itself (Carlson et al., 2008). So it is essential to characterize the size and agglomeration/aggregation tendency of synthesised NPs in the culture media for accurate biological behaviour.

5.2.2 Shape dependent interactions

Few researchers have investigated the effect of particle shape and aspect ratio on the uptake and internalisation by the cells. They have demonstrated that the threshold radius varies with particle shape (cylindrical and spherical) and that there is an optimal particle size for cells to wrap a membrane around the particles during endocytosis or cell internalization (Gao et al., 2005, Chithrani et al., 2006, Decuzzi and Ferrari, 2007, Decuzzi and Ferrari, 2008). They further concluded that the particle intake would depend on the orientation of the particle near the cell membrane. For example, the intake of nanorods or cylindical particles would depend on the basis that whether the rods were perpendicular or parallel to the cell surface when in contact. In the former case, it is believed to favour the endocytosis process. Particles with high aspect ratio undergo longer wrapping times than spherical nanoparticles due to greater

energy required for their engulfment, and therefore take longer time to internalize (Chithrani and Chan, 2007, Kumar et al., 2014). A study by Das et al. explored various cellular responses with different size and shape of nanoceria. They analysed cell proliferation of human umbilical vein endothelial cells (HUVECs) using ceria nanospheres, nanocubes, stars and rods and observed that with the exception of ceria nanorods, other size and shaped nanoparticles did not reveal any overt toxicity towards HUVEC cells whereas exposure to ceria nanorods led to a slight reduction in cell proliferation. Proliferation of endothelial cells is the critical first step involved in angiogenesis (angiogenesis is the formation of new blood vessels from existing blood vessels and is critical for many physiological and patho-physiological processes) (Das et al., 2012). In another in *vitro* study using ceria nanorods, the aspect ratio of nanorods played a major role towards toxicity. Nanorods (both synthesised using hydrothermal methodology with cerium chloride as cerium source) with an aspect ratio 1–16 did not induce any cellular response. However, nanorods with an aspect ratio 22 and 31 induced pro-inflammatory (IL-1β) production and cytotoxicity. Higher aspect ratio nanorods ≥22 (at lengths ≥200 nm) damaged lysosomes and therefore induced inflammatory response to the cells. Hence, shape of the NPs could also influence the cellular response.

5.2.3 Surface charge and surface modification dependent interactions

There are studies which looked at the surface chemistry of particles in relation to their interactions with biological systems. Patil et al. observed variations in bovine serum albumin (BSA) protein adsorption with different positive and negative surface charged ceria samples (Patil et al., 2007) (Albumin protein is an important component of the bovine serum used in cell culture media). Protein adsorption on the surface of the nanoparticles mainly depends on electrostatic interaction, hydrophobic interaction and specific chemical interactions between

protein and the nanoparticle surface (Kumar et al., 2014). They observed that positively surface charged nanoceria (prepared using hydrothermal method) adsorbed more proteins, whereas negatively surface charged nanoceria (prepared using micremulsion method) did not significantly adsorb proteins and further during cell internalization studies (A549 cell line; human alveolar basal epithelial cells), negative surface charged nanoparticles showed higher cellular uptake as compared to positive surface charged nanoceria. This could be attributed to the fact that like protein adsorption, NP uptake by cells also depends upon the electrostatic interaction of nanoceria with the cell membrane. In another study by Dowding et al., three differently sized nanoceria were synthesised using simple wet lab methodologies. The surface charge of these samples were HMT-nanoceria (~34 mV) > nanoceria2 (~30 mV) > nanoceria1 (18 mV), however in cell culture media, they showed a very similar distribution of charge (8–10 mV). Moreover, during cellular uptake studies in human umbilical vein endothelial cells line (HUVECs), HMT-nanoceria were found to show higher uptake, followed by nanoceria2 and minimum amount were observed in case of nanoceria1 (analyzed using ICP-MS). Another interesting point is that though HMT-nanoceria were found to have higher cell internalization, the size of HMT-nanoceria were bigger that nanoceria1 and nanoceria2.

There are some other studies who have looked at the effect of surface modifications on cellular response. Although nothing specific to ceria could be found, Wagner et al. (Wagner et al., 2007) examined cellular interaction of aluminium oxide and aluminium nanoparticles, including their effect on cell viability and cell phagocytosis, with reference to particle size and composition on alveolar macrphages. Gratton et al. (Gratton et al., 2008) suggested that high aspect ratio pegylated hydrogel particles undergo internalization rapidly. From these

results, it can be concluded that size, shape, surface modification and surface charge play an important role in cell-nanoparticle interaction.

5.2.4 Interaction between NPs and serum proteins

It is known that when the nanoparticles enter a biological fluid, they interact with proteins of the biological fluid along with other constituents such as nucleic acids or lipids. This nanoparticle-protein interaction leads to the adsorption of proteins on the nanoparticle surface forming a protein-nanoparticle complex. The formation of such nanoparticle–protein complexes has been studied by many workers and the complex is often referred to as a –protein corona" (Cedervall et al., 2007a, Cedervall et al., 2007b, Lynch et al., 2007, Sahoo et al., 2007, Lynch and Dawson, 2008). The concept of protein corona is important in shaping the surface properties, charges, resistance to aggregation and hydrodynamic size of nanoparticles (Nel et al., 2009). For example, the coated proteins may undergo conformational changes leading to a new bioentity, hence altering the nanoparticle surface completely and hence biological behaviour (Lynch et al., 2007, Cedervall et al., 2007b, Lundqvist et al., 2008). The adsorbed protein may provide extra stability to the particle thereby increasing its life span within the biological fluids. The corona formation may lead to an increase in hydrodynamic size of the NPs as well as a complete change in surface charge (Wiogo et al., 2012). A survey of the literature on nanoparticle-protein binding also shows that the proteins associated with a particle possess a wide range of affinities for the particle surface, resulting in a range of different residence times for proteins at a nanoparticle surface. The residence time and the exchange of proteins processes may redistribute from one compartment to another, such as upon uptake into cells from the cell culture media, or upon transport from the cytosol to the nucleus (Lynch and Dawson, 2008), however, these may also be size or shape dependent. Other factors such as electrostatic interaction, hydrophobic

interaction and specific chemical interactions between protein and the adsorbent also play an important role in protein adsorption (Arai and Norde, 1990, Zhang et al., 2006, Xu and Siedlecki, 2007). There are studies in literature which looked at the interactions and protein binding kinetics of serum proteins with a number of engineered NPs as a function of their physicochemical properties. Albumin protein is one of the most abundant protein present in serum. Many studies have used bovine serum albumin (BSA) as a model to determine the binding affinity of proteins (Patil et al., 2007, Tantra et al., 2010, Kreyling et al., 2014). The studies suggest that that BSA offers steric stabilisation of nanoparticles (Schulze et al., 2008, Jiang et al., 2009). Tantra et al demonstrated material dependent affinity of serum albumin, they also demonstrated that adsorption of BSA led to subsequent de-agglomeration of the sub-micron ZnO clusters into smaller fragments, even breaking them up into individual isolated nanoparticles (Tantra et al., 2010). Another study looked at the protein absorption on bare and functionalised MNPs and found more protein absorption on the bare surfaces as compared to the functionalised particles (Wiogo et al., 2012). According to literature, by and large, the amount and identity of the protein adsorbed on the NP surface seems to determine the uptake of the NP (Saptarshi et al., 2013). The nature of the proteins in the corona may be determined by the local chemical property of the nanomaterial. However, even for a fixed material type, the size of the particle, and its surface modification are able to entirely change the nature of the biologically active proteins in the corona, and thereby possibly also the biological impacts (Lundqvist et al., 2008).

5.2.5 Internalisation pathways of nanoparticles

Several pathways are known to be associated with the cellular entry of nanoparticles depending upon the particular cell line used, age, cellular environment and/or the physiochemical characteristics of the specific particles being tested eg, size, shape,

composition and surface characteristics (Dausend et al., 2008, Xia et al., 2008b, Nel et al., 2009, Johnston et al., 2010, Iversen et al., 2011, Kuhn et al., 2014). The term endocytosis describes two different cellular uptake mechanisms: pinocytosis, which involves the uptake of fluids and molecules within vesicles and phagocytosis, which is responsible for engulfing large particles (e.g., microorganisms, particles, apoptotic bodies). Pinocytosis covers macropinocytosis, clathrin-mediated endocytosis, caveolin-mediated endocytosis and clathrin- and caveolin-independent endocytosis (Figure 5.1). Macropinocytosis involves the internalisation of large areas of the plasma membrane together with significant amounts of fluid, since uncoated vesicles can be bigger than coated ones, thus allowing endocytosis of larger objects (>150 nm) (Swanson and Watts, 1995, Mercer and Helenius, 2012). Clathrin-mediated endocytosis (CME), is the process involving specific receptors that recognize and internalize cargo into –coated pits", formed by the assembly of a cytosolic coat protein, clathrin, which constitutes the main assembly unit. These coated pits invaginate and pinch off to form vesicles that later fuse with endoplasmic compartments such as early endosomes, endosomes or with lysosomes (Huang et al., 2004, Granseth et al., 2006, Granseth et al., 2007). Caveolae-mediated endocytosis involves clustering of lipid raft components on the plasma membrane into so called caveolae, which are flask-shaped invaginations, formed as a result of the interactions of different proteins, mainly caveolin, with the cellular membrane. Caveolae are extremely abundant at the surface of endothelial cells, and internalisation via this pathway is induced by specific ligands such as cholera toxin and simian virus-40, and this is considered to be the predominant pathway of entry for particles above 200 nm (Orlandi and Fishman, 1998, Nabi and Le, 2003, Rejman et al., 2004). Other uptake pathways include clathrin- and caveolae-independent endocytosis, in which other types of cholesterol-rich microdomains on the plasma membrane are involved, rather than caveolae. These domains are generally referred to as lipid rafts, small structures of 40–50 nm in diameter, that diffuse

on the cell surface and then these small rafts can be captured by, and internalized within an endocytic vesicle (Schnitzer et al., 1995, Romer et al., 2007, Lundmark et al., 2008, Doherty and Lundmark, 2009).

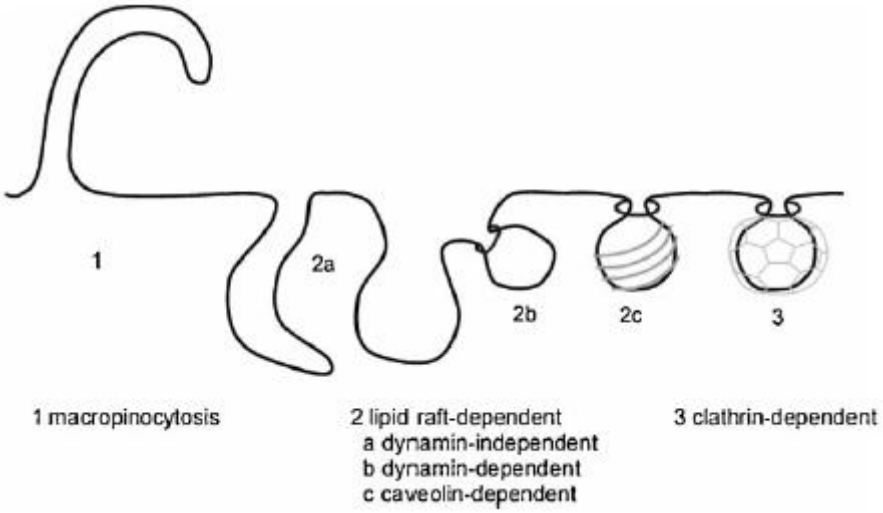

Figure 5.1 Mechanisms of endocytosis. The three main pathways are macropinocytosis, lipid raft-dependent mechanisms, and the clathrin-dependent pathway, adapted from (Dausend et al., 2008)

Many pharmacological inhibitors (eg amiloride blocks macropinocytosos, chlorpromazine known to block CME, genistein inhibits caveolae pinching etc) and markers (eg transferrin to identify clatherin-coated pits and caveolin to detect caveolae etc) are often used to investigate which endocytic mechanism is responsible for cellular uptake of nanoparticles (Jackson et al., 1996). This approach is far too often based on the assumption that these inhibitors have specific effects on a given endocytic mechanism, for more details refer to (Iversen et al., 2011). As far as the A549 cell line in particular is concerned, a lot of nanoparticle uptake and internalisation studies have been carried out using this cell line with different nanoparticles (shape and size) with some explaining the mechanism and some not. In particular clathrin mediated endocytosis has been found to be a predominant internalisation pathway for A549 cell line, however, some studies showing caveolae-mediated endocytosis

were also found (Smith et al., 2012, Kuhn et al., 2014). Experimental studies in literature have demonstrated different modes of intracellular trafficking and, possibly, entering mechanisms depending on the particle size and material including the possibility of a cell type to use multiple pathways simultaneously to internalise the same NPs (Rothen-Rutishauser et al., 2007, dos Santos et al., 2011).

In the present study, an attempt has been made to (1) Assess the behaviour of synthesised ceria NPs in human lung epithelial cell culture medium and (2) Look into the effect of shape, size and surface chemistry of ceria NPs on the uptake and internalization by A549 cells. DLS was used to measure the hydrodynamic diameter, polydispersity index (PdI) and electrophoretic mobility of the NPs in the water as well in the culture media whereas reflectance confocal microscopy (RCM) was used in this work to detect the aggregation behaviour and visualise the uptake and internalsation of ceria nanoparticles by the human lung epithelial cells (also known as HeLa A549 cells).

5.3 Material and methodology

The serum containing media (SCM) and serum free media (SFM) used in these experiments were provided by Dr Julie Mazzolini from school of biosciences, University of Birmingham. The composition of SCM and SFM are as below

5.3.1 Serum Containing Media (SCM)

5.3.1.1 DMEM 4.5g/L Glucose w/ L-Glutamine 500ml (Lonza) - Dulbecco's modified eagle's medium (DMEM) formulation is a modification of basal medium eagle (BME) that contains four-times the concentrations of the amino acids and vitamins. Table 5.1 illustrates the composition of DMEM as obtained from Lonza.

5.3.1.2 0.5% Penicillin-Streptomycin (Invitrogen) - The antibiotics penicillin and streptomycin are used to prevent bacterial contamination of cell cultures due to their effective combined action against gram-positive and gram-negative bacteria. This product is formulated to contain 10,000 units penicillin and 10 mg streptomycin/mL solubilized in a proprietary citrate buffer.

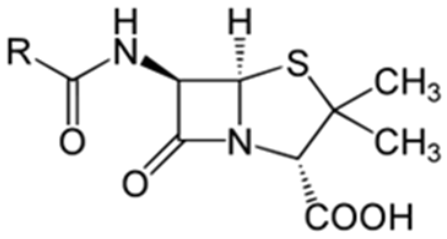

Penicillin

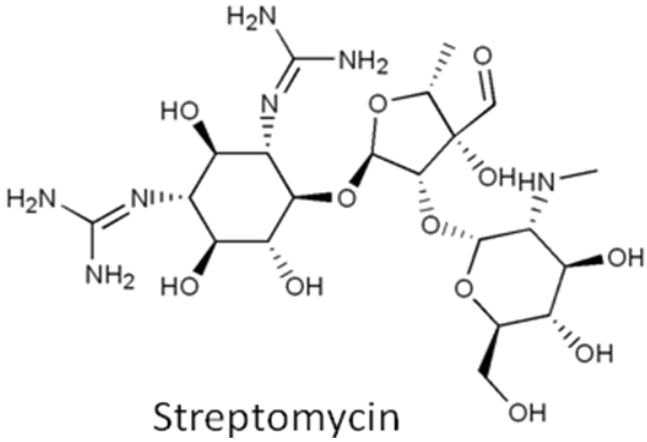

Streptomycin

5.3.1.3 10% Foetal Bovine Serum (Biosera)- Fetal bovine serum (FBS) is a cocktail of most of the factors required for cell attachment, growth and proliferation and is thus used as an almost universal growth supplement effective for most types of human and animal (including insect) cells. Animal serum is an extremely complex mixture of a large number of constituents, low and high molecular weight biomolecules, with different, physiologically balanced growth-promoting and growth-inhibiting activities. The sera most widely used are bovine sera of adult or newborn animals, or of foetal origin (FBS) (Brunner et al., 2010). The major functions of serum in culture media are to provide (i) hormonal factors stimulating cell growth and proliferation and promoting differentiated functions, (ii) transport proteins carrying hormones (e.g. transcortin), minerals and trace elements (e.g. transferrin) and lipids (e.g. lipoproteins), (iii) attachment and spreading factors, acting as germination points for cell

attachment and (iv) stabilising and detoxifying factors needed to maintain pH or to inhibit proteases either directly, such as α-antitrypsin or α2-macroglobulin, or indirectly, by acting as an unspecific sink for proteases and other (toxic) molecules

5.3.2 Serum Free Media (SFM)

5.3.2.1 DMEM 4.5g/L Glucose w/ L-Glutamine 500ml (Lonza)

5.3.2.2 0.5% Penicillin-Streptomycin (Invitrogen)

Table 5.1 Composition of DMEM, adapted from http://bio.lonza.com/uploads/tx_mwaxmarketingmaterial/Lonza_ProductDataSheets_Formulation_-_Dulbeccos_Modified_Eagles_Medium_DMEM_12-604.pdf

5.3.3 Adenocarcinomic human alveolar basal epithelial cells (A459)

Cells were purchased from the Health Protection Agency Culture Collection, Salisbury, UK. Adenocarcinomic human alveolar basal epithelial cells (A459) were grown in a complete Dulbecco‘s modified eagles medium (DMEM, Lonza) supplemented with 10% fetal bovine

serum (FBS, Biosera) and 1% of penicillin streptomycin (Gibco). This work was carried out with the help of Dr Julie Mazzolini from School of Biosciences, University of Birmingham.

5.3.4 Laboratory techniques and sterilisation

All media were prepared under the clean laminar hood with disposable sterile plastic ware and filtered using a filter system (500 ml, 0.22 μm pore size) from Corning and kept at 4^{o}C throughout. The floor of the laminar flow cabinet was treated with an aqueous 70% ethanol solution to prevent any bacterial contamination.

All the glassware and plastic required for the experiments was washed before and after use with 10% nitric acid (HNO3) for a minimum of 24 hrs and then rinsed thoroughly with ultrapure water ensuring no traces of acid remained. The glassware was then air dried and kept in sterile boxes until next use. Cerium oxide suspensions were made in sterile water and apart from that no extensive sterilisation techniques such as higher temperature treatments has been carried out on any of the ceria samples. This is in order to avoid any further changes to the physicochemical properties of the characterised samples.

5.3.5 Ceria NPs used

Six of our samples of cerium oxide nanoparticles were used for dispersion and stability studies in the cell culture media and cellular uptake by A549 cells. Three nanocube samples C1, C2 and C3, two nanospheres S1 and S2 and a nanorod sample R1 has been used. The synthesis and characterisation of these particles has had been previously discussed in chapter 3. Their size obtained by TEM and hydrodynamic diameter obtained from DLS are summarised in Table 5.2

5.3.6 Characterisation

DLS was used to measure the hydrodynamic diameter and polydispersity index (PdI) of the NPs in the water as well in the culture media. The electrophoretic mobility of the particles was measured using Zetasizer nano from Malvern instruments. The zeta potential measurements have been carried out for both pristine as well as particles treated with SCM and SFM. At least three measurements were made in each case and the data were averaged. Reflectance confocal microscopy (RCM) was used in this work to detect the aggregation behaviour and visualise the uptake and internalsation of ceria nanoparticles by the human lung epithelial cells (also known as HeLa A549 cells).

Table 5.2 Ceria NPs used for aggregation studies and cellular uptake by A549 cells

Sample code	Morphology	Size (nm)	
		DLS	TEM
C1	Nanocube	93.7±0.8	30.8±7.3
C2	Nanocube	113.4±0.5	20.6±7.3
C3	Nanocube	132.8±3.2	15.8±4.6
S1	Nanosphere	85.5±0.4	4.5±2.5
S2	Nanosphere	89.0±0.3	6.0±3.0
R1	Nanorod	338.7±6.2	83.0±56.0(Length) 16.0±6.0(width)

5.4 Stability studies of ceria NPs in cell culture media

Dispersion and aggregation behaviour of ceria NPs in cell culture media which is serum containing media (SCM) and serum-free media (SFM) was studied at 37 ^{0}C by DLS for 1

hour. This temperature and time period were chosen to mimic the conditions during uptake assays. The ceria nanoparticles were suspended in sterile distilled water at concentrations of 10 mg ml^{-1}. Stock solutions of ceria nanoparticles (10 mg ml^{-1}) prepared in sterile distilled water were sonicated for 1 min using Branson 1510 ultrasonic bath (details in chapter 2 section) and suitable amount of ceria NPs was added into SCM or SFM to form a final concentration of 500 μg ml^{-1}. The mixtures were immediately moved to DLS system for *in situ* monitoring of the variation of hydrodynamic diameter of ceria NPs and understand their stability with time. Six independent samples were measured using the same procedure. The particles used in cell culture studies remain submerged in cell culture media for 1 hour at 37 ^{0}C. These culture medium contain salts, various small molecules, serum proteins as well as other macromolecules. So the time-course of the stability experiments was designed to investigate the kinetics of aggregation and the influence of medium components on the particle size as a function of time. The data has been collected at 20, 40 and 60 minutes after the addition and the temperature was set at 37 ^{0}C.

5.4.1 Results and discussion of stability tests of ceria NPs in SCM and SFM

DLS was used to measure the hydrodynamic diameter and polydispersity index (PdI) of the NPs in the water as well as in the culture media. DLS was also run for pure SCM and SFM. Figure 5.2 shows the size distribution by intensity data observed for pure SCM and SFM. SCM shows a distinct double peak and a mean diameter of around 161.9 nm. This could be due to the scattering from the bovine serum albumin (BSA) in the serum solution. The electrophoretic mobility of the pure SCM and SFM was measured using Zetasizer nano from Malvern instruments. The zeta potential measurements came out to be -0.846±0.405 mV at pH +7.4 and -1.62±0.96 mV at pH +7.3 for SCM and SFM respectively.

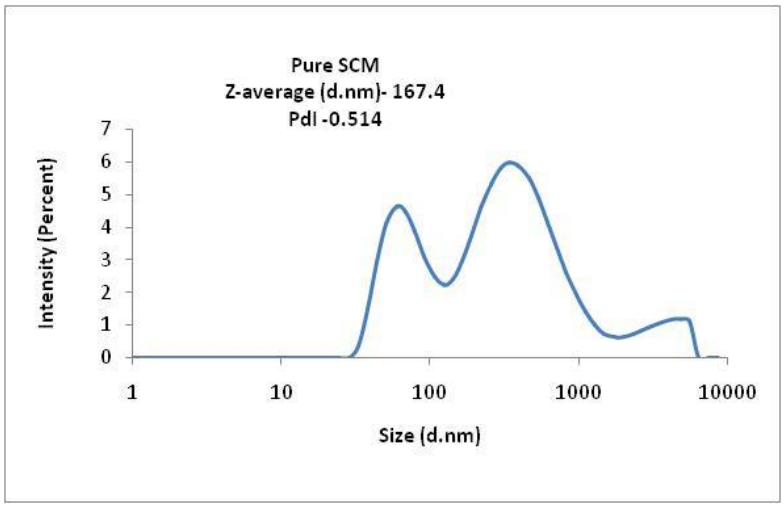

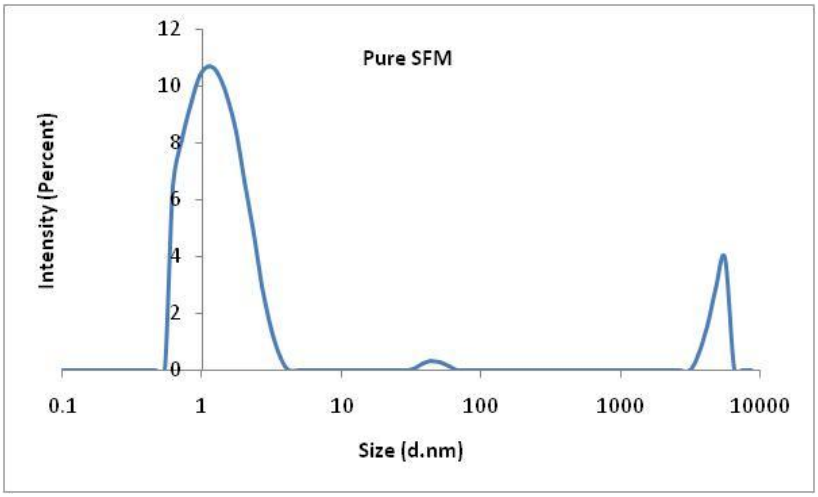

Figure 5.2 Size distribution by intensity obtained with DLS for SCM and SFM, each coloured line represents an average of minimum three measurements

The stability tests for the nanocubes (C1, C2, and C3), nanospheres (S1 and S2), and nanorods (R1) in SCM and SFM showed that the hydrodynamic diameter increases quickly in the first 20 minutes for both SCM as well as SFM (table 5.3 and 5.4). However, the aggregation rate is faster in the latter. The detailed study on sample basis is discussed below.

5.4.1.1 Stability results for nanocubes C1: The hydrodynamic diameter for pristine nanocubes (C1) in ultrapure water is 98 nm. When dispersed in SCM, there is an abrupt rise in particle size (1894 nm) in the first 20 minutes and then particle size slightly dropped down

to 1653 nm after 40 minutes and then increased to 1717 nm after 60 minutes in the SCM at 37^0C. The polydispersity index for these measurements is higher (0.550). However when dispersed in SFM for same duration and at same temperature, the aggregation rate is faster than in SCM. The particle size quickly reached to 5033 nm in the first 20 minutes and then further increased to 5743 nm after 40 minutes and 6815 nm after 60 minutes of the study, when dispersed in SFM. The PDI observed is smaller (0.199) indicating that the sample is less polydisperse. The change and trend in particle diameter as obtained by DLS, when dispersed in SCM and SFM is tabulated in tables 5.3 and 5.4 respectively. Figure 5.3 (a) shows size distribution by intensity data obtained for C1 in ultra pure water, SCM and SFM. The electrophoretic mobility of the particles in ultra pure water as well as the particles treated with SCM and SFM was measured using Zetasizer nano from Malvern instruments. The zeta potential for pristine nanocubes (C1) dispersed in water is 5.71±0.16 mV at pH+6.9. However it turned to almost neutral when dispersed in SCM (-1.34±0.13mV) at pH+7.2 and SFM (-0.28±0.05mV) at pH+7.2.

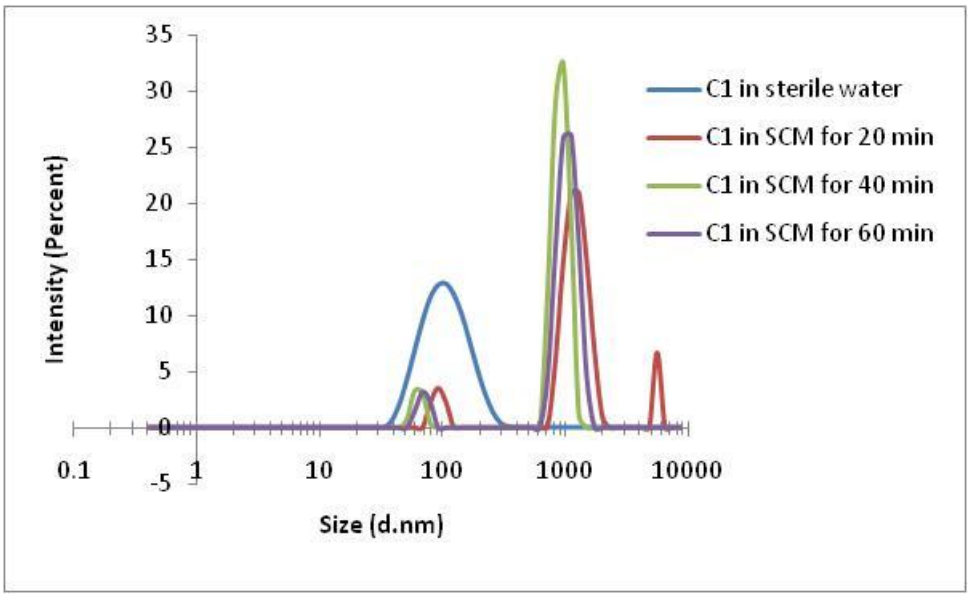

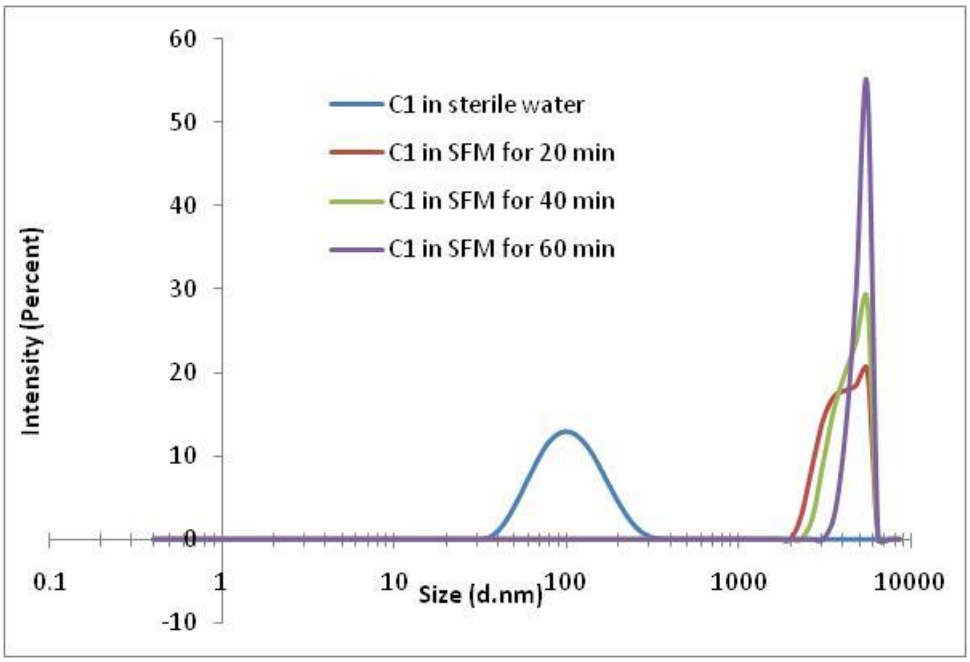

Figure 5.3 (a) Size distribution by intensity data obtained with DLS for nanocubes C1 in sterile water, SCM and SFM, each coloured line represents an average of minimum three measurements

Table 5.3 Trend and change in hydrodynamic diameter and polydispersity index (PdI) for the nanocubes (C1, C2, and C3), nanospheres (S1 and S2), and nanorods (R1) in SCM over a period of 60 minutes, as obtained by DLS

Time in minutes	Size in serum containing media (SCM) (nm)					
	C1	C2	C3	S1	S2	R1
20	1894±114 PdI:0.567	1776±122 PdI:0.402	959±12 PdI:0.271	92±23 PdI:0.680	450±12 PdI:0.348	1207±19 PdI:0.397
40	1653±145 PdI:0.587	1996±91 PdI:0.411	937±14 PdI:0.250	106±61 PdI:0.733	453±10 PdI:0.317	1160±13 PdI:0.389
60	1717±86 PdI:0.533	2105±101 PdI:0.372	958±9 PdI:0.233	122±41 PdI:0.635	453±16 PdI:0.362	1164±11 PdI:0.369

Table 5.4 Trend and change in hydrodynamic diameter and polydispersity index (PdI) for the nanocubes (C1, C2, and C3), nanospheres (S1 and S2), and nanorods (R1) in SFM over a period of 60 minutes, as obtained by DLS

Time in minutes	Size in serum free media (SFM) (nm)					
	C1	C2	C3	S1	S2	R1
20	5033±1478 PdI:0.199	296±41 PdI:1.000	2858±826 PdI:0.714	1491±120 PdI:0.233	4646±828 PdI:0.146	2141±423 PdI:0.373
40	5743±907 PdI:0.207	276±23 PdI:1.000	3112±310 PdI:0.223	66±13 PdI:0.240	2308±720 PdI:0.408	1310±266 PdI:0.373
60	6815±758 PdI:0.188	255±82 PdI:1.000	3540±288 PdI:0.157	1578±422 PdI:1.000	2742±470 PdI:0.267	825±521 PdI:0.375

5.4.1.2 Stability results for C2: The hydrodynamic diameter for pristine nanocubes (C2) in ultrapure water is 114 nm. When dispersed in SCM, there is rise in particle size (1776 nm) in the first 20 minutes and then particle size further increased to 1996 nm after 40 minutes and then increased to 2015 nm after 60 minutes in the SCM at 37^0C. However when dispersed in SFM for same duration and at same temperature, the aggregation rate is much quicker than in SCM. This is indicated by the high PdI, also the Z-average obtained did not match with the intensity distributions obtained indicating very strong and quick aggregation. As discussed in the methodology chapter (Chapter 2), intensity distributions need to cited in such conditions. The particle size reached to 296 nm in the first 20 minutes and then dropped to 276 nm after 40 minutes and then again dropped to 255 nm after 60 minutes of the study, when dispersed in SFM. However, it was found that nanocubes C2 are less stable than C1 in both SCM and SFM. The change and trend in particle diameter as obtained by DLS, when dispersed in SCM

and SFM is tabulated in tables 5.3 and 5.4 respectively. Figure 5.3 (b) shows size distribution by intensity data obtained for C2 in ultra pure water, SCM and SFM. The zeta potential for pristine nanocubes (C2) dispersed in water is 26.9±1.72 mV at pH+7.1. However it turned to neutral when dispersed in SCM (-1.38±0.11 mV) at pH+7.2 and SFM (-0.33±0.03 mV) at pH+7.2.

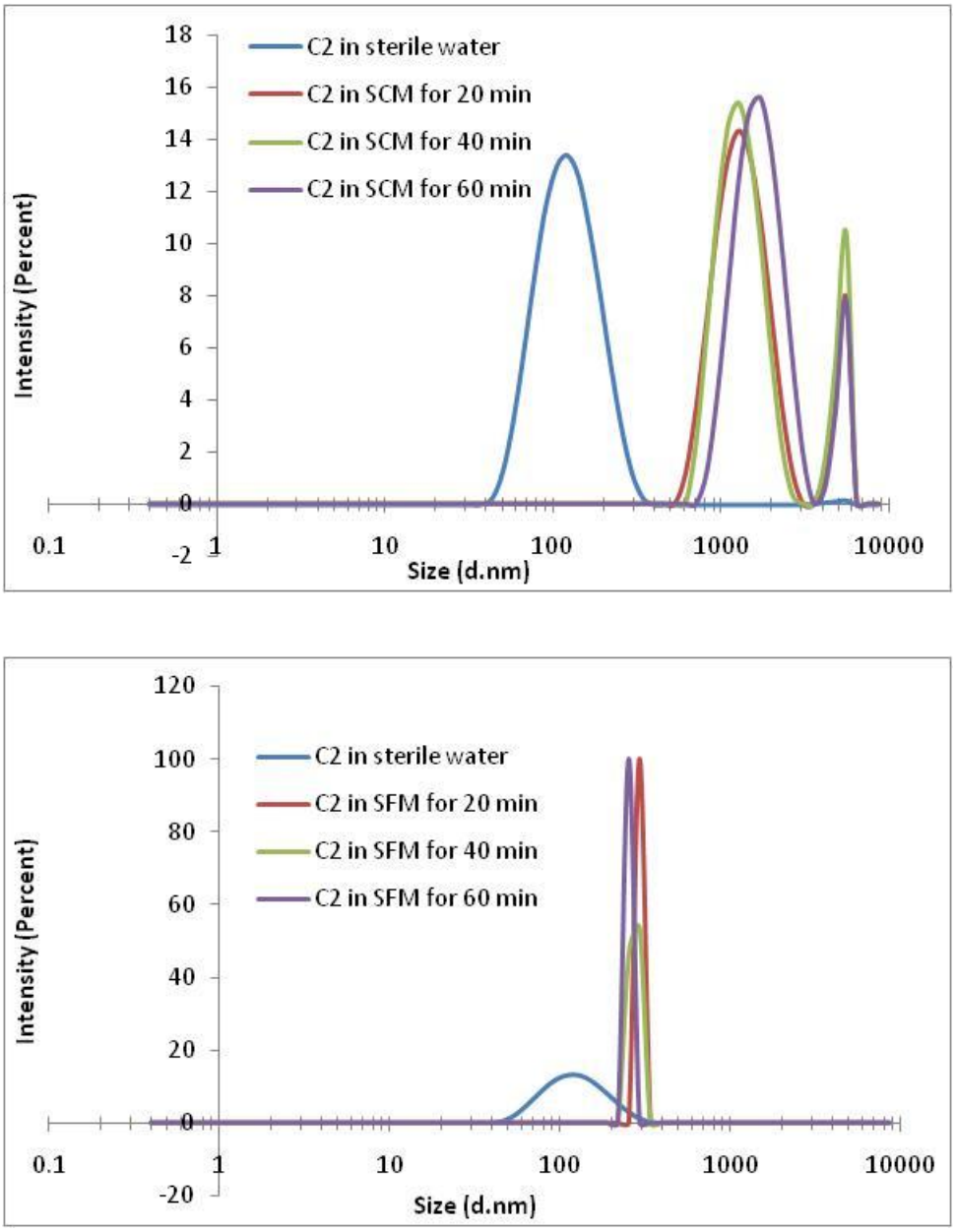

Figure 5.3 (b) Size distribution by intensity data obtained with DLS for nanocubes C2 in sterile water, SCM and SFM, each coloured line represents an average of minimum three measurements

5.4.1.3 Stability results for C3: The hydrodynamic diameter for pristine nanocubes (C3) in ultrapure water is 133 nm. When dispersed in SCM, there is a rise in particle size (959 nm) in the first 20 minutes and then particle size slightly decreased to 937 nm after 40 minutes and then again increased to 958 nm after 60 minutes in the SCM at 37^0C. The results indicate that the particle in sample C3 were not aggregating after first 20 minutes in the SCM as the particle size remains almost consistent after 40 minutes and 60 minutes in the SCM. However when dispersed in SFM for same duration and at same temperature, the aggregation rate is much quicker than in SCM. The particle size reached to 2858 nm in the first 20 minutes and then further increased to 3112 nm after 40 minutes and then again increased to 3540 nm after 60 minutes of the study, when dispersed in SFM. However, it was found that nanocube sample C3 was comparatively more stable than nanocube samples C1 and C2 in SFM (see table 5.5) i.e in terms of stability order, C3>C1>C2 when dispersed in SFM. C3 is also more stable than C1 and C2 in SCM and the order of stability is very similar to SCM, C3>C1>C2. The change and trend in particle diameter as obtained by DLS, when dispersed in SCM and SFM is tabulated in tables 5.3 and 5.4 respectively. Figure 5.3 (c) shows size distribution by intensity data obtained for C3 in ultra pure water, SCM and SFM.

The zeta potential measurements of C3 showed that these nanocubes are negatively charged as compared to C1 and C2 (both positively charges). The zeta potential for pristine nanocubes (C3) dispersed in water is -2.20±0.041 mV at pH+7.2. However it turned to almost neutral when dispersed in SCM (-1.43±0.14 mV) at pH+7.3 and SFM (-0.51±0.03 mV) at pH+7.2.

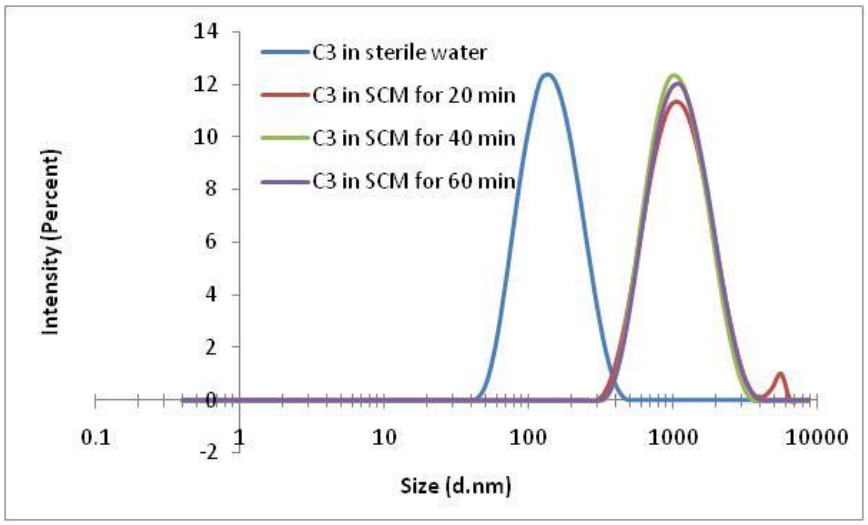

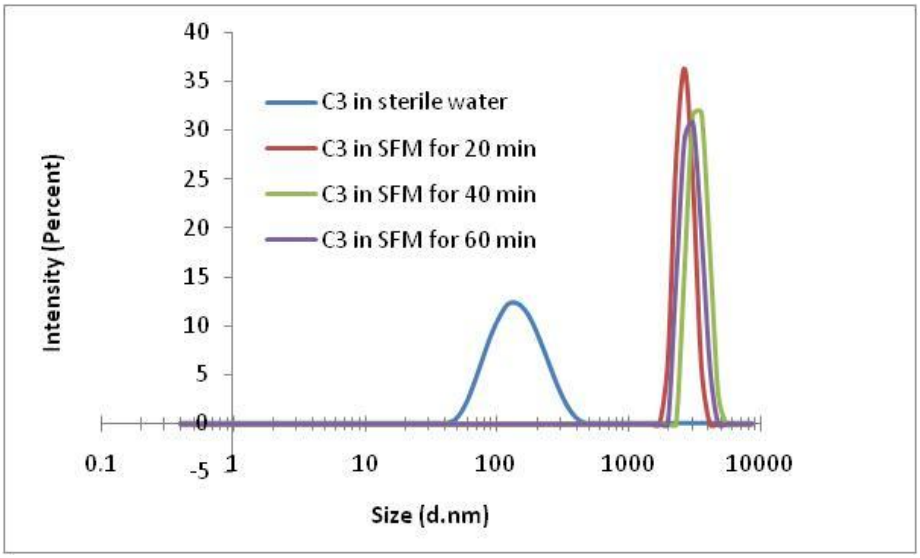

Figure 5.3 (c) Size distribution by intensity data obtained with DLS for nanocubes C3 in sterile water, SCM and SFM, each coloured line represents an average of minimum three measurements

5.4.1.4 Stability results for nanospheres S1: The hydrodynamic diameter for pristine nanospheres (S1) in ultrapure water is 86 nm. When dispersed in SCM, there is a sudden rise in aggregation, as indicated by the high PdI values obtained for the suspensions after 20, 40 and 60 minutes in SCM (Table 5.3). The high Z-average values obtained (8989nm) in the first 20 minutes of treatment with SCM are not in agreement with the intensity distributed values (93 nm) obtained by DLS indicating very quick and strong aggregation. This is also

evident from the high PdI values obtained (0.733). As per recommendations in literature, intensity distributed sizes with high PdI obtained have been quoted in table 5.3. The results indicate that the particles in sample S1 quickly aggregated to larger sizes. When dispersed in SFM for same duration and at same temperature, the aggregation rate for S1 in SFM appeared to be very much similar to that in SCM. The particle size quickly reached to 1491 nm in the first 20 minutes and then dropped to 66 nm after 40 minutes and then increased to 1578 nm after 60 minutes of the study, when dispersed in SFM. The pattern indicated sample instability in SFM and is also confirmed with high PdI values obtained after 60 minutes in SFM. The data indicates that that S1 is unstable when dispersed in SCM and SFM. The change and trend in particle diameter as obtained by DLS, when dispersed in SCM and SFM is tabulated in tables 5.3 and 5.4 respectively. Figure 5.3 (d) shows size distribution by intensity data obtained for S1 in ultra pure water, SCM and SFM.

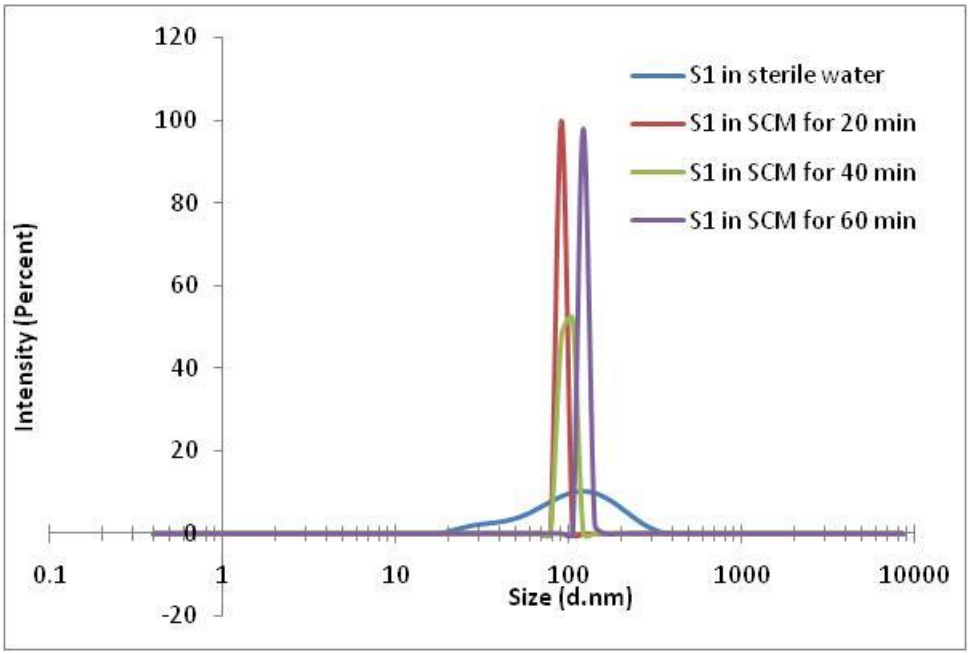

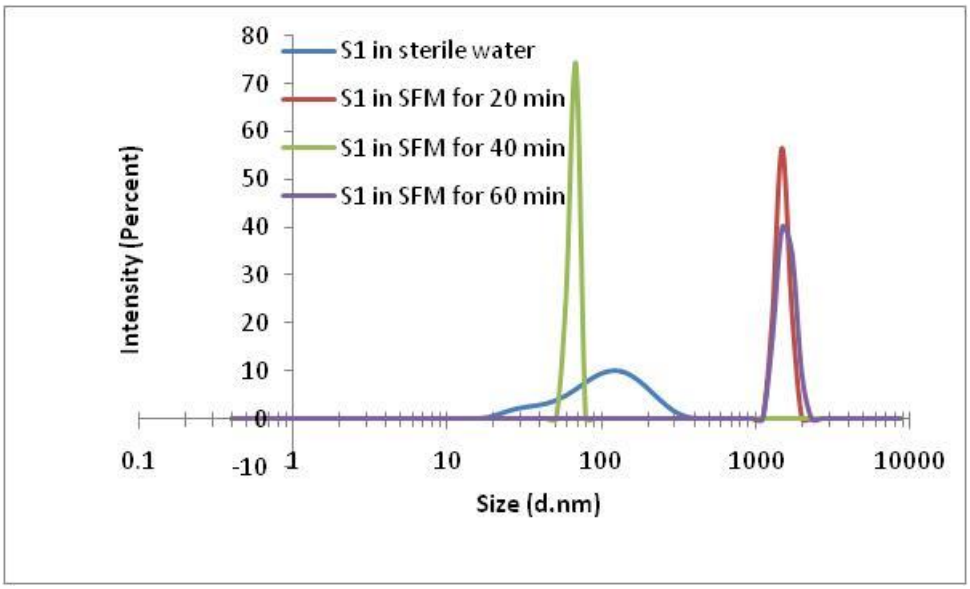

Figure 5.3 (d) Size distribution by intensity data obtained with DLS for nanosheres S1 in sterile water, SCM and SFM, each coloured line represents an average of minimum three measurements

5.4.1.5 Stability results for nanospheres S2: The hydrodynamic diameter for pristine nanospheres (S2) in ultrapure water is 89 nm. When dispersed in SCM, there is a rise in hydrodynamic diameter (450 nm) in the first 20 minutes and then particle size slightly increased to 453 nm after 40 minutes and then stayed static at 453 nm after 60 minutes in the SCM at 37^0C. The results indicate that the particles in sample S2 are stable when dispersed in SCM. The results indicate that the particle in sample S2 were not aggregating after first 20 minutes in the SCM as the particle size remains almost consistent after 40 minutes and 60 minutes in the SCM. However when dispersed in SFM for same duration and at same temperature, the aggregation rate is quicker than in SCM. The particle size reached to 4646 nm in the first 20 minutes and then decreased to 2308 nm after 40 minutes and then again increased to 2742 nm after 60 minutes into the study, when dispersed in SFM. Figure 5.3 (e) indicates the presence of multiple peaks in size distribution by intensity data obtained after 40

and 60 minutes of treatment with SFM. The indicates that S2 is more stable in SCM as compared to SFM.

Both nanosphere samples S1 and S2 are PEG capped but with different molecular weights of PEG. S1 is capped with PEG 1500 (MW) and S2 is capped with PEG 600 (MW). Both the samples have been synthesised by sonochemical method using the same cerium precursor but have showed different stability regime when dispersed in SCM and SFM. Stability data shows that S2 is more stable than S1 in both SCM and SFM. The change and trend in particle diameter for S1, as obtained by DLS, when dispersed in SCM and SFM is tabulated in tables 5.3 and 5.4 respectively. Figure 5.3 (e) shows size distribution by intensity data obtained for S2 in ultra pure water, SCM and SFM.

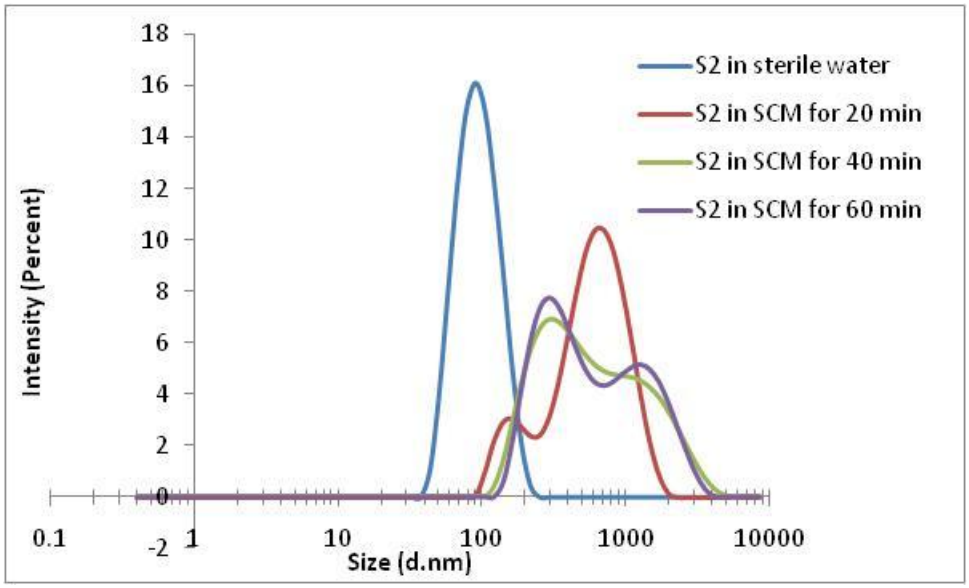

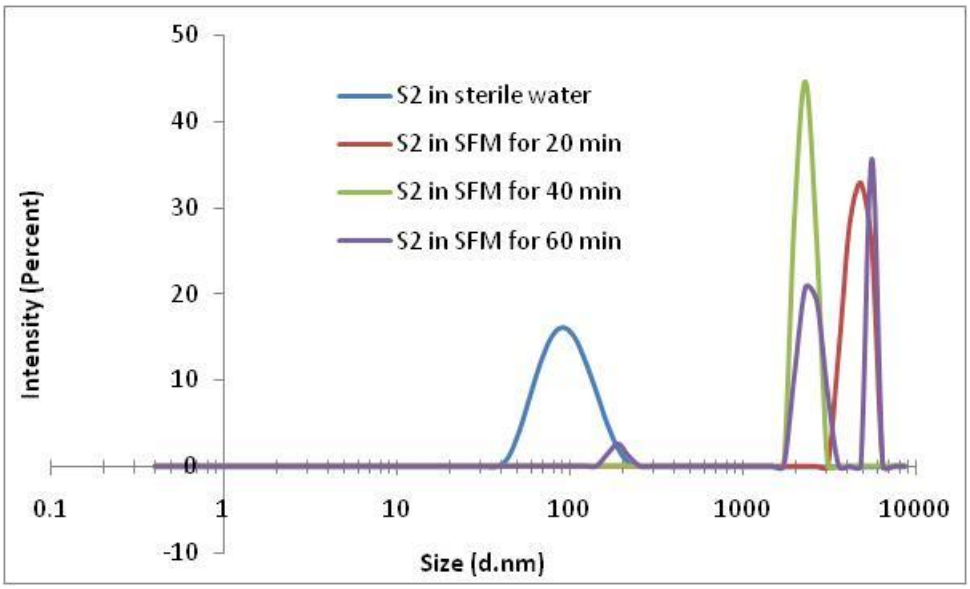

Figure 5.3 (e) Size distribution by intensity data obtained with DLS for nanosheres S2 in sterile water, SCM and SFM, each coloured line represents an average of minimum three measurements

5.4.1.6 Stability results for nanorods R1: The hydrodynamic diameter for pristine nanorods (R1) in ultrapure water is 339 nm. When dispersed in SCM, there is a rise in hydrodynamic diameter (1207 nm) in the first 20 minutes and then particle size slightly decreased to 1160 nm after 40 minutes and then stayed static at 1164 nm after 60 minutes in the SCM at 37^0C. The results indicate that the particle in sample R1 were not aggregating after first 20 minutes in the SCM as the particle size remains almost consistent after 40 minutes and 60 minutes in the SCM. However when dispersed in SFM for same duration and at same temperature, the aggregation rate is quicker than in SCM. The particle size reached to 2141 nm in the first 20 minutes and then decreased to 1310 nm after 40 minutes and then again decreased to 825 nm after 60 minutes into the study, when dispersed in SFM. The Z-average values obtained are not in agreement with the size distributions by intensity data, the pattern indicates sample instability in SFM. The results indicate that R1 is more stable in SCM as compared to SFM. The change and trend in particle diameter for R1, as obtained by DLS, when dispersed in

SCM and SFM is tabulated in tables 5.3 and 5.4 respectively. Figure 5.3 (f) shows size distribution by intensity data obtained for R1 in ultra pure water, SCM and SFM.

The zeta potential for pristine nanorods (R1) dispersed in water is -3.00±0.072 mV at pH+7.0. However it turned to (-1.27±0.08 mV) at pH+7.3 when dispersed in SCM and (-0.42±0.07 mV) at pH+7.2 when dispersed in SFM.

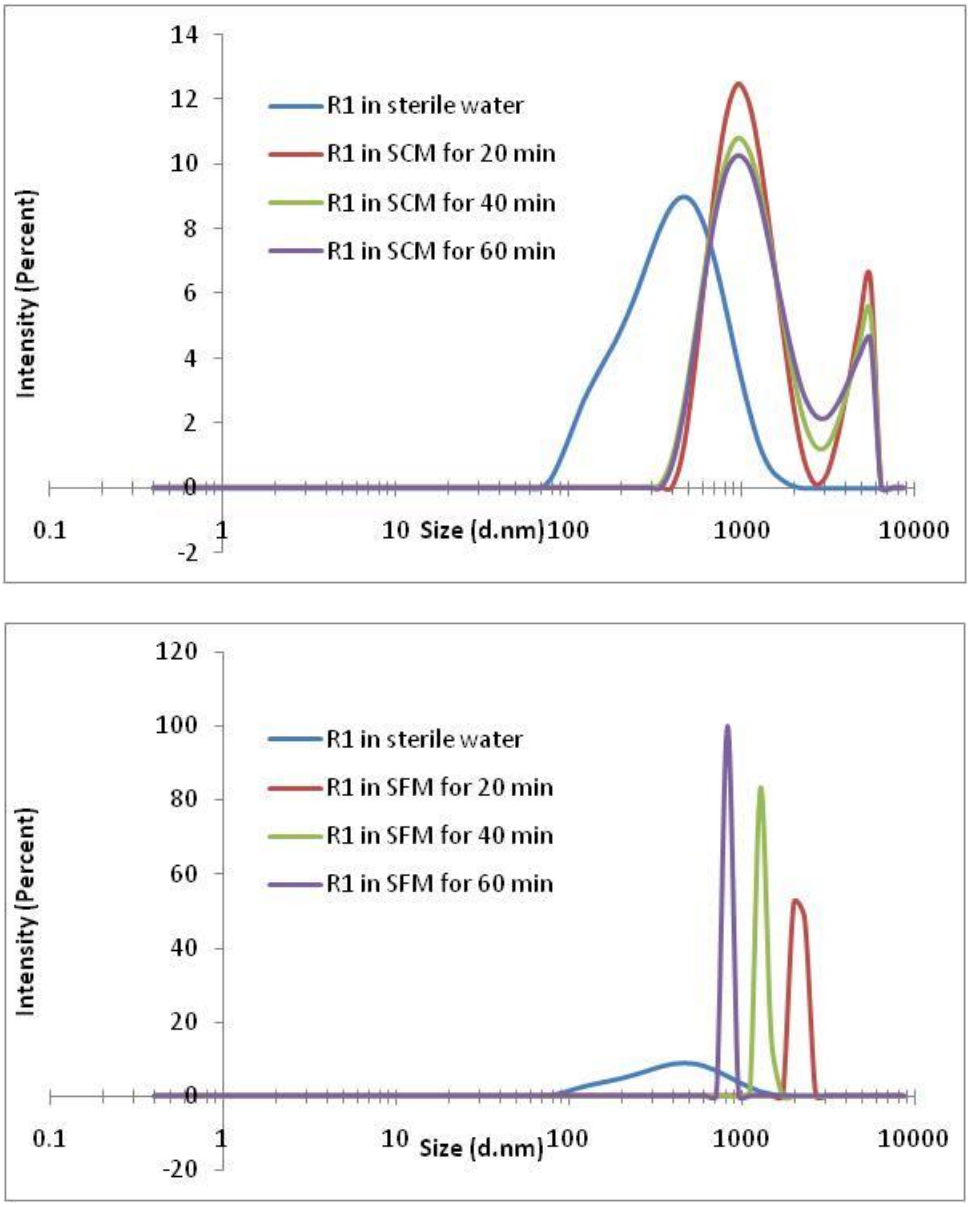

Figure 5.3 (f) Size distribution by intensity data obtained with DLS for nanorods R1 in sterile water, SCM and SFM, each coloured line represents an average of minimum three measurements

Figure 5.4 and 5.5 illustrate the change and trend in particle diameter for the nanocubes (C1, C2, and C3), nanospheres (S1 and S2), and nanorods (R1) when dispersed in SCM and SFM respectively, over a period of 60 minutes. The zeta potential mesurements are summarised in table 5.5.

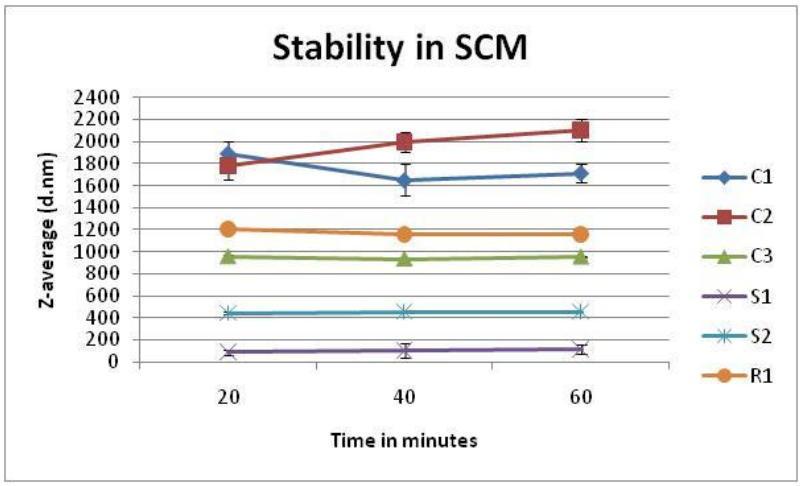

Figure 5.4 Illustration of the change and trend in particle diameter for nanocubes (C1, C2, and C3), nanospheres (S1 and S2), and nanorods (R1) in SCM over a period of 60 minutes (by DLS). The stability order is S2>C3>R1>C1>C2>S1

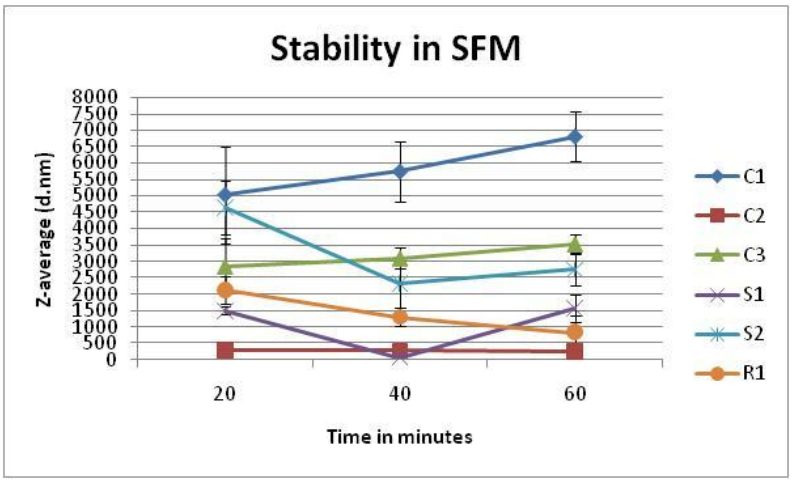

Figure 5.5 Illustration of the change and trend in particle diameter for nanocubes (C1, C2, and C3), nanospheres (S1 and S2), and nanorods (R1) in SFM over a period of 60 minutes (by DLS). The stability order is C3>C2>C1>S2>R1>S1

Table 5.5 Change in the zeta-potential of the investigated ceria samples pre and post treatment with SCM and SFM

	Sample	Zeta Potential (mV)					
	Pure SCM	-0.846±0.405 (pH+7.4)					
	Pure SFM	-1.62±0.96 (pH+7.3)					
Morphology		Pristine NPs	pH	In SCM	pH	In SFM	pH
Nanocube	C1	+5.71±0.16	+6.9	-1.34±0.13	+7.2	-0.28±0.05	+7.2
Nanocube	C2	+26.9±1.72	+7.1	-1.38±0.11	+7.2	-0.33±0.03	+7.2
Nanocube	C3	-2.20±0.041	+7.2	-1.43±0.14	+7.3	-0.51±0.03	+7.2
Nanosphere	S1	+0.024±0.012	+7.9	-1.46±0.07	+7.4	-0.69±0.09	+7.3
Nanosphere	S2	+0.094±0.023	+7.3	-1.40±0.03	+7.3	-0.39±0.01	+7.2
Nanorod	R1	-3.00±0.072	+7.0	-1.27±0.08	+7.3	-0.42±0.07	+7.2

5.5 Agglomeration detection and visualisation by reflectance confocal microscopy (RCM)

Aggregation behaviour of all the six samples (nanocubes C1, C2, and C3, nanospheres S1 and S2, and nanorods R1) has also been observed and visualised using reflectance confocal microscopy (RCM). Unlike other studies, TEM could not be used here as the SCM and SFM formed a concentrated thick layer on the grid surface leading to the depletion of the carbon coating and due to limitations of the experiment, samples could not be diluted. TEM grids were prepared using drop method. A drop of the NP sample dispersed in cell culture media was put on the holey carbon grid and left for air drying while kept covered to prevent contamination. We found that both SCM and SFM lead to the depletion of carbon coating on the grid. We also tried tweaking the grid preparation method by leaving the sample on the grid for only few minutes but this also didn't solve the problem. However, RCM proved to be an effective technique to visualise the aggregation behaviour.

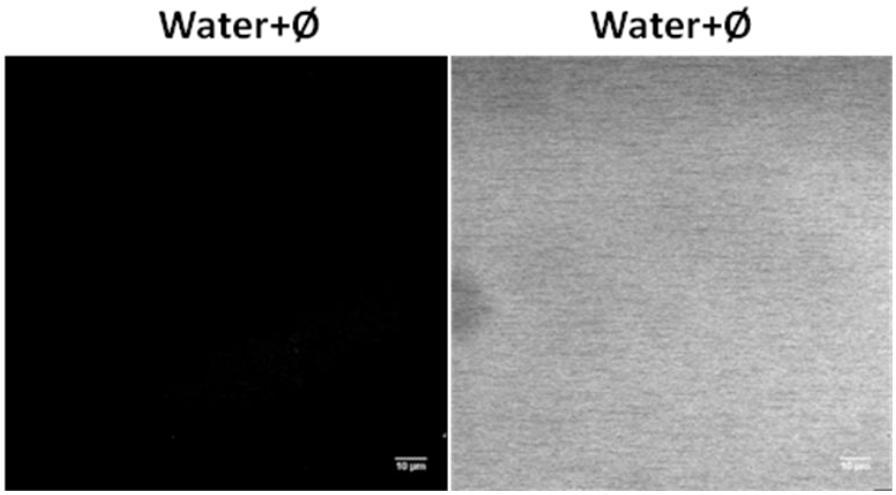

Figure 5.6 (a) Con-focal reflectance microscopy images and corresponding bright field images of sterile water only.

The nanoparticle sample was mounted on the clean slide by putting a drop of the pristine particles suspended in water and then later covering it with a coverslip. A similar procedure was used for particles treated with SCM and SFM. Before the sample imaging, a blank slide was imaged with a drop of ultra pure water to eliminate any chances of false reflectance by dust or any unwanted particles and was saved as a background image. The blank image is illustrated in figure 5.6 (a) and reveals no signal or reflectance. The confocal microscopy images for the investigated samples are illustrated in figures 5.6 (b-g).

Reflectance confocal image acquisitions were obtained using the laser 488 and the reflectance option from confocal microscope (Zeiss LSM 710 Confocor 3) equipped with an oil immersion objective (PLAPO 63x/1.40 oil DIC M27). Z-series of images were taken at 0.2 μm increment (more details about the technique have been discussed in chapter 2).

5.5.1 Results and discussion: This method potentially allows us to image the true dispersion of ceria NPs in water or culture media and identify any agglomerates. There are, however, several disadvantages with this technique. Transmission electron microscopy can easily provide individual measurements of the particles and one can quantify the aggregates size, so a quantitative comparison can be easily made between individual particles and aggregates but in this case, the resolution is not very high and so the quantification of size and shape is not straightforward. However, the images obtained can provide some visual information about the particle behaviour in complex media. Figure 5.6 (b-g) illustrate the reflectance confocal microscopy images for all the six ceria samples illustrated in table 5.1. The images clearly depict the aggregation behaviour of synthesised particles in SCM and SFM. It is evident from all the images that the particles in sample C1, C2, C3, S2 and S1 are more stable in SCM as compared to when treated with SFM except sample S1 which does not show much difference in reflectance images when dispersed in both SCM and SFM. In the images, the individual

particles from the pristine sample as well as the stable particles in SCM can be easily identified and distinguished between the comparatively larger particles obtained on treatment with SFM (A large number of white dots can be seen on a dark background). The inset images also provide a better picture of the particle distribution in the sample. In figures 5.6 (b-g), the first column represents the reflectance image of pristine particles dispersed in sterile water along with the corresponding brightfield image, the second and third columns represent the reflectance by the sample treated with SFM and SCM along with their bright field images respectively. The results obtained cannot be directly compared with those obtained by DLS because the data obtained by RCM cannot be quantified.

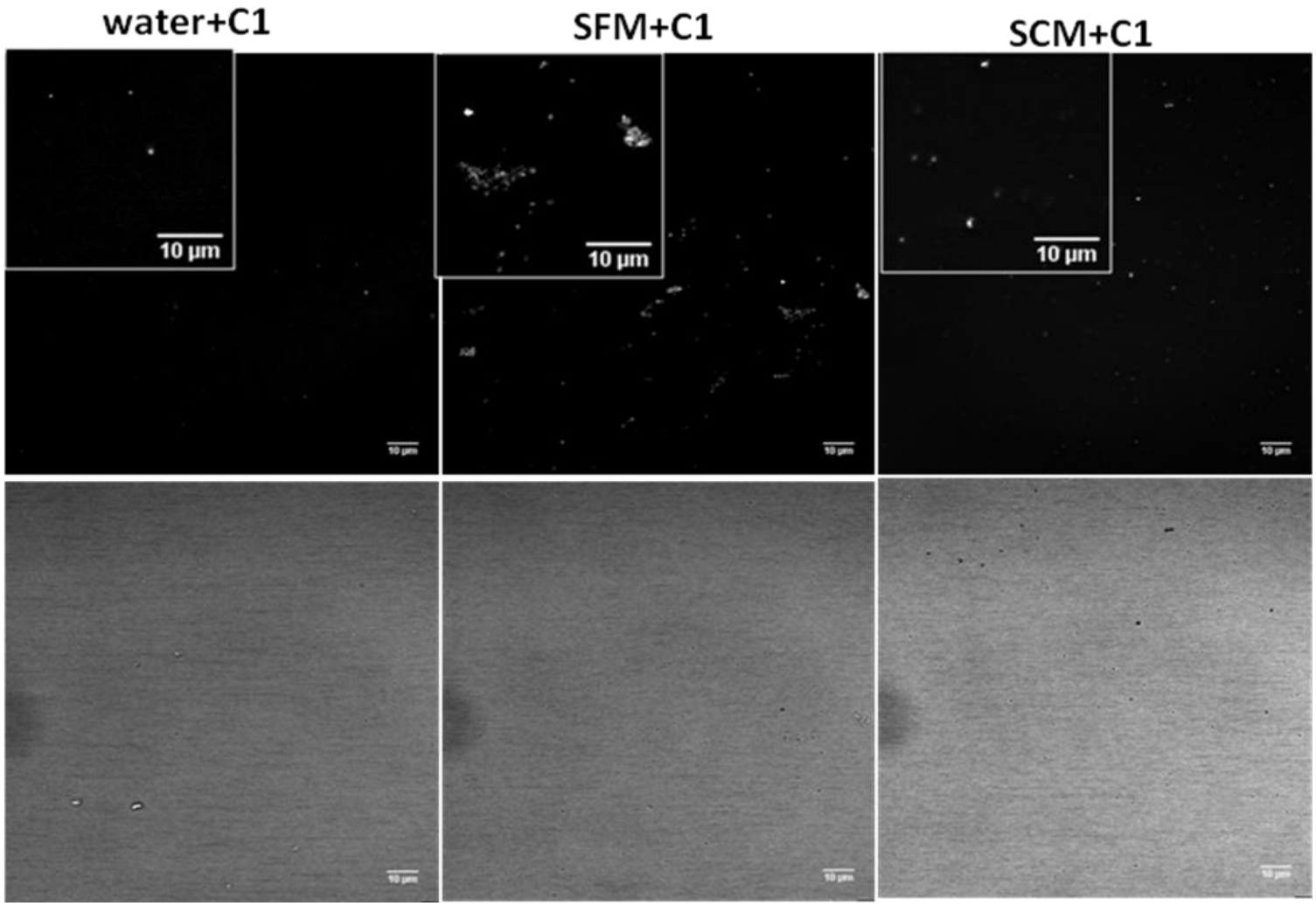

Figure 5.6 (b) Con-focal reflectance microscopy images and corresponding bright field images of C1 in sterile water, SFM and SCM

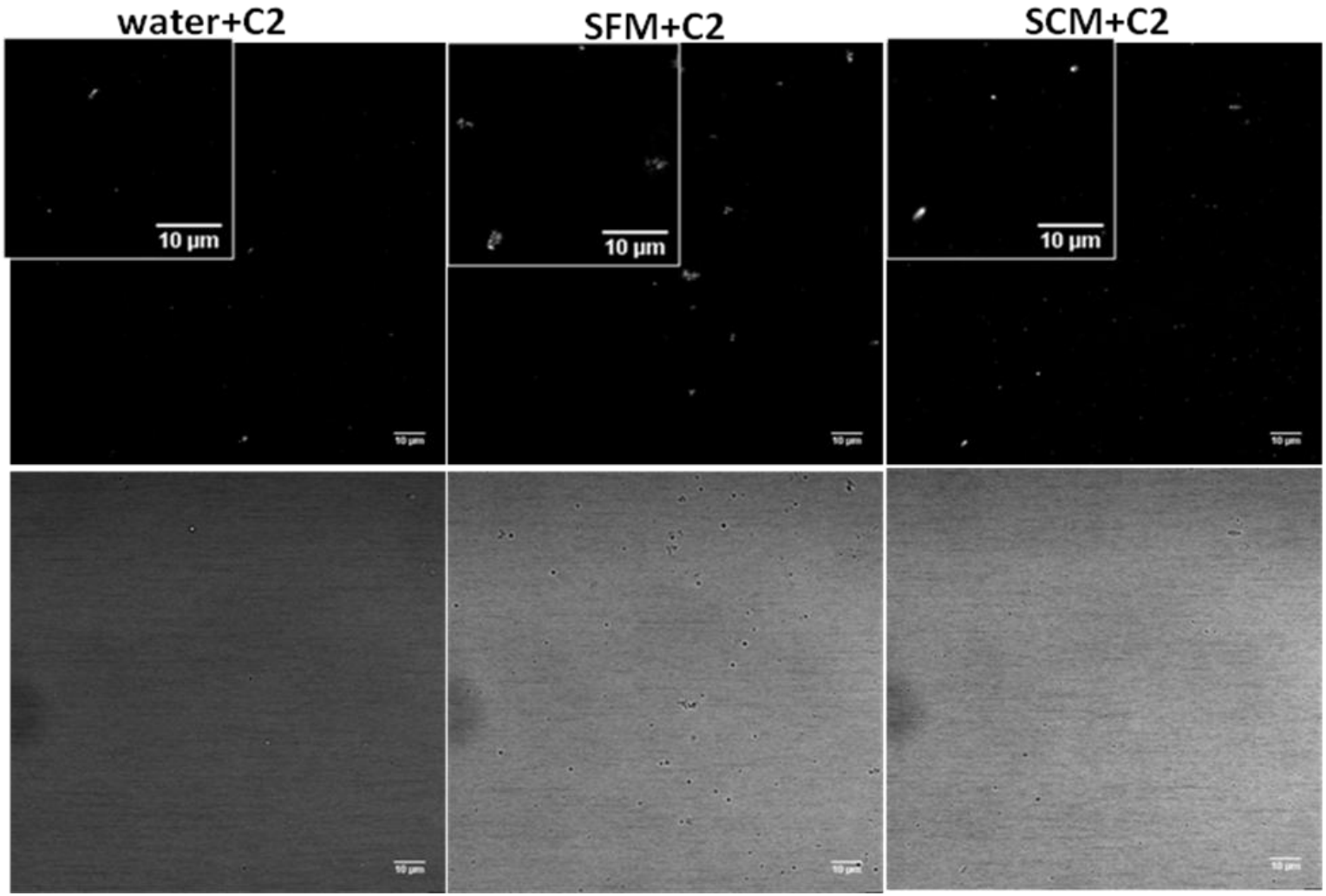

Figure 5.6 (c) Con-focal reflectance microscopy images and corresponding bright field images of C2 in sterile water, SFM and SCM

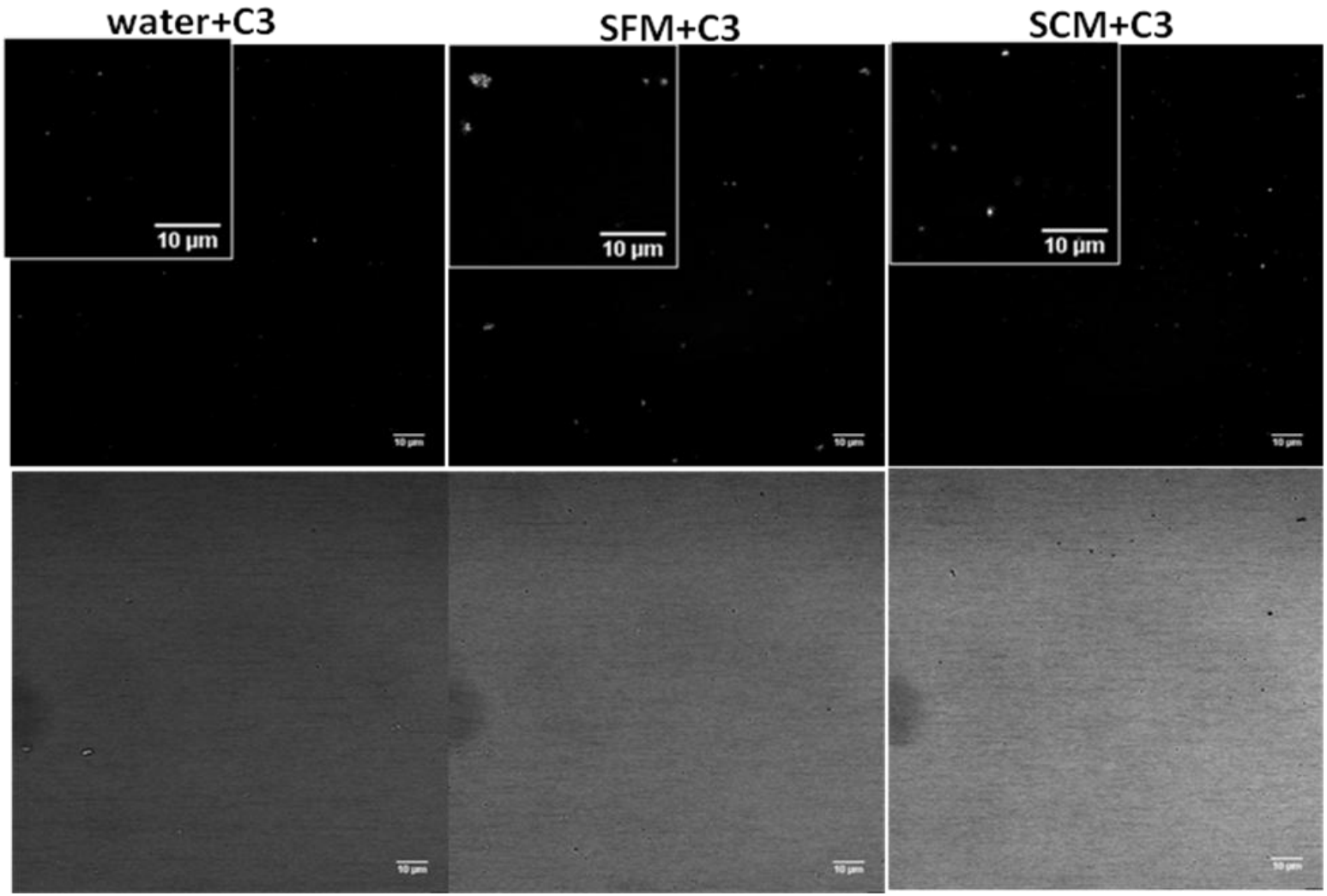

Figure 5.6 (d) Con-focal reflectance microscopy images and corresponding bright field images of C3 in sterile water, SFM and SCM

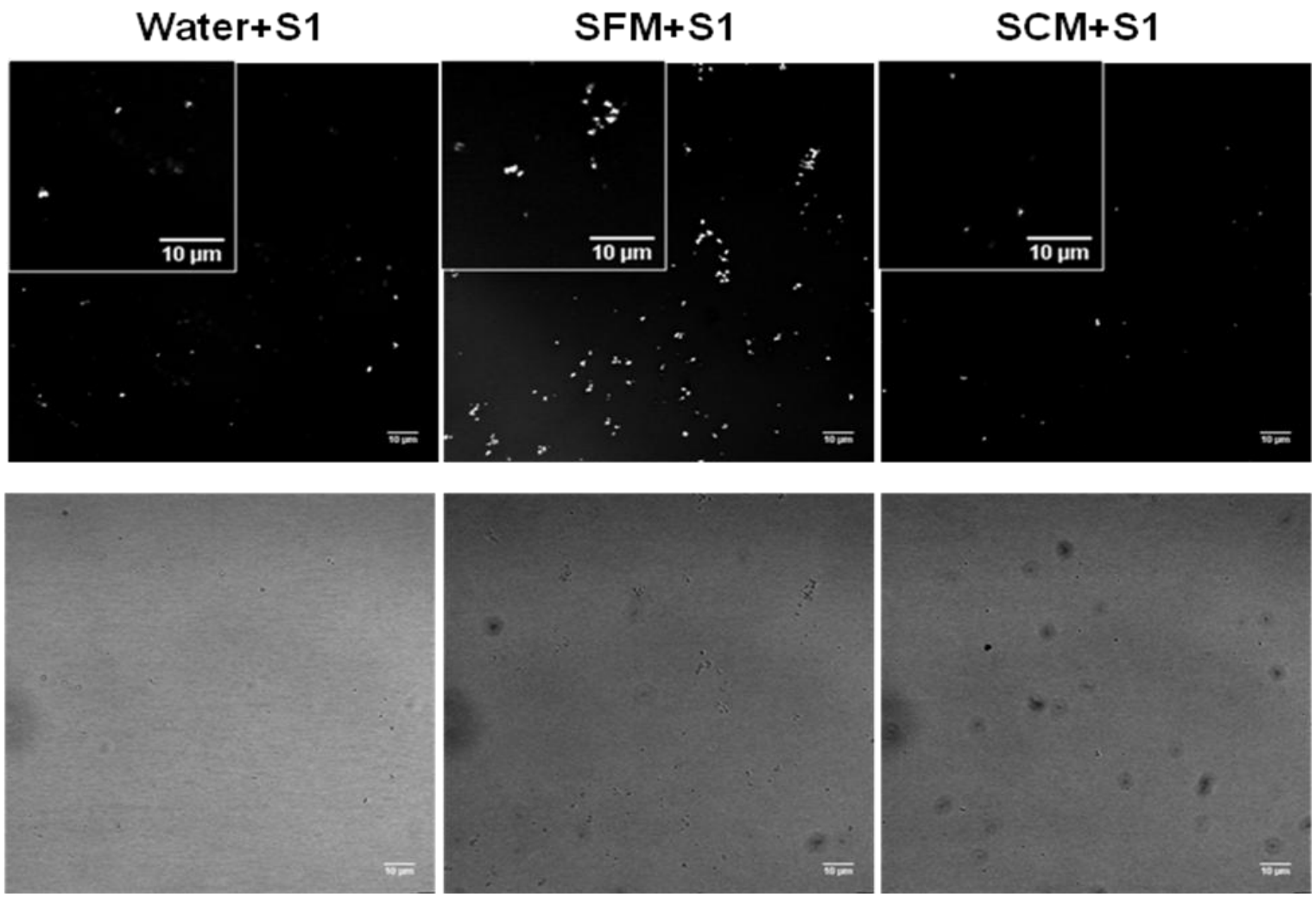

Figure 5.6 (e) Con-focal reflectance microscopy images and corresponding bright field images of S1 in sterile water, SFM and SCM

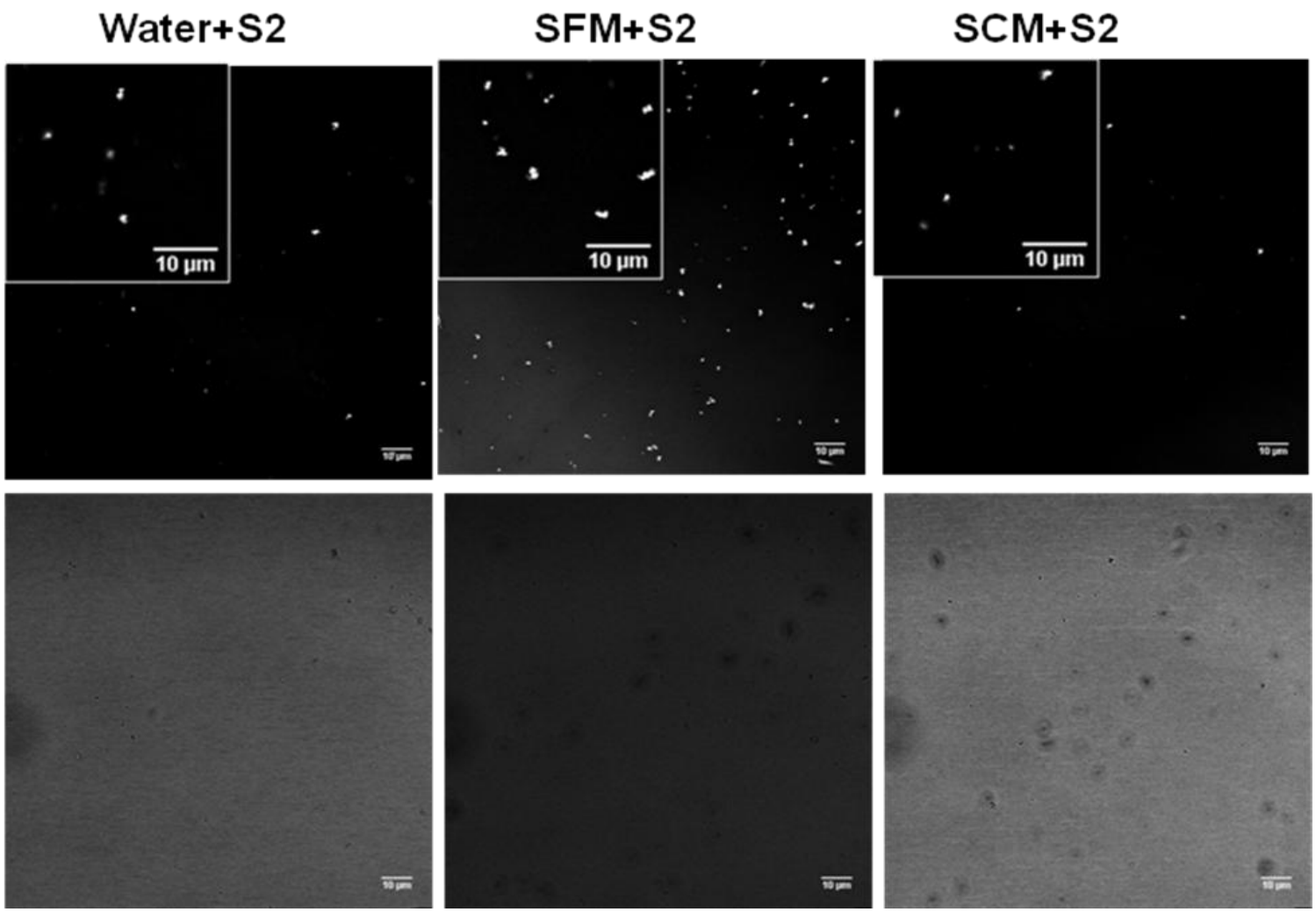

Figure 5.6 (f) Con-focal reflectance microscopy images and corresponding bright field images of S2 in sterile water, SFM and SCM

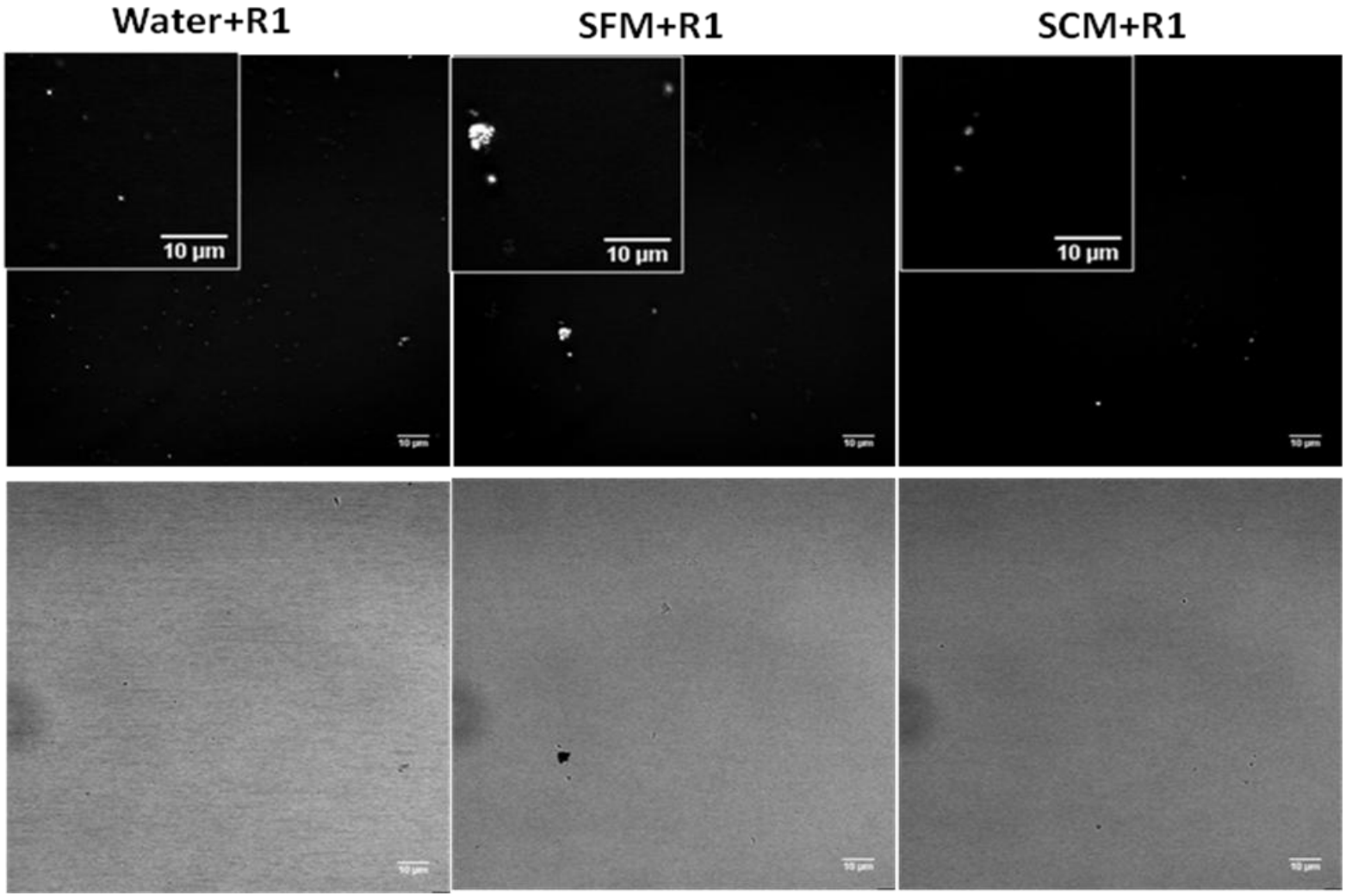

Figure 5.6 (g) Con-focal reflectance microscopy images and corresponding bright field images of R1 in sterile water, SFM and SCM

5.6 Uptake and internalisation of ceria NPs by HeLa A549 cells

5.6.1 Cerium oxide uptake assay

Stock solutions of ceria nanoparticles (10 mg ml^{-1}) prepared in sterile distilled water were sonicated for 1 min using an ultrasonic bath and diluted to the required concentration using serum-containing media (SCM). HeLa cells were incubated in SCM in the presence or absence of ceria NPs at a final concentration of 500 μg ml^{-1} at 37 ^{0}C for 60 min in a 5% CO2 incubator. Cells were washed with SCM then left for 1h at 37 °C in SCM. Exposure was conducted for 30 min at 37 °C, 5% CO_2, and then cells were washed twice with phosphate-buffered saline 1X, PBS (Lonza), to remove any ceria particles outside the cells. The cells were then fixed in 4% parafornaldehyde (PFA) for 10 min at room temperature and then washed with Ammonium chloride (NH_4Cl) then with PBS and mounted on microscope slides in Vectashield Mounting Media with DAPI (VECTOR Laboratories). The samples were examined under a confocal microscope (Zeiss LSM 710 Confocor 3) equipped with Ar and He/Ne lasers.

5.6.1.1 Concentration of ceria nanoparticles

In the larger FABLE study, when ceria uptake experiments were started, we performed experiments based on incubation of A549 cells with increasing nanoparticle concentrations to determine a nanoparticle concentration that does not induce cytotoxicity and allows visualising ceria NPs by reflectance microscopy. We found out that 500 μg ml^{-1} was the lowest concentration that we could use to clearly visualise the internalised ceria nanoparticles by reflectance microscopy without inducing any cytotoxicity.

5.6.2 Results and discussion of uptake studies

Figure 5.7 shows the brightfield, reflectance and corresponding merged images in the same scale and position of HeLa cells incubated in SCM for 60 min at 37 ºC. This is a representative image of how the A549 cells look using the confocal reflectance microscopy.

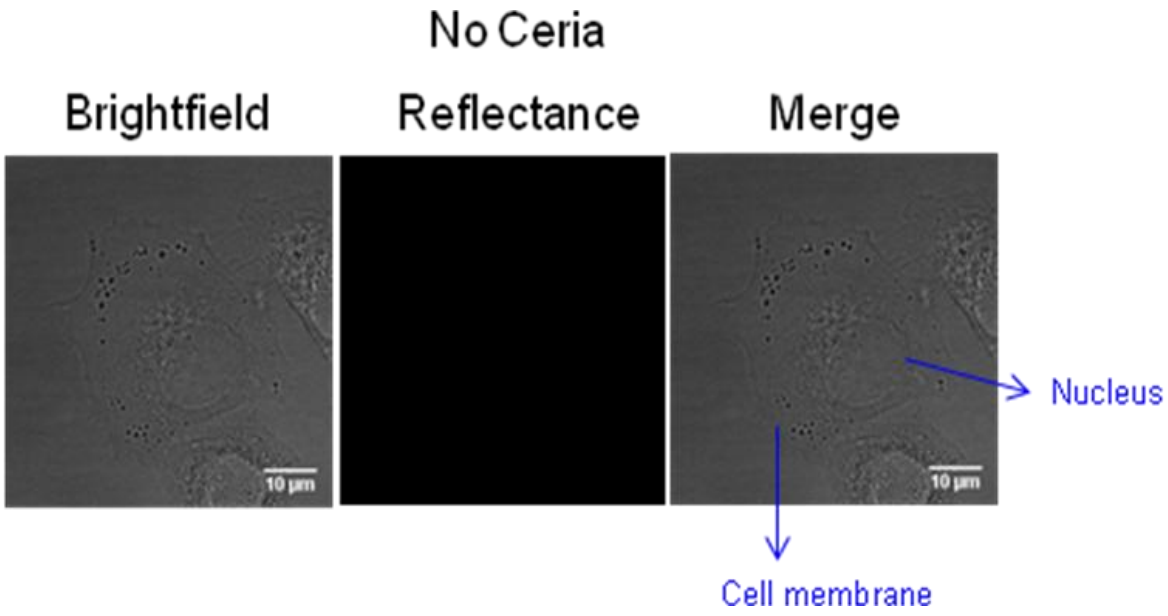

Figure 5.7 Confocal reflectance microscopy images along with the corresponding bright field and merged images of A549 cells in the absence of ceria NPs.

Result of in vitro cellular uptake of ceria NPs are shown in Figure 5.8 (a-f). The CRM images indicate that particles with sizes (<10nm) have shown internalisation and uptake by the A549 cells. Sample S1 (PEG 1500 capped nanospheres) showed complete uptake as is evident from figure 5.8 (d) whereas sample S2 (PEG 600 capped nanospheres) and C3 (nanocubes) were partially uptaken by the A549 cells, figures 5.8 (e and c) respectively. The results can be compared to the stability data obtained by DLS (table 5.3). Sample S1 showed least stability in SCM with very high polydispersity index by DLS. Whereas, S2 and C3 showed, comparatively more stability with particle sizes of 450 nm and 947 nm respectively and

hence partial uptake. Based on stability results, we expected that serum stabilised particles would remain suspended in the cell culture plate in the supernatant SCM and may or may not interact with the cell surface, however this is not the case here. Further, it was found that after internalisation in S1, S2 and C3, the nanoparticles are localised only in cytoplasm. None of the particles were seen in the nucleus. The bright white spots from the ceria NPs are clearly visible in the reflectance images. The red dots in the merged images correspond to the ceria NPs and indicate the entry of ceria NPs in A549 cells for sample S1 and partial uptake for S2 and C3. Partial uptake refers to that some of the particles were uptaken by the cells and some particles can be seen outside the cell membrane. No internalisation was observed for samples C1, C2 and R1. The images reveal that the samples C1, C2 and R1, aggregated during incubation and the big aggregates are present either outside the cell or attached to the cell membrane and there was no uptake. These differences in cellular uptake could be ascribed to so many factors such as the size, shape, surface composition and surface charge of the particles and even cell response during uptake assays and have been discussed in the conclusion section. The results are summarised in table 5.6

Table 5.6 Illustration of cell response (A549) towards particles of different shapes and sizes

Sample code	Morphology	Size (nm)			Uptake by A549 cells
		(TEM) particles in water	(DLS) particles in water	(DLS) particles in SCM	
C1	Nanocube	31±8	94±1	1754±125	No uptake
C2	Nanocube	21±8	114±1	1959±168	No uptake
C3	Nanocube	16±5	133±4	952±13	Partial uptake
S1	Nanosphere	5±3	86±1	107±15	Uptake
S2	Nanosphere	6±3	89±1	451±5	Partial uptake
R1	Nanorod	83±56 (Length) 16±6 (width)	339±7	1177±27	No uptake

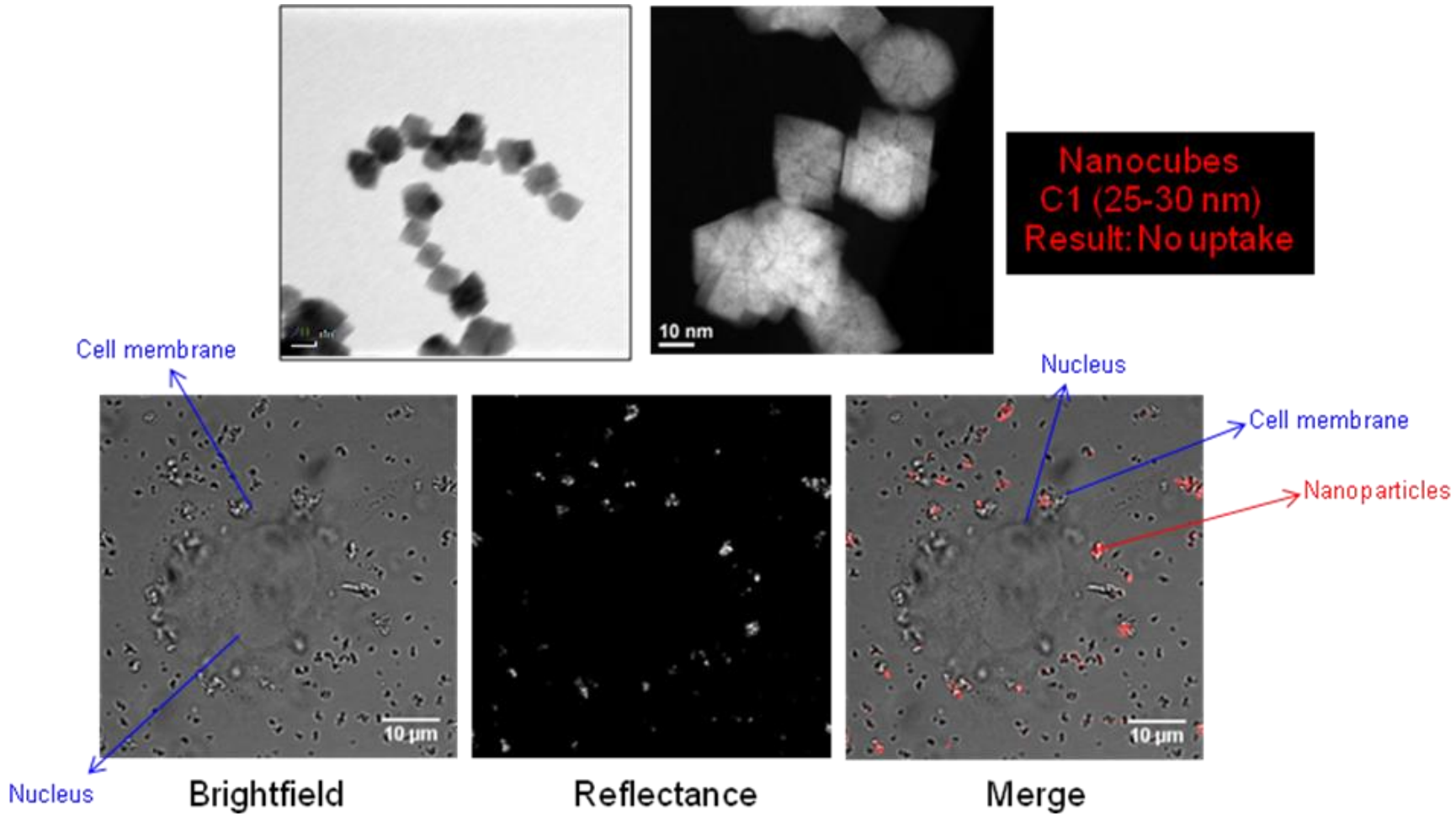

Figure 5.8 (a) Representative HRTEM images of C1 (top row) and confocal reflectance microscopy images along with the corresponding bright field and merged images of NPs in cells in cellular uptake tests. The white dots in reflectance image and the red dots in the merged image represent the ceria NPs.

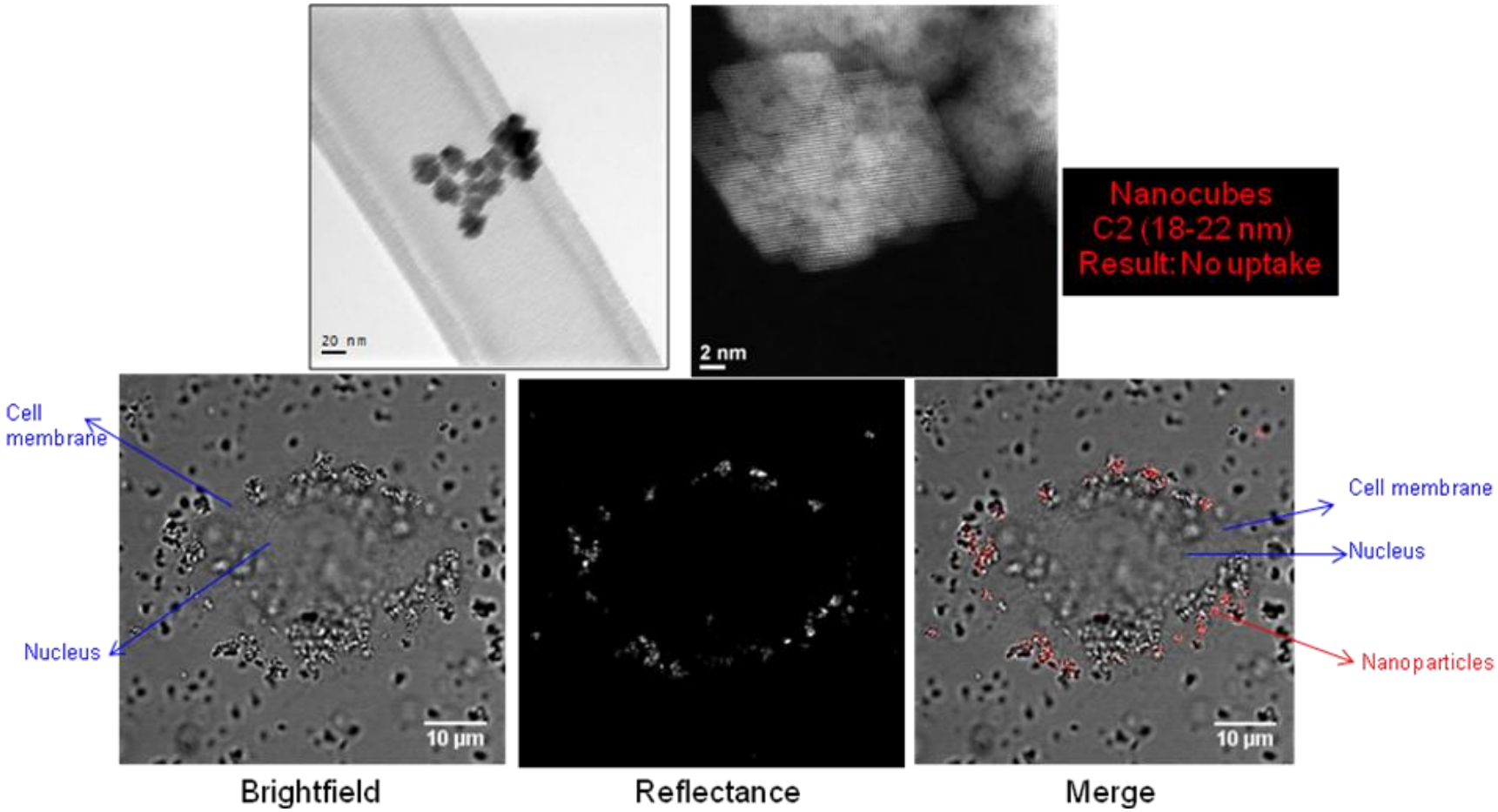

Figure 5.8 (b) Representative HRTEM images of C2 (top row) and confocal reflectance microscopy images along with the corresponding bright field and merged images of NPs in cells in cellular uptake tests. The white dots in reflectance image and the red dots in the merged image represent the ceria NPs.

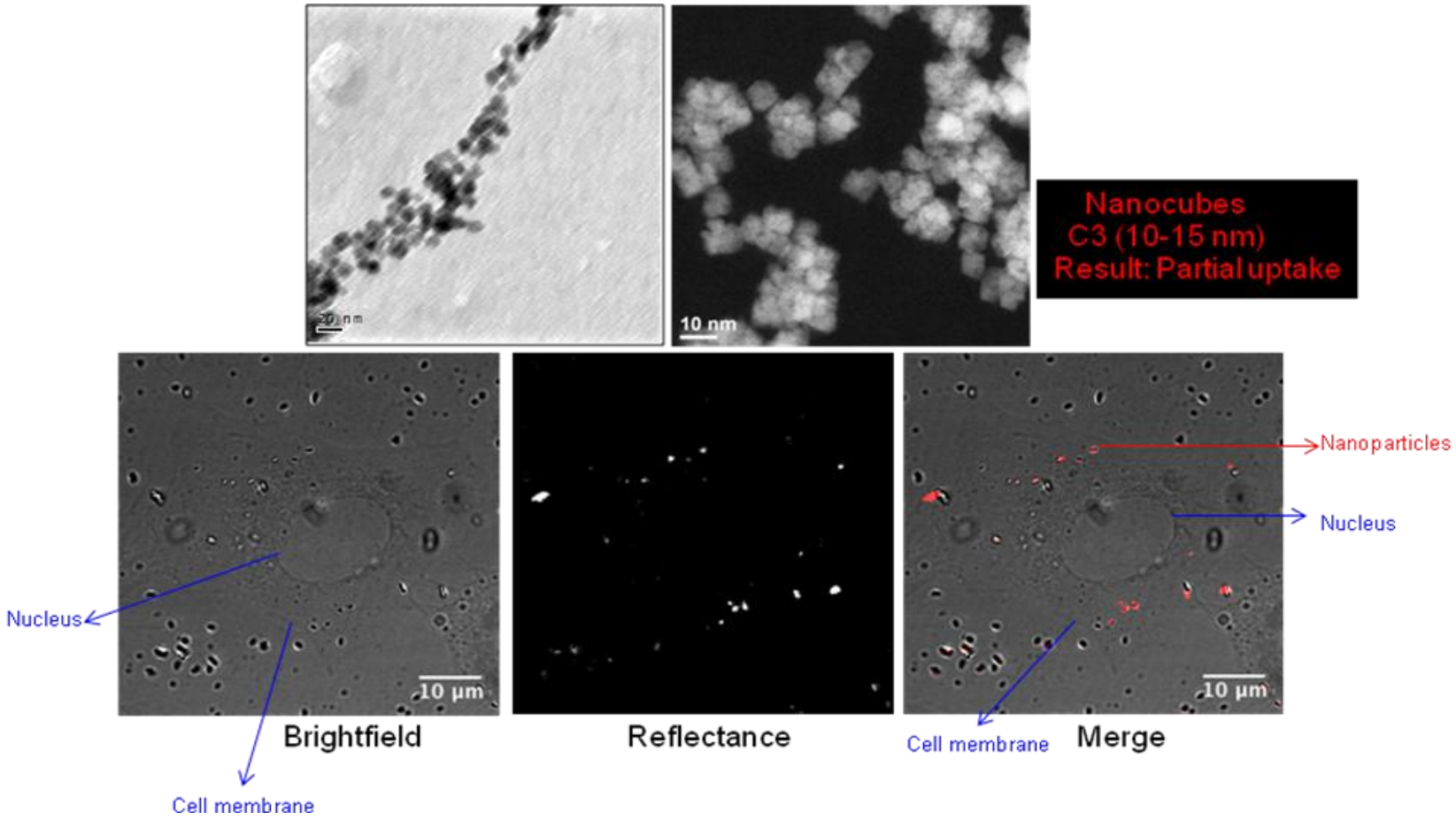

Figure 5.8 (c) Representative HRTEM images of C3 (top row) and confocal reflectance microscopy images along with the corresponding bright field and merged images of NPs in cells in cellular uptake tests. The white dots in reflectance image and the red dots in the merged image represent the ceria NPs.

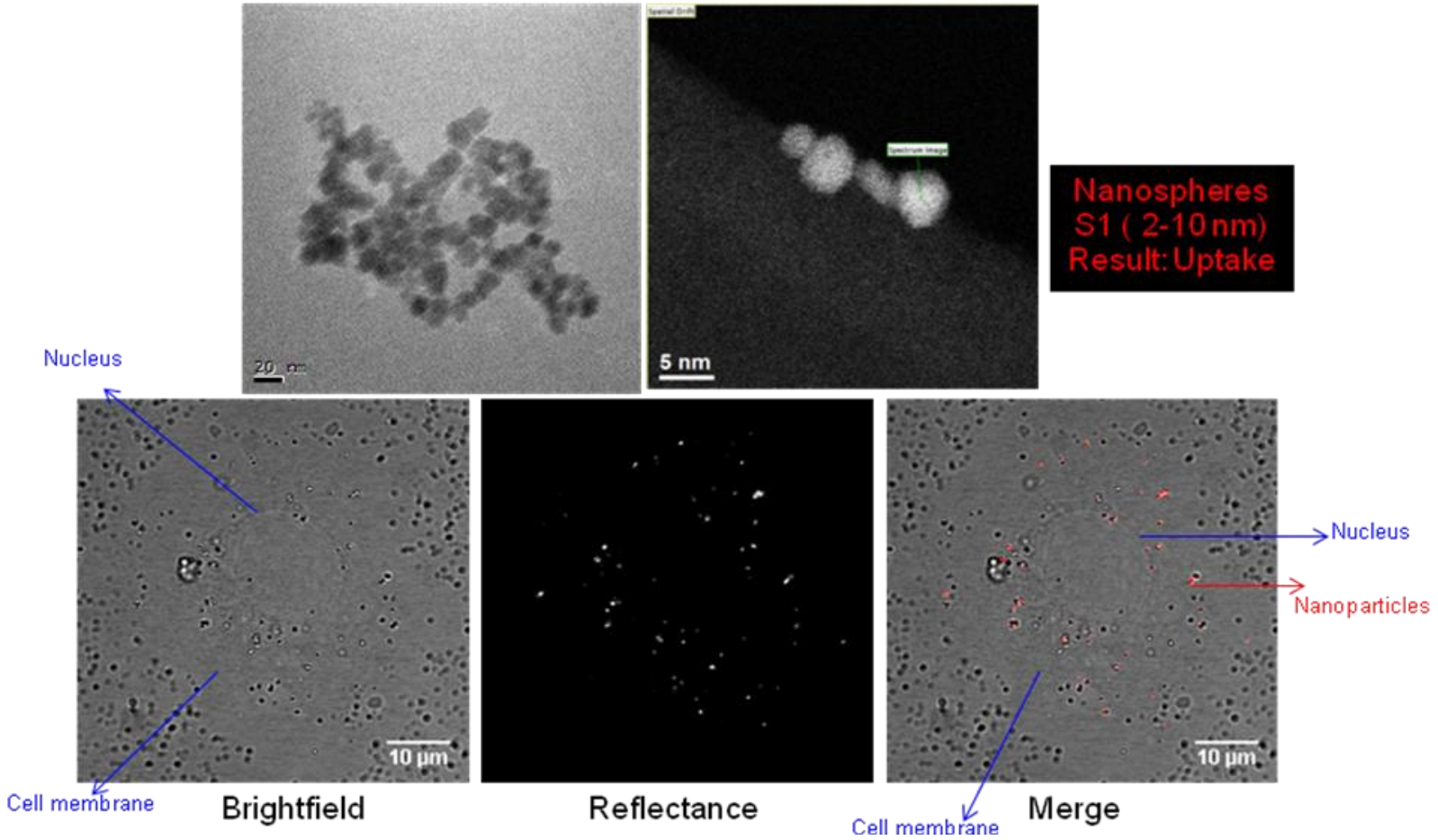

Figure 5.8 d) Representative HRTEM images of S1 (top row) and confocal reflectance microscopy images along with the corresponding bright field and merged images of NPs in cells in cellular uptake tests. The white dots in reflectance image and the red dots in the merged image represent the ceria NPs.

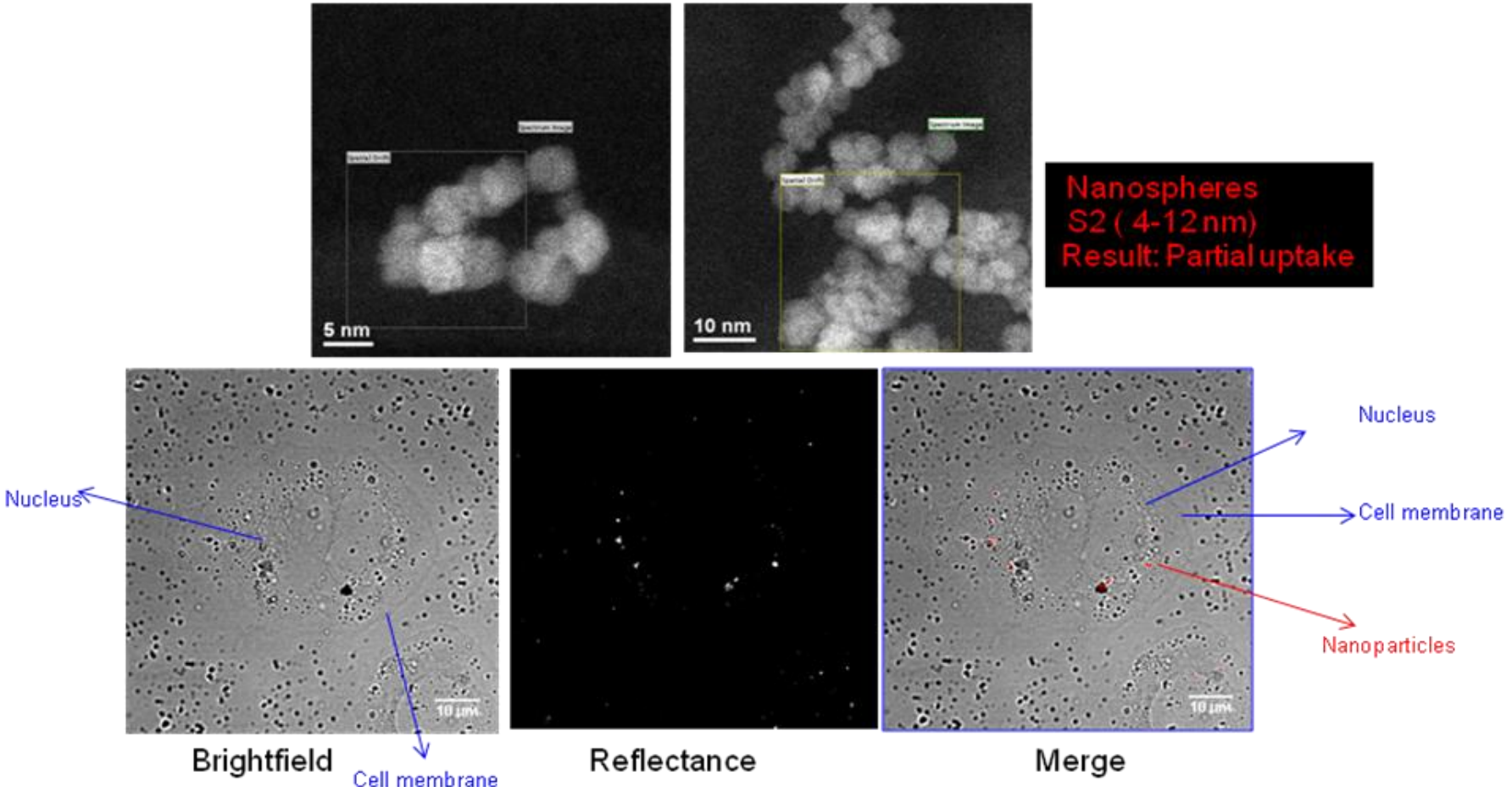

Figure 5.8 e) Representative HRTEM images of S2 (top row) and confocal reflectance microscopy images along with the corresponding bright field and merged images of NPs in cells in cellular uptake tests. The white dots in reflectance image and the red dots in the merged image represent the ceria NPs.

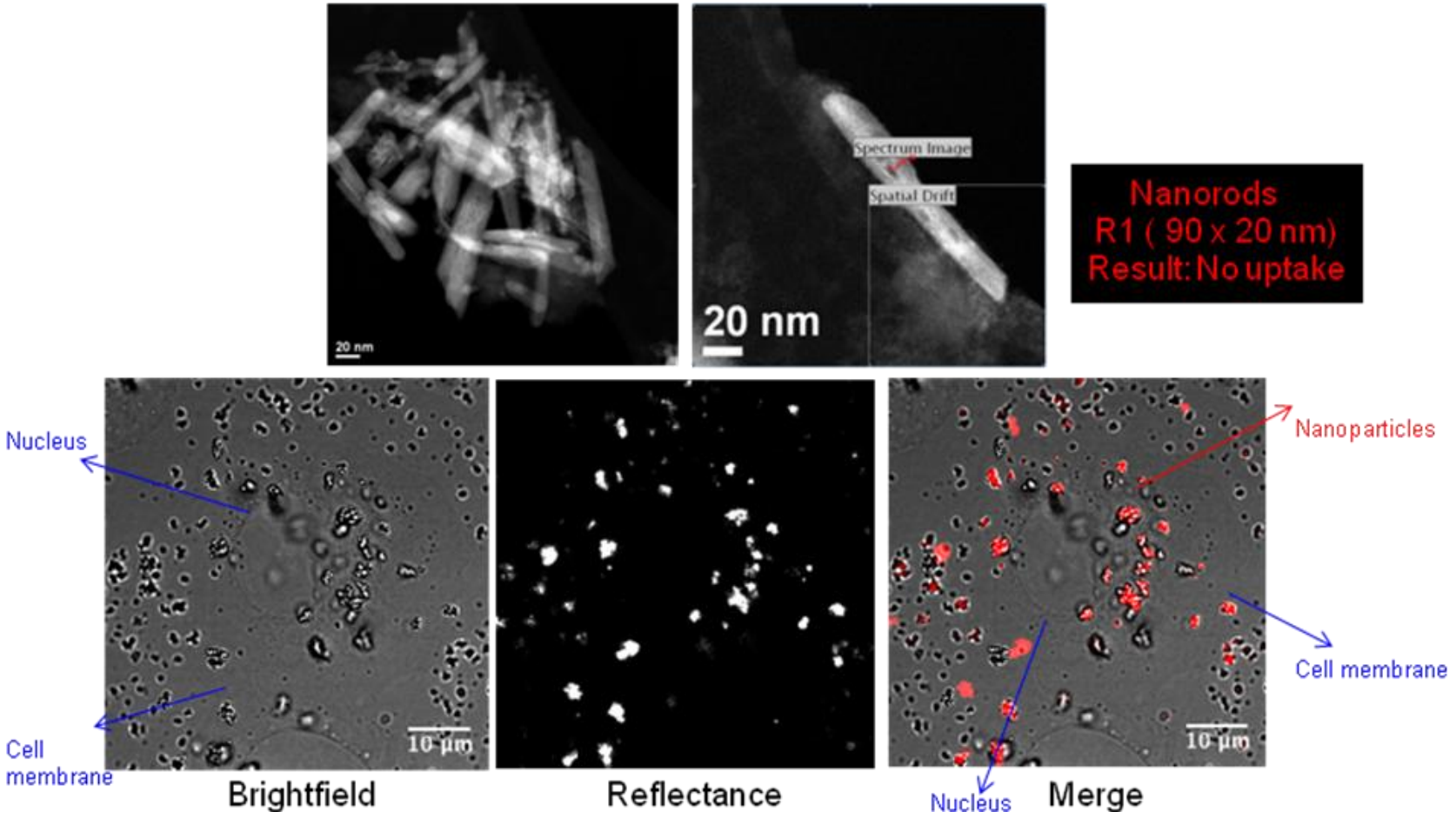

Figure 5.8 f) Representative HRTEM images of R1 (top row) and confocal reflectance microscopy images along with the corresponding bright field and merged images of NPs in cells in cellular uptake tests. The white dots in reflectance image and the red dots in the merged image represent the ceria NPs.

5.7 Conclusions

As discussed above, the characterization of NPs in pristine conditions as well as in complex media is essential for the toxicity assessments. Studies have shown that the size, shape, surface reactivity, solubility, and degree of aggregation impart for their differential response in biological systems. In this study, NPs have been dispersed and characterised in cell culture media to mimic the realistic conditions during uptake assays in order to better understand the behaviour of NPs when treated with the biological media. We have assessed the ceria nanoparticle agglomeration in the serum containing media and serum free media and their cellular interaction and uptake by human lung epithelial cells using six different types of ceria NPs with different shapes and sizes, three nanocube samples (C1, C2 and C3), two nanosphere samples (S1 and S2) and a nanorod sample (R1). DLS was used to measure the hydrodynamic diameter and polydispersity index (PdI) of the NPs in the water as well in the culture media. The electrophoretic mobility of the particles was measured using Zetasizer nano from Malvern instruments. The zeta potential measurements have been carried out for both pristine as well as particles treated with SCM and SFM whereas reflectance confocal microscopy (RCM) was used in this work to detect the aggregation behaviour and visualise the uptake and internalsation of ceria nanoparticles by the human lung epithelial cells (also known as HeLa A549 cells).

In-situ DLS study reveals that most of the particles form a comparatively stable suspension in SCM whereas their treatment with SFM leads to large aggregates except sample S1 (nanospheres) which showed instability in both SCM and SFM (table 5.3 and 5.4). This stability by serum could be attributed to the presence of albumin protein in the serum which is previously known to stabilise the particles (Lynch and Dawson, 2008, Patil et al., 2007). A

dynamic layer of protein or a corona is known to adsorb on the particle surface leading to stability. This was discussed in detail in section 5.2.4 above.

All the three nanocube samples, C1, C2 and C3, have been synthesised by homogenous precipitation method using the same precursors but in different concentrations (details in chapter 3) leading to three different sized nanocubes. However their stability behaviour was different in SCM and SFM (table 5.3 and 5.4). It was found that nanocube sample C3 was comparatively more stable than C1 and C2 in both SCM as well as SFM and the order of stability is C3>C1>C2. This could be attributed to the surface charge modification of these particles when in contact with SCM and SFM. Both C1 and C2 were positively charged pre treatment with the cell culture media whereas C3 was negatively charged. However SCM and SFM has great impact on the surface charge of these particles post treatment. The results are in table 5.5.

Both nanosphere samples S1 and S2, are PEG capped, but with different molecular weights of PEG. S1 is capped with PEG 1500 (MW) and S2 is capped with PEG 600 (MW). Both the samples have been synthesised by sonochemical method using the same cerium precursor but have showed different stability regime when dispersed in SCM and SFM. Stability data shows that S2 is more stable than S1 in both SCM and SFM (table 5.5). The results demonstrate that increase in chain length of the stabiliser due to an increase in molecular weight also plays an important role towards the stability of the particles. Also the zeta potential measurement show that both S1 and S2 acquired the charge of SCM and SFM post treatmemt.

The order of stability for all the six samples in SCM is S2>C3>R1>C2>C1>S1 whereas in SFM is C1>S2>R1>C3>C2>S1 (as obtained by DLS). Zeta potential was measured in order to gain some insight into the mechanism of nanoparticle size stabilisation. The electrophoretic mobility measurement for pristine particles varied from positive to slightly negative. After treatment with SCM the zeta potential for all the samples turned to almost zero at pH 7.3±0.1. The difference between the zeta potential observed for SCM and SFM is very less. so it is very hard to tell the difference in the presence and absence of serum. The hydrodynamic diameter, polydispersity index (PdI) and zeta potential of the NPs obtained pre and post-treatment with SCM and SFM is detailed in table 5.5. Similar kind of results were obtained on visualising the aggregation behaviour of particles in SCM and SFM using reflectance confocal microscopy. Due to lack of quantification data by RCM, the results cannot be compared with DLS. The experimental data obtained from RCM is illustrated in figures 5.6 (b-g).

The results from in vitro ceria uptake experiments conclude that particles with sizes (<10nm) are completely internalised and uptaken by the A549 cells. Sample S1 (PEG 1500 capped nanospheres) showed complete uptake, figure 5.8 (d), whereas sample S2 (PEG 600 capped nanospheres) and C3 (nanocubes) were partially uptaken by the A549 cells, figures 5.8 (e and c) respectively. The results can be compared to the stability data obtained by DLS (table 5.5). Sample S1 showed least stability in SCM with very high polydispersity index by DLS. Whereas, S2 and C3 showed, comparatively more stability with particle sizes of 446 nm and 971 nm respectively and hence partial uptake. The uptake process involves attachment of the particles on the cell surface followed by internalisation. No internalisation was observed for samples C1, C2 and R1. The images reveal that the samples C1, C2 and R1 aggregated during incubation and the big aggregates are present either outside the cell or attached to the

cell membrane and there was no uptake. This indicate that shape of the particles can have profound effect on uptake by the cells, the particles got attached to the cell membrane but were not internalised. The shape dependent uptake was ranked as spheres>cubes>rods. This could be attributed to the high aspect ratio of cubes and rods. The idea is consistent with some other findings in the literature which concluded that particles with high aspect ratio exhibit reduced or no endocytosis. The intake of nanorods or cylindical particles would also depend on the basis that whether the rods were perpendicular or parallel to the cell surface when in contact. In the former case, it is believed to favour the endocytosis process. Particles with high aspect ratio undergo longer wrapping times than spherical nanoparticles due to greater energy required for their engulfment, and therefore take longer time to internalize. Surface modifications may also enhance or inhibit the uptake process as proteins present in the serum exhibit selective binding affinities to different surface modifications. Protein adsorption on the surface of the nanoparticles mainly depends on electrostatic interaction, hydrophobic interaction and specific chemical interactions between protein and the nanoparticle surface ehich are surface dependent. Both nanosphere samples S1 and S2 are PEG capped but with different molecular weights. However, S1 (capped with PEG1500) showed a great amount of internalisation whereas S2 (capped with PEG 600) was partially uptaken. The results demonstrate that increase in chain length of the stabiliser due to an increase in molecular weight affects the uptake process. Similarly, nanocube samples C1, C2 and C3, were synthesised by same method (homogenous precipitation) using the same precursors but in different concentrations (details in chapter 3) leading to three different sized nanocubes. However their stability behaviour was different in SCM and hence difference in uptake. Sample S1 has shown a great amount of internalisation, sample S2 and C3 showed partial uptake whereas samples C1, C2 and R1 showed the presence of large aggregates and are present either outside the cell or are attached to the cell membrane and do not get

internalised. The uptake images clearly depict that the internalised particles are localised in the cytoplasm and do not seem to enter the nucleus of A549 cells. The data further concludes that the internalisation seems to be more size dependent and to some extent shape and capping dependent. The order of ceria uptake by A549 in all the NP samples is S1>S2>C3>R1>C2>C1.

The above results clearly demonstrate that size, shape, aggregation behaviour, surface composition and surface charge of the particles play an important role towards cell-nanoparticle interaction or cellular responses.

6 Conclusions and future work

6.1 Overview

Nanotechnology and the use of nanoparticles (NPs) has remarkably increased in the past few years and is attracting a lot of public interest. As a result, NPs are increasingly being released into the environment. Ceria NPs, due to their widespread applications, have also attracted a lot of concern about their toxic effects on both human health and environment. Cerium is a a rare earth inner transition metal that is being used in its oxide form to create novel nanomaterials. Cerium occurs in two oxidation states, Ce (III) and Ce (IV), and has the unique ability to readily switch between these two states in the absence and presence of oxygen. It is commonly referred as CeO_{2-x}. Though most of the cerium is present as Ce (IV), the reactive sites are presumed to be redox active and present in the Ce (III) state in the absence of oxidants. There is some contradiction in literature about the oxidant /antioxidant behaviour of nanoceria and the toxicity and protective role of ceria NPs have both been related to the oxidation state of the surface atoms (Ce (III)/Ce (IV)). It is speculated that the reactivity of the surface associated Ce (III) sites is the most likely source of reactive oxygen species, leading to toxicity/protective role but the exact mechanism is not known. So, there are large gaps in knowledge of whether Ce (III) or Ce (IV) is responsible for such toxic behaviours, their toxicological mechanism and safety assessment.

6.2 Conclusions

The work done in this thesis aimed to investigate some of the above issues that are important in better understanding of the environmental and health effects of nanoceria. A systematic

study was carried out and the conclusions drawn at different steps of the study are outlined below:

6.2.1 Aim 1: To synthesise shape and size selected ceria nanoparticles, both with and without capping agents.

In light of the fact that nanoceria is capable of oxygen storage, which is size and shape dependent (Mai et al., 2005) and that nanoceria can reveal different biological response depending on its physico-chemical characteristics, we produced different sized and shaped ceria NPs coated with capping agents, with different strengths of interaction between core and capping agent/no capping agent and with both steric and charge stabilization using sonochemical, thermal hydrolysis and precipitation methods.

The concentration of the precursors, specially the oxidising agent or reducing agent, reaction time, temperature and even some non-thermodynamic variables such as stirring speed and rate of addition of the oxidant to the reaction mixture showed to play an important role towards the shape and size of the particles formed. All these parameters were carefully recorded for future studies.

6.2.2 Aim 2: Physico-chemical characterization of the manufactured ceria NPs for their size, shape, aggregation, surface charge, composition and oxidation state.

Given the dynamics that are well known to occur within ceria suspensions, it is really important to perform accurate measurements on the size, shape, morphology, aggregation/ agglomeration, surface charge and dissolution (and related parameters) behaviour of these NPs in their pristine form. We found that particles with similar shape but different sizes, synthesised using the same set of precursors and reaction conditions but at different concentration of the precursors lead to different surface charge of the suspension and it varied

from being highly positive charged (large particles) to negative charged (small particle). We found that oxidation state is related to size. The oxidation state of ceria NPs is not uniform throughout the particle and the amount of Ce (III) increases as the particle size decreases, with particles ≤ 2nm to be completely Ce (III). Therefore, oxidation state of ceria could be engineered by synthesising monodispersed NPs with desired sizes which can be further used in specific studies to better understand the toxic behaviour and toxicological mechanism of these NPs.

6.2.3 Aim 3: Quantification of the Ce (III) and Ce (IV) ratios in as-synthesised samples using STEM-EELS and XPS and the technique comparison.

One of the objectives of this study was to ascertain if Ce (III) and Ce (IV) oxidation states of different sized and shaped cerium oxide can be consistently determined using both EELS and XPS. Also, given the uncertainties and contradictions in literature, use of two complimentary methods for the determination and quantification of oxidation state, would allow us to be more accurate.

Both the techniques provided useful information about the Ce (III) and Ce (IV) ratios in the samples. EELS, because of its spatial resolution to analyse individual particles on a 'per particle' basis, was found to be a suitable technique for oxidation state quantification in a localised way whereas XPS was effectively used to quantify ceria oxidation states from the bulk samples. Other general issues associated with nanoparticle analysis such as sample dehydration prior to the study for XPS measurements and beam damage during EELS experiments were also highlighted. We now have a batch of ceria NPs with known size,

shape, morphology, surface charge and oxidation state data. These NPs can be sent to other groups for various toxicological studies.

6.2.4 Aim 4: Dispersion and aggregation studies of ceria nanoparticles in cell culture media (serum containg media (SCM) and serum free media (SFM))

We reported and discussed the dispersion behaviour of some of the synthesised nanoceria (with known physico-chemical properties) in serum containing media (SCM) and serum free media (SFM). *In situ* DLS studies and reflectance confocal microscopy images revealed that most of the particles formed a comparatively stable suspension in SCM whereas their treatment with SFM leads to large aggregates. The surface charge of the ceria suspensions was greatly influenced after their treatment with SCM and SFM and converted from highly positive charged (for example, for nanocube C2, 26.9±1.72 mV) to slightly negative charge post treatment with both SCM (C2= -1.38±0.11 mV) and SFM (C2= -0.33±0.03 mV). The stability behaviour was also found to be different for NPs of same shape and size capped with PEG of different molecular weights (PEG 1500 and PEG 600). Our study has shown that the size, surface charge and presence of capping agent in the suspension impart for their stability in cell culture media. The characterization of NPs in pristine conditions as well as in cell culture media is essential for the toxicity assessments.

6.2.5 Aim 5: Uptake and internalisation studies of ceria NPs in human lung epithelial cells (Adenocarcinomic human alveolar basal epithelial cells, A549)

The results from *in vitro* ceria uptake experiments concluded that particles with sizes (<10nm) are internalised and uptaken by the A549 cells. The results when compared to the stability data revealed that the NPs which were completely uptaken were the ones which

showed least stability in SCM during *in situ* DLS experiments. However, the NPs which showed stability in SCM were partially uptaken by the cells. We believe that the stable NPs remain suspended in the supernatant SCM present in the cell plate and do not reach the bottom and hence are not readily available for cellular interactions. The uptake images depicted that the internalised particles were localised in the cytoplasm and did not enter the nucleus of A549 cells. The results concluded that the internalisation seemed to be more size dependent and to some extent shape and capping dependent. The study clearly demonstrated that size, shape, aggregation behaviour, surface composition and surface charge of the particles play an important role towards cell-nanoparticle interaction or cellular responses.

6.3 Future work

Some X-ray absorption studies (XAS) studies have been performed on selected ceria samples for oxidation state determination, with the help of United States Environmental Protection Agency (USEPA). The results are awaiting. They would also add to the current pool of techniques used for oxidation state quantification. Future work may involve looking at the effect of aging in the synthesised ceria suspensions, specially oxidation state and also the change in oxidation state in complex media. Further work may involve assessing the behaviour and stability of the synthesised NPs at environmentally relevant concentrations, chronic and acute toxicity tests of the studied NPs in A549 cells and other cell lines. We now have a batch of ceria NPs with known size, shape, morphology, surface charge and oxidation state data. These NPs can be sent to other groups for various toxicological studies. A summary of the all the data generated and discussed in this thesis is outlined in table 6.1.

Table 0.1 A summary of the all the data generated and discussed in this thesis

Sample code	Synthesis type	Precursors	Reaction temperature (°C)	Stirring hours	Product morphology	DLS	TEM	Size/ shape quantification	STEM-EELS Images and spectra	XPS	Dispersion and stability studies in cell culture media using DLS and RCM		Uptake and internalisation studies in A549 cells
											SCM	SFM	
C1	Homogenous precipitation	$Ce(NO_3)_3 \cdot 6H_2O$ + HMTA Ratio 1: 10	70	7	Nanocube	✓	✓	✓	✓ Particle scans	✓	✓	✓	✓
C2	Homogenous precipitation	$Ce(NO_3)_3 \cdot 6H_2O$ + HMTA Ratio 1: 20	70	7	Nanocube	✓	✓	✓	✓ Particle scans	✓	✓	✓	✓
C3	Homogenous precipitation	$Ce(NO_3)_3 \cdot 6H_2O$ + HMTA Ratio 1: 40	70	7	Nanocube	✓	✓	✓	✓ Particle scans	✓	✓	✓	✓
S1	Sonochemical	$Ce(NO_3)_3 \cdot 6H_2O$ + PEG 1500 + NaOH	Room Temperature (25)	4	Nanosphere	✓	✓	✓	✓ Particle scans	✓	✓	✓	✓

S2	Sonochemical	$Ce(NO_3)_3 \cdot 6H_2O$ + PEG 600 + NaOH	Room Temperature (25)	4	Nanosphere	✓	✓	✓	✓ Particle scans	✓	✓	✓	✓
S3	Homogenous precipitation	$Ce(NO_3)_3 \cdot 6H_2O$ + Ethylenediamine	Room Temperature (25)	24	Nanosphere	✓	✓	✓	✓ Particle and area scans	✓			
S4	Co-precipitation	$Ce(NO_3)_3 \cdot 6H_2O$ + Ethylenediamine	100	7	Nanosphere	✓	✓	✓	✓ Area scans	✓			
R1	Co-precipitation	$Ce(NO_3)_3 \cdot 6H_2O$ + Ethylenediamine + Water	100	7	Nanorod	✓	✓	✓	✓ Particle scans	✓	✓	✓	✓
S5	Hydrolysis	Ammonium Ce(IV) nitrate + NaOH	Room Temperature (25)	24	Nanosphere	✓	✓	✓	✓ Area scans	✓			
C4	Thermal hydrolysis	Ammonium Ce(IV) nitrate +	100	7	Nanocube	✓	✓	✓	✓ Particle scans				

		NaOH											
S6	Co-precipitation	$Ce(NO_3)_3 \cdot 6H_2O$ + Ammonia	Room Temperature (25)	1	Nanosphere	✓	✓	✓	✓ Particle scans				
S7	precipitation	$Ce(NO_3)_3 \cdot 6H_2O$ + NaOH	Room Temperature (25)	48	Nanosphere	✓	✓		✓ Area scans	✓			
R2	precipitation	$Ce(NO_3)_3 \cdot 6H_2O$ + NaOH	50	48	Mixture of nanosphere and nanorods	✓	✓		✓				

References

AITKEN, R. J., CHAUDHRY, M. Q., BOXALL, A. B. A. & HULL, M. 2006. Manufacture and use of nanomaterials: current status in the UK and global trends. *Occupational Medicine,* 56**,** 300-306.

AITKEN, R. J., HANKIN, S. M., LANG TRAN, C., DONALDSON, K., STONE, V., CUMPSON, P., JOHNSTONE, J., CHAUDHRY, Q., CASH, S. & GARROD, J. 2008. A multidisciplinary approach to the identification of reference materials for engineered nanoparticle toxicology. *Nanotoxicology,* 2**,** 71-78.

ALILI, L., SACK, M., KARAKOTI, A. S., TEUBER, S., PUSCHMANN, K., HIRST, S. M., REILLY, C. M., ZANGER, K., STAHL, W., DAS, S., SEAL, S. & BRENNEISEN, P. 2011. Combined cytotoxic and anti-invasive properties of redox-active nanoparticles in tumor-stroma interactions. *Biomaterials,* 32**,** 2918-2929.

ALIVISATOS, A. P. 1996. Semiconductor Clusters, Nanocrystals, and Quantum Dots. *Science,* 271**,** 933-937.

AMIN, K. A., HASSAN, M. S., AWAD, E.-S. T. & HASHEM, K. S. 2011. The protective effects of cerium oxide nanoparticles against hepatic oxidative damage induced by monocrotaline. *International journal of nanomedicine* [Online], 6. Available: http://europepmc.org/abstract/MED/21289991

ARAI, T. & NORDE, W. 1990. The behavior of some model proteins at solid—liquid interfaces 2. Sequential and competitive adsorption. *Colloids and Surfaces,* 51**,** 17-28.

ARNOLD, M. C., BADIREDDY, A. R., WIESNER, M. R., DI GIULIO, R. T. & MEYER, J. N. 2013. Cerium oxide nanoparticles are more toxic than equimolar bulk cerium oxide in Caenorhabditis elegans. *Arch Environ Contam Toxicol,* 65**,** 224-33.

ASATI, A., SANTRA, S., KAITTANIS, C., NATH, S. & PEREZ, J. M. 2009. Oxidase-like activity of polymer-coated cerium oxide nanoparticles. *Angewandte Chemie (International ed. in English),* 48**,** 2308-2312.

AUFFAN, M., ROSE, J., BOTTERO, J.-Y., LOWRY, G. V., JOLIVET, J.-P. & WIESNER, M. R. 2009a. Towards a definition of inorganic nanoparticles from an environmental, health and safety perspective. *Nature nanotechnology,* 4**,** 634-641.

AUFFAN, M., ROSE, J., ORSIERE, T., DE MEO, M., THILL, A., ZEYONS, O., PROUX, O., MASION, A., CHAURAND, P., SPALLA, O., BOTTA, A., WIESNER, M. R. & BOTTERO, J.-Y. 2009b. CeO2 nanoparticles induce DNA damage towards human dermal fibroblasts in vitro. *Nanotoxicology,* 3**,** 161-171.

AUFFAN, M., ROSE, J., WIESNER, M. R. & BOTTERO, J.-Y. 2009c. Chemical stability of metallic nanoparticles: A parameter controlling their potential cellular toxicity in vitro. *Environmental Pollution,* 157**,** 1127-1133.

BAALOUSHA, M., JU-NAM, Y., COLE, P. A., GAISER, B., FERNANDES, T. F., HRILJAC, J. A., JEPSON, M. A., STONE, V., TYLER, C. R. & LEAD, J. R. 2012a. Characterization of cerium oxide nanoparticles-part 1: size measurements. *Environ Toxicol Chem,* 31**,** 983-93.

BAALOUSHA, M., JU-NAM, Y., COLE, P. A., HRILJAC, J. A., JONES, I. P., TYLER, C. R., STONE, V., FERNANDES, T. F., JEPSON, M. A. & LEAD, J. R. 2012b. Characterization of cerium oxide nanoparticles-part 2: nonsize measurements. *Environ Toxicol Chem,* 31**,** 994-1003.

BAALOUSHA, M., LE COUSTUMER, P., JONES, I. & LEAD, J. R. 2010. Characterisation of structural and surface speciation of representative commercially available cerium oxide nanoparticles. *Environmental Chemistry,* 7**,** 377-385.

BAALOUSHA, M. & LEAD, J. R. 2009. Overview of Nanoscience in the Environment. *In:* LEAD, J. R. & SMITH, E. (eds.) *Environmental and Human Health Impacts of Nanotechnology*. Chichester, UK: Wiley.

BADAWY, A. M. E., LUXTON, T. P., SILVA, R. G., SCHECKEL, K. G., SUIDAN, M. T. & TOLAYMAT, T. M. 2010. Impact of Environmental Conditions (pH, Ionic Strength, and Electrolyte Type) on the Surface Charge and Aggregation of Silver Nanoparticles Suspensions. *Environmental Science & Technology,* 44**,** 1260-1266.

BAER, D. R. 2011. Surface Characterization of Nanoparticles: critical needs and significant challenges. *Journal of surface analysis (Online),* 17**,** 163-169.

BARNARD, A. S. 2006. Nanohazards: Knowledge is our first defence. *Nat Mater,* 5**,** 245-248.

BÊCHE, E., CHARVIN, P., PERARNAU, D., ABANADES, S. & FLAMANT, G. 2008. Ce 3d XPS investigation of cerium oxides and mixed cerium oxide (CexTiyOz). *Surface and Interface Analysis,* 40**,** 264-267.

BLEIWAS, D. I. 2013. Potential for recovery of cerium contained in automotive catalytic converters. Open-File Report 2013: U.S. Geological Survey.

BORCHERT, H., FROLOVA, Y. V., KAICHEV, V. V., PROSVIRIN, I. P., ALIKINA, G. M., LUKASHEVICH, A. I., ZAIKOVSKII, V. I., MOROZ, E. M., TRUKHAN, S. N., IVANOV, V. P., PAUKSHTIS, E. A., BUKHTIYAROV, V. I. & SADYKOV, V. A. 2005. Electronic and Chemical Properties of Nanostructured Cerium Dioxide Doped with Praseodymium. *The Journal of Physical Chemistry B,* 109**,** 5728-5738.

BORM, P., KLAESSIG, F. C., LANDRY, T. D., MOUDGIL, B., PAULUHN, J., THOMAS, K., TROTTIER, R. & WOOD, S. 2006a. Research Strategies for Safety Evaluation of Nanomaterials, Part V: Role of Dissolution in Biological Fate and Effects of Nanoscale Particles. *Toxicological Sciences,* 90**,** 23-32.

BORM, P. J. A., ROBBINS, D., HAUBOLD, S., KUHLBUSCH, T., FISSAN, H., DONALDSON, K., SCHINS, R., STONE, V., KREYLING, W., LADEMANN, J., KRUTMANN, J., WARHEIT, D. & OBERDORSTER, E. 2006b. The potential risks of nanomaterials: a review carried out for ECETOC. *Particle and fibre toxicology* [Online], 3. Available: http://europepmc.org/abstract/MED/16907977

BORTOLINI, C. 2014. Preparation and characterization of peptide aggregations and their Au-labelled complex by transmission electron microscopy. *in Microscopy: advances in scientific research and education***,** 868-874.

BRAYNER, R., FERRARI-ILIOU, R., BRIVOIS, N., DJEDIAT, S., BENEDETTI, M. F. & FIÉVET, F. 2006. Toxicological Impact Studies Based on Escherichia coli Bacteria in Ultrafine ZnO Nanoparticles Colloidal Medium. *Nano Letters,* 6**,** 866-870.

BREGGIN, L. K. & CAROTHERS, L. 2006. Governing Uncertainty: The Nanotechnology Environmental, Health and Safety Challenge. *Columbia journal of environmental law,* 31.

BRUNNER, D., FRANK, J., APPL, H., SCHÖFFL, H., PFALLER, W. & G., G. 2010. Serum-free cell culture: the serum-free media interactive online database. *ALTEX.* ALTEX.

BUMAJDAD, A., EASTOE, J. & MATHEW, A. 2009. Cerium oxide nanoparticles prepared in self-assembled systems. *Adv Colloid Interface Sci,* 147-148**,** 56-66.

BURROUGHS, P., HAMNETT, A., ORCHARD, A. F. & THORNTON, G. 1976. Satellite structure in the X-ray photoelectron spectra of some binary and mixed oxides of lanthanum and cerium. *Journal of the Chemical Society, Dalton Transactions***,** 1686-1698.

CAMPBELL, C. T. & PEDEN, C. H. F. 2005. Oxygen Vacancies and Catalysis on Ceria Surfaces. *Science,* 309**,** 713-714.

CARLSON, C., HUSSAIN, S. M., SCHRAND, A. M., K. BRAYDICH-STOLLE, L., HESS, K. L., JONES, R. L. & SCHLAGER, J. J. 2008. Unique Cellular Interaction of Silver Nanoparticles: Size-Dependent Generation of Reactive Oxygen Species. *The Journal of Physical Chemistry B,* 112**,** 13608-13619.

CASSEE, F. R., CAMPBELL, A., BOERE, A. J. F., MCLEAN, S. G., DUFFIN, R., KRYSTEK, P., GOSENS, I. & MILLER, M. R. 2012. The biological effects of subacute inhalation of diesel exhaust following addition of cerium oxide nanoparticles in atherosclerosis-prone mice(). *Environmental Research,* 115**,** 1-10.

CEDERVALL, T., LYNCH, I., FOY, M., BERGGÅRD, T., DONNELLY, S. C., CAGNEY, G., LINSE, S. & DAWSON, K. A. 2007a. Detailed identification of plasma proteins adsorbed on copolymer nanoparticles. *Angew Chem Int Ed,* 46.

CEDERVALL, T., LYNCH, I., LINDMAN, S., BERGGÅRD, T., THULIN, E., NILSSON, H., DAWSON, K. A. & LINSE, S. 2007b. Understanding the nanoparticle-protein corona using methods to quantify exchange rates and affinities of proteins for nanoparticles. *Proc Natl Acad Sci USA,* 104.

CHAMPION, J. A. & MITRAGOTRI, S. 2006. Role of target geometry in phagocytosis. *Proceedings of the National Academy of Sciences of the United States of America,* 103**,** 4930-4934.

CHAN, W. C. W. & NIE, S. 1998. Quantum Dot Bioconjugates for Ultrasensitive Nonisotopic Detection. *Science,* 281**,** 2016-2018.

CHAUDHRY, Q., AITKEN, R., HANKIN, S., DONALDSON, K., OLSEN, S., BOXALL, A., KINLOCH, I. & FRIEDRICHS, S. 2009. Nanolifecycle: A Lifecycle Assessment Study Of The Route And Extent Of Human Exposure Via Inhalation For Commercially Available Products And Applications Containing Carbon Nanotubes. UK.

CHAUDHRY, Q., BOXALL, A., AITKEN, R. AND HULL, M. 2005. A scoping study into the manufacture and use of nanomaterials in the UK, Central Science Laboratory, York. *DEFRA*.

CHAUDHURY, K., BABU K, N., SINGH, A. K., DAS, S., KUMAR, A. & SEAL, S. Mitigation of endometriosis using regenerative cerium oxide nanoparticles. *Nanomedicine: Nanotechnology, Biology and Medicine,* 9**,** 439-448.

CHEN, H.-I. & CHANG, H.-Y. 2004. Homogeneous precipitation of cerium dioxide nanoparticles in alcohol/water mixed solvents. *Colloids and Surfaces A: Physicochemical and Engineering Aspects,* 242**,** 61-69.

CHEN, J., PATIL, S., SEAL, S. & MCGINNIS, J. F. 2006. Rare earth nanoparticles prevent retinal degeneration induced by intracellular peroxides. *Nature nanotechnology,* 1**,** 142-150.

CHEN, P.-L. & CHEN, I. W. 1993. Reactive Cerium(IV) Oxide Powders by the Homogeneous Precipitation Method. *Journal of the American Ceramic Society,* 76**,** 1577-1583.

CHITHRANI, B. D. & CHAN, W. C. W. 2007. Elucidating the Mechanism of Cellular Uptake and Removal of Protein-Coated Gold Nanoparticles of Different Sizes and Shapes. *Nano Letters,* 7**,** 1542-1550.

CHITHRANI, B. D., GHAZANI, A. A. & CHAN, W. C. W. 2006. Determining the Size and Shape Dependence of Gold Nanoparticle Uptake into Mammalian Cells. *Nano Letters,* 6**,** 662-668.

CHO, W.-S., DUFFIN, R., POLAND, C. A., HOWIE, S. E. M., MACNEE, W., BRADLEY, M., MEGSON, I. L. & DONALDSON, K. 2010. Metal oxide nanoparticles induce unique inflammatory footprints in the lung: important implications for nanoparticle testing. *Environmental health perspectives,* 118**,** 1699-1706.

COLLIN, B., AUFFAN, M., JOHNSON, A. C., KAUR, I., KELLER, A. A., LAZAREVA, A., LEAD, J. R., MA, X., MERRIFIELD, R. C., SVENDSEN, C., WHITE, J. C. & UNRINE, J. M. 2014. Environmental release, fate and ecotoxicological effects of manufactured ceria nanomaterials. *Environ. Sci.: Nano*.

COLON, J., HERRERA, L., SMITH, J., PATIL, S., KOMANSKI, C., KUPELIAN, P., SEAL, S., JENKINS, D. W. & BAKER, C. H. 2009. Protection from radiation-induced pneumonitis using cerium oxide nanoparticles. *Nanomedicine : nanotechnology, biology, and medicine,* 5**,** 225-231.

COMMISSION, E. 2012. Commission Staff Working Paper: Types and Uses of Nanomaterials, Including Safety Aspects. Brussels.

CONESA, J. 1995. Computer modeling of surfaces and defects on cerium dioxide. *Surface Science,* 339**,** 337-352.

CORMA, A., ATIENZAR, P., GARCIA, H. & CHANE-CHING, J.-Y. 2004. Hierarchically mesostructured doped CeO2 with potential for solar-cell use. *Nat Mater,* 3**,** 394-397.

CREWE, A. V., ISAACSON, M. & JOHNSON, D. 1969. A Simple Scanning Electron Microscope. *Review of Scientific Instruments,* 40**,** 241-246.

D'ANGELO, B. S., SANDRO; BENEDETTI, ELISABETTA; DI LORETO, SILVIA; PHANI, R. A.; FALONE, STEFANO; AMICARELLI, FERNANDA; CERÚ, MARIA PAOLA; CIMINI, ANNAMARIA 2009. Cerium Oxide Nanoparticles Trigger Neuronal Survival in a Human Alzheimer Disease Model By Modulating BDNF Pathway. *Current Nanoscience,* 5.

DARLINGTON, T. K., NEIGH, A. M., SPENCER, M. T., GUYEN, O. T. N. & OLDENBURG, S. J. 2009. Nanoparticle characteristics affecting environmental fate and transport through soil. *Environmental Toxicology and Chemistry,* 28**,** 1191-1199.

DAS, M., PATIL, S., BHARGAVA, N., KANG, J.-F., RIEDEL, L. M., SEAL, S. & HICKMAN, J. J. 2007. Auto-catalytic ceria nanoparticles offer neuroprotection to adult rat spinal cord neurons. *Biomaterials,* 28**,** 1918-1925.

DAS, S., SINGH, S., DOWDING, J. M., OOMMEN, S., KUMAR, A., SAYLE, T. X. T., SARAF, S., PATRA, C. R., VLAHAKIS, N. E., SAYLE, D. C., SELF, W. T. & SEAL, S. 2012. The induction of angiogenesis by cerium oxide nanoparticles through the modulation of oxygen in intracellular environments. *Biomaterials,* 33**,** 7746-7755.

DAUSEND, J., MUSYANOVYCH, A., DASS, M., WALTHER, P., SCHREZENMEIER, H., LANDFESTER, K. & MAILÄNDER, V. 2008. Uptake Mechanism of Oppositely Charged Fluorescent Nanoparticles in HeLa Cells. *Macromolecular Bioscience,* 8**,** 1135-1143.

DE MESSEMAEKER, J., PUT, S., VAN-GENECHTEN, D., VAN ROMPAEY, Y., NELIS, D., STRAUVEN, Y. & VAN TENDELOO, G. 2011. *Doped Ceria Abrasives with Controlled Morphology and Preparation Thereof*. US 12/866,485.

DECUZZI, P. & FERRARI, M. 2007. The role of specific and non-specific interactions in receptor-mediated endocytosis of nanoparticles. *Biomaterials,* 28**,** 2915-2922.

DECUZZI, P. & FERRARI, M. 2008. The Receptor-Mediated Endocytosis of Nonspherical Particles. *Biophysical Journal,* 94**,** 3790-3797.

DELUGA, G. A., SALGE, J. R., SCHMIDT, L. D. & VERYKIOS, X. E. 2004. Renewable Hydrogen from Ethanol by Autothermal Reforming. *Science,* 303**,** 993-997.

DERJAGUIN, B. & LANDAU, L. 1993. Theory of the stability of strongly charged lyophobic sols and of the adhesion of strongly charged particles in solutions of electrolytes. *Progress in Surface Science,* 43**,** 30-59.

DESHPANDE, S., PATIL, S., KUCHIBHATLA, S. V. N. T. & SEAL, S. 2005. Size dependency variation in lattice parameter and valency states in nanocrystalline cerium oxide. *Applied Physics Letters,* 87**,** 133113-133113-3.

DOHERTY, GARY J. & LUNDMARK, R. 2009. GRAF1-dependent endocytosis. *Biochemical Society Transactions,* 37**,** 1061-1065.

DONG, X. H., G. ; DECAI, Y. ; DASHU, Y. 1997. Synthesis and Properties of Cerium Oxide Nanometer Powders by Pyrolysis of Amorphous Citrate. *J. Mater. Sci. Technol,* 13**,** 113.

DOS SANTOS, T., VARELA, J., LYNCH, I., SALVATI, A. & DAWSON, K. A. 2011. Effects of Transport Inhibitors on the Cellular Uptake of Carboxylated Polystyrene Nanoparticles in Different Cell Lines. *PLoS ONE,* 6**,** e24438.

DOWDING, J. M., DAS, S., KUMAR, A., DOSANI, T., MCCORMACK, R., GUPTA, A., SAYLE, T. X. T., SAYLE, D. C., VON KALM, L., SEAL, S. & SELF, W. T. 2013. Cellular Interaction and Toxicity Depend on Physicochemical Properties and Surface Modification of Redox-Active Nanomaterials. *ACS Nano,* 7**,** 4855-4868.

EGERTON, R. 2005. *Physical principles of electron microscopy*, Springer.

EGERTON, R. F. 1996. *Electron Energy Loss Spectroscopy in the Electron Microscope,* New York, Plenum.

EGERTON, R. F., LI, P. & MALAC, M. 2004. Radiation damage in the TEM and SEM. *Micron,* 35**,** 399-409.

EINSTEIN, A. 1905. Theory of Brownian Motion. *Ann. der Physik*.

EL-SAYED, I. H., HUANG, X. & EL-SAYED, M. A. 2005. Surface Plasmon Resonance Scattering and Absorption of anti-EGFR Antibody Conjugated Gold Nanoparticles in Cancer Diagnostics: Applications in Oral Cancer. *Nano Letters,* 5**,** 829-834.

EOM, H.-J. & CHOI, J. 2009. Oxidative stress of CeO2 nanoparticles via p38-Nrf-2 signaling pathway in human bronchial epithelial cell, Beas-2B. *Toxicology letters,* 187**,** 77-83.

EUROPEAN COMMISSION 2011. Commission Recommendation of 18 October 2011on the definition of nanomaterial. *Official Journal of the European Union,* 275**,** 38-40.

FABREGA, J., FAWCETT, S. R., RENSHAW, J. C. & LEAD, J. R. 2009. Silver Nanoparticle Impact on Bacterial Growth: Effect of pH, Concentration, and Organic Matter. *Environmental Science & Technology,* 43**,** 7285-7290.

FARRÉ, M., GAJDA-SCHRANTZ, K., KANTIANI, L. & BARCELÓ, D. 2009. Ecotoxicity and analysis of nanomaterials in the aquatic environment. *Analytical and Bioanalytical Chemistry,* 393**,** 81-95.

FENG, X., SAYLE, D. C., ZHONG, L. W., PARAS, M. S., SANTORA, B., SUTORIK, A. C., SAYLE, T. X. T., YI, Y., YONG, D., XUDONG, W. & YIE-SHEIN, H. 2006. Converting Ceria Polyhedral Nanoparticles into Single-Crystal Nanospheres. *SCIENCE,* 312**,** 1504-1508.

FORTNER, J. A., BUCK, E. C., ELLISON, A. J. G. & BATES, J. K. 1997. EELS analysis of redox in glasses for plutonium immobilization. *Ultramicroscopy,* 67**,** 77-81.

FUTURE MARKETS, I. 2012. The Global Market for Nanomaterials 2002–2016: Production volumes, revenues and end user markets

Global.

GAISER, B. K., BISWAS, A., ROSENKRANZ, P., JEPSON, M. A., LEAD, J. R., STONE, V., TYLER, C. R. & FERNANDES, T. F. 2011. Effects of silver and cerium dioxide micro- and nano-sized particles on Daphnia magna. *J Environ Monit,* 13**,** 1227-35.

GAO, H., SHI, W. & FREUND, L. B. 2005. Mechanics of receptor-mediated endocytosis. *Proceedings of the National Academy of Sciences of the United States of America,* 102**,** 9469-9474.

GAO, P., KANG, Z., FU, W., WANG, W., BAI, X. & WANG, E. 2010. Electrically Driven Redox Process in Cerium Oxides. *Journal of the American Chemical Society,* 132**,** 4197-4201.

GARVIE, L. A. J. & BUSECK, P. R. 1999. Determination of Ce4+/Ce3+ in electron-beam-damaged CeO2 by electron energy-loss spectroscopy. *Journal of Physics and Chemistry of Solids,* 60**,** 1943-1947.

GARVIE, L. A. J. & CRAVEN, A. J. 1994. Electron-beam-induced reduction of Mn4+ in manganese oxides as revealed by parallel EELS. *Ultramicroscopy,* 54**,** 83-92.

GENG, Y., DALHAIMER, P., CAI, S., TSAI, R., TEWARI, M., MINKO, T. & DISCHER, D. E. 2007. Shape effects of filaments versus spherical particles in flow and drug delivery. *Nat Nano,* 2**,** 249-255.

GOJOVA, A., LEE, J.-T., JUNG, H. S., GUO, B., BARAKAT, A. I. & KENNEDY, I. M. 2009. Effect of cerium oxide nanoparticles on inflammation in vascular endothelial cells. *Inhalation toxicology,* 21 Suppl 1**,** 123-130.

GOTTSCHALK F, S. T., SCHOLZ RW, NOWACK B 2009. Modelled environmental concentrations of engineered nanomaterials (TiO2, ZnO, Ag, CNT, fullerenes) for different regions. *Environ. Sci. Technol.,* 43**,** 9216–9222.

GRANSETH, B., ODERMATT, B., ROYLE, STEPHEN J. & LAGNADO, L. 2006. Clathrin-Mediated Endocytosis Is the Dominant Mechanism of Vesicle Retrieval at Hippocampal Synapses. *Neuron,* 51**,** 773-786.

GRANSETH, B., ODERMATT, B., ROYLE, S. J. & LAGNADO, L. 2007. Clathrin-mediated endocytosis: the physiological mechanism of vesicle retrieval at hippocampal synapses. *The Journal of Physiology,* 585**,** 681-686.

GRATTON, S. E. A., ROPP, P. A., POHLHAUS, P. D., LUFT, J. C., MADDEN, V. J., NAPIER, M. E. & DESIMONE, J. M. 2008. The effect of particle design on cellular internalization pathways. *Proceedings of the National Academy of Sciences,* 105**,** 11613-11618.

GRULKE, E., REED, K., BECK, M., HUANG, X., CORMACK, A. & SEAL, S. 2014. Nanoceria: factors affecting its pro- and anti-oxidant properties. *Environ. Sci.: Nano,* 1**,** 429-444.

GURR, J.-R., WANG, A. S. S., CHEN, C.-H. & JAN, K.-Y. 2005. Ultrafine titanium dioxide particles in the absence of photoactivation can induce oxidative damage to human bronchial epithelial cells. *Toxicology,* 213**,** 66-73.

HAIGH, S. J., YOUNG, N. P., SAWADA, H., TAKAYANAGI, K. & KIRKLAND, A. I. 2011. Imaging the active surfaces of cerium dioxide nanoparticles. *Chemphyschem,* 12**,** 2397-9.

HAKUTA, Y., ONAI, S., TERAYAMA, H., ADSCHIRI, T. & ARAI, K. 1998. Production of Ultra-fine Ceria Particles by Hydrothermal Synthesis Under Supercritical Conditions. *Journal of Materials Science Letters,* 17**,** 1211-1213.

HAN, W.-Q., WU, L. & ZHU, Y. 2005. Formation and Oxidation State of CeO2-x Nanotubes. *Journal of the American Chemical Society,* 127**,** 12814-12815.

HANDY, R., OWEN, R. & VALSAMI-JONES, E. 2008a. The ecotoxicology of nanoparticles and nanomaterials: current status, knowledge gaps, challenges, and future needs. *Ecotoxicology,* 17**,** 315-325.

HANDY, R. D. & SHAW, B. J. 2007. Toxic effects of nanoparticles and nanomaterials: Implications for public health, risk assessment and the public perception of nanotechnology. *Health, Risk & Society,* 9**,** 125-144.

HANDY, R. D., VON DER KAMMER, F., LEAD, J. R., HASSELLOV, M., OWEN, R. & CRANE, M. 2008b. The ecotoxicology and chemistry of manufactured nanoparticles. *Ecotoxicology,* 17**,** 287-314.

HANSEN, S., MICHELSON, E., KAMPER, A., BORLING, P., STUER-LAURIDSEN, F. & BAUN, A. 2008. Categorization framework to aid exposure assessment of nanomaterials in consumer products. *Ecotoxicology,* 17**,** 438-447.

HANSEN, S. F., BAUN, A., MICHELSON, E.S, KAMPER, A., BORLING, P., STUER-LAURIDSEN, F. 2008b. Nanomaterials in Consumer Products: Categorization and Exposure Assessment. *Nanotechnology Risks and Benefits,* 363-372.

HARDAS, S. S., BUTTERFIELD, D. A., SULTANA, R., TSENG, M. T., DAN, M., FLORENCE, R. L., UNRINE, J. M., GRAHAM, U. M., WU, P., GRULKE, E. A. & YOKEL, R. A. 2010. Brain distribution and toxicological evaluation of a systemically delivered engineered nanoscale ceria. *Toxicological sciences : an official journal of the Society of Toxicology,* 116**,** 562-576.

HASSELLÖV, M. & KAEGI, R. 2009. Analysis and Characterization of Manufactured Nanoparticles in Aquatic Environments. *Environmental and Human Health Impacts of Nanotechnology.* John Wiley & Sons, Ltd.

HECKERT, E. G., KARAKOTI, A. S., SEAL, S. & SELF, W. T. 2008a. The role of cerium redox state in the SOD mimetic activity of nanoceria. *Biomaterials,* 29**,** 2705-2709.

HECKERT, E. G., SEAL, S. & SELF, W. T. 2008b. Fenton-Like Reaction Catalyzed by the Rare Earth Inner Transition Metal Cerium. *Environmental Science & Technology,* 42**,** 5014-5019.

HECKMAN, K. L., DECOTEAU, W., ESTEVEZ, A., REED, K. J., COSTANZO, W., SANFORD, D., LEITER, J. C., CLAUSS, J., KNAPP, K., GOMEZ, C., MULLEN, P., RATHBUN, E., PRIME, K., MARINI, J., PATCHEFSKY, J., PATCHEFSKY, A. S., HAILSTONE, R. K. & ERLICHMAN, J. S. 2013. Custom Cerium Oxide Nanoparticles Protect against a Free Radical Mediated Autoimmune Degenerative Disease in the Brain. *ACS Nano,* 7**,** 10582-10596.

HERMAN, G. S. 1999. Characterization of surface defects on epitaxial CeO2(001) films. *Surface Science,* 437**,** 207-214.

HIRANO, M., FUKUDA, Y., IWATA, H., HOTTA, Y. & INAGAKI, M. 2000. Preparation and Spherical Agglomeration of Crystalline Cerium(IV) Oxide Nanoparticles by Thermal Hydrolysis. *Journal of the American Ceramic Society,* 83**,** 1287-1289.

HIRANO, M. & KATO, E. 1999. Hydrothermal Synthesis of Nanocrystalline Cerium(IV) Oxide Powders. *Journal of the American Ceramic Society,* 82**,** 786-788.

HIRST, S. M., KARAKOTI, A., SINGH, S., SELF, W., TYLER, R., SEAL, S. & REILLY, C. M. 2013. Bio-distribution and in vivo antioxidant effects of cerium oxide nanoparticles in mice. *Environ Toxicol,* 28**,** 107-18.

HIRST, S. M., KARAKOTI, A. S., TYLER, R. D., SRIRANGANATHAN, N., SEAL, S. & REILLY, C. M. 2009. Anti-inflammatory properties of cerium oxide nanoparticles. *Small (Weinheim an der Bergstrasse, Germany),* 5**,** 2848-2856.

HOECKE, K. V., QUIK, J. T. K., MANKIEWICZ-BOCZEK, J., SCHAMPHELAERE, K. A. C. D., ELSAESSER, A., MEEREN, P. V. D., BARNES, C., MCKERR, G., HOWARD, C. V., MEENT, D. V. D., RYDZYŃSKI, K., DAWSON, K. A., SALVATI, A., LESNIAK, A., LYNCH, I., SILVERSMIT, G., SAMBER, B. D., VINCZE, L. & JANSSEN, C. R. 2009. Fate and Effects of CeO2 Nanoparticles in Aquatic Ecotoxicity Tests. *Environmental Science & Technology,* 43**,** 4537-4546.

HOSOKAWA, M. 2007. *Nanoparticle Technology Handbook* Elsevier.

HTTP://WWW.SLIDESHARE.NET/PERKINELMER/POSTER-NANOMATERIALS 2012.

PerkinElmer Inc.

HU, X., GUO, T., FU, X. & HU, X. 2003. Nanoscale oxide structures induced by dynamic electric field on Si with AFM. *Applied Surface Science,* 217**,** 34-38.

HUANG, F., KHVOROVA, A., MARSHALL, W. & SORKIN, A. 2004. Analysis of Clathrin-mediated Endocytosis of Epidermal Growth Factor Receptor by RNA Interference. *Journal of Biological Chemistry,* 279**,** 16657-16661.

HUSSAIN, S. M., BRAYDICH-STOLLE, L. K., SCHRAND, A. M., MURDOCK, R. C., YU, K. O., MATTIE, D. M., SCHLAGER, J. J. & TERRONES, M. 2009. Toxicity Evaluation for Safe Use of Nanomaterials: Recent Achievements and Technical Challenges. *Advanced Materials,* 21**,** 1549-1559.

INABA, H. & TAGAWA, H. 1996. Ceria-based solid electrolytes. *Solid State Ionics,* 83**,** 1-16.

IVERSEN, T.-G., SKOTLAND, T. & SANDVIG, K. 2011. Endocytosis and intracellular transport of nanoparticles: Present knowledge and need for future studies. *Nano Today,* 6**,** 176-185.

JACKSON, A. P., BLACKBOURN, H. D., HAWKINS, S. F. C. & HUGHES, M. J. G. 1996. Receptor-mediated endocytosis. *In:* LEE, A. G. (ed.) *Biomembranes: A Multi-Volume Treatise.* JAI.

JEMEC, A., DROBNE, D., REMŠKAR, M., SEPČIĆ, K. & TIŠLER, T. 2008. Effects of ingested nano-sized titanium dioxide on terrestrial isopods (Porcellio scaber). *Environmental Toxicology and Chemistry,* 27**,** 1904-1914.

JIANG, J., OBERDÖRSTER, G. & BISWAS, P. 2009. Characterization of size, surface charge, and agglomeration state of nanoparticle dispersions for toxicological studies. *Journal of Nanoparticle Research,* 11**,** 77-89.

JOHNSTON, H. J., SEMMLER-BEHNKE, M., BROWN, D. M., KREYLING, W., TRAN, L. & STONE, V. 2010. Evaluating the uptake and intracellular fate of polystyrene nanoparticles by primary and hepatocyte cell lines in vitro. *Toxicology and Applied Pharmacology,* 242**,** 66-78.

JU-NAM, Y. & LEAD, J. R. 2008. Manufactured nanoparticles: An overview of their chemistry, interactions and potential environmental implications. *Science of The Total Environment,* 400**,** 396-414.

KAR, S. P., C. AND SANTRA, S. 2009. Direct Room Temperature Synthesis of Valence State Engineered Ultra-Small Ceria Nanoparticles: Investigation on the Role of Ethylenediamine as a Capping Agent. *Journal of Physical Chemistry C,* 113**,** 4862–4867.

KARAKOTI, A., SINGH, S., DOWDING, J. M., SEAL, S. & SELF, W. T. 2010a. Redox-active radical scavenging nanomaterials. *Chemical Society Reviews,* 39**,** 4422-4432.

KARAKOTI, A. S., DAS, S., THEVUTHASAN, S. & SEAL, S. 2011. PEGylated inorganic nanoparticles. *Angew Chem Int Ed Engl,* 50**,** 1980-94.

KARAKOTI, A. S., MUNUSAMY, P., HOSTETLER, K., KODALI, V., KUCHIBHATLA, S., ORR, G., POUNDS, J. G., TEEGUARDEN, J. G., THRALL, B. D. & BAER, D. R. 2012. Preparation and Characterization Challenges to Understanding Environmental and Biological Impacts of Nanoparticles. *Surf Interface Anal,* 44**,** 882-889.

KARAKOTI, A. S., SINGH, S., KUMAR, A., MALINSKA, M., KUCHIBHATLA, S. V. N. T., WOZNIAK, K., SELF, W. T. & SEAL, S. 2009. PEGylated Nanoceria as Radical Scavenger with Tunable Redox Chemistry. *Journal of the American Chemical Society,* 131**,** 14144-14145.

KARAKOTI, A. S., TSIGKOU, O., YUE, S., LEE, P. D., STEVENS, M. M., JONES, J. R. & SEAL, S. 2010b. Rare earth oxides as nanoadditives in 3-D nanocomposite scaffolds for bone regeneration. *Journal of Materials Chemistry,* 20**,** 8912-8919.

KARHANEK, M., KEMP, J. T., POURMAND, N., DAVIS, R. W. & WEBB, C. D. 2005. Single DNA Molecule Detection Using Nanopipettes and Nanoparticles. *Nano Letters,* 5**,** 403-407.

KATUSIC, S., KROELL, M., KRAEMER, M., HEBERER, S., STAAB, E. & MICHAEL, G. 2009. *Cerium oxide powder and cerium oxide dispersion*. US 11/502,568.

KLABUNDE, K. J. & RICHARDS, R. M. 2009. *Nanoscale materials in chemistry,* Hoboken, New Jersey, John Wiley & Sons, Inc.

KLAINE, S. J., ALVAREZ, P. J. J., BATLEY, G. E., FERNANDES, T. F., HANDY, R. D., LYON, D. Y., MAHENDRA, S., MCLAUGHLIN, M. J. & LEAD, J. R. 2008. Nanomaterials in the environment: Behavior, fate, bioavailability, and effects. *Environmental Toxicology and Chemistry,* 27**,** 1825-1851.

KNOLL, M. A. E. R., M. KNOLL, E. RUSKA 1932. The electron microscope. *Zeitschrift Fur Physik,* 78**,** 318-339.

KONINKLIJKE. 2012. *Transmission Electron Microscopy* [Online].

KORSVIK, C., PATIL, S., SEAL, S. & SELF, W. T. 2007. Superoxide dismutase mimetic properties exhibited by vacancy engineered ceria nanoparticles. *Chemical communications (Cambridge, England)***,** 1056-1058.

KREYLING, W. G., FERTSCH-GAPP, S., SCHÄFFLER, M., JOHNSTON, B. D., HABERL, N., PFEIFFER, C., DIENDORF, J., SCHLEH, C., HIRN, S., SEMMLER-BEHNKE, M., EPPLE, M. & PARAK, W. J. 2014. In vitro and in vivo interactions of selected nanoparticles with rodent serum proteins and their consequences in biokinetics. *Beilstein Journal of Nanotechnology,* 5**,** 1699-1711.

KUHN, D. A., VANHECKE, D., MICHEN, B., BLANK, F., GEHR, P., PETRI-FINK, A. & ROTHEN-RUTISHAUSER, B. 2014. Different endocytotic uptake mechanisms for nanoparticles in epithelial cells and macrophages. *Beilstein Journal of Nanotechnology,* 5**,** 1625-1636.

KUMAR, A., DAS, S., MUNUSAMY, P., SELF, W., BAER, D. R., SAYLE, D. C. & SEAL, S. 2014. Behavior of nanoceria in biologically-relevant environments. *Environ. Sci.: Nano*.

KUNTSCHE, J., HORST, J. C. & BUNJES, H. 2011. Cryogenic transmission electron microscopy (cryo-TEM) for studying the morphology of colloidal drug delivery systems. *International Journal of Pharmaceutics,* 417**,** 120-137.

LAACHIR, A., PERRICHON, V., BADRI, A., LAMOTTE, J., CATHERINE, E., LAVALLEY, J. C., EL FALLAH, J., HILAIRE, L., LE NORMAND, F., QUEMERE, E., SAUVION, G. N. & TOURET, O. 1991. Reduction of CeO2 by hydrogen. Magnetic susceptibility and Fourier-transform infrared, ultraviolet and X-ray

photoelectron spectroscopy measurements. *Journal of the Chemical Society, Faraday Transactions,* 87**,** 1601-1609.
LABERTY-ROBERT, C., LONG, J. W., LUCAS, E. M., PETTIGREW, K. A., STROUD, R. M., DOESCHER, M. S. & ROLISON, D. R. 2005. Sol−Gel-Derived Ceria Nanoarchitectures: Synthesis, Characterization, and Electrical Properties. *Chemistry of Materials,* 18**,** 50-58.
LADEMANN, J., WEIGMANN, H. J., SCHÄFER, H., MÜLLER, G. & STERRY, W. 2000. Investigation of the Stability of Coated Titanium Microparticles Used in Sunscreens. *Skin Pharmacology and Physiology,* 13**,** 258-264.
LAMER, V. K. & DINEGAR, R. H. 1950. Theory, Production and Mechanism of Formation of Monodispersed Hydrosols. *Journal of the American Chemical Society,* 72**,** 4847-4854.
LAZAREVA, A. & KELLER, A. A. 2014. Estimating Potential Life Cycle Releases of Engineered Nanomaterials from Wastewater Treatment Plants. *ACS Sustainable Chemistry & Engineering,* 2**,** 1656-1665.
LEDIN, A., KARLSSON, S, DUKER, A AND ALLARD, B 1994. Measurements In-Situ of Concentration and Size Distribution of Colloidal Matter in Deep Groundwaters by Photon-Correlation Spectroscopy. *Water Research,* 28**,** 1539-1545.
LIN, D. & XING, B. 2008. Root Uptake and Phytotoxicity of ZnO Nanoparticles. *Environmental Science & Technology,* 42**,** 5580-5585.
LIN, H.-W., HWU, W.-H. & GER, M.-D. 2008. The dispersion of silver nanoparticles with physical dispersal procedures. *Journal of Materials Processing Technology,* 206**,** 56-61.
LIN, W., HUANG, Y.-W., ZHOU, X.-D. & MA, Y. 2006. Toxicity of cerium oxide nanoparticles in human lung cancer cells. *International journal of toxicology,* 25**,** 451-457.
LU, Z., KARAKOTI, A., VELARDE, L., WANG, W., YANG, P., THEVUTHASAN, S. & WANG, H.-F. 2013. Dissociative Binding of Carboxylic Acid Ligand on Nanoceria Surface in Aqueous Solution: A Joint In Situ Spectroscopic Characterization and First-Principles Study. *The Journal of Physical Chemistry C,* 117**,** 24329-24338.
LUNDMARK, R., DOHERTY, G. J., HOWES, M. T., CORTESE, K., VALLIS, Y., PARTON, R. G. & MCMAHON, H. T. 2008. The GTPase-Activating Protein GRAF1 Regulates the CLIC/GEEC Endocytic Pathway. *Current Biology,* 18**,** 1802-1808.
LUNDQVIST, M., STIGLER, J., ELIA, G., LYNCH, I., CEDERVALL, T. & DAWSON, K. A. 2008. Nanoparticles size and surface properties determine the protein corona with possible implications for biological impacts. *Proc Natl Acad Sci USA,* 105.
LYNCH, I., CEDERVALL, T., LUNDQVIST, M., CABALEIRO-LAGO, C., LINSE, S. & DAWSON, K. A. 2007. The nanoparticle - protein complex as a biological entity; a complex fluids and surface science challenge for the 21st century. *Adv Colloid Interfac,* 134.
LYNCH, I. & DAWSON, K. A. 2008. Protein-nanoparticle interactions. *Nano Today,* 3**,** 40-47.
MA, J. Y., ZHAO, H., MERCER, R. R., BARGER, M., RAO, M., MEIGHAN, T., SCHWEGLER-BERRY, D., CASTRANOVA, V. & MA, J. K. 2011. Cerium oxide nanoparticle-induced pulmonary inflammation and alveolar macrophage functional change in rats. *Nanotoxicology,* 5**,** 312-325.
MAI, H. X., SUN, L. D., ZHANG, Y. W., SI, R., FENG, W., ZHANG, H. P., LIU, H. C. & YAN, C. H. 2005. *J. Phys. Chem. B,* 109**,** 24380.

MANOUBI, T., COLLIEX, C. & REZ, P. 1990. Quantitative electron energy loss spectroscopy on M45 edges in rare earth oxides. *Journal of Electron Spectroscopy and Related Phenomena,* 50**,** 1-18.

MARTIN, P. & LEIBOVICH, S. J. 2005. Inflammatory cells during wound repair: the good, the bad and the ugly. *Trends in Cell Biology,* 15**,** 599-607.

MASUI, T., FUJIWARA, K., MACHIDA, K.-I., ADACHI, G.-Y., SAKATA, T. & MORI, H. 1997. Characterization of Cerium(IV) Oxide Ultrafine Particles Prepared Using Reversed Micelles. *Chemistry of Materials,* 9**,** 2197-2204.

MAVROCORDATOS, D., PERRET, D. & LEPPARD, G. G. 2007. Strategies and Advances in the Characterisation of Environmental Colloids by Electron Microscopy Denis Mavrocordatos. *In:* WILKINSON, K. J. & LEAD, J. R. (eds.) *Environmental Colloids and Particles.* John Wiley & Sons, Ltd.

MAVROCORDATOS. D, W. P. A. M. B. 2004. Analysis of environmental particles by atomic force microscopy, scanning and transmission electron microscopy. *Water Science & Technology,* 50**,** 9-18.

MAXIT, B. 2010. Particle size measurements of dark and concentrated dispersions by dynamic light scattering. *Spotlight.*

MAYNARD, A. & KUEMPEL, E. 2005. Airborne Nanostructured Particles and Occupational Health. *Journal of Nanoparticle Research,* 7**,** 587-614.

MAYNARD, A. D. 2006. Nanotechnology: assessing the risks. *Nano Today,* 1**,** 22-33.

MCCARTNEY, K. S. 2003. Catalytic converter theory, operation and testing: Bear River Converters. November 16, 2011.

MCCORMICK, P. G. & TZUZUKI, T. 2003. *Milling; nanosized grains of precursor metal compound uniformly dispersed in nonreactant diluent; heat conversion to metal oxide; dissolution removal of diluent; such as cerium oxide from cerium hydroxide and sodium chloride*. US 09/700,124.

MERCER, J. & HELENIUS, A. 2012. Gulping rather than sipping: macropinocytosis as a way of virus entry. *Current Opinion in Microbiology,* 15**,** 490-499.

MERRIFIELD, R. C., WANG, Z. W., PALMER, R. E. & LEAD, J. R. 2013. Synthesis and characterization of polyvinylpyrrolidone coated cerium oxide nanoparticles. *Environ Sci Technol,* 47**,** 12426-33.

MINSKY, M. 1988. Memoir on Inventing the Confocal Scanning Microscope. *Scanning,* 10**,** 128-138.

MISRA, S. K., DYBOWSKA, A., BERHANU, D., LUOMA, S. N. & VALSAMI-JONES, E. 2012. The complexity of nanoparticle dissolution and its importance in nanotoxicological studies. *Sci Total Environ,* 438**,** 225-32.

MORONES, J. R., ELECHIGUERRA, J. L., CAMACHO, A., HOLT, K., KOURI, J. B., RAMÍREZ, J. T. & YACAMAN, M. J. 2005. The bactericidal effect of silver nanoparticles. *Nanotechnology,* 16**,** 2346.

MUELLER, N. C. & NOWACK, B. 2008. Exposure Modeling of Engineered Nanoparticles in the Environment. *Environmental Science & Technology,* 42**,** 4447-4453.

MULLINS, D. R., OVERBURY, S. H. & HUNTLEY, D. R. 1998. Electron spectroscopy of single crystal and polycrystalline cerium oxide surfaces. *Surface Science,* 409**,** 307-319.

NABI, I. R. & LE, P. U. 2003. Caveolae/raft-dependent endocytosis. *The Journal of Cell Biology,* 161**,** 673-677.

NAVARRO, E., BAUN, A., BEHRA, R., HARTMANN, N., FILSER, J., MIAO, A.-J., QUIGG, A., SANTSCHI, P. & SIGG, L. 2008. Environmental behavior and

ecotoxicity of engineered nanoparticles to algae, plants, and fungi. *Ecotoxicology,* 17**,** 372-386.
NEL, A., XIA, T., MÄDLER, L. & LI, N. 2006. Toxic Potential of Materials at the Nanolevel. *Science,* 311**,** 622-627.
NEL, A. E., MADLER, L., VELEGOL, D., XIA, T., HOEK, E. M. V., SOMASUNDARAN, P., KLAESSIG, F., CASTRANOVA, V. & THOMPSON, M. 2009. Understanding biophysicochemical interactions at the nano-bio interface. *Nat Mater,* 8**,** 543-557.
NEUTZE, R., WOUTS, R., VAN DER SPOEL, D., WECKERT, E. & HAJDU, J. 2000. Potential for biomolecular imaging with femtosecond X-ray pulses. *Nature,* 406**,** 752-757.
NIEDERBERGER, M. 2007. Nonaqueous Sol–Gel Routes to Metal Oxide Nanoparticles. *Accounts of Chemical Research,* 40**,** 793-800.
NIKON. Introduction to confocal microscopy.
NIU, J., AZFER, A., ROGERS, L. M., WANG, X. & KOLATTUKUDY, P. E. 2007. Cardioprotective effects of cerium oxide nanoparticles in a transgenic murine model of cardiomyopathy. *Cardiovascular research,* 73**,** 549-559.
NIU, J., WANG, K. & KOLATTUKUDY, P. E. 2011. Cerium oxide nanoparticles inhibit oxidative stress and nuclear factor-κB activation in H9c2 cardiomyocytes exposed to cigarette smoke extract. *The Journal of pharmacology and experimental therapeutics,* 338**,** 53-61.
NOBBMANN, U. 2014. *Malvern.*
NOWACK, B. & BUCHELI, T. D. 2007. Occurrence, behavior and effects of nanoparticles in the environment. *Environmental Pollution,* 150**,** 5-22.
NWANESHIUDU ADAOBI, K. C., SAKAMOTO FERNANDA H. , ANDERSON R. ROX , SCHWARZENBERGER KATHRYN AND YOUNG ROGER C. 2012. Introduction to Confocal Microscopy. *The Society for Investigative Dermatology,* 132**,** 1-5.
OBERDORSTER, G. 2012. Nanotoxicology: in vitro-in vivo dosimetry. *Environ Health Perspect,* 120**,** A13; author reply A13.
OBERDÖRSTER, G., MAYNARD, A., DONALDSON, K., CASTRANOVA, V., FITZPATRICK, J., AUSMAN, K., CARTER, J., KARN, B., KREYLING, W., LAI, D., OLIN, S., MONTEIRO-RIVIERE, N., WARHEIT, D., YANG, H. & GROUP, A. R. F. T. I. R. F. R. S. I. N. T. S. W. 2005a. Principles for characterizing the potential human health effects from exposure to nanomaterials: elements of a screening strategy. *Particle and Fibre Toxicology,* 2**,** 8-8.
OBERDÖRSTER, G., OBERDÖRSTER, E. & OBERDÖRSTER, J. 2005b. Nanotoxicology: An Emerging Discipline Evolving from Studies of Ultrafine Particles. *Environmental Health Perspectives,* 113**,** 823-839.
ORLANDI, P. A. & FISHMAN, P. H. 1998. Filipin-dependent Inhibition of Cholera Toxin: Evidence for Toxin Internalization and Activation through Caveolae-like Domains. *The Journal of Cell Biology,* 141**,** 905-915.
OWEN R & RD, H. 2007. Formulating the problems for environmental risk assessment of nanomaterials. *Environ Sci Techol,* 41**,** 5582-5588.
OWEN, R. & DEPLEDGE, M. 2005. Nanotechnology and the environment: Risks and rewards. *Marine Pollution Bulletin,* 50**,** 609-612.
PAN, Y., NEUSS, S., LEIFERT, A., FISCHLER, M., WEN, F., SIMON, U., SCHMID, G., BRANDAU, W. & JAHNEN-DECHENT, W. 2007. Size-Dependent Cytotoxicity of Gold Nanoparticles. *Small,* 3**,** 1941-1949.
PAPARAZZO, E. 2011. On the curve-fitting of XPS Ce(3d) spectra of cerium oxides. *Materials Research Bulletin,* 46**,** 323-326.

PARENT, R. A. 1992. *Comparative Biology of the Normal Lung*, CRC Press.
PARK, B., DONALDSON, K, DUFFIN, R, TRAN, L, KELLY, F, MUDWAY, I, MORIN, JP, GUEST, R, JENKINSON, P, SAMARAS, Z, GIANNOULI, M, KOURIDIS, H & MARTIN, P 2008. Hazard and risk assessment of a nanoparticulate cerium oxide-based diesel fuel additive - A case study. *INHALATION TOXICOLOGY,* 20**,** 547-566.
PARK, B., MARTIN, P., HARRIS, C., GUEST, R., WHITTINGHAM, A., JENKINSON, P. & HANDLEY, J. 2007. Initial in vitro screening approach to investigate the potential health and environmental hazards of Enviroxtrade mark - a nanoparticulate cerium oxide diesel fuel additive. *Particle and fibre toxicology* [Online], 4. Available: http://europepmc.org/abstract/MED/18053256

PARK, E.-J., CHOI, J., PARK, Y.-K. & PARK, K. 2008. Oxidative stress induced by cerium oxide nanoparticles in cultured BEAS-2B cells. *Toxicology,* 245**,** 90-100.
PARK EJ, C. W., JEONG J, YI JH, CHOI K, KIM Y, PARK K. 2010. Induction of inflammatory responses in mice treated with cerium oxide nanoparticles by intratracheal instillation. *Journal of Health Science,* 56**,** 387–396.
PARK, J.-G., KATOH, T., LEE, W.-M., JEON, H. & PAIK, U. 2003. Surfactant Effect on Oxide-to-Nitride Removal Selectivity of Nano-abrasive Ceria Slurry for Chemical Mechanical Polishing. *Japanese Journal of Applied Physics,* 42**,** 5420.
PARK, S., VOHS, J. M. & GORTE, R. J. 2000. Direct oxidation of hydrocarbons in a solid-oxide fuel cell. *Nature,* 404**,** 265-267.
PARK, S. W., MYEONG, W. J., BAIK, J. S., CHUNG, C. M. & SONG, K. H. 2010. *Concentrate of fine ceria particles for chemical mechanical polishing and preparing method thereof*. US 10/557,940.
PATIL, S., SANDBERG, A., HECKERT, E., SELF, W. A. & SEAL, S. 2007. Protein adsorption and cellular uptake of cerium oxide nanoparticles as a function of zeta potential. *Biomaterials.,* 26**,** 4600-4607.
PATNAIK, P. 2003. *Handbook of Inorganic Chemicals*, McGraw-Hill.
PENGO, P., POLIZZI, S., BATTAGLIARIN, M., PASQUATO, L. & SCRIMIN, P. 2003. Synthesis, characterization and properties of water-soluble gold nanoparticles with tunable core size. *Journal of Materials Chemistry,* 13**,** 2471-2478.
PENNYCOOK, S. J., LUPINI, A. R., VARELA, M., BORISEVICH, A., PENG, Y., OXLEY, M. P., VAN BENTHEM, K. & CHISHOLM, M. F. 2007. Scanning Transmission Electron Microscopy for Nanostructure Characterization. *In:* ZHOU, W. & WANG, Z. (eds.) *Scanning Microscopy for Nanotechnology.* Springer New York.
PEREZ, J. M., ASATI, A., NATH, S. & KAITTANIS, C. 2008. Synthesis of biocompatible dextran-coated nanoceria with pH-dependent antioxidant properties. *Small (Weinheim an der Bergstrasse, Germany),* 4**,** 552-556.
PHENRAT, T., SALEH, N., SIRK, K., TILTON, R. D. & LOWRY, G. V. 2006. Aggregation and Sedimentation of Aqueous Nanoscale Zerovalent Iron Dispersions. *Environmental Science & Technology,* 41**,** 284-290.
PIERSCIONEK, B. K., KEENAN, J., YASSEEN, A., COLHOUN, L.M., LI, Y.B., SCHACHAR, R.A. AND CHEN, W. 2010. CeO2 nanoparticles have no detrimental effect on eye lens proteins. *Current Analytical Chemistry,* 6**,** 172-176.
PIPAN-TKALEC, Ž., DROBNE, D., JEMEC, A., ROMIH, T., ZIDAR, P. & BELE, M. 2010. Zinc bioaccumulation in a terrestrial invertebrate fed a diet treated with particulate ZnO or ZnCl2 solution. *Toxicology,* 269**,** 198-203.

PIRMOHAMED, T., DOWDING, J. M., SINGH, S., WASSERMAN, B., HECKERT, E., KARAKOTI, A. S., KING, J. E., SEAL, S. & SELF, W. T. 2010. Nanoceria exhibit redox state-dependent catalase mimetic activity. *Chem Commun (Camb),* 46**,** 2736-8.

PITKETHLY, M. 2009. Nanotechnology, regulation and the environment. *Materials Today,* 12**,** 23.

POLEZHAEVA, O. S., YAROSHINSKAYA, N. V. & IVANOV, V. K. 2008. Formation mechanism of nanocrystalline ceria in aqueous solutions of cerium(III) nitrate and hexamethylenetetramine. *Inorganic Materials,* 44**,** 51-57.

POPOV, A. P., PRIEZZHEV, A. V., LADEMANN, J. & MYLLYLÄ, R. 2005. TiO 2 nanoparticles as an effective UV-B radiation skin-protective compound in sunscreens. *Journal of Physics D: Applied Physics,* 38**,** 2564.

POWERS, K. W., BROWN, S. C., KRISHNA, V. B., WASDO, S. C., MOUDGIL, B. M. & ROBERTS, S. M. 2006. Research strategies for safety evaluation of nanomaterials. Part VI. Characterization of nanoscale particles for toxicological evaluation. . *Toxicol Sci,* 90**,** 296-303.

POWERS, K. W., PALAZUELOS, M., MOUDGIL, B. M. & ROBERTS, S. M. 2007. Characterization of the size, shape, and state of dispersion of nanoparticles for toxicological studies. *Nanotoxicology,* 1**,** 42-51.

REJMAN, J., ZUHORN ANS, I. S., OBERLE, V. & HOEKSTRA, D. 2004. Size dependent internalization of particles via the pathways of clathrin- and caveolae-mediated endocytosis. *Biochem J,* 377.

RIEDL, T., GEMMING, T. & WETZIG, K. 2006. Extraction of EELS white-line intensities of manganese compounds: Methods, accuracy, and valence sensitivity. *Ultramicroscopy,* 106**,** 284-291.

RIMAN, R. E., SUCHANEK, W. L. & LENCKA, M. M. 2002. Hydrothermal crystallization of ceramics. *Annales de Chimie Science des Matériaux,* 27**,** 15-36.

ROCO, M. C. 2003. Nanotechnology: convergence with modern biology and medicine. *Curr Opin Biotechnol* 14**,** 337–346.

RÖHDER, L. A., BRANDT, T., SIGG, L. & BEHRA, R. 2014. Influence of agglomeration of cerium oxide nanoparticles and speciation of cerium(III) on short term effects to the green algae Chlamydomonas reinhardtii. *Aquatic Toxicology,* 152**,** 121-130.

ROMEO, M., BAK, K., FALLAH, J. E., NORMAND, F. L. & HILAIRE, L. 1993. XPS Study of the Reduction of Cerium Dioxide. *SURFACE AND INTERFACE ANALYSIS,* 20**,** 508-512.

ROMER, W., BERLAND, L., CHAMBON, V., GAUS, K., WINDSCHIEGL, B., TENZA, D., ALY, M. R. E., FRAISIER, V., FLORENT, J.-C., PERRAIS, D., LAMAZE, C., RAPOSO, G., STEINEM, C., SENS, P., BASSEREAU, P. & JOHANNES, L. 2007. Shiga toxin induces tubular membrane invaginations for its uptake into cells. *Nature,* 450**,** 670-675.

ROTELLO, V. 2003. *Nanoparticles: Building Blocks for Nanotechnology.,* New York, Springer.

ROTHEN-RUTISHAUSER, B., MÜHLFELD, C., BLANK, F., MUSSO, C. & GEHR, P. 2007. Translocation of particles and inflammatory responses after exposure to fine particles and nanoparticles in an epithelial airway model. *Particle and Fibre Toxicology,* 4**,** 1-9.

ROYAL, S. 2004. Nanoscience and nanotechnologies: opportunities and uncertainties. The Royal Society, London, UK: The Royal Society & The Royal Academy of Engineering.

RYMAN-RASMUSSEN, J. P., RIVIERE, J. E. & MONTEIRO-RIVIERE, N. A. 2006. Penetration of Intact Skin by Quantum Dots with Diverse Physicochemical Properties. *Toxicological Sciences,* 91**,** 159-165.

SAFI, M., SARROUJ, H., SANDRE, O., MIGNET, N. & BERRET, J. F. 2010. Interactions between sub-10-nm iron and cerium oxide nanoparticles and 3T3 fibroblasts: the role of the coating and aggregation state. *Nanotechnology,* 21**,** 145103.

SAHOO, B., GOSWAMI, M., NAG, S. & MAITI, S. 2007. Spontaneous formation of a protein corona prevents the loss of quantum dot fluorescence in physiological buffers. *Chemical Physics Letters,* 445**,** 217-220.

SAHU, T., SINGH BISHT, S., RANJAN DAS, K. & KERKAR, S. 2013. Nanoceria: Synthesis and Biomedical Applications. *Current Nanoscience,* 9**,** 588-593.

SAKTHIVEL, T., DAS, S., KUMAR, A., REID, D. L., GUPTA, A., SAYLE, D. C. & SEAL, S. 2013. Morphological Phase Diagram of Biocatalytically Active Ceria Nanostructures as a Function of Processing Variables and Their Properties. *ChemPlusChem,* 78**,** 1446-1455.

SAKURADA, T., HOSAKA, D. & CHINONE, K. 2012. *Method of producing oxide particles, slurry, polishing slurry, and method of polishing substrate*. US 12/226,545.

SALATA, O. V. 2004. Applications of nanoparticles in biology and medicine. *Journal of Nanobiotechnology,* 2**,** 3-3.

SAMIEE, S. & GOHARSHADI, E. K. 2012. Effects of different precursors on size and optical properties of ceria nanoparticles prepared by microwave-assisted method. *Materials Research Bulletin,* 47**,** 1089-1095.

SAPTARSHI, S., DUSCHL, A. & LOPATA, A. 2013. Interaction of nanoparticles with proteins: relation to bio-reactivity of the nanoparticle. *Journal of Nanobiotechnology,* 11**,** 1-12.

SAUER, H., BRYDSON, R., ROWLEY, P. N., ENGEL, W. & THOMAS, J. M. 1993. Determination of coordinations and coordination-specific site occupancies by electron energy-loss spectroscopy: An investigation of boron—oxygen compounds. *Ultramicroscopy,* 49**,** 198-209.

SAVOLAINEN, K., ALENIUS, H., NORPPA, H., PYLKKÄNEN, L., TUOMI, T. & KASPER, G. 2010. Risk assessment of engineered nanomaterials and nanotechnologies—A review. *Toxicology,* 269**,** 92-104.

SCHNITZER, J. E., LIU, J. & OH, P. 1995. Endothelial Caveolae Have the Molecular Transport Machinery for Vesicle Budding, Docking, and Fusion Including VAMP, NSF, SNAP, Annexins, and GTPases. *Journal of Biological Chemistry,* 270**,** 14399-14404.

SCHUBERT, D., DARGUSCH, R., RAITANO, J. & CHAN, S.-W. 2006. Cerium and yttrium oxide nanoparticles are neuroprotective. *Biochemical and biophysical research communications,* 342**,** 86-91.

SCHULZE, C., SCHULZE, C., KROLL, A., SCHULZE, C., KROLL, A., LEHR, C.-M., SCHÄFER, U. F., BECKER, K., SCHNEKENBURGER, J., SCHULZE ISFORT, C., LANDSIEDEL, R. & WOHLLEBEN, W. 2008. Not ready to use – overcoming pitfalls when dispersing nanoparticles in physiological media. *Nanotoxicology,* 2**,** 51-61.

SCHWABE, F., TANNER, S., SCHULIN, R., ROTZETTER, A., STARK, W., VON QUADT, A. & NOWACK, B. 2015. Dissolved cerium contributes to uptake of Ce in the presence of differently sized CeO2-nanoparticles by three crop plants. *Metallomics,* 7**,** 466-477.

SERVICE, R. F. 1996. Small Clusters Hit the Big Time. *Science,* 271**,** 920-922.

SHAFIROVICH, E., DIAKOV, V. & VARMA, A. 2006. Combustion of novel chemical mixtures for hydrogen generation. *Combustion and Flame*, 415-418.

SHANMIN, G. E. A. 2003. Preparation of CuAlO 2 nanocrystalline transparent thin films with high conductivity. *Nanotechnology,* 14.

SMIJS, T. G. & PAVEL, S. 2011. Titanium dioxide and zinc oxide nanoparticles in sunscreens: focus on their safety and effectiveness. *Nanotechnology, Science and Applications,* 4, 95-112.

SMITH, P. J., M, G., WIGGINS, H. L., GOWER, F., THORLEY, J. A., STOLPE, B., MAZZOLINI, J., DYSON, R. J. & RAPPOPORT, J. Z. 2012. Cellular entry of nanoparticles via serum sensitive clathrin-mediated endocytosis, and plasma membrane permeabilization. *International Journal of Nanomedicine,* 7, 2045-2055.

SUCHANEK, W. L., LENCKA, M., MCCANDLISH, L., PFEFFER, R. L., OLEDZKA, M., MIKULKA-BOLEN, K., ROSSETTI, G. A. & RIMAN, R. E. 2005. Hydrothermal Deposition of 〈001〉 Oriented Epitaxial Pb(Zr,Ti)O3 Films under Varying Hydrodynamic Conditions. *Crystal Growth & Design,* 5, 1715-1727.

SUN, Y., MAYERS, B. & XIA, Y. 2003a. Metal Nanostructures with Hollow Interiors. *Advanced Materials,* 15, 641-646.

SUN, Y., MAYERS, B. & XIA, Y. 2003b. Transformation of Silver Nanospheres into Nanobelts and Triangular Nanoplates through a Thermal Process. *Nano Letters,* 3, 675-679.

SURESH, A. K., PELLETIER, D. A., WANG, W., MOON, J.-W., GU, B., MORTENSEN, N. P., ALLISON, D. P., JOY, D. C., PHELPS, T. J. & DOKTYCZ, M. J. 2010. Silver Nanocrystallites: Biofabrication using Shewanella oneidensis, and an Evaluation of Their Comparative Toxicity on Gram-negative and Gram-positive Bacteria. *Environmental Science & Technology,* 44, 5210-5215.

SUZUKI, T., KOSACKI, I., ANDERSON, H. U. & COLOMBAN, P. 2001. Electrical Conductivity and Lattice Defects in Nanocrystalline Cerium Oxide Thin Films. *Journal of the American Ceramic Society,* 84, 2007-2014.

SWANSON, J. A. & WATTS, C. 1995. Macropinocytosis. *Trends in Cell Biology,* 5, 424-428.

TAN, H., VERBEECK, J., ABAKUMOV, A. & VAN TENDELOO, G. 2012. Oxidation state and chemical shift investigation in transition metal oxides by EELS. *Ultramicroscopy,* 116, 24-33.

TANTRA, R., TOMPKINS, J. & QUINCEY, P. 2010. Characterisation of the de-agglomeration effects of bovine serum albumin on nanoparticles in aqueous suspension. *Colloids and Surfaces B: Biointerfaces,* 75, 275-281.

TARNUZZER, R. W., COLON, J., PATIL, S. & SEAL, S. 2005. Vacancy engineered ceria nanostructures for protection from radiation-induced cellular damage. *Nano letters,* 5, 2573-2577.

THILL, A., ZEYONS, O., SPALLA, O., CHAUVAT, F., ROSE, J., AUFFAN, M. & FLANK, A. M. 2006. Cytotoxicity of CeO2 Nanoparticles for Escherichia coli. Physico-Chemical Insight of the Cytotoxicity Mechanism. *Environmental Science & Technology,* 40, 6151-6156.

TOURINHO, P. S., VAN GESTEL, C. A. M., LOFTS, S., SVENDSEN, C., SOARES, A. M. V. M. & LOUREIRO, S. 2012. Metal-based nanoparticles in soil: Fate, behavior, and effects on soil invertebrates. *Environmental Toxicology and Chemistry,* 31, 1679-1692.

TRATNYEK, P. G. & JOHNSON, R. L. 2006. Nanotechnologies for environmental cleanup. *Nano Today,* 1, 44-48.

TROVARELLI, A. 1996. Catalytic properties of ceria and CeO2-containing materials. *Catalysis Reviews-Science and Engineering,* 38**,** 439-520.

TURNER, S., LAZAR, S., FREITAG, B., EGOAVIL, R., VERBEECK, J., PUT, S., STRAUVEN, Y. & VAN TENDELOO, G. 2011. High resolution mapping of surface reduction in ceria nanoparticles. *Nanoscale,* 3**,** 3385-90.

UEKAWA, N., UETA, M., WU, Y. J. & KAKEGAWA, K. 2004. Characterization of CeO2 Fine Particles Prepared by the Homogeneous Precipitation Method with a Mixed Solutionof Ethylene Glycol and Polyethylene Glycol. *Journal of Materials Research,* 19**,** 1087-1092.

ULRICH, A. & WICHSER, A. 2003. Analysis of additive metals in fuel and emission aerosols of diesel vehicles with and without particle traps. *Analytical And Bioanalytical Chemistry,* 377**,** 71-81.

US-EPA 2005. Nanotechnology white, external review draft. US Environmental Protection Agency, Washington DC: Science Policy Council, US Environmental Protection Agency.

VEISEH, O., SUN, C., GUNN, J., KOHLER, N., GABIKIAN, P., LEE, D., BHATTARAI, N., ELLENBOGEN, R., SZE, R., HALLAHAN, A., OLSON, J. & ZHANG, M. 2005. Optical and MRI Multifunctional Nanoprobe for Targeting Gliomas. *Nano Letters,* 5**,** 1003-1008.

VERDON, E., DEVALETTE, M. & DEMAZEAU, G. 1995. Solvothermal synthesis of cerium dioxide microcrystallites: effect of the solvent. *Materials Letters,* 25**,** 127-131.

VERWEY EJW, O. J. 1948. *Theory of the stability of lyophobic colloids: the interaction of sol particles having an electric double layer,* New York, Elsevier publishing company Inc.

VON ARDENNE, M. 1938. Das Elektronen-Rastermikroskop. *Zeitschrift für Physik,* 109**,** 553-572.

WAGNER, A. J., BLECKMANN, C. A., MURDOCK, R. C., SCHRAND, A. M., SCHLAGER, J. J. & HUSSAIN, S. M. 2007. Cellular Interaction of Different Forms of Aluminum Nanoparticles in Rat Alveolar Macrophages. *The Journal of Physical Chemistry B,* 111**,** 7353-7359.

WAKEFIELD, G., GREEN, M., LIPSCOMB, S. & FLUTTER, B. 2004. Modified titania nanomaterials for sunscreen applications – reducing free radical generation and DNA damage. *Materials Science and Technology,* 20**,** 985-988.

WANG, H., WICK, R. L. & XING, B. 2009. Toxicity of nanoparticulate and bulk ZnO, Al2O3 and TiO2 to the nematode Caenorhabditis elegans. *Environmental Pollution,* 157**,** 1171-1177.

WASHINGTON, C. 1992. *Particle size analysis in pharmaceutics and other industries: theory and practice,* New York; London: Ellis Horwood, 1992.

WIJNHOVEN, S. W. P., DEKKERS, S., HAGENS, W. I. & DE JONG, W. H. 2009. Exposure to nanomaterials in consumer products. The Netherlands: Center for Substances and Integrated Risk Assessment.

WILLANDER, M., NUR, O., LOZOVIK, Y. E., AL-HILLI, S. M., CHIRAGWANDI, Z., HU, Q. H., ZHAO, Q. X. & KLASON, P. 2005. Solid and soft nanostructured materials: Fundamentals and applications. *Microelectronics Journal,* 36**,** 940-949.

WIOGO, H. T. R., LIM, M., BULMUS, V., GUTIÉRREZ, L., WOODWARD, R. C. & AMAL, R. 2012. Insight into Serum Protein Interactions with Functionalized Magnetic Nanoparticles in Biological Media. *Langmuir,* 28**,** 4346-4356.

WU, L., WIESMANN, H., MOODENBAUGH, A., KLIE, R., ZHU, Y., WELCH, D. & SUENAGA, M. 2004. Oxidation state and lattice expansion of CeO2-x nanoparticles as a function of particle size. *Physical Review B,* 69.

WU, N.-C., SHI, E.-W., ZHENG, Y.-Q. & LI, W.-J. 2002. Effect of pH of Medium on Hydrothermal Synthesis of Nanocrystalline Cerium(IV) Oxide Powders. *Journal of the American Ceramic Society,* 85**,** 2462-2468.

XIA, T., KOVOCHICH, M., LIONG, M., MÄDLER, L., GILBERT, B., SHI, H., YEH, J. I., ZINK, J. I. & NEL, A. E. 2008a. Comparison of the mechanism of toxicity of zinc oxide and cerium oxide nanoparticles based on dissolution and oxidative stress properties. *ACS nano,* 2**,** 2121-2134.

XIA, T., KOVOCHICH, M., LIONG, M., ZINK, J. I. & NEL, A. E. 2008b. Cationic Polystyrene Nanosphere Toxicity Depends on Cell-Specific Endocytic and Mitochondrial Injury Pathways. *ACS Nano,* 2**,** 85-96.

XU, L.-C. & SIEDLECKI, C. A. 2007. Effects of surface wettability and contact time on protein adhesion to biomaterial surfaces. *Biomaterials,* 28**,** 3273-3283.

XUE, Y., LUAN, Q., YANG, D., YAO, X. & ZHOU, K. 2011. Direct Evidence for Hydroxyl Radical Scavenging Activity of Cerium Oxide Nanoparticles. *The Journal of Physical Chemistry C,* 115**,** 4433-4438.

YAKOVLEV, S., BALSARA, N. P. & DOWNING, K. H. 2012. Limits of spatial and compositional resolution of electron energy loss spectroscopy of soft materials. *Ultramicroscopy,* 116**,** 39-46.

YANG, G., MÖBUS, G. & HAND, R. J. 2006. Cerium and boron chemistry in doped borosilicate glasses examined by EELS. *Micron,* 37**,** 433-441.

YIN, L., WANG, Y., PANG, G., KOLTYPIN, Y. & GEDANKEN, A. 2002. Sonochemical Synthesis of Cerium Oxide Nanoparticles—Effect of Additives and Quantum Size Effect. *Journal of Colloid and Interface Science,* 246**,** 78-84.

YOKEL, R. A., FLORENCE, R. L., UNRINE, J. M., TSENG, M. T., GRAHAM, U. M., WU, P., GRULKE, E. A., SULTANA, R., HARDAS, S. S. & BUTTERFIELD, D. A. 2009. Biodistribution and oxidative stress effects of a systemically-introduced commercial ceria engineered nanomaterial. *Nanotoxicology,* 3**,** 234-248.

ZASOSKI, R. J. 2008. Zeta potential. *In:* CHESWORTH, W. (ed.) *Encyclopedia of Soil Science.* Springer Netherlands.

ZHANG, D., FU, H., SHI, L., FANG, J. & LI, Q. 2007. Carbon nanotube assisted synthesis of CeO2 nanotubes. *Journal of Solid State Chemistry,* 180**,** 654-660.

ZHANG, D. F., H.; SHI, L.; PAN, C.; LI, Q.; CHU, Y. AND YU, W. 2007. Synthesis of CeO2 Nanorods via Ultrasonication Assisted by Polyethylene Glycol. *Inorganic chemistry,* 46**,** 2446-2451.

ZHANG, F., WANG, P., KOBERSTEIN, J., KHALID, S. & CHAN, S.-W. 2004. Cerium oxidation state in ceria nanoparticles studied with X-ray photoelectron spectroscopy and absorption near edge spectroscopy. *Surface Science,* 563**,** 74-82.

ZHANG, H., HE, X., ZHANG, Z., ZHANG, P., LI, Y., MA, Y., KUANG, Y., ZHAO, Y. & CHAI, Z. 2011a. Nano-CeO2 exhibits adverse effects at environmental relevant concentrations. *Environ Sci Technol,* 45**,** 3725-30.

ZHANG, J., NAKA, T., OHARA, S., KANEKO, K., TREVETHAN, T., SHLUGER, A. & ADSCHIRI, T. 2011b. Surface ligand assisted valence change in ceria nanocrystals. *Physical Review B,* 84.

ZHANG, X., BAI, R. & TONG, Y. W. 2006. Selective adsorption behaviors of proteins on polypyrrole-based adsorbents. *Separation and Purification Technology,* 52**,** 161-169.

ZHANG, Y.-W., SI, R., LIAO, C.-S., YAN, C.-H., XIAO, C.-X. & KOU, Y. 2003. Facile Alcohothermal Synthesis, Size-Dependent Ultraviolet Absorption, and Enhanced CO Conversion Activity of Ceria Nanocrystals. *The Journal of Physical Chemistry B,* 107**,** 10159-10167.

ZHOU, F., NI, X., ZHANG, Y. & ZHENG, H. 2007. Size-controlled synthesis and electrochemical characterization of spherical CeO2 crystallites. *Journal of Colloid and Interface Science,* 307**,** 135-138.

APPENDIX A: XPS survey spectra of different nanoceria samples: Nanocubes (C1-C3), Nanosphere (S1-S5 and S7) and Nanorod (R1)

C1

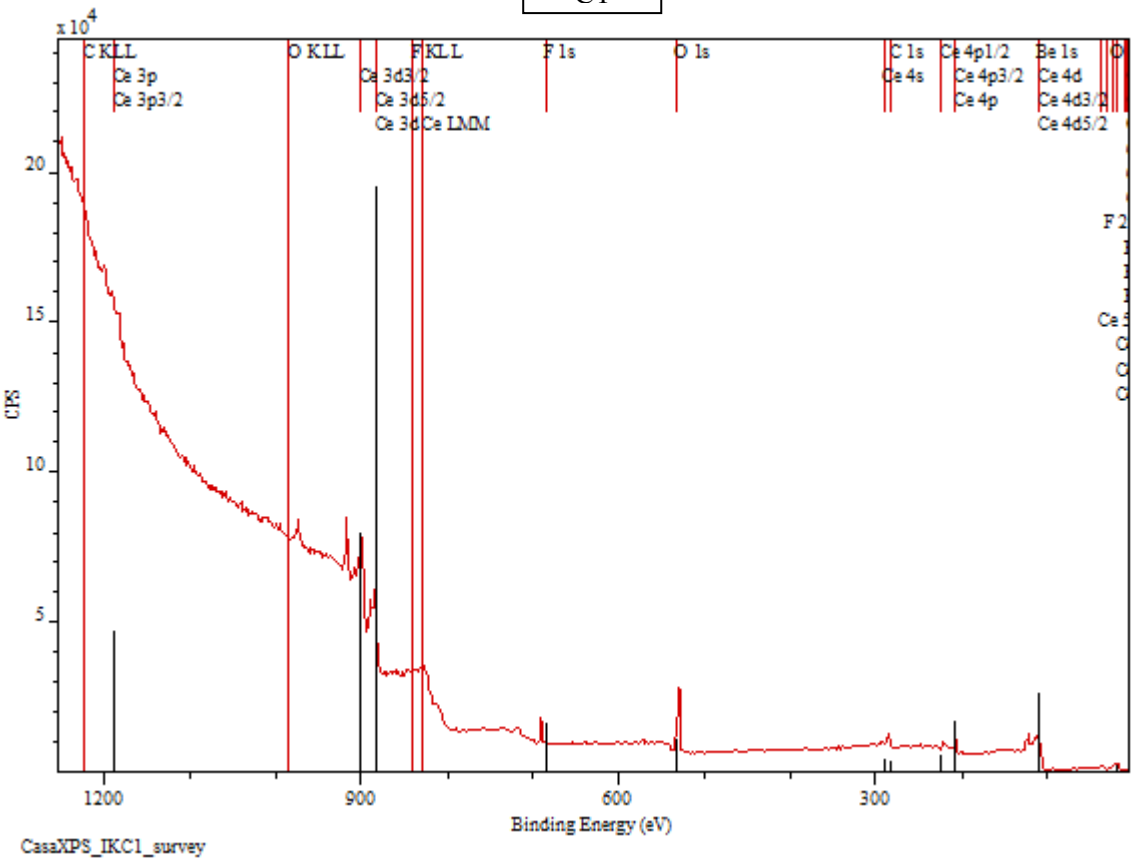

C2

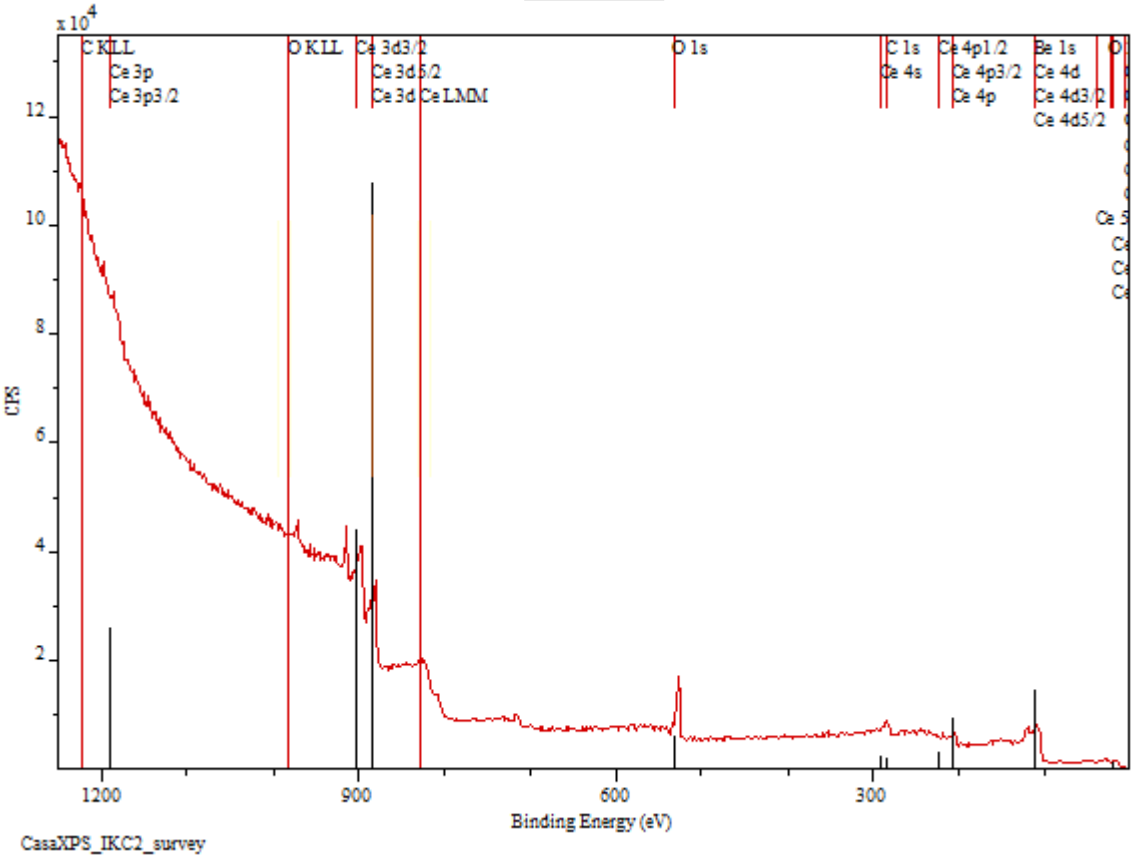

CasaXPS_IKC2_survey

C3

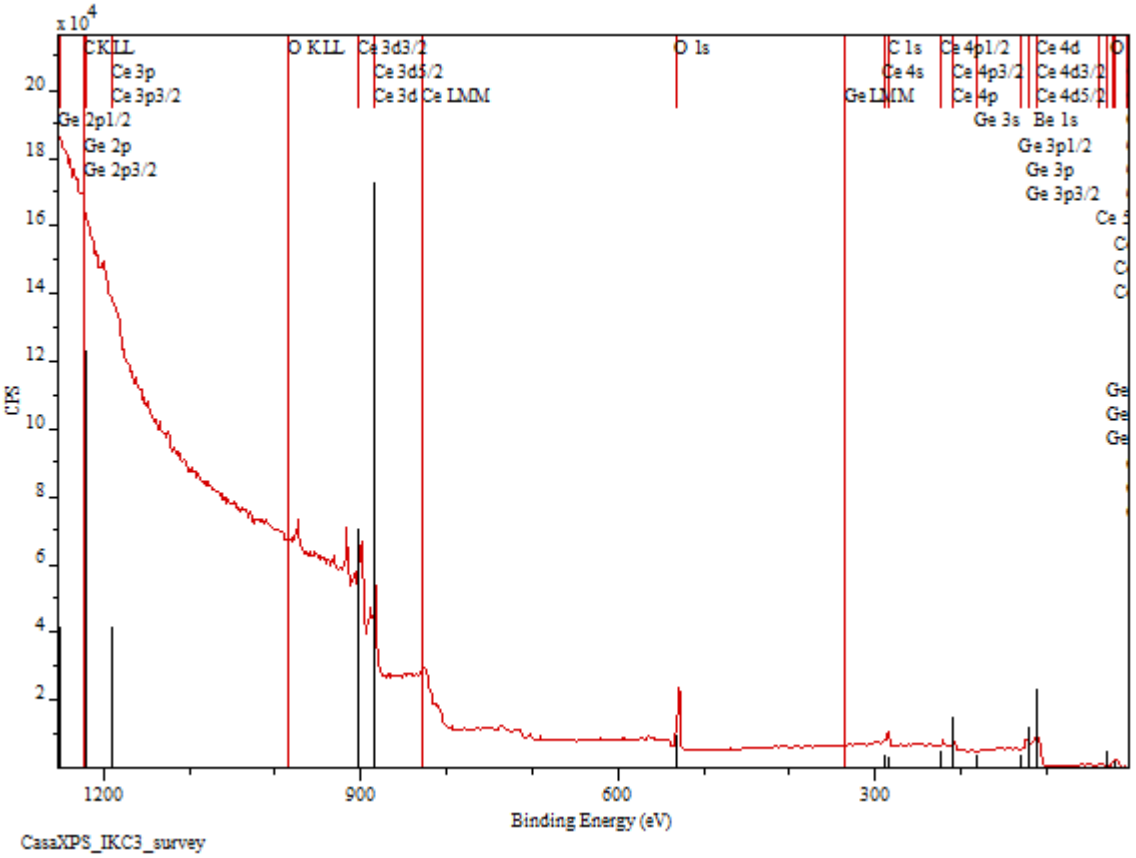

CasaXPS_IKC3_survey

S1

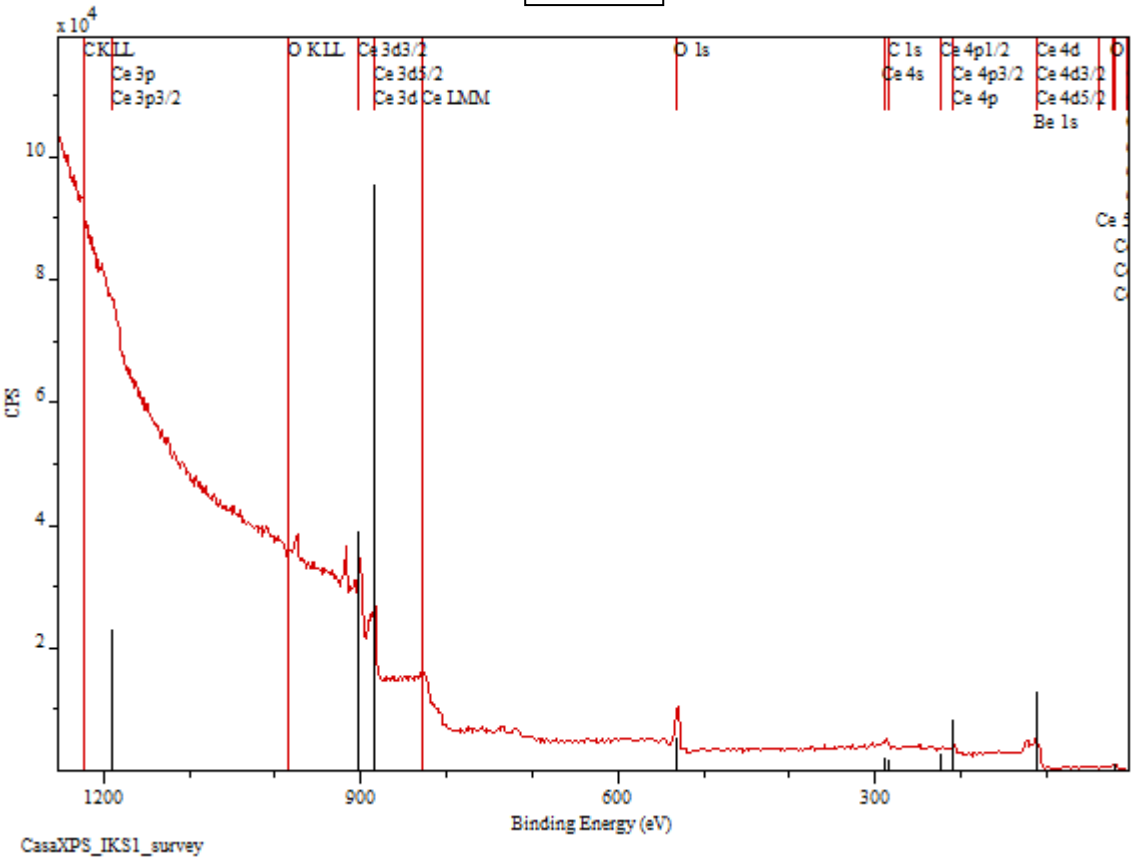
x 10^4
C KLL
Ce 3p
Ce 3p3/2
O KLL
Ce 3d3/2
Ce 3d5/2
Ce 3d
Ce LMM
O 1s
C 1s
Ce 4s
Ce 4p1/2
Ce 4p3/2
Ce 4p
Ce 4d
Ce 4d3/2
Ce 4d5/2
Be 1s
CPS
Binding Energy (eV)
CasaXPS_IKS1_survey

S2

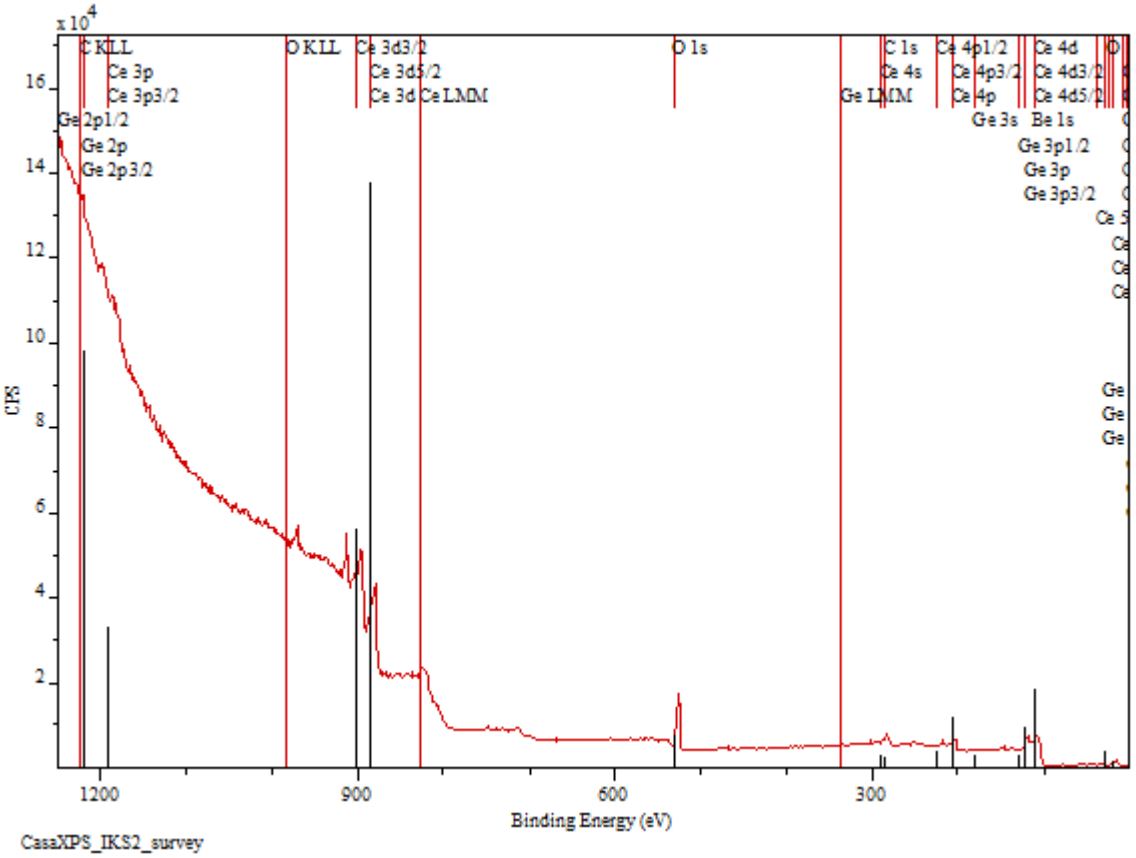
x 10^4
C KLL
Ce 3p
Ce 3p3/2
O KLL
Ce 3d3/2
Ce 3d5/2
Ce 3d
Ce LMM
O 1s
C 1s
Ce 4s
Ge LMM
Ce 4p1/2
Ce 4p3/2
Ce 4p
Ce 4d
Ce 4d3/2
Ce 4d5/2
Ge 3s
Be 1s
Ge 3p1/2
Ge 3p
Ge 3p3/2
Ge 2p1/2
Ge 2p
Ge 2p3/2
CPS
Binding Energy (eV)
CasaXPS_IKS2_survey

S3

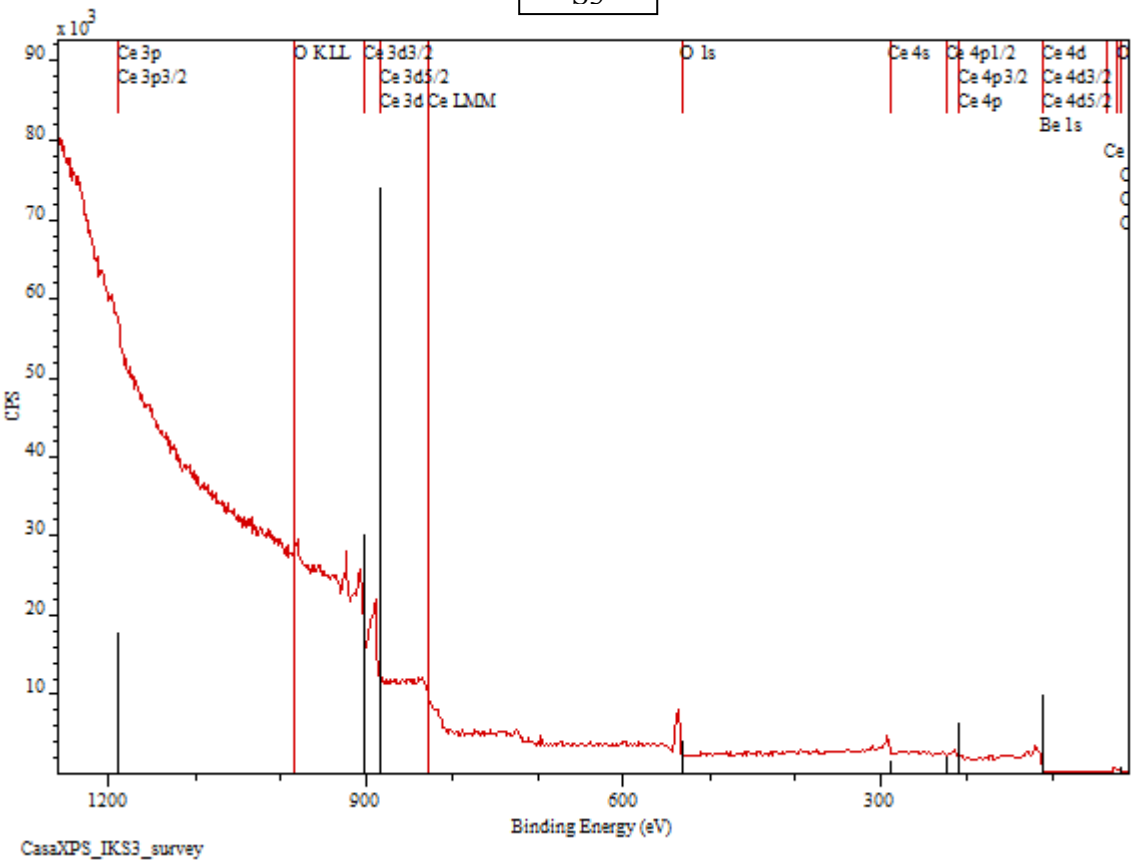
x 10^3
CPS
Ce 3p
Ce 3p3/2
O KLL
Ce 3d3/2
Ce 3d5/2
Ce 3d Ce LMM
O 1s
Ce 4s
Ce 4p1/2
Ce 4p3/2
Ce 4p
Ce 4d
Ce 4d3/2
Ce 4d5/2
Be 1s
Binding Energy (eV)
CasaXPS_IKS3_survey

S4

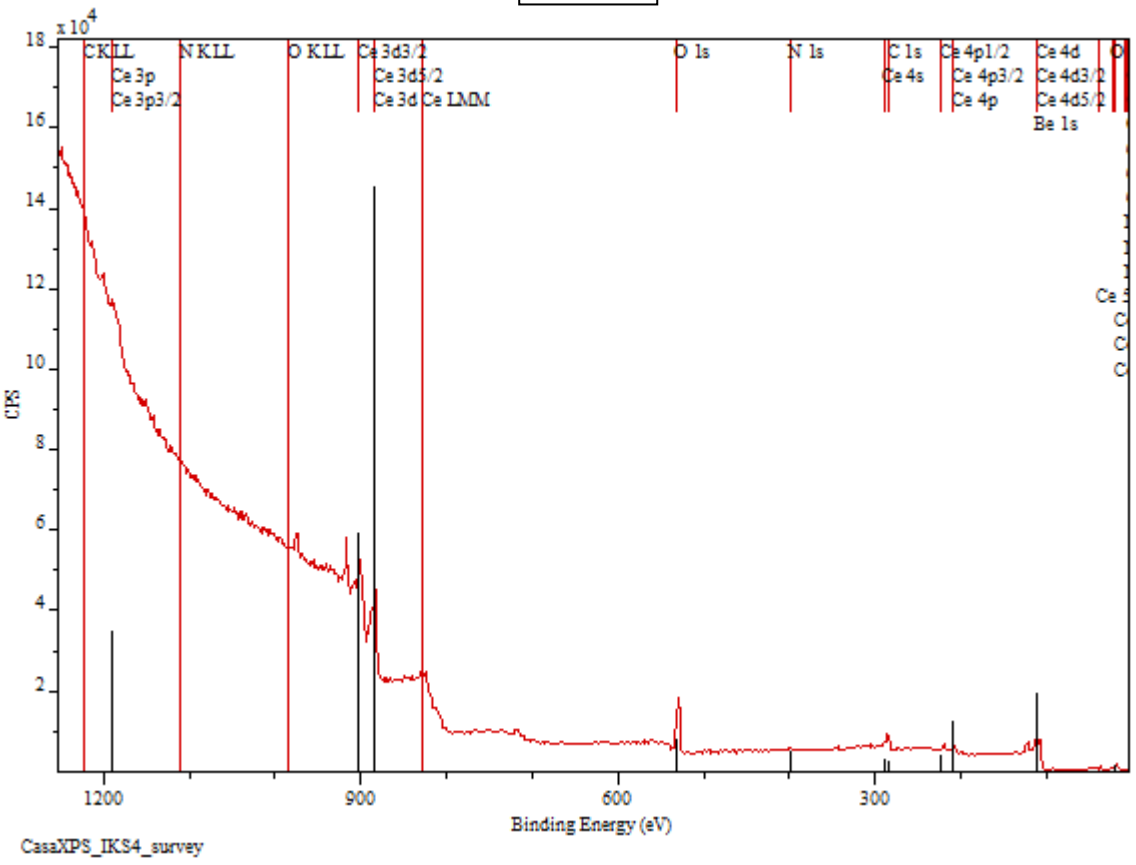
x 10^4
CPS
C KLL
Ce 3p
Ce 3p3/2
N KLL
O KLL
Ce 3d3/2
Ce 3d5/2
Ce 3d Ce LMM
O 1s
N 1s
C 1s
Ce 4s
Ce 4p1/2
Ce 4p3/2
Ce 4p
Ce 4d
Ce 4d3/2
Ce 4d5/2
Be 1s
Binding Energy (eV)
CasaXPS_IKS4_survey

S5

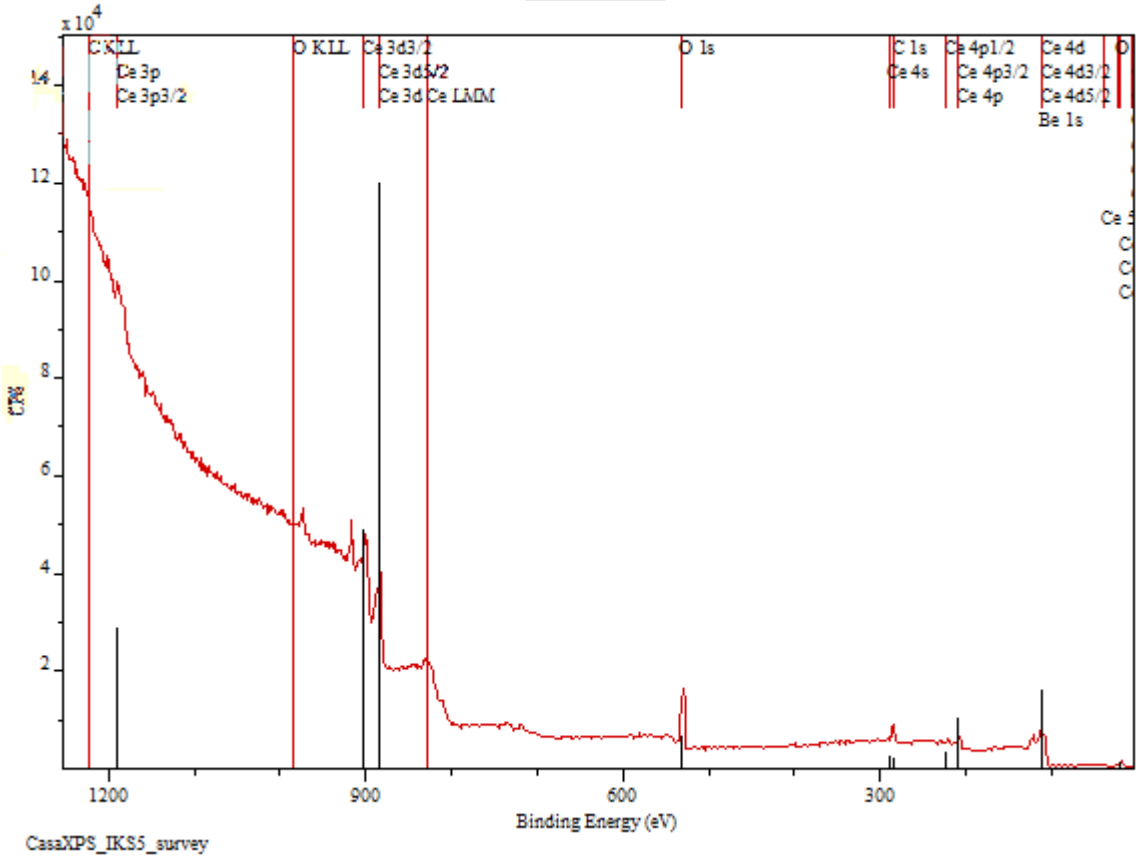

CasaXPS_IKS5_survey

S7

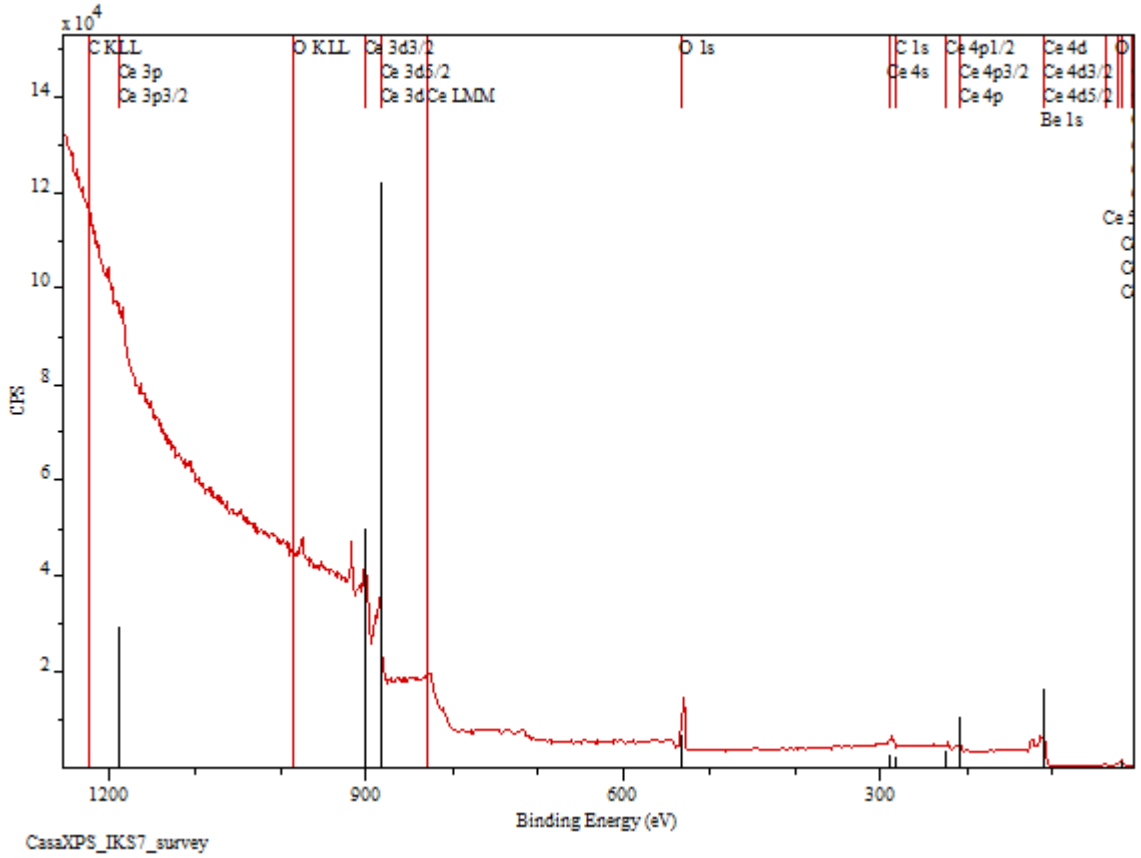

CasaXPS_IKS7_survey

R1

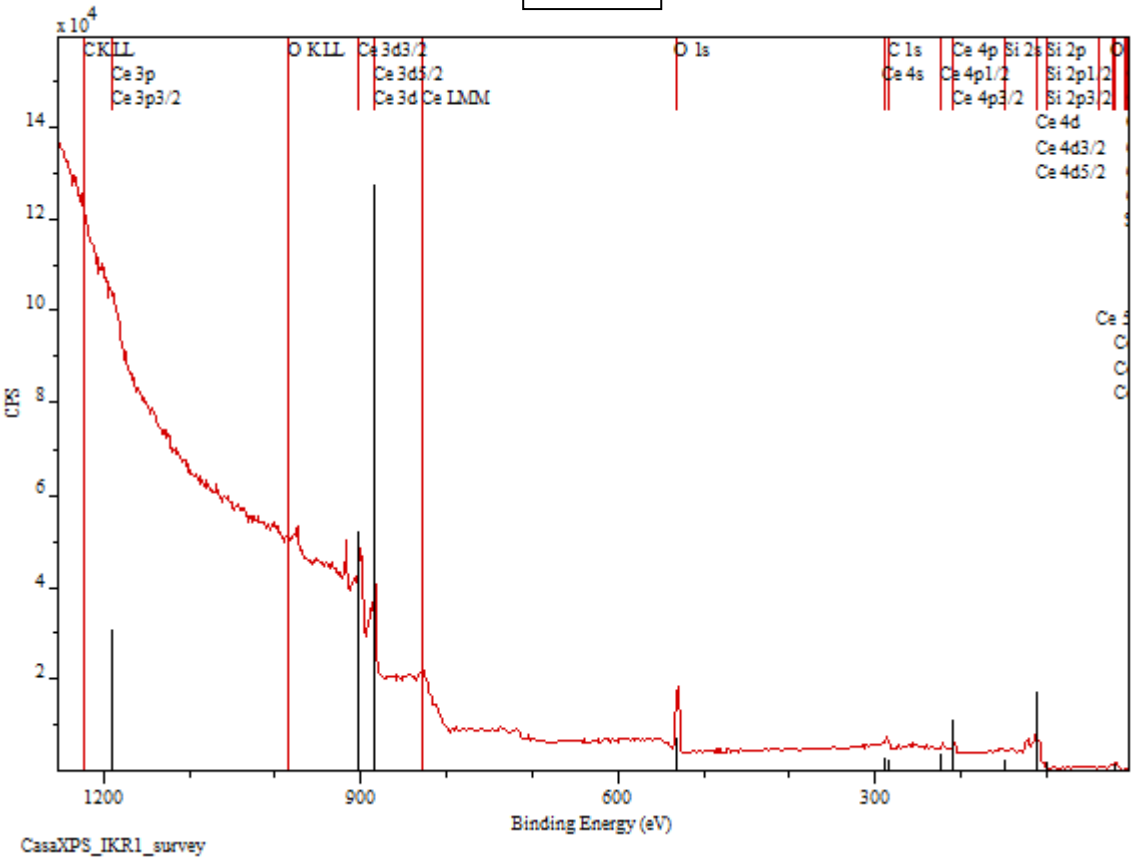
x 10^4
C KLL
Ce 3p
Ce 3p3/2
O KLL
Ce 3d3/2
Ce 3d5/2
Ce 3d
Ce LMM
O 1s
C 1s
Ce 4s
Ce 4p
Ce 4p1/2
Ce 4p3/2
Si 2s
Si 2p
Si 2p1/2
Si 2p3/2
Ce 4d
Ce 4d3/2
Ce 4d5/2
CPS
14
12
10
8
6
4
2
1200
900
600
300
Binding Energy (eV)
CasaXPS_IKR1_survey

APPENDIX B: EELS spectrum with weak signals

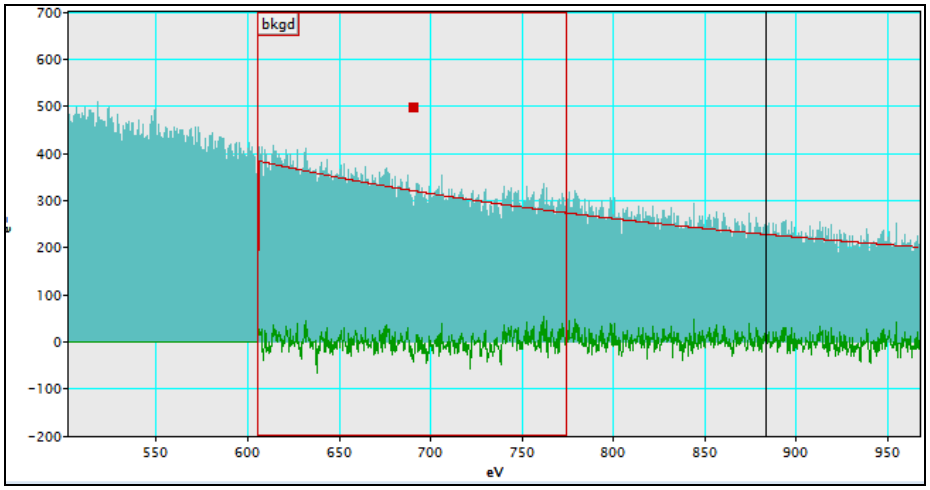

S3 Particle 2(A)

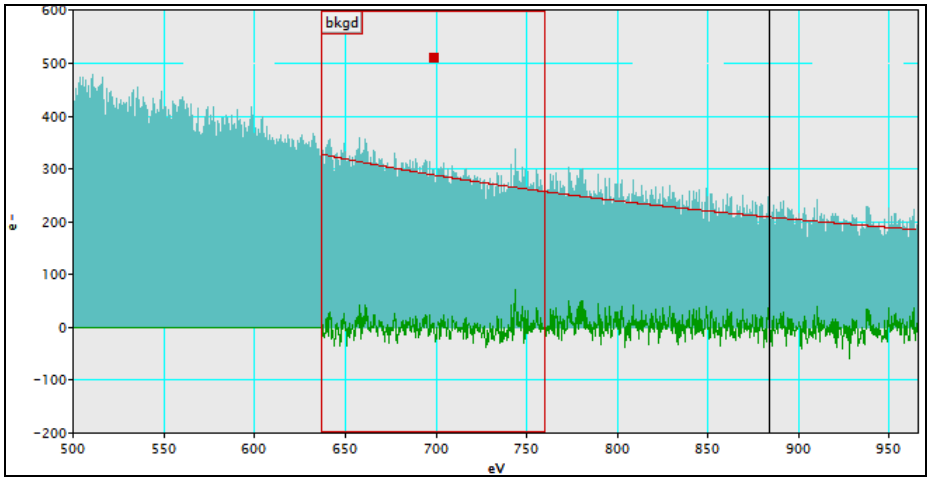

S3 Particle 2(C)

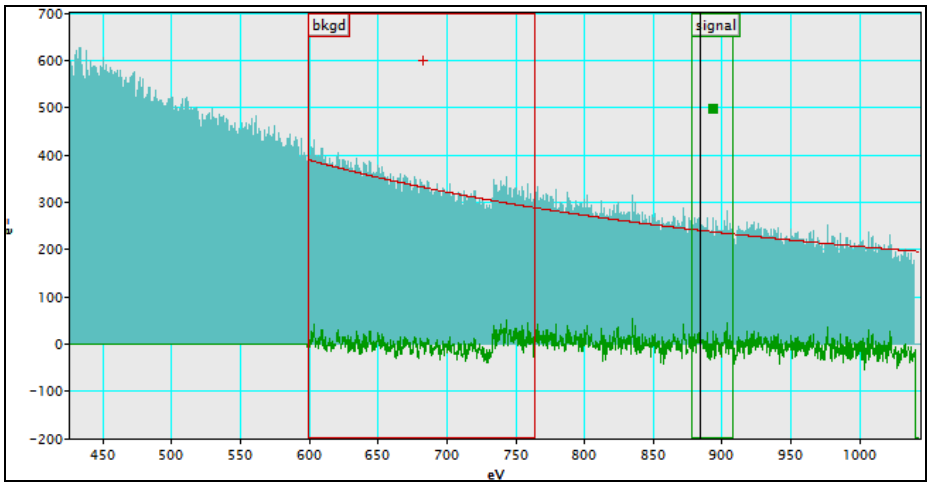

S3 Particle 5(A)

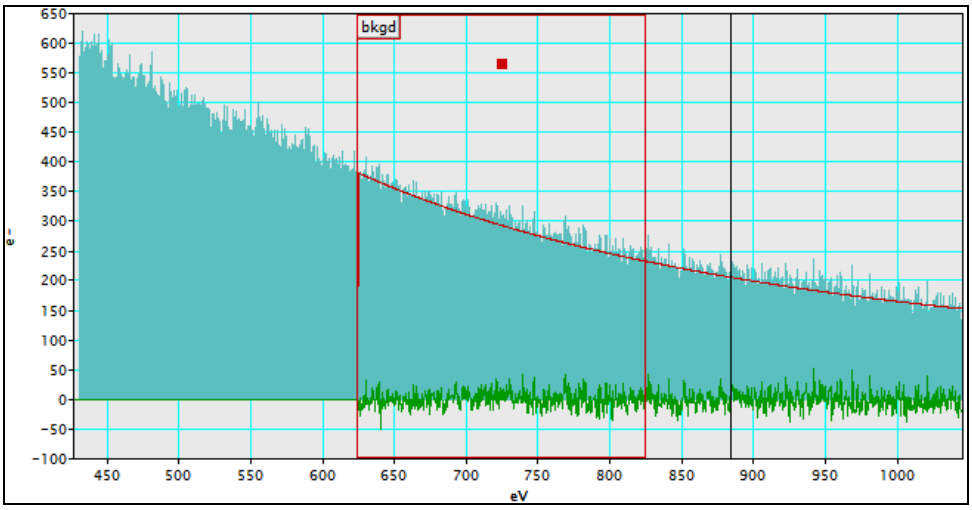

S3 Particle 5(C)

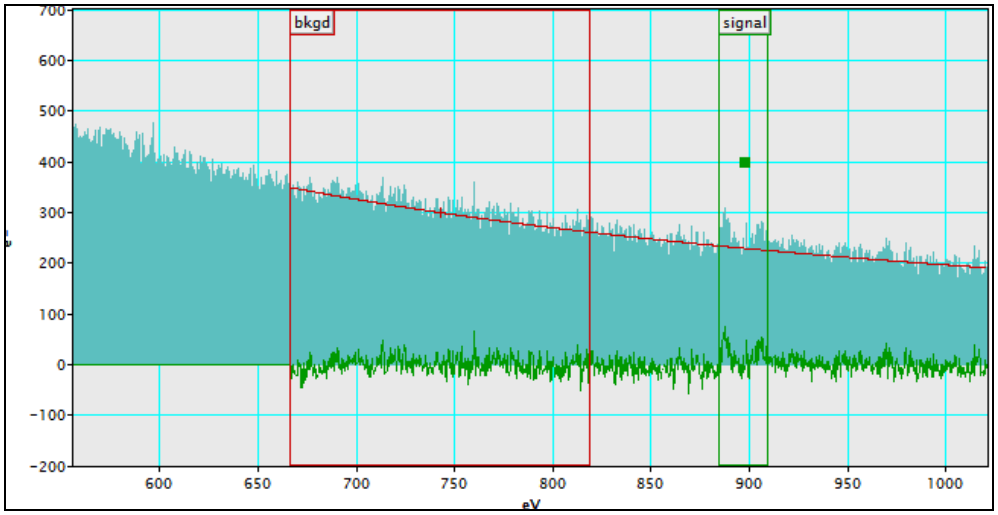

S3 Particle 7(A)

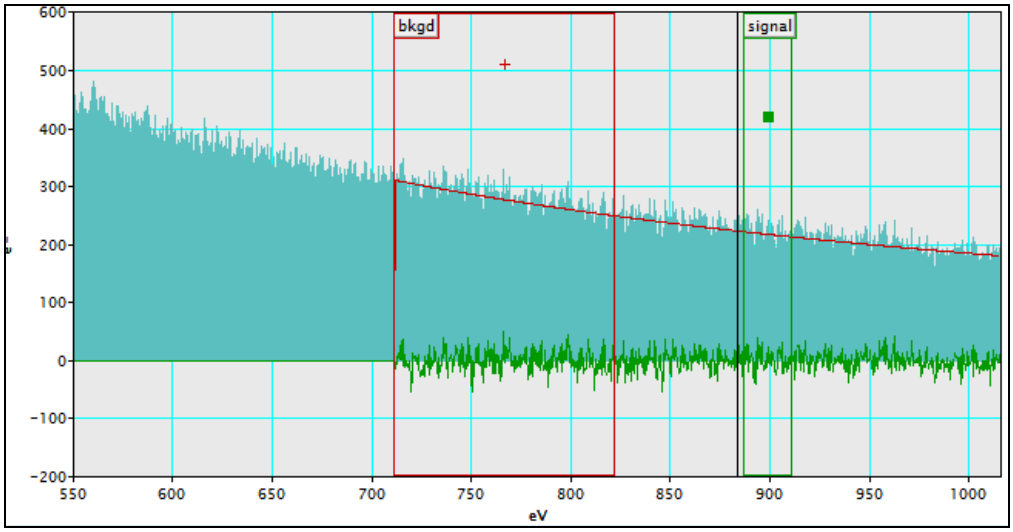

S3 Particle 7(C)

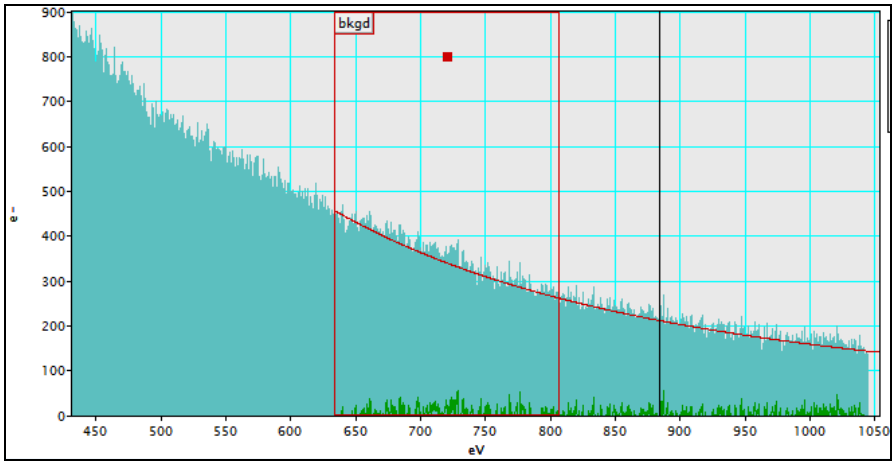

S6 Particle 1(C)

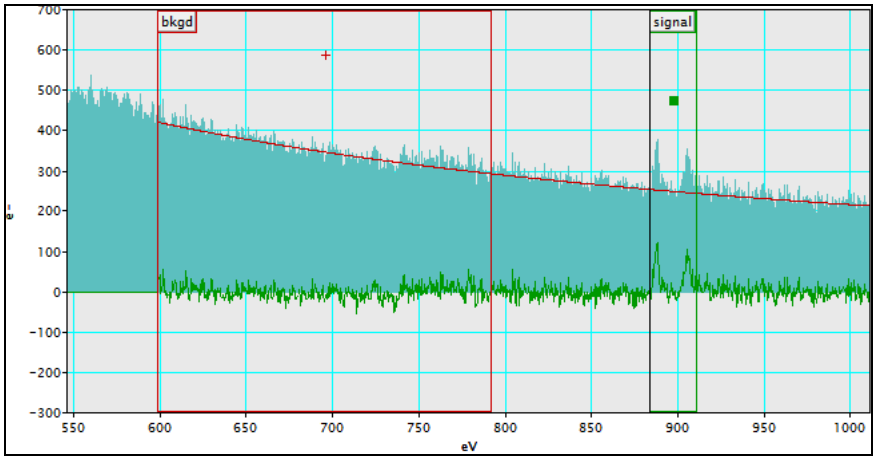

C4 Particle 3(A)

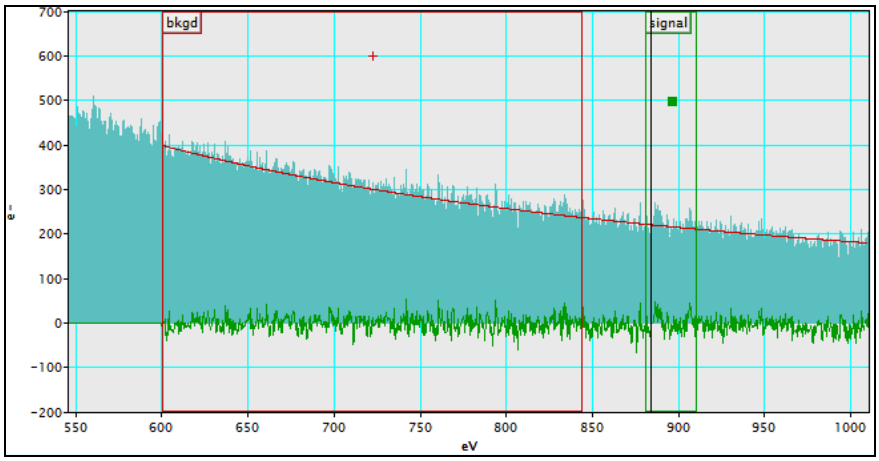

C4 Particle 3(B)

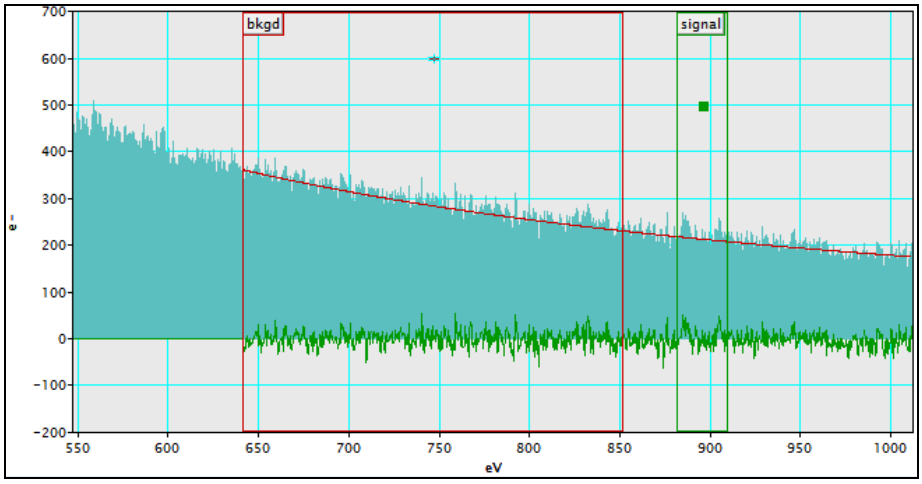

C4 Particle 3(C)

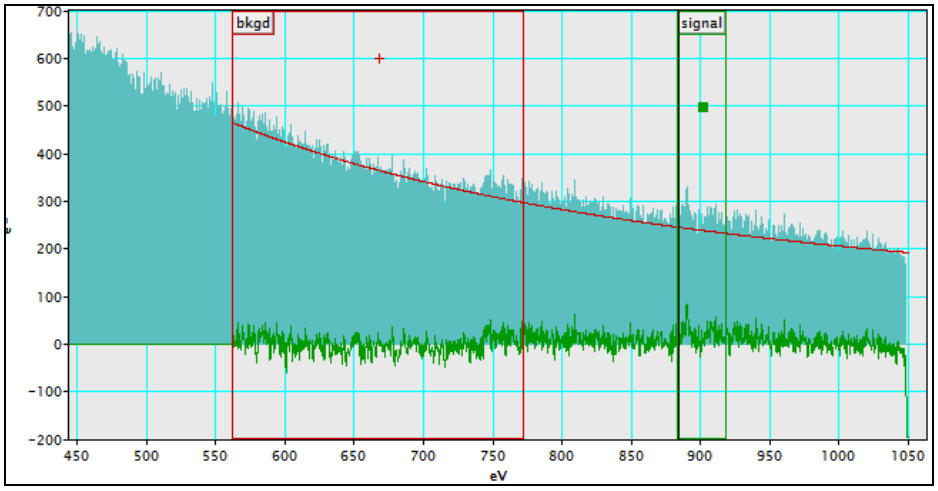

C4 Particle 4(A)

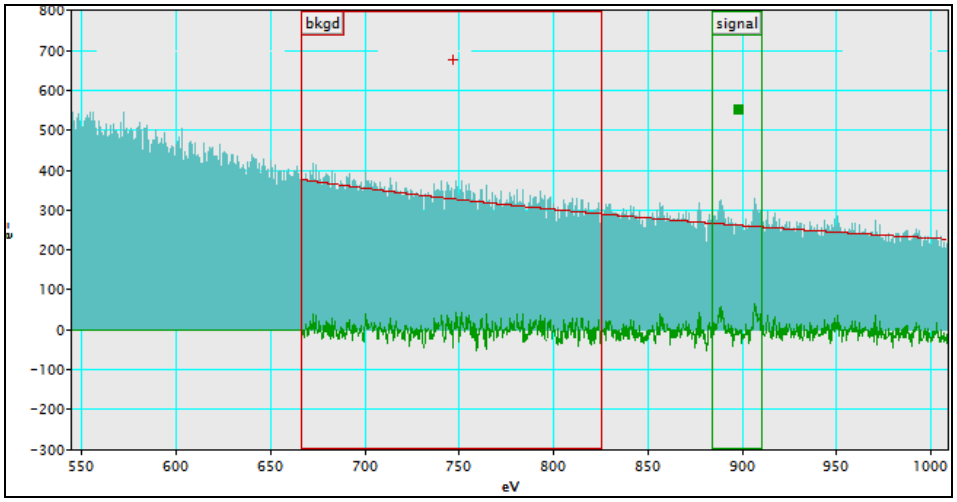

C4 Particle 4(B)

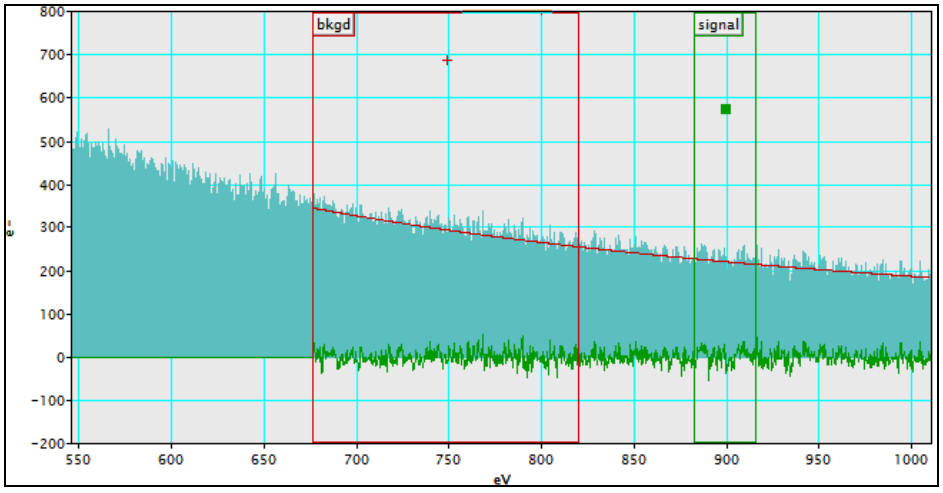

C4 Particle 4(C)

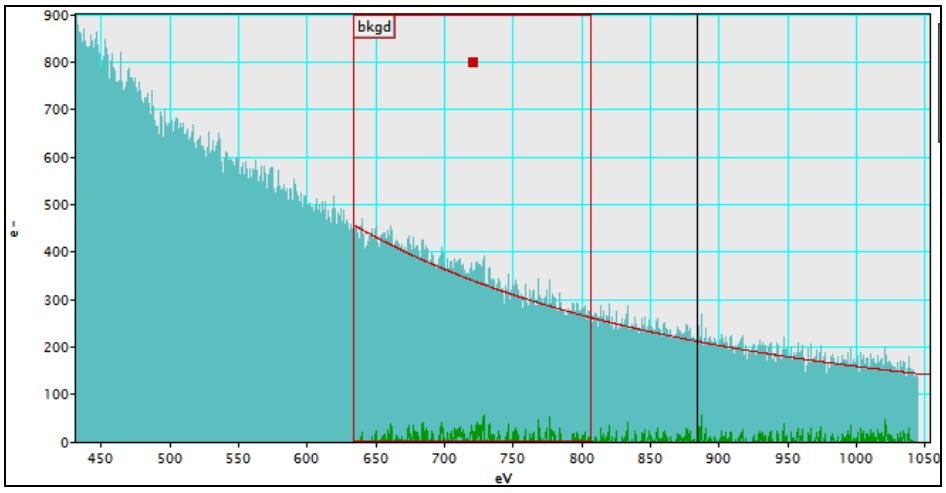

S6 Particle 1(C)

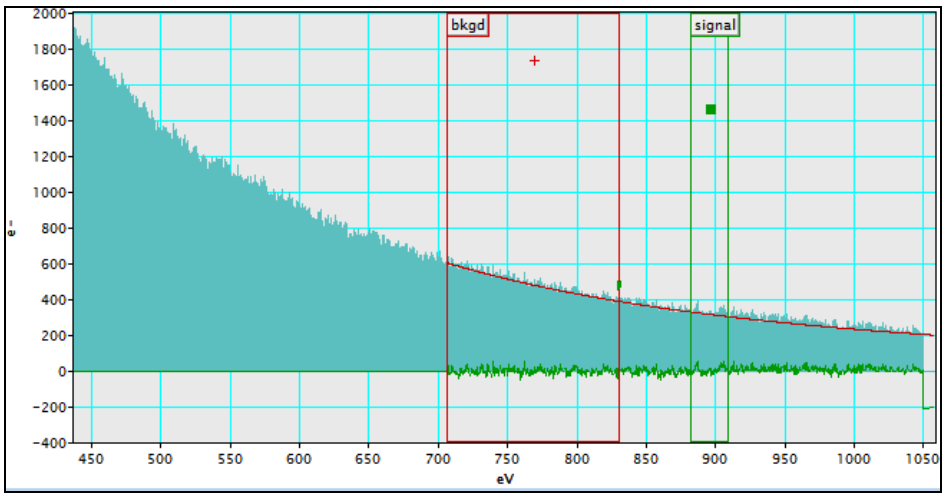

S6 Particle 7(C)

APPENDIX C: Shape and size quantification by imageJ

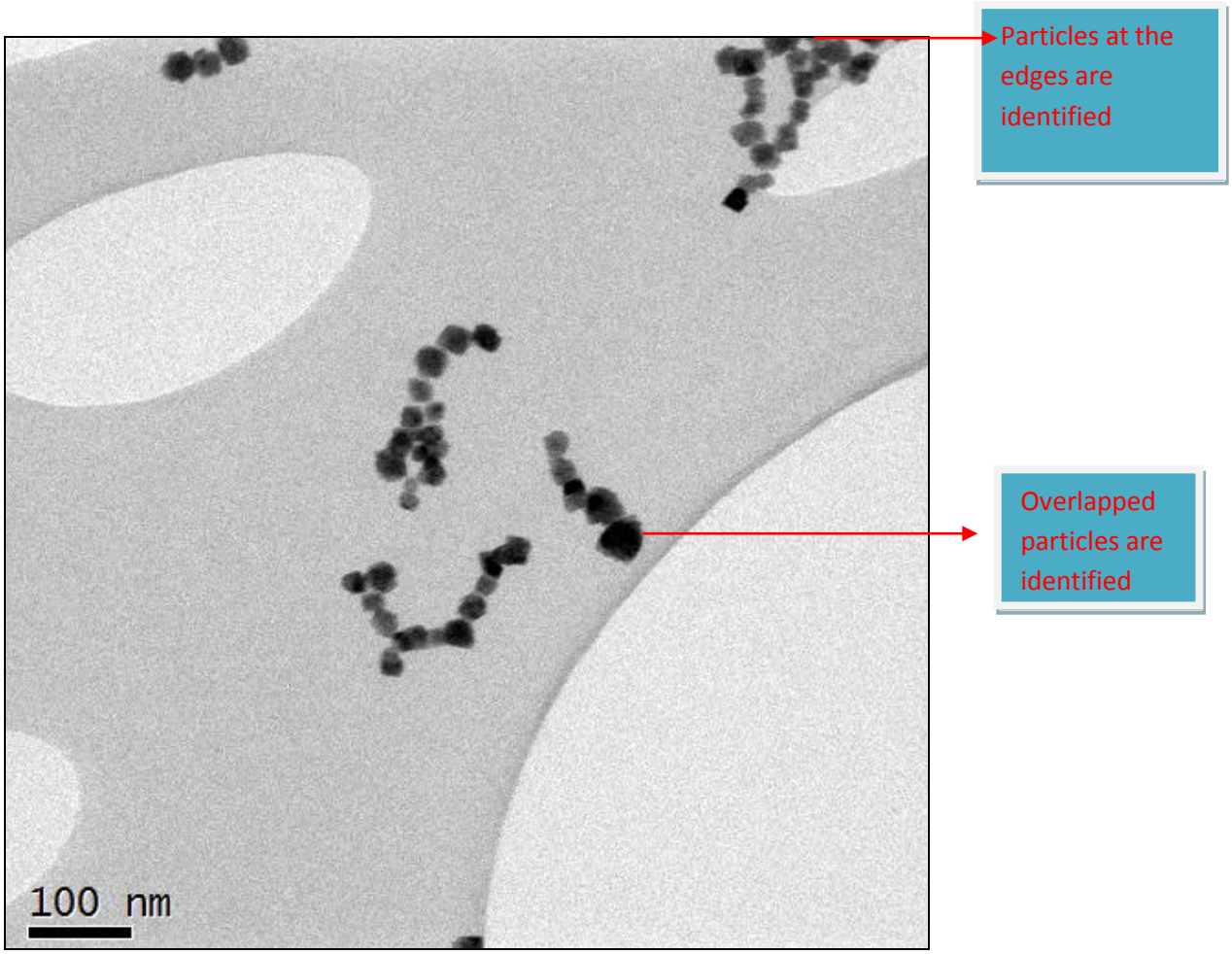

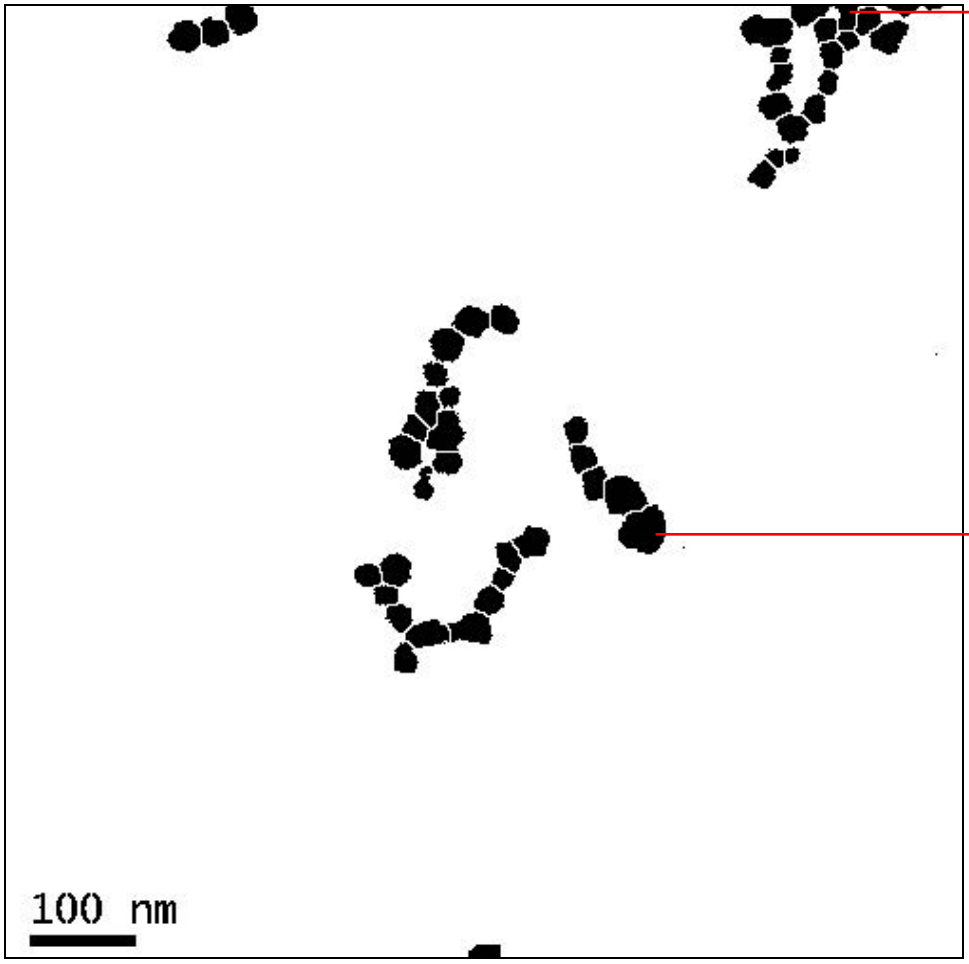
Particles at the edges were discarded
Overlapped particles are discarded
100 nm

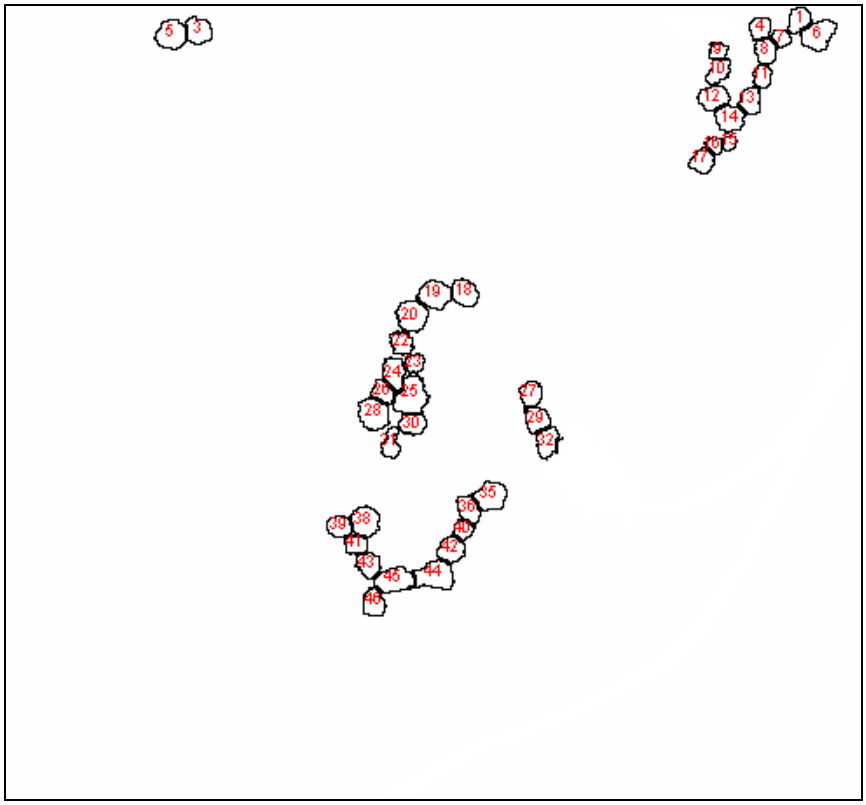

The diameters, areas, circularity, roundness values are then automatically calculated by imageJ

APPENDIX D: Beam damage during line scans in S5

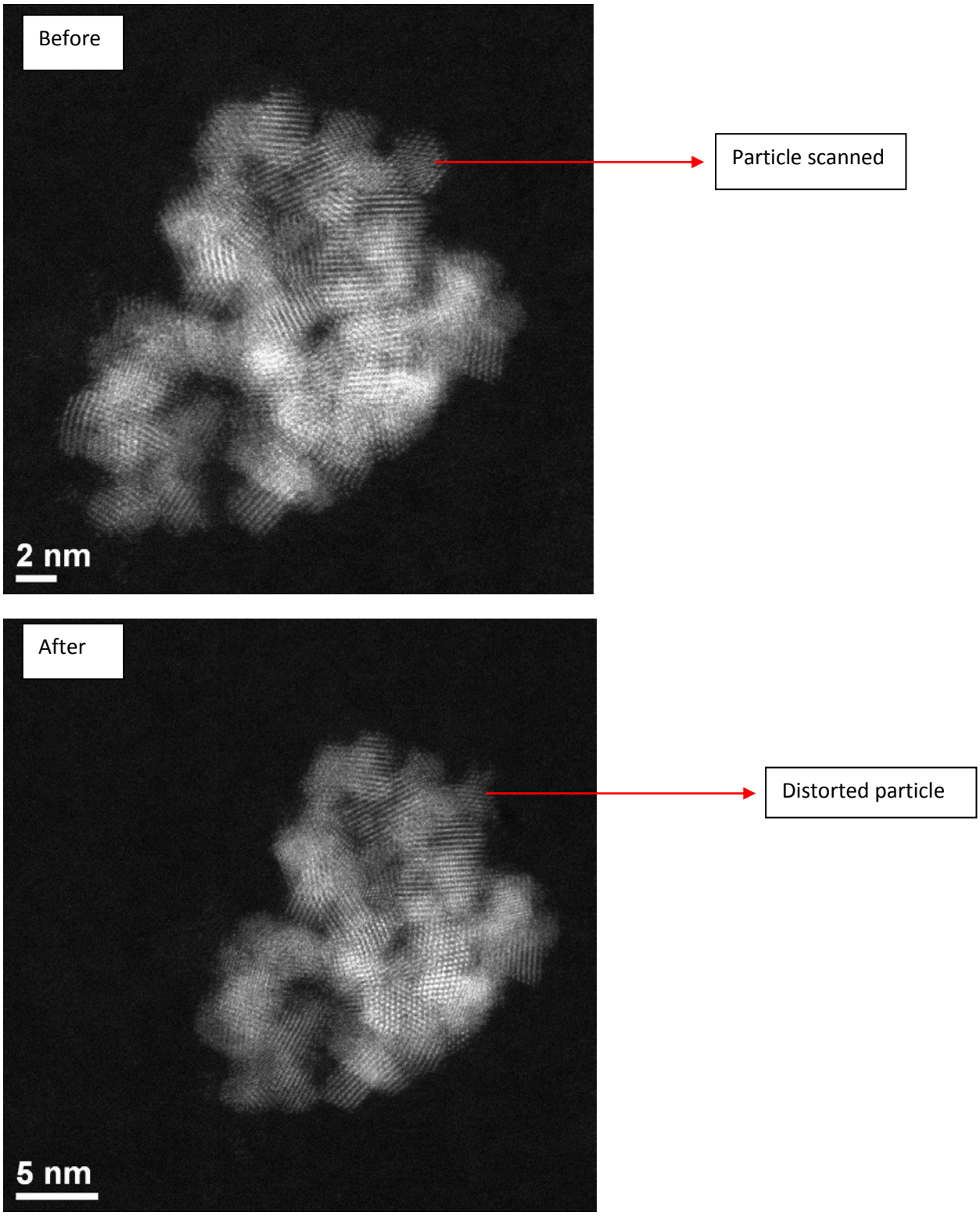

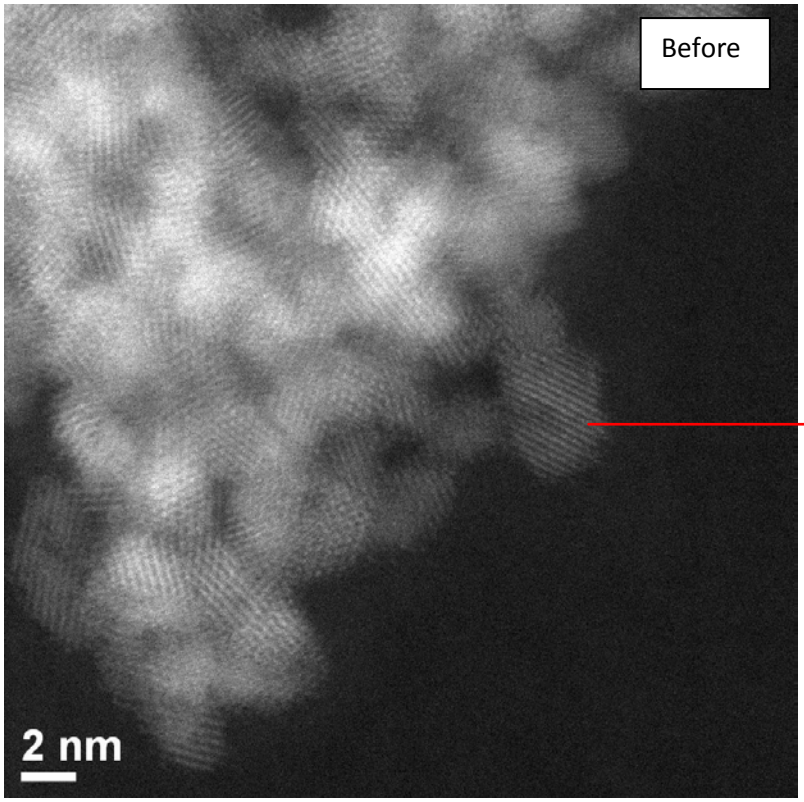
Before
Particle scanned
2 nm

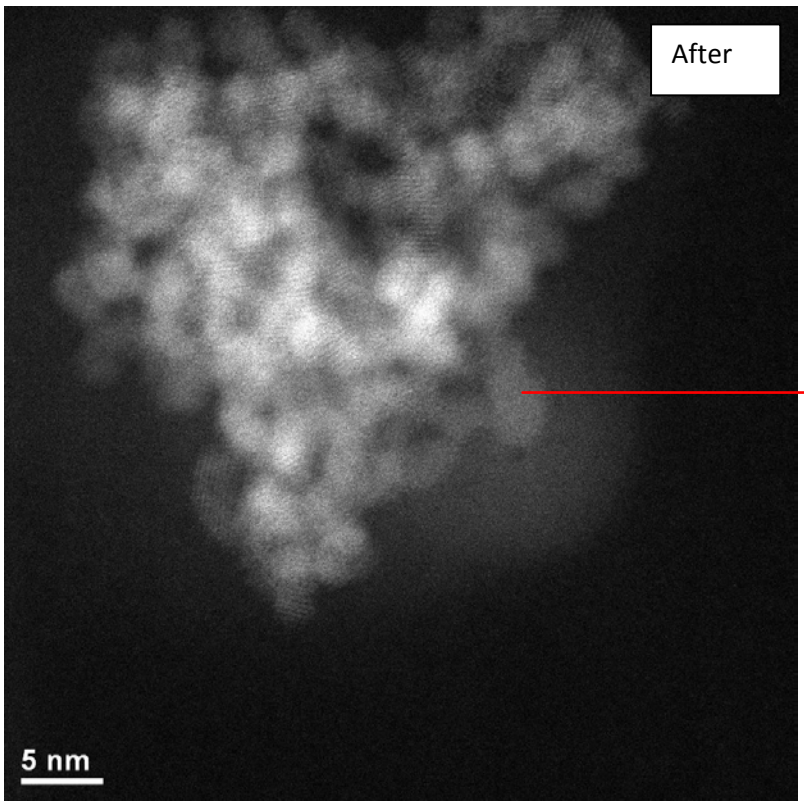
After
Distorted particle
5 nm

APPENDIX E: No beam damage observed during area scans in S5

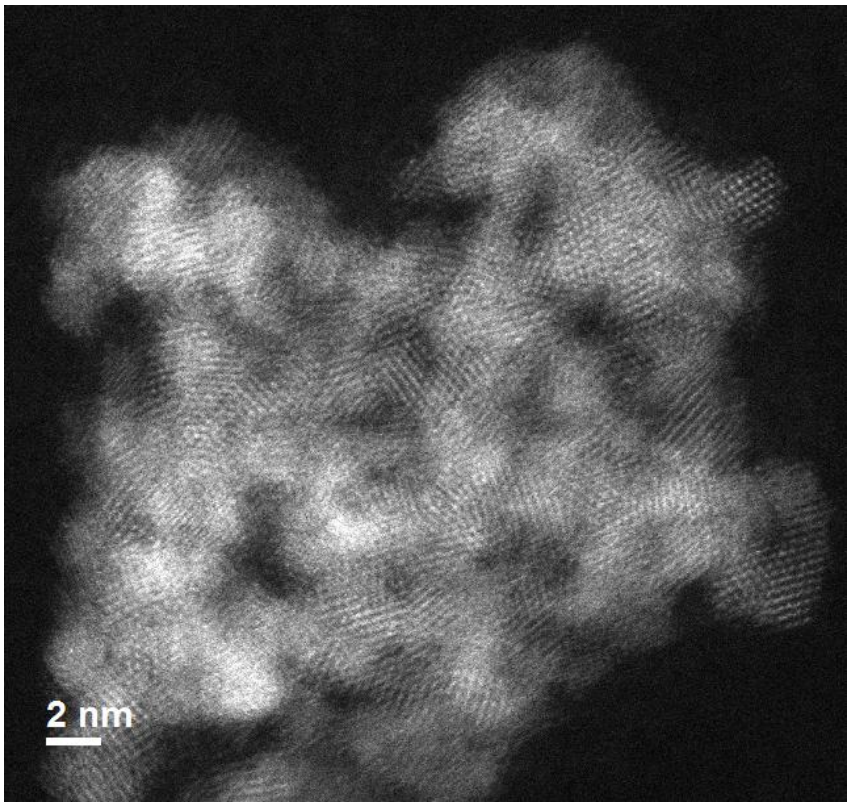

Area 1

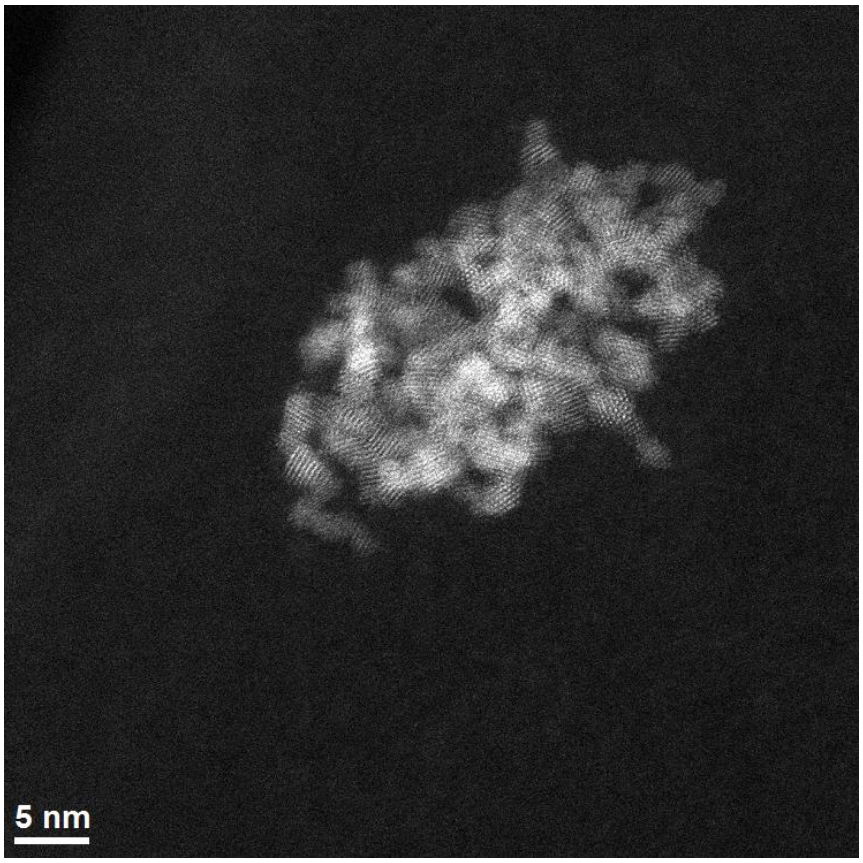

Area 2

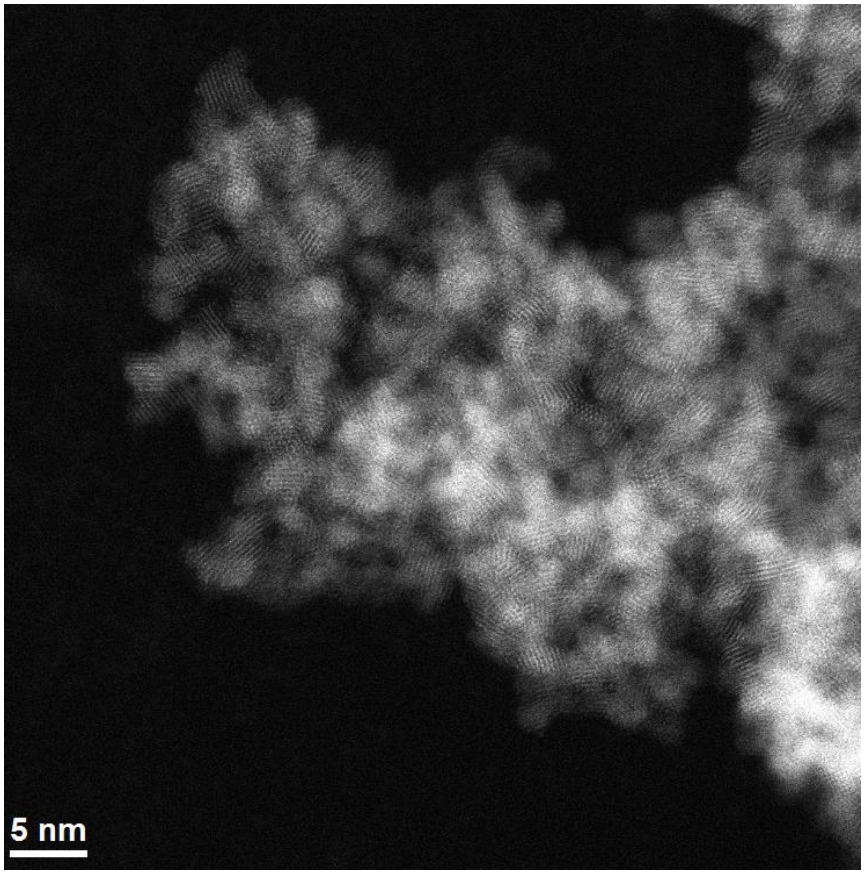

Area 3

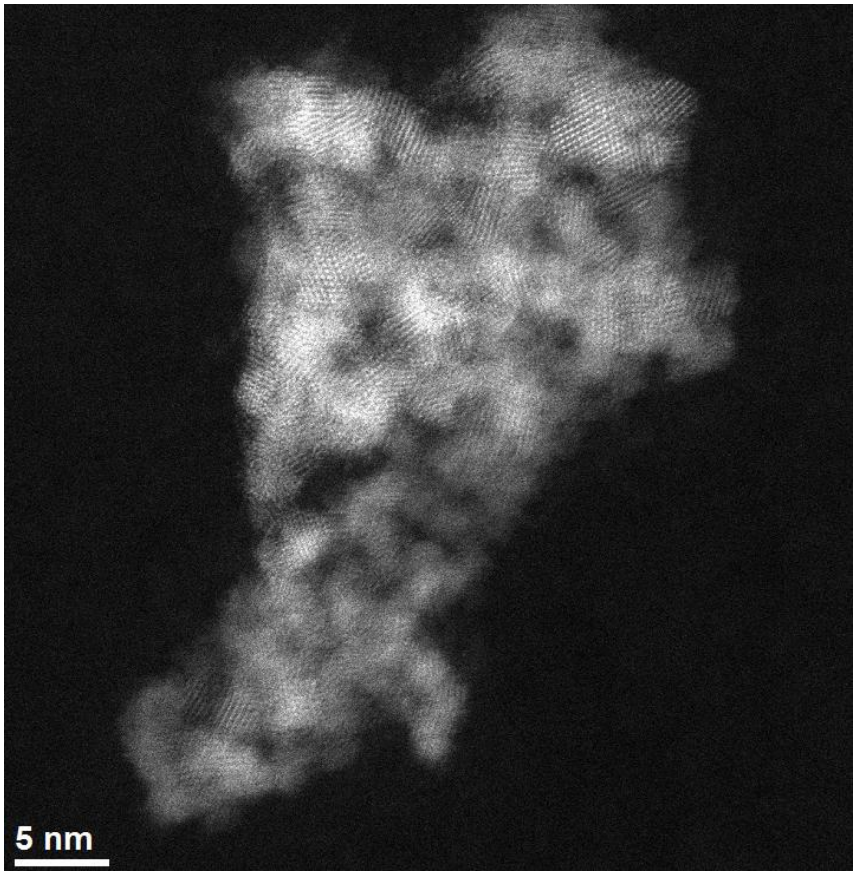

Area 4

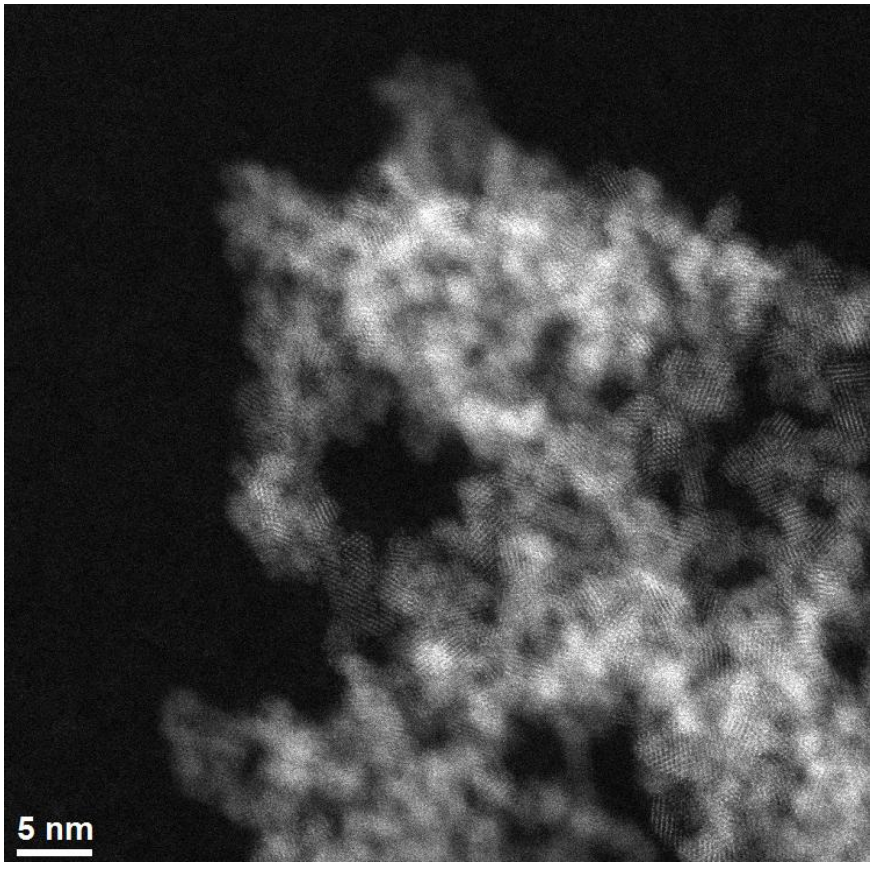

Area 5

APPENDIX F: Publications and conference presentations during this period

Publications

1. Collin, B., Auffan, M., Johnson, A.C., **Kaur, I**., Keller, A.A., Lazareva, A., Lead, J.R., Ma, X., Merrifield, R.C., Svendson, C., White, J.C. & Unrine, J.M. 2014. Environmental release, fate and ecotoxicological effects of manufactured ceria nanomaterials. *Environ. Sci.: Nano*., *1, 533-548*

Conference presentations

1. **I. Kaur**, J.R. Lead and E. Valsami-Jones, –Understanding the surface chemistry of nanoceria using STEM-EELS and XPS", 9th ICEENN, South Carolina, USA, September 2014 (Oral presentation).
2. **I. Kaur,** J.R Lead and E. Valsami-Jones, –Synthesis and characterisation of ceria nanoparticles using various microscopic and spectroscopic techniques", FABLE steering group meeting December, 2013 (Oral presentation).
3. **I. Kaur**, J.R Lead and E. Valsami-Jones, –Quantifying Ceria oxidation states using STEM-EELS and XPS", Workshop on nano-ceria, Sustainable Nanotechnology Organization (SNO), Santa Barbara, California, November 2013 (Oral presentation).
4. **I. Kaur**, J.R. Lead and E. Valsami-Jones, –Understanding the surface chemistry of nanoceria using STEM-EELS and XPS", Indoor and outdoor pollution annual review meeting, Solihull, UK, July 2014 (Poster).

5. **I. Kaur,** J.R Lead and E. Valsami-Jones, –Synthesis and characterisation of ceria nanocubes", Nanotechnology symposium 2013 organised by Royal Society of Chemistry, December 2013 (Poster).
6. **I. Kaur**, J.R Lead and E. Valsami-Jones, –Quantifying Ceria oxidation states using STEM-EELs and XPS", 2nd Sustainable Nanotechnology Organization conference (SNO), Santa Barbara, California, November 2013 (Poster).
7. **I. Kaur,** J.R Lead and E. Valsami-Jones, " Multi-method approach: Synthesis and characterisation of Cerium Oxide nanoparticles", United Kingdom Surface Analysis Forum (UKSAF) meeting, January 2013, Diamond light Source, Oxford, UK (Poster).
8. **I. Kaur,** J.R Lead and E. Valsami-Jones, –Understanding the surface chemistry of ceria nanorods using a multi-method approach", 7th International Conference on the Environmental Effects of Nanoparticles and Nanomaterials (ICEENN), 10-12 September 2012, Banff, Alberta, Canada (Poster).